TDFD
TÜRK DOĞA ve FEN DERGİSİ

TURKISH JOURNAL OF NATURE AND SCIENCE

TJNS
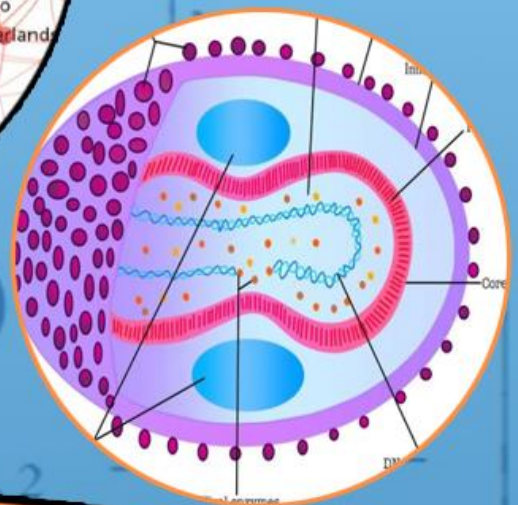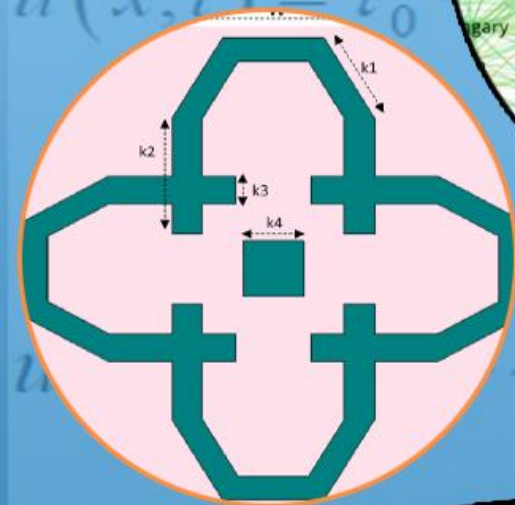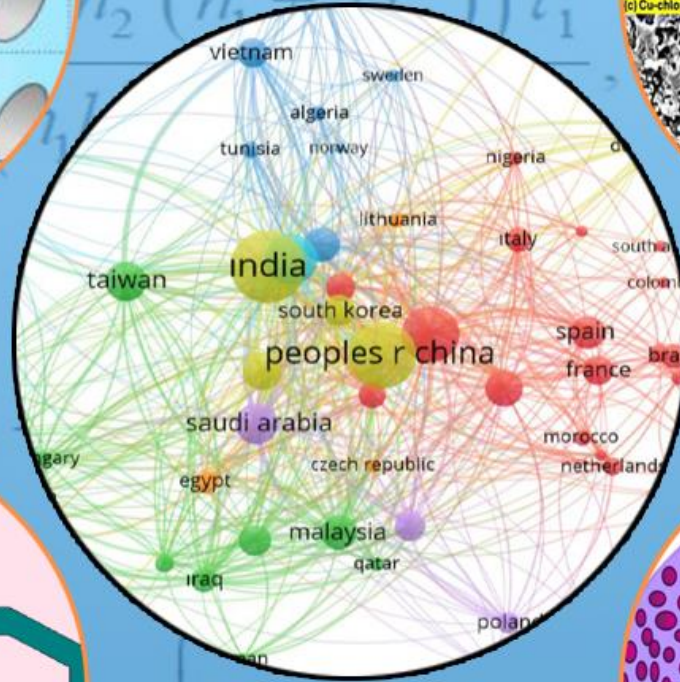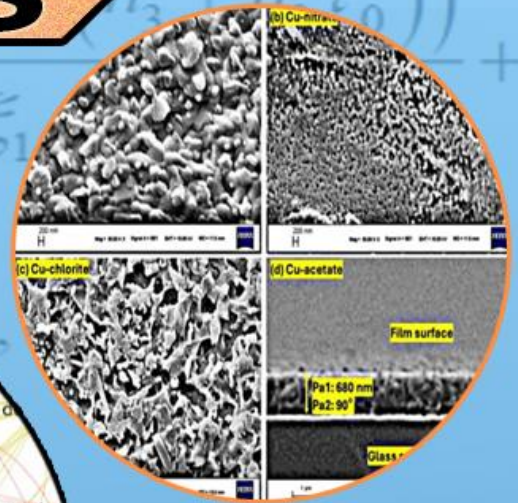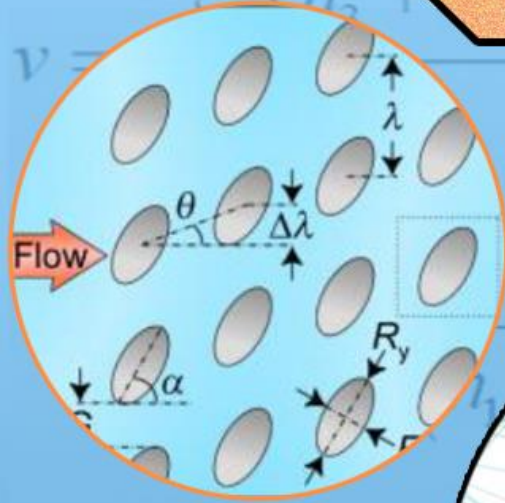
$$\tau_0 = \tau_0$$

$$-\xi \left(h_2 + \right)$$

$$v =$$

$$h_2^2 \left(h_1 h_2^2 + h_3 \right) \xi_1$$

$$h_2^2 \left(h_1 + 2\tau_1 \right) \tau_1$$

$$u(x,t) = \tau_0$$

$$2(\alpha_1 + \alpha_2)$$

$$\frac{\tau_1}{4}$$

TÜRK DOĞA VE FEN DERGİSİ

Amaç

Türk Doğa ve Fen Dergisi, Dergipark tarafından yayınlanan Bingöl Üniversitesi Fen Bilimleri Enstitüsüne ait ulusal ve hakemli bir dergidir. Türk Doğa ve Fen Dergisi, Türkiye ve dünyanın her yerinden gelen doğa ve fen bilimlerinin her alanında özgün, yayımlanmamış, yayımlanmak üzere başka yere gönderilmemiş makale, derleme ve sempozyum değerlendirmesi gibi çalışmaların bilim alemine sunulması amacıyla kurulmuştur.

Kapsam

Türk Doğa ve Fen Dergisinde Mühendislik, Ziraat, Veterinerlik, Fen ve Doğa Bilimleri alanlarından olmak üzere Türkçe ve İngilizce hazırlanmış orijinal makale, derleme ve sempozyum değerlendirmesi gibi çalışmalar yayımlanır. Türk Doğa ve Fen Dergisi sadece online sistemde yayınlanmakta olup ayrıca kağıt baskısı bulunmamaktadır.

Merhaba…

Türk Doğa ve Fen Dergisi, Dergipark tarafından yayınlanmakta olup Bingöl Üniversitesi Fen Bilimleri Enstitüsüne aittir. Bahar ve güz dönemi olmak üzere yılda iki defa çıkarılan ulusal hakemli bir dergi olarak ilk sayısını 2012 bahar döneminde yayımlamıştır. Türk Doğa ve Fen Dergisi, Türkiye ve dünyanın her yerinden gelen doğa ve fen bilimlerinin her alanında özgün, yayımlanmamış, yayımlanmak üzere başka yere gönderilmemiş makale, derleme ve sempozyum değerlendirmesi gibi çalışmaların bilim alemine sunulması amacıyla kurulmuştur. İlk sayısından bugüne kesintisiz olarak faaliyetlerini sürdürmektedir.

Türk Doğa ve Fen Dergisi sadece online sistemde yayınlanmakta olup ayrıca kağıt baskısı bulunmamaktadır. Dergimize gelen her çalışma öncelikle Turnitin intihal programında taranmaktadır. Dergimizde editörlerin, hakemlerin ve yazarların, uluslararası yayım etik kurallarına uyması ve makalelerin yazım kurallarına uyumlu olması zorunluluğu vardır.

Yazarlar yayımlanmak üzere dergimize gönderdikleri çalışmaları ile ilgili telif haklarını zorunlu olarak Bingöl Üniversitesi Türk Doğa ve Fen Dergisi'ne devretmiş sayılırlar. Yazarlardan herhangi bir ücret talep edilmemektedir. Yazarların değerlendirmeleri, dergimizin resmi görüşü olarak kabul edilemez. Çalışmaların her türlü sorumluluğu yazarlarına aittir. Araştırma ürünleri için etik kurul raporu gerekli ise, çalışma üzerinde bu raporun alınmış olduğu belirtilmeli ve kurul raporu sisteme kaydedilmelidir. Araştırma ile ilgili intihal, atıf manipülasyonu, sahte veri uydurma vb. suistimallerin tespit edilmesi halinde yayım ve etik ilkelerine göre davranılır. Bu durumda çalışmanın yayımlanmasını önlemek, yayımdan kaldırmak ya da başka işlemler yapmak için gerekli işlemler takip edilmektedir.

Dergimizde, kaynak gösteriminde uluslararası Vancouver sistemine geçilmiştir. Ayrıca dergimiz, Creative Commons ile lisanslanmak suretiyle dergimizde yayımlanan makalelerin paylaşımı, kaynak gösterimi ve yayımlanmasında dergi ve yazar haklarını korumaya almıştır. 2018 yılı güz döneminden itibaren makaleler, uluslararası yazar kimlik numarası ORCID No'su ile yayımlanmaktadır.

Dergi ekibi, dergimizin ulusal ve uluslararası indekslerce taranan bir dergi olması yönünde çalışmalarını titizlikle sürdürmektedir. Dergimize gösterilen ilgi bu yönde bizleri teşvik etmeye devam edecektir.

Prof. Dr. Zafer ŞİAR

Bingöl Üniversitesi, Fen-Edebiyat Fakültesi, Matematik Bölümü
E-Mail: zsiar@bingol.edu.tr

Prof. Dr. Uğur ÇAKILCIOĞLU

Munzur Üniversitesi, Pertek Sakine Genç Meslek Yüksekokulu, Bitki Morfolojisi
ve Anatomisi Bölümü
E-Mail: ucakilcioglu@yahoo.com

Doç. Dr. Kamuran DİLSİZ

Bingöl Üniversitesi, Fen-Edebiyat Fakültesi, Fizik Bölümü
E-Mail: kdilsiz@bingol.edu.tr

Doç. Dr. Şükran KONCA

Bakırçay Üniversitesi, Mühendislik ve Mimarlık Fakültesi, Temel Bilimler,
Matematik Bölümü
E-Mail: sukran.konca@bakircay.edu.tr

Doç. Dr. İdris YAZGAN

Kastamonu Üniversitesi, Fen Edebiyat Fakültesi, Biyoloji

E-Mail: idrisyazgan@gmail.com

Doç. Dr. Abdulcabbar YAVUZ

Gaziantep Üniversitesi, Mühendislik Fakültesi, Metalurji ve Malzeme Mühendisliği
E-Mail: ayavuz@gantep.edu.tr

Doç. Dr. Bünyamin ALIM

Bayburt Üniversitesi, Teknik Bilimler Meslek Yüksekokulu, Elektrik ve Enerji
Bölümü
E-Mail: balim@bayburt.edu.tr

Doç. Dr. Mustafa Şükrü KURT

Erzurum Teknik Üniversitesi, Fen Fakültesi, Temel Bilimler
E-Mail: mustafa.kurt@erzurum.edu.tr

Doç. Dr. Sinan SAĞIR

Karamanoğlu Mehmetbey Üniversitesi, Fizik

E-Mail: sinansagir@kmu.edu.tr / sinan.sagir@cern.ch

Doç. Dr. Murat AYDEMİR

Erzurum Teknik Üniversitesi, Fen Fakültesi, Temel Bilimler

E-Mail: murat.aydemir@erzurum.edu.tr

Mühendislik Bilimleri

Prof. Dr. Figen KOREL

İzmir Yüksek Teknoloji Enstitüsü, Gıda Mühendisliği Bölümü
E-Mail: figenkorel@iyte.edu.tr

Prof. Dr. Kubilay ASLANTAŞ

Afyon Kocatepe Üniversitesi, Teknoloji Fakültesi, Makine Mühendisliği Bölümü
E-Mail: aslantas@aku.edu.tr

Prof. Dr. Hamit Özkan GÜLSOY

Marmara Üniversitesi, Teknoloji Fakültesi, Metalurji ve Malzeme Mühendisliği
Bölümü
E-Mail: ogulsoy@marmara.edu.tr

Prof. Dr. Ali Adnan HAYALOĞLU

İnönü Üniversitesi, Mühendislik Fakültesi, Gıda Mühendisliği Bölümü
E-Mail: adnan.hayaloglu@inonu.edu.tr

Prof. Dr. Barbara SAWICKA

University of Life Sciences in Lublin, Department of Plant Production Technology
and Commodities Sciences
E-Mail: barbara.sawicka@gmail.com

Prof. Dr. İbrahim GÜNEŞ

Giresun Üniversitesi, Mühendislik Fakültesi, İnşaat Mühendisliği Bölümü
E-Mail: ibrahim.gunes@giresun.edu.tr

Doç. Dr. Serhat ŞAP

Bingöl Üniversitesi, Teknik Bilimler Meslek Yüksekokulu, Elektrik ve Enerji
Bölümü
E-Mail: ssap@bingol.edu.tr

Doç. Dr. Sırma YEĞİN

Ege Üniversitesi, Mühendislik Fakültesi, Gıda Mühendisliği Bölümü
E-Mail: sirma.yegin@ege.edu.tr

Doç. Dr. Hasan OĞUL

Sinop Üniversitesi, Mimarlık ve Mühendislik Fakültesi, Nükleer Enerji
Mühendisliği
E-Mail: hogul@sinop.edu.tr

Doç. Dr. Murat YILMAZTEKİN

İnönü Üniversitesi, Mühendislik Fakültesi, Gıda Mühendisliği Bölümü
E-Mail: murat.yilmaztekin@inonu.edu.tr

Doç. Dr. Ferhat AYDIN

Sakarya Uygulamalı Bilimler Üniversitesi, Teknoloji Fakültesi, İnşaat
Mühendisliği Bölümü
E-Mail: ferhata@subu.edu.tr

Dr. Öğr. Üyesi Nurullah DEMİR

Bingöl Üniversitesi, Mühendislik ve Mimarlık Fakültesi, Gıda Mühendisliği
Bölümü
E-Mail: ndemir@bingol.edu.tr

Doç. Dr. Ahmet GÜNER

Bingöl Üniversitesi, Mühendislik ve Mimarlık Fakültesi, Elektrik ve Elektronik
Mühendisliği Bölümü
E-Mail: aguner@bingol.edu.tr

Dr. Öğr. Üyesi Tahir AKGÜL

Sakarya Uygulamalı Bilimler Üniversitesi, Teknoloji Fakültesi, İnşaat
Mühendisliği Bölümü
E-Mail: tahirakgul@subu.edu.tr

Dr. Erhan Sulejmani

University of Tetova, Faculty of Food Technology and Nutrition
E-Mail: erhan.sulejmani@unite.edu.mk

Dr. Hacène Medjoudj

Larbi Ben M'Hidi University of Oum El Bouaghi, Food Science Department
E-Mail: medjoudjh@yahoo.com

Dr. Avinash Lakshmikanthan

Nitte Meenakshi Institute of Technology, Department of Mechanical Engineering,
Karnataka, India
E-Mail: avinash.laks01@gmail.com

Dr. Manjunath Patel GC

PES Institute of Technology and Management, Department of Mechanical
Engineering, Karnataka, India
E-Mail: manju09mpm05@gmail.com

Sağlık Bilimleri

Doç. Dr. Aydın Şükrü BENGÜ

Bingöl Üniversitesi, Sağlık Hizmetleri Meslek Yüksekokulu, Tıbbi Hizmetler ve
Teknikler
E-Mail: abengu@bingol.edu.tr

Dr. Öğr. Üyesi Dilhun Keriman ARSERİM UÇAR

Bingöl Üniversitesi, Sağlık Bilimleri Fakültesi, Beslenme ve Diyetetik Bölümü
E-Mail: dkucar@bingol.edu.tr

Dr. Öğr. Üyesi Abdullah TUNÇ

Bingöl Üniversitesi, Sağlık Bilimleri Fakültesi, İş Sağlığı ve Güvenliği Bölümü
E-Mail: atunc@bingol.edu.tr

Dr. Öğr. Üyesi Ramazan GÜNDOĞDU

Bingöl Üniversitesi, Sağlık Hizmetleri Meslek Yüksekokulu, Eczane Hizmetleri
E-Mail: rgundogdu@bingol.edu.tr

Dr. Alexander HERGOVICH

UCL Cancer Institute, Faculty of Medical Sciences, Department of Cancer Biology,
UCL, London, UK
E-Mail: a.hergovich@uc.ac.uk

Dr. Valenti GOMEZ

UCL Cancer Institute, Faculty of Medical Sciences, Department of Oncology, UCL, London, UK
E-Mail: valentin.gomez@ucl.ac.uk

Veterinerlik Bilimleri

Prof. Dr. Fatih Mehmet KANDEMİR

Atatürk Üniversitesi, Veteriner Fakültesi, Veteriner Hekimliği Temel Bilimler
E-Mail: fmehmet.kandemir@atauni.edu.tr

Doç. Dr. Akın KIRBAŞ

Bozok Üniversitesi, Veteriner Fakültesi, Klinik Bilimler Bölümü
E-Mail: akindahiliye55@yahoo.com

Doç. Dr. Emrah Hicazi AKSU

Atatürk Üniversitesi, Veteriner Fakültesi, Klinik Bilimler Bölümü
E-Mail: emrahaksu@atauni.edu.tr

Ziraat Bilimleri

Doç. Dr. Zeynep DUMANOĞLU

Bingöl Üniversitesi, Ziraat Fakültesi, Biyosistem Mühendisliği Bölümü
E-Mail: zdumanoglu@bingol.edu.tr

Prof. Dr. Kağan KÖKTEN

Bingöl Üniversitesi, Ziraat Fakültesi, Tarla Bitkileri Bölümü
E-Mail: kahafe1974@yahoo.com

Prof. Dr. Mustafa SÜRMEN

Adnan Menderes Üniversitesi, Ziraat Fakültesi, Tarla Bitkileri Bölümü
E-Mail: mustafa.surmen@adu.edu.tr

Prof. Dr. Banu YÜCEL

Ege Üniversitesi, Ziraat Fakültesi, Hayvan Yetiştirme Anabilim Dalı, Zootekni Bölümü
E-Mail: banu.yucel@ege.edu.tr

Prof. Dr. Hakan İNCİ

Bingöl Üniversitesi, Ziraat Fakültesi, Zootekni Bölümü
E-Mail: hinci@bingol.edu.tr

TEKNİK EDİTÖRLER

Dr. Nimetullah KORKUT

Bingöl Üniversitesi, BİNUZEM, Bilgisayar Teknolojileri
E-Mail: nkorkut@bingol.edu.tr

DİL EDİTÖRÜ

Dr. Öğr. Üyesi Ahmet KESMEZ
Bingöl Üniversitesi, Yabancı Diller Yüksekokulu, İngilizce Bölümü
E-Mail: akesmez@bingol.edu.tr

Türk Doğa ve Fen Dergisi
Turkish Journal of Nature and Scienc

www.dergipark.gov.tr/tdfd

İÇİNDEKİLER/CONTENTS

Maybe a New Target for Gliomas: AQP1

Saniye Elvan ÖZTÜRK¹* (iD)

¹ Aksaray University, Faculty of Science and Letters, Department of Molecular Biology and Genetics, Aksaray, Türkiye
Saniye Elvan ÖZTÜRK ORCID No: 0000-0003-4399-8299
Corresponding author: selvanozturk@aksaray.edu.tr

21

Evaluatıon of Yield Performance of Some Local Chickpea Varieties In Silifke Ecological Conditions

Gülay ZULKADİR¹* (iD) **, İnci KARATAŞ¹** (iD) **, Leyla İDİKUT²** (iD)

¹ Mersin University, Applied Technology and Management School of Silifke, Organic Farming Management Department, Mersin, Türkiye
¹ Mersin University, Applied Technology and Management School of Silifke, Organic Farming Management Department, Mersin, Türkiye
² Kahramanmaras Sutcu Imam Universitesi, Faculty of Agriculture, Field Crops Department, Kahramanmaras, Türkiye
Gülay ZULKADİR ORCID No: 0000-0003-3488-4011
İnci KARATAŞ ORCID No: 0009-0008-8229-2575
Leyla İDİKUT ORCID No: 0000-0002-0685-7158

Corresponding author: gulayzulkadir@gmail.com

32

The Potential Prognostic Value of Glutatione-S Transferase Izoenzymes in Non-small Cell Lung Cancer

Aydın KESKIN¹ (iD) **, Pınar KAYGIN¹** (iD) **, Kayhan BAŞAK²** (iD) **Fatma ÇAKMAK KAZANCI³** (iD) **, Sezen YILMAZ SARIALTIN⁴** (iD) **, Onur DIRICAN⁵*** (iD) **, Abbas Ali HUSSEINI⁶** (iD) **, Muharrem ATLI¹** (iD) **, Can YILMAZ⁷** (iD) **, Serpil OĞUZTÜZÜN¹** (iD)

¹ Department of Biology, Faculty of Arts and Sciences, Kirikkale University, Kirikkale, Türkiye
² Department of Pathology, Kartal Dr. Lütfi Kırdar City Hospital, Turkish Ministry of Health, University of Health Sciences, İstanbul, Türkiye
³ Medical Pathology Clinic, Çerkezkoy State Hospital, Tekirdağ, Türkiye
⁴ Department of Toxicology, Faculty of Pharmacy, Ankara University, Ankara, Türkiye
⁵ Department of Pathology Laboratory Techniques, Vocational School of Health Services, Istanbul Gelişim University, Istanbul, Türkiye.
⁶ Life Sciences and Biomedical Engineering Application and Research Centre, Istanbul Gelisim University, Istanbul, Türkiye.
⁷ Department of Molecular Biology and Genetics, Yüzüncü Yıl University, Van, Türkiye
Aydın KESKİN ORCID No: 0000-0003-2360-7692
Pınar KAYGIN ORCID No: 0000-0003-0127-1753
Kayhan BAŞAK ORCID No: 0000-0003-1960-8924
Fatma ÇAKMAK KAZANCI ORCID No: 0000-0001-5064-0952
Sezen YILMAZ SARIALTIN ORCID No: 0000-0002-8387-4146
Onur DİRİCAN ORCID No: 0000-0003-0511-6611
Abbas Ali HUSSEINI ORCID No: 0000-0002-8861-7106
Muharrem ATLI ORCID No: 0000-0002-2453-1370
Can YILMAZ ORCID No: 0000-0002-0028-6614
Serpil OĞUZTÜZÜN ORCID No: 0000-0002-5892-3735

Corresponding author: odirican@gelisim.edu.tr

48

Investigation of Quality Parameters of Soil Sample Collected from Akdağmadeni/Bulgurlu Village District of Yozgat Province

Büşra ŞENSOY GÜN[1,2*] , **Beyza YORULMAZ[1,3]** , **Arda AYTİMUR[1]** , **Belgin TUNALI[2]**

[1]Bilecik Şeyh Edebali University, Central Research Laboratory Application and Research Center, Bilecik 11100, Türkiye
[2]Burdur Mehmet Akif Ersoy University, Department of Nanoscience and Nanotechnology, Burdur 15030, Türkiye
[3]Bilecik Şeyh Edebali University, Faculty of Science, Department of Molecular Biology and Genetics, Bilecik 11100, Türkiye
Büşra ŞENSOY GÜN ORCID No:0000-0001-5190-9490
Beyza YORULMAZ ORCID No: 0009-0007-0579-5446
Arda AYTİMUR ORCID No: 0000-0001-6995-6164
Belgin TUNALI ORCID No: 0000-0003-0768-679X

*Corresponding author: busra.sensoygun@bilecik.edu.tr

Effect of K and Si Applications on Plant Development, Na and K Content and Some Antioxidant (SOD, CAT, APX) Activities of Wheat (Triticum aestivum L.) Plant Exposed to Salt Stress

Orhan İNİK[1*] , **Mehmet Ali Bozkurt[2]**

[1] Department of Soil Science and Plant Nutrition, Faculty of Agriculture, Bingol University, Bingol/Türkiye
[2]Department of Soil Science and Plant Nutrition, Faculty of Agriculture, Yüzüncü Yıl University, Van/Türkiye
Orhan İNİK ORCID No: 0000-0003-1473-1392
Mehmet Ali BOZKURT ORCID No: 0000-0003-3923-857X

*Corresponding author: oinik@bingol.edu.tr

A Study on OSH Performance Measurement by PROMETHEE Method in Coal-Fired Thermal Power Plants

Nagihan ERSOY[1*]

[1] Manisa Celal Bayar University, Soma Meslek Yüksekokulu, Occupational Health and Safety Department, Manisa, Türkiye

Nagihan Ersoy ORCID No: 0000-0002-9807-9786

*Corresponding author: nagihanersoy89@gmail.com

Diagnostic Process of Periprosthetic Joint Infection in Painful Arthroplasty Patients Referred to a Tertiary Care Center: Orthopedics and Pathology Perspective

Berna ERITEN [1] , Serdar MENEKŞE[2]*

[1] Şehit Prof. Dr. İlhan Varank Education and Research Hospital, Pathology Department, İstanbul, Türkiye
[2] Adana Seyhan State Hospital, Orthopedics and Traumatology Department, Adana, Türkiye
Berna ERITEN ORCID ID: 0000-0003-3710-1502
Serdar MENEKŞE ORCID ID: 0000-0002-4121-8917

Corresponding author: dr.serdarmenekse@gmail.com

83

Experimental Investigation of the Thermal Performance of Iron Oxide-Water Nanofluid Subjected To a Magnetic Field in a Horizontal Tube

Hamza ERTÜRK[1] , Tarkan KOCA[2]*

[1] İnonu University, Engineering Faculty, Mechanical Engineering Department, Malatya, Türkiye
[2] İnonu University, Engineering Faculty, Mechanical Engineering Department, Malatya, Türkiye
Hamza ERTÜRK ORCID No: 0009-0001-0517-9949
Tarkan KOCA ORCID No: 0000-0002-6881-4153

Corresponding author: tarkan.koca@inonu.edu.tr

89

Design of A New Metamaterial and Investigation of Its Effect on The Gain of A Circular Patch Antenna

Bülent URUL[1]*

[1] Isparta University of Applied Sciences University, Vocational School of Technical Sciences, Electronics and Automation Department, Isparta, Türkiye
Bülent URUL ORCID No: 0000-0003-2656-2450

Corresponding author : bulenturul@isparta.edu.tr

96

Cascade Control of Single Input Multi Output Buck Converter for Synchronous Charging Applications of Battery/Ultracapacitor Hybrid Energy Storage Systems

Muhammed Reşit ÇORAPSIZ[1*] iD

[1] Erzurum Technical University, Faculty of Engineering and Architecture, Department of Electrical & Electronics Engineering, Erzurum, Türkiye
Muhammed Reşit ÇORAPSIZ ORCID No: 0000-0001-5477-5299

Corresponding author: r.corapsiz@erzurum.edu.tr

103

Investigation of the Effects of Environmental and Geothermal Resource Temperature on Carnot Efficiency

Mert GÜRTÜRK [1] iD **, Murat ERDEM [2*]** iD

[1] Fırat University, Technology Faculty, Department of Energy Systems Engineering, Elazığ, Türkiye
[2] Fırat University, Vocational School of Technical Sciences, Elazığ, Türkiye
Mert GÜRTÜRK ORCID No: 0000-0003-0380-5704
Murat ERDEM ORCID No: 0000-0003-0287-1881

Corresponding author: muratrdm01@gmail.com

117

Effects of *Berberis vulgaris* L. Extract on the Physicochemical, Sensory, and Textural Properties of Raw and Cooked Patties

Kübra CINAR TOPCU[1*] iD **, Gamze UGUR[2]** iD

[1] Bayburt University, Aydıntepe Vocational School, Department of Food Science, Bayburt, Türkiye
[2] Bayburt University, Aydıntepe Vocational School, Food Technology, Bayburt, Türkiye
Kübra CINAR TOPCU ORCID No: 0000-0002-3715-8739
Gamze UGUR ORCID No: 0009-0009-9238-9589

Corresponding author: kcinar@bayburt.edu.tr

127

Renewable Energy and Hydrogen Storage System Analysis for Carbon Neutral Campuses with HOMER

Faruk BARLAZ[1*] iD **, Yahya AKIL[2]** iD **, Cem HAYDAROĞLU[3]** iD **, Heybet KILIÇ[2]** iD

[1] Dicle University, Institute of Science, Diyarbakır, Türkiye
[2] Dicle University, Department of Electrical Energy and Energy, Diyarbakır, Türkiye
[3] Dicle University, Department of Electrical and Electronics Engineering, Diyarbakır, Türkiye

Faruk BARLAZ ORCID No: 0009-0003-2703-0234
Yahya AKIL ORCID No: 0000-0002-7497-6458
Cem HAYDAROĞLU ORCID No: 0000-0003-0830-5530
Heybet KILIÇ ORCID No: 0000-0002-6119-0886

Corresponding author: cem.haydaroglu@dicle.edu.tr

136

Antioxidant Activity, Amino Acid Composition and Trace Element Levels of *Verbascum lasianthum* Boiss. ex Bentham from Erzincan, Türkiye

Tugrul Cagri AKMAN[1*] [ID]

[1] Erzincan Binali Yıldırım University, Faculty of Pharmacy, Department of Analytical Chemistry, Erzincan, Türkiye
Tugrul Cagri AKMAN ORCID No: 0000-0002-5439-950X

Corresponding author: eczcagri87@gmail.com

146

Development of an Effective Deep Learning Model for COVID-19 Detection from CT Images

Tanju CEYLAN*[ID] **, Özkan İNİK[2]** [ID]

[1] Tokat Gaziosmanpaşa University, Department of Computer Engineering, Tokat, Türkiye
[2] Tokat Gaziosmanpaşa University, Department of Computer Engineering, Tokat, Türkiye
Tanju CEYLAN ORCID No: 0009-0001-3843-5785
Özkan İNİK ORCID No: 0000-0003-4728-8438

Corresponding author: tanju.ceylan@gop.edu.tr

156

Determination of Wave Parameters of Bandirma Bay Using Wave Prediction Methods

Selahattin Alp ERKURTULMUS[1*] [ID] **, Emre PESMAN[2]** [ID]

[1] Yalova University, Altinova Vocational School, Ship Construction Program, Yalova, Türkiye
[2] Karadeniz Technical University, Surmene Faculty of Marine Sciences, Naval Arch. and Marine Eng. Department, Trabzon, Türkiye
Selahattin Alp ERKURTULMUS ORCID No: 0000-0001-5129-7228
Emre PESMAN ORCID No: 0000-0003-3529-3619

Corresponding author: alp.erkurtulmus@yalova.edu.tr

167

Determination of Serum Vaspin Levels in Diabetic Rats and Investigation of Possible Relationships Between Vaspin and Some Other Adipocytokines

Gülsüm ASİLKAN KALDIK[1*] [ID] **, Abdurrahman ŞERMET[2]** [ID]

[1] Bingöl University, Vocational School of Health Services, Elderly Care Department, Bingöl, Türkiye
[2] Dicle University, Medicine Faculty, Physiology Department, Diyarbakır, Türkiye
Gülsüm ASİLKAN KALDIK ORCID No: 0000-0002-1179-7719
Abdurrahman ŞERMET ORCID No: 0000-0001-5579-8310

Corresponding author: gasilkan@bingol.edu.tr

174

Artificial Intelligence-Assisted Multi-Criteria Decision-Making Methodology: From Research Trends to the Future Roadmap

Mahmut BAYDAŞ[1*] ID , Nazlı ERSOY[2] ID

[1] Necmettin Erbakan University, Faculty of Applied Sciences, Department of Accounting and Finance Management, Konya, Türkiye
[2] Osmaniye Korkut Ata University, Faculty of Economics and Administrative Sciences, Department of Business Administration, Osmaniye, Türkiye
Mahmut BAYDAŞ ORCID No: 0000-0001-6195-667X
Nazlı ERSOY ORCID No: 0000-0003-0011-2216

Corresponding author: mbaydas@erbakan.edu.tr

180

Does High Blood Pressure Have an Effect on Intervertebral Fibrocartilage Histology?

Erhan ŞAHİN[1*] ID , Damla Gül FINDIK[2] ID , Özlem TÜRELİK[3] ID

[1:] Bilecik Seyh Edebali University, Faculty of Medicine, Histology and Embryology Department, Bilecik, Türkiye
[2:] Bilecik Seyh Edebali University, Faculty of Medicine, Histology and Embryology Department, Bilecik, Türkiye
[3:] Bilecik Seyh Edebali University, Faculty of Medicine, Pathology Department, Bilecik, Türkiye
Erhan SAHIN ORCID No: 0000-0003-2152-0542
Damla Gul FINDIK ORCID No: 0000-0001-8028-627X
Ozlem TURELIK ORCID No: 0000-0001-6057-9171

Corresponding author: erhansahinn@gmail.com

192

Deterministic Lateral Displacement System with Inclined Elliptical Obstacles for Efficient Size-Based Separation of Microparticles

Döne SAYARCAN[1*] ID , Ahmet CİCEK[2] ID , Nurettin KOROZLU[2] ID

[1] Opticianry Programme, Gölhisar Vocational School of Health Services, Burdur Mehmet Akif Ersoy University, Burdur, Türkiye
[2] Department of Nanoscience and Nanotechnology, Art and Science Faculty, Burdur Mehmet Akif Ersoy University, Burdur, Türkiye
Döne SAYARCAN ORCID No: 0000-0001-7000-0354
Ahmet CİCEK No: 0000-0002-7686-0045
Nurettin KOROZLU No: 0000-0002-0899-0227

Corresponding author: donesayarcan@mehmetakif.edu.tr

197

Rare Cardiac Tumor: Diagnosis And Management Of Atrial Myxoma With Computerized Tomography

Ahmet BAYTOK[1*] iD

[1] Karapınar State Hospital, Radiology Department, Konya, Türkiye
Ahmet BAYTOK ORCID No: 0000-0003-1615-5771

Corresponding author: drahmetbaytok@gmail.com

204

Monkeypox Virus: Current Status And Global Health Ipmlications

Semih Eriten[1] iD

[1] Sultanbeyli State Hospital, Emergency Department. İstanbul, Türkiye
Semih Eriten: 0000-0001-8516-372X

Corresponding author: semiheriten@hotmail.com

208

Türk Doğa ve Fen Dergisi
Turkish Journal of Nature and Science
www.dergipark.gov.tr/tdfd

Effect of Leonardite Material Doses on The Elimination of Salt Stress in Groundnut (*Arachis Hypogaea* L.)

Erkan BOYDAK [1*] iD , Bahar ENES [2] iD , Ali Rıza DEMİRKIRAN [3] iD

[1]Bingöl University, Faculty of Agriculture, Department of Field Crops, Bingöl, Türkiye
[2]Bingöl University, Institute of Science, Bingöl, Türkiye
[3]Bingöl University, Faculty of Agriculture, Department of Soil Science and Plant Nutrition, Bingöl, Türkiye
Erkan BOYDAK ORCID NO: 0000-0002-3466-5356
Bahar ENES ORCID NO: 0000-0002-2151-7223
Ali Rıza DEMİRKIRAN ORCID NO: 0000-0002-0086-0137

*Corresponding author: eboydak@bingol.edu.tr

Abstract: This study was established as a pot experiment with 4 replicates according to the coincidence plots factorial experimental design to investigate the positive and negative effects of sodium clor (NaCI) salt and leonardite material doses prepared at different rates on the development of NC-7 groundnut variety in the summer season of 2021. 5 different leonardite doses (0 kg/da, 25 kg/da, 50 kg/da, 75 kg/da and 100 kg/da) and 4 different NaCI doses (0 mM, 50 mM, 100 mM and 150 mM) were applied. As a result of the study; plant height 10.06-12.36 (cm), number of branches 3.00-3.78 (pcs/plant), seedling wet weight 5.66-8.94 (g), seedling dry weight 4.42-7.27 (g), leaf area index 36.62-47, 53 (cm2), root length 26.31-45.93 (cm), root wet weight 0.44-2.52 (g), K content 0.957-1.337 (%), sodium (Na) content 386.25-699.05 (mg/kg). According to the data obtained in the experiment; NaCI salt application had a significant effect on seedling dry weight, seedling wet weight, Na and root wet weight. Leonardite application had significant effect on plant height, root length, potassium (K) and root wet weight. Leonardite x NaCI interaction had significant effect on root length, root wet weight, seedling dry weight, K (%) content and Na (mg/kg) content.

1

Yerfıstığı (*Arachis Hypogaea* L.)'nda Leonardit Materyali Dozlarının Tuz Stresini Gidermede Etkisi

Öz: Bu çalışma 2021 yılı yaz sezonunda farklı oranlarda hazırlanmış NaCI tuzu ve leonardit materyali dozlarının NC-7 yerfıstığı çeşidinin gelişimi üzerine olumlu ve olumsuz etkilerini araştırmak için saksı denemesi şeklinde tesadüf parselleri faktöriyel deneme desenine göre 4 tekerrürlü olarak kurulmuştur. 5 farklı leonardit dozu (0 kg/da, 25 kg/da, 50 kg/da, 75 kg/da ve 100 kg/da hesabına göre) ve 4 farklı NaCI dozu (0 mM, 50mM, 100mM ve 150mM) uygulanmıştır. Çalışma sonucunda; bitki boyu 10.06-12.36 (cm), dal sayısı 3.00-3.78 (adet/bitki), fide yaş ağırlığı 5.66-8.94 (g), fide kuru ağırlığı 4.42-7.27 (g), yaprak alanı indeksi 36.62-47.53 (cm^2), kök uzunluğu 26.31-45.93 (cm), kök yaş ağırlığı 0.44-2.52 (g), K oranı 0.957-1.337 (%), Na oranı 386.25-699.05 (mg/kg), arasında değiştiği gözlenmiştir. Denemede elde edilen verilere göre; NaCI tuzu uygulaması fide kuru ağırlığı, fide yaş ağırlığı, Sodyum (Na) ve kök yaş ağırlığına önemli etkide bulunmuştur. Leonardit uygulaması bitki boyu, kök uzunluğu, K (potasyum) ve kök yaş ağırlığına önemli etkide bulunmuştur. Leonardit x NaCI interaksiyonuna bakıldığında ise kök uzunluğu, kök yaş ağırlığı, fide kuru ağırlığı, K (%) oranı ve Na(mg/kg) miktarı önemli bulunmuştur.

1. INTRODUCTION

The origin of the peanut is South America. It is the region extending from southern Bolivia to northern Argentina. It is thought that peanuts were taken from North America to Europe by Spanish sailors [1]. Peanut is a plant that grows in tropical and subtropical regions from its natural growing area and likes plenty of light and warmth and does not like cold. As temperatures increase, growing times shorten and photosynthesis decreases in extreme temperatures, resulting in a decrease in yield. Peanut plant needs a total temperature requirement of 3000°-4500°C during the growing period [2].

Biochar is a soil conditioner. Leonardite has been accepted as a soil conditioner as a result of recent studies [3]. Leonardite is very high in phosphorus (P2O5) and calcium carbonate contents in terms of plant nutrients but poor in potassium (K). Soil reactions (pH) are around neutral [4]. Leonardite plays an important role in correcting soil colour, aerating compacted soil and reducing soil salinity [3]. Humic substances generally contribute to plant development and ecosystem balance by improving the physical, chemical and biological properties of the soil [5]. With the ability of humic acid to bond with metals, nutrient losses occurring in the soil are prevented and the amount of fertiliser to be used is reduced [6]. Leonardite, due to its high water retention capacity, prevents the irrigation water away from the soil and provides low water consumption [7].

Salinity problem is more common in arid and semi-arid regions and 10 million hectares of land are lost every year in the world due to salinity [8]. Salinity is an important stress factor that has a negative effect on plant growth, development, bud formation, leaf area and stomata and causes significant decreases in yield [9]. Excessive and incorrect fertilisation used in agriculture also causes salinisation in the soil [10]. In order to eliminate the negative effects of salinity, it is necessary to apply improving substances to the plant growth environment. Recently, studies on organic matter applications have been intensified [11]. It is seen that different concentrations of humic acid are used in studies carried out to determine the effects of humic acid on salinity [12]. The nutritive functions of humic acids occur especially in the passage of macro and micronutrients to the plant [13]. When groundnut (Arachis hypogaea L.) is exposed to salt stress, which is common in soils, especially in arid climates, significant crop loss occurs. Salinity can disrupt the ionic and osmotic balance in the cell, causing damage to functional-structural proteins and cell membrane and alteration in cell membrane fluidity [14]. Salt stress can affect the peanut plant directly or indirectly. Leaves and stems of plants affected by salinity may appear stunted. [15]. Like many plants, groundnut plant is most sensitive to water stress during flowering and pod filling [16].

Some previous scientific researches on the subject of the study are presented below. NaCI salt application was found to be significant on root wet weight and number of branches at 0.01 level, while it was significant on root length and seedling dry weight at 0.05 level. Biochar treatment was significant on root wet weight, seedling wet weight, K (%) ratio at 0.01 level, while it was significant on root length and leaf area at 0.05 level. In Biochar x NaCI interaction, root fresh weight, number of branches, seedling fresh weight and K (%) ratio were found significant at 0.01 level, while Na (mg/kg) ratio was found significant at 0.05 level [17]. It was reported that 3000 kg leonardite application per decare before sowing caused an increase in the amounts of macro and micro elements in the plant, 1000 kg/da application had the highest effect on grain weight and grain yield of the plant, and the highest value was obtained at 3000 kg/da dose on biomass and wet weight [18].

It was determined that the germination rate and emergence rate prolonged with increasing salt doses and this negatively affected seedling development [16]. 100 mM, 200 mM, 300 mM 3 different NaCl doses were applied and values such as germination time (days), average emergence time (days) and sensitivity index increased significantly with increasing salt doses, while values such as emergence rate (%), seedling wet weight (g), root wet weight (g), seedling length (mm), root length (mm), seedling dry weight (g) and root dry weight (g) decreased [19]. Four doses of sodium chloride (NaCl) (0 mM, 50 mM, 100 mM and 150 mM) and four doses of leonardite (0 g/kg, 20 g/kg, 30 g/kg and 40 g/kg) were used in salt stress. Leonardite material and salt doses significantly affected shoot wet weight, root wet weight, root length and shoot length. It was determined that leonardite applications had a positive effect on plant growth and ion uptake in plants exposed to salt [20]. The effect of leonardite applications on root and stem wet weight, root and stem length, root and stem dry weight, leaf area index of plants exposed to salt stress was found to be statistically significant [21]. Leonardite applications significantly increased the phosphorus (P), nitrogen (N) and organic matter content of the soil, while it showed a certain increase in terms of potassium (K), but no statistically significant difference was found [22].

7 different salt doses (0 mM, 25 mM, 50 mM, 75 mM, 100 mM, 125 mM, 150 mM NaCl) were applied and it was determined that Na (Sodium) accumulated in the aboveground plant parts starting from 25 mM salt dose in all genotypes, and it was determined that 25 mM NaCl dose had a positive effect on some traits, but it was determined that plant development was negatively affected with the increase in salt doses in all genotypes [23]. Leonardite and nitrogen doses had no effect on the number of branches, plant height, branch height and 1000 grain weight [24]. It was found that as the dose of organic materials increased, the total nitrogen, plant-available phosphorus, organic matter, extractable potassium and pH of the soil increased, and the effect of organic material applications on all parameters examined, except nitrogen and pH, was obtained from the highest hazelnut husk, while the lowest was obtained from biochar applications [25].

It was determined that the stem weight decreased by 21.4%, plant height by 21.6% and root length by 30% above 4 dS m^{-1} and 8 dS m^{-1}, respectively. The increase in salt content in irrigation water caused an increase in Na content in the leaves and roots of plants [26]. Na was

2

found in high amounts in roots, leaves and stems with increasing salt content. There was a significant decrease in Ca, K and Mg in leaves. It was shown that the studied varieties of faba bean, which are moderately sensitive to salt, were moderately affected by ambient salinity and did not have a protective mechanism against salinity [27]. The proline, Na, CI and P concentrations of the cultivars exposed to salt stress increased and K concentration decreased [28].

2. MATERIAL AND METHOD

This research was established in June-July 2021 in the campus area of Bingöl University Faculty of Agriculture in the form of a pot experiment under open air conditions and NC-7 peanut variety, leonardite biochar as Leonardite material and NaCI salt for salt application were used in the experiment. The soils used in the pots were first sieved through 4 mm sieves and transferred to 5 kg pots. The experiment was established on 12 June 2021. NC-7 peanut variety was registered by the Western Mediterranean Agricultural Research Institute Directorate in 1991 [29].

Table 1. Climate data for Bingöl province

Months	Monthly average Temperature (°C)		Monthly relative humidity (%)		Monthly total Precipitation (mm)	
	2021 year	Long years average	2021 year	Long years average	2021 year	Long years average
June	24.4	22.2	30.2	44.3	1.8	21.1
July	28.4	26.7	28.6	37.2	0.2	6.9
August	27.3	26.7	31.0	36.0	3.9	4.9

*:Long-term average for 1990-2020 (thirty-one years of data analysed)

The average temperature value recorded in June and July was 24.4-28.4°C in 2021 and the long-term average temperature was 22.2-26.7°C. The amount of precipitation was 1.8-0.2 mm in 2021 and the long-term average was 21.1- 6.9 mm. Relative humidity was 30.2-28.6% in 2021 and the long-term average was 44.3-37.2%.

Table 2. Soil analysis results

pH	Organic mat. (%)	Salinity (%)	Lime (%)	K (kg/da)	P (kg/da)
8.09	0.36	0.011	6.91	18.18	2.86
Slightly alkaline	Az	unsalted	medium	medium	low

According to Table 2, the soil structure was slightly alkaline, organic matter content was low, no salt, lime and potassium content was medium and phosphorus content was low.

The pot experiment was carried out in 4 replicates according to the random plots factorial experiment design with 5 different leonardite doses (0 kg/da (control), 25 kg/da, 50 kg/da, 75 kg/da, 100 kg/da) and 4 different NaCI doses (0 Mm, 50 Mm, 100 Mm, 150 Mm). The soils used in the pots were dried under natural conditions and analysed. Five peanut seeds were sown in each pot and diluted after germination and 3 plants were left in each pot. The pots were irrigated with tap water until they reached the field capacity and NaCI solution was added to the pots after irrigation. The pots were watered once a week and the plants were harvested during the flowering period.

Plant height (cm), number of branches (number), seedling wet weight (g), leaf area index (cm2), root length (cm), root wet weight (g), seedling dry weight (g), plant sodium (Na) content, plant potassium (K) content and plant phosphorus (P) content were determined. Data analyses were performed using JMP Statistical Package Programme.

3. RESULTS AND DISCUSSION

3.1. Plant Height (cm)

Table 3 shows the mean values of leonardite and NaCI treatments on plant height of groundnut. According to the table, the highest average plant height was obtained from L4 with 11.39 cm and the lowest average plant height was obtained from L1 with 10.40 cm. The highest mean plant height of NaCI treatment was obtained from NO with 11.33 cm and the lowest mean plant height was obtained from N1 with 10.68 cm.

Table 3. Mean Values of plant height of Peanut in Leonardite and NaCI Treatments and Resulting Groups

Leonardit	NaCI				
	N0	N1	N2	N3	Average
L0	11.73	11.56	10.83	10.60	11.18 AB
L1	10.06	10.17	10.44	10.94	10.40 B
L2	11.06	10.70	10.61	10.83	10.80 AB
L3	11.46	10.47	11.89	11.31	11.28 A
L4	12.36	10.53	11.91	10.74	11.39 A
Average	11.33	10.68	11.14	10.89	

Our findings are in agreement with [26] who reported that salt doses up to 400 mM did not significantly affect stem length, but increasing salt doses after 400 mM decreased stem length, [20] who found the effect of salt and leonardite applications on plant height statistically significant, [30] who found the effect of leonardite and oak charcoal applications on plant height statistically significant.

[17] investigated the effect of biochar and NaCl applications on plant height of peanut under Bingöl conditions. As a result of the study, the effect of biochar x NaCl application on plant height was not found significant. The highest mean plant height value was obtained from B250 biochar application with 11.78 cm, while the lowest value was obtained from B500 and B1000 applications with 11.20 cm. The highest mean plant height value of NaCl treatment was obtained from N0 treatment with 11.59 cm, while the lowest value was obtained from N3 treatment with 11.07 cm. It was determined that increasing salt content did not have a significant effect on plant height of groundnut.

3.2. Number of Branches (Number/Plant)

Table 4 shows the mean values of the number of branches of peanut for leonardite and NaCl treatments. According to this table, the highest average number of branches of leonardite treatment was obtained from L0 treatment with 3.56 and the lowest average number of branches was obtained from L1 treatment with 3.35. The highest average number of branches of NaCl treatment was obtained from N2 and N3 treatments with 3.53 and the lowest average number of branches was obtained from N0 treatment with 3.38.

Table 4. Mean Values of Number of Branches of Peanut in Leonardite and NaCl Treatments and Resulting Groups

Leonardit	NaCl				
	N0	N1	N2	N3	Average
L0	3.67	3.44	3.33	3.78	3.56
L1	3.00	3.33	3.56	3.50	3.35
L2	3.33	3.45	3.67	3.67	3.53
L3	3.11	3.39	3.56	3.44	3.38
L4	3.78	3.39	3.56	3.28	3.50
Average	3.38	3.40	3.53	3.53	

Our findings; Our results are similar to those of [17] who found the effect of different salt doses applied to peanut on branching to be statistically significant and the effect of different biochar doses on branching to be statistically significant, [22] who applied different doses of leonardite to Java variety of bean and found the effect of leonardite on branching to be statistically significant and did not find the branching data statistically significant in Volare variety, [24] who applied different leonardite doses to sesame plant and found the effect of leonardite on branching to be statistically significant.

3.3. Seedling Wet Weight (g)

Table 5 shows the mean values of seedling wet weight of peanut for leonardite and NaCl treatments. According to this table, the highest seedling wet weight average of leonardite treatment was obtained from L4 treatment with 7.30 g, while the lowest seedling wet weight average was obtained from L3 treatment with 6.81 g. The highest seedling wet weight of NaCl treatment was obtained from N2 treatment with 7.79 g, while the lowest seedling wet weight average was obtained from N1 treatment with 6.70 g.

Table 5. Mean Values of Seedling Wet Weight of Peanut in Leonardite and NaCl Treatments and Resulting Groups

Leonardit	NaCl				
	N0	N1	N2	N3	Average
L0	7.57	7.52	6.51	7.48	7.27
L1	6.34	6.65	8.23	7.31	7.13
L2	6.77	7.36	7.31	6.27	6.93
L3	6.33	6.31	7.96	6.65	6.81
L4	7.46	5.66	8.94	7.13	7.30
Average	6.89 AB	6.70 B	7.79 A	6.97 AB	

Our findings are in harmony with the studies conducted by [17] who stated that there was an increase in seedling wet weight with the increase in biochar material applied to peanut, [30] who stated that there was an increase in seedling wet weight by applying leonardite and oak charcoal to tomato, [18] who stated that there was an increase in seedling wet weight by applying leonardite to chickpea, [20] who stated that there was an increase in seedling wet weight in parallel with the increase in the amount of leonardite applied to beans.

3.4. Leaf Area Index (cm^2)

According to Table 6, the mean leaf area values of leonardite and NaCl treatments of groundnut are shown in the table. Accordingly, the highest mean leaf area of leonardite treatment was obtained from L3 treatment with 43.60 cm^2 and the lowest mean leaf area was obtained from L1 treatment with 40.29 cm^2. The highest mean leaf area of NaCl treatment was obtained from N2 treatment with 43.73 cm2 and the lowest mean leaf area was obtained from N3 treatment with 40.05 cm^2.

Table 6. Mean Values of Leaf Area Index of Peanut in Leonardite and NaCl Treatments and Resulting Groups

Leonardit	NaCl				
	N0	N1	N2	N3	Average
L0	41.50	41.22	42.85	42.74	42.08
L1	40.43	39.97	40.39	40.38	40.29
L2	42.96	41.76	42.25	40.96	41.98
L3	47.07	42.13	45.65	39.56	43.60
L4	42.69	40.62	47.53	36.62	41.87
Average	42.93	41.14	43.73	40.05	

Our findings are in agreement with [17] who reported that the effect of biochar material on leaf area in peanut, to which salt and biochar were applied at different rates, was different under saline conditions, and that while it gave the highest value in some applications (B0), this value decreased and increased again in the following applications, and [21] who reported that the leaf area index of the amount of salt applied at different rates in beans was obtained from 0 mM (control) application.

4

3.5. Root Length (cm)

According to Table 7, the mean root length values of leonardite and NaCI treatments of groundnut are shown in the table. According to the table, the highest root length average of leonardite treatment was obtained from L0 treatment with 39.20 cm, while the lowest root length average was obtained from L4 treatment with 28.93 cm. The highest root length average of NaCI treatment was obtained from N1 with 35.66 cm, while the lowest root length average was obtained from N0 with 32.01 cm.

Table 7. Mean Values of Root Lenght of Peanut in Leonardite and NaCI Treatments and Resulting Groups

Leonardit	NaCI				
	N0	N1	N2	N3	Average
L0	36.94 abc	45.93 a	41.10 ab	32.82 abc	39.20 A
L1	35.90 abc	30.28 bc	30.45 bc	33.60 abc	32.56 B
L2	31.11 bc	33.49 abc	31.48 bc	34.89 abc	32.74 B
L3	29.78 bc	39.36 abc	31.94 bc	28.69 bc	32.44 B
L4	26.31 c	29.22 bc	29.28 bc	30.90 bc	28.93 B
Average	32.01	35.66	32.85	32.18	

Our findings; [16] who reported a decrease in root length depending on the amount of salt applied at different doses to different rapeseed varieties, [17] who stated that biochar used to manage salinity stress in root length with different doses of salt and biochar application in peanut has a positive effect up to B750 application dose and can manage the stress of salinity up to N3 dose, which is the last dose of salt applications, [21] who reported that root length decreased with the increase in the amount of salt in beans, [26], [21] who reported that root length decreased with the increase in the amount of salt applied at different doses in bean.

As a result of the interaction of leonardite and salt treatments, the highest root length was 45.93 cm in L0N1 treatment and the lowest root length was 26.31 cm in L4N0 treatment. This situation explains that the root length was the highest in the first dose of salt application without leonardite, and the root length decreased in the other cases where leonardite and salt increased.

3.6. Root Wet Weight (g)

According to Table 8, the average root wet weight values of leonardite and NaCI treatments of groundnut are shown in the table. According to this table, the highest root wet weight average of leonardite treatment was obtained from L0 treatment with 1.99 g, while the lowest root wet weight average was obtained from L4 treatment with 0.92 g. The highest root wet weight average of NaCI treatment was obtained from N0 treatment with 1.52 g, while the lowest root wet weight average was obtained from N1 treatment with 1.03 g.

Table 8. Mean Values of Root Wet Weight of Peanut in Leonardite and NaCI Treatments and Resulting Groups

Leonardit	NaCI				
	N0	N1	N2	N3	Average
L0	2.52 a	1.92 b	1.68 b	1.85 b	1.99 A
L1	1.93 b	0.44 g	0.71 fg	0.72 efg	0.95 B
L2	1.16 c	0.94 c-f	0.83 def	0.86 c-f	0.95 B
L3	0.98 c-f	0.96 c-f	1.09 cd	0.95 c-f	0.99 B
L4	1.02 cde	0.86 c-f	0.98 c-f	0.84 def	0.92 B
Average	1.52 A	1.03 B	1.06 B	1.04 B	

Our findings are in accordance with [16] who reported a decrease in root wet weight parallel to the amount of salt applied to different rapeseed varieties at different doses, [17] who reported that root wet weight decreased with the increase in the amount of salt applied to peanut, [17] who reported that root wet weight increased with the increase in the amount of biochar, [31] who reported a decrease in root wet weight of eggplant grown in saline soils.

As a result of the interaction of leonardite with salt treatments, the highest root wet weight of 2.52 g was obtained from L0N0 application and the lowest root wet weight of 0.44 g was obtained from L1N1 application. This situation explains that the root wet weight was the highest in the absence of leonardite and salt applications, while the root wet weight decreased in the other cases where leonardite and salt increased.

3.7. Seedling Dry Weight (g)

Table 9 shows the mean values of seedling dry weight of peanut for leonardite and NaCI treatments. According to the table, the highest seedling dry weight average of leonardite application was obtained from L0 application with 6.22 g, while the lowest seedling dry weight average was obtained from L1 application with 5.67 g. The highest seedling dry weight average of NaCI treatment was obtained from N2 treatment with 6.62 g, while the lowest seedling dry weight average was obtained from N1 treatment with 5.28 g.

Table 9. Mean Values of Seedling Dry Weight of Peanut in Leonardite and NaCI Treatments and Resulting Groups

Leonardit	NaCI				
	N0	N1	N2	N3	Average
L0	6.28 abc	6.35 abc	6.04 abc	6.21 abc	6.22
L1	5.26 abc	4.42 c	6.76 abc	6.23 abc	5.67
L2	5.98 abc	6.34 abc	5.96 abc	6.32 abc	6.15
L3	6.27 abc	4.59 c	7.06 ab	5.81 abc	5.93
L4	6.24 abc	4.71 bc	7.27 a	6.27 abc	6.12
Average	6.01 AB	5.28 B	6.62 A	6.17 A	

As a result of the interaction of leonardite with salt treatments, the highest seedling dry weight of 7.27 g and the lowest root wet weight of 4.42 g and 4.59 g were obtained from L4N2 and L1N1 and L3N1 treatments, respectively. This shows that the seedling wet weight of leonardite increased despite the salt treatments, and the lowest values were determined in the first (N1) dose of salt in different doses of leonardite.

Our findings are in agreement with [17] who stated that there was no negative effect of salinity on seedling dry weight in peanut with different doses of salt and biochar application, [30] who stated that seedling dry weight increased with the increase in the amount of leonardite applied to tomato, [20] who stated that seedling dry weight decreased with the increase in the amount of salt in beans with different doses of salt and leonardite and increased with the increase of leonardite.

3.8. Determination of Sodium (Na) in Plant (mg/kg)

As a result of the interaction of Leonardite with salt treatments, the highest Na contents in the above-ground part of the seedling were obtained from L0N2 and L3N3 treatments as 699.05 mg/kg and 692.10 mg/kg, respectively. The lowest sodium content was obtained from L2N1 treatment as 386.25 mg/kg. This situation explains that leonardite and salt applications increased sodium content at certain levels and decreased it at some doses (L2N1). According to these results, when the sodium content is taken into consideration, it shows that leonardite applications can be applied in saline environments and under saline conditions by paying attention to the application doses (Table 10).

Table 10. Mean Values of Determination of Sodium (Na) in Plant of Peanut in Leonardite and NaCI Treatments and Resulting Groups

Leonardit	NaCI				
	N0	N1	N2	N3	Average
L0	424.75 ab	521.15 ab	699.05 a	525.35 ab	542.56
L1	625.10 ab	453.20 ab	432.45 ab	649.25 ab	540.00
L2	538.65 ab	386.25 b	582.45 ab	529.15 ab	509.13
L3	563.75 ab	525.30 ab	597.95 ab	692.10 a	594.78
L4	649.55 ab	598.35 ab	474.80 ab	620.70 ab	570.85
Average	560.36 AB	484.85 B	557.34 AB	603.31 A	

Our findings are similar to those of [26] who reported that the amount of Na in leaves and roots increased with increasing salt content in irrigation water in peanut, [20] who reported that the amount of Na increased with increasing salt doses in bean and there was a positive relationship between leonardite and salt, [27] who reported that sodium accumulated in roots, leaves and stems with increasing salt content in broad bean, [28], [23] who stated that the amount of Na increased in the above-ground evening with increasing salt doses in pea, [17] who stated that Na element increased with salt application to peanut and biochar applications had a positive effect on the sodium intake of the plant.

3.9. Determination of Potassium (K) in Plant (%)

Table 11 shows the mean values of K (%) of peanut for leonardite and NaCI treatments. According to this table, the highest K (%) average of leonardite application was obtained from L1 application with 1.248 and the lowest K (%) average was obtained from L4 application with 1.008. The highest K (%) average of NaCI application was obtained from N0 application with 1.169 and the lowest K (%) average was obtained from N3 application with 1.139.

Table 11. Mean Values of Determination of Potassium (K) in Plant of Peanut in Leonardite and NaCI Treatments and Resulting Groups

Leonardit	NaCI				
	N0	N1	N2	N3	Average
L0	1.170 a-d	1.257 ab	1.140 a-d	1.247 ab	1.203 A
L1	1.237 ab	1.157 a-d	1.260 ab	1.337 a	1.248 A
L2	1.257 ab	1.260 ab	1.147 a-d	1.147 a-d	1.203 A
L3	1.200 abc	1.107 bcd	1.070 bcd	1.007 cd	1.096 B
L4	0.980 cd	0.977 d	1.117 a-d	0.957 d	1.008 C
Average	1.169	1.151	1.147	1.139	

As a result of the interaction of Leonardite with salt treatments, the highest potassium content in the above-ground part of the seedling was obtained as 1.337 % from L1N3 treatment. The lowest potassium contents were obtained from L4N1 and L4N3 treatments as 0.977 and 0.957 %, respectively. This situation explains that potassium was accumulated in the above-ground part of the plant at the L1 dose of leonardite and N3 application of salt, and this situation (potassium content) decreased with the increase of leonardite. According to these results, leonardite applications in terms of potassium content can be applied in saline environments or saline water conditions by paying attention to the application doses.

Our findings are similar to those of [20] who stated that leonardite material applied at certain doses increased the K content in beans and decreased the positive effect of leonardite in parallel with the increase in the amount of salt, [32] who stated that the ash remaining at 5% and below increases the potassium concentration in the soil with the use of coal ash in agricultural areas, [25], [17], who reported that salinity did not have a significant effect on the potassium intake of the plant, while biochar applications increased the potassium content at certain levels, the salinity stress was reduced in the B250 application.

3.10. Determination of Phosphorus (P) in Plants (%)

The effects of salt stress on phosphorus content in the plant and the effects of leonardite applications in reducing it were examined and found to be statistically significant. With salt applications, the average phosphorus content increased at N1 dose, decreased at N2 dose and increased again at N3 dose. With Leonardite applications, the average phosphorus contents increased in L1, L2 and L3 applications and decreased slightly in L4 application compared to the control. When the effects of interaction were analysed, the lowest phosphorus content was found in L0N0 application and the highest phosphorus content was found in L3N3 application.

Table 12. Mean Values of Determination of Phosphorus (P) in Plant of Peanut in Leonardite and NaCI Treatments and Resulting Groups

Leonardit	NaCI				
	N0	N1	N2	N3	average
L0	0.278 f	0.290 def	0.279 ef	0.297 c-f	0.286 C
L1	0.327 a-d	0.340 ab	0.311 a-f	0.339 abc	0.329 A
L2	0.310 a-f	0.320 a-f	0.322 a-f	0.322 a-d	0.319 AB
L3	0.290 def	0.332 a-d	0.321 a-e	0.352 a	0.324 AB
L4	0.313 a-f	0.318 a-f	0.307 b-f	0.303 b-f	0.310 B
Average	0.304 C	0.320 AB	0.308 BC	0.322 A	

It can be concluded that leonardite doses have positive effects on salt tolerance depending on plant growth parameters and nutrient contents such as phosphorus. Perennial ground cover plants Alchemilla mollis and Nepeta x faassenii (Catmint 'Walker's Low') were treated with salt (0, 50, 100, 200 and 400 mM NaCl) and it was determined that salt increased P content in A. mollis and decreased P content in N. x faassenii [33]. Sesleria caerulea (L., Ard.) and Koeleria glauca (Spreng, DC.) were treated with salt (0, 5, 10, 15, 30 g NaCl.dm^{-3}) and it was reported that leaf P content decreased [34]. The effects of proline (100 mM) and phosphorus (P; 10 and 100 mg kg^{-1} sand) application on growth, P content and ion balance of maize (30/87 hybrid) under salt stress were investigated. Salt stress caused a significant decrease in shoot and root P content. However, proline and P application significantly improved plant P content [35]. In a study, humic acid (0, 750 and 1500 mg.kg^{-1}) and phosphorus (0, 50, 100 and 150 mg.kg^{-1}) were applied to pepper seedlings (Demre variety) grown under salt stress (8 mM NaCl). Humic acid application significantly increased shoot P content of pepper seedlings. Humic acid is a product containing many elements that increase the fertility of the soil and increase the usefulness of nutrients, affect plant growth and yield and improve the harmful effects of salt stress [36].

4. CONCLUSION

In the study, it was determined that the leonardite material applied to the soil at certain doses improved the soil and contributed to the soil physically, chemically and biologically. It was also observed that it had a positive effect on the early developmental stages of the peanut plant used in the study. Considering the soil improving effect of Leonardite material, it will provide an important benefit by minimising the use of chemical inputs for sustainable agriculture. Leonardite applications can improve the detrimental effects of salt stress on groundnut seedlings and leonardite, which contains substances that have a positive effect on plant growth such as humic acid, can be an economical and simple application to reduce the problems of growing groundnut in moderately saline soils.

Acknowledgement

REFERENCES

[1] Pearman, G. The migration of plants. In: The cultural history of plants. (Eds. Prance S G, Nesbitt M). Routledge publisher, New York; 2005.

[2] Arıoğlu H, Kurt C, Bakal H, Onat B, Güllüoğlu L. Çukurova Bölgesi Ana Ürün Koşullarında Yapılan Yerfıstığı Tarımında Farklı Hasat Zamanlarının Verim ve Bazı Tarımsal Özelliklere Etkisi. Türkiye 10. Tarla Bitkileri Kongresi, 10-13 Eylül, Konya; 2013. p. 183-188.

[3] Demirkıran AR, Özbay N, Demir Y. Leonardit ve İnorganik Gübrelemenin Domates Bitkisinin Gelişimi Üzerine Etkileri Tr. Doğa ve Fen Dergisi 2012;1(2): 110-114.

[4] Olivella MA, Del Rio JC, Palacios J, Vairavamoorthy MA, Des Las Heras.. Characterization of Humic Acid from Leonardite Coal: An Integrated Study of PY–GC–MS–XPS and XANES Techniques, Jounnal of Analytical and Applied Prolyses 2002;63:59-68.

[5] Özdemir A. Humic Acid and Fulvic Acid Production from Lignites. Ankara. Ankara University; 2011.

[6] Akıncı Ş. Hümik Asitler, Bitki Büyümesi ve Besleyici Alımı. Fen Bilimleri Dergisi 2011; 23(1), 46-56.

[7] Engin VT. Cöcen Eİ, İnci U.. Türkiye'de Leonardit. Sakarya Üniversitesi Fen Edebiyat Dergisi 2012;1, 435-443.

[8] Akgül H. Tuzluluk Ziraat Mühendisliği Dergisi, Ankara 2003; Sayı 340, p.1.

[9] Allakhverdiev SI, Sakamoto A, Nishiyama Y, Inaba M, Murata N. Ionic and Osmotic Effects of Naclinduced İnactivation of Photosystems and Iı in (Synechococcus Sp.) Plant Physiol. 2000;123: 1047–1056."

[10] Kalefetoğlu T, Ekmekçi Y. Bitkilerde Kuraklık Stresinin Etkileri ve Dayanıklılık Mekanizmaları. Fen Bilimleri Dergisi. 2005;18(4): 723-740."

[11] Korkmaz A, Karagöl A, Horuz A. Artan NaCl Stres

Şartlarında Besin Çözeltisine Ilave Edilen Humik Asitin Domates Bitkisinin Verim ve Bazı Meyve Kalite Özellikleri Üzerine Etkileri. Anadolu Tarım Bilim. Derg.2016; 31, 275- 282."

[12] Akıncı Ş. Humik Asitlerin Stres Altındaki Bitkilerin Büyümesine ve Besleyicilerin Alınmasına Etkileri ı: Tuzluluk. Marmara Fen Bilimleri Dergisi.2017; 4, 134-143.

[13] Çelik C. Production and Characterisation of Humic Acid (Ha) and Fulvic Acids (Fa) from Olive Black Juice. Adana: University of Çukurova; 2010.

[14] Mahajan S, Tuteja N. Cold, Salinity and Drought Stresses: An Overview. Archives of Biochemistry and Biophysics.2005;444 (2), 139-158.

[15] Oummu Kulthum AHM. The Effect of NaCl Salinity on the Growth and Development of Groundnut (Arachis hypogaea L.) Seedlings. Gaziantep: University of Gaziantep; 2018.

[16] Balcı A, Boydak E. Farklı Kolza (Brassica Napus L.) Genotiplerinde NaCI Konsantrasyonlarının Çimlenme ve Çıkış Üzerine Etkisi. Kahramanmaraş Sütçü İmam Üniversitesi Tarım ve Doğa Dergisi.2021;4(5):1011–1020.

[17] Aslan S. The Effect of Orange Biochar Material Doses on the Elimination of Salt Stress in Groundnut (Arachis hypogaea L.) Plants. Bingöl: University of Bingöl; 2023.

[18] Gürocak EN. Effects of Leonardite as Organic Material on Chickpea Plant Growth. Bingöl: University of Bingöl; 2022.

[19] Kurtuluş M, Boydak E. Bazı Aspir (Carthamus tinctorius L.) Çeşitlerinde Farklı Tuz Konsantrasyonlarının Çimlenme ve Çıkış Üzerine Etkisi. Türk Tarım ve Doğa Bilimleri Dergisi.2022; 9(3): 696–704.

[20] Kiyas Ü. Effect of Different Leonardite and Salt Levels on Bean Seedling Growth. Bingöl: University of Bingöl; 2020.

[21] Oral E, Tunçtürk R, Tunçtürk M, Kulaz H. "Silisyum Ön Uygulamalarının Fasulyede (Phaseolus Vulgaris L.) Tuzluluğa Dayanıklı Üzerine Etkisi. Kahramanmaraş Sütçü İmam Üniversitesi Tarım ve Doğa Dergisi. 2020;3(6):1616–25.

[22] İmamoğlu S. Effect of Different Leonardite Applications on Bean Yield and Quality. Bursa: Uludağ University; 2019.

[23] Zambi H. Effect of Different NaCl Concentrations on Plant Growth of Some Pea (Pisum Sativum) Varieties and Genotypes. Ordu: University of Ordu; 2019.

[24] Işık M. Effect of Leonardite and Nitrogen Application on Yield and Quality Characteristics of Sesame Crop under Second Crop Conditions. Adana: University of Çukurova; 2019.

[25] Tarakçıoğlu C, Özenç DB, Yılmaz, FI, Kulaç S, Aygün S. Fındık Kabuğundan Üretilen Biyokömürün Toprağın Besin Maddesi Kapsamı Üzerine Etkisi. Anadolu Journal of Agricultural Sciences. 2019;34,107–17.

[26] Aydınşakır K, Büyüktaş D, Dinç N. Karaca C. Impact of Salinity Stress on Growing, Seedling Development and Water Consumption of Peanut (Arachis Hypogaea Cv. NC-7). Akdeniz Üniversitesi Ziraat Fakültesi Dergisi. 2015;28(2):25-32.

[27] Bulut F. The Effect of Salinity on Seedling Development and Uptake of Some Minerals in Broad Bean (Vicia Faba L.). Istanbul. Marmara University; 2007.

[28] Özcan H, Turan MA, Koç Ö, Çıkılı Y, Taban S. Tuz Stresinde Bazı Nohut (Cicer aietinum L. cvs.) Çeşitlerinin Gelişimi ve Prolin, Sodyum, Klor, Fosfor ve Potasyum Konsantrasyonlarındaki Değişimler. Turk J. Agric. For. 2000;24 /6, 649- 654.

[29] Kadiroğlu, A. [Internet]; 2023 [cited 2023 july 12]. Available from: https://arastirma.tarimorman.gov.tr/batem/Belgeler/Kutuphane/Teknik%20Bilgiler/yerfistigi%20yetistiriciligi.pdf

[30] Öztürk A. Effects of Leonardite and Oak Charcoal Treatments on Bingol Guldar Tomato Seedlings. Bingöl: University of Bingöl; 2022.

[31] Özyavuz M. Determination of the Effect of Biochar (Bıochar) Applications on Eggplant Plant and Chemical Properties of Soil. Şanlıurfa: University of Harran; 2017.

[32] Yılmaz S. Kömür Külünün Toprakların Kimyasal Özelliklerine ve Bitki Gelişimine Etkisi. Tekirdağ: Namık Kemal University; 2015.

[33] Eom SH, Setter TL, DiTommaso A, Weston LA. Differential growth response to salt stress among selected ornamentals. Journal of plant nutrition.2007;30(7), 1109-1126.

[34] Henschke M. Response of ornamental grasses cultivated under salinity stress. Acta Scientiarum Polonorum. Hortorum Cultus.2017;16(1). 95-103.

[35] Naz M, Hussain S, Ashraf I, Farooq M. Exogenous application of proline and phosphorus help improving maize performance under salt stress. Journal of Plant Nutrition.2023;46(10), 2342-2350.

[36] Çimrin KM, Türkmen Ö, Turan M, Tuncer B. Phosphorus and humic acid application alleviate salinity stress of pepper seedling. African Journal of Biotechnology. 2010;9(36).5845-5851

8

Türk Doğa ve Fen Dergisi
Turkish Journal of Nature and Science
www.dergipark.gov.tr/tdfd

A Method for n-Dimensional Reconstruction of Scalar Field Proposals

Burçin DOĞAN [iD]

Malatya Turgut Özal University, Faculty of Engineering and Natural Sciences, Department of Engineering Basic
Sciences, Malatya, Türkiye
Burçin DOĞAN ORCID No: 0000-0001-8386-213X

burcin.dogan@ozal.edu.tr

Abstract: In the present study, we mainly implement a correspondence between two different concepts of dark energy via the reverse engineering technique. Expressing the self-potential of scalar fields in analytical form is a very important and mathematically challenging problem. In conclusion, after performing the required mathematical calculations, we show that one can find exact expressions for a scalar field function and its self-interacting potential by making use of such correspondence.

Skaler Alan Tasarılarının n-Boyutlu İnşaası İçin Bir Yöntem

Öz: Bu çalışmada, esas olarak iki farklı karanlık enerji kavramı arasında tersine mühendislik tekniği ile bir ilişki kurulmuştur. Skaler alanların öz potansiyelini analitik formda ifade etmek oldukça önemli ve matematiksel zorluklar içeren bir problemdir. Sonuç olarak, gerekli matematiksel hesaplamaları tamamladıktan sonra, bu tür eşleştirmelerden yararlanarak bir skaler alan fonksiyonu ve onun öz-etkileşim potansiyeli için kesin ifadelerin bulunabileceği gösterilmiştir.

9

1. INTRODUCTION

It is generally known that, in a free fall motion, a particle follows a geodesic in spacetime. The concepts of geodesic and spacetime are linked by the metric:

$$ds^2 = g_{\mu\nu}dx^\mu dx^\nu, \qquad (1.1)$$

where ds^2, $g_{\mu\nu}$ and x^μ respectively indicate the proper interval, metric tensor and a four-vector. It is significant to emphasize here that we have three possible kinds of proper interval:

1) $ds^2 < 0$ *: spacelike,*
2) $ds^2 = 0$ *: lightlike (or null),*
3) $ds^2 > 0$ *: timelike.*

In the present work, we focus on an n-dimensional Friedmann-Robertson-Walker (nFRW henceforth) type Kaluza-Klein metric [1]:

$$ds^2 = dt^2 - b^2(t)\left[\frac{dr^2}{1 - kr^2} + r^2 dx_m^2\right], \qquad (1.2)$$

where $n = m + 2$ is the number of spacetime dimension and

$$dx_m^2 = dy_1^2 + \sin^2 y_1 dy_2^2 + ... + \sin^2 y_{m-1} dy_m^2. \qquad (1.3)$$

It is understood that the above interval represents an isotropic and homogenous universe [1]. Moreover, $b(t)$ shows the cosmic scale factor and k is known as the spatial curvature parameter, which can be normalized to three different values -1, 0, $+1$. Here, the case $k = 0$ indicates that $(m + 2)$-dimensional space-time has a flat fabric. On the other hand, $k = -1$ and $k = +1$ cases denote open and closed manifolds, respectively.

In 1915, making use of the diverse frameworks of classical mechanics, Einstein introduced a field equation describing the geometry of spacetime [2]:

$$R_{\mu\nu} - \frac{1}{2}g_{\mu\nu}R = \kappa\{(\rho + p)u_\mu u_\nu - pg_{\mu\nu}\}, \qquad (1.4)$$

where $R_{\mu\nu}$ is the Ricci tensor, R denotes the curvature

scalar, ρ represents the energy density and p indicates the pressure. Also, $\kappa = 8\pi G$, where G is known as the universal gravitational constant. As a matter of fact, Einstein field equations was described by considering $(3+1)$-dimensional Riemannian geometry. Besides, the most recent cosmological observations strongly indicates an accelerated expansion epoch of the universe [3-8] and a large number of scientists believe that dark energy and dark matter are responsible for this mysterious nature of cosmos. In this context, extra dimensional point of view is one of the most studied theoretical candidates of the dark energy [9]. In addition to this idea, there are some other theoretical candidates: scalar fields [10-12], modified gravity [13-16], unified energy densities [17-19] etc. In this work, we mainly discuss our attention on investigating the dynamical evolution of a scalar field dark energy model from the nFRW perspective. As we mentioned before, the scalar field idea is one of the most significant dark energy candidates, which means these proposals may be taken into account as an effective description of the accelerated expansion phase of the cosmos. In physics, there are various scalar field definitions, but, it is so hard to get an exact relation for the self-interacting potential of a scalar field by making use of fundamental theories. On this purpose, we perform an investigation in order to obtain exact expressions for the self-interacting potential of a scalar field model via n-dimensional framework.

2. MATERIAL AND METHOD

Theorem 2.1. *n-dimensional description of a scalar field model can be obtained via the Reverse Engineering method. Thus, one can reconstruct any scalar field model with the help of this technique.*

Proof. First of all, we focus on the n-dimensional field equations [1]:

$$\frac{(n-2)(n-1)}{2}\{H^2 + \frac{k}{b^2}\} = \kappa\rho, \tag{2.1}$$

$$(n-2)\{\dot{H} + H^2\} + \frac{(n-2)(n-3)}{2}\{H^2 \\ + \frac{k}{b^2}\} = -\kappa p. \tag{2.2}$$

Here, $H = \frac{\dot{b}}{b}$ is the cosmic Hubble parameter and the dot indicates a derivative with respect to the cosmic time t. In order to write a relation for the equation-of-state (EoS henceforth) parameter, i.e. $\omega = \frac{p}{\rho}$, we can use equations (2.1) and (2.2). It is generally known that this parameter yields very interesting conclusions in modern cosmology. From this point of view, we need this quantity in further calculations. So, making use of equations (2.1) and (2.2) gives

$$\omega = -\frac{(n-2)\{\dot{H} + H^2\} + \frac{(n-2)(n-3)}{2}\{H^2 + \frac{k}{b^2}\}}{\frac{(n-2)(n-1)}{2}\{H^2 + \frac{k}{b^2}\}}. \tag{2.3}$$

It is important to mention at this point that the condition for the late-time speedy expansion epoch is $\omega < -\frac{1}{3}$ [20].

Now, we are in a position to consider scalar field dark energy models and we use the quintessence type scalar field description [12] as an example in this section. For the quintessence field, the corresponding energy density and pressure are written [21-22] respectively as given below;

$$\rho_Q = \frac{\dot{\varphi}^2}{2} + v(\varphi), \tag{2.4}$$

$$p_Q = \frac{\dot{\varphi}^2}{2} - v(\varphi). \tag{2.5}$$

Therefore, it can be written that

$$\omega_Q = \frac{\dot{\varphi}^2 - 2v}{\dot{\varphi}^2 + 2v}. \tag{2.6}$$

One can see from here that the universe has a speedy expansion phase for the case $\dot{\varphi}^2 < v$ if we have the condition $\omega < -\frac{1}{3}$ [22-23].

At this step, we can now perform the reverse engineering method for the n-dimensional description of the quintessence scalar field model. Subsequently, we should assume $\rho_Q = \rho$ and $\omega_Q = \omega$, because both of these scenarios are proposed to explain nature of the dark energy. Consequently, from equations (2.4) and (2.5) together with $p = \rho\omega$, we get

$$\dot{\varphi}^2 = (1 + \omega_Q)\rho_Q = (1 + \omega)\rho, \tag{2.7}$$

$$v(\varphi) = \frac{1}{2}(1 - \omega_Q)\rho_Q = \frac{1}{2}(1 - \omega)\rho. \tag{2.8}$$

Now, we substitute expressions (2.1), (2.2) and (2.3) into the above results which lead to

$$\dot{\varphi}^2 = \frac{(n-2)}{\kappa b^2}[k + \dot{b}^2 - b\ddot{b}], \tag{2.9}$$

$$v = \frac{(n-2)}{2\kappa b^2}[(n-2)(k + \dot{b}^2) + b\ddot{b}]. \tag{2.10}$$

As it is seen from the above expressions, we can obtain an exact relation for the self-interacting potential via the reverse engineering method.

10

3. RESULTS

In the previous section, we give a correspondence between the quintessence proposal and the n FRW scenario. It is important to emphasize here that our investigation can be extended by considering other well-known dark energy descriptions such as the tachyon, dilaton and the $k-$essence type scalar field models etc.

(i) $n-$dimensional tachyonic model

$$\dot{\varphi}^2 = (1+\omega_T) = (1+\omega), \qquad (3.1)$$

$$v = \rho_T (1-\dot{\varphi}^2)^{\frac{1}{2}} = \rho\sqrt{-\omega}. \qquad (3.2)$$

(ii) $n-$dimensional dilaton field

$$\frac{h}{2}\dot{\varphi}^2 e^{\delta\varphi} = \frac{\omega_{n-1}}{3\omega_{n-1}} = \frac{\omega-1}{3\omega-1}, \qquad (3.3)$$

where h and δ are positive constants.

(iii) $n-$dimensional $k-$essence definition,

$$f(\varphi) = \frac{\rho_k}{3\chi^2 - \chi} = \frac{\rho}{3\chi^2 - \chi}, \qquad (3.4)$$

where

$$\chi = \frac{\omega_k - 1}{3\omega_k - 1} = \frac{\omega - 1}{3\omega - 1}. \qquad (3.5)$$

4. DISCUSSION AND CONCLUSION

It is known that our universe expands with an accelerated velocity and there is no theory explaining the entire nature of dark universe successfully. In this context, the scalar field models and extra dimensional frameworks are possible theoretical candidates [13,14,16-18,24,25]. In the present work, we have shown that one can redefine any scalar field dark energy models in the n FRW type framework and obtain exact expressions for the corresponding scalar field and its self-interacting potential. It can be said that such calculations are important to discuss how various cosmological proposals are related to each other.

REFERENCES

[1] Singh GP, Kotambkar S, Srivastava D, Pradhan A, A New Class of Higher Dimensional Cosmological Models of Universe with Variable G and Λ terms, Rom. Journ. Phys., Vol. 53, Nos. 3â€``4, (2008), 607â€``618.

[2] Einstein A, Zur Allgemeinen Relativitätstheorie, Preussische Akademie der Wissenschaften., 47, (1915), 778.

[3] Ade PAR, et al., Planck 2013 results. XII. Diffuse component separation A & A 571, A12 (2014), DOI:10.1051/0004-6361/201321580.

[4] Ade PAR, et al., Planck 2015 results. XIII. Cosmological parameters A & A 594, A13 (2016), DOI: 10.1051/0004-6361/201525830.

[5] Allen SW, et al., Constraints on dark energy from Chandra observations of the largest relaxed galaxy clusters, Mon. Not. R. Astron. Soc., 353 (2) (2004), 457-467.

[6] Bennet CL, et al., First Year Wilkinson Microwave Anisotropy Probe (WMAP) Observations: Preliminary Maps and Basic Results, Astrophys. J. Suppl., (2003), 148, 1.

[7] Perlmutter S, et al., Measurements of Ω and Λ from 42 High-Redshift Supernovae, Astrophys. J., (1998), 517-565.

[8] Tegmark M, et al., Cosmological Parameters from SDSS and WMAP, Phys. Rev. D., (2004), 69, 103501.

[9] Keskin AI, Saltı M, Cosmographic nature of the early universe from extra dimensional perspective, Physics Letters B., 791, (2019),

[10] doi.org/10.1016/j.physletb.2019.02.024, 80-85.

[11] Caldwell RR, A Phantom Menace? Cosmological consequences of a dark energy component with super-negative equation of state, Phys.Lett. B., 545, (2002), 23-29.

[12] Chiba T, Okabe T and Yamaguchi M, Kinetically driven quintessence, Phys. Rev. D., 62, 023511(2000).

[13] Copeland EJ, Sami M and Tsujikawa S, Dynamics of Dark Energy, Int. Journal of Modern Phys. D., 15, 11 (2006), 1753-1935.

[14] Abedi H and M. Saltı M, Multiple field modified gravity and localized energy in teleparallel framework, Gen. Rel. Grav., 47:93, (2015).

[15] Askin M, Abedi H and Saltı M, Thermodynamics in $f(T,\theta)$ Gravity, Rom. J. Phys., 60 (2015), 44-55.

[16] Boisseau B, et al., Reconstruction of a Scalar-Tensor Theory of Gravity in an Accelerating Universe, Phys Rev Lett., 2000, 85(11):2236-9.

[17] Capozziello S, et al., $f(R)$ Cosmology with Torsion,â€,Physica Scripta, 78(6) 2008.

[18] Askin M, Salti M and Aydogdu O, Cosmology via thermodynamics of polytropic gas, Modern Physics Letters A., 32, 1750177, 2017.

[19] Christensen Dalsgaard J, Lecture Notes on Stellar Structure and Evolution, Aarhus Univ. Press, 2004.

[20] Yu A, Kamenshchik A, Moschella U, Pasquier V, An alternative to quintessence, Physics Letters B., 511, 2001, 265-268.

[21] Tripathi A, Sangwan A and Jassal HK, Dark energy equation of state parameter and its evolution at low redshift, Journal of Cosmology and Astroparticle Physics, 06 (2017) 012.

[22] Carrillo JAE, Silva JM and Lima JAS, Astronomy and Relativistic Astrophysics: New Phenomena and New States of Matter in the Universe, in Proceedings of the Third Workshop (Joo Pessoa, Paraba, Brazil, 3-6 October 2007), 183-192.

[23] Jamil M, Karami K and Sheykhi A, Restoring New

11

Agegraphic Dark Energy in RS II Braneworld, Int. J. Theor. Phys., 50 (2011) 3069-3077.

[24] Pasqua A, Khodam-Mohammadi A, Jamil M, Myrzakulov R, Interacting Ricci dark energy with logarithmic correction, Astrophysics and Space Science, 340 (2012) 199-208.

[25] Zengin B, Askin M, Salti M and Aydogdu O, Thermal Device Beyond the Carnot Limit, Proceedings of the National Academy of Sciences, India Section A: Physical Sciences, 93 (2023) 177-183.

[26] Askin M, Salti M and Aydogdu O, Polytropic Carnot heat engine, Modern Physics Letters A 34 (2018) 1950197.

Impact of Different Cu Sources on the Structure, Surface Morphology, Optical and Photocatalytic Characteristics of Sol-Gel Derived CuO Thin Films

Sultan GÖKTAŞ[1*] iD , Gülsen ŞAHİN[2] iD

[1] Harran University, Faculty of Arts and Science, Department of Chemistry, Şanlıurfa, Türkiye
[2] Adiyaman University, Faculty of Education, Department of Mathematics and Science Education, Adıyaman, Türkiye
Sultan GÖKTAŞ ORCID No: 0009-0000-7084-9710
Gülsen ŞAHİN ORCID No: 0000-0003-4891-041X

*Corresponding author: sultangoktas@harran.edu.tr

Abstract: In this study, the impact of different Cu sources has been scrutinized on the structure, surface morphology, optical, and photocatalytic properties of CuO thin films, synthesized by sol-gel dip coating have been investigated. X-ray diffraction (XRD), scanning electron microscopy (SEM), energy dispersive spectroscopy (EDS) mapping, and UV–Vis spectroscopy were utilized to scrutinize them. The XRD patterns showed that the CuO films had a monoclinic CuO phase with a polycrystalline nature and their crystalline quality depended on the used Cu-source. Comparatively, the highest crystalline quality was observed for CuO film derived from the Cu-acetate source. The EDS and elemental mapping analysis exhibited the presence of Cu and O atoms within the film composition, randomly distributed on the film facets. As observed from the SEM analysis, the surface morphologies and grain sizes of CuO films were mainly changed by the Cu chemical source used. Variation in UV–Vis absorbance reflects different surface morphology and defect levels as the Cu-source was changed. The synthesized nanostructured CuO thin films showed highly varied photocatalytic activities and degradation rate of methylene blue dye solution under solar radiation. Among all synthesized CuO thin films, derived by using a Cu-chlorite source showed the highest photocatalytic efficacy within 150 min.

Farklı Cu kaynaklarının sol-jel ile türetilmiş CuO ince filmlerin yapısına, yüzey morfolojisine, optik ve fotokatalitik özelliklerine etkisi

Öz: Bu çalışmada, sol-jel daldırarak kaplama yöntemi ile sentezlenen CuO ince filmlerin yapısı, yüzey morfolojisi, optik ve fotokatalitik özelliklerine farklı bakır kaynaklarının etkisi incelenmiştir. X-ışını kırınım difraksiyonu (XRD), taramalı elektron mikroskobu (SEM), enerji dağılımlı spektroskopi (EDS), haritalama ve UV-Vis spektroskopisi gibi çeşitli analiz yöntemleri onların özelliklerini incelemek için kullanılmıştır. XRD desenleri, CuO filmlerinin polikristal yapıya sahip monoklinik CuO fazına sahip olduğunu ve kristal kalitesinin büyük ölçüde kullanılan Cu kaynağına bağlı olduğunu gösterdi. Karşılaştırmalı olarak, en yüksek kristal kalitesi, Cu-asetat kaynağından türetilen CuO filmi için gözlemlendi. EDS ve element haritalama analizleri film bileşiğinde, film yüzeyine rastgele dağılan Cu ve O atomlarının varlığını gösterdi. CuO filmlerinin yüzey morfolojileri ve tane boyutları, SEM analizlerinden gözlemlendiği gibi, esas olarak kullanılan Cu kimyasal kaynağına göre değişti. UV-Vis soğrulma spektrumundaki değişiklik, Cu kaynağı değiştikçe farklı yüzey morfolojilerini ve kusur seviyelerini yansıtır. Sentezlenen nanoyapılı CuO ince filmleri, oldukça değişken fotokatalitik aktiviteler ve güneş ışınımı altında metilen mavisi çözeltisinin bozunumun oranları gösterdi. Sentezlenen tüm CuO ince filmleri arasında Cu-klorit kaynağı kullanılarak üretilen film, 150 dakikada en yüksek fotokatalitik verimi gösterdi.

13

1. INTRODUCTION

In the last decade, there has been a critical excursion to improve particularly well-organized, affordable, durable, safe photocatalysts and catalysts for large plate degradation of detrimental azo dyes and nitro aromatic compositions from wastewater [1-3]. It is reported that among all the metal oxide-based semiconductors ZnO and TiO₂ are the most explored photocatalysts to remove harmful organic pollutants within the water [4-5]. Reduced employment of sunlight arising from the wide optical band gaps of ZnO and TiO₂ restrict their efficacy as photocatalysts [6]. To overcome this limitation narrow optical band gap semiconductors viz. CuO and Cu₂O have acquired profound notice. Especially, the uniqueness of CuO nanoparticles is even though they are metallic in bulk they behave like semiconductors when they are in nanosize. In addition, the main reason for selecting CuO among other transition metals oxides is its semiconductivity, providing the usability in optoelectronic devices. Furthermore, Copper (Cu) is ample in nature in an immersion of approximately 60 g per ton and durable on the Earth's crust and the nanosized CuO, having relatively smaller size and larger surface area to volume ratio, showing better photocatalytic and antimicrobial activity compared to the other metal oxides.

CuO is a semiconductor known as p-type. This semiconductor can be found in three separate phases such as CuO, Cu₂O, and Cu₄O₃ [7-8]. Among these phases, CuO, which is the most likely to be found, crystallizes in a monoclinic structure. The lattice parameters vary as a=4.684 Å, b=3.425 Å, c=5.129 Å and β=99.28°. It has also been reported that the band gap of this phase is around 2.1 eV [9]. It has also been observed that the nanoscale forms of the structure have high absorption but low transmittance (20 %) in the visible region. In addition, the refractive index in the same region can vary between 2 and 2.5 [9]. Due to these superior properties, CuO is widely used in various applications such as solar cells, lithium-ion batteries, gas sensors, and glucose sensors [10]. Moreover, the physicochemical characteristic of their nanostructures makes them promising materials for possible optoelectronic and photocatalytic applications [11-12]. CuO nanocrystalline thin films can be used for the large-scale diminishing of pollutants from wastewater and several types of solar cells.

CuO thin films are frequently preferred in several applications due to their properties such as Cu components being abundant in nature, being environmentally friendly, and non-toxic. Various thin film production methods have been used to synthesize CuO thin films. These methods can be listed as follows; chemical vapor deposition, electrodeposition, thermal oxidation, reactive magnetron sputtering, molecular beam epitaxy, ultrasonic spray pyrolysis, and also sol-gel. Among these methods, the sol-gel technique is potentially more preferred due to its useful, simple, uncomplicated, non-complicated, and economical method for obtaining CuO thin films Additionally, the dip coating process represents an effective method for coating large surfaces [13-17].

The photocatalytic performance of semiconductor thin film photocatalysts is highly upon on agents viz. facet morphology, crystallite/grain size, degree of crystallinity, active surface area, etc. [18–20]. For example, the photocatalytic behavior of CuO nano-whiskers thin film was reported by Mukherjee et al. [21]. In the reported study, the CuO nano-whiskers thin film showed a photocatalytic efficiency of 84 % for degradation of Rhodamine B (RhB) within 260 min under visible light. Similarly, CuO thin films having star like morphology showed 95 % photocatalytic efficiency in 210 min towards the photodegradation of methylene blue (MB) [22]. On the other hand, in nanowire-shaped CuO thin films, the MB removal efficacy reached 95.6 % in 210 min as reported by Wang et al [23]. It was reported that CuO nanostructures with flower-like shapes exhibited a high MB degradation efficiency of 98 % in 90 min [24]. Recently, the effect of annealing temperature on the photodegradation ability of CuO has been examined. The CuO degradation efficiency towards malachite green and MB was improved with increased annealing temperature due to the enhanced surface area of the CuO thin films [25]. More recently, Komaraiah et al. [26] have prepared CuO thin films having different film thicknesses, derived by spin coater technique, for degradation of the MB and Methyl orange under visible light. The maximum photocatalytic efficiency of 89.91 % was reported.

Herein, CuO thin films with different surface morphology were produced by sol-gel dip coating process using different Cu sources. The influences of the Cu-sources on the morphological, structural, optical, and photocatalytic behavior for the degradation of MB dye in water have been examined. According to our best knowledge, the influence of the different Cu sources on the above-mentioned properties has not been scrutinized yet. Therefore, investigating the influences of different Cu-sources on the morphological, structural, optical, and photocatalytic properties is highly attractive to get highly efficient, economical, stable, and reusable photocatalytic thin films for large-scale remove of organic pollutants and hazardous chemicals from wastewater.

2. MATERIAL AND METHOD

2.1. Synthesis Method of CuO Thin films

CuO thin films were grown by sol-gel dip coating method using 2-methoxyethanol (C₃H₈O₃), ethanolamine (C₂H₇NO), and different zinc sources such as copper (II) acetate monohydrate ((CH₃COO)₂Cu.H₂O), nitrate trihydrate (Cu(NO₂).3H₂O), and chlorite dihydrate (CuCl₂ .2H₂O). All used chemicals were analytically graded and not subjected to further purification, were used to grow the main solution of the thin films. To prepare different film solutions, 0.05 M of each of these zinc sources were separately dissolved in C₃H₈O₃ using a magnetic stirrer with a hot plate at room temperature for 30 min. Then a certain amount of the C₃H₈O₃ was added to each solution as a stabilizer. The final solutions were aged for 24 h overnight with continuous stirring on the hot plate at room temperature using magnetic rotators. The obtained last mixtures are completely homogeneous and transparent

(no suspended or insoluble particles were observed in them) and also have various coloring (blue, green, and pink) due to using different Cu-salt sources. Afterward, the mixture solutions were poured into 50 ml wells for coating on the glass substrates that were previously cleaned by washing them in an ultrasonic acetone and methanol bath. Finally, the clean glass substrates were deposited by a dip coating method using the final mixture solutions at 400 °C. The deposited film samples were sintered in the air atmosphere at 500 °C for 1 h. From now the deposited film samples will be called Cu-acetate, Cu-nitrate, and Cu-chlorite in this text according to used copper (II) acetate monohydrate ($(CH_3COO)_2Cu.H_2O$), nitrate trihydrate ($Cu(NO_2).3H_2O$), and chlorite dihydrate ($CuCl_2 .2H_2O$) chemical sources.

2.2. Characterization Techniques of CuO Thin Films

X-ray diffraction, XRD (Rigaku Ultima III (40 kV, 40 mA, and 1.54 A°)) diffractometer was used to check crystal phases and impurities in CuO thin films obtained by sol-gel dipping technique. Scanning electron microscopy, SEM (Zeiss Evo 50, 200 kV) was used for surface analysis and determination of the film thickness (from a cross-section of the film samples) of CuO thin samples. EDX (energy dispersion X-ray spectrophotometry) and elemental mapping methods were used to perform elemental analysis in the films. On the other hand, a UV-Vis spectrophotometer was used to determine the optical properties of the films (300-1100 nm wave) and to take absorption measurements of methylene blue (MB) dye after the photocatalytic process.

2.3. Photocatalytic Measurements of CuO Thin Films

To prepare the MB solution, 1.25 mg/L MB was dissolved in 100 ml of pure water using a magnetic stirrer at room temperature. It was then stirred until properly dissolved. The pH of the mixture (using a Hanna pH meter (HI2211 pH/ORP meter)) was regulated by the desired NaOH content. According to studies in the literature, MB undergoes best photodegradation at pH = 11 [27, 28].

The photocatalytic degradation behavior of MB was assessed in water under 200 W visible light using CuO thin films as a photocatalyst. For this study, 1.25 mg/L of MB solution in 100 mL of deionized water was made ready in a flask made up of glass and synthesized CuO thin films were submerged in this solution. This vial was left in a dark condition for 30 min to get an equilibrium of adsorption–desorption. Then it was exposed to sunlight for 30 min intervals. The absorption of MB solutions before and after various 30-min irradiation times was guided and examined using a UV–Vis spectroscopy (PerkinElmer Lambda 25) coupled to the distinctive absorption of the MB top at 664 nm. The efficacy of the CuO nanocrystalline photocatalysts was computed using the formula of $\eta = [(1-(C/C_0))]x100$.

Here, C_0 and C are the main absorption peaks of MB and represent the intensity of MB before and after photocatalysis, respectively.

3. RESULTS

3.1. Structural and Morphological Studies

The XRD patterns of CuO thin films obtained using different chemical sources are given in Figure 1. The XRD patterns showed that CuO thin films crystallize in the monoclinic CuO phase and crystallization (crystallite size) varies depending on the Cu chemical source used. Polycrystalline and nanostructured CuO thin films with (110), (002), (111), ($\bar{2}$02), (021), ($\bar{1}$13), and (220) miller indices (matched well with JCPDF card #89-5899, and ICSD card #087126) and preferred to crystallize at a higher rate along the plane side of (002) [2].
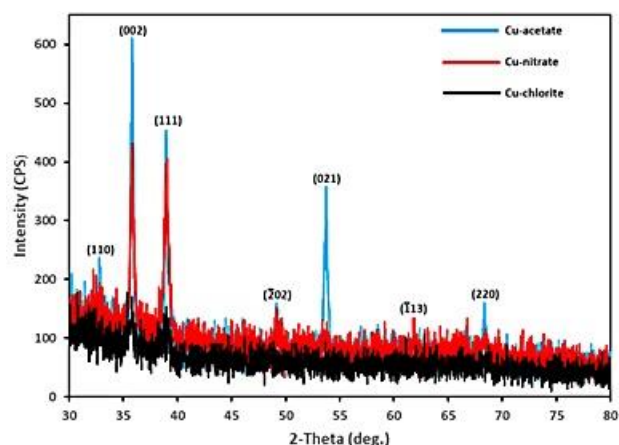
Figure 1. XRD patterns of CuO thin film samples Cu-acetate, Cu-nitrate, and Cu-chlorite

The crystallite size was calculated from the chief x-ray diffraction peak, having high peak intensity, at $2\theta = 35.70°$- $35.70°$ using Scherrer's formula [13].

$$D = 0.9\lambda/\beta\cos(\theta) \quad (1)$$

where β is FWHM, λ is the wavelength of the incident X-ray, and θ is the diffraction angle. The micro-strain ($\varepsilon = \beta\cos(\theta)$), and dislocation density ($\delta=1/D^2$) of the CuO films were evaluated [5] and given in Table 1.

Table 1. The full-width half-maximum, diffraction angle, crystallite size, dislocation density, micro-strain, and lattice parameter of the prepared CuO nanocrystalline thin film samples Cu-acetate, Cu-nitrate, and Cu-chlorite.

Cu-source	FWHM ($\beta°$)	2θ(deg.)	D_{hkl}(nm)	$\delta x10^{-3}$	$\varepsilon x 10^{-3}$	a (Å)
Acetate	0.28	35.70	30.00	11.11	2.640	4.779
Nitrate	0.43	35.76	19.53	26.21	4.243	4.729
Chlorite	0.78	35.80	10.76	86.37	7.919	4.717

It was observed that the examined SEM surface morphologies of nano-structured CuO thin films varied depending on the type of Cu chemical source used (Fig. 2a-c). Although the surfaces of these films are dense and homogeneous with some cracks and surface roughness have been observed. It can be seen from Fig.2a that the nanostructured CuO thin film prepared with copper acetate has denser and larger grains than those prepared with other Cu-source chemicals (Cu-nitrate and Cu-chlorite).

15
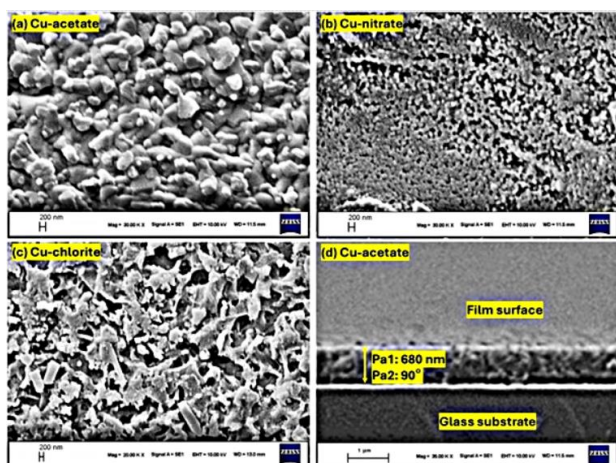
Figure 2. SEM images of the synthesized CuO thin film samples Cu-acetate (a), Cu-nitrate (b), Cu-chlorite (c), and the film thickness of Cu-chlorite film sample.

EDX and mapping technique results are presented in Fig. 3a-d. EDX spectra of the Cu-acetate film sample was given in Fig. 3a and confirmed the presence of Cu (51.40 at. %) and O (48.60 at. %) atoms in the film samples (Fig. 3a). The presence of the Au atom is due to the conductive contact used. In addition, it is understood from the mapping results that Cu (red) and O (green) atoms are distributed homogeneously on the film facet (Fig. 3b). The distribution of the Cu and O atoms was also given in different images as seen in Fig. 3c and 3d, respectively. Furthermore, the black spots or other colors show that the elements do not organize or flow in only mark contentment.
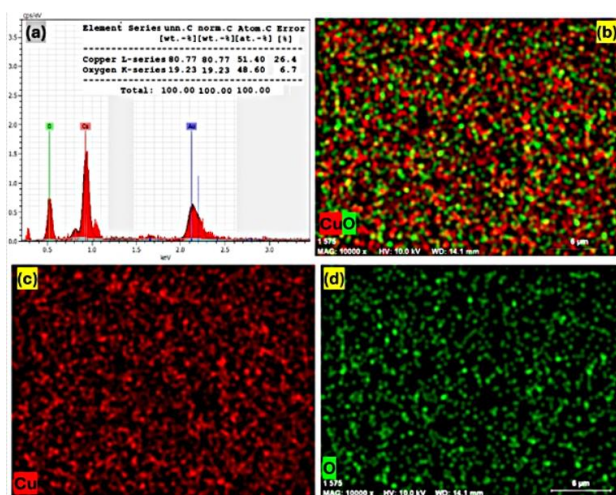
Figure 3. EDX spectra of the synthesized Cu-chlorite film sample (a), total color mapping (b), and color mapping of Cu (c) and O (d).

3.2. UV-Vis Measurements

UV–Vis absorption spectroscopy was carried out to monitor the optical response of the deposited CuO nanostructured thin film. The absorbance spectra of the prepared with acetate, nitrate, and chloride starting chemical sources, depending on wavelength and starting chemical type, are given in Fig. 4a. Tauc plots were utilized for the resolving of band gap values of CuO nanocrystalline films [32, 33]. The estimated bandgap values calculated as 1.51, 1.72 eV, and 1.66 eV for the

Cu-acetate, Cu-nitrate, and Cu-chlorite thin films, respectively (see Fig. 4b).
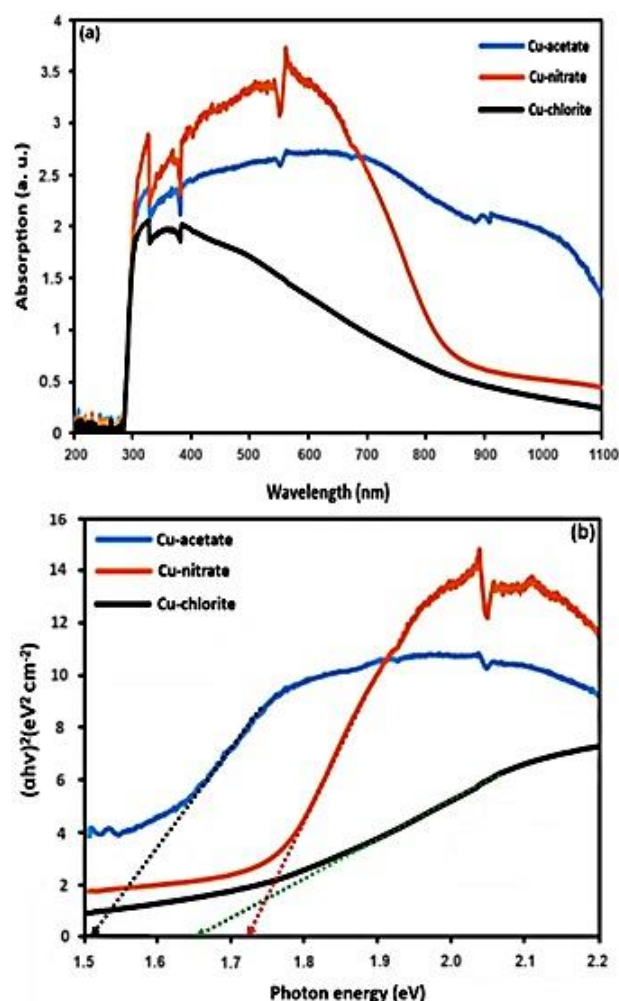
Figure 4. (a) UV–Visible absorption spectra of the synthesized CuO thin film samples Cu-acetate, Cu-nitrate, and Cu-chlorite, (b) Tauc curves of the synthesized samples.

3.3. Evaluation of Photocatalytic Studies

Photocatalytic actions of CuO thin films were scrutinized by degradation of MB dye under visible light radiation. Visible light radiation-induced swaps in the absorption spectrum of MB solution both for CuO thin film samples Cu-acetate, Cu-nitrate, and Cu-chlorite are given in Fig. 5 (a–c). The absorption at 664 nm is moderately impaired with increasing exposure time. The synthesized sample Cu-chlorite was observed to be the best photocatalyst and partially degraded MB in 150 min.

16
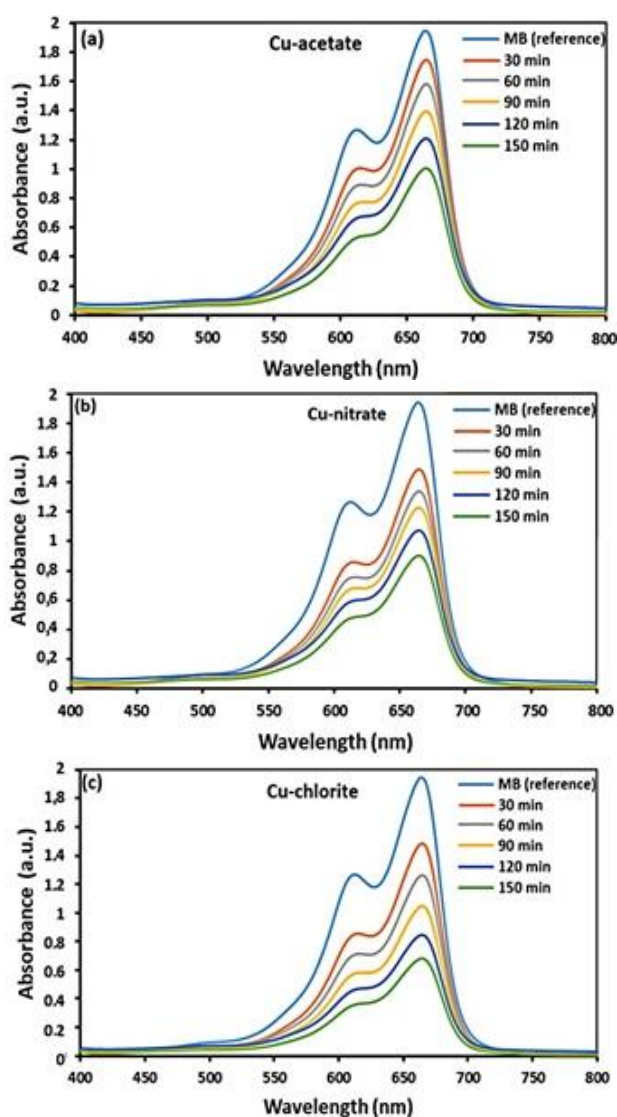
Figure 5. Absorption spectra of MB in the existence of CuO thin film samples Cu-acetate (a), Cu-nitrate (b), and Cu-chlorite (c).

Accordingly, the highest degradation ratio was observed in Fig. 5c. So, the highest MB degrade ratio was observed for the Cu-chlorite photocatalyst as its highest active surface area due to having nanorods-like shaped facet morphology and having relatively lower crystallite size. Therefore, the changes may be nearly same but the intensity variation is different by time for the used 3 samples.

The kinetics (C/Co versus time) of the photocatalytic degradation of MB by the synthesized CuO samples are exhibited in Fig. 6 (a). As can be seen from it, the C/Co ratio reduces according to the Cu-acetate, Cu-nitrate, and Cu-chlorite samples. A relatively fast reduction has been observed for the Cu-chlorite sample.

The first order rate constant for the degradation of MB was estimated by utilizing the formula [34]:

$$C/C_0 = \exp(-kt) \qquad (2)$$

where k reflects the rate constant, C and C_0 represent the first and final concentration of dye, respectively.

The rate constants for the degradation of MB by the CuO thin film photocatalysts such as Cu-acetate, Cu-nitrate, and Cu-chlorite are computed as 0.0078, 0.009 and 0.0114 min^{-1}, respectively (Fig. 6(b)). The variation in the efficacy of CuO thin films for MB degradation with the radiation time is exhibited in Fig. 6(c). The computed values according to the efficacy formula, described in our previous ref [34] are 52.50, 57.00, and 68.50 % for the Cu-acetate, Cu-nitrate, and Cu-chlorite film samples, respectively. These results show that CuO nanostructured thin film prepared by Cu-chlorite precursor is the most efficient photocatalyst for the solar-driven degradation of MB dye in water.

Figure 6. Variation in C/C_0 of MB with time for different photocatalysts under sunlight illumination (a), rate constant (b), and efficiency (c) of the prepared photocatalysts for the degradation of MB.

The rate constants for the degradation of MB by the CuO thin film photocatalysts such as Cu-acetate, Cu-nitrate, and Cu-chlorite are computed as 0.0078, 0.009 and 0.0114 min^{-1}, respectively (Fig. 6(b)). The variation in the efficacy of CuO thin films for MB degradation with the radiation time is exhibited in Fig. 6(c). The computed values according to the efficacy formula, described in our

previous ref [34] are 52.50, 57.00, and 68.50 % for the Cu-acetate, Cu-nitrate, and Cu-chlorite film samples, respectively. These results show that CuO nanostructured thin film prepared by Cu-chlorite precursor is the most efficient photocatalyst for the solar-driven degradation of MB dye in water.

4. DISCUSSION AND CONCLUSION

The D reduces by changing the Cu-source type and the D of the Cu-acetate sample has the highest value among all the prepared film samples. The ε and δ values of the film samples decrease by enhancement of the D values reflecting deterioration of the crystalline quality of the film samples with varying Cu-source type. A slight decrement in a lattice constant is observed due to the reduction of the D.

It is seen in the SEM measurement results that the grain sizes vary between approximately 100-400 nm. The observed different grain shapes were mainly attributed to the used Cu-source. The trend in grain size variation is nearly the same with the analysis of XRD showing a good agreement between the SEM and XRD results. However, it was determined that the grain sizes observed by SEM were larger than the crystal size calculated based on XRD data. This is due to grain sizes containing more than one crystallite [29]. Moreover, the thickness of the produced films is about 680 nm as seen in Fig. 2d, which corresponds to the Cu-acetate film sample.

According to the optical absorption of the films varies depending on the type of starting chemical exhibiting the starting chemical sources influence the light-capacity of the produced CuO thin film samples. The highest absorption in the visible region was observed for the film sample prepared with Cu-nitrate chemical co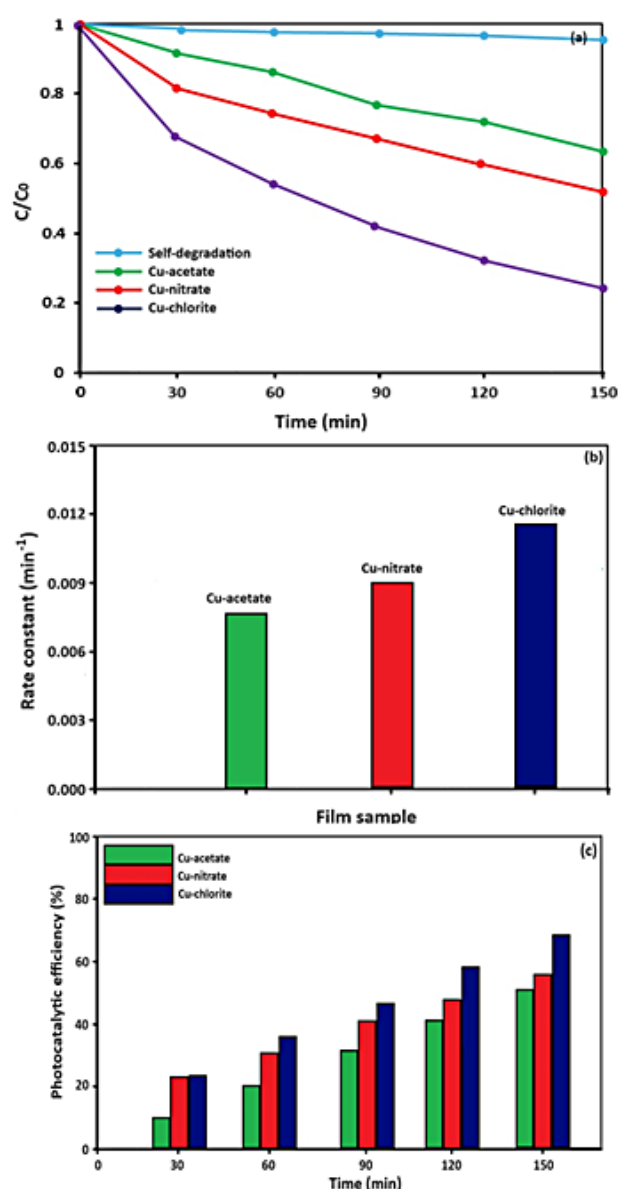mpared to the other film samples. On the other hand, among all the film samples the highest absorption at wavelengths higher than the visible region was observed in the film prepared with Cu-acetate precursor chemical. While the increase in optical absorption is directly related to the structure of the material, it is also closely related to the increase in crystal defects and the rate of crystallization [8, 30, 31]. It is understood from the absorption spectra that the absorption edge of the films varies depending on the type of starting chemical used.

The film samples show a narrow bandgap and permit good solar spectral absorption, leading to an increment of solar energy driven photocatalytic efficiency. The E_g values are in good agreement with previous reports on the CuO thin films [34].

The variations in the Figure 5 are depended on several factors and the decreasing in their intensity reflects the degradation of the MB within the MB dye solution. These factors are highly depending on the surface morphology and the crystallite size of the photocatalyst as well as the defect concentrations. It is expected the variations need to be same but the intensity of them should be decreased by time, reflecting degraded MB contents monotonically.

The possible procedure of dye degradation by CuO nanocrystalline thin film photocatalyst is diagrammatically exhibited in Fig. 7. In this mechanism, electrons are excited to the conduction band depending on the radiation of sunlight. The photo-induced electrons react with the O_2 absorbed creating superoxide radicals ($*O^{-2}$), whereas the holes interact with H_2O molecules and facet hydroxyl groups generating hydroxyl radicals ($*OH$). The ($*O^{-2}$) and $*OH$ radicals are accountable for the noticed dye degradation [35, 36].
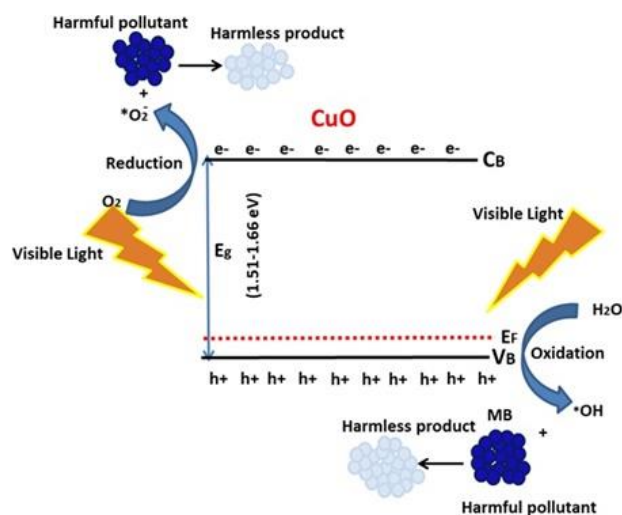
Figure 7. Proposed process of photocatalytic degradation of organic MB dye by CuO thin film.

The investigated characteristics such as optical, structural, and morphological have major influences on the photocatalytic activity of CuO nanostructures. The mean grain/crystallite size of CuO nanostructured thin film upon the sintering temperature and time [37–39]. The E_g, light absorption capability, crystallization and the facet area of CuO nanocrystalline thin films modify their photocatalytic activity.

Reduction in the E_g results in the uncomplicated movement of electrons in the CuO nanocrystalline, leading to an upgrade in the photocatalytic activity. Sahu et al. [25] reported that the CuO nanostructured thin film sintered at 400 °C exhibited better photocatalytic behavior as compared to other samples because of its smaller band gap and higher light absorption ability. In the present study, different surface areas due to different crystallite/grain sizes, narrow band gap, and increased use of light assisting better adsorption of MB dye molecule in the CuO nanocrystalline film synthesized by Cu-chlorite source are chiefly accountable for its relatively enhanced photocatalytic efficacy toward the degradation of MB dye in water.

In conclusion, the nanocrystalline CuO thin films were prepared using sol-gel dip coating technique and different Cu-chemical sources under air ambient. Depending on the used Cu-chemical sources, notable moderations in the surface morphology, optical, structural, and photocatalytic activity of CuO nanocrystalline thin film were found. CuO nanocrystalline thin film synthesized by Cu-chlorite source showed superb behavior for the photocatalytic debasement of MB dye in water. The

degradation of MB in the existence of Cu-chlorite nanocrystalline thin film sintered at 500 ℃ occurs in 150 min beneath sunlight radiation. The enhanced photocatalytic activity of the Cu-chlorite nanocrystalline thin film is ascribed to its relatively high surface area/low crystallite size, narrow E_g (1.66eV), refined usage of sunlight, and increased adsorption of MB dye owing to the increased formation of relatively higher active surface area of Cu-chlorite nanocrystalline at the film facet. The synthesized CuO nanocrystalline thin films can be used in photocatalytic degradation of harmful organic contaminants from wastewater because of their handle, economic, environmentally friendly, and stability.

Acknowledgement

REFERENCES

[1] Kwan I, Mapstone J. Visibility aids for pedestrians and cyclists: a systematic review of randomised controlled trials. Accid Anal Prev. 2004;36(3):305-12.

[2] Lachheb H, Puzenat E, Houas A, Ksibi E, Elaloui E, Guillard C, et al. Photocatalytic degradation of various types of dyes (alizarin S, crocein orange G, methyl red, congo red, methylene blue) in water by UV-irradiated titania. Appl. Catal B: Environ. 2002; 39:75-90.

[3] Goktas S, Goktas A. A comparative study on recent progress in efficient ZnO based nanocomposite and heterojunction photocatalysts: A review. J Alloy Compd. 2021; 863: 158734.

[4] Banazadeh A, Salimi H, Khaleghi M, Haghighi SS. Highly efficient degradation of hazardous dyes in aqueous phase by supported palladium nano catalyst-a green approach. J Environ Chem Eng. 2016; 4:2178-2186.

[5] Göktaş S, Aslan F. Kimyasal çöktürme yöntemiyle belirli karboksilik asitlerden organosiklotrifosfazen üretimi ve kimyasal özellikleri. Harran üniversitesi mühendislik dergisi, 2019; 4(3):19-28.

[6] Goktas A, Modanlı S, Tumbul A, Kilic A. Facile synthesis and characterization of ZnO, ZnO: Co, and ZnO/ZnO: Co nano rod-like homojunction thin films: Role of crystallite/grain size and microstrain in photocatalytic performance. J Alloy and Compd. 2022; 893:162334.

[7] Faisal M, Khan SB, Rahman MM, Jamal A, Asiri AM, Abdullah MM. Smart chemical sensor and active photo-catalyst for environmental pollutants. Chem Eng J. 2011; 173:178-184.

[8] Shariffudin SS, Khalid SS, Sahat NM, Sarah MSP, Hashim H. Preparation and characterization of nanostructured CuO thin films using sol-gel dip coating, IOP Conf Series: Mater. Sci. Eng. 2015:99;012007.

[9] Vikas P, Datta J, Shailesh P, Manik C, Prsad G, Sanjay P. Nanocrystalline CuO thin films for H2S

[10] Lidia A, Davide B, Manuel B, Gregorio B, Cinzia S, Eugenio T. A sol–gel approach to nanophasic copper oxide thin films, Thin Solid Films. 2003; 442:48–52.

[11] Jessica LR, Jorge M, Guerrero-V, María de LMG, Francisco S, Aguirre-Tostado et al. G, Gutiérrez H., Israel M-S., Amanda, CC. Optical and microstructural characteristics of CuO thin films by sol gel process and introducing in non-enzymatic glucose biosensor applications. Optik. 2021; 229:166238.

[12] Zaman S, Zainelabdin A, Amin G, Nur O, Willander M. Efficient catalytic effect of CuO nanostructures on the degradation of organic dyes. J Phys Chem Solids 2012; 73:1320-1325.

[13] Xu C, Sun J, Gao L, J Power Sources 2011;196:5138.

[14] Goktas S, Tumbul A, Goktas A. Growth technique–induced highly c-axis-oriented ZnO: Mn, ZnO:Fe and ZnO:Co thin films: a comparison of nanostructure, surface morphology, optical band gap, and room temperature ferromagnetism. J Supercond Nov Magn 2023;36: 1875.

[15] Bayansal F, Taşköprü, T Şahin B, Çetinkara HA. Effect of cobalt doping on nanostructured CuO thin films. Metall Mater Trans A. 2014; 45:3670.

[16] Şahin G, Göktaş S, Calculation of structural parameters and optical constants of size dependent ZrO2 nanostructures. GJES. 2024; 10(1)114–124.

[17] Goktas A, Role of simultaneous substitution of Cu2+ and Mn^{2+} in ZnS thin films: defects-induced enhanced room temperature ferromagnetism and photoluminescence. Phys. E: Low-Dimens. Syst. Nanostructures. 2020; 117:113828.

[18] Goktas A, High-quality solution-based Co and Cu co-doped ZnO nanocrystalline thin films: Comparison of the effects of air and argon annealing environments. J Alloy Compd. 2018;735: 2038-2045.

[19] Bensouici F, Bououdina M, Dakhel AA, Tala-Ighil R, Tounane M, Iratni A, et al. Optical, structural and photocatalysis properties of Cu-doped TiO2 thin films. Appl. Surf. Sci. 2017; 395:110–116.

[20] Goktas A, Modanlı S, Tumbul A, Kilic A. Facile synthesis and characterization of ZnO, ZnO: Co, and ZnO/ZnO: Co nano rod-like homojunction thin films: Role of crystallite/grain size and microstrain in photocatalytic performance. J. Alloy Compd. 2022; 893:162334.

[21] Mikailzade F, Önal F, Maksutoglu M, Zarbali M, Göktaş A. Structure and magnetization of polycrystalline La0.66Ca0.33MnO3 and La0.66Ba0.33MnO3 films prepared using sol-gel technique. J Supercond Nov Magn. 2018; 31:4141–4145.

[22] Mukherjee N, Show B, Maji SK, Madhu U, Bhar SK, Mitra BC, et al. CuO nano-whiskers: electrodeposition, Raman analysis, photoluminescence study and photocatalytic activity, Mater Lett. 2011; 65:3248–3250.

[23] Wang Y, Jiang T, Meng D, Yang J, Li Y, Ma Q, et al. Fabrication of nanostructured CuO films by

19

electrodeposition and their photocatalytic properties, Appl Surf Sci. 2014;317:414–421.

[24] Wang Y, Jiang T, Meng D, Jin H, Yu D. Controllable fabrication of nanowirelike CuO film by anodization and its properties. Appl Surf Sci. 2015; 349:636–643.

[25] Gao F, Zhu L, Li H, Xie H. Hierarchical flower-like CuO film: one-step room temperature synthesis, formation mechanism and excellent optoelectronic properties. Mater Res Bull. 2017; 93:342–351.

[26] Kavita S, Shipra Choudhar S, Khan A, Akhilesh P, Satyabrata M. Thermal evolution of morphological, structural, optical and photocatalytic properties of CuO thin films. Nano-Struct. Nano-Obj. 2019; 17:92–102.

[27] Komaraiah D, Sayanna R. Structural, optical properties and photocatalytic activity of spin-coated CuO thin films. Adv Nat Sci: Nanosci. Nanotechnol. 2023; 14:015006.

[28] Göktaş S, Sahin G. Methylene blue concentration and pH-induced photocatalytic degradation of methylene blue without photocatalyst under visible light. Inter. J Adv Nat. Sci. Eng. Res. 2023;7(6):176-181.

[29] Tumbul A, Aslan E, Göktaş A, Mutlu IH, Arslan F, Aslan F. Chemically derived quinary $Cu_2Co_{1-x}Na_xSnS_4$ photon absorber material and its photocatalytic application. Appl Phys A. 2024;130:225.

[30] Goktas A, Aslan F, Mutlu IH. Annealing effect on the characteristics of $La_{0.67}Sr_{0.33}MnO_3$ polycrystalline thin films produced by the sol–gel dip-coating process. J Mater Sci: Mater Electron. 2012; 23:605–611.

[31] Sekhar CR, Preparation of copper oxide thin film by the sol–gel-like dip technique and study of their structural and optical properties. Sol. Energy Mater. Sol. Cells. 2001; 68(3–4): 307.

[32] Goktas A, Aslan F, Tumbul A. Nanostructured Cu-doped ZnS polycrystalline thin films produced by a wet chemical route: the influences of Cu doping and film thickness on the structural, optical and electrical properties. J Sol-Gel Sci Technol. 2015; 75:45.

[33] Wang Z, Pischedda V, Saxena SK, Lazor P. X-ray diffraction and Raman spectroscopic study of nanocrystalline CuO under pressures, Solid State Commun. 2002; 121:275–279.

[34] Goktas A, Sol–gel derived $Zn_{1-x}Fe_xS$. Diluted magnetic semiconductor thin films: compositional dependent room or above room temperature ferromagnetism, Appl. Surf. Sci. 2015; 340:151-159.

[35] Göktaş S, Synergic effects of pH, reaction temperature, and various light sources on the photodegradation of methylene blue without photocatalyst: a relatively high degradation efficiency. Chem Africa. 2024; 1-13.

[36] Maryam K-S, Alireza N-E. Comparative study on the increased photoactivity of coupled and supported manganese-silver oxides onto a natural zeolite nanoparticle. J Mol Catal. A: Chem. 2016;(418–419):103-114.

[37] Goktas S, Metilen mavisi organik boyasinin güneş ışığında katalizörsüz yıkımı. Inter. Conf. Eng. Nat. Soc. Sci. 2023; 1, 364-367.

[38] Huang H, Tu S, Zeng C, Zhang T, Reshak HA, Zhang Y, Macroscopic polarization enhancement promoting photo-and piezoelectric-induced charge separation and molecular oxygen activation, Angew Chem Inter Ed. 2017;56:11860–11864.

[39] Goktas A, Aslan F, Mutlu IH. Effect of preparation technique on the selected characteristics of $Zn_{1-x}Co_xO$ nanocrystalline thin films deposited by sol–gel and magnetron sputtering. J. alloy compd. 2014; 615:765-778.

[40] Aslanoglu M, Goktas S, Karabulut S, Kutluay A. Cyclic voltammetric determination of noradrenaline in pharmaceuticals using poly (3-acetylthiophene)-modified glassy carbon electrode. Chem. Analityczna, 54(4), 643-653.

Türk Doğa ve Fen Dergisi
Turkish Journal of Nature and Science

Maybe a New Target for Gliomas: AQP1

Saniye Elvan ÖZTÜRK[1*] [iD]

[1] Aksaray University, Faculty of Science and Letters, Department of Molecular Biology and Genetics, Aksaray, Türkiye
Saniye Elvan ÖZTÜRK ORCID No: 0000-0003-4399-8299
Corresponding author: selvanozturk@aksaray.edu.tr

Abstract: Gliomas are the most common and aggressive tumors of the central nervous system, with poor prognosis. Studies on their diagnosis and treatment are critical. This study investigates the roles of Aquaporin family members, specifically AQP1 and AQP4, in gliomas using in silico methods. Expression levels of AQPs in Low-Grade Glioma (LGG) and Glioblastoma Multiforme (GBM) glioma subtypes were analyzed using GEPIA, UCSC Xena, Gliovis, cBioPortal, and Ivy GAP tools. Findings revealed that AQP1 and AQP4 expressions were significantly higher in tumor tissues compared to normal tissues in LGG and GBM datasets. Survival and prognosis analyses showed AQP1 levels were lower in the Oligodendrogram subtype of LGG, whereas both AQP1 and AQP4 levels were elevated in other subtypes. These results highlight AQP1 and AQP4 as key contributors to glioma pathogenesis and patient survival. While AQP4 is already known, AQP1 emerges as a potential novel biomarker or drug target for aggressive gliomas. Future studies should further explore its therapeutic potential.

21

Gliomlar için Belki Yeni Bir Hedef: AQP1

Öz: Gliomlar, merkezi sinir sisteminin en yaygın ve agresif tümörleridir ve prognozları genellikle kötüdür. Bu nedenle, gliomların tanı ve tedavisine yönelik çalışmalar büyük önem taşımaktadır. Bu çalışmada, in silico yöntemlerle Aquaporin ailesi üyeleri, özellikle AQP1 ve AQP4'ün gliomlardaki rolleri incelenmiştir. LGG ve GBM gliom alt tiplerinde AQP ekspresyon seviyeleri GEPIA, UCSC Xena, Gliovis, cBioPortal ve Ivy GAP analiz araçlarıyla değerlendirilmiştir. Bulgular, AQP1 ve AQP4 gen ekspresyonlarının LGG ve GBM veri setlerinde tümör dokularında normal dokulara kıyasla daha yüksek olduğunu göstermiştir. Sağkalım ve prognoz analizleri, AQP1 seviyelerinin LGG'nin Oligodendrogram alt tipinde düşük, diğer tüm alt tiplerde ise AQP1 ve AQP4 seviyelerinin yüksek olduğunu ortaya koymuştur. Bu sonuçlar, AQP1 ve AQP4'ün gliom patogenezi ve hasta sağkalımında önemli roller oynadığını göstermektedir. AQP4'ün yanı sıra AQP1 de agresif gliomlara karşı yeni bir biyobelirteç veya ilaç hedefi olarak değerlendirilebilir. Bu genlerin terapötik potansiyeli, gelecekteki çalışmalarda araştırılmalıdır.

1. INTRODUCTION

Gliomas, the most common tumors of the central nervous system, also make up 80% of the most deadly malignant brain tumors [1, 2]. It has been observed that the age, gender, ethnicity and other factors affecting the incidence vary between about 2-10/100,000 [3, 4]. When classified histopathologically, they can be divided up to 4 degrees, although they can generally be classified into low-grade gliomas (LGGs) (astrocytomas, oligodendrogliomas and oligoastrocytomas) and glioblastoma multiforme (GBMs) [5, 6]. LGG has a 5-year overall survival rate of approximately 60%, while GBM has a median survival of

14.6 months. Therefore, GBM can be described as the most aggressive brain tumor [5, 7]. Examining the survival based on grades, it has been shown that grade 4 has the worst rate among others and that approximately 7% of patients can survive in the next 5 years [8, 9]. Another bad news is that patients with a diagnosis of LGG may evolve to GBM within 5-10 years. During this process, many gene expression changes occur, and it is important to understand the course of the disease by monitoring their changes [10]. The most known glioblastoma markers have been studied as O-6-methylguanine-DNA methyltransferase (MGMT) promoter methylation, Epidermal growth factor receptor

(EGFR) changes, and isocitrate dehydrogenase 1 (IDH1) and isocitrate dehydrogenase 2 (IDH2) mutations [11, 12], but new genes need to be investigated and applied as biomarkers to accelerate the diagnosis and treatment of gliomas of varying degrees.

With the widespread use of RNA sequencing studies, it has become increasingly easy to monitor and compare changes in gene expression. When examined in terms of clinical oncology, the advantages of this situation are known in terms of discovering new genes effective in tumors, monitoring the effects of applied therapeutic agents and making discoveries related to tumor prognosis [13-15]. Differentially expressed genes (DEGs) are obtained after many bioinformatic analyses and database usage used to carry out these studies [16, 17]. It is obtained by examining the signal pathways and interaction networks of their effects on the tumor, after comparative examination of these obtained genes. New gene discoveries create new targets for tumors and thus new hopes for improved patient survival [18, 19].

Although it is known that aquaporins (AQP) can play different roles in various tissues, they are most commonly involved in water balance, as well as in fat metabolism, cell proliferation, migration and adhesion [20-22]. AQPs, which are water-selective transmembrane transport channel proteins, are a family of 13 proteins with high conservativity. Of these, only AQP1, AQP4 and AQP9 are found in the brain in mammals [23]. The AQP1 and AQP4 as classical aquaporins are selective for water, urea, gases, H_2O_2, ammonia, and charged particles. The AQP9 is one of the groups of listed as aquaglyceroporins and permeable for water, glycerol, and, in some cases, urea, lactate, or H_2O_2 [22].

Given the therapy-resistant nature of GBM and the potential for LGG to progress into GBM, it becomes imperative to emphasize research concerning these diseases and gain insight into potential drug target proteins and genes. One notable aspect of studies on differentially expressed genes is their capacity to pinpoint genes exhibiting distinct expression patterns between normal and tumor tissues. This capability facilitates comparative analysis and the identification of genes and proteins that exhibit significant variations, making them potential candidates for drug targeting.

Moreover, it's of utmost importance not only to spot individual genes with significant differences but also to identify those that are interconnected and collectively influential. Biological studies have established that proteins can compensate for each other's functions. Therefore, rather than concentrating solely on a single protein or gene, investigating pathways and interconnected genes that function in tandem is another crucial aspect of drug targeting.

The primary objective of this study is to assess the expression status of transmembrane transporter proteins like AQP1 and AQP4 in GBM and LGG, in conjunction with both individual and correlated known genes associated with these diseases. This comprehensive approach aims to provide a deeper understanding of potential drug targets.

2. MATERIAL AND METHOD

2.1. Gene Expression Analysis of AQP Family Genes in Glioma and Normal Tissues

The gene expression profiles of human aquaporins in LGG and GBM datasets were analyzed with the Gene Expression Profiling Interactive Analysis (GEPIA) platform (http://gepia.cance r- pku.cn/). Normal and tumor samples were compared to determine the differences [24]. Expression levels in tumors were assessed using The Cancer Genome Atlas (TCGA) dataset whereas transcript levels in healthy tissue samples were obtained from the Genotype Tissue Expression (GTEx) project. The cut-off of p value and fold change were defined as 0.05 and 1.5, respectively.

2.2. AQP1 and AQP4 Gene Expressions Based on Histology

Samples from the TCGA-LGG dataset were analyzed using the GlioVis (http://gliov is.bioin fo.cnio.es/) web application.18 AQP1 and AQP4 expressions in patients having different histologies were assessed and plotted as log2(norm_count+1). In the current analysis, 188 patients with Oligodendroglioma, 129 patients with Oligoastrocytoma, 193 patients with Astrocytoma and in total 510 patients were included in the expression query. Samples from the TCGA-GBM dataset (RNA-seq platform) were analyzed using the GlioVis (http://gliov is.bioin fo.cnio.es/) web application [25]. AQP1 and AQP4 expressions in patients having different histologies were assessed and plotted as log2 (norm_count+1). In the current analysis, 4 patients with non-tumor, 156 patients with GBM and in total 160 patients were included in the query.

2.3. AQP1 and AQP4 Transcript Level Analyses Based on Molecular Subtype

For glioma subtype analysis TCGA-LGG and TCGA-GBM datasets were used. TCGA- LGG dataset includes 85 patients with IDHmut-codel, 141 patients with IDHmut-non-codel, 55 patients with IDHwt subtypes, and in total 281 patients were included for this analysis. TCGA- GBM dataset includes 56 patients with Classical, 51 patients with Mesenchymal, 46 patients with Proneural subtypes and in total 156 patients were included for this analysis. Samples were analyzed using the GlioVis (http://gliov is.bioinfo.cnio.es/) web application [25].

2.4. Overall Survival Analyses of AQP1 and AQP4

Patients' overall survival Kaplan-Meier plots were drawn to the UCSC Xena browser using records of primary tumor samples obtained from the TCGA-LGG, TCGA-GBM and TCGA-GBMLGG cohorts. The median for each gene in the selected cohort was used for groups [26].

22

2.5. Correlation Analysis of AQP1 and AQP4 Gene Transcript Levels

Correlation between AQP1 and AQP4 transcript levels were determined by retrieving gene expression RNAseq illuminaHiseq data on primary tumors in the TCGA- LGG and TCGA- GBM cohorts from GlioVis. A log2(X + 1) transformed RSEM normalized count was depicted on both axes. Pearson tests were used for correlation analyses [25].

2.6. AQP4 Correlated Genes and Protein Interaction Analyses

AQP1 and 4 and their correlated genes (filtered by r>0.5 for AQP1 and r>0.6 for AQP4) were obtained from The Ivy Glioblastoma Atlas Project (IVY GAP) [27]. STRING v11.5 (Search Tool for the Retrieval of Interacting Genes) was used to examine protein–protein interaction networks [28]. Functional annotation analysis was performed using DAVID v6.7 (Database for Annotation, Visualization, and Integrated Discovery), which provides a comprehensive set of functional annotation tools to understand the biological significance associated with large lists of genes or proteins [29].

2.7. Statistical Analysis

GraphPad Prism 9 was used for statistical analysis in the study. Kruskal Wallis test was applied for comparisons between groups, and Dunn's post hoc test was applied for multiple comparisons. Comparison between two groups was made using Student's t-test. All values are represented as mean ± SD.

Kaplan–Meier curves were plotted using the UCSC Xena database. The difference between the curves was determined by the Log-rank test. Correlation analysis was performed by calculating Pearson correlation coefficients. $p < 0.05$ indicates statistical significance.

3. RESULTS

3.1. The Expressions of AQP1 & AQP4 in Different Human Cancers

The expression levels of AQP1 were observed as increased in tumor tissues of Cholangio carcinoma (CHOL), Glioblastoma multiforme (GBM), Brain Lower Grade Glioma (LGG), Liver hepatocellular carcinoma (LIHC), Pancreatic adenocarcinoma (PAAD), Pheochromocytoma and Paraganglioma (PCPG), Stomach adenocarcinoma (STAD), Testicular Germ Cell Tumors (TGCT) and Thymoma (THYM) (Figure 1A). AQP4 was found to be higher in tumor tissue in CHOL, GBM, LGG, PCPG, THYM and Uterine Carcinosarcoma (UCS) human cancer types (Figure 1B).

As a result of the comparison of the expressions of the AQP family genes in the brain parts, although the cerebellar hemisphere and cerebellum are slightly different from the other parts, in general, it has been observed that AQP1 and AQP4 show very high activity in almost all brain regions (Figure 1C). The most striking difference in the cerebellar hemisphere and cerebellum is the higher expression of AQP7 compared to other brain tissues.

23
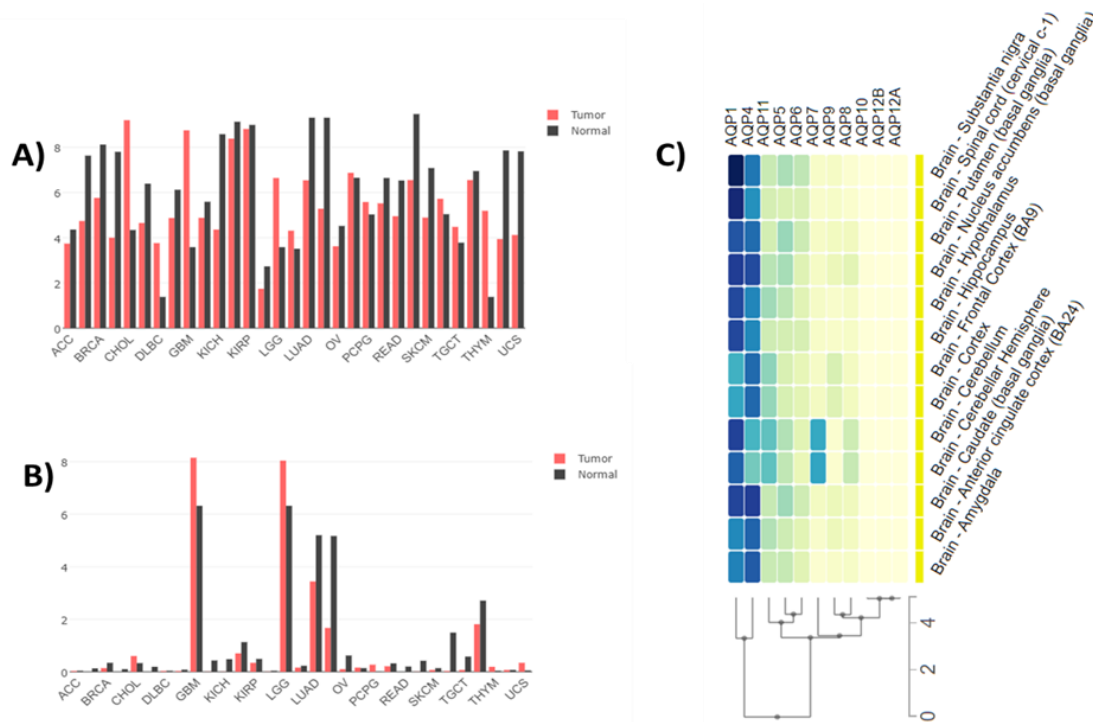
Figure 1. (A) AQP1 and **(B)** AQP4 expression levels in Human Cancers by GEPIA. **(C)** Comparison of the expressions of AQP family genes in brain regions using GTEx portal.

3.2. AQP Family Genes in LGG and GBM Platforms Have Different Expression Results in Glioblastoma and Normal Tissue Samples

It is known that intercellular and intracellular traffic is very rapid in cancer. One of the protein families responsible for these traffics is aquaporins. Depending on the increase in cancer cell activities, the increase of these proteins, which are responsible for transport, may be specific to some types of cancer or cancer tissues. Considering this situation, it aims to establish a

relationship by looking at the expression rates of AQP family genes in glioblastoma cancers and their significance levels.

In the expression profiles comparison, it is observed that the gene expression levels of AQP1 and AQP4 are highly expressed in both LGG and GBM datasets compared to the others (Figure 2). It is observed that the amount of AQP1 in tumor tissue is quite significant compared to normal tissue. According to Figure 2, AQP11 is another highly expressed aquaporin after AQP1 and AQP4.

Figure 2. The expression profiles of human AQP1-12 (12A and 12B) in LGG and GBM platforms. The transcript levels of AQP family members in LGG and GBM tumors and normal tissues were analyzed using the GEPIA database.

Considering the significance of expression levels of AQP genes in tumor and normal tissues in LGG and GBM datasets, AQP1 and AQP4 seem to be remarkable in both datasets. Figure 3 (A-M) shows the differential expression levels of all AQP genes in LGG and GBM datasets. Figure 5A (AQP1) and Figure 3D (AQP4) were statistically

significantly higher in tumor tissue than in normal tissue. Although AQP5 and AQP6 were higher in tumor tissue in both datasets, the results were not statistically significant. AQP7,8,11,12A and 12B appear to be higher in normal tissue, but the results are also not statistically significant in these groups. Overall, these data highlight the possible roles of AQP1 and AQP4 in glioma progression.
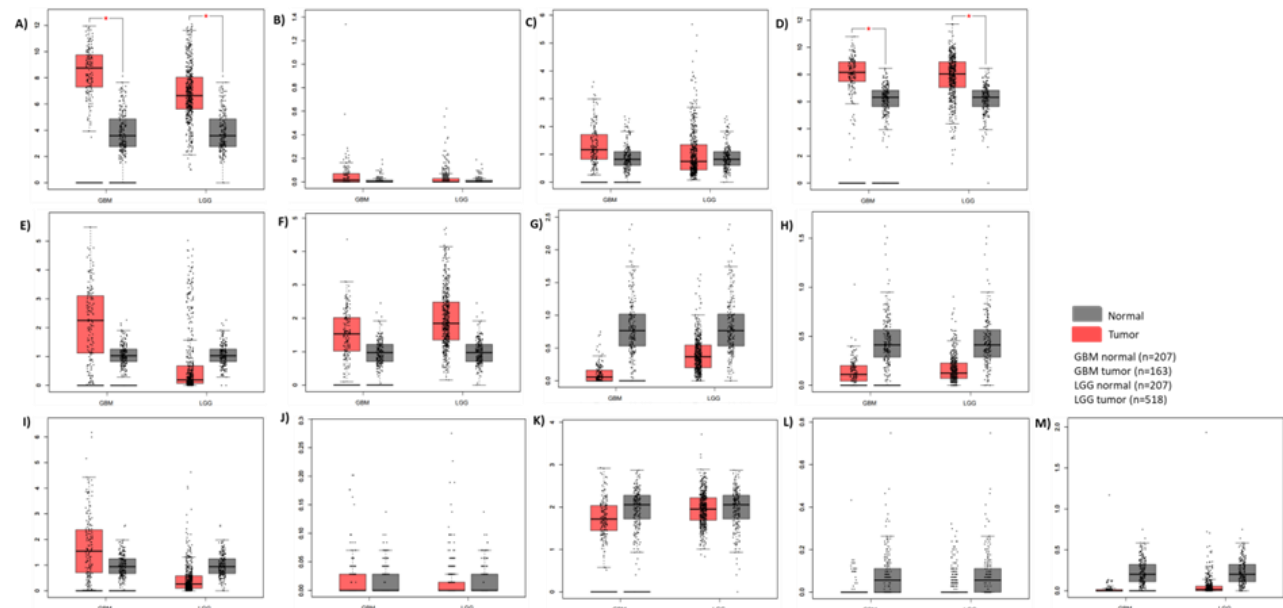
Figure 3. The differential expressions of AQP family members in LGM and GBM tumor tissues compared to normal counterparts. The expression levels of AQPs in LGM and GBM were analyzed using the GEPIA database. Box plots showing the expression profile of (A) AQP1, (B) AQP2, (C) AQP3, (D) AQP4, (E) AQP5, (F) AQP6, (G) AQP7, (H) AQP8, (I) AQP9, (J) AQP10, (K) AQP11, (L) AQP12A, (M) AQP12B in tumor and healthy tissues. The asterisk (*) shows statistical significance ($p<0.05$).

3.3. High AQP1 and Low AQP1 in GBM & Low AQP1 and AQP4 in LGG are related with better prognosis

To assess the prognostic values of the AQP1 and AQP4 genes in two different datasets (GBM and LGG), Kaplan-Meier plots were generated to visualize the overall survival (OS) patterns (Figure 4). It was observed that increased AQP1 expression in the GBM dataset (Figure 4A) had a positive impact on the overall survival curve. Similarly, the effect of AQP4 on overall survival in the GBM dataset was found to contribute (Figure 4B). In the overall survival plots of the LGG dataset, lower gene expression levels for both AQP1 and AQP4 were associated with longer OS (Figure 4C-D).
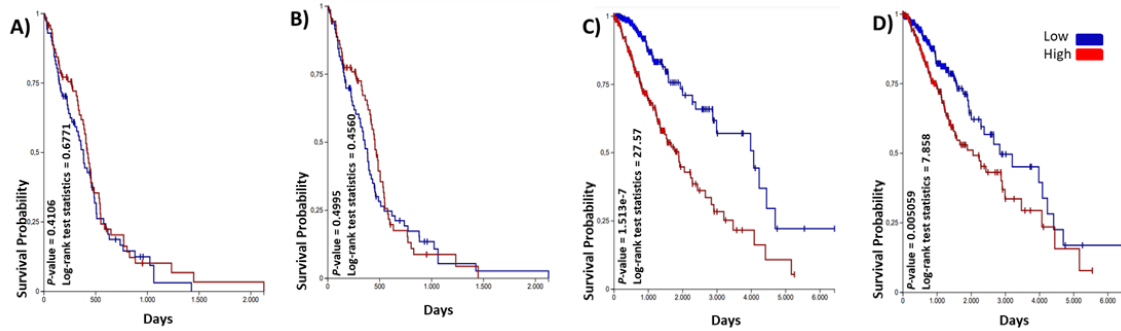
Figure 4. AQP1 and AQP4 effect on overall survival in TCGA-GBM and TCGA-LGG datasets. A) AQP1 GBM overall survival, B) AQP4 GBM overall survival, C) AQP1 LGG overall survival, D) AQP4 LGG overall survival

3.4. The Expression Patterns of AQP1 and AQP4 in Datasets Based on Histology, Subtypes and Grade of Glioma

The GBM dataset was analyzed histologically and subtype-based in terms of AQP1 and AQP4 gene expressions. The histology-based analysis of AQP1 expression showed a statistically significant difference between the non-tumor and tumor groups (Figure 5A). However, there was no significant change in AQP4 mRNA expression between the non-tumor and tumor groups (Figure 5C).

Subtype-based analyses were also conducted, yielding controversial results. According to Figure 5B, there was no statistically significant difference in the expression ratios of AQP1 among the subtypes. However, AQP4 displayed significant differences between the subtype groups. Notably, the Classical and Mesenchymal subtypes exhibited a significant difference in AQP4 expression ($p<0.01$) (Figure 5D). The most significant difference was observed between the Classical and Preneural groups ($p<0.01$).
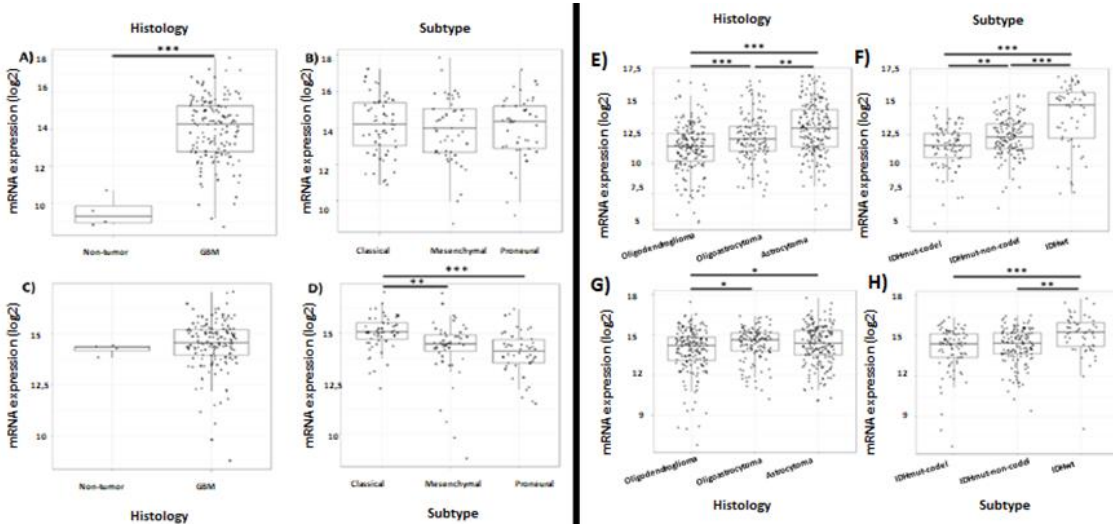
Figure 5. The expression results of AQP1 and AQP4 genes in the TCGA-GBM dataset by using the GlioVis platform. A) AQP1 gene expressions result in histology-based, B) AQP1 gene expressions result subtype-based, C) AQP4 gene expressions result in histology-based, D) AQP4 gene expressions result subtype-based. The expression results of AQP1 and AQP4 genes in the TCGA-LGG dataset by using the GlioVis platform. E) AQP1 gene expressions result in histology-based, F) AQP1 gene expressions result subtype-based, G) AQP4 gene expressions result in histology based, H) AQP4 gene expressions results subtype based. The table shows the difference between pairs, the 95% confidence interval and the p-value of the pairwise comparisons. ***$p<0.001$; **$p<0.01$. Not significant results were not shown on graphics. No significant results were not shown on graphics.

The analysis of the LGG dataset yielded highly satisfactory results. At least two subgroups in the graphs displayed significant values, particularly in the case of AQP1 gene expression. Significant values were observed in every comparison, both in terms of histology and subtype (Figure 5E and F). Although AQP4 showed lower statistics in histology-based analyses, two comparisons yielded significant results, except for the Oligoastrocytoma and Astrocytoma comparison (Figure 5G). In the subtype-based analysis, comparing the

25

presence of wild-type and mutated status for the AQP4 gene expression level revealed significant results in both cases (Figure 5H).
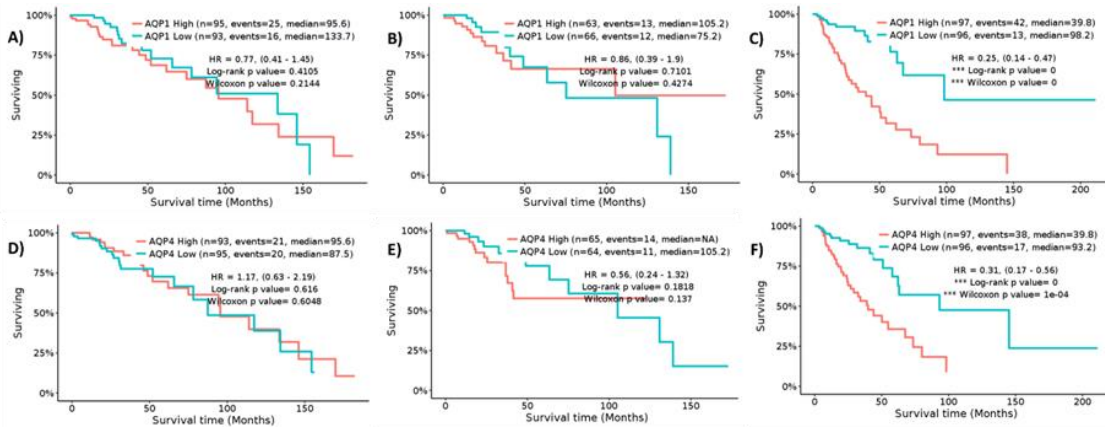
Figure 6. The survival graphics of histology-based LGG dataset A) Oligodendroglioma-AQP1 B) Oligoastrocytoma-AQP1 C) Astrocytoma-AQP1 D) Oligodendroglioma-AQP4 E) Oligoastrocytoma-AQP4 F) Astrocytoma-AQP4.
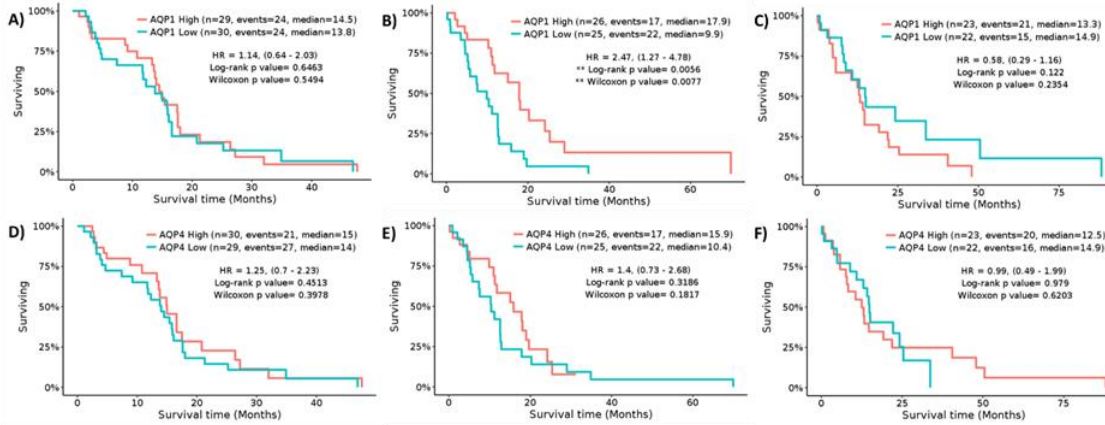
Figure 7. The survival graphics of histology GBM subtype based GBM dataset A) Classical-AQP1 B) Mesenchymal-AQP1 C) Proneural-AQP1 D) Classical-AQP4 E) Mesenchymal-AQP4 F) Proneural-AQP4.

3.5. Correlation of the AQP1 and AQP4 gene expression levels in TCGA-GBM and TCGA-LGG datasets

The correlation of the expression levels of the AQP1 and AQP4 genes was investigated in the TGCA-GBM and TCGA-LGG datasets. In the TCGA-GBM dataset, a lower gene expression correlation value was obtained with r=0.46 (Figure 8A). The correlation between AQP1 and AQP4 was relatively higher in the TCGA-LGG dataset (Figure 8B).
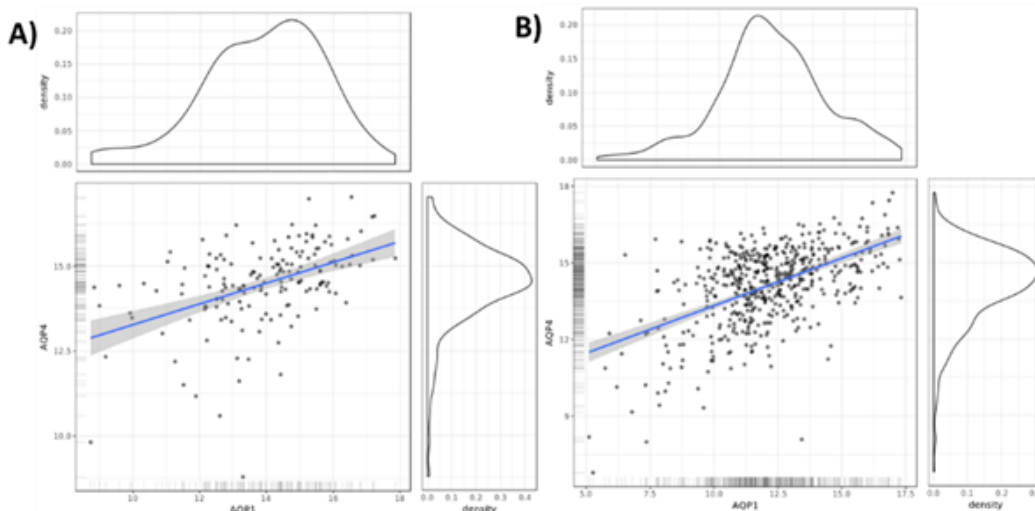
Figure 8. Correlation of AQP1 and AQP4 levels in A) TCGA_ GBM (r= 0.46) and B) TCGA_ LGG (r= 0.53) datasets. Pearson's test was used for correlation analyses.

26

3.6. AQP1, AQP4 and their correlated genes and their protein interaction analyses

Genes correlated with AQP1 (r=0.5) and AQP4 (r=0.6) were listed separately by The Ivy Glioblastoma Atlas Project. The 86 genes were listed for AQP1, while 100 genes were listed for AQP4. The DAVID tool was used to search for the functional annotations of these lists. Thus, the roles of genes that are separately correlated with AQP1 and AQP4 in cellular components, molecular function and biological processes have been annotated.

As expected in the cellular component analysis, cell membrane and membrane-related parts were more enriched for both AQP1 and AQP4 (Table 1 and Table 2).

After analyzing the results of the Cellular component analysis of AQP1 and its correlated genes, several prominent locations were identified. The Plasma membrane, Endosome, Integral component of the plasma membrane, Extracellular region, and Extracellular space were found to be the major cellular components, each constituting more than 10 percent of the total (Table 1). The Membrane and Cell membrane were listed as the major cellular components of AQP4 and correlate (Table 2). Although p-value<0.05 for both aquaporins in Molecular Function and Biological Process results, enrichment scores were listed as quite high. Of these, only AQP1's Cell Adhesion, listed in Biological Process, was able to exceed the 10 percent limit (Table 1).

Table 1. Functional annotation of AQP1 and its correlated proteins functional annotation results with DAVID (2023q2). (Red marked ones are significant in terms of p-value and/or enrichment score values are less than 0.05.)

| Category	Term Name	Count (%)	PValue	Enrichment Score
CELLULAR COMPONENT	Plasma membrane	36 (46,8)	5,70E-05	9,00E-03
	Endosome	7 (9,1)	1,00E-03	8,10E-02
	An integral component of plasma membrane	14 (18,2)	1,70E-03	8,90E-02
	Extracellular region	17 (22,1)	4,10E-03	1,60E-02
	Extracellular space	15 (19,5)	9,60E-03	2,70E-02
	Neuronal cell body	6 (7,8)	1,00E-02	2,70E-02
	Basolateral plasma membrane	5 (6,5)	1,30E-02	2,80E-02
	Extracellular matrix	5 (6,5)	1,40E-02	2,80E-02
	Astrocyte end-foot	2 (2,6)	1,80E-02	3,10E-02
	Caveola	3 (3,9)	3,00E-02	4,40E-02
	Membrane	21 (27,3)	3,00E-02	4,40E-02
	Perineuronal net	2 (2,6)	3,50E-02	4,70E-02
	Neuron projection	5 (6,6)	4,30E-02	5,10E-02
	Perinuclear region of cytoplasm	7 (9,1)	4,80E-02	5,10E-02
	Lysosomal lumen	3 (3,9)	4,80E-02	5,10E-02
	Integral component of membrane	27 (35,1)	5,50E-02	5,30E-02
	Golgi lumen	3 (3,9)	5,70E-02	5,30E-02
	Filopodium membrane	2 (2,6)	6,30E-02	5,50E-02
	Filopodium tip	2 (2,6)	7,30E-02	6,10E-02
	Extracellular exosome	13 (16,9)	9,60E-02	7,70E-02
MOLECULAR FUNCTION	Glyceraldehyde-3-phosphate dehydrogenase (NAD+) (non-phosphorylating) activity	2 (2,6)	2,60E-02	1,00E+00
	Water transmembrane transporter activity	2 (2,6)	2,60E-02	1,00E+00
	Beta-amyloid binding	2 (2,6)	4,20E-02	1,00E+00
	GTPase activating protein binding	2 (2,6)	5,60E-02	1,00E+00
	Aldehyde dehydrogenase (NAD) activity	2 (2,6)	5,60E-02	1,00E+00
	Water channel activity	2 (2,6)	6,30E-02	1,00E+00
	Peptidase inhibitor activity	2 (2,6)	7,30E-02	1,00E+00
	Semaphorin receptor binding	2 (2,6)	8,40E-02	1,00E+00
	Hyaluronic acid binding	2 (2,6)	9,10E-02	1,00E+00
	Phosphatidylinositol phospholipase C activity	2 (2,6)	9,40E-02	1,00E+00
	Channel activity	2 (2,6)	9,40E-02	1,00E+00
	Inward rectifier potassium channel activity	2 (2,6)	9,40E-02	1,00E+00
BIOLOGICAL PROCESS	Cell adhesion	9 (11,7)	1,20E-03	7,80E-01
	Skeletal system development	4 (5,2)	1,40E-02	1,00E+00
	Cell migration	5 (6,5)	2,00E-02	1,00E+00
	Retina development in camera-type eye	3 (3,9)	2,10E-02	1,00E+00
	Cellular water homeostasis	2 (2,6)	2,60E-02	1,00E+00
	Hippocampus development	3 (3,9)	2,80E-02	1,00E+00
	Negative regulation of neuron projection development	3 (3,9)	2,80E-02	1,00E+00
	Intracellular signal transduction	6 (7,8)	2,90E-02	1,00E+00
	Potassium ion transport	3 (3,9)	3,30E-02	1,00E+00
	Alpha-linolenic acid metabolic process	2 (2,6)	3,70E-02	1,00E+00
	Bergmann glial cell differentiation	2 (2,6)	4,10E-02	1,00E+00
	Multicellular organismal water homeostasis	2 (2,6)	4,10E-02	1,00E+00
	Cell cycle	5 (6,5)	4,70E-02	1,00E+00
	Adaptive thermogenesis	2 (2,6)	4,80E-02	1,00E+00
	Carbon dioxide transport	2 (2,6)	5,10E-02	1,00E+00
	Synapse maturation	2 (2,6)	5,90E-02	1,00E+00
	Sodium ion transmembrane transport	3 (3,9)	6,80E-02	1,00E+00
	Renal water homeostasis	2 (2,6)	6,90E-02	1,00E+00
	Positive regulation of neuron projection development	3 (3,9)	7,20E-02	1,00E+00
	Water transport	2 (2,6)	8,30E-02	1,00E+00
	Glial cell differentiation	2 (2,6)	8,60E-02	1,00E+00
	Potassium ion transmembrane transport	3 (3,9)	8,90E-02	1,00E+00
	Ion transport	3 (3,9)	9,80E-02	1,00E+00

*Red lines are statistically significant groups ($p<0.05$).

27

Table 2. Functional annotation of AQP4 and its correlated proteins functional annotation results with DAVID (2023q2). (Red marked ones are significant in terms of p-value and/or enrichment score values are less than 0.05.)

Category	Term Name	Count (%)	PValue	Enrichment Score
CELLULAR COMPONENT	Membrane	63 (68,5)	3,20E-07	7,30E-06
	Cell membrane	40 (43,5)	7,00E-07	8,10E-06
	Microsome	4 (4,3)	1,80E-02	1,40E-01
	Cytoskeleton	12 (13)	5,90E-02	3,40E-01
	Endoplasmic reticulum	11 (12)	1,00E-01	4,60E-01
MOLECULAR FUNCTION	Developmental protein	12 (13)	9,20E-03	1,50E-01
	Developmental protein	12 (13)	9,20E-03	1,50E-01
	Actin-binding	6 (6,5)	1,30E-02	1,50E-01
	Ion channel	6 (6,5)	3,40E-02	1,00E-02
BIOLOGICAL PROCESS	Cell adhesion	9 (9,8)	2,80E-03	6,30E-02
	Symport	5 (5,4)	2,90E-03	6,30E-02
	One-carbon metabolism	3 (3,3)	4,40E-03	6,40E-02
	Transport	19 (20,7)	1,10E-02	1,10E-01
	Neurogenesis	6 (6,5)	1,40E-02	1,10E-01
	Ion transport	9 (9,8)	1,50E-02	1,10E-01
	Differentiation	8 (8,7)	8,40E-02	5,30E-01

*Red lines are statistically significant groups ($p<0.05$).

The common 31 genes in both AQP1 and AQP4-related gene lists were examined for protein-protein interactions using the STRING database. The most interacted genes with AQP1 and AQP4 were ADCYAP1R1, KCNJ16, FAM107A, ALDH1L1, S100B in Figure 9A. In addition, GPR56 and TSAPN3 were also associated with each other.
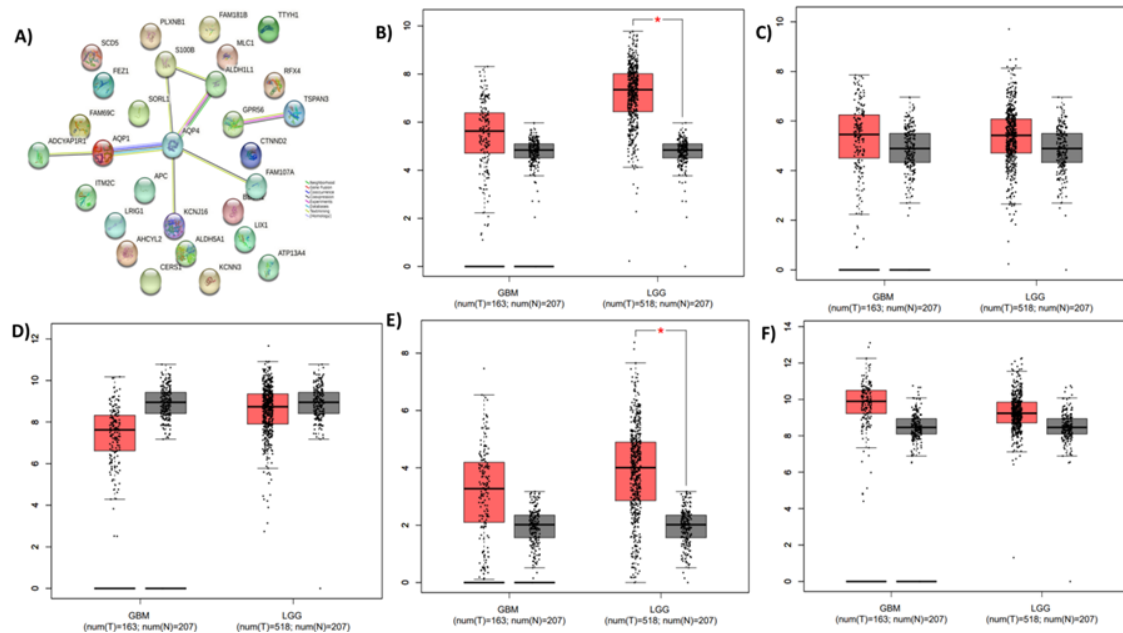
Figure 9. Common AQP1 and AQP4 related genes and their interaction and expression values. A) Protein-protein interactions of common genes in the list of AQP1 and AQP4 correlated genes using STRING v11.5. Most interacted genes with AQP1&4 were selected for further analyses. The expression pattern of (B) ADCYAP1R1, (C) ALDH1L1, (D) FAM107A, (E) KJN16 and (F) S100B in GBM and LGG datasets using the GEPIA database. The asterisk (*) shows statistical significance ($p<0.05$).

4. DISCUSSION AND CONCLUSION

Discussion

Among the central nervous system tumors in humans, diffuse gliomas are the most common. These include GBM (associated with poor prognosis) and LGGs (associated with better prognosis) that are at risk of developing into GBM in the future. Changes in many genes and molecular pathways are required for this differentiation [10]. In this study, the changes of AQP1 and AQP4 between LGG and GBM were compared and whether they could be used as biomarkers and/or therapeutic targets was investigated. Individuals with GBM have much shorter overall survival periods than those with LGG because of factors such as fast development, high invasiveness, and resistance to treatment [30]. LGG also leads to the secondary subtype of GBM, which contains primary and secondary subtypes. Previous researches have also revealed that IDH mutation, TP53 mutation, and 19q deletion are some of the most prevalent modifications in the creation of the secondary type [12, 14, 31]. Although there may be similarities between LGG and GBM in terms of gene expression, there are also very significant differences, as shown above. Therefore, it is important to recognize these differences and investigate biomarkers and potential therapeutic targets.

Although ion channel pharmacology has been used in the clinic for a long time, the idea of aquaporins being used in the clinic is still a developing idea [32-34]. In this study, which focused on the classical AQPs, AQP1 and AQP4, the expression levels of both genes in different cancer types were examined (Figure 1). Accordingly, it shows that both AQP1 and AQP4 are highly expressed in tumor tissue in GBM and LGG types (Figure 1A). On the other hand, since both cancers are glioma types, the expression status of the members of the aquaporin family in the brain was compared (Figure 1B). The results obtained show that the expression of AQP1 and AQP4 are aquaporins that are actively used in almost all tissues of the brain. AQP11 is right next to it. However, it has been observed that two regions of the brain (brain-cerebellum and brain-cerebellar hemisphere) can be targeted by AQP7, which is highly expressed in these regions. Therefore, while AQP1 and AQP4 can be used in studies that can target almost the entire brain, it is thought that AQP7 can be used more specifically in targeting these two regions of the brain.

While the aquaporins associated with the brain are AQP1-AQP4-AQP9 according to the literature, when the expression levels of aquaporins in LGG and GBM datasets are examined in our study, it is striking that the ones with the highest expression are AQP1-AQP4 and AQP11 (Figure 2). Unlike the others in the LGG and GBM datasets, AQP9 was observed to be higher in normal tissue in LGG and tumor tissue in GBM.

When the significance of gene expression levels of the AQP family in GBM and LGG were compared, it was found that only the expression levels of AQP1 (Figure 3A) and AQP4 (Figure 3D) differed significantly in tumor and normal tissue comparisons. It has been shown that this significant difference is found to be higher in tumor tissue than in normal ones.

In this study, in which the effects of the above-mentioned two genes on the overall survival graphs of the patients were also examined, it was found that AQP1 and AQP4 did not have significant effects in GBM-type glioma (Figure 4A-B). On the other hand, when looking at the LGG type, it was observed that there were relatively positive effects on overall survival in scenarios where the expression of both genes was low (Figure 4C-D).

It was investigated whether there was a significant difference between AQP1 and AQP4 gene levels for both GBM and LGG datasets in histology and subtype levels (Figure 5). According to the data obtained, it was observed that a very significant (p<0.001) difference in the GBM dataset of AQP1 was only in the histology-based set. In the same histology-based set, no significant difference was observed for AQP4. When the subtype-based set was analyzed in the GBM dataset, it was observed that the expression of AQP4 showed significant variation between Classical and Mesenchymal subtypes and between Classical and Preneural subtypes. The Classical subtype was observed to have higher expression levels than the other subtypes. As a result of the analysis of the LGG dataset, it was found that almost all groups

showed significant differences for both AQP1 and AQP4 genes. It was observed that AQP1 was expressed lower in Oligodendrograms and had increased expression status in other histological groups. In the groups with IDH-wt, both genes were found to have higher expression compared to the other groups.

The amount of AQP1 and the degree of malignancy were also strongly correlated by Saadoun et al (2002)[35]. As observed in the astrocytoma group, where there was a significant difference based on histological subtype for AQP1 and AQP4 in the LGG dataset, survival was higher in the scenario with low expression of AQP1 and AQP4. Apart from these, no significant effect was found in other subtypes (Figure 6). When the same study was performed on the GBM dataset, it was observed that the high level of AQP1 could be associated with patient survival only in the Mesenchymal type. According to these findings, there is a significant difference in AQP1 levels between the relatively early stages of the disease (LGG dataset) and the late stage of the disease (GBM dataset). AQP1 water channel blockers could therefore be used as potent anti-brain tumor edema agents, according to several groups [35-37]. However, according to our study, besides being used as edema agents, it can prolong patient life by increasing survival. By using this change in gliomas due to disease progression, drug targeting or changing AQP1 expressions can affect prognosis and survival.

When the common genes associated with AQP1 and AQP4 were examined, it was observed that the expression of 31 genes changed. It was found that 5 of them were directly related to AQP1 and AQP4 proteins at the protein level. These are ADCYAP1R1, ALDH1L1, FAM107A, KJN16 and S100B. When the expression levels of these 5 genes in the LGG and GBM datasets were examined, it was observed that only the expressions of ADCYAP1R1 and KJN16 changed significantly in the LGG dataset.

Spence and his friends have found that ADCYAP1R1 has a QTL background for inheritance in their rat studies. Both AQP1 (7p15-->p14)[38] and ADCYAP1R1 (7p14.3)[39] genes are located on chromosome 7 in humans. Therefore these two genes may be inherited together and possibly have roles in similar mechanisms. ADCYAP1R1 is a G-coupled protein on the plasma membrane responsible for controlling human stress responses [40, 41] and also this protein was considered as a prognostic marker for gliomas in 2020 [42]. Considering that AQP1 may play a similar role, it can be thought that the increases that occur at the level of these two genes in tumor conditions are to protect glial cells from the stress conditions caused by the tumor.

KJN16 gene encodes a channel protein named Kir5.1. This protein is mainly responsible for potassium homeostasis and pH-electrolyte balances [43]. Possible mutations on this gene cause several disorders such as hypercapnia/hypoxia, and seizure. To explain it from the perspective of our study, statistically significant results in gliomas of this gene, which was previously thought to have therapeutic potential [43] in other studies, were observed. Its mutation status in gliomas and their

29

contributions to gliomas can be investigated in more detail and its use as a drug target can be examined.

In summary, it has been found that AQP1, like AQP4, has effects on gliomas, with significant differences, especially in the LGG type. Conditions with lower AQP1 and AQP4 levels are more favorable for disease progression. Therefore, it has been shown that AQP1 can be used as a therapeutic target in common glioma studies. Therefore, this study will be a starting point for further studies.

CONCLUSION

This study conducted a systematic bioinformatics analysis of DEGs between LGG and GBM. Notably, it observed differential expression of AQP1 and AQP4 aquaporin family members in diffuse gliomas for the first time. Furthermore, it revealed significant differences in the associations of expression levels according to different subtypes among aquaporins. In the LGG subtype, low expression of AQP1 and high expression of ADCYAP1R1 gene, which is correlated with AQP1, has been shown to be advantageous in terms of survival. However, in the GBM dataset, high expression of AQP1 is associated with increased survival in mesenchymal types. Based on these findings, it can be concluded that AQP1 is more promising than AQP4 in terms of being a treatment target and usability as a prognostic marker. While this study, which analyzes existing data from the literature, offers valuable insights into the potential of aquaporins as drug targets and markers, further experimental verification studies are needed.

Author contributions
SEO: Conceptualization, data analysis, and manuscript writing.

Conflict Of Interest
The authors declare that they have no competing interests.

Ethical Statement
Not applicable.

Funding
This study did not receive any funding from a particular source.

Consent to participate
Not applicable.

Consent for publication
Not applicable.

Data Availability Statement
The manuscript contains all data supporting the reported results. The raw data used in this study are available online in the GTEx, TCGA LGG, TCGA GBM cohorts and Rembrandt dataset. Additional questions can be directed to the relevant author(s).

REFERENCES

[1] Ostrom, Q.T., et al., CBTRUS Statistical Report: Primary Brain and Other Central Nervous System Tumors Diagnosed in the United States in 2011-2015. Neuro Oncol, 2018. 20(suppl_4): p. iv1-iv86.

[2] Louis, D.N., et al., The 2021 WHO Classification of Tumors of the Central Nervous System: a summary. Neuro Oncol, 2021. 23(8): p. 1231-1251.

[3] Molinaro, A.M., et al., Genetic and molecular epidemiology of adult diffuse glioma. Nat Rev Neurol, 2019. 15(7): p. 405-417.

[4] Ostrom, Q.T., et al., The epidemiology of glioma in adults: a "state of the science" review. Neuro Oncol, 2014. 16(7): p. 896-913.

[5] Claus, E.B. and P.M. Black, Survival rates and patterns of care for patients diagnosed with supratentorial low-grade gliomas: data from the SEER program, 1973-2001. Cancer, 2006. 106(6): p. 1358-63.

[6] Venneti, S. and J.T. Huse, The evolving molecular genetics of low-grade glioma. Adv Anat Pathol, 2015. 22(2): p. 94-101.

[7] Perry, J.R., et al., Short-Course Radiation plus Temozolomide in Elderly Patients with Glioblastoma. N Engl J Med, 2017. 376(11): p. 1027-1037.

[8] Ostrom, Q.T., et al., CBTRUS Statistical Report: Primary Brain and Other Central Nervous System Tumors Diagnosed in the United States in 2012-2016. Neuro Oncol, 2019. 21(Suppl 5): p. v1-v100.

[9] Sant, M., et al., Survival of European patients with central nervous system tumors. Int J Cancer, 2012. 131(1): p. 173-85.

[10] Dubois, L.G., et al., Gliomas and the vascular fragility of the blood brain barrier. Front Cell Neurosci, 2014. 8: p. 418.

[11] Dahlrot, R.H., et al., Prognostic value of O-6-methylguanine-DNA methyltransferase (MGMT) protein expression in glioblastoma excluding nontumour cells from the analysis. Neuropathol Appl Neurobiol, 2018. 44(2): p. 172-184.

[12] Eckel-Passow, J.E., et al., Glioma Groups Based on 1p/19q, IDH, and TERT Promoter Mutations in Tumors. N Engl J Med, 2015. 372(26): p. 2499-508.

[13] Garcia-Escudero, R. and J.M. Paramio, Gene expression profiling as a tool for basic analysis and clinical application of human cancer. Mol Carcinog, 2008. 47(8): p. 573-9.

[14] Kim, Y.W., et al., Identification of novel synergistic targets for rational drug combinations with PI3 kinase inhibitors using siRNA synthetic lethality screening against GBM. Neuro Oncol, 2011. 13(4): p. 367-75.

[15] Weeraratna, A.T., Discovering causes and cures for cancer from gene expression analysis. Ageing Res Rev, 2005. 4(4): p. 548-63.

[16] Cheng, W., et al., Bioinformatic profiling identifies an immune-related risk signature for glioblastoma. Neurology, 2016. 86(24): p. 2226-34.

[17] Li, J., et al., TCPA: a resource for cancer functional proteomics data. Nat Methods, 2013. 10(11): p. 1046-7.

[18] Zhang, Y., et al., S100A gene family: immune-related prognostic biomarkers and therapeutic targets for low-grade glioma. Aging (Albany NY), 2021. 13(11): p. 15459-15478.

[19] Zhu, H., et al., TUBA1C is a Prognostic Marker in Low-grade Glioma and Correlates with Immune Cell Infiltration in the Tumor Microenvironment. Front Genet, 2021. 12: p. 759953.

[20] Charlestin, V., et al., Aquaporins: New players in breast cancer progression and treatment response. Front Oncol, 2022. 12: p. 988119.

[21] Moon, C.S., D. Moon, and S.K. Kang, Aquaporins in Cancer Biology. Front Oncol, 2022. 12: p. 782829.

[22] Varricchio, A. and A.J. Yool, Aquaporins and Ion Channels as Dual Targets in the Design of Novel Glioblastoma Therapeutics to Limit Invasiveness. Cancers (Basel), 2023. 15(3).

[23] Magni, F., et al., AQP1 expression analysis in human diseases: implications for proteomic characterization. Expert Rev Proteomics, 2008. 5(1): p. 29-43.

[24] Tang, Z., et al., GEPIA: a web server for cancer and normal gene expression profiling and interactive analyses. Nucleic Acids Res, 2017. 45(W1): p. W98-W102.

[25] Bowman, R.L., et al., GlioVis data portal for visualization and analysis of brain tumor expression datasets. Neuro Oncol, 2017. 19(1): p. 139-141.

[26] Goldman, M.J., et al., Visualizing and interpreting cancer genomics data via the Xena platform. Nat Biotechnol, 2020. 38(6): p. 675-678.

[27] Puchalski, R.B., et al., An anatomic transcriptional atlas of human glioblastoma. Science, 2018. 360(6389): p. 660-663.

[28] Szklarczyk, D., et al., STRING v11: protein-protein association networks with increased coverage, supporting functional discovery in genome-wide experimental datasets. Nucleic Acids Res, 2019. 47(D1): p. D607-D613.

[29] Dennis, G., Jr., et al., DAVID: Database for Annotation, Visualization, and Integrated Discovery. Genome Biol, 2003. 4(5): p. P3.

[30] Werner, J.M., et al., Expression of FAS-L Differs from Primary to Relapsed Low-grade Gliomas and Predicts Progression-free Survival. Anticancer Res, 2017. 37(12): p. 6639-6648.

[31] Reon, B.J., et al., Expression of lncRNAs in Low-Grade Gliomas and Glioblastoma Multiforme: An In Silico Analysis. PLoS Med, 2016. 13(12): p. e1002192.

[32] Kourghi, M., et al., Bumetanide Derivatives AqB007 and AqB011 Selectively Block the Aquaporin-1 Ion Channel Conductance and Slow Cancer Cell Migration. Mol Pharmacol, 2016. 89(1): p. 133-40.

[33] Pei, J.V., et al., Differential Inhibition of Water and Ion Channel Activities of Mammalian Aquaporin-1 by Two Structurally Related Bacopaside Compounds Derived from the Medicinal Plant Bacopa monnieri. Mol Pharmacol, 2016. 90(4): p. 496-507.

[34] Salman, M.M., et al., Recent breakthroughs and future directions in drugging aquaporins. Trends Pharmacol Sci, 2022. 43(1): p. 30-42.

[35] Saadoun, S., et al., Aquaporin-4 expression is increased in oedematous human brain tumours. J Neurol Neurosurg Psychiatry, 2002. 72(2): p. 262-5.

[36] Oshio, K., et al., Expression of the aquaporin-1 water channel in human glial tumors. Neurosurgery, 2005. 56(2): p. 375-81; discussion 375-81.

[37] Boon, K., et al., Identification of astrocytoma associated genes including cell surface markers. BMC Cancer, 2004. 4: p. 39.

[38] Deen, P.M., et al., The human gene for water channel aquaporin 1 (AQP1) is localized on chromosome 7p15-->p14. Cytogenet Cell Genet, 1994. 65(4): p. 243-6.

[39] Brabet, P., et al., Localization of the human pituitary adenylate cyclase-activating polypeptide receptor (PACAP1-R) gene to 7p15-p14 by fluorescence in situ hybridization. Genomics, 1996. 38(1): p. 100-2.

[40] Gonzalez, P. and K.G. Martinez, The role of stress and fear in the development of mental disorders. Psychiatr Clin North Am, 2014. 37(4): p. 535-46.

[41] Oyola, M.G. and R.J. Handa, Hypothalamic-pituitary-adrenal and hypothalamic-pituitary-gonadal axes: sex differences in regulation of stress responsivity. Stress, 2017. 20(5): p. 476-494.

[42] Hu, G., et al., Prognostic Markers Identification in Glioma by Gene Expression Profile Analysis. J Comput Biol, 2020. 27(1): p. 81-90.

[43] Staruschenko, A., M.R. Hodges, and O. Palygin, Kir5.1 channels: potential role in epilepsy and seizure disorders. Am J Physiol Cell Physiol, 2022. 323(3): p. C706-C717.

Türk Doğa ve Fen Dergisi
Turkish Journal of Nature and Science
www.dergipark.gov.tr/tdfd

Evaluation of Yield Performance of Some Local Chickpea Varieties In Silifke Ecological Conditions

Gülay ZULKADİR[1*] iD , **İnci KARATAŞ[1]** iD , **Leyla İDİKUT[2]** iD

[1] Mersin University, Applied Technology and Management School of Silifke, Organic Farming Management Department, Mersin, Türkiye
[2] Kahramanmaras Sutcu Imam Universitesi, Faculty of Agriculture, Field Crops Department, Kahramanmaraş, Türkiye
Gülay ZULKADİR ORCID No: 0000-0003-3488-4011
İnci KARATAŞ ORCID No: 0009-0008-8229-2575
Leyla İDİKUT ORCID No: 0000-0002-0685-7158

Corresponding author: gulayzulkadir@gmail.com

Abstract: This study was conducted in 2022 in the arid conditions of Silifke district, Mersin. The experiment included 14 chickpea varieties planted in a randomized complete block design with three replications. According to the research results, flowering time average to 130.74 days, pod setting time to 141.30 days, plant height to 39.98 cm, first pod height to 23.80 cm, number of branches per plant to 2.79 pieces, number of pods per plant to 9.14 pieces, number of seeds per pod to 0.75 pieces, pod length to 2.24 cm, thousand seed weight to 301.86 g, grain yield per decare to 80.14 kg, harvest index to 35.09%, root length to 9.05 cm, disease degree to 0.67, protein content to 16.14%, starch content to 42.14%, fat content to 5.41%, ash content to 2.56%, fiber content to 6.49%, and moisture content ranging to 11.40%. In conclusion, the Aksu variety was found to be more suitable under Silifke ecological conditions based on the evaluated characteristics and demonstrated higher yield compared to other varieties. Further scientific research on the Aksu variety suggests its potential widespread cultivation under Silifke conditions.

32

Bazı Nohut Ceşitlerinin Silifke Ekolojik Kosullarında Verim Performansının Değerlendirilmesi

Anahtar Kelimeler
Cicer arietinum L.,
Adaptasyon,
Verim,
Verim unsurları,
Silifke

Öz: Bu çalışma, 2022 yılında, Mersin'in Silifke ilçesinde kıraç şartlarda kurulmuştur. Denemede 14 adet nohut çeşidi kullanılmış olup, tesadüf blokları deneme planına gore 3 tekerrürlü olarak ekimi yapılmıştır. Araştırma sonuçlarına göre, çiçeklenme süresi ortalama 130.74 gün, bakla bağlama süresi 141.30 gün, bitki boyu 39.98 cm, ilk bakla yüksekliği 23.80 cm, bitkide dal sayısı 2.79 adet, bitkide bakla sayısı 9.14 adet, baklada tane sayısı 0.75 adet, bakla uzunluğu 2.24 cm, bin tane ağırlığı 301.86 g, dekara tane verimi 80.14 kg, hasat indeksi 35.09%, kök uzunluğu 9.05 cm, hastalık derecesi 0.67, protein oranı 16.14%, nişasta oranı 42.14%, yağ oranı 5.41%, kül oranı 2.56%, lif oranı 6.49% ve nem miktarlarının 11.40% olarak tespit edilmiştir. Sonuç olarak, Silifke ekolojik koşullarında nohut çesitlerinin incelenen özelliklerine göre Aksu çeşidi daha uygun bulunmuş ve verim açısında diğer çeşitlere göre daha çok verim verdiği görülmüştür. Aksu çeşidi üzerinde daha çok bilimsel araştırmalar yapılarak Silifke koşullarında yaygın olarak ekimi yapılabileceği öngörülmektedir.

1. INTRODUCTION

Currently, our planet is home to approximately 8 billion people [1], and it is estimated that by 2030, this number will reach 8.6 billion, and by 2050, it will almost exceed 9.8 billion [2]. We will increasingly face the demand to produce more food for more people with fewer resources, and to meet this growing demand, we will need to prioritize high-quality products. Chickpea is one of the important products, and it is a good source of energy, protein, minerals, vitamins, and fiber. It also contains potentially beneficial phytochemicals for health. [3]. Chickpeas play a leading role in global food security by filling the protein gap in the daily food rations of the populations in India and Sub-Saharan Africa [4]. The designed chickpea-based infant follow-on formula meets the WHO/FAO requirements for complementary foods and the EU regulations for follow-on formulas with minimal additions of fat, minerals, and vitamins. It uses chickpeas as a common source of carbohydrates and protein, making it more economical and affordable for developing countries without compromising nutritional quality [5].

Chickpea plant is a very important vegetable protein source, although the amount of use varies depending on the development status of the countries. Among legumes, chickpea is preferred to legumes in some regions due to its multiple uses [6]. Chickpea is considered unique because of its high protein content, which accounts for almost 40% of its weight. Furthermore, chickpeas have health beneficial effects that include reducing cardiovascular, diabetic and cancer risks.

This species is widely distributed in the world and is cultivated almost everywhere [7]. Turkey is an important gene center [8]. However, according to TEPGE (Tarimsal Ekonomi ve Politika Gelistirme Enstitüsü), 2023 data, it was cultivated on 15 million ha in the world. World cultivation areas have increased by 3.00% in the last five years. Accordingly, when evaluated on a country basis, the country with the highest cultivation area in 2021 is India with 10.90 million ha. This value constitutes approximately 73.00% of the total chickpea cultivation area. Other countries with significant cultivation areas are Pakistan, Russia, Turkey, Iran, Iran, Myanmar, Australia and Ethiopia. Turkey accounts for only 4.00% of the total chickpea cultivation area in the world. While there has been an increase in the world's cultivation areas in the last five years, Turkey ranks 4th with an area of 482,000 ha-1 and constitutes approximately 3.20% of the total cultivation areas in the world [9].

Chickpea is a very important food source for human and animal nutrition and plays an important role in soil sustainability, especially in arid and semi-arid regions. Chickpea can grow in arid and semi-arid areas with rainfall without the need for irrigation. Thanks to this feature, chickpea is included in the crop rotation and reduces fallow areas. Thus, in 2018, by receiving incentives for agricultural production, chickpea is being cultivated in many areas from sea level to high areas [10]. However, the yield obtained varies greatly depending on genotype, year and environmental factors. This situation has led researchers to work on the selection of suitable conditions, suitable cultivation methods and suitable varieties.

Mersin is one of the provinces with significant chickpea production. According to TUIK (Türkiye İstatistik Kurumu) data, Mersin was the leading province with the highest chickpea production in Turkey until 2012, while in 2022 it ranked 11th with 97,356 cultivation area according to TEPGE [11]. In this context, the steady decline in chickpea cultivation areas in Mersin stands out.

In the province of Mersin, the highest chickpea production is carried out in the districts of Gulnar and Silifke" [12]. The lands used as agricultural land in Silifke are concentrated in Goksu Valley, Goksu Delta and coastal areas. The agricultural land is more in Goksu Delta due to the high amount of alluvial soils. With the effect of irrigation, strawberries, citrus fruits, peanuts and various vegetables are grown in these areas. In the areas where the elevation increases, cereals and legume crops (wheat, barley, chickpea) come to the forefront due to the inadequacy of temperature and irrigation [13].

In this context, the aim of this study is to examine 14 different varieties of chickpea plants in terms of yield and yield elements in Silifke ecological conditions and to determine which variety is suitable for the conditions of the region. The aim is to develop this selected variety through scientific research and to ensure its widespread cultivation in this region.

In this context, the importance of this study is as follows; chickpea plant is a plant with adaptation limitations and not all varieties give the same yield everywhere. Therefore, measuring the adaptation abilities of the improved varieties to the region, determining their yield potentials, and identifying suitable varieties will provide a scientific basis for breeding studies to be conducted in the region and inform producers about varieties suitable for the region.

The first objective of this research is to determine the feasibility of chickpea cultivation in the coastal and barren regions of Silifke. Accordingly, it has been determined which variety adapts better and whether the yield obtained will be satisfactory for the producers

2. MATERIAL AND METHOD

This study was carried out between October-December 2022 as winter sowing under Silifke conditions. 'Aksu, Seckin, Inci, Kusmen-99, Damla-89, Cevdetbey-98, Canitez, Ubet, Gulumser, Borabey, Zuhal, Sezenbey, Sari-98 and Yasa-05' varieties were used in the study.

When examining the long-term climate data (1991-2020) and the climate data for the year 2022 for the Silifke district of Mersin [14], it was found that the average

33

monthly temperature during the growing season (October, November, and December) of 2022 was 21.15°C, while the long-term average was 19.6°C. Comparing these, it was observed that the temperature was 1.5°C higher." During the growing season encompassing September, October, November, and December, the average monthly maximum temperature was 30.8°C, while the long-term average was 34.7°C. Comparing these, it was observed that the temperature was 4.7°C lower. While the total rainfall was 115.4 mm, the long-term average total rainfall was 274.8 mm, indicating a 58% decrease in total rainfall in 2022 compared to long-term averages. During the growing season, the average relative humidity was 52.12%, whereas the long-term average relative humidity was 56.15%. It was recorded that the relative humidity in 2022 showed a 7% decrease compared to long-term averages.

In the study, the selected varieties were sown in 3 replications according to the randomized blocks experimental design. In the sowing process; the distance between rows of each plot was set as 45 cm, the distance between rows was set as 5 cm, the number of rows in the plot was set as 4, and the length of the plot was set as 4 m.

According to the results of the soil analysis of the cultivation area, it was found that it had a calcareous structure, insufficient organic matter, alkaline, and very poor drainage. It was observed that plant roots could not develop comfortably in this soil, which was very dense due to the lack of cultivation for a long time. Therefore, 18-46 DAP fertilizer was applied at the rate of 6 kg phosphorus per decare during sowing, and before flowering, 46% urea was applied at a rate of 3 kg per decare.

In the study, various traits such as flowering duration, Pod Setting Time, plant height, first pod height, number of branches per plant, number of pods per plant, number of seeds per pod, pod length, thousand-seed weight, seed yield, root length, disease degree, protein content, starch content, oil content, ash content, fiber content, and moisture content were examined. Observations were made from 5 plants selected from each plot according to the Technical Instructions for Agricultural Values Measurement Trials determined by the Turkish Ministry of Agriculture and Rural Affairs, General Directorate of Protection and Control, Seed Registration and Certification Center Directorate.

2.1. Statistical Analysis

The values of the examined traits were subjected to analysis of variance using SAS package program according to the randomized block design and the differences between the averages were tested according to DUNCAN multiple comparison method at p<0.01 significance level. In addition, correlation analysis and Principal Component Analysis (PCA) of the relationships between traits were performed using PAST 4 program.

3. RESULTS AND DISCUSSION

The results obtained from this study, which evaluated the performance of various chickpea varieties in the coastal regions near Silifke, are presented below.

3.1. Flowering Time (days)

The presence of differences in flowering timetimes and the statistical analysis results for the grouping of these differences are presented in Table 1. According to the variance analysis results, the flowering time of the varieties were found to be statistically significant at the 1% significance level. On the other hand, differences were also observed between the blocks, but these differences were found to be significant at the 5% level.

Table 1. Analysis of variance, mean values, and groupings for flowering duration, pod setting time, and plant height of chickpea varieties

No	Varieties	Flowering Duration (days)	Pod Setting Time (days)	Plant Height (cm)
1	Aksu	128.67 ef	139.67 ef	**46.70 a**
2	Seckin	128.67 ef	140.50 c-f	38.13 ef
3	Inci	**133.33 a**	**143.53 a**	40.83 de
4	Kusmen-99	131.00 a-e	**138.70 f**	**29.77 ı**
5	Damla-89	129.33 c-f	141.73 a-d	41.50 cd
6	Cevdetbey-98	**133.33 a**	141.67 a-d	43.33 b-d
7	Aydin-92	131.33 a-d	140.00 d-f	45.93 ab
8	Ubet	129.00 d-f	**139.40 f**	41.53 cd
9	Gulumser	132.67 ab	142.03 a-c	45.30 ab
10	Borabey	131.00 a-e	142.10 a-c	33.55 h
11	Zuhal	130.50 b-f	141.50 b-e	34.85 gh
12	Sezenbey	**128.50 f**	143.00 ab	43.73 bc
13	Sari-98	131.67 a-c	142.80 ab	36.33 fg
14	Yasa-05	131.33 a-d	141.50 b-e	38.20 ef
Average		130.74	141.30	39.98
% CV		0.98	0.70	3.83
F	Varieties	5.31**	6.33**	32.60**
Value	Blocks	5.10*	0.31	0.79

**: p<0.01; *: p<0.05 statistically significant within error limits.

When examining the average values of the flowering time of chickpea varieties, it was determined that the flowering time varied between 125.50 and 133.33 days, with the average flowering duration of the varieties being 130.74 days. Among these varieties, 'Sezenbey' was the variety with the shortest flowering period and was in a separate group from the other varieties. On the other hand, the varieties with the longest flowering period were 'Inci' and 'Cevdetbey-98'.

The findings we obtained regarding the duration until flowering were evaluated with previous studies. Accordingly, it has been stated in various studies conducted under Adana conditions that the flowering duration can vary between 97.70 and 171.30 days depending on the genotypes [15; 16; 17]. However, under Sırnak-İdil conditions, the average flowering duration was determined to be 139.90 days [18]. On the other hand, in a study conducted under Ankara conditions, Aydogan [16] reported that the number of days to flowering ranged from 59.00 to 67.3 days, Gurbuz [17] reported 55.8 days under Bingol ecological conditions, Patan [18] reported 56.7 to 67.0 days under

Erzurum conditions, and Karakan Kaya [19] reported 57.0 to 62.3 days under Elazığ conditions.

In general, it has been observed that flowering time differ in each study. This is thought to be significantly influenced by the selection of varieties, planting time, agricultural procedures, and the climatic and soil characteristics of the growing location. Thus, both similarities and differences with other studies have been observed. However, it is clearly evident from the comparison of this study with other studies that the number of days until flowering is more or less similar in similar ecologies and with the same genotypes.

3.2. Pod Setting Time (days)

The variance analysis results and average values related to pod setting times are given in Table 1. Accordingly, it was found that the pod setting times of the examined varieties were statistically very significant ($p < 0.01$). It was determined that the pod setting times of the varieties varied between 138.70 - 143.53 days and the average pod setting time of all varieties was 141.30 days. It was observed that the variety 'Kusmen-99' had the shortest pod setting time, and the second shortest Pod Setting Time was found to be 'Ubet' with 139.40 days. It was also noted that these two varieties were not statistically different from each other. The variety 'Inci' had the longest pod setting time and was placed in a separate group from all other varieties.

The data obtained in this study are similar to the data of Oztas [20], who stated that the pod setting time varied between 164.00-177.00 days for chickpea varieties sown in November in Harran Plain. Additionally, it also shows similarity to the data expressed by Yigit [21], who reported the pod setting periods of chickpea varieties to be 82.00-111.00 days in a study conducted to determine the yield performance of some chickpea varieties under the ecological conditions of Kırsehir. However, it is found to be higher than the data of Ozgun et al. [22] who reported that the pod setting time varied between 50.00-11.00 days in their study sown in April. This may be due to the fact that the vegetation season in summer is shorter than in winter and therefore the pod setting time is shortened [23].

3.3. Plant Height (cm)

The results of the variance analysis, mean values, and formed groups of the data related to the plant heights of the varieties are presented in Table 1. Accordingly, it was observed that the variation among the varieties was statistically significant at the $p < 0.01$ level, indicating high diversity in this area. The average plant height values varied between 29.77 - 46.70 cm and the average plant height of all varieties was 39.97 cm. The highest plant height was found to be 'Aksu' variety and the lowest plant height was found to be 'Kusmen-99' variety. Both varieties were in separate groups. The second lowest plant height value was observed in 'Borabey' variety and 'Borabey' was in a separate group. All other varieties were in intermediate groups.

In studies related to plant height values, Erden [24] found that plant heights ranged from 38.1 to 52.8 cm under Siirt conditions, while Beysari [25] found that plant heights ranged from 41.4 to 46.6 cm under Bingol conditions. Additionally, Beykara [26] reported plant heights ranging from 37.42 to 44.00 cm, Gurbuz [17] from 30.3 to 42.3 cm, Dinc [27] from 28.96 to 41.26 cm under Van conditions, Yasar [28] from 34.17 to 42.53 cm under Diyarbakir conditions, and Karakan Kaya [19] found plant heights ranging from 41.2 to 56.9 cm under Elazığ conditions. All these studies indicate that plant height values vary greatly, and these variations are significantly influenced by genotype and environment.

3.4. First Pod Height (cm)

The variance analysis results of the first pod height data for chickpea varieties grown in Silifke district are presented in Table 2. According to the results of this analysis, the variation among varieties for first pod height was found to be statistically significant at the $p < 0.01$ level. first pod height values varied between 20.85 - 28.37 cm and the average was 23.80 cm. The variety with the highest first pod height was 'Aydin-92', followed by the 'Aksu' variety with 28.07 cm. These two varieties were found to be in the same group, statistically indistinguishable from each other. The lowest first pod height was obtained from the 'Zuhal' variety.

When the studies conducted by other researchers on the first pod height were examined, it was seen that Dinc [27] determined that the first pod height varied between 19.13-25.33 cm under Van ecological conditions, Beysari [25] determined 20.80-29.90 cm under Bingol conditions, Yasar [28] determined 15.27-20.20 cm under Diyarbakir ecological conditions, and Gurbuz [17] determined 14.00-28.20 under Bingol conditions. The first pod height values obtained by researchers are in parallel with the values obtained in this study. However, in studies conducted by Bakoglu and Aycicek [29] under Bingol conditions, by Bicer and Anlarsal [30] under Diyarbakir conditions, by Vural and Karasu [31] under Isparta ecological conditions, and by Canci and Toker [32] under Antalya conditions, the average first pod height was determined to be 17.8 cm, 16.63 cm, 16.70 cm, and 18.50 cm, respectively. These values are lower than the values obtained in our study. The first pod height characteristic is related to plant height, and both characteristics are directly related to the genetic potential of the variety. They are also significantly influenced by cultural practices during the growth period and especially by rainfall [33].

3.5. Number of Branches Per Plant (pieces)

Data on the number of branches of the varieties used in the experiment were obtained and subjected to analysis of variance. The results obtained are given in Table 2. According to this table, it was seen that the variation between varieties was significant at $p < 0.05$ level. According to the data obtained, the number of branches per plant of each variety varied between 1.80 - 4.10 pieces and the average number of branches was 2.79

pieces. In terms of number of branches, the lowest value was obtained from 'Yasa-05' and the highest value was obtained from 'Sezenbey' cultivar. Except for these two varieties, all other varieties were in the transition groups in terms of this trait.

When the studies conducted were evaluated, Demirci and Bildirici [34] determined the number of branches of 2.00-3.30 pieces in 14 chickpea varieties under Sanliurfa conditions, Sozen and Karadavut [35] determined 1.40-3.50 pieces in 62 chickpea genotypes, Tetik [36] determined 4.60-6.80 piecesin 16 chickpea varieties.

Bakoglu and Aycicek [29] reported that the number of branches varied between 2.30-3.53 pieces in a study conducted with 8 chickpea varieties under dry conditions in Bingol; Bicer and Anlarsal [30] obtained the number of main branches as 1.8-3.2 pieces in a study conducted with 48 chickpea genotypes in Diyarbakır. Onder and Ucer [37] found that the number of main branches per plant for 5 chickpea varieties ranged from 3.50 to 9.50 pieces under Konya ecological conditions; Karakoy [38] determined that the number of branches per plant varied between 2.85 and 4.65 pieces in a study conducted under Adana conditions. In other studies on the number of main branches per plant, Bicer [39] obtained values between 1.80-3.20 pieces, Arshad et al. [40] between 2.40-3.95 pieces and Kacar et al. [41] obtained values between 2.58 and 3.23 pieces. The values for the number of main branches per plant obtained by the researchers are similar to those obtained in this study. However, when examining the study conducted by Aydogan [42] under Eskisehir ecological conditions, it is observed that the number of main branches per plant in the chickpea varieties included in the study ranged from 6.50 to 12.80 pieces. The values obtained for this characteristic in our study are lower than those obtained by the researcher, and it was concluded that these values were obtained as a result of different ecological and climatic factors, although the other varieties were different and the Inci variety was common.

3.6. Number of Pods Per Plant (pieces)

The presence of differences in the number of pods per plant and the statistical analysis results aimed at grouping these differences are presented in Table 2. According to the results of variance analysis, the number of pods per plant of the varieties was found to be statistically significant at $p < 0.01$ significance level.

It was recorded that the average values of pods per plant among the varieties varied between 2.47 - 13.10 pieces, and the general value of these values was 9.14 pieces (Table 2). The lowest number of pods was obtained from Kusmen-99 and the highest number of pods was obtained from 'Sezenbey' variety. These varieties were placed in different groups because they showed significant differences from each other and from all other varieties. However, the varieties 'Aksu', 'Seckin', 'Inci', 'Cevdetbey-98', and 'Gulumser' were found to have the same number of pods statistically. The varieties 'Aydin-

92', 'Zuhal', and 'Yasa-05' also shared the same values statistically.

The number of pods of a plant is one of the most important traits determining grain yield compared to other yield components and has a positive and significant relationship with the number of grains in the plant [43]. Although various environmental and climatic factors influence the number of pods in a plant, many studies suggest that the genetic potential of the variety is the determining factor.

Some researchers have reported varying numbers of pods per plant in their studies. For example, Demirci and Bildirici [34] found that the number of pods per plant ranged from 6.90 to 13.00 for 14 genotypes under Sanliurfa conditions. Sozen and Karadavut [35] reported a range of 8.00 to 32.00 pods per plant for 62 genotypes. Aydogan [42] observed a range of 23.80 to 75.30 pods per plant for 11 chickpea genotypes under Eskisehir conditions. Tetik [36] found that the number of pods per plant ranged from 11.10 to 23.50 for 16 different genotypes. Bicaksiz [44] reported that the number of pods per plant varied from 15.60 to 19.90 pieces under Eskisehir conditions. Patan [18] observed a range of 12.70 to 25.90 piece pods per plant under Erzurum conditions. Bakoglu [29] found that the number of pods per plant ranged from 6.10 to 15.00. Although the findings of the researchers were slightly above the values obtained in this study, they were partially similar. However, in the study conducted under Erzurum conditions, the average number of pods per plant was 29.00 [45], in the study conducted in Sanliurfa it was 26.40 [20], in the research conducted under Bursa ecological conditions it was 29.50 [41], in the study conducted in Bingol it was 12.42 [29], and in the study conducted under Diyarbakir ecological conditions, the average number of pods per plant was 19.05 [46]. These values are observed to be higher than the values obtained in our study. The discrepancy between the results of the literature and the results of the current study can be attributed to the genotypic differences among the varieties and environmental conditions.

3.7. Number of Grains Per Pod (piece)

A grouping analysis based on averages was performed due to significant variability in the number of grains per pod among the varieties, and the results are presented in Table 2. When examining the table, it could be seen that the number of grains per pod varied between 0.54 and 1.08 piece, and the average number of grains per pod of the varieties was 0.75 piece. It was recorded that the highest number of grains per pod was found in the 'Damla-89' variety, while the lowest value was found in the 'Cevdetbey-98' variety. Additionally, it was determined that these two varieties significantly differed from each other and from the other varieties, placing them in separate groups. All other varieties were found to be in transitional groups.

The number of grains in the pod may show different characteristics depending on the genotype of the variety.

Mostly, there may be two pods with small seeds and one pod with large seeds [47]. In this context, a review of the literature reveals that studies have reported the number of seeds per pod as follows: Demirci and Bildirici [34] 1.00-1.30 seeds pod^{-1}, Ceran [48] 0.86 seeds pod^{-1}, Patan [18] 0.94 seeds pod^{-1}, Beysari [25] 1.03 seeds pod^{-1}, and Erdemci [49] 1.01-1.03 seeds pod^{-1}. Additionally, other studies have reported values ranging from 0.82 to 1.15 seeds per pod [50] [51] [29]which are largely similar to our findings.

3.8. Pod Length (cm)

Data on pod length for different varieties were subjected to variance analysis, and the results are presented in Table 3. According to this, it was determined that there was no statistical difference in pod length among the varieties and that all had the same pod length. However, The average values of pod length of the varieties are given in Table 3. As seen in the table, pod length values varied between 1.96 (Damla-89) - 2.50 (Sari-98) cm, however, the overall average of the varieties was 2.24 cm. Differences at the 5% level were observed between the blocks.

When the literature is reviewed, Ozgun [22] in his study conducted under Diyarbakir conditions reported pod lengths ranging from 2.27 to 3.00 cm. This finding is similar to the findings of our study.

3.9. Thousand Grain Weight (g)

After the harvest, the thousand grain weight data for each variety was obtained and variance analysis was conducted. The results are presented in Table 3. According to these results, significant differences (p<0.01) were found in the thousand grain weights of the varieties.

The average values of thousand grain weights for the varieties and the groups formed according to Duncan's multiple comparison test are detailed in Table 3. The thousand grain weight values varied between 258.17 - 395.33 g according to the varieties and the average was 301.86 g. The lowest thousand grain weight was obtained from 'Inci' variety. However, it was determined that there was no statistical difference between the following varieties 'Kusmen-99' (260.08 g), 'Damla-89' (261.42 g), 'Gulumser' (265.08 g) and 'Borabey' (265.08 g) and they were in the same group. On the other hand, the highest thousand grain weight was obtained from 'Cevdetbey-98'.

In many cereal and edible legume crops, thousand grain weight values are one of the most important parameters related to yield. In this respect, thousand grain weight values are especially examined in the studies. When examining the studies of other researchers on this subject, Demirci and Bildirici [34] determined the thousand grain weight as 98.20-295.50 g in 14 different chickpea genotypes, Aydogan [42] as 246.00-427.00 g in 11 different genotypes, Sozen and Karadavut [35] as 267.00-470.00 g in 62 chickpea genotypes, while Erden

[24] reported the hundred seed weight as 27.90-39.60 g and Bicaksiz [44] as 40.40-44.00 g. In general, it has been understood that both our findings and the findings of other researchers show great variability. This situation suggests that it is due to genotypic differences, ecological conditions, and cultural practices.

3.10. Grain Yield Per Decare (kg)

The values for grain yield per decare, which is one of the most important characteristics in cultivation, were subjected to variance analysis to investigate the significance of differences among varieties, and the results are presented in Table 3. With the emergence of significant differences, a grouping analysis of the average values was conducted, and the results are also given in Table 3. As seen in Table 3, the grain yield per decare for the varieties was found to be statistically highly significant.

When Table 3 was analyzed, it was observed that grain yield values varied between 23.84 - 116.91 kg and the general average value of the varieties was 80.14 kg. It was recorded that the best variety in terms of grain yield per decare was 'Aksu'. The other varieties with the highest values were 'Seckin' with 116.26 kg and 'Ubet' with 110.41 kg, but these two varieties were in the intermediate group after 'Aksu'. The lowest grain yield was obtained from 'Kusmen-99' variety.

Grain yield is a criterion examined in all studies since it is the main element of cultivation and production. In this regard, when evaluating all studies related to chickpea cultivation, considering different genotypes, ecologies, and cultural practices for grain yield, Mart et al. [52] reported values between 117.60-202.30 kg da^{-1}, Topcu and Akcura [53] reported 327.00 kg da^{-1}, Gunes et al. [54] reported 400.00 kg da^{-1} and above, Demirci and Bildirici [34] reported values between 140.70-398.70 kg da^{-1}, Topcu [55] reported values between 97.50-327.00 kg da^{-1}, Tetik [36] reported values between 45.60-103.10 kg da^{-1}, Aydogan [42] reported values between 72.00-197.00 kg da^{-1}, and Gundogdu Gurbuz [56] reported values between 26.20-85.20 kg da^{-1}. Grain yield significantly increases with agricultural procedures such as irrigation and fertilization, especially with sufficient irrigation during the branching process, flowering, and pod-setting periods [57].

3.11. Harvest Index (%)

The variance analysis results and the average values for harvest index for different varieties are provided in Table 3. The analysis indicates that the harvest index shows statistically significant differences at the p<0.05 significance level for all varieties (Table 3).

On the other hand, the average harvest index of the varieties varied between 26.35 - 42.72% and the average of all varieties was 35.09% (Table 3). The highest harvest index value was obtained from 'Seckin' variety, while 'Ubet' variety with 42.71% and 'Aksu' variety with 40.78% were the varieties with the highest harvest index

and were statistically in the same group. The lowest harvest index value was obtained from 'Kusmen-99' variety and all other varieties were in the intermediate group.

Another parameter related to yield is the harvest index. Researchers' findings on this criterion vary. In some studies, it was recorded that the harvest index value in Sırnak-Idil conditions was between 26.00-41.50% [58],

the average harvest index values in Siirt conditions were between 34.70 and 44.50% [24], and in the study conducted in Central Anatolia, it was between 39.67-45.82% [44]. Tetik [36] also reported that the harvest index varied between 12.60-33.30% and Yigitoglu [59] between 45.20-49.07%. Our findings are similar to the findings of other researchers in terms of the similarity of our research conditions.

Table 2. Variance analysis, mean values, and groupings of chickpea varieties for first pod height, number of branches per plant, number of pods per plant, and number of seeds per pod

No	Varieties	First Pod Height (cm)	Number of Branches per Plant (pieces)	Number of Pods per Plant (pieces)	Number of Seeds per Pod (pieces)
1	Aksu	**28.07 a**	2.73 b-e	10.73 c	0.79 b-d
2	Seckin	21.67 de	2.53 b-e	10.20 c	0.84 bc
3	Inci	23.20 b-e	2.33 c-e	10.13 c	0.82 bc
4	Kusmen-99	22.47 c-e	2.20 de	**2.47 f**	1.00 ab
5	Damla-89	25.07 bc	3.07 a-d	11.13 bc	**1.08 a**
6	Cevdetbey-98	23.17 b-e	2.73 b-e	10.40 c	**0.54 d**
7	Aydin-92	**28.37 a**	2.20 de	8.20 d	0.68 cd
8	Ubet	21.77 de	3.20 a-d	12.47 ab	0.64 cd
9	Gulumser	25.80 ab	2.70 b-e	10.30 c	0.69 cd
10	Borabey	22.05 c-e	3.50 a-c	5.80 e	0.76 b-d
11	Zuhal	**20.85 e**	3.60 ab	8.30 d	0.63 cd
12	Sezenbey	24.55 b-d	**4.10 a**	**13.10 a**	0.67 cd
13	Sari-98	22.87 b-e	2.40 b-e	7.07 de	0.77 b-d
14	Yasa-05	23.35 b-e	**1.80 e**	7.70 d	0.65 cd
Average		**23.80**	2.79	**9.14**	0.75
% CV		6.80	23.19	9.01	17.76
F Value	Variety	5.31**	2.88*	34.67**	3.62**
	Block	5.10*	0.77	0.20	2.53

**: $p < 0.01$; *: $p < 0.05$ statistically significant within error limits.

Table 3. Analysis of variance, mean values, and formed groups for pod length, thousand grain weight, yield per decare, harvest index, root length, and disease degree of chickpea varieties

	Varieties	Pod Length (cm)	Thousand Grain Weight (g)	Yield per Decare (kg)	Harvest Index (%)	Root Length (cm)	Disease Degree
1	Aksu	2.327 a-c	321.582 c	**116.91 a**	**40.8 a**	8.500 bc	**0.000 e**
2	Seckin	2.278 a-c	305.167 d	116.26 ab	**42.721 a**	**11.500 a**	0.500 c-e
3	Inci	2.207 a-c	**258.167 f**	87.07 a-e	36.042 ab	**12.375 a**	1.000 a-d
4	Kusmen-99	2.267 a-c	**260.083 f**	**23.84 f**	**26.347 b**	8.889 bc	1.500 ab
5	Damla-89	**1.958 c**	261.417 f	88.91 a-e	35.519 ab	8.556 bc	0.633 c-e
6	Cevdetbey-98	2.317 a-c	**395.333 a**	91.22 a-d	33.284 ab	9.653 b	1.067 a-c
7	Aydin-92	2.240 a-c	301.167 de	65.34 c-e	30.379 ab	**7.942 c**	**0.000 e**
8	Ubet	2.053 bc	348.000 b	110.41 ab	**42.711 a**	**7.633 c**	0.500 c-e
9	Gulumser	2.290 a-c	**265.083 f**	79.90 b-e	35.361 ab	8.583 bc	**0.000 e**
10	Borabey	2.200 a-c	**265.083 f**	53.52 ef	33.423 ab	8.800 bc	**0.000 e**
11	Zuhal	2.390 ab	290.833 e	67.19 c-e	32.898 ab	8.650 bc	0.267 de
12	Sezenbey	2.120 a-c	309.917 d	101.07 a-c	31.755 ab	**8.167 c**	0.800 b-d
13	Sari-98	**2.500 a**	343.750 b	59.65 de	37.498 ab	8.783 bc	**1.667 a**
14	Yasa-05	2.180 a-c	300.417 de	60.64 de	32.583 ab	8.625 bc	1.500 ab
Average		2.238	301.857	80.14	35.093	9.047	0.674
% CV		8.975	2.017	23.89	18.458	7.944	59.071
F Value	Variety	4.91*	131.96**	5.87**	1.55*	10.14**	6.80**
	Block	1.39*	0.71	1.42	0.28	0.49	1.54

**: $p < 0.01$; *: $p < 0.05$ statistically significant within error limits.

3.12. Root Length (cm)

The results of the analysis of variance, average values and the distribution of these values among the groups obtained after determining the root lengths of the varieties are given in Table 3. According to the results of analysis of variance, root lengths of the varieties showed significant ($p < 0.01$) differences.

Table 3 shows that the average root length values of the varieties varied between 7.63 - 12.38 cm and the overall average was 9.05 cm. Accordingly, it was determined that the variety with the highest root length was 'Inci', followed by 'Seckin' with 11.50 cm and these two varieties were statistically indistinguishable from each other. The lowest root length value belonged to the variety 'Ubet', while 'Aydin-92' (7.94 cm) and 'Sezenbey' (8.17 cm) were in the same group with 'Aydin-92' (7.94

cm) and they were statistically indistinguishable from each other.

When the previous studies were examined, Sanlı and Kaya [58] reported that the root length value was between 10.60-13.30 cm in their experiments. Our findings are similar to the findings reported by the researchers. Kacar [59] stated that depending on the plant species and growing season, if there is not enough moisture in the soil surrounding the root, the root may increase its vertical or horizontal elongation with the same force to reach water. Therefore, it is understood that irrigation conditions and soil structure also have important effects.

3.13. Degree of Disease

The data related to the degree of disease were made according to the 1-5 scale and the evaluation was made based on these data. Variance analysis results of the obtained data are given in Table 3.

According to this, it was recorded that the degree of disease of the varieties was statistically significant at 1% significance level.

The table (Table 3) showing the averages of the disease degrees of the varieties and their distribution among the groups is given below. Accordingly, it was determined that the disease degrees varied between 0.00 - 1.67 according to the varieties. The general disease degree of all varieties was determined as 0.67. It was recorded that the variety with the highest tolerance to the disease agent was 'Sari-98' and the most sensitive varieties were 'Aksu, Aydin-92, Gulumser and Borabey'.

When the previous studies were examined, Baylan [60] tried to determine the response of chickpea to anthracnose disease by sowing chickpea population suitable for the regional conditions at different times in Diyarbakir. As a result of the research, it was determined that the disease index of 'ILC-482' variety increased in 1997 compared to the previous year and was 7.67-7.00-6.75 and 6.50 in December, January, February and March, respectively, and varied depending on the air temperature and humidity. Yasar [28], in his study conducted under Diyarbakir conditions, reported that he detected moderate damage (small spots of burns on the lower leaves) in 'EGE-3002, EGE-3012 and Diyar 95' varieties.

3.14.   Protein Content (%)

The results of the analysis in which the differences in protein ratio were determined according to the varieties are given in Table 4. According to this table, it was determined that the differences in protein ratio were statistically very significant.

According to the average values of the protein ratios of the varieties and the duncan multiple comparison test of these averages, it was determined that the protein ratios varied between 14.22 – 19.48% among the varieties and

the general average of the varieties was 16.14%. While the lowest protein rate was observed in 'Aksu' variety, the highest protein rate was observed in 'Kusmen-99' variety. In general, it was determined that all varieties except 'Seckin' (15.35%) and 'Inci' (15.36%) were in different groups, but 'Seckin' and 'Inci' were in the same group and statistically indistinguishable from each other. Regarding protein ratios, Mart et al. [52] reported that the protein ratios of genotypes in their study conducted in Sanliurfa ranged between 21.7% and 26.5%. Gurbuz [17] found protein ratios between 16.6% and 22.1% under Bingol conditions, Sari [61] reported protein ratios between 13.60% and 18.90% under Samsun conditions, Dinc [27] found protein ratios between 20.32% and 24.35% under the ecological conditions of Van, and Yagmur and Kaydan [62] reported protein ratios in chickpea genotypes grown in Van province ecology ranging between 10.30% and 15.30%. The values obtained by these researchers were found to be partially consistent with the findings of our experiment. It is believed that the differences in findings are due to factors such as genotype, environment.

3.15. Starch Content (%)

The results of variance analysis and the distribution of groups based on the average starch ratio of chickpea varieties are presented in Table 4. According to these results, the starch ratios were found to be statistically significant among the varieties at the p<0.01 level.

Starch ratios varied between 38.00 - 44.69% depending on the varieties and the general average was 42.14%. While the variety with the lowest starch ratio was 'Kusmen-99', the highest value was obtained from 'Ubet' variety. However, 'Zuhal' variety with 44.64% was the variety with the second highest starch ratio and it was determined that it was statistically no different from 'Ubet' variety since it was in the same group with 'Ubet' variety.

When other studies were examined, In their study on chickpea yield quality, Karayel et al. [63] reported that the starch content of the seeds ranged between 48.5% and 50.23%. These values are partially similar to the values obtained in our study. Aksakalli [64] reported in his study that changes in starch content are related to protein content, indicating that higher protein content correlates with higher starch content.

39

Table 4. Analysis of variance, average values, and grouping of chickpea varieties for protein content, starch content, fat content, ash content, fiber content, and moisture content

No	Varieties	Protein Content (%)	Starch Content (%)	Fat Content (%)	Ash Content (%)	Fiber Content (%)	Moisture Content (%)
1	Aksu	**14.22 m**	41.05 f	5.42 c	2.64 b	**6.93 a**	**12.02 a**
2	Seckin	15.35 h	40.14 g	5.24 g	2.57 b-d	**6.96 a**	11.37 de
3	Inci	15.36 h	43.15 c	5.33 de	2.50 c-e	6.257 e	11.57 b
4	Kusmen-99	**19.48 a**	**38.00 h**	**4.56 h**	**2.93 a**	**6.94 a**	11.33 d-g
5	Damla-89	14.84 k	42.90 c	**5.69 a**	2.44 e	6.02 f	11.36 d-f
6	Cevdetbey-98	17.12 d	41.24 f	5.31 ef	2.56 b-d	**5.87 g**	11.44 cd
7	Aydin-92	16.46 g	43.77 b	**5.75 a**	2.48 c-e	6.41 d	**11.07 ı**
8	Ubet	14.33 l	**44.69 a**	5.55 b	2.47 de	6.04 f	11.42 c-e
9	Gulumser	15.05 j	42.18 d	**5.70 a**	**2.45 e**	6.74 b	11.30 e-g
10	Borabey	17.38 c	42.06 de	5.38 cd	2.61 b	6.59 c	11.52 bc
11	Zuhal	15.24 ı	**44.64 a**	5.25 fg	2.57 bc	6.46 d	11.57 b
12	Sezenbey	17.74 b	41.89 e	**5.70 a**	2.48 c-e	6.38 d	11.15 hı
13	Sari-98	16.77 e	41.11 f	5.29 e-g	2.63 b	6.81 b	11.20 gh
14	Yasa-05	16.56 f	43.14 c	5.60 b	2.52 c-e	6.41 d	11.23 f-h
	Average	16.14	42.14	5.41	2.56	6.49	11.40
	% CV	0.38	0.35	0.72	1.99	0.84	0.634
F Value	Variety	1786.94**	459.16**	188.18**	18.01**	129.47**	31.66**
	Block	0.01	1.19	0.12	0.48	4.56*	2.94

**: $p<0.01$; *: $p<0.05$ statistically significant within error limits.

3.16. Fat Content (%)

The results of the variance analysis for the fat content of the varieties, the average values for each variety, and the resulting groups are presented in Table 4. According to these results, the fat content showed significant ($p<0.01$) differences among the varieties.

Here, it was observed that the fat content values among the varieties varied between 4.56 - 5.75% and the overall average was 5.41%. 'Kusmen-99' was recorded as the variety with the lowest fat content. On the other hand, the highest fat content was observed in 'Aydin-92' and it was in the same group with 'Gulumser' (5.70%), 'Sezenbey' (5.70%) and 'Damla-89' (5.69%).

When previous studies are examined, Dinc [27] reported that the fat content in seeds ranged between 4.01% and 4.93%. Research indicates that fat content in edible legumes is generally low. However, Ozdemir [65] stated that the fat content in chickpeas is around 5%. In this context, it is observed that the values obtained in our study are consistent with those obtained in previous studies.

3.17. Ash Content (%)

Variance analysis results of the ash content data for some chickpea varieties grown under Silifke ecological conditions are presented in Table 4. Accordingly, it was determined that the ash content values showed significant ($p<0.01$) variability among the varieties.
It was determined that the average ash content values varied between 2.45 – 2.93% according to the varieties and the general average of the varieties was 2.56%. The lowest ash content was obtained from the 'Gulumser' variety and the second lowest ash content value was obtained from the 'Damla-89' variety with 2.44% and these two varieties were statistically indistinguishable from each other. On the other hand, the highest ash content was obtained from 'Kusmen-99' variety.

Sarimurat [66], in his study conducted under the ecological conditions of Van, reported that the ash content values ranged from 3.83% to 6.00%. Karayel et al. [63] found that the ash content varied between 2.88% and 3.00%. Sepetoglu [67] reported that the average ash content in seeds was around 3.5%. The results from these studies show some similarity with the findings of our research.

3.18. Fiber Content (%)

The results of the analysis of variance for the fiber content data of chickpea varieties, the average values of the fiber content data of the varieties and the groups formed are given in Table 4. As seen in the table, the fiber content of the varieties were significantly ($p<0.01$) different from each other.

It is observed that the average fiber content of the varieties varied between 5.87% and 6.96% and the general average was 6.49%. The variety with the highest fiber content was 'Seckin', followed by 'Kusmen-99' with 6.94% and 'Aksu' with 6.93% and they were in the same group. 'Cevdetbey-98' variety had the lowest fiber content.

When other studies were examined, Deshpande et al. [68] reported that the average rate of fiber in chickpea was 3.9% and Ertas [69] reported that the fiber content was 3.65%. El-Adawy [70] reported that the amount of fiber in the seed was 3.82%. These results were found to be lower than the findings of our study.

3.19. Moisture Content (%)

The results of the analysis of variance, average values and statistical distribution of moisture content among cultivars are given in Table 4. When the table is examined, it is noted that the moisture content varied significantly among the varieties.
It was observed that the moisture content values varied between 11.07% and 12.02% according to the varieties

and the general average was 11.40%. The lowest moisture content was obtained from 'Aydin-92' and the highest moisture content was obtained from 'Aksu' variety.

When the studies were examined, Ghavidel and Prakash [71] reported that the moisture content of chickpea was 9.90% and Kilincer [72] reported that the moisture values of the samples varied between 4.47-11.13%. These results are similar to the findings of this study.

3.20. Correlation Analysis

The relationships between the yield and quality characteristics of the varieties used in the trial were determined by correlation analysis, and the results are presented in Table 5.

When Table 5 is examined, it can be seen that there is a positive and significant (p<0.01) correlation between pod setting time and flowering time (r = 0.402**); plant height and first pod height (r = 0.6976**), number of pods per plant (r = 0.7381**), yield per decare (r = 0.5946**), and oil content (r = 0.7202**). These findings are consistent with those reported by Gurbuz [17], Yasar [28], Yesilgun [73], and Eser et al. [74].

It has been determined that there is a significant positive correlation between the height of the first pod and the oil content (r = 0.4302**); the number of branches per plant and the number of pods (r = 0.3940**); the number of pods per plant and grain yield per decare (r = 0.8157**), harvest index (r = 0.4132**), starch content (r = 0.4436**), and oil content (r = 0.6733**); grain yield per decare and harvest index (r = 0.7127**) and oil content (r = 0.4021**); disease degree and protein content (r = 0.4375**); protein content and ash content (r = 0.5869**); starch content and oil content (r = 0.6664**); ash content and fiber content (r = 0.5604**). Our findings are similar to those of Yasar [28].

It has been determined that there is a significant negative correlation between flowering duration and grain yield per decare (r = -0.4366**); plant height and protein content (r = -0.5154**) and ash content (r = -0.6541**); the number of pods per plant and protein content (r = -0.6255**), ash content (r = -0.6938**) and fiber content (r = -0.4533**); the number of seeds per pod and thousand seed weight (r = -0.4444**); grain yield per decare and protein content (r = -0.5971**) and ash content (r = -0.4482**); harvest index and protein content (r = -0.5122**); protein content and starch content (r = -0.5697**), oil content (r = -0.4999**) and moisture content (r = -0.4413**); starch content and ash content (r = -0.7130**) and fiber content (r = -0.5917**); oil content and ash content (r = -0.8485**) and fiber content (r = -0.4166**). It has been observed that when one of these values increases, the other significantly decreases. The negative and significant correlation between grain yield and thousand seed weight found in our study is consistent with the results obtained by Guler et al. [75] and Altinbas and Tosun [76]. In contrast, Beysari [25], Yucel et al. [77], Hassan

et al. [78] and Saleem et al. [79] have reported a positive and significant correlation in their findings.

The statistically positive and significant (p<0.05) relationships between the traits are as follows. These are: Pod Setting Time and oil content (r = 0.3226*); plant height and starch content (r = 0.3301*); number of branches per plant and grain yield per decare (r = 0.3795*) and harvest index (r = 0.3279*); number of pods per plant and thousand seed weight (r = 0.3195*); pod length and fiber content (r = 0.3103*); thousand seed weight and grain yield per decare (r = 0.3373*); disease severity and ash content (r = 0.3228*). These findings are consistent with the results obtained by Yesilgun [73].

On the other hand, a negative relationship at the 5% significance level was determined between flowering duration and harvest index (r = -0.3778*); Pod Setting Time and ash content (r = -0.3585*); plant height and disease severity (r = -0.3532*); first pod height and disease severity (r = -0.3074*); number of seeds per pod and starch content (r = -0.3570*); disease severity and starch content (r = -0.3048*); and oil content (r = -0.3647*).

3.21. Principal Component Analysis (PCA)

In this study, where the performance of different chickpea varieties was evaluated based on yield and quality characteristics in Silifke district, the PCA (Principal Component Analysis) was applied to the obtained data. The results are presented in Table 6, and the graphical representation of these values is shown in Figure 1.

The first three principal components calculated for yield and quality characteristics explained approximately 59.00% of the total variation among the evaluated traits. Respectively, the number of pods per plant (0.37), ash content (-0.35), oil content (0.34), plant height (0.32), grain yield per decare (0.32), and protein content (-0.30) made significant contributions to the first principal component (PC1), which explained about 33.00% of the total variation.

The second component (PC2) accounted for approximately 14.42% of the total variation. The traits contributing the most to the variation among the varieties were moisture content (0.41), harvest index (0.36), fiber content (0.35), and flowering duration (-0.34). The third component (PC3) explained about 11.35% of the total variation. Root length (0.41), pod length (0.38), and thousand grain weight (0.37) were found to significantly influence the distribution of the varieties along the third axis based on their differences.

Table 5: Correlation of the examined characteristics of the varieties with each other

	Flowering Duration	Pod Setting Time	Plant Height	First Pod Height	Number of Branches per Plant	Number of Pods per Plant	Number of Seeds per	Pod Length	Thousand Grain Weight	Yield per Decare	Harvest Index	Root Length	Disease Degree	Protein Content	Starch Content	Fat Content	Ash Content	Fiber Content
Pod Setting Time	0.402**	1.0000																
Plant Height	-0.0813	0.0636	1.0000															
First Pod Height	-0.1149	-0.1399	0.6976**	1.0000														
Number of Branches per Plant	-0.2592	0.2120	0.0327	-0.2855	1.0000													
Number of Pods per Plant	-0.2593	0.2383	0.7381**	0.1873	0.3940**	1.0000												
Number of Seeds per	-0.1446	-0.2163	-0.2690	0.0951	-0.2152	-0.2688	1.0000											
Pod Length	0.0911	-0.0602	-0.1022	0.0315	0.0069	-0.2355	-0.0162	1.0000										
Thousand Grain Weight	-0.0259	-0.0852	0.2948	-0.0237	0.0132	0.3195*	-0.4444**	0.2046	1.0000									
Yield per Decare	-0.4366**	0.0859	0.5946**	0.1176	0.3795*	0.8157**	-0.2141	-0.0768	0.3373*	1.0000								
Harvest Index	-0.3778*	0.0019	0.2319	-0.1317	0.3279*	0.4132**	-0.0843	0.1504	0.2238	0.7127**	1.0000							
Root Length	0.2472	0.2552	-0.1292	-0.2660	-0.1743	-0.0211	0.1763	0.0917	-0.1455	0.1350	0.1899	1.0000						
Disease Degree	0.1674	0.2010	-0.3532*	-0.3074*	-0.2156	-0.2483	-0.0727	-0.0501	0.1649	-0.1694	-0.1216	0.1231	1.0000					
Protein Content	0.1956	-0.0083	-0.5154**	-0.1669	-0.0643	-0.6255**	0.0651	0.0892	-0.0532	-0.5971**	-0.5122**	-0.0623	0.4375**	1.0000				
Starch Content	0.0224	0.2118	0.3301*	0.0225	0.1983	0.4436**	-0.3570*	-0.1959	0.0304	0.1906	0.1092	-0.2241	-0.3048*	-0.5697**	1.0000			
Fat Content	-0.0798	0.3226*	0.7202**	0.4302**	0.1951	0.6733**	-0.2578	-0.2437	0.0801	0.4021**	0.1588	-0.2925	-0.3647*	-0.4999**	0.6664**	1.0000		
Ash Content	0.0204	-0.3585*	-0.6541**	-0.2134	-0.1177	-0.6938**	0.2271	0.2472	-0.0859	-0.4482**	-0.2518	0.0288	0.3228*	0.5869**	-0.7130**	-0.8485**	1.0000	
Fiber Content	-0.1650	-0.2235	-0.2908	0.0869	-0.1770	-0.4533**	0.2217	0.3103*	-0.2948	-0.1864	0.0255	0.0833	-0.0390	0.1624	-0.5917**	-0.4166**	0.5604**	1.0000
Moisture Content	-0.1586	-0.1338	0.0750	0.0586	0.0940	0.0904	-0.0072	0.0809	0.0138	0.2944	0.2579	0.1774	-0.2405	-0.4413**	-0.0289	-0.2233	0.1911	0.1549

Table 6: Principal Component Analysis Results for Examined Traits According to Research Findings

Traits	PC 1	PC 2	PC 3
Flowering Time	-0.11	**-0.35**	0.30
Pod Setting Time	0.08	-0.31	0.24
Plant Height	**0.32**	-0.01	-0.01
First Pod Height	0.14	0.03	-0.28
Number of Branches	0.15	0.01	-0.15
Number of Pods per Plant	**0.37**	0.04	0.09
Number of Seeds per Pod	-0.14	0.23	-0.29
Pod Length	-0.16	0.07	**0.38**
Thousand Seed Weight	0.10	-0.03	**0.37**
Yield per Decare	**0.32**	0.26	0.17
Harvest Index	0.22	**0.36**	0.26
Root Length	-0.06	0.11	**0.41**
Disease Degree	-0.21	-0.19	0.24
Protein Content	**-0.30**	-0.24	-0.09
Starch Content	0.27	-0.23	-0.03
Oil Content	**0.34**	-0.20	-0.15
Ash Content	**-0.35**	0.21	-0.01
Fiber Content	-0.20	**0.34**	-0.04
Moisture Content	0.05	**0.41**	0.14
Eigenvalues	6.35	2.74	2.16
Variance (%)	33.40	14.42	11.35
Cumulative Variance (%)	33.396	47.819	59.173

The differences between varieties in terms of the examined traits were quite high (Figure 2). Different varieties stood out for different traits. Figure 1 shows that varieties numbered 1, 2, 4, 7, 8, 12, and 14 are distributed at extreme points concerning the examined traits. Evaluating the traits, the 'Aksu' (1) variety showed significantly high values for plant height, first pod height, harvest index, yield per decare, moisture content, and fiber content compared to other varieties. However, it had lower values for protein content and disease degree. The 'Kusmen-99' (4) variety had high values for ash content and protein content but very low values for pod setting time, plant height, number of pods per plant, thousand seed weight, harvest index, yield per decare,

starch content, and oil content. The 'Ubet' (8) variety excelled in harvest index and starch content, but showed lower values for pod setting time and root length. The 'Sezenbey' (12) variety had high values for the number of branches per plant and the number of pods per plant, but low values for flowering duration and root length. In the 'Aydin-92' (7) variety, the first pod height was high, while root length, disease degree, and moisture content were low. The 'Seckin' (2) variety was distinctly different from others due to its high values in fiber content, root length, and harvest index. Lastly, the 'Yasa-05' (14) variety stood out from other varieties due to its low values in the number of branches per plant, seed yield per decare, moisture content, and harvest index.

4. CONCLUSIONS

When the results of the research were evaluated in general, it was determined that 'Aksu' variety was more suitable for the conditions of the region and showed superior characteristics compared to other varieties in terms of many traits examined. After 'Aksu', 'Seckin', 'Inci' and 'Aydin-91' varieties were the most suitable varieties. Since the lowest values were obtained from 'Kusmen-99' variety, its cultivation is not recommended. In addition, it is thought that Zuhal, Yasa-05, Borabey, Sari-98 and Cevdet-98 varieties should not be preferred. As a result of the study, it is predicted that the cultivation of 'Aksu' variety may be useful in barren and infertile soils in the region. However, in order to obtain more detailed and precise results, it is recommended that the experiment should be repeated for at least two more years and/or different studies should be carried out in different locations.

43
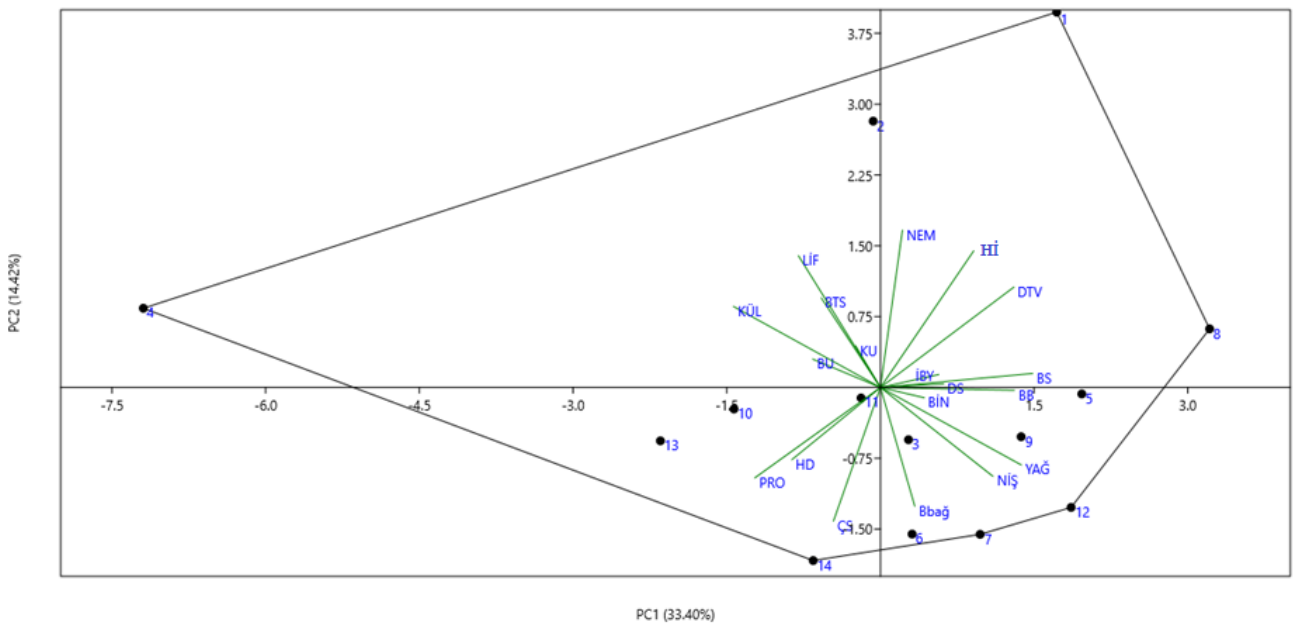
Figure 1. Principal Component Graph of the Examined Traits of the Varieties
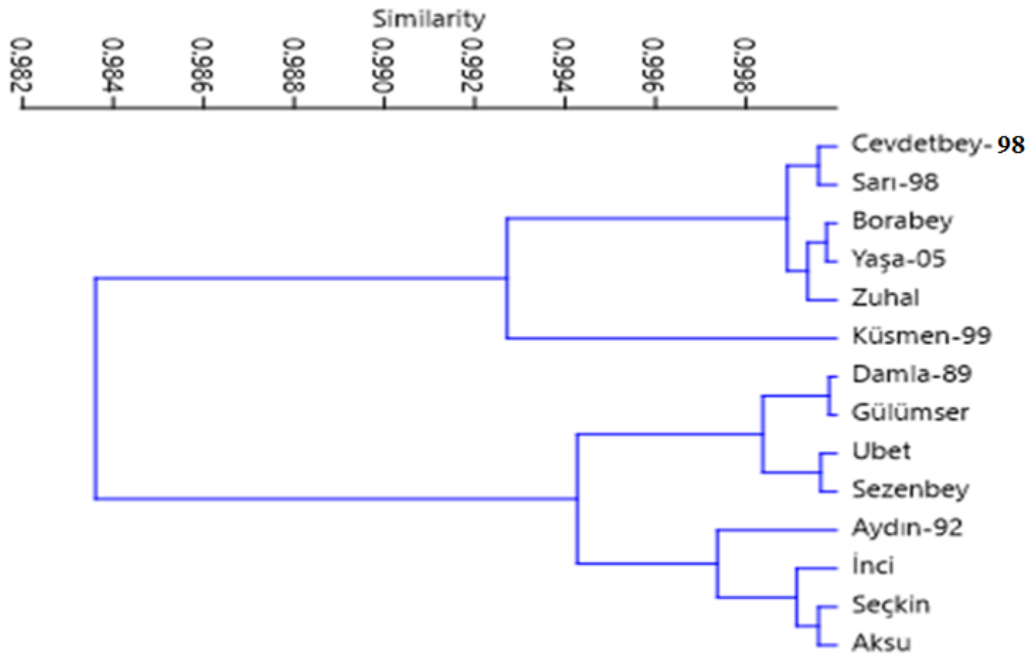
Figure 2. Cluster analysis based on the examined characteristics of the varieties

Acknowledgement

REFERENCES

[1] UNFPA. Dunya nufus durumu raporu. 2023 [cited 2023 Oct 29]. Available: https://turkiye.unfpa.org/tr/swop-%C3%B6zet-2023.

[2] Anonymous. Tarim ve Orman Bakanlığı. Ankara, 2021a.

[3] Wood J, Grusak M. Nutrional value chickpea. Chickpea Breeding and Management, CAB International. Wallingford. 2007; 101-142.

[4] Dogan A. Yoksullar lehine buyumede tarimin rolu: Sahra-altı Afrika ornegi. Karamanoglu Mehmetbey Universitesi İktisadi ve İdari Bilimler Fakultesi Dergisi. 2009; 11(16): 21-38.

[5] Malunga LN, Bar-El Dadon S, Zinal E, Berkovich Z, et al. The potential use of chickpeas in development of infant follow-on formula. Nutrition Journal. 2014; 22(13): 8.

[6] Siddique M, Hamid A, Islam M. Drought stress effects on water relation of wheat. Botanical Bulletin- Academia Sinica Taipei. 2000; 41(1): 35-39.

[7] Singh S, Singh I, Kapoor K, Gaur P, Chaturvedi S, Singh N, Sandhu J. Chicpea. Broadening the Genetic Base of Grain Legumes. 2014; 51-73.

[8] E. Karagul, «Turkiye yemeklik tane baklagil genetik kaynakları,» ANADOLU Ege Tarımsal Arastırma Enstitusu Dergisi, cilt 27, no. 1, p. 56 – 70, 2017.

[9] Burucu D. Urun Raporu NOHUT 2021. TEPGE Yayın No: 342, 2021.

[10] Sayilgan C, Kocaturk M. Sahil ve gecit kusagına uygun tescilli ve yerel nohut cesitlerinin Bati Akdeniz Bolgesi'nde yazlik ekim verim performanslarinin degerlendirilmesi. Derim. 2019; 36(2): 207-216.

[11] TEPGE. T.C. Tarim ve Orman Bakanligi Tarimsal Ekonomi ve Politika Gelistirme Enstitusu Mudurlugu. 2023. Available: https://arastirma.tarimorman.gov.tr/tepge/Menu/27/Tarim-Urunleri-Piyasalari.

[12] Mart D, Cansaran E, Karakoy T, Simsek M. Cukurova ve Orta Anadolu bolgesinden toplanan yerel nohut (Cicer arietinum L.) populasyonlarinin bazi onemli agronomik ve morfolojik ozelliklerinin belirlenmesi, seleksiyonu ve kalitatif karekterlerinin karakterizasyonu. Tarla Bitkileri Merkez Arastirma Enstitusu Dergisi. 2007; 16(1-2): 61-72.

[13] Anonymous. Mersin İl Tarim Mudurlugu. Mersin, 2009.

[14] Anonymous. Mersin Meteoroloji Il Mudurlugu. Mersin, 2021.

[15] Anlarsal A E, Yucel C, Ozveren D. Cukurova kosullarinda bazi nohut (Cicer arietinum L.) hatlarinin verim ve verimle ilgili ozelliklerinin saptanmasi uzerine bir arastirma. Turkiye 3. Tarla Bitkileri Kongresi, 15-20 Kasım, Adana. 1999.

[16] Mart D. Cukurova kosullarinda nohut (Cicer arietinum L.)'de bazi onemli ozellikler yonunden genotip x cevre interaksiyonlari ve uyum yeteneklerinin saptanmasi uzerine bir arastirma. Adana: Cukurova Universitesi, Fen Bilimleri Enstitusu; 2000.

[17] Karakoy T. Cukurova ve Orta Anadolu Bolgelerinden toplanan bazi yerel nohut (Cicer arietinum L.) genotiplerinin verim ve verimle ilgili ozelliklerinin belirlenmesi uzerine bir arastirma. Adana: Cukurova Universitesi, Fen Bilimleri Enstitusu; 2008.

[18] Matur I. Sirnak-Idil kosullarinda bazi nohut hat ve cesitlerinin verim ve verim unsurlarinin

degerlendirilmesi. Sirnak: Sirnak Universitesi, Fen Bilimleri Enstitusu; 2021.

[19] Aydogan A. Genis ve dar yaprakli kabuli tip nohut (Cicer arietinum L.) cesit ve hatlarinda verim ve kalite ozelliklerinin belirlenmesi. Ankara: Ankara Universitesi Fen Bilimleri Enstitusu; 2012.

[20] L. G. Gurbuz, Bingol ekolojik kosullarında bazı nohut (Cicer arietinum L.) cesitlerinin verim ve kalite ozelliklerinin belirlenmesi, Bingol: Bingol Universitesi Fen Bilimleri Enstitusu, 2018.

[21] Patan F. Tescilli bazi nohut (Cicer arietinum L.) cesitlerinin Erzurum ekolojik kosullarina adaptasyonu. Erzurum: Ataturk Universitesi, Fen Bilimleri Enstitusu; 2014.

[22] Karakan Kaya F. Bazi nohut (Cicer arietinum L.) cesitlerinin Elazig kosullarindaki verim ve adaptasyon yeteneklerinin belirlenmesi. Bingol: Bingol Universitesi, Fen Bilimleri Enstitusu; 2014.

[23] Oztas E, Bucak B, Al V, Kahraman A. Farklı nohut (Cicer arietinum L.) cesitlerinin Harran ovası kosullarinda kisa dayaniklilik, verim ve diger ozelliklerinin belirlenmesi. Harran Universitesi Ziraat Fakultesi Dergisi. 2007; 11(3/4): 84-85.

[24] Yigit M. Bazi nohut cesitlerinin farkli tohum iriligi ve ekim zamanlarinda verim ve kalite performanslarinin belirlenmesi., Kirsehir: Kirsehir Ahi Evran Universitesi Fen Bilimleri Enstitusu; 2018.

[25] Ozgun O. Diyarbakir Bismil kosullarinda damla sulama ve farklı ekim tarihlerinin nohutta (Cicer arietinum L.) verim ve verim ogelerine etkisi, Erzurum: Ataturk Universitesi Fen Bilimleri Enstitusu; 2004.

[26] Yurur N, Karasu A. Ekim zamaninin nohutun bazi agronomik ozelliklerine etkisi. Uludag Universitesi Ziraat Fakultesi Dergisi. 1995; 11: 95-107.

[27] Erden Z. Siirt ekolojik kosullarinda nohudun (Cicer arietinum L.) cesit ve adaptasyon ozelliklerinin belirlenmesi. Van: Yuzuncu Yıl Universitesi Fen Bilimleri Enstitusu; 2014.

[28] Beysari V. Bazi nohut (Cicer arietinum L.) cesitlerinin Bingol kosullarindaki verim ve adaptasyon yeteneklerinin belirlenmesi. Bingol : Bingol Universitesi Fen Bilimleri Enstitusu; 2012.

[29] Beykara İ. Bingol ekolojik kosullarinda farkli ekim zamanlarinin bazi nohut (Cicer arietinum L.) genotiplerinde verim ve verim ozelliklerine etkisi. Bingol : Bingol Universitesi Fen Bilimleri Enstitusu; 2019.

[30] Dinc A. Turkiye'de tescil edilmis bazi nohut (Cicer arietinum L.) cesitlerinin Van kosullarinda verim ve verim ogelerinin belirlenmesi. Van: Yuzuncu Yıl Universitesi Fen Bilimleri Enstitusu; 2014.

[31] Yasar M. Diyarbakir ekolojik kosullarinda bazi nohut (Cicer arietinum L.) hat ve cesitlerinin verim ve verim ogelerinin belirlenmesi uzerine bir arastırma. Adana: Cukurova Universitesi, Fen Bilimleri Enstitusu; 2010.

[32] Bakoglu A, Aycicek M. Bingol ekolojik kosularinda bazi nohut (Cicer arietinum L.) cesitlerinin verim ve verim ogeleri uzerine bir arastırma. Firat Universitesi Fen ve Muhendislik Bilimleri Dergisi. 2005; 17(1): 107-113.

[33] Bicer B T, Anlarsal A E. Bazı nohut (Cicer arietinum L.) koy cesitlerinde bitkisel ve tarimsal ozelliklerin belirlenmesi. Ankara Universitesi Ziraat Fakultesi Tarım Bilimleri Dergisi. 2004; 10(4): 289-396.

[34] Vural H, Karasu A. Variability studies in chickpea (Cicer arietinum L.) varieties grown in Isparta of Turkey. Revista UDO Agricola. 2007; 7(1) 35-40.

[35] Canci H, Toker C. Evaluation of annual wild Cicer species for drought and heat resistance under field conditions. Genetic Resources and Crop Evolution. 2009; 56: 1-6.

[36] Peker G N. Ileri duzey nohut genotiplerinde verim ve kalite calismalari. Kirsehir : Kirsehir Ahi Evran Universitesi Fen Bilimleri Enstitusu, 2022.

[37] Demirci O, Bildirici N. Sanliurfa ekolojik degerlendirmelerinde yetistirilen nohut (Cicer arietinum L.) cesitlerinin verim ve verim unsurlarının belirlenmesi. Avrupa Bilim ve Teknoloji Dergisi. 2020; 20: 656-662.

[38] Sozen O, Karadavut U. Kırsehir ekolojik kosullarinda yetistirilen bazi nohut genotiplerinin verim ogeleri korelasyon ve path analizi. 21. Yuzyilda Fen ve Teknik Dergisi. 2019; 6(12): 29-40.

[39] Tetik S. Turkiye'de tescil edilmis bazi nohut cesitlerinin Bolu sartlarında verim ve bazi verim ogelerinin tespit edilmesi. Bolu: Bolu Abant İzzet Baysal Universitesi Fen Bilimleri Enstitusu, 2019.

[40] Onder M, Ucer F. Konya ekolojik sartlarinda bazi nohut cesitlerinin ikinci urun olarak yetistirilmesi. Selcuk Universitesi Ziraat Fakultesi Dergisi. 1999; 13(18): 1-8.

[41] Bicer B T. Diyarbakir yoresinde toplanan bazi nohut yerel cesitlerinde onemli bitkisel ve tarimsal ozelliklerin belirlenmesi uzerine bir arastirma. Adana: Cukurova Universitesi Fen Bilimleri Enstitusu, 2001.

[42] Arshad M, Bakhsh A, Ghafoor A. Path coefficient analysis in chickpea (Cicer arietinum L.) under rainfed conditions. Pakistan Journal of Botany. 2004; 36(1): 75-81.

[43] Kacar O, Goksu E, Azkan N. Bursa'da kislik olarak yetistirilebilecek nohut (Cicer arietinum L.) hatlarinin belirlenmesi. Uludag Universitesi. Zir. Fak. Dergisi. 2005; 19(2): 33-45.

[44] Aydogan Y. Eskisehir ekolojik kosullarinda bazi nohut (Cicer arietinum L.) cesitlerinin tarimsal ozelliklerinin ve ozellikler arasi iliskilerin belirlenmesi. Kirsehir : Kirsehir Ahi Evran Universitesi, Fen Bilimleri Enstitusu, 2019.

[45] Talebi R, Fayaz F, Jelodar N. Correlation and path coeficients analysis of yield and yield components of chickpea (Cicer arietinum L.) under dry land condition in the west of Iran. 2007; 6(7): 1151-1154.

[46] Bicaksiz Y. Bazi Nohut (Cicer arietinum L.) cesitlerinin orta Anadolu kosullarina adaptasyonu, Eskisehir:Eskisehir Osmangazi Universitesi, 2010.

[47] Babagil G E. Erzurum ekolojik kosullarinda bazi nohut (Cicer arietinum L.) cesitlerinin verim ve verim ozellikleri incelenmesi. Anadolu Tarım Bilim Dergisi. 2011; 26(2): 122-127.

45

[48] Bicer BT, Anlarsal AE. Diyarbakir yoresi nohut (Cicer arietinum L.) koy populasyonlarinin tarimsal, morfolojik ve fenolojik ozellikler icin degerlendirilmesi. Harran Universitesi Ziraat Fakultesi Dergisi. 2005; 9(3): 1-8.

[49] Eser D. Yemeklik tane baklagiller. Ankara: Ankara Universitesi Ziraat Fakultesi Ders Notu, 1978.

[50] Ceran F. Farkli zamanlarda ekilen nohut cesitlerinin (Cicer arietinum L.) bazi tarimsal ozelliklerinin belirlenmesi. Konya: Selcuk Universitesi-Fen Bilimleri Enstitusu, 2015.

[51] Erdemci I. Guneydogu Anadolu Bolgesi kosullarinda farkli nohut (Cicer arietinum L.) genotiplerinin yazlik ve kislik ekimlerinde bazi tarimsal ve teknolojik ozelliklerinin belirlenmesi. Adana: Cukurova Universitesi-Fen Bilimleri Enstitusu, 2012.

[52] Altinbas M, Sepetoglu H, Karasu A. Nohutta verim ogelerinin farkli cevre kosullarinda verime etkileri uzerinde bir calisma. Turkiye III.Tarla Bitkileri Kongresi, Adana, 1999.

[53] Altınbas M, Sepetoglu H H. Kislik ekime uygun nohut gelistirmede bazi tarimsal ozellikler icin genotipik ve cevresel etki degerdirmesi. Ege Universitesi Ziraat Fakultesi Dergisi. 2002; 39(3): 33-40.

[54] Mart D, Oktem A, Akın R, Turkeri M, Atmaca E, Mart S, Karakoy T. Sanliurfa'da tescilli bazi nohut (Cicer arietinum L.) cesitlerinin verim, morfolojik ve kalite ozelliklerinin degerlendirilmesi. Turk Tarım ve Doga Bilimleri Dergisi. 2023; 10(1): 152-160.

[55] Topcu M, Akcura M. Bazi nohut cesitlerinin verim ve verim unsurlarinin incelenmesi. COMU, Ziaraat Fakultesi Dergidi. 2022; 10(1): 191-198.

[56] Gunes A, Tekatlı M, Erturk E, Kilinc C. Kahramanmaras kosullarinda bazi ileri nohut (Cicer arietinum L.) genotiplerinde tarimsal ozelliklerin incelenmesi. Turk Tarim ve Doga Bilimleri Dergisi. 2022; 9(1): 119-131.

[57] Topcu M. Bazi nohut (Cicer arietinum L.) cesitlerinin Edirne kosullarinda verim ve verim unsurlarının incelenmesi. Canakkale: COMU, Fen Bilimleri Enstitusu, 2019.

[58] Gundogdu Gurbuz L. Bingol Ekolojik Kosullarinda Bazi Nohut (Cicer arietinum L.) Cesitlerinin Verim ve Kalite Ozelliklerinin Belirlenmesi. Bingol: Bingol Universitesi Fen Bilimleri Enstitusu, 2018.

[59] Yagmur M, Engin M. Nohut (Cicer arietinum L.)'ta fosfor ve azot dozlari ile bakteri (Rhizobium ciceri) asilamanin bazi morfolojik ozellikler ile tane verimi uzerine etkileri ve bazi bitkisel ozellikler arasındaki iliskiler. Yuzuncu Yil Universitesi Ziraat Fakultesi Tarım Bilimleri Dergisi. 2005; 15(2): 103-112.

[60] Sakar S. Sırnak-İdil kosullarinda kislik ve erken ilkbaharda yetistirilen nohut cesitlerinin verim ve verimle ilgili ozelliklerinin belirlenmesi. Sırnak: Sırnak Universitesi Lisansustu Egitim Enstitusu, 2022.

[61] Yigitoglu D. Kahramanmaras kosullarinda farkli bitki sikliklarinin kislik ve yazlik ekilen bazi nohut cesitlerinde (Cicer arietinum L.) verim ve verim ile ilgili ozelliklere etkisi. Adana: Cukurova

Universitesi Fen Bilimleri Enstitusu, Tarla Bitkileri Anabilim Dalı, 2006.

[62] Sanlı A, Kaya M. Tohum Uygulamaları İle Farkli Ekim Zamanlarinin Nohut Cicer arietinum L.' un Bazi Agronomik Ozellikler Uzerine Etkileri. Suleyman Demirel Universitesi Ziraat Fakultesi Dergisi. 2008; 3: 42-51.

[63] Kacar B. Bitki fizyolojisi. Ankara: Ankara Universitesi Ziraat Fakultesi Yayınları 1153, 1989.

[64] Baylan B. Diyarbakir kosullarinda nohut ekim zamanı ile antraknoz hastaligi (Ascochyta rabiei (pass) labr.) arasındaki iliskinin belirlenmesi. Diyarbakır: Dicle Universitesi, Fen Bilimleri Enstitusu, 1998.

[65] Sari H. Bazı yemeklik tane baklagillerin gelisme donemlerine gore farkli bitki kisimlarinda ham protein iceriklerinin belirlenmesi. Samsun: Ondokuz Mayıs Universitesi Fen Bilimleri Enstitusu, 2015.

[66] Yagmur M, Kaydan D. Plant growth and protein ratio of spring sown chickpeawith various combinations of rhizobium inoculation, nitrogen fertilizer and irrigation under rainfed condition. African Journal of Agricultural Research. 2010; 6(12): 2648-2654.

[67] Karayel R, Uzun A, Bozoglu H. Nohut (Cicer arietinum L.)'un verim ve kalitesine ahir gubre dozlarinin etkisi. BSEU Fen Bilimleri Dergisi 7, Milli Mucadele ve TBMM'nin Acılısının 100. Yılı Anısına-100. Yıl Ozel Sayisi. 2020; 279-288.

[68] Agsakallı A. Farkli ekim sikligi ve gubre dozlarinin bazi nohut genotiplerinde verim, verim unsurları ve kalite uzerine etkileri. Erzurum: Ataturk Universitesi, Fen Bilimleri Enstitusu, 1995.

[69] Ozdemir S. Yemeklik Baklagiller. İstanbul: Hasad Yayıncılık., 2006.

[70] Sarimurat M S. Van ekolojik kosullarinda yetistirilen bazi nohut (Cicer arietinum L.) cesitlerinin verim ve kalite ozelliklerinin belirlenmesi. Van: Van Yuzuncu Yıl Universitesi, Fen Bilimleri Enstitusu, 2017.

[71] Sepetoglu H. Nohutta cesit ve bitki sikliginin buyume ve verim uzerine etkisi. Ege Universitesi, Ziraat Fakultesi Dergisi. 1988; 19(2): 71-76.

[72] Deshpande S S, Damodaran S. Structure digestibility relationship of legume 7S proteins. Advanced in Cereal Science and Technology. 1990; 10(3): 156.

[73] Ertas N. Nohut (Cicer Arietinum L.) fasulye (Phaseolus vulgaris L.) ve soya fasulyesinden (Glycine max L.) uretilen baklagil bulgurlarinin uretim metotlarinin standardizasyonu ile bazi kalitatif ve besinsel ozelliklerinin belirlenmesi. Konya: Selcuk Universitesi, Fen Bilimleri Enstitusu, 2010.

[74] El-Adawy T A. Nutritional composition and antinutritional factors of chickpeas (Cicer arietinum L.) undergoing different cooking methods and germination. Plant Foods for Human Nutrition. 2002; 57(83): 97.

[75] Ghavidel RA, Prakash J. The impact of germination and dehulling on nutrients, antinutrients, in vitro iron and calcium bioavailability and in vitro starch

46

and protein digestibility of some legume seeds. LWT-Food Science and Technology. 2007; 40: 1292-1299.

[76] Kilincer F. Cimlendirilmis bazi tahil ve baklagillerin besinsel ve fonksiyonel ozellikleri uzerine bir arastırma. Konya: Necmettin Erbakan Universitesi Fen Bilimleri Enstitusu, 2018.

[77] Yesilgun S. Cukurova bolgesinde bazi kislik nohut (Cicer arietinum L.) hat ve cesitlerinin bitkisel ve tarimsal ozelliklerinin saptanması. Adana: Cukurova Universitesi, Fen Bilimleri Enstitusu, 2006.

[78] Eser D, Gecit HH, Emekliler HY. Evaluation of chickpea landraces in Turkey. Chickpea Newsletter Jun. Icn. 1991; 24: 22-23.

[79] Guler M, Adak M, Ulukan H. Determining relationships among yield and some yield components using path coefficient analysis in chickpea (Cicer arietinum L.). European Journal of Agronomy. 2001; 14: 161-166.

[80] Altınbas M, Tosun M. Nohutta ileri generasyonlarda verim ile verim ogeleri arasindaki iliskiler uzerine bir degerlendirme. Journal of Agriculture Faculty of Ege University. 2002; 39(2): 33-40.

[81] Yucel D, Anlarsal AM, Yucel C. Genetic variability, correlation and path analysis of yield and yield components in chickpea (Cicer arietinum L.). Turkish Journal of Agriculture and Forestry. 2006; 30: 183-188.

[82] Hassan M, Atta BM, Shah TM, Haq MA, Syed H, Alam SS. Correlation and path coefficient studies in induced mutants of chickpea (Cicer arietinum L.). Pakistan Journal of Botany. 2005; 37(2): 293-298.

[83] Saleem M, Tahir MHN, Kabir R, Javid M, Shahzod K. Interrelationships and path analysis of yield attributes in chickpea (Cicer arietinum L.). International Journal of Agriculture & Biology. 2002; 4(3): 404-406.

47

Türk Doğa ve Fen Dergisi
Turkish Journal of Nature and Science
www.dergipark.gov.tr/tdfd

The Potential Prognostic Value of Glutatione-S Transferase Izoenzymes in Non-small Cell Lung Cancer

Aydın KESKIN[1] , **Pınar KAYGIN [1]** , **Kayhan BAŞAK [2]** **Fatma ÇAKMAK KAZANCI [3]** , **Sezen YILMAZ SARIALTIN [4]** , **Onur DIRICAN[5*]** , **Abbas Ali HUSSEINI [6]** , **Muharrem ATLI[1]** , **Can YILMAZ[7]** , **Serpil OĞUZTÜZÜN[1]**

[1]Department of Biology, Faculty of Arts and Sciences, Kirikkale University, Kirikkale, Türkiye
[2]Department of Pathology, Kartal Dr. Lütfi Kırdar City Hospital, Turkish Ministry of Health, University of Health Sciences, İstanbul, Türkiye
[3]Medical Pathology Clinic, Çerkezkoy State Hospital, Tekirdağ, Türkiye
[4]Department of Toxicology, Faculty of Pharmacy, Ankara University, Ankara, Türkiye
[5]Department of Pathology Laboratory Techniques, Vocational School of Health Services, Istanbul Gelişim University, Istanbul, Türkiye.
[6]Life Sciences and Biomedical Engineering Application and Research Centre, Istanbul Gelisim University, Istanbul, Türkiye.
[7] Department of Molecular Biology and Genetics, Yüzüncü Yıl University, Van, Türkiye
Aydın KESKİN ORCID No: 0000-0003-2360-7692
Pınar KAYGIN ORCID No: 0000-0003-0127-1753
Kayhan BAŞAK ORCID No: 0000-0003-1960-8924
Fatma ÇAKMAK KAZANCI ORCID No: 0000-0001-5064-0952
Sezen YILMAZ SARIALTIN ORCID No: 0000-0002-8387-4146
Onur DİRİCAN ORCID No: 0000-0003-0511-6611
Abbas Ali HUSSEINI ORCID No: 0000-0002-8861-7106
Muharrem ATLI ORCID No: 0000-0002-2453-1370
Can YILMAZ ORCID No: 0000-0002-0028-6614
Serpil OĞUZTÜZÜN ORCID No: 0000-0002-5892-3735

Corresponding author: odirican@gelisim.edu.tr

(Received: 14.11.2024, Accepted: 14.12.2024, Online Publication: 26.03.2025)

Keywords	**Abstract:** To investigate correlations between GST isozyme levels and tumor markers to evaluate the prognostic value of GST isozymes. This retrospective study analyzed clinical data from 40 patients with adenocarcinoma and squamous cell carcinoma. Tumor and adjacent healthy tissue samples were immunohistochemically stained to profile GST enzymes (Sigma, Omega, Pi, Mu) and caspase-3, Bcl-2, p38, p53. Associations between protein expression levels and patient characteristics were examined, and correlations between GST enzymes and Caspase-3, Bcl-2, p38, p53 were analyzed. Significant immunohistochemical differences were found between tumorous and healthy tissues for all markers. GST enzymes (GSTS, GSTO, GSTP, GSTM) were predominantly expressed in tumorous tissues, with GSTO and GSTP showing high expression levels. Compared to SCC tissues, GSTP expression is around 30% higher in AC tissues. In contrast, GSTO expression increases by around 25% in second-stage tumors, particularly in AC tissues. Correlation analysis revealed significant positive associations between Bcl-2 and caspase-3, p38, GSTS, between caspase-3 and GSTP, and between p38 and GSTM in tumor tissues. The study supports the prognostic value of GST isozymes in NSCLC.
Lung Cancer, Glutatione-S Transferase, Caspase-3, Bcl-2, p38, p53	

Küçük Hücreli Dışı Akciğer Kanserinde Glutatione-S Transferaz İzoenzimlerinin Potansiyel Prognostik Değeri

Öz: GST izozimlerinin prognostik değerini değerlendirmek için GST izozim düzeyleri ile tümör belirteçleri arasındaki korelasyonları araştırmak. Bu retrospektif çalışmada adenokarsinom ve skuamöz hücreli karsinomu olan 40 hastanın klinik verileri analiz edilmiştir. Tümör ve komşu sağlıklı doku örnekleri, GST enzimlerinin (Sigma, Omega, Pi, Mu) ve kaspaz-3, Bcl-2, p38, p53'ün profilini çıkarmak için immünohistokimyasal olarak boyandı. Protein ekspresyon düzeyleri ile hasta özellikleri arasındaki ilişkiler incelenmiş ve GST enzimleri ile Kaspaz-3, Bcl-2, p38, p53 arasındaki korelasyonlar analiz edilmiştir. Tüm belirteçler için tümörlü ve sağlıklı dokular arasında anlamlı immünohistokimyasal farklılıklar bulunmuştur. GST enzimleri (GSTS, GSTO, GSTP, GSTM) ağırlıklı olarak tümörlü dokularda eksprese edilmiş, GSTO ve GSTP yüksek ekspresyon seviyeleri göstermiştir. SCC dokularıyla karşılaştırıldığında, GSTP ekspresyonu AC dokularında yaklaşık %30 daha yüksektir. Buna karşılık, GSTO ekspresyonu ikinci evre tümörlerde, özellikle de AC dokularında yaklaşık %25 oranında artmaktadır. Korelasyon analizi, tümör dokularında Bcl-2 ile kaspaz-3, p38, GSTS arasında, kaspaz-3 ile GSTP arasında ve p38 ile GSTM arasında anlamlı pozitif ilişkiler olduğunu ortaya koymuştur. Çalışma, KHDAK'de GST izozimlerinin prognostik değerini desteklemektedir.

1. INTRODUCTION

Tumors arising in the lung parenchyma or within the bronchi are referred to as lung cancer, or bronchogenic carcinoma. Lung neoplasms are the primary cause of cancer incidence and death globally [1].

Many of the more advanced methods of pathologic diagnosis have resulted in a more accurate pathologic and genetic categorization of lung tumors, opening the door to more effective therapeutic options. This has been made possible by the introduction of immunohistochemistry and molecular testing throughout the classification. The 2021 WHO Classification of Thoracic Tumors includes following main titles:: papillomas, adenomas, precursor glandular lesions, adenocarcinoma in situ, adenocarcinomas (AC), invasive nonmucinous adenocarcinoma, squamous precursor lesions, squamous cell carcinomas (SCC), large cell carcinomas (LCC), adenosquamous carcinomas, sarcomatoid carcinomas, salivary gland-type tumors, neuroendocrine tumors, neuroendocrine carcinomas (e.g., small cell carcinoma, SCLC, and large cell neuroendocrine carcinoma, LCNEC), tumors of ectopic tissues (malonoma and meningioma), mesenchymal tumors specific to the lung, and PEComatous tumors [2]. AC, SCC, and LCC are subtypes of non-small-cell lung carcinoma (NSCLC), which makes up 85% of all cases of lung cancer [3].

The pathology of adenocarcinomas is characterised by the formation of neoplastic glands, the expression of pneumocyte marker (thyroid transcription factor 1 (TTF-1) with or without napsin expression), or intracytoplasmic mucin. On cytology, squamous cell pathology is indicated by the presence of keratin and/or intercellular desmosomes [4]. Both of them requires the immunohistochemical (IHC) evidence of expression of some current markers such as p38 [5,6] caspase-3[7-9], Bcl-2 [10-11] and p53 [12-14]. However, despite the fact that these markers are widely employed, some

publications have critical views on their prognostic efficacy as well as negative attitudes [15,16]. The key takeaway is that there is a constant mention of the need for additional IHC markers that can serve as substitutes for these and other related popular indicators, or that, when combined, can improve prognostic outcomes.

A multiple gene family of phase II enzymes known as glutathione transferases (GSTs) catalyses endogenous glutathione detoxification processes and shields cellular macromolecules from cytotoxic and carcinogenic chemicals. The six gene families that make up the cytosolic GST isozymes are alpha (GSTA), mu (GSTM), theta (GSTT), pi (GSTP), omega (GSTMO), and one membrane-associated microsomal GST, which are categorised based on their biochemical properties [17]. Abnormal expression and GST polymorphisms have been linked to a number of human diseases, including malignant tumors. Many tumors have increased GST expression, which is linked to poor prognosis, treatment resistance, and cell proliferation [18]. There are few studies on the prognostic value of GST isozymes in lung cancer, despite the fact that many cancer types, including myeloid leukaemia, stomach, urinary bladder, breast, and nasopharyngeal carcinoma, have had this information evaluated and reported [19-23]. However, it is still possible to modify the risk of lung cancer by changing the structure, function, or expression levels of specific isozymes [24].

In the current study, the expressions of p38, p53, Bcl-2 and caspase-3, which are generally accepted cancer markers, as well as GSTO1, GSTM1, GSTP1 and GSTS1 isozymes were detected in two different types of NSCLC tumor samples, AC and SCC. The expression levels of those proteins in cancerous tissues were comparatively examined by using peripheral tissue as control group for each patient and the prognostic values of GST isozymes were analyzed by cross comparisons.

49

2. MATERIAL AND METHOD

2.1. The sources of specimens

The Kartal Dr. Lütfi Kırdar City Hospital Pathology Clinic in Istanbul, Turkey, identified and treated 40 patients with 20 AC and 20 SCC for the study. The clinical information and state of follow-up were reviewed in the patient's medical file. The median duration of follow-up was 24 months (between 2017-2019). Clinical staging, adequate follow-up information, and slides showing the histology of the tumor were available to all patients. Each patient was staged at the time of surgery using regional lung tissue dissection. The patient's cancer stage was ascertained using the TNM staging method created by the American Joint Committee on Cancer. Of the 40 cases, 29 were men and 11 were women. The mean age of the patients was 67.20 ± 1.36 years, with 62.5% of them being over 65. Of the 40 lung tumors that underwent surgical removal, 13 were in stage 1A, 7 in stage 1B, 8 in stage 2A, 9 in stage 2B, and 3 in stage 3A. 3.67 ± 0.38 cm is the average tumor diameter. Table 1 summarises the following information: patient age and gender; cancer grade; localization, invasion, involvement, in situ, metastasis, and neoadjuvant states; tumor size and stage; and patient survival states.

Table 1. Demographic and clinical data of patients

Data	Category	n (%)
Demographic data		
Gender	Female	11 (27.5%)
	Male	29 (72.5%)
Age	≤65	15 (37.5%)
	>65	25 (62.5%)
Clinical data		
Diagnosis	AC	20 (50%)
	SCC	20 (50%)
Grade	Acinar	5 (12.5%)
	Keratinized	10 (25.0%)
	Lepidic	5 (12.5%)
	Non-keratinized	10 (25.0%)
	Papiller	5 (12.5%)
	Solid	5 (12.5%)
Localization	Right AC	1 (2.5%)
	Right lower lobe	11 (27.5%)
	Right upper lobe	12 (30.0%)
	Left AC	2 (5.0%)
	Left lower lob	2 (5.0%)
	Left upper lob	11 (27.5%)
	Upper lobe	1 (2.5%)
Vascular invasion	Yes	13 (32.5%)
	No	27 (67.5%)
Neural invasion	Yes	9 (22.5%)
	No	31 (77.5%)
Bronchial involvement	Yes	11 (27.5%)
	No	29 (72.5%)
Pleural involvement	Yes	12 (30.0%)
	No	28 (70.0%)
in situ	Yes	4 (10.0%)
	No	36 (90.0%)
Metastasis	Yes	13 (32.5%)
	No	27 (67.5%)
Tumor size	T1A	11 (27.5%)
	T1B	5 (12.5%)
	T2A	12 (30.0%)
	T2B	4 (10.0%)
	T3	8 (20.0%)
Lymph node metastasis	N0	29 (72.5%)
	N1	7 (17.5%)
	N2	3 (7.5%)
Stage	No data	1 (2.5%)
	1A	13 (32.5%)
	1B	7 (17.5%)
	2A	8 (20.0%)
	2B	9 (22.5%)
	3A	3 (7.5%)
Neoadjuvant	Yes	2 (5.0%)
	No	38 (95.0%)
Survival status	Dead	9 (22.5%)
	Alive	31 (77.5%)
n % AC SCC	number of patients number of patients in the specified group / total number of patients adenocarcinoma squamous cell carcinoma	

2.2. Immunohistochemical analyses

The specimens that were surgically removed were routinely embedded in paraffin blocks and preserved in 10% formalin. After being sliced at 4 μm, tissue sections were stained with hematoxylin and eosin. Endogenous peroxidase activity was inhibited for immunohistochemistry by soaking the sections in 1% hydrogen peroxide (v/v) in methanol for ten minutes at room temperature (RT). Following that, the sections were rinsed with distilled water for five minutes. A household pressure cooker was used to accomplish antigen retrieval for three minutes using 0.01 M citrate buffer (pH 6.0). The sections were treated with super block (SHP125) (ScyTek Laboratories, USA) at room temperature for 10 minutes in order to prevent nonspecific background staining. The sections were incubated with diluted primary antibody anti-bcl-2 (Boster, USA, dilution 1:250), Anti-caspase-3 (Genex, USA, dilution 1:500), Anti-p38 (Santa Cruz, USA, dilution 1:500), Anti-p53 (Boster, USA, dilution 1:200) and Anti-GSTP (Boster, USA, dilution 1:1000), Anti-GSTM (Santa Cruz, USA, dilution 1:500), Anti-GSTO (Abcam, USA, dilution 1:200), Anti-GSTS (Santa Cruz, USA, dilution 1:50), for 1 hour at room temperature (RT). The sections were incubated at RT for biotinylated link antibody (SHP125) (ScyTek Laboratories, USA) following a 15-minute washing in TBS. Streptavidin/HRP complex (SHP125) (ScyTek Laboratories, USA) was then used as a course of treatment. To observe peroxidase activity in the tissues, diaminobenzidine (DAB) was utilised. Following a brief hematoxylin counterstain, the sections were dried and mounted. The degree of immunostaining of tumor cells was assessed as follows: The intensity of the cytoplasmic staining is 1 for weak, 2 for moderate, and 3 for strong. The intensity of immunostaining for GST Pi, GST Mu, GST Sigma, GST Omega, caspase 3, p38, Bcl-2 were assessed using the following scale: (Figure 1A-G) 1 = weak, 2 = moderate, 3 = strong. Immunohistochemical p53 reactivity was evaluated as follows: (null) for negative staining (no protein expression), (wild) for weak staining, (mutant) for strong staining (Figure 1H).
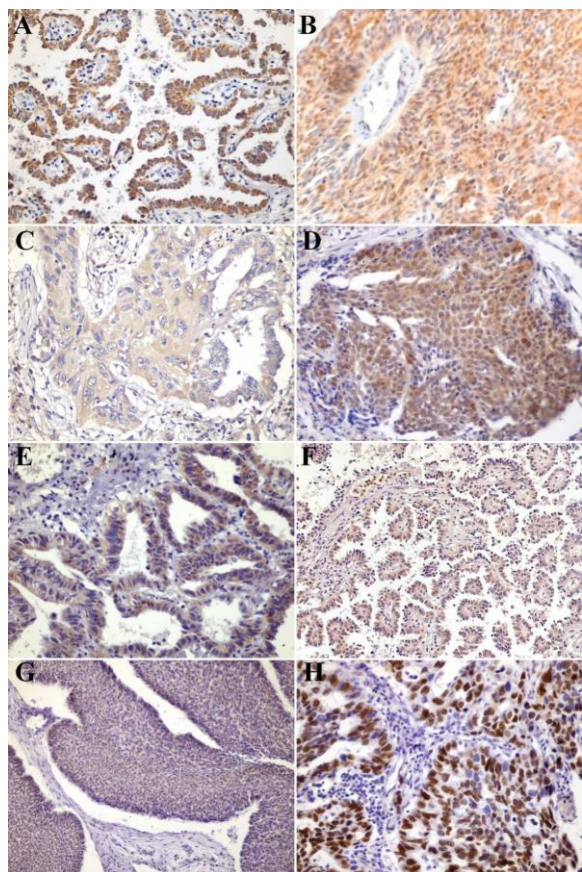
50

Figure 1. Composite figures of immunohistochemical staining results of (A) GST Pi, (B) GST Mu, (C) GST Sigma, (D) GST Omega (E) caspase 3, (F) p38, (G) Bcl-2, (H) p53

2.3. Statistical analyses

IBM® SPSS® Statistics 25.0 was used to conduct statistical analyses. Our investigation included normal tissues and SCC and AC tumors from 40 patients. The findings are given as mean +/- standard error of mean (SEM). Data that has been categorised according to clinical and demographic traits is presented as percentages and numbers. The Shapiro-Wilk test was used to assess the data's distribution patterns. Using the Levene test, homogeneity of variances was investigated. The Mann-Whitney U test was used to compare pairs when the assumptions of the parametric test were not met. The Chi-square test was used to investigate the association between category variables. Correlation analyses were conducted using Spearman's rank correlation test. The accepted threshold for statistical significance was $p < 0.05$.

3. RESULTS

Bcl-2, Caspase-3, p38 expressions in tumor and normal tissues were examined immunohistochemically and expression levels were evaluated (Table 3). Weak Bcl-2 expression was found in 12.5% of tumor tissues and moderate Bcl-2 expression was found in 7.5%. Bcl-2 expression was not detected in any of the normal tissues. Bcl-2 expression of tumor tissues is statistically significantly higher than that of normal tissues ($p = 0.003$). Caspase-3 was weakly expressed in 20% of tumor tissues and moderately expressed in 2.5%. Caspase-3 expression was not found in normal tissues. Caspase-3 expression in tumor tissues is statistically significantly higher than in normal tissues ($p = 0.002$). p38 was expressed weakly in 52.5% of tumor tissues, moderately in 25%, and strongly in 10%. While weak p38 expression is seen in 7.5% of normal tissues, there are no tissues where it is expressed at moderate or strong levels. The p53 expression of tumor tissues is statistically significantly higher than that of normal tissues ($p < 0.001$). The p53 staining patterns of tumor tissues were evaluated and described as mutant (more than 40% of the positive cells), null (less than 40% of the positive cells) and wild (40% of the positive cells).

51

Table 2. Bcl-2, caspase-3, p38, p53 expression levels of tumor and normal tissues determined by immunohistochemistry

IHC Score	Bcl-2 Tumor	Bcl-2 Normal	Caspase-3 Tumor	Caspase-3 Normal	p38 Tumor	p38 Normal	p53 Staining pattern	p53 Tumor
0	32/40 (%80.0)[a]	40/40 (%100)[a]	31/40 (%77.5)[a]	40/40 (%100)[a]	5/40 (%12.5)[a]	37/40 (%92.5)[a]	Mutant	12/40 (%30.0)[a]
1	5/40 (%12.5)[a]	-	8/40 (%20.0)[a]	-	21/40 (%52.5)[a]	3/40 (%7.5)[a]	Null	20/40 (%50.0)[a]
2	3/40 (%7.5)[a]	-	1/40 (%2.5)[a]	-	10/40 (%25.0)[a]	-	Wild	8/40 (%20.0)[a]
3	-	-	-	-	4/40 (%10.0)[a]	-		
Avg.	0.28 ± 0.09[b*] (0-2)[c]	-	0.25 ± 0.08[b*] (0-2)[c]	-	1.33 ± 0.13[b*] (0-3)[c]	0.08 ± 0.04[b] (0-1)[c]		
p-value	*0.003*		*0.002*		*<0.001*			
T/P value	-		-		*16.63*			

Total n = 40
Scoring was made according to the staining intensity of the tissues. 0: no staining, 1: weak positive, 2: moderate positive, 3: strong positive
(*) $p < 0.05$ is statistically significant according to the Mann-Whitney U test
(a)   number of samples stained at the specified score / total number of samples
(b)   Mean ± SEM
(c)   min – max

GSTS, GSTO, GSTP and GSTM expressions of tumor and normal tissues were evaluated immunohistochemically (Table 3). While weak and moderate GSTS expression was found in 70% of tumor tissues, weak and moderate GSTS expression was observed in 42.5% of normal tissues. Although the T/P ratio was 1.35, there was no significant difference between the GSTS expression levels of tumor and normal tissues ($p = 0.051$). GSTO was weakly expressed in 55% of tumor tissues and moderately expressed in 37.5%.

While medium and strong levels of GST-O expression were not observed in normal tissues, weak expression was observed in only 1 tissue. GSTO expressions of tumor tissues were found to be significantly higher than that of normal tissues (p<0.001). It was observed that GSTP was expressed weakly in 37.5% of tumor tissues, moderately in 17.5%, and strongly in 37.5%. While strong GSTP expression was not observed in normal tissues, weak expression was detected in 7.5% of the tissues and

moderate expression was detected in 5% of the tissues. GSTP showed significantly higher expression in tumor tissues than in normal tissues (p<0.001). While GSTM was expressed weakly in 10% of tumor tissues, moderately in 7.5%, and strongly in 5.2%, it was observed that it was not expressed at all in normal tissues. The expression of GSTM in tumor tissues was found to be significantly higher than in normal tissues (p = 0.003).

Table 3. Immunohistochemically detected GSTS, GSTO, GSTP and GSTM expression levels of tumor and normal tissues

IHC Score	GSTS Tumor	GSTS Normal	GSTO Tumor	GSTO Normal	GSTP Tumor	GSTP Normal	GSTM Tumor	GSTM Normal
0	5/40 (%12.5)[a]	16/40 (%40.0)[a]	3/40 (%7.5)[a]	38/40 (%95.0)[a]	3/40 (%7.5)[a]	35/40 (%87.5)[a]	32/40 (%80.0)[a]	40/40 (%100)[a]
1	28/40 (%70.0)[a]	17/40 (%42.5)[a]	22/40 (%55.0)[a]	1/40 (%2.5)[a]	15/40 (%37.5)[a]	3/40 (%7.5)[a]	4/40 (%10.0)[a]	-
2	7/40 (%17.5)[a]	7/40 (%17.5)[a]	15/40 (%37.5)[a]	-	7/40 (%17.5)[a]	2/40 (%5.0)[a]	3/40 (%7.5)[a]	-
3	-	-	-	-	15/40 (%37.5)[a]	-	1/40 (%2.5)[a]	-
Avg.	1.05 ± 0.09 (0-2)[c]	0.78 ± 0.12 (0-2)[c]	1.30 ± 0.10* (0-2)[c]	0.03 ± 0.03 (0-1)[c]	1.85 ± 0.16* (0-3)[c]	0.18 ± 0.08 (0-2)[c]	0.33 ± 0.12* (0-3)[c]	-
p-value	0.051		<0.001		<0.001		0.003	
T/P value	1.35		43.33		10.28		-	

Total n = 40
Scoring was made according to the staining intensity of the tissues. 0: no staining, 1: weak positive, 2: moderate positive, 3: strong positive.
(*) p<0.05 is statistically significant according to the Mann-Whitney U test
([a]) number of samples stained at the specified score / total number of samples
([b]) Mean ± SEM
([c]) min – max

Correlation analyzes were performed between Bcl-2, Caspase-3, p38, GSTS, GSTO, GSTP, GSTM expressions

of tumor and normal tissues; and the results are stated in Table 4.

Table 4. Correlation analyzes of IHC expressions in tumor and normal tissues

		Bcl-2	Caspase-3	p38	p38	GSTS	GSTS	GSTO	GSTO	GSTP	GSTP	GSTM
Bcl-2 Tumor	r	1.000	**0.468****	**0.387***	**0.342***	**0.402***	-0.031	0.043	-0.082	0.137	-0.023	0.272
	p		**0.002**	**0.014**	**0.031**	**0.010**	0.850	0.793	0.620	0.399	0.889	0.089
Caspase-3 Tumor	r	**0.468****	1.000	0.223	0.289	0.058	0.177	0.001	-0.082	**0.451****	-0.203	0.184
	p	**0.002**		0.166	0.071	0.722	0.273	0.997	0.619	**0.003**	0.210	0.254
p38 Tumor	r	**0.387***	0.223	1.000	**0.359***	0.307	-0.031	0.058	-0.071	0.046	-0.161	**0.374***
	p	**0.014**	0.166		**0.023**	0.054	0.848	0.724	0.670	0.779	0.322	**0.017**
p38 Normal	r	**0.342***	0.289	**0.359***	1.000	0.148	0.080	0.005	-0.047	-0.039	-0.107	0.136
	p	**0.031**	0.071	**0.023**		0.363	0.623	0.977	0.777	0.810	0.510	0.404
GSTS Tumor	r	**0.402***	0.058	0.307	0.148	1.000	-0.101	0.216	-0.027	0.197	0.120	0.090
	p	**0.010**	0.722	0.054	0.363		0.534	0.181	0.869	0.224	0.462	0.582
GSTS Normal	r	-0.031	0.177	-0.031	0.080	-0.101	1.000	-0.147	-0.180	0.011	0.240	-0.117
	p	0.850	0.273	0.848	0.623	0.534		0.366	0.272	0.946	0.136	0.474
GSTO Tumor	r	0.043	0.001	0.058	0.005	0.216	-0.147	1.000	0.195	0.228	0.097	-0.070
	p	0.793	0.997	0.724	0.977	0.181	0.366		0.234	0.157	0.550	0.669
GSTO Normal	r	-0.082	-0.082	-0.071	-0.047	-0.027	-0.180	0.195	1.000	0.191	-0.062	-0.075
	p	0.620	0.619	0.670	0.777	0.869	0.272	0.234		0.244	0.707	0.648
GSTP Tumor	r	0.137	**0.451****	0.046	-0.039	0.197	0.011	0.228	0.191	1.000	-0.030	0.281
	p	0.399	**0.003**	0.779	0.810	0.224	0.946	0.157	0.244		0.854	0.079
GSTP Normal	r	-0.023	-0.203	-0.161	-0.107	0.120	0.240	0.097	-0.062	-0.030	1.000	-0.187
	p	0.889	0.210	0.322	0.510	0.462	0.136	0.550	0.707	0.854		0.247
GSTM Tumor	r	0.272	0.184	**0.374***	0.136	0.090	-0.117	-0.070	-0.075	0.281	-0.187	1.000
	p	0.089	0.254	**0.017**	0.404	0.582	0.474	0.669	0.648	0.079	0.247	
r		correlation coefficient										
p		limit of significance (sign. (2-tailed))										
(*)		The correlation was significant at the 0.05 level (2-tailed).										
(**)		The correlation was significant at the 0.01 level (2-tailed).										

Positive and significant correlations were found between Bcl-2 and caspase-3, p38 and GSTS expressions in tumor tissues (p<0.05). A positive and significant correlation was determined between caspase-3 and GSTP expressions in tumor tissues (r=0.451, p=0.003). A positive and significant correlation was found between p38 and GSTM expressions in tumor tissues (r=0.374, p=0.017). A positive and significant correlation was also observed between p38 expressions of tumor and normal tissues (r = 0.359, p = 0.023).

4. DISCUSSION

The global epidemiology of lung cancer need ongoing surveillance due to its exceptional disease burden and the regional variations in trends for ageing, smoking, and population growth. When categorizing lung malignancies for treatment and preventive measures, the histology and molecular markers of the disease are crucial factors.

GST isozymes have attracted the interest of cancer researchers because they are expressed in all cell types and are abundant in aggressive cancer cells, implying that they play an important role in tumor growth and pathogenicity. The expression levels of several common cancer markers and GSTs, separately in AC and SCC, were assessed in the current study in connection with certain patient demographic information, and some conclusions were drawn. Regardless of the type of lung cancer, it has been noted that the expression of the GSTP and GSTO isozymes differs in male and female patients. Specifically, the expression of the GSTP isozyme was found to be approximately 11% greater in female patients, whilst the GSTO isozyme was 13% higher in male patients. Gender-related expression differences have also been demonstrated in other studies; e.g. according to Pan et al.,[25] lung cancer patients' null genotypes of GSTT and GSTM were associated with a gender-related risk [25].

Comparing the expressions of GSTO and GSTP isozymes for SCC and AC tumors, it was shown that, while taking into account the values obtained in AC tissues, GSTO was 7.7% higher in SCC tissue samples. Conversely, the GSTP isozyme exhibited the most intriguing data, with a 32.4% increase in expression in AC tissues relative to SCC. Wang et al. [26] noted the upregulation of GSTP in their recent study using lung cancer organoids and reported that it might be a significant target protein, particularly in chemotherapy trials [26]. Human lung squamous-cell carcinoma resistance to chemotherapeutic drugs is associated with an overexpression of GSTP[27]. This significant enzyme may have a role in both the diagnosis and treatment planning of lung cancer, according to the results of the current study. It should be highlighted, nonetheless, that not all cancer types would support this kind of inference, and that it might differ in the instance of lung cancer based on additional factors such the cancer's stage.

In fact, our investigation revealed that variations in the GSTP isozyme were observed in both AC and SCC first- and second-stage malignant tissues (1A and 1B and 2A and 2B, respectively). While GSTP expression was shown to be roughly 7% greater in second stage sample tissues compared to first stage tissues in SCC tumors, it was found to be approximately 9% higher in first stage samples in AC tissues than in second stage tissues. Rybárová et al.[28] reported a similar outcome for non-small cell lung cancer. In cancer samples, they discovered a statistically significant connection between GSTP1 and histological grade (p = 0.025); also, the adenocarcinoma samples exhibited the greatest GSTP1 expression (77%) based on histopathological type [28]. Although there is limited evidence for GSTP's predictive power, there is data supporting its use as a prognostic biomarker overall [29].

A correlation between the levels of GSTO expression and the histopathological grade was found in the present study. GSTO expression in second-stage tissues was 16.1% greater than in first-grade tissues, regardless of the type of NSCLC. More significantly, the GSTO expression level found in second-grade SCC tissues is roughly 24% greater than in first-grade tissues when classified based on cancer types. These findings suggest that GSTO protein levels, similar to GSTP, have the potential to be employed as a marker in non-small cell lung cancer diagnosis and stage assessment. When compared to control tissues, there was a statistically significant increase in GSTO expression in tumor tissues. It is therefore a target for medicinal uses. GSTO1 controls the JAK/STAT3 signalling pathway, which may play a significant part in NSCLC. As a result, blocking GSTO1 expression levels could be a cutting-edge treatment approach for NSCLC [30].

In NSCLC targeted cancer therapy, p38 is a protein that is regularly investigated for its functions in malignant cell proliferation or transformation. p38 is a protein frequently studied in NSCLC targeted cancer therapy for its roles in malignant cell growth or transformation [5,31,32]and p38 inhibition can be a potent therapeutic strategy against NSCLC [33,34]. We discovered that the expression of this significant marker protein was 11.3% higher in AC type cancer tissues than in SCC tissues. Furthermore, upon reexamining the expression in these AC tissues for the first and second stages, we observed a 25.5% higher rate of p38 protein detection in first-grade tissues relative to second-grade tissues. A comparable examination for SCC was performed again, and in second-grade tissues, p38 was found to be about 9% higher. It has, also, been shown that the mutant form of p53, another important tumor suppressor gene like p38, is more frequent in AC tissues than in SCC.

Evidence in this study reveals a significant elevation of Bcl-2, caspase-3, and p38 expression in tumor tissue. Moreover, the mutant allele of p53 was associated with lower expression of p53 in tumor tissue, with a higher frequency in men. These results emphasize that these proteins, known as biomarkers in cancer pathology, may also have prognostic value in lung cancer. Research indicates that patients with non-small cell lung cancer (NSCLC) who exhibit positive expression of Bcl-2 tend to experience a more favorable prognosis compared to

those with negative Bcl-2 expression [35,36]. However, the influence of Bcl-2 expression on the survival outcomes of stage I NSCLC patients appears to be less pronounced. While Bcl-2 expression shows promise as a prognostic biomarker in lung cancer, especially in NSCLC, its precise prognostic value across various stages and types of lung cancer requires validation through further large-scale clinical trials.

Studies have shown that high caspase-3 expression is associated with apoptosis of tumor cells and may lead to a better prognosis in patients with NSCLC [37,38]. While caspase-3 is a key player in apoptotic cell death, its expression levels in lung cancer have been linked to patient outcomes, highlighting its potential as a prognostic marker in the management of NSCLC. Research indicates that p38 MAPK, particularly the isoform p38α, shows elevated expression in lung cancer tissues, with significant associations with tumor stage and prognosis [39]. Additionally, the prognostic value of p38 in lung cancer has been highlighted, with activated p38 showing increased levels in tumors compared to normal tissues, suggesting its relevance as a prognostic marker in NSCLC [40]. Patients with lung cancer who exhibit p53 mutations or abnormal p53 expression generally experience a poorer prognosis and may also demonstrate increased resistance to chemotherapy and radiation therapy [42,43]. Since p53 is a tumor suppressor gene that regulates cell division and apoptosis, its lower expression due to mutations could contribute to unchecked cell proliferation and tumor progression. Additionally, the observation of higher frequency in men could suggest gender-specific differences in the genetic and molecular characteristics of the tumor.

Bcl-2 was positively correlated with GSTS expression, while caspase-3 and p38 showed a positive correlation with GSTP and GSTM, respectively. There is a solid body of opinion about the connection between p38 and GSTM proteins. Studies suggest that GSTM proteins, particularly GSTM1, play a role in modulating stress-activated signals and the p38 signaling pathway by interacting with key proteins like Ask1. Heat shock-induced dissociation of GSTM1 from Ask1 can affect the activation of the p38 pathway. This indicates a functional relationship between p38 and GSTM proteins in cellular signaling pathways [43-45].

This study highlights several clinical features of cancer dynamics at the molecular level for the first time. Evidence from research results revealed caspase-3 was expressed higher in AC patients and among acinar tumor tissues. GSTS was significantly higher in vascular invasion and metastasis, while in pleural invasion GSTP was higher. The available information suggests that caspase-3 expression is associated with tumorigenesis and prognosis in certain cancers, but does not allow for a direct comparison between AC and SCC [7,38]. While the search results support the idea that caspase-3 expression is elevated in acinar tumors compared to normal tissues [46]. They do not directly justify the claim that caspase-3 expression is notably higher in acinar tumor tissues compared to keratinized and non-keratinized SCC tissues.

To determine these specific relationships, further research focusing on this aspect would be necessary.

In a lung adenocarcinoma study performed with these markers on tissues surgically obtained from 166 patients, the significance of the protein level expression of Caspase-3, p53 and Bcl-2 revealed the effectiveness of these markers involved in the apoptosis pathway. This suggests that a correlation can be established with regard to positive contributions to prognosis, particularly in the context of lung cancers [12].

In a separate study by Oğuztüzün et al., immunohistochemical staining characteristics of glutathione-S-transferase alpha, pi, mu, theta, and p53 were investigated in 50 patients with primary lung carcinoma. A comparison of normal and tumor tissues from these cases revealed that glutathione-S-transferase alpha, pi, mu, theta expressions were significantly higher in tumor cells than in normal cells, while p53 expression did not differ significantly between the two tissue types[47].

4. CONCLUSION

Lung cancer is the most common cancer to be diagnosed and the leading cause of cancer-related deaths globally, with an estimated 2.20 million new cases and 1.79 million deaths annually [48]. Although some encouraging molecular markers have been found, there isn't a single marker that can accurately predict a patient's prognosis or response to treatment for those who suffer this terrible disease. With a better understanding of the molecular biology of lung cancer, more tailored therapies may be developed. Age, stage, and performance status are examples of traditional prognostic indicators that are still unquestionably useful; nevertheless, the discovery of additional markers may serve to further improve this and direct treatment decisions [49].

The current study's findings may point to the utility of two GST isozymes, GSTO and GSTP, in the diagnosis and treatment of non-small cell lung cancer. Compared to SCC tissues, GSTP expression is around 30% higher in AC tissues. In contrast, GSTO expression increases by around 25% in second stage tumors, particularly in AC tissues.

The study incorporates a wide array of established cancer associated proteins p38, p53, Bcl-2, and caspase-3 along with a novel focus on glutathione transferases (GSTs), offering a comprehensive understanding of molecular markers in lung cancer pathology. The study explores the association between marker expression levels and various clinical parameters, providing insights into potential prognostic indicators and therapeutic targets in lung cancer. While the study examines the expression levels of various markers, it does not directly assess their prognostic significance or impact on patient outcomes over time, limiting the interpretation of their clinical relevance. The study is conducted at a single pathology clinic, which may limit the diversity of patient populations and tumor characteristics, potentially

54

influencing the extrapolation of findings to broader populations. Although the study identifies correlations between marker expression levels, it does not delve into the functional implications of these associations or mechanistic insights into cancer pathogenesis, warranting further investigation.

REFERENCES

[1] Thandra KC, Barsouk A, Saginala K, Aluru JS, & Barsouk A. (Epidemiology of lung cancer. Contemporary Oncology. 2021; *25*(1): 45. https://doi.org/10.5114/WO.2021.103829

[2] Nicholson AG, Tsao MS, Beasley MB, Borczuk AC, Brambilla E, Cooper WA, et al. The 2021 WHO Classification of Lung Tumors: Impact of Advances Since 2015. Journal of Thoracic Oncology : Official Publication of the International Association for the Study of Lung Cancer. 2022; 17(3): 362–387. https://doi.org/10.1016/J.JTHO.2021.11.003

[3] Zappa C, & Mousa SA. Non-small cell lung cancer: current treatment and future advances. Translational Lung Cancer Research. 2016; *5*(3): 288. https://doi.org/10.21037/TLCR.2016.06.07

[4] Siddiqui F, Vaqar S, Siddiqui AH . Lung Cancer. Cambridge Handbook of Psychology, Health and Medicine, Second Edition, 605–606, 2023. https://doi.org/10.1017/CBO9780511543579.138

[5] Greenberg AK, Basu S, Hu J, Yie TA, Kam MTW, Rom WN, Lee TC. Selective p38 activation in human non-small cell lung cancer. American Journal of Respiratory Cell and Molecular Biology. 2002;26(5): 558–564. https://doi.org/10.1165/AJRCMB.26.5.4689

[6] Kato S, Yokoyama S, Hayakawa Y, Li L, Iwakami Y, Sakurai H, Saiki I. P38 pathway as a key downstream signal of connective tissue growth factor to regulate metastatic potential in non-small-cell lung cancer. Cancer Science, 2016;107(10): 1416–1421. https://doi.org/10.1111/CAS.13009

[7] Huang J-S, Yang C-M, Wang J-S, Liou H-H, Hsieh I-C, Li G-C, et al. Caspase-3 expression in tumorigenesis and prognosis of buccal mucosa squamous cell carcinoma. Oncotarget. 2017; 8(48): 84237–84247. https://doi.org/10.18632/ONCOTARGET.20494

[8] Joseph B, Ekedahl J, Lewensohn R, Marchetti P, Formstecher P, Zhivotovsky B. Defective caspase-3 relocalization in non-small cell lung carcinoma. Oncogene. 2001;20(23): 2877–2888. https://doi.org/10.1038/SJ.ONC.1204402

[9] Takata T, Tanaka F, Yamada T, Yanagihara K, Otake Y, Kawano Y, et al. Clinical significance of caspase-3 expression in pathologic-stage I, nonsmall-cell lung cancer. International Journal of Cancer. 2001a; 96 Suppl(SUPPL.); 54–60. https://doi.org/10.1002/IJC.10347

[10] Anagnostou VK, Lowery FJ, Zolota V, Tzelepi V, Gopinath A, Liceaga C, Panagopoulos N, et al. High expression of BCL-2 predicts favorable outcome in non-small cell lung cancer patients with non squamous histology. BMC Cancer. 2010;*10*(1): 1–11. https://doi.org/10.1186/1471-2407-10-186/TABLES/2

[11] Sun PL, Sasano H, Gao H. Bcl-2 family in non-small cell lung cancer: its prognostic and therapeutic implications. Pathology International. 2017; 67(3): 121–130. https://doi.org/10.1111/PIN.12507

[12] Cakir E, Yilmaz A, Demirag F, Oguztuzun S, Sahin S, Yazici UE, Aydin M. Prognostic significance of micropapillary pattern in lung adenocarcinoma and expression of apoptosis-related markers: caspase-3, bcl-2, and p53. APMIS : Acta Pathologica, Microbiologica, et Immunologica Scandinavica. 2011; 119(9): 574–580. https://doi.org/10.1111/J.1600-0463.2011.02778.X

[13] Kim C H, Lee H S, Park JH, Choi JH, Jang SH, Park YB, et al. Prognostic role of p53 and Ki-67 immunohistochemical expression in patients with surgically resected lung adenocarcinoma: a retrospective study. Journal of Thoracic Disease. 2015; 7(5): 822. https://doi.org/10.3978/J.ISSN.2072-1439.2015.05.02

[14] Zhu CQ, Shih W, Ling CH, Tsao MS. Immunohistochemical markers of prognosis in non-small cell lung cancer: a review and proposal for a multiphase approach to marker evaluation. Journal of Clinical Pathology. 2006a; *59*(8): 790–800. https://doi.org/10.1136/JCP.2005.031351

[15] Ma X, Le Teuff G, Lacas B, Tsao MS, Graziano S, Pignon JP, et al . Prognostic and Predictive Effect of TP53 Mutations in Patients with Non-Small Cell Lung Cancer from Adjuvant Cisplatin-Based Therapy Randomized Trials: A LACE-Bio Pooled Analysis. Journal of Thoracic Oncology : Official Publication of the International Association for the Study of Lung Cancer.2016;11(6): 850–861. https://doi.org/10.1016/J.JTHO.2016.02.002

[16] Zhu CQ, Shih W, Ling CH, & Tsao MS. Immunohistochemical markers of prognosis in non-small cell lung cancer: a review and proposal for a multiphase approach to marker evaluation. Journal of Clinical Pathology. 2006b; *59*(8): 790. https://doi.org/10.1136/JCP.2005.031351

[17] Singh RR, Reindl KM. Glutathione S-Transferases in Cancer. Antioxidants (Basel, Switzerland). 2021;10(5): 701. https://doi.org/10.3390/ANTIOX10050701

[18] Zeng B, Ge C, Li R, Zhang Z, Fu Q, Li Z, Lin Z, Liu L, Xue Y, Xu Y, He J, Guo H, Li C, Huang W, Song X, & Huang Y. Knockdown of microsomal glutathione S-transferase 1 inhibits lung adenocarcinoma cell proliferation and induces apoptosis. Biomedicine & Pharmacotherapy. 2020; *121*: 109562. https://doi.org/10.1016/J.BIOPHA.2019.109562

[19] Albarakati N, Khayyat D, Dallol A, Al-Maghrabi J, & Nedjadi T.The prognostic impact of GSTM1/GSTP1 genetic variants in bladder Cancer. BMC Cancer. 2019; *19*(1): 1–11. https://doi.org/10.1186/S12885-019-6244-6/TABLES/5

[20] Chen Y, Li B, Wang J, Liu J, Wang Z, Mao Y, Liu S, Liao X, Chen J. Identification and verification of

the prognostic value of the glutathione S-transferase Mu genes in gastric cancer. Oncology Letters. 2020; 20(4): https://doi.org/10.3892/OL.2020.11961

[21] Hsu CH, Chen CL, Hong RL, Chen KL, Lin JF, Cheng AL.Prognostic value of multidrug resistance 1, glutathione-S-transferase-pi and p53 in advanced nasopharyngeal carcinoma treated with systemic chemotherapy. Oncology. 2002;62(4):305–312. https://doi.org/10.1159/000065061

[22] Huang J, Tan PH, Thiyagarajan J, Bay BH. Prognostic Significance of Glutathione S-Transferase-Pi in Invasive Breast Cancer. Modern Pathology.2003; 16(6): 558–565. https://doi.org/10.1097/01.mp.0000071842.83169.5a

[23] Voso M T, D'Alo F, Putzulu R, Mele L, Scardocci A, Chiusolo P, et al. (2002). Negative prognostic value of glutathione S-transferase (GSTM1 and GSTT1) deletions in adult acute myeloid leukemia. Blood. 2002; 100(8): 2703–2707. https://doi.org/10.1182/BLOOD.V100.8.2703

[24] Wang Y, Spitz MR, Schabath MB, Ali-Osman F, Mata H, & Wu X. Association between glutathione S-transferase p1 polymorphisms and lung cancer risk in Caucasians: a case-control study. Lung Cancer. 2003; 40(1): 25–32. https://doi.org/10.1016/S0169-5002(02)00537-8

[25] Pan C, Zhu G, Yan Z, Zhou Y, Liu Z. Glutathione S-Transferase T1 and M1 Polymorphisms Are Associated with Lung Cancer Risk in a Gender-Specific Manner. Oncology Research and Treatment. 2014;37(4): 164–169. https://doi.org/10.1159/000361083

[26] Wang SQ, Chen JJ, Jiang Y, Lei ZN, Ruan YC, Pan Y, et al. Targeting GSTP1 as Therapeutic Strategy against Lung Adenocarcinoma Stemness and Resistance to Tyrosine Kinase Inhibitors. Advanced Science (Weinheim, Baden-Wurttemberg, Germany). 2023; 10(7): https://doi.org/10.1002/ADVS.202205262

[27] Inoue T, Ishida T, Sugio K, Maehara Y, Sugimachi K. Glutathione S Transferase Pi Is a Powerful Indicator in Chemotherapy of Human Lung Squamous-Cell Carcinoma. Respiration. 1995;62(4): 223–227. https://doi.org/10.1159/000196451

[28] Rybárová S, Hodorová I, Mihalik J, Mirossay L. MRP1 and GSTp1 expression in non-small cell lung cancer does not correlate with clinicopathological parameters: A Slovakian population study. Acta Histochemica. 2014;116(8): 1390–1398. https://doi.org/10.1016/J.ACTHIS.2014.09.002

[29] Jankova L, Robertson G, Chan C, Tan KL, Kohonen-Corish M, Fung CLS, et al . Glutathione S-transferase Pi expression predicts response to adjuvant chemotherapy for stage C colon cancer: A matched historical control study. BMC Cancer. 2012;12(1): 1–9. https://doi.org/10.1186/1471-2407-12-196/TABLES/3

[30] Wang K, Zhang FL, Jia W. Glutathione S-transferase ω 1 promotes the proliferation, migration and invasion, and inhibits the apoptosis of non-small cell lung cancer cells, via the JAK/STAT3 signaling pathway. Molecular Medicine Reports, 2021; 23(1): 1–7. https://doi.org/10.3892/MMR.2020.11709

[31] Mora Vidal R, Regufe da Mota S, Hayden A, Markham H, Douglas J, Packham G, Crabb SJ. Epidermal Growth Factor Receptor Family Inhibition Identifies P38 Mitogen-activated Protein Kinase as a Potential Therapeutic Target in Bladder Cancer. Urology. 2018; 112: 225.e1-225.e7. https://doi.org/10.1016/J.UROLOGY.2017.10.041

[32] Zarczynska I, Gorska-Arcisz M, Cortez A J, Kujawa KA, Wilk A M, Skladanowski A C, Stanczak A, Skupinska M, Wieczorek M, Lisowska K M, Sadej R, & Kitowska K. P38 mediates resistance to fgfr inhibition in non-small cell lung cancer. Cells. 2021; 10(12): 3363. https://doi.org/10.3390/CELLS10123363/S1

[33] Fang Y, Wang J, Wang G, Zhou C, Wang P, Zhao S, et al. Inactivation of p38 MAPK contributes to stem cell-like properties of non-small cell lung cancer. Oncotarget. 2017; 8(16): 26702. https://doi.org/10.18632/ONCOTARGET.15804

[34] Sunaga N, Miura Y, Tsukagoshi Y, Kasahara N, Masuda T, et al. Dual inhibition of MEK and p38 impairs tumor growth in KRAS-mutated non-small cell lung cancer. Oncology Letters. 2019; 17(3): https://doi.org/10.3892/OL.2019.10009

[35] Feng C, Wu J, Yang F, Qiu M, Hu S, Guo S, Wu J, Ying X, Wang J. Expression of Bcl-2 is a favorable prognostic biomarker in lung squamous cell carcinoma. Oncology Letters. 2018; 15(5): 6925. https://doi.org/10.3892/OL.2018.8198

[36] Zhang J, Wang S, Wang L, Wang R, Chen S, Pan B, Sun Y, Chen H. Prognostic value of Bcl-2 expression in patients with non-small-cell lung cancer: a meta-analysis and systemic review. OncoTargets and Therapy. 2015; 8: 3361. https://doi.org/10.2147/OTT.S89275

[37] Takata T, Tanaka F, Yamada T, Yanagihara K, Otake Y, Kawano Y, et al. Clinical significance of caspase-3 expression in pathologic-stage I, nonsmall-cell lung cancer. International Journal of Cancer. 2001b; 96 Suppl(SUPPL.), 54–60. https://doi.org/10.1002/IJC.10347

[38] Yoo J, Kim CH, Song SH, Shim BY, Jeong YJ, Ahn MI, et al. Expression of Caspase-3 and c-myc in Non-Small Cell Lung Cancer. Cancer Research and Treatment : Official Journal of Korean Cancer Association. 2004;36(5): 303. https://doi.org/10.4143/CRT.2004.36.5.303

[39] Sahu V, Mohan A, Dey S. p38 MAP kinases: plausible diagnostic and prognostic serum protein marker of non small cell lung cancer. Experimental and Molecular Pathology. 2019;107:118–123. https://doi.org/10.1016/J.YEXMP.2019.01.009

[40] Liu H, Tong X, Zhao H, Li Y, Zhang L. P2-080: Prognostic value of Smad4 and p38 proteins in Non-Small Cell Lung Cancer. Journal of Thoracic Oncology. 2007;2(8): S522. https://doi.org/10.1097/01.jto.0000283544.26342.98

[41] Ahrendt SA, Hu Y, Buta M, McDermot MP, Benoit N, Yang SC, et al. p53 mutations and survival in stage I non-small-cell lung cancer: results of a

prospective study. Journal of the National Cancer Institute. 2003;*95*(13):961–970. https://doi.org/10.1093/JNCI/95.13.961

[42] Mogi A, Kuwano H. TP53 mutations in nonsmall cell lung cancer. Journal of Biomedicine and Biotechnology. 2011;Jan18,2011:583929 https://doi.org/10.1155/2011/583929

[43] Bhattacharya P, Madden JA, Sen N, Hoyer PB, Keating AF. Glutathione S-transferase class μ regulation of apoptosis signal-regulating kinase 1 protein during VCD-induced ovotoxicity in neonatal rat ovaries. Toxicology and Applied Pharmacology. 2013;*267*(1): 49–56. https://doi.org/10.1016/J.TAAP.2012.12.013

[44] Dorion S, Lambert H, Landry J. Activation of the p38 signaling pathway by heat shock involves the dissociation of glutathione S-transferase Mu from Ask1. The Journal of Biological Chemistry.2002;277(34): 30792–30797. https://doi.org/10.1074/JBC.M203642200

[45] Luo HY, Tang WL, Xiang L, Peng LL, Wu D, Zhu ZY, Gu, HT, et al . Comprehensive analysis of the correlation between GSTM1 and tumor immunity in colon cancer. Journal of Gastrointestinal Oncology, 2022;13(6): 3025–3037. https://doi.org/10.21037/JGO-22-1060/COIF

[46] Jakubowska K, Guzińska-Ustymowicz K, Famulski W, Cepowicz D, Jagodzińska D, Pryczynicz A. Reduced expression of caspase-8 and cleaved caspase-3 in pancreatic ductal adenocarcinoma cells. Oncology Letters. 2016;11(3): 1879. https://doi.org/10.3892/OL.2016.4125

[47] Oguztüzun S, Aydin M, Demirag F, Yazici Ü, Özhavzali M, Kiliç M, Işcan M. The expression of GST isoenzymes and p53 in non-small cell lung cancer. Folia Histochemica et Cytobiologica. 2010;*48*(1): 122–127. https://doi.org/10.2478/V10042-008-0084-6

[48] Cancer Today. (n.d.). Retrieved February 19, from https://gco.iarc.fr/today/en, 2024.

[49] Scott A, Salgia R. Biomarkers in lung cancer: from early detection to novel therapeutics and decision making. Biomarkers in Medicine.2008;2(6): 577. https://doi.org/10.2217/17520363.2.6.577

57

Türk Doğa ve Fen Dergisi
Turkish Journal of Nature and Science
www.dergipark.gov.tr/tdfd

BİNGÖL UNIVERSITY

Investigation of Quality Parameters of Soil Sample Collected from Akdağmadeni/Bulgurlu Village District of Yozgat Province

Büşra ŞENSOY GÜN[1,2*] ID **, Beyza YORULMAZ[1,3]** ID **, Arda AYTİMUR[1]** ID **, Belgin TUNALI[2]** ID

[1]Bilecik Şeyh Edebali University, Central Research Laboratory Application and Research Center, Bilecik, Türkiye
[2]Burdur Mehmet Akif Ersoy University, Department of Nanoscience and Nanotechnology, Burdur, Türkiye
[3]Bilecik Şeyh Edebali University, Faculty of Science, Department of Molecular Biology and Genetics, Bilecik, Türkiye
Büşra ŞENSOY GÜN ORCID No:0000-0001-5190-9490
Beyza YORULMAZ ORCID No: 0009-0007-0579-5446
Arda AYTİMUR ORCID No: 0000-0001-6995-6164
Belgin TUNALI ORCID No: 0000-0003-0768-679X

Corresponding author: busra.sensoygun@bilecik.edu.tr
(Received: 09.08.2024, Accepted: 16.12.2024, Online Publication: 26.03.2025)

Abstract: In our study, the chemical composition and soil quality parameters of the soil sample obtained by mixing soil samples taken from 30 cm depth from certain parts of the land at 39°48'20.8"N and 35°53'44.0"E locations of Yozgat/Akdağmadeni Bulgurlu Village in Turkey were investigated. After the soil sample was dried at room temperature, it was sieved with 10 and 60 mesh sieves, respectively. The chemical content of the soil sample was determined by an X-Ray Fluorescence (XRF) Spectroscopy as 40.98% silicon oxide (SiO_2), 13.27% aluminum oxide (Al_2O_3) and 11.04% calcium oxide (CaO). The concentrations of copper (Cu), zinc (Zn), chromium (Cr), manganese (Mn) and lead (Pb) metals in the soil sample were determined by atomic absorption spectroscopy (AAS) using the leaching method by adding nitric acid. The pH, lime, saturation values and the amount of organic, inorganic matter and some elemental of the soil sample were examined. In order to determine the morphological characteristics of the soil sample, color imaging was performed and the soil structure was examined with Stereo microscopy. As a result of the analysis, it was determined that the soil sample was heavy red clay, slightly alkaline, unsalted, calcareous, high in potassium and very low in organic matter and phosphorus. The aim of this study is to contribute to the development of correct fertilization and soil improvement strategies in agricultural practices in the region by determining the soil properties and soil quality of the land.

Yozgat İli Akdağmadeni İlçesi Bulgurlu Köyünden Toplanan Toprak Örneğinin Kalite Parametrelerinin İncelenmesi

Öz: Çalışmamızda, Türkiye'deki Yozgat/Akdağmadeni Bulgurlu Köyünün 39°48'20.8"N ve 35°53'44.0"E konumlarındaki arazinin belirli bölgelerinden 30 cm derinlikten alınan toprak numunelerinin karıştırılması ile elde edilen toprak örneğinin kimyasal bileşimi ve toprak kalite parametrelerinin incelendi. Toprak örneği oda sıcaklığında kurutulduktan sonra sırasıyla 10 ve 60 mesh eleklerle elendi. Toprak örneğinin kimyasal içeriği X-Işını Floresansı (XRF) Spektrometresi ile %40.98 Silisyum oksit (SiO_2), %13.27 alüminyum oksit (Al_2O_3) ve %11.04 kalsiyum oksit (CaO) olarak tespit edildi. Atomik absorpsiyon spektroskopisi (AAS) ile toprak örneğinin içerisindeki bakır (Cu), çinko (Zn), krom (Cr), mangan (Mn) ve kurşun (Pb) metal konsantrasyonları nitrik asit eklenerek liç yöntemi ile tayin edildi. Toprak örneğinin pH, kireç, doygunluk değerleri, organik, inorganik kompanentler ve bazı elementel madde miktarları incelendi. Toprak örneğinin morfolojik özelliklerini belirlemek amacıyla renk ölçümü yapıldı ve stereo mikroskopi ile toprak yapısı incelendi. Analizler soncu toprak örneğinin ağır kırmızı kil, hafif alkalin, tuzsuz, kireçli, yüksek potasyum ve organik madde ile fosfor bakımından çok az olduğu tespit edilmiştir. Bu çalışmanın amacı arazinin toprak özelliklerini ve toprak kalitesini belirleyerek bölgedeki tarımsal uygulamalarda doğru gübreleme ve toprak iyileştirme stratejilerinin geliştirilmesine katkı sağlamaktır.

1. INTRODUCTION

Soil, like a living system, is a natural system with complex and dynamic processes [1]. The minerals, gases, organic matter, microorganisms, and water that sustain these dynamic processes in the soil are its fundamental components [2]. Additionally, it contains essential elements such as carbon (C), oxygen (O), and hydrogen (H), which are crucial for plant nutrition [3]. An ideal soil comprises 45% mineral, 5% organic matter and 50% pores [4].

Soils contain approximately 1 to 6% organic matter [5, 6]. The presence of organic matter in the soil provides essential nutrients for plants, buffers soil pH, increases water retention capacity and enhances soil aeration, thereby improving soil productivity [7, 8]. The frequently changing pH in soil determines some physicochemical and biological processes that sustain soil productivity and plant growth. Macro nutrients (N, P, K, Ca, Mg and S) present in a soil with low pH are less bioavailability than at higher pH levels. The pH of the soil between 6 and 7.5 is ideal for plant growth, but there are some plants that can tolerate, and even prefer more acidic and basic conditions [9-13]. Microelements found in the soil, apart from macroelements, play an important role in plant growth and development. Microelements such as iron (Fe), zinc (Zn), manganese (Mn), copper (Cu), boron (B), molybdenum (Mo), chlorine (Cl) and nickel (Ni) take part in the regulation of cellular functions in plants. For example, Fe and Zn are critically important in enzyme activity and photosynthesis processes. Mn and Cu play a role in reducing oxidative stress in plant cells, while B is necessary for cell wall formation and pollen development. Mo supports nitrogen metabolism, while Cl is important in ion balance and photosynthesis. Ni is necessary for urea metabolism and enzyme functions. Depending on soil quality, deficiency or excess of these elements can affect plant yield and product quality. Soils with rich organic matter content generally provide an environment where microelements are naturally more accessible. However, increasing agricultural practices and the use of high-yield crop varieties cause microelement deficiencies to become more common. Therefore, proper management of microelements is critical for both plant nutrition and sustainable agricultural practices [14, 15].

The inorganic components of mineral soils are generally sand, silt and clay. The proportion of these different components determines the structure of the soil and its subsequent chemical, physical and biological properties [16, 17]. All these characteristics are important for agriculture. Not all soils are suitable for agriculture; agricultural soils must contain specific proportions of macro and micro nutrients. Ideal soils for agriculture are those in which mineral components (sand: 0.05–2 mm, silt: 0.002–0.05 mm, clay: <0.002 mm), soil organic matter, air and water components are balanced [18, 19]. Soil granule sizes are directly related to soil fertility. The physical structure of the soil affects basic processes such as plant root growth and the movement of water and nutrients. In this case, granule sizes determine the porosity, water holding capacity and air permeability of the soil (Gündüz 2019; Negiş 2020; taş 2022). Soils

containing equal amounts of sand, silt and clay are fertile and suitable for agriculture. Soils rich in sand are characterized by their wide pores, enhancing water drainage, yet they cannot retain a significant amount of nutrients in the soil. In contrast, soils rich in clay increase water retention capacity and provide the essential nutrients for many plants [19, 20].

Clay minerals are colloidal structures with a charged surface and high surface area. They are the most reactive inorganic components found in soil [21, 22]. The most common minerals are iron (Fe), aluminum (Al) and manganese (Mn) oxides [23]. Clay soils composed of silicon alumina structures. Additionally, depending on the type of clay, they contain varying amounts of elements such as Scandium (Sc), Chromium (Cr), Copper (Cu), Titanium (Ti), Gallium (Ga), Zirconium (Zr), Manganese (Mn), Magnesium (Mg), Strontium (Sr), and Lead (Pb) [24, 25].

In a study conducted to assess the potential for quince and grape cultivation in the Karanlıkdere Valley of Yozgat Şefaatli district, soil analysis and land use status were examined. Suitability for vineyard and garden investments was assessed and projects on alternative products were developed. As a result, the soils in the region were found to be sufficient in terms of potassium, calcium and iron, but showed deficiencies in nutrients such as nitrogen, phosphorus, magnesium and zinc. The high pH value reduced the usefulness of some nutrients. Zinc fertilization and appropriate fertilization programs are critical to increasing soil fertility [26]. In another study, the relationship between organic matter content, erodibility and some soil properties of the soils where rosehip plants grow in Yozgat province was investigated. Organic matter, macro and micro nutrients, pH, lime, electrical conductivity and erosion factors were analyzed in surface soil samples taken from 30 points. As a result of the study, the soils were generally sufficient in terms of nutrients and the organic matter content varied between 2.28% and 9.87%. Organic matter showed a negative relationship with pH and erosion factor and a positive relationship with Mn and Zn. This situation revealed that organic matter content is important in soil nutrient balance and resistance to erosion [27].

This study investigated the chemical composition and soil quality parameters of the soil samples collected from Bulgurlu Village. To determine the morphological properties of the soil sample, color measurement was performed and the soil structure was examined with stereo microscopy. The chemical components present in the soil samples were determined using XRF analysis. Samples taken from the soil were prepared using the leaching method for the analyses of total Mn, Cr, Pb, Cu, and Zn metals, which were then analyzed using AAS. Soil quality was determined by examining parameters such as pH, saturation, salinity, lime content, phosphate, potassium and organic matter. The aim of this study is to contribute to the development of correct fertilization and soil improvement strategies in agricultural practices in the region by determining the soil properties and soil quality of the land.

59

2. MATERIAL AND METHOD

2.1. Preparation of Soil Sample

In order to determine the soil quality and to conduct analyses, soil samples were taken from 10 points (every 10 steps) marked at a depth of 30 cm (blue points) in the field land in Figure 1 located at the coordinates of 39°48'20.8"N and 35°53'44.0"E in Bulgurlu Village, Akdağmadeni District, Yozgat Province, Central Anatolia Region of Turkey, in July, and these areas were advanced by drawing zigzags as indicated by Kaçar [28].After the collected samples were mixed homogeneously to represent the general condition of the field, the obtained sample was left to dry at room temperature. The dried soil sample was used for analysis by passing through 10 and 60 mesh sieves, respectively [28, 29, 30].
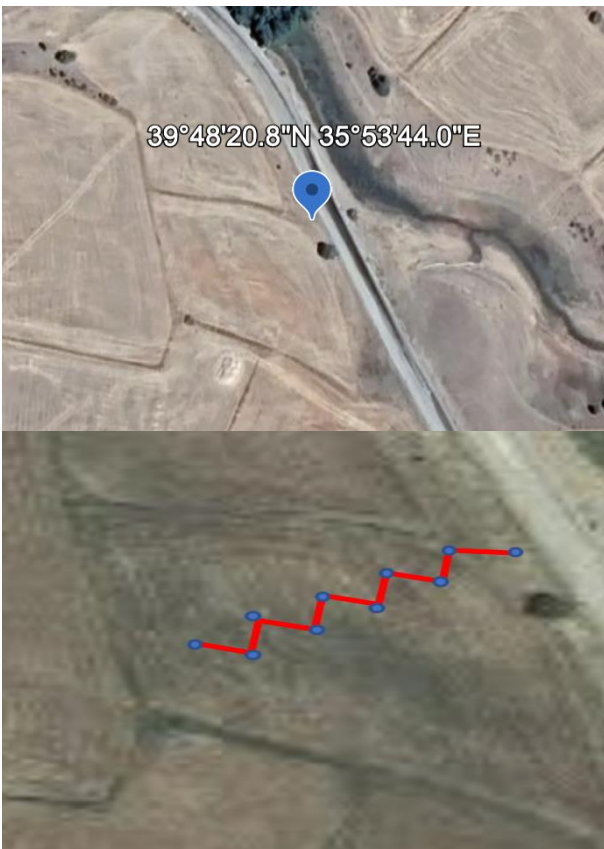

Figure 1. Google Earth map of the location where the soil sample was taken

In order to determine the morphological properties of the unsieved and sieved soil, color measurement was performed with a Konica Minolta device and the soil structure was examined with LEICA S6 D Stereo microscopy [31].

2.2. XRF Analysis

To calculate the loss on ignition (LOI) of the finely powdered soil sample, it was dried in the incubator at 105 °C for 2 h. The empty crucible was weighed and kept in the muffle furnace at a rate of 10 °C min^{-1} to 1050 °C for 1 hour. It was then cooled in a desiccator and weighed again. These processes were repeated until the crucibles reached a stable weight. Subsequently, 1 g of clay sample was added to the crucible that had reached constant weight and was placed back in the muffle furnace at 1050 °C [32]. After cooling in a desiccator and weighing, the loss on ignition was calculated according to the equality 1 below;

$$\frac{(M_2) - (M_3)}{(M_2) - (M_1)} \%100 = LOI \qquad (1)$$
$$M_1 = mass\ of\ the\ empty\ crucible\ (g)$$
$$M_2 = mass\ of\ the\ empyt\ crucible + dried\ sample\ (g)$$
$$M_3 = mass\ of\ the\ empyt\ crucible + ignited\ sample\ (g)$$

For XRF analysis, lithium tetraborate was added to the soil sample whose ignition loss was calculated and glassy pellet was obtained with the fusion device. The elemental composition of the prepared sample was determined by XRF spectroscopy using Panalytical Axios Max minerals equipment.

2.3. Heavy Metal Analysis

For AAS analysis, unsieved and sieved soil samples were prepared using the leaching method. 1 gram of each unsieved and sieved soil sample was weighed, and 200 ml of nitric acid (Reagent pure, 65%) was added. The acidified soil samples were shaken at 400 rpm at room temperature for 2, 3, and 12 hours. After shaking, the soil samples were allowed to settle at room temperature to enable the soil particles to precipitate to the bottom of the flask [33, 34]. The supernatant liquids were then taken and diluted to specific ratios. Calibration curves, prepared standard compounds of Mn, Cu, Cr, Zn and Pb were created in detail and AAS analysis of soil samples was developed with Perkin Elmer / Elmer Analyst 800 device.

2.4. Soil Quality Parameter Analysis

The raw soil sample was sieved using the dry sieving method and pH, phosphorus, potassium, saturation, salt content, lime percentage and organic matter percentage were determined in accordance with standard methods. In order to determine the water holding capacity of the soil sample, experiments were carried out with air-dry soil in accordance with the Turkish Standard TS 8333. pH measurement was made using the method suggested by Yurdakul to determine the acidity or alkalinity level of the soil. For the lime content in the soil, TS EN ISO 10693 standard was modified and the amount of salt in the soil was determined by measuring the electrical conductivity in samples turned into mud according to the TS 8334 standard. The available soil phosphorus content that can be taken by plants was also measured according to the Olsen method. This method was determined by extracting phosphorus with sodium bicarbonate and measuring its concentration spectrophotometrically. The organic matter content of the soil was determined by measuring the amount of available potassium according to the TS 8336 standard and its concentration according to the TS 8341 standard [28, 35-37].

3. RESULTS

Sieved and unsieved soil samples were examined under a stereo microscope (**Figure 2**). In the stereo microscopy analysis of the soil samples, there is an almost homogeneous image in the sieved soil sample in **Figure 2B**, while the particle sizes of the unsieved soil are in different distributions in **Figure 2A** [38,39].
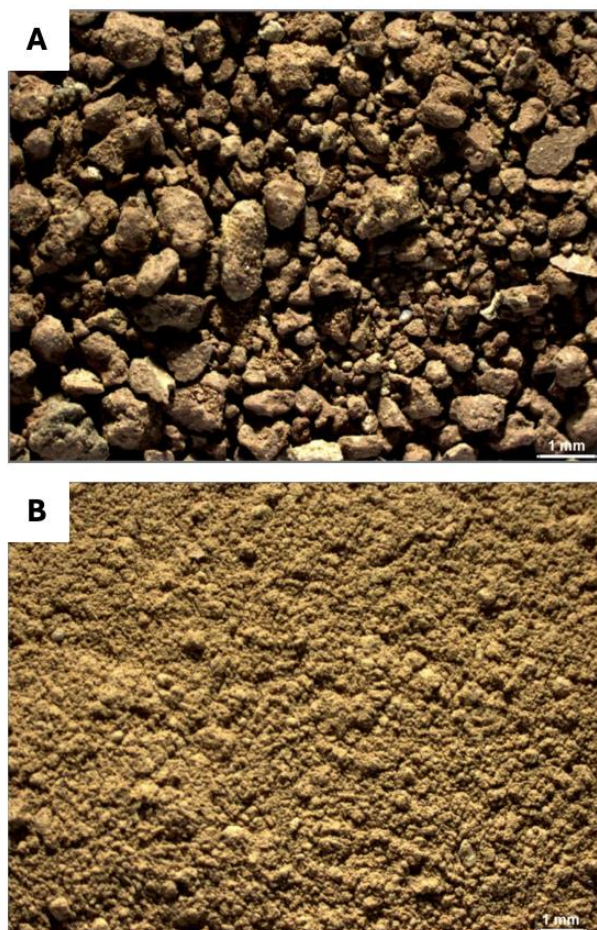

Figure 2. Stereo microscopy analysis **A)** unsieved soil sample B) sieved soil sample

Colour measurements of sieved and unsieved soil samples were analysed according to the absolute colour system L*, a* and b*' method (L* = brightness], a* = green-red and b* = yellow-blue) [40]. Color measurement values of sieved and unsieved soil samples are given in **Table 1.**

Table 1. Colour measurement values of sieved and unsieved soil samples

Colour parameters	Unsieved soil	Sieved soil
L	58.7	63.1
a	13.3	16.6
b	34.2	42.5

The chemical composition of the clay was determined by X-Ray Fluorescence Spectroscopy using Panalytical Axios Max Minerals equipment. The finely powdered clay sample was mixed with lithium tetraborate for chemical analysis and the LOI was calculated as 21.84% by calcination at 1000°C. The results of the XRF analysis performed to determine the chemical composition of the minerals present in the soil sample are given in **Table 2**.

It is observed that the majority of the soil sample consists of SiO_2, Al_2O_3 and CaO, respectively.

Table 2. XRF results of clay sample

Compound Name	Concentration (unit)	Absolute Error (unit)
SiO_2	40.98%	0.1%
Al_2O_3	13.27%	0.1%
CaO	11.04%	0.09%
Fe_2O_3	5.385%	0.07%
MgO	4.232%	0.06%
K_2O	1.749%	0.04%
TiO_2	0.4752%	0.02%
Na_2O	0.4270%	0.02%
P_2O_5	0.1653%	0.01%
SO_3	0.1133%	0.01%
MnO	917.4 mg kg^{-1}	90 mg kg^{-1}
Cl	900.9 mg kg^{-1}	90 mg kg^{-1}
SrO3	450.7 mg kg^{-1}	60 mg kg^{-1}
Cr_2O_3	399 mg kg^{-1}	60 mg kg^{-1}
NiO	285.2 mg kg^{-1}	50 mg kg^{-1}
CuO	170.6 mg kg^{-1}	40 mg kg^{-1}
ZnO	108.6 mg kg^{-1}	30 mg kg^{-1}

Common heavy metals contained in 6 soil samples prepared by the leaching method using AAS spectroscopy are given in **Table 3**. According to the results, metals were mostly detected better in samples treated with acid for 12 hours compared to those treated for 2 and 3 hours [41, 42]. When comparing the AAS analysis results of raw and sieved soil samples, similar metal values were detected in both samples. The highest Mn and the lowest Cr metal were found in both raw and sieved soil sample.

Table 3. Concentration of certain metals in the soil sample (mg kg^{-1})

Sample	Mn	Pb	Cu	Cr	Zn
Raw soil 2 h	73.9± 0.017	3.320±0.038.	4.940± 0.009	-	6.350±0.013
Raw soil 3 h	71.55± 0.013	4.040±0.163	5.12±0.06	-	6.480±0.015
Raw soil 12 h	92.55± 0.008	4.750±0.027	5.26±0.032	-	5.930±0.005
Sifted soil 2 h	79.050 ±0.01	3.670±0.062	5.77±0.005	-	6.650 ± 0.013
Sifted soil 3 h	87.1±0.008	2.720±0.043	4.380± 0.017	2.630± 0.200	6.840 ± 0.029
Sifted soil 12 h	92.700 ±0.01	3.09± 0.053	5.310± 0.011	4.750± 0.412	6.340± 0.011

As a result of the experiment conducted on the soil sample, it is shown in **Table 4** that the soil is alkaline, calcareous, salt-free and clay in structure, and that phosphate and potassium, which are macro nutrients, are present in the soil sample, albeit in small amounts. In this case, it is seen that the soil sample is in clay form as a result of both XRF and soil analysis. As a result of the analysis, it was determined that the soil sample had a heavy red clay structure, was slightly alkaline, salt-free, calcareous, had high air content, and had very low organic matter and phosphorus content. The analysis results of your soil show that the current plant characteristics are not suitable in some ways, but can be improved.

Table 4. Soil quality parameters

Analysis name	Result	Assessment
Saturation	140.15	Heavy clay
pH	8.25	Slightly alkaline
Lime%	20.76	Highly calcareous
Salt%	0.042	Saltless
FOSFAT (P_2O_5) kg da^{-1}	1.72	low
Organic matter%	0.63	low
POTASSIUM (K_2O) kg da^{-1}	54.6	Hight

4. DISCUSSION AND CONCLUSION

According to the XRF analysis of the soil sample, the main component of the soil sample is found to be 40.98% SiO_2. Additionally, the soil sample contains 13.27% Al_2O_3 and 11.04% CaO. Upon examining the soil color, it is observed that the color of the soil is red. Clays consist of alumina silica structures. The red color of red clay is attributed to the presence of iron within it [12, 13]. Consequently, these components indicate that the sample is red clay.

Soil fertility is determined based on certain parameters, including micro and macro elements, saturation, salt content, pH, and organic matter. Micro and macro (nitrogen, phosphorus, potassium, etc.) elements play an crucial role in plant nutrition. Micro elements are found in lower amounts in soil compared to macro elements. Microelements such as nickel, boron, zinc, chromium, manganese, copper, chlorine and iron are sufficient to be present in the soil even at low concentrations for plant development [1, 4, 5]. AAS analysis was conducted to examine the total Mn, Cu, Cr, Zn, and Pb metal contents of the soil sample. Mn metal was detected in the highest amount of 92.7 mg kg^{-1} in the sieved clay treated with acid for 12 hours, while Cu, Pb and Zn were detected in similar proportions in six samples. However, while Cr metal was not detected in raw clay samples, it was detected in trace amounts in sieved clay samples treated with acid for 3 and 12 hours. This variation can be attributed to the different durations of treatment with nitric acid for AAS analysis.

Heavy clay was found as a result of the saturation level of the soil sample. Compared to sandy soils, clayey soils have a higher water retention capacity. Soils with high water retention capacity enable plant roots to penetrate deeper into the soil, thus affecting soil fertility [43, 44]. Upon examination of the soil sample for salt content, it was evaluated as salt-free. In soils with high salt concentrations, it reduces the permeability of water and accelerates its evaporation. This situation causes the vegetation to become weak and spindly [44]. The fact that our soil sample has a low salt content and a high water retention capacity will ensure that the products that can be grown on it will be productive. Soils have a pH between 0 and 14, depending on their composition. Plants generally thrive in pH ranges between 5.5 and 6.5. Each soil has unique pH value, determining the type of plant species grown. The pH value of our soil sample was found to be 8.25 slightly alkaline. Organic substances in soil are formed as a result of the decomposition of animals and plants residues by bacteria in the soil. Fertile soil should contain an average of 5% organic matter [5, 43]. The organic matter content of our soil sample was found to be low at 0.63%. The very low organic matter content in our

soil sample prevents the agricultural plants on it from developing as a result of malnutrition. This issue can be addressed by fertilizing the soil with barn manure.

Phosphorus (P) and potassium (K) are two essential elements that complement each other but have different functions in plant growth and development. Phosphorus plays a central role in energy production and transfer and is necessary for vital processes such as photosynthesis, respiration, DNA and RNA synthesis. Plants usually take phosphorus in the form of phosphate ($H_2PO_4^-$ or HPO_4^{2-}), which is obtained from organic matter or phosphate minerals found in soluble form in the soil. Phosphorus has critical effects such as promoting root development and supporting early plant growth processes. Potassium regulates cellular water balance, supports enzyme activities and controls the opening and closing mechanisms of stomata. These properties increase the resistance of plants to water stress and diseases. In addition, potassium supports fruit and seed development and increases product quality. Phosphorus is especially effective in the early growth period, while potassium is more critical in the maturity and stress management processes of the plant. Both elements are necessary for optimum plant growth and their balanced presence in soil is vital for plant development. Regular soil analysis for these elements and use of appropriate fertilization methods are critical steps for sustainable agriculture and productivity. Potassium and phosphate are essential macro-nutrients for plant growth, root resilience, and increased water retention capacity [43-46]. Total phosphate amount of our soil sample was found to be very low at 1.74 kg da^{-1}, while the potassium amount was found to be high at 54.6 kg da^{-1} [47] Our soil sample contains a high amount of lime at 20.76%. This situation is caused by the calcium carbonate ($CaCO_3$) contained in the soil. Calcium ions (Ca^{+2}) are necessary for plant nutrition and increasing soil granulation. Ca^{+2} ions contribute to the soil to yield more crops and control soil pH [47, 48].

In a study conducted to evaluate the soil fertility in Turkiye, it was found that the soil structure throughout Turkiye is generally sandy-clayey loam, non-saline, slightly alkaline, lime and low in organic matter. Additionally, it was determined that the total P content is low while K is high [48-51]. Analysis of our soil sample revealed that the soil structure is heavy clayey, non-saline, highly lime, with high potassium content, and deficient in organic matter and phosphate. The high content of silicon dioxide and aluminum oxide, as indicated by XRF analysis, supports its clayey structure, while the presence of significant amounts of calcium oxide reinforces its calcareous nature. Additionally, AAS analysis identified some of the micro-nutrient metals present in the soil.

Acknowledgement

REFERENCES

[1] Al-Kaisi MM, Lal R, Olson KR, Lowery B. Fundamentals and functions of soil environment. In: Soil health and intensification of agroecosytems. 2017;1-23.

[2] Needelman BA. What Are Soils? Nature Education Knowledge. 2013;4(3):2.

[3] Ontl TA, Schulte LA. Soil Carbon Storage. Nature Education Knowledge. 2012;3(10):35.

[4] Shahane AA, Shivay YS. Soil health and its improvement through novel agronomic and innovative approaches. Frontiers in agronomy. 2021;3:680456.

[5] Brady NC, Weil RR. The Nature and Properties of Soil. 13th ed. Prentice Hall; 2002.

[6] Huntley BJ. Soil, water and nutrients. In: Ecology of Angola: Terrestrial Biomes and Ecoregions. Springer International Publishing; 2023. pp. 127-147.

[7] Gerke J. The central role of soil organic matter in soil fertility and carbon storage. Soil Systems. 2022;6(2):33.

[8] Pimentel D, Burgess M. Maintaining sustainable and environmentally friendly fresh produce production in the context of climate change. In: Global Safety of Fresh Produce. Woodhead Publishing; 2014. pp. 133-139.

[9] Brady NC, Weil RR. The Nature and Property of Soils. Prentice Hall; 1999.

[10] Neina D. The role of soil pH in plant nutrition and soil remediation. Applied and Environmental Soil Science. 2019;2019:5794869.

[11] Förstner U. Land contamination by metals—global scope and magnitude of problem. In: Allen HE, Huang CP, Bailey GW, Bowers AR, eds. Metal Speciation and Contamination of Soil. CRC Press, Inc.; 1995. pp. 1-33.

[12] Gillman GP. An analytical tool for understanding the properties and behaviour of variable charge soils. Soil Research. 2007;45(2):83-90.

[13] Bronick CJ, Lal R. Soil structure and management: A review. Geoderma. 2005;124(1-2):3-22.

[14] Thapa S, Bhandari A, Ghimire R, Xue Q, Kidwaro F, Ghatrehsamani S, Maharjan B, Goodwin M. Managing micronutrients for improving soil fertility, health, and soybean yield. *Sustainability*. 2021;13:11766.

[15] Che J, Ricachenevsky FK, Deng F. Editorial: Micronutrients movement from soil to the grains: Role of plant membrane transporters. *Front Plant Sci*. 2023;14:1179674.

[16] Tian J, Lou Y, Gao Y, Fang H, Liu S, Xu M, et al. Response of soil organic matter fractions and composition of microbial community to long-term organic and mineral fertilization. Biology and Fertility of Soils. 2017;53:523-532.

[17] White JG, Zasoski RJ. Mapping soil micronutrients. Field Crops Research. 1999;60(1-2):11-26.

[18] Parikh SJ, James BR. Soil: The foundation of agriculture. Nature Education Knowledge. 2012;3(10):2.

[19] Al-Hamed S, Wahby M, Al-Sulaiman M, Aboukarima A. Prediction of soil fractions (sand, silt and clay) in surface layer based on natural radionuclides concentration in the soil using adaptive neuro fuzzy inference system. Open Journal of Soil Science. 2014;4(07):215.

[20] Churchman GJ. Game changer in soil science. Functional role of clay minerals in soil. Journal of Plant Nutrition and Soil Science. 2018;181(1):99-103.

[21] Nelson PN, Baldock A, Oades JM, Churchman GJ, Clarke P. Dispersed clay and organic matter in soil: Their nature and associations. Soil Research. 1999;37(2):289-316.

[22] Schulze DG. Minerals in Soil Environments. In: Dixon JB, Weed SB, eds. Soil Science Society of America; 1989.

[23] Omoniyi IM, Oludare SMB, Oluwaseyi OM. Determination of radionuclides and elemental composition of clay soils by gamma- and X-ray spectrometry. SpringerPlus. 2013;2:74.

[24] Senesil GS, Baldassarre G, Senesi N, Radina B. Trace element inputs into soils by anthropogenic activities and implications for human health. Chemosphere. 1999;39(2):343-377.

[25] Karataş R. Toprak, Bitki ve Su Örneklerinin Alımı ve Laboratuvara Taşınma Teknikleri. Süleyman Demirel Üniversitesi Fen Bilimleri Enstitüsü; 2013.

[26] [ORAN, Orta Anadolu Kalkınma Ajansı. Yozgat ili Şefaatli ilçesi Karanlıkdere Vadisi arazilerinin değerlendirilmesi ve kullanım planlaması. Kayseri: ORAN; 2017.

[27] Yakupoğlu T, Koç A, Kara Z. Relationships between some general properties and erosion susceptibility of soils where wild rosehip grows in Yozgat province. *Bozok Journal of Agriculture and Natural Sciences*. 2023;2(2):73-84.

[28] Kaçar B. Bitki Toprak ve Gübre Analizleri 3: Fiziksel ve Kimyasal Toprak Analizleri. 2016

[29] Li F, Liang X, Li H, et al. Enhanced soil aggregate stability limits colloidal phosphorus loss potentials in agricultural systems. Environmental Science and Pollution Research. 2020;32:17.

[30] Kawałko D, Gruszka D, Waroszewski J, Kabała C. Application of portable colorimeter for identification of mollic horizon and mollic-based soil groups. Soil Science Annual. 2023;74:1-9.

[31] Genç ŞC, Kayacı K, Yıldırım Y. Mineralogical and technological properties of the Konya clays, Central Turkey. Journal of Thermal Analysis and Calorimetry. 2022;147:1887-1897.

[32] Demır G, Çoruh S, Ergun ON. Leaching behavior and immobilization of heavy metals in zinc leach residue before and after thermal treatment. Environmental Progress. 2008;27(4):479-486.

[33] Ünal Ö. Recovery of metallic values in RAM memory by hydrometallurgical methods [thesis]. İstanbul: Istanbul Technical University; 2015.

[34] Sastre J, Sahuquillo A, Vidal M, Rauret G. Determination of Cd, Cu, Pb and Zn in environmental samples: Microwave-assisted total digestion versus aqua regia and nitric acid extraction. *Anal Chim Acta*. 2002;462(1):59–72. https://doi.org/10.1016/s0003-2670(02)00307-0

[35] Yurdakul İ. Toprak Gübre Su Bitki Organik Materyal ve. Mikrobiyoloji Analiz Metotları

63

Laboratuvar El Kitabı, Tarım ve Orman Bakanlığı Tarımsal Araştırmalar ve Politikalar Genel Müdürlüğü Toprak Gübre ve Su Kaynakları Merkez Araştırma Enstitüsü Müdürlüğü; 2018.

[36] Olsen SR, Cole V, Watanable FS, Dean LA. Estimation of avaible phosphorus in soils by extraction with sodium bicarbonate, United States Department of Agriculture. Washington, United States of America; 1954

[37] Tüzüner A. Toprak ve su analiz laboratuvarları el kitabı. Tarım Orman ve Köy İşleri Bakanlığı, Köy Hizmetleri Genel Müdürlüğü; 1990.

[38] De Oliveira Morais PA, Souza DM de, de Melo Carvalho MT, Emoke Madari B, Oliveira AE de. Predicting Soil Texture Using Image Analysis. Microchemical Journal. 2019. https://doi.org/10.1016/j.microc.2019.01.009

[39] Suptijah P, Suseno SH, Anwar C, et al. JPHPI: J. Pengolahan Hasil Ikan Perikanan Indonesia. 2013;16(2):183-191. https://doi.org/10.17844/jphpi.v16i2.8053

[40] Brady NC. The Nature and Properties of Soils. 10th ed. Macmillan Publishing Company; 1990.

[41] Ünal Ö. Recovery of metallic values in RAM memory by hydrometallurgical methods [thesis]. İstanbul: Istanbul Technical University; 2015.

[42] He F, Ma B, Wang C, Zuo Y, Chen Y. Dissolution behavior and porous kinetics of limonitic laterite during nitric acid atmospheric leaching. *Minerals Engineering*. 2022;185:107671.

[43] Kantarcı MD. Toprak İlmi. İstanbul Üniversitesi, Orman Fakültesi; 2000.

[44] McCauley A, Jones C, Jacobsen J. Nutrient Management. Montana State University Extension Service. Publication, 4449-9; 2009. pp. 1-16.

[45] Boşgelmez A, Boşgelmez İİ, Savaşçı S, Paslı N. Ekoloji – II (Toprak). Başkent Klişe Matbaacılık; 2001.

[46] Aktaş M, Ateş A. Bitkilerde Beslenme Bozuklukları Nedenleri Tanınmaları. Nurol Matbaacılık A.Ş.; 1998.

[47] Sun F, Sun N, Ma X, Zhou B, Zhu P, Gao H, Xu M. The Application of Fertilizer Phosphorus Affected Olsen P and the Phosphorus Fractions of Hedley Method in Black Soil. Agronomy, 12, 3146; 2022.

[48] Eyüpoğlu F. Türkiye Topraklarının Verimlilik Durumu. Başbakanlık Köy Hizmetleri Genel Müdürlüğü; 1999.

[49] Boşgelmez A, Boşgelmez İ İ, Savaşçı S ve Paslı N., (2001). Ekoloji – II (Toprak), Başkent KlişeMatbaacılık, Kızılay-Ankara.

[50] Kantarcı M D (2000). Toprak İlmi. İÜ Toprak İlmi ve Ekoloji Anabilim Dalı, İ Ü Yayın No. 4261, OrmanFakültesi Yayın No. 462, İstanbul, 420 s.

[51] Yıldız, K., Kuh, M., Tan, S., & Ay, G. (2020). The soil characteristics of some of Silene L. species grown in Turkey. *Biological Diversity and Conservation*, *13*(3), 252–263.

64

Türk Doğa ve Fen Dergisi
Turkish Journal of Nature and Science

BINGÖL UNIVERSITY

Effect of K and Si Applications on Plant Development, Na and K Content and Some Antioxidant (SOD, CAT, APX) Activities of Wheat (Triticum aestivum L.) Plant Exposed to Salt Stress

Orhan İNİK[1*] (iD), Mehmet Ali Bozkurt[2] (iD)

[1] Bingol University, Faculty of Agriculture, Department of Soil Science and Plant Nutrition, Bingöl, Türkiye
[2] Yüzüncü Yıl University, Faculty of Agriculture, Department of Soil Science and Plant Nutrition, Van, Türkiye
Orhan İNİK ORCID No: 0000-0003-1473-1392
Mehmet Ali BOZKURT ORCID No: 0000-0003-3923-857X

*Corresponding author: oinik@bingol.edu.tr

Abstract: The problem of salinity in our soil is increasing day by day. This problem has become even more important with global climate change. Plants are the ones most affected by this problem. Salinity affects many metabolic activities in a very complex way by causing stress in plants. Reactive oxygen species, especially formed by salt stress, cause serious damage to plant cells. They use antioxidative enzymes such as catalase (CAT), ascorbate peroxidase (APX), and superoxide dismutase (SOD) to protect the plant from this stress. The aim of this research is to determine the effects of potassium and silicon applications on some antioxidant enzyme activities in wheat plant in salty conditions. In the experiment conducted under potted conditions, increasing doses of salt (0 and 100 mM NaCl), potassium (0, 150,300 ppm K) and silicon (0, 75, 150 ppm Si) were applied to the wheat plant. According to the results obtained, SOD activity increased with the 100 mM NaCl, 150 mg/kg K, 0 mg/kg Si, and 300 mg/kg Si applications. The effect of salt application on CAT activity was not found to be significant compared to control. APX activity was generally increased with the addition of salt. However, the increase in APX activity due to 100 mM NaCl administration decreased significantly with increasing silicon doses when 150 mg/kg potassium treatment was kept constant. This suggests that K and Si applications can be beneficial in alleviating salt stress.

65

Tuz Stresindeki Buğday (Triticum aestivum L.) Bitkisinin Bitki Gelişimi, Na ve K İçeriği ve Bazı Antioksidan (SOD, CAT, APX) Aktiviteleri Üzerine K ve Si Uygulamalarının Etkisi

Öz: Topraklarımızdaki tuzluluk sorunu her geçen gün artmaktadır. Küresel iklim değişikliğiyle birlikte bu sorun daha da önemli hale gelmiştir. Bu sorundan en çok etkilenen ise bitkilerdir. Tuzluluk, bitkilerde strese neden olarak birçok metabolik aktiviteyi çok karmaşık bir şekilde etkilemektedir. Özellikle tuz stresinin oluşturduğu reaktif oksijen türleri, bitki hücrelerinde ciddi hasarlara neden olmaktadır. Bitkiler bu stresten korunmak için katalaz (CAT), askorbat peroksidaz (APX) ve süperoksit dismutaz (SOD) gibi antioksidan enzimleri kullanırlar. Bu araştırmanın amacı, tuzlu koşullarda buğday bitkisinde bazı antioksidan enzim aktiviteleri üzerine potasyum ve silisyum uygulamalarının etkilerini belirlemektir. Saksı koşullarında yapılan deneyde buğday bitkisine artan dozlarda tuz (0 ve 100 mM NaCl), potasyum (0, 150,300 ppm K) ve silisyum (0, 75, 150 ppm Si) uygulanmıştır. Elde edilen sonuçlara göre, SOD aktivitesi 100 mM NaCl, 150 mg/kg K, 0 mg/kg Si ve 300 mg/kg Si uygulamalarıyla artmıştır. Tuz uygulamasının CAT aktivitesi üzerine etkisi kontrole göre anlamlı bulunmamıştır. APX aktivitesi genel olarak tuz ilavesiyle artmıştır. Ancak, 100 mM NaCl uygulamasına bağlı APX aktivitesindeki artış, 150 mg/kg potasyum uygulaması sabit tutulduğunda artan silikon dozlarıyla anlamlı şekilde azalmıştır. Bu durum, K ve Si uygulamalarının tuz stresini hafifletmede faydalı olabileceğini düşündürmektedir.

1. INTRODUCTION

Plants show their best development under optimal conditions. Depending on the flexibility of normal metabolism, although they can continue to grow in the face of daily and seasonal changes, their constant or occasional exposure to an unexpected condition may result in diseases, damage or physiological changes that affect their development and survival [1]. The factors that create these unfavorable conditions are referred to as 'stress'. [2-5].
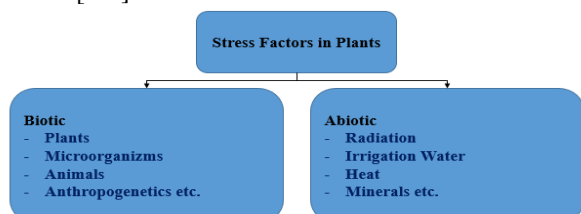

Figure 1. Stress Factors Affecting Plants [6-7]

Stress factors affecting plants are divided into two groups as biotic and abiotic (Figure 1). Of these factors, minerals from abiotic stresses are second with a rate of 20% after the stress factor that most affects usable areas caused by drought. The most important mineral that causes stress is salinity, which occurs in soils [7-8]. Salinity, together with the increasing human population, is one of the stress factors that significantly restrict the production of food products by jeopardizing efficient agriculture in our world. Excessive salinity in the soil affects the development of plants by causing structural, physiological and biochemical changes [9]. Both in the world and in our country, the yield is decreasing day by day in the agricultural lands and some areas are completely out of production due to excessive salinization. There is a salinity problem in 2-2.5 million ha of agricultural area in Turkey [10]. This problem is increasing due to chemical fertilizers used in agricultural areas, pesticides, intensive and unconscious irrigation in agricultural lands, destruction of the natural vegetation of a region and opening it to agricultural lands [11-14].

Salt stress inhibits plant growth and development by causing osmotic and ionic stress [15]. The increase in the amount of salt in the root rhizosphere first causes osmotic stress, which leads to a decrease in the amount of usable water, which is also called "physiological drought" [16]. The decrease in the amount of available water leads to reduced cell expansion and a slowdown in shoot development.

During the ion stress phase that occurs in the continuation of osmotic stress, nutrient deficiency or nutrient imbalance occurs in plants when Na and Cl ions increasing in the environment cause an antagonistic effect with the necessary nutrients such as K^+, Ca^{+2} and NO_3^- [17-18]. In particular, this effect significantly inhibits the plant's potassium (K^+) uptake [9,19].
One of the reasons for the stress observed in plants in salty conditions is the inhibition of the uptake, transportation and use of nutrients by plants. In one study, it was determined that the growth decline observed in the barley plant grown in a salty environment was largely due to salt-induced Mn deficiency [20]. In addition, P uptake and movement in soil-grown plants decreased as salt concentration increased [21].

Many studies have been done and are still being done to eliminate the damage of salinity in the soil. In addition to growing salinity-resistant halophyte plants, it can prevent the damage caused by salt stress in the soil in some applications. For example, it is believed that the salt tolerance of plants is related to the limitation in Na intake and that K plays an important role in this limitation. In a study conducted by Litifi et al. (1992) [22], it was seen that potassium regulation, increased K/Na ratio in the plant and salt tolerance increased. It has been determined that salt-tolerant varieties absorb more K than sensitive varieties, and that K plays an important role in drought and salt stress tolerance [23]. Under saline conditions, increasing the turgor pressure in plant tissues, which is a natural defense mechanism, and protecting turgor come to the forefront. Likewise, studies conducted to date have shown that silicone (Si) has beneficial effects on healthy plant growth and development. Silicon has been proven to increase plant tolerance to salt stress and drought [24-25]. It is stated that if Si is added to saline soils, silicon reacts with Na and significantly reduces Na uptake and transport, as well as increases K uptake and reduces the Na/K ratio in the plant. In addition, many studies report that Si reduces oxidative stress in plants [26-34].

Although there are various studies in which K and Si applications are discussed individually in the prevention of salt stress, there are almost no studies investigating K×Si interaction. The aim of this study is to determine the effect of K×Si interaction on some antioxidant enzyme activity in the plant in order to eliminate the damages caused by salinity in the wheat plant.

2. MATERIAL AND METHOD

The trial was carried out in pots under the conditions of the climate room at Yüzüncü Yıl University Faculty of Agriculture. Alparslan Wheat variety plant was used as the plant in the research. The experiment was carried out in randomized plots according to the factorial design with 4 replications. Plants are grown in pots that can weigh up to 1 kg. In the study, a total of 144 pots consisting of two pots were used each repeatedly. The climate room is set to be 14 hours day, 10 hours at night, relative humidity 60%, temperature 25-27 ^{0}C.

The mortar used in the trial was prepared by mixing soil, sand and peat in a ratio of 2: 2:1. In the experiment, 50 ppm P was given to all pots in the form of P (triple superphosphate) as basic fertilization (Figure 2.a).
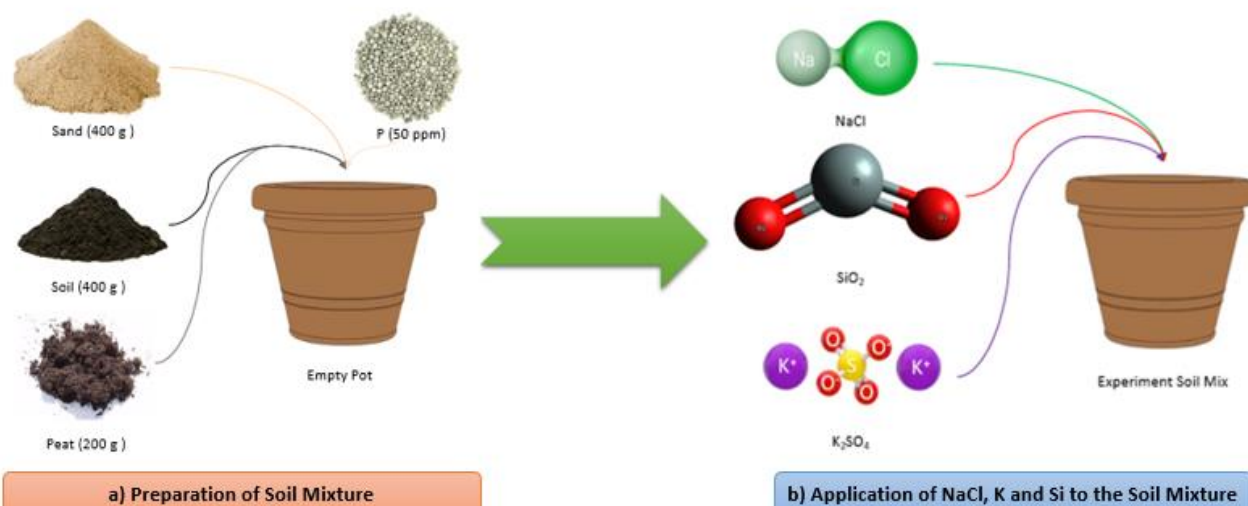
66

Figure 2: Preparation of soil mixture and application of NaCl, K and Si before planting seeds in pots

Six seeds are planted in a 1 kg plastic pot. After germination is completed three plants are left in each pot. After six weeks of development, the plants were harvested by cutting from the soil surface. Samples for enzyme analysis were taken from the youngest leaves of the plant before harvest and stored in a -82 ^{0}C freezer.

Salt was applied in two levels (0 and 100 mM) as NaCI. Potassium was applied at 3 levels (0, 150, 300 ppm K) with control as K_2SO_4. Silicon application was applied at 3 levels (0, 75, 150 ppm Si) with control as SiO_2 (Figure 2.b; Table 1).

Table 1. Experiment pattern topics

$NaCl_0 K_0 Si_0$ (kontrol)	10- $NaCl_1 K_0 Si_0$ (100 mM NaCl)
$NaCl_0 K_0 Si_1$ (75 ppm Si)	11- $NaCl_1 K_0 Si_1$ (100 mM NaCl + 75 ppm Si)
$NaCl_0 K_0 Si_2$ (150 ppm Si)	12- $NaCl_1 K_0 Si_2$ (100 mM NaCl + 150 ppm Si)
$NaCl_0 K_1 Si_0$ (150 ppm K)	13- $NaCl_1 K_1 Si_0$ (100 mM NaCl +150 ppm K)
$NaCl_0 K_1 Si_1$ (150 ppm K + 75 ppm Si)	14- $NaCl_1 K_1 Si_1$ (100 mM NaCl +150 ppm K + 75 ppm Si)
$NaCl_0 K_1 Si_2$ (150 ppm K + 150 ppm Si)	15- $NaCl_1 K_1 Si_2$ (100 mM NaCl +150 ppm K + 150 ppm Si)
$NaCl_0 K_2 Si_0$ (300 ppm K)	16- $NaCl_1 K_2 Si_0$ (100 mM NaCl +300 ppm K)
$NaCl_0 K_2 Si_1$ (300 ppm K + 75 ppm Si)	17- $NaCl_1 K_2 Si_1$ (100 mM NaCl +300 ppm K + 75 ppm Si)
$NaCl_0 K_2 Si_2$ (300 ppm K + 150 ppm Si)	18- $NaCl_1 K_2 Si_2$ (100 mM NaCl +300 ppm K + 150 ppm Si)

As stated by Jakson (1958), the pH values in the experimental soil were determined by diluting the pH values with pure water in a ratio of 1/2.5 [35]. Lime (%) was detected using Scheibler's calcimeter, as noted by Hızalan and Ünal (1966) [36]. EC (dS/m), using the 1/2.5 method was determined by a handheld electrical constantimeter [37]. Organic matter was determined according to the modified Walkley-Black method [38]. Total nitrogen was determined according to the Kjeldahl method [37] and the available phosphorus was determined according to the Sodium bicarbonate method [39]. Exchangeable potassium (C), calcium (Ca), magnesium (Mg) and sodium (Na) were determined in the Atomic Absorption Spectrophotometer by shaking with 1 N Ammonium acetate according to Thomas (1982) [40]. Available microelements (Fe, Mn, Zn and Cu) in soil samples were determined by reading the prepared solutions with the 0.05 M DTPA method, pH adjusted to 7.3, on an atomic absorption spectrophotometer (AAS). [37]. Some analyses of the trial soil are given in Table 2.

Table 2. Some features of the experiment soil

Properties	Experimental Soil
pH (1/2.5)	8.26
EC (dS/m)	0.80
$CaCO_3$ (%)	13.6
Organic Madder (%)	6.27
Total N (%)	0.15
Available P (mg/kg)	13.3
Exchangeable Cations (ppm)	
K	732
Ca	23709
Mg	749
Na	459
Extractable with DTPA (ppm)	
Fe	19.3
Zn	0.46
Cu	0.47
Mn	5.16

Catalase (CAT) activity in plant leaves was determined by measuring the change in absorbance due to H2O2 decrease at a wavelength of 240 nm [41]. Superoxide Dismutase (SOD) Activity was determined by inhibition of nitroblue tetrazolium (NBT) at a wavelength of 560 nm [42]. Ascorbate Peroxidase (APX) Activity was measured

by H_2O_2 reduction due to ascorbic acid [43]. After the statistical analysis of the obtained findings was determined by SPSS package program, the significance of the difference between the averages of the applications was made with Duncan multiple comparison test ($P < 0.05$) [44].

3. RESULTS

3.1. Plant Productivity

Some of the images of the experiment are in Figure 3. The effect of salt stress on plant development is clearly visible (Figure 3a).

$NaCl_0K_2Si_1$ application increased plant growth compared to $NaCl_0K_2Si_2$ application (figure 3.b.).
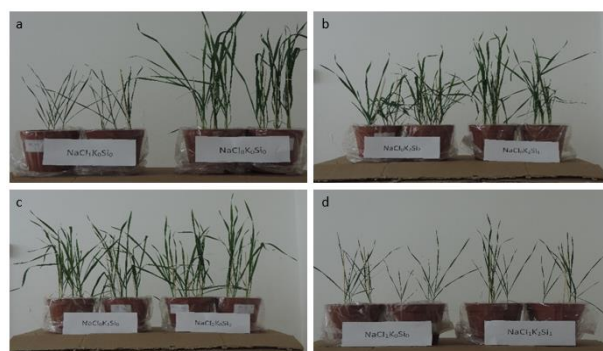

Figure 3. Some images of plant development.

Variance analysis results regarding the effects of NaCl, K, Si and the double and triple interactions of these applications on plant fresh weight, plant dry weight and plant height are shown in Table 3.

Table 3. Variance analysis results regarding the effects of NaCl, K and Si applications on plant fresh weight, dry weight and plant height.

Variation Source	S.D.	Fresh Weight		Dry Weight		Plant Height	
		Mean of Squares	F Value	Mean of Squares	F Value	Mean of Squares	F Value
NaCl	1	1445.3	6512.2***	33.6	3304.7***	4403.6	1356.2***
K	2	1.303	5.872**	0.000	0.03 ns.	19.55	6.02**
Si	2	0.554	2.495 ns.	0.040	3.94 *	8.46	2.60 ns.
NaClxK	2	0.564	2.543 ns.	0.060	5.93**	29.01	8.94***
NaClxSi	2	0.097	0.439 ns.	0.003	0.25 ns.	0.25	0.08 ns.
KxSi	4	0.232	1.047 ns.	0.010	0.95 ns.	2.73	0.84 ns.
NaClxKxSi	4	0.153	0.687 ns.	0.041	4.01**	5.00	1.54 ns.
Error	54	0.222		0.010		3.25	
Total	71						

*: Important at $p < 0.05$, **: Important at $p < 0.01$, ***: Important at $p < 0.001$, ns: non significant

Variance analysis results regarding the effects of NaCl, K, Si and the double and triple interactions of these applications on plant fresh weight, plant dry weight and plant height are shown in Table 3. While the effect of NaCl ($P < 0.001$) and K ($P < 0.01$) applications on plant fresh weight was found to be statistically significant, the effect of other applications was not found to be significant. The fresh plant weight, which was determined as 10.9 grams in the $NaCl0Si0K0$ application, decreased significantly to 1.58 grams in the $NaCl_1Si_0K_0$ application. Increasing potassium doses in both salt-free ($NaCl_0$) and salty ($NaCl_1$) conditions caused a decrease in plant fresh weight. The effect of Si doses on plant fresh weight was not found to be significant (Table 4.).

The effect of NaCl ($P < 0.001$), Si ($P < 0.05$), NaClxK ($P < 0.01$) and NaClxKxSi ($P < 0.01$) applications on plant dry weight was found to be significant (Table 3.). The dry weight of the plant, which was determined as 1.59 grams in the $NaCl_0Si_0K_0$ application, decreased significantly to 0.28 grams in the $NaCl_1Si_0K_0$ application. At constant potassium level (K_1) under salt-free conditions, Si_1 application significantly increased plant dry weight compared to other silicon doses.

Table 4. Effect of NaCl, K and Si applications on plant fresh weight (g/pot)

Si Doses (mg/kg)	K Doses (mg/kg)	$NaCl_0$	$NaCl_1$
		Average	Average
Si_0	K_0	A 10.91 a	A 1.580 a *
	K_1 (150)	A 10.05 b	A 1.100 b *
	K_2 (300)	A 10.26 b	A 1.248 b *
Si_1 (75)	K_0	B 10.40 a	B 1.230 a *
	K_1 (150)	A 10.35 a	A 1.110 a *
	K_2 (300)	A 9.79 a	A 1.392 a *
Si_2 (150)	K_0	B 10.53 a	B 1.198 ab *
	K_1 (150)	A 9.85 b	A 1.215 a *
	K_2 (300)	A 9.56 b	B 0.980 b *

a,b, c: The difference between potassium levels that take on different lowercase letters at the same silicon and NaCl level is important ($p < 0.05$).
A, B,C: The difference between different capitalized silicon levels at the same potassium and NaCl levels is important ($p < 0.05$).
*: The difference between NaCl1 administration and control (NaCl0) is significant ($p < 0.05$).

When the K_0 dose was kept constant under saline conditions, Si_1 application significantly increased the plant dry weight compared to other silicon doses. Similarly, when $NaCl_1K_1$ application was kept constant,

plant dry weight increased significantly with increasing silicon doses (Table 5.). These results show that the NaClxKxSi interaction is important on plant dry weight.

Table 5. Effect of NaCl, K and Si applications on plant dry weight (g/pot)

Si Doses (mg/kg)	K Doses (mg/kg)	$NaCl_0$	$NaCl_1$
		Average	Average
Si_0	K_0	A 1.59 a	B 0.282 a *
	K_1 (150)	B 1.55 a	B 0.227 b *
	K_2 (300)	A 1.66 a	A 0.240 b *
Si_1 (75)	K_0	A 1.54 b	A 0.452 a *
	K_1 (150)	A 1.83 a	A 0.260 b *
	K_2 (300)	A 1.71 ab	A 0.235 b *
Si_2 (150)	K_0	A 1.63 a	B 0.262 a *
	K_1 (150)	B 1.60 a	A 0.267 a *
	K_2 (300)	A 1.69 a	A 0.252 a *

a,b, c: The difference between potassium levels that take on different lowercase letters at the same silicon and NaCl level is important (p<0.05).
A, B,C: The difference between different capitalized silicon levels at the same potassium and NaCl levels is important (p<0.05).
*: The difference between NaCl1 administration and control (NaCl0) is significant (p<0.05).

The effects of NaCl (P<0.001), K (P<0.01) and NaClxK (P<0.001) applications on plant height were found to be statistically significant (Table 3.). The plant height, which was determined as 40.6 cm in the $NaCl_0Si_0K_0$ application, decreased significantly to 25.2 cm in the $NaCl_1Si_0K_0$ application. In salt-free conditions, when NaCl and Si doses were kept constant, increasing potassium doses caused plant height to decrease.

The effect of increasing potassium doses at constant silicon level under saline conditions on plant height was not found to be significant. The effect of silicon doses at constant potassium level on plant height was found to be insignificant in both salt-free and salty conditions (Table 6.).

Table 6. Effect of NaCl, K and Si applications on plant height (cm)

Si Doses (mg/kg)	K Doses (mg/kg)	$NaCl_0$	$NaCl_1$
		Average	Average
Si_0	K_0	A 40.625 a	A 25.225 a *
	K_1 (150)	B 39.625 ab	A 22.475 a *
	K_2 (300)	A 37.850 b	A 22.775 a *
Si_1 (75)	K_0	A 40.650 a	A 22.650 a *
	K_1 (150)	A 39.875 a	A 23.325 a *
	K_2 (300)	B 36.850 b	A 24.900 a *
Si_2 (150)	K_0	A 40.075 a	A 22.300 a *
	K_1 (150)	A 39.050 a	A 22.475 a *
	K_2 (300)	A 35.325 b	A 23.025 a *

a,b, c: The difference between potassium levels that take on different lowercase letters at the same silicon and NaCl level is important (p<0.05).
A, B,C: The difference between different capitalized silicon levels at the same potassium and NaCl levels is important (p<0.05).
*: The difference between NaCl1 administration and control (NaCl0) is significant (p<0.05).

3.2. Na and K Content in Plants

The effects of NaCl, K, Si and the double and triple interactions of these applications on the potassium (K) and sodium (Na) content in the plant can be seen in Table 7.

Table 7. Variance analysis results of the effects of NaCl, K and Si applications on K and Na content in the plant

Variation Source	S.D.	K		Na	
		Mean of Squares	F Value	Mean of Squares	F Value
NaCl	1	17.0	111.3 ***	12.69	1815.8***
K	2	0.695	9.02**	0.85	120.3 ***
Si	2	0.177	6.61 ns.	0.42	60.14***
NaClxK	2	0.436	26.3 *	1.07	152.9 ***
NaClxSi	2	0.001	3.21ns.	0.40	56.47***
KxSi	4	0.518	26.0 **	0.62	89.20***
NaClxKxSi	4	0.271	4.21*	0.62	88.33***
Error	54	0.093		0.01	
Total	71				

*: Important at p<0.05, **: Important at p<0.01 , ***: Important at p<0.001, ns: non significan

The effect of NaCl (P<0.001), K (P<0.01), NaClxK (P<0.05), KxSi (P<0.01) and NaClxKxSi (P<0.05) applications on the potassium content in the plant is statistically significant. was found (Table 7.). Under salt-free conditions, potassium doses at a fixed dose of Si_0

caused a decrease in plant potassium content compared to the control, while increasing potassium doses, keeping the Si_2 dose constant, significantly increased the potassium content in the plant compared to the control. In saline conditions, when the silicon dose was generally kept

constant, increasing potassium doses increased the plant potassium content compared to the control.

This increase was found to be statistically significant at Si_0 and Si_1 doses compared to the control (K_0) (Table 8.). The effect of all variation sources on sodium in the plant was found to be significant ($P<0.001$) (Table 7.). Increasing potassium applications at a constant silicon dose under salt-free conditions significantly reduced plant sodium content. Application of Si_1 at a fixed K_0 dose significantly increased the sodium content in the plant compared to other silicon doses. Increasing potassium applications at a fixed silicon dose under saline conditions generally significantly increased the sodium content of the plant.

Table 8. Effect of NaCl, K and Si applications on potassium content in plants (%)

Si Doses (mg/kg)	K Doses (mg/kg)	NaCl$_0$ Average	NaCl$_1$ Average
	K_0	A 2.38 a	A 1.15 b *
Si_0	K_1 (150)	A 2.12 b	B 0.79 c *
	K_2 (300)	A 2.18 b	A 1.80 a *
	K_0	A 2.17 a	A 0.80 b *
Si_1 (75)	K_1 (150)	A 1.95 a	B 0.86 b *
	K_2 (300)	A 2.05 a	B 1.56 a *
	K_0	B 1.75 b	A 0.91 a *
Si_2 (150)	K_1 (150)	A 2.41 a	A 1.50 a *
	K_2 (300)	A 2.32 a	C 1.20 a *

a,b, c: The difference between potassium levels that take on different lowercase letters at the same silicon and NaCl level is important (p<0.05).
A, B,C: The difference between different capitalized silicon levels at the same potassium and NaCl levels is important (p<0.05).
*: The difference between NaCl1 administration and control (NaCl0) is significant (p<0.05).

When the K_0 dose was kept constant, the highest sodium content was determined in the Si_1 dose, while when the K_2 dose was kept constant, the highest sodium content was obtained with the Si_2 application (Table 9.).

Table 9. Effect of NaCl, K and Si applications on sodium content in plants (%)

Si Doses (mg/kg)	K Doses (mg/kg)	NaCl$_0$ Average	NaCl$_1$ Average
	K_0	B 0.088 a	B 0.642 a *
Si_0	K_1 (150)	A 0.087 a	A 0.783 a *
	K_2 (300)	A 0.053 b	B 0.749 a *
	K_0	A 0.120 a	A 0.827 b *
Si_1 (75)	K_1 (150)	A 0.089 b	B 0.661 c *
	K_2 (300)	A 0.055 c	B 0.992 a *
	K_0	B 0.101 a	B 0.581 b *
Si_2 (150)	K_1 (150)	A 0.100 a	B 0.666 b *
	K_2 (300)	A 0.061 b	A 0.407 a *

a,b, c: The difference between potassium levels that take on different lowercase letters at the same silicon and NaCl level is important (p<0.05).
A, B,C: The difference between different capitalized silicon levels at the same potassium and NaCl levels is important (p<0.05).
*: The difference between NaCl1 administration and control (NaCl0) is significant (p<0.05).

3.3. Antioxidant Enzyme Activity

The effect of NaCl, K, Si and the double and triple interactions of these applications on SOD, CAT and APX enzymes in the plant is seen in Table 3.

The effect of NaCl ($P<0.01$), K ($P<0.001$), Si ($P<0.01$), NaClxK ($P<0.01$) and NaClxKxSi ($P<0.001$) applications on SOD enzyme in the plant was found to be statistically significant (Table 10).

Table 10. Variance analysis results of the effect of NaCl, K and Si applications on SOD, CAT and APX enzyme activations in the plant

Variation Source	S.D.	SOD Mean of Squares	SOD F Value	CAT Mean of Squares	CAT F Value	APX Mean of Squares	APX F Value
NaCl Doses	1	0.09	12.78**	0.001	6.40*	4.84	73.51***
K Doses	2	0.17	22.91***	0.003	24.15	0.81	12.31***
Si Doses	2	0.04	5.87**.	0.001	6.90**	0.62	9.39***
NaClxK	2	0.05	6.99**	0.001	11.14***	0.61	9.28***
NaClxSi	2	0.01	1.73ns.	1.60	0.13ns.	0.50	7.63**
KxSi	4	0.01	0.75ns.	0.00	2.84*	0.93	14.12***
NaClxKxSi	4	0.08	10.90***	9.30	0.80 ns.	0.38	5.76**
Error	54	0.01		0.00		0.07	
Total	71						

*: Important at p<0.05, **: Important at p<0.01 , ***: Important at p<0.001, ns: non significant

When the silicon doses are kept constant separately in salty conditions, the difference created by the K_1 dose in potassium applications is found to be statistically significantly higher than other doses. The highest SOD activity at a constant dose of K_1 in saline conditions was determined at the dose of no silicon (Si_0). When the K_2 dose was kept constant, the difference between the silicon doses and the Si_1 dose was found to be significant and high (Figure 4 and Table 11).
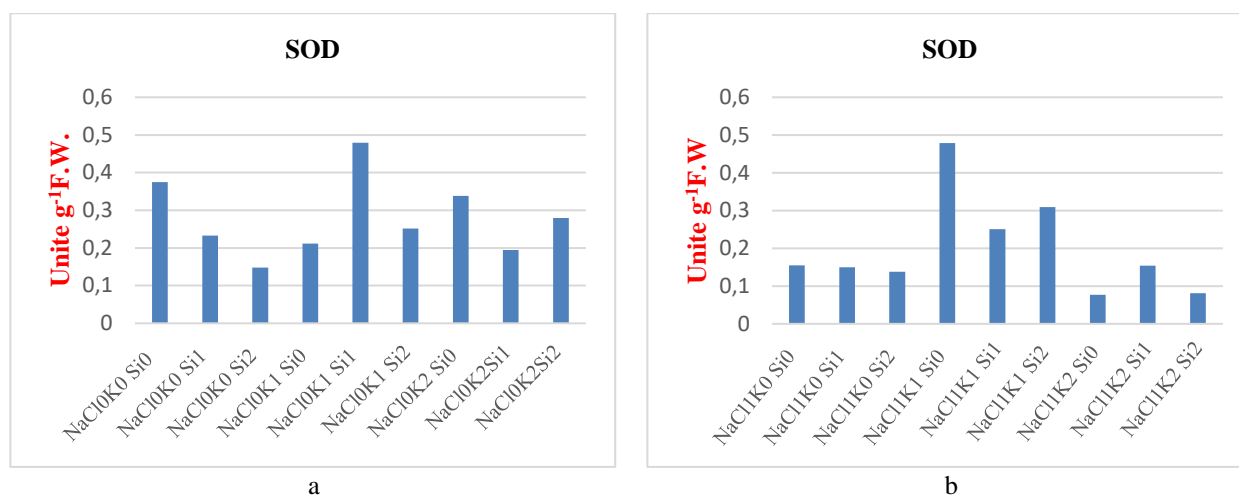
Figure 4. SOD enzyme activity in the plant; a. Effect of unsalted KxSi interactions, b. Effect of 100 mM NaCl saline KxSi interactions

Table 11. Effect of NaCl, K and Si applications on superoxide dismutase (SOD) enzyme activity in the plant (Unite g-1F.W.)

Si Doses (mg/kg)	K Doses (mg/kg)	$NaCl_0$ Average	$NaCl_1$ Average
Si_0	K_0	A 0.375 a	A 0.155 b *
	K_1 (150)	B 0.212 a	A 0.479 a *
	K_2 (300)	A 0.338 a	B 0.077 c *
Si_1 (75)	K_0	AB 0.233 b	A 0.150 b *
	K_1 (150)	A 0.480 a	B 0.251 a *
	K_2 (300)	B 0.195 b	A 0.154 b
Si_2 (150)	K_0	B 0.148 a	A 0.138 b
	K_1 (150)	B 0.252 a	B 0.309 a
	K_2 (300)	B 0.208 a	B 0.081 b *

a,b, c: The difference between potassium levels that take on different lowercase letters at the same silicon and NaCl level is important ($p<0.05$).
A, B,C: The difference between different capitalized silicon levels at the same potassium and NaCl levels is important ($p<0.05$).
*: The difference between $NaCl_1$ administration and control ($NaCl_0$) is significant ($p<0.05$).

The effect of NaCl ($P<0.05$), K ($P<0.01$), Si ($P<0.01$), NaClxK ($P<0.001$) and KxSi ($P<0.05$) applications on CAT enzyme in the plant was found to be important (Table 10). While salt application did not affect CAT activity in general, the addition of salt to only the K_0-Si_1 application group significantly increased CAT activity. The CAT activity obtained by K_2-Si_1 application under salt-free conditions was found to be statistically significantly different from other applications.
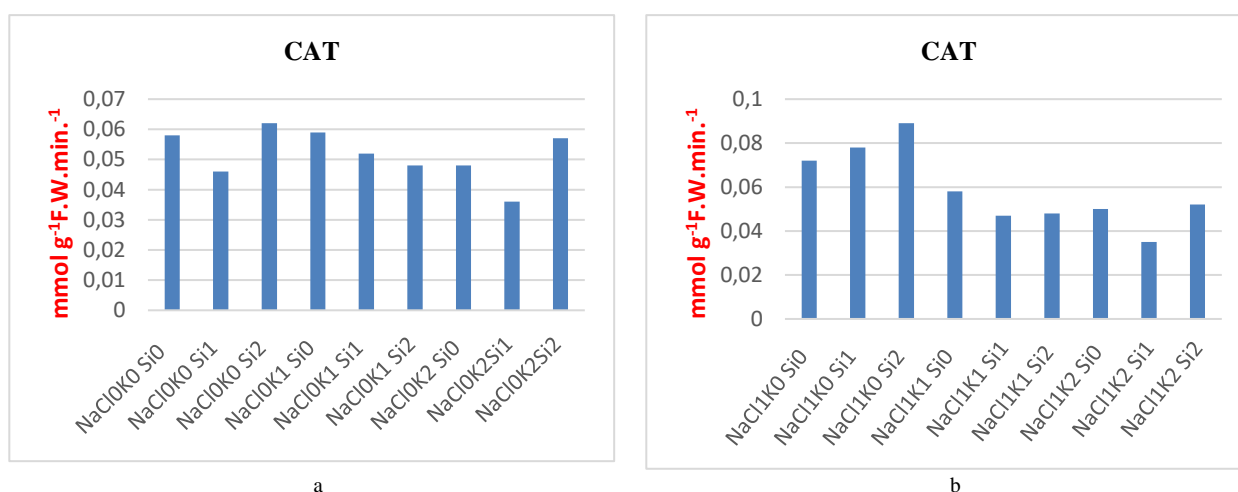
Figure 5. CAT enzyme activity in the plant; a. Effect of unsalted KxSi interactions, b. Effect of 100 mM NaCl saline KxSi interactions

When the level of silicon (Si_0, Si_1 and Si_2) was kept constant under saline conditions, increased potassium doses significantly reduced CAT Catalase activity decreased significantly from 0.078 mmol g^{-1}F.W.min.$^{-1}$ in the K_0-Si_1 interaction group to 0.035 mmol g^{-1}F.W.min.$^{-1}$ in the K_2-Si_1 interaction group. Increased doses of silicon in pots where potassium was applied under the same conditions significantly increased CAT activity (Figure 5 and Table 12).

The effect of all variation sources on APX enzyme in the plant was found to be significant (Table 10). When the Si_0 dose from silicon applications was kept constant under unsalted ($NaCl_0$) conditions, increased potassium doses

increased APX activity, while increased potassium levels at constant Si1 and Si2 doses led to a decrease in APX activity. The difference of Si2 dose in silicon applications when K_0 dose was kept constant from potassium applications, the difference caused by reducing Si1

activity when K_1 dose was kept constant, and the increase in activity obtained with Si_0 dose when K_2 dose was kept constant were found to be statistically important.

Table 12. Effect of NaCl, K and Si applications on catalase (CAT) enzyme activity in the plant (mmol g^{-1}F.W.min.$^{-1}$)

Si Doses (mg/kg)	K Doses (mg/kg)	$NaCl_0$ Average	$NaCl_1$ Average
Si_0	K_0	A 0.058 a	B 0.072 a
	K_1 (150)	A 0.059 a	A 0.058 ab
	K_2 (300)	A 0.048 a	A 0.050 b
Si_1 (75)	K_0	A 0.046 a	AB 0.078 a *
	K_1 (150)	A 0.052 a	A 0.047 b
	K_2 (300)	A 0.037 b	B 0.035 b
Si_2 (150)	K_0	A 0.063 a	A 0.089 a
	K_1 (150)	A 0.049 a	A 0.048 b
	K_2 (300)	A 0.057 a	A 0.052 b

a,b, c: The difference between potassium levels that take on different lowercase letters at the same silicon and NaCl level is important (p<0.05).
A, B,C: The difference between different capitalized silicon levels at the same potassium and NaCl levels is important (p<0.05).
*: The difference between NaCl1 administration and control (NaCl0) is significant (p<0.05).
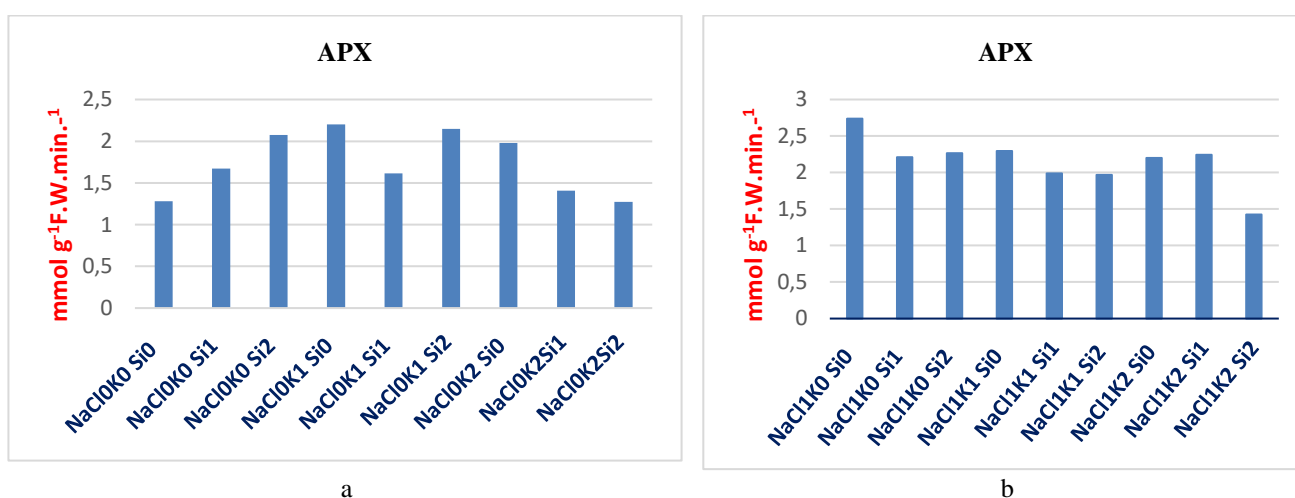

a

b

Figure 6. APX enzyme activity in the plant; a. Effect of unsalted KxSi interactions, b. Effect of 100 mM NaCl saline KxSi interactions

Considering the effects of these applications in saline conditions, the difference between silicon applications was found to be insignificant when the K_0 dose was kept constant. The difference of Si0 dose when K_1 dose was kept constant and the difference of all silicon doses when K_2 dose was kept constant were found to be statistically

significant and the lowest activity was obtained with Si_2 administration (1.425 mmol g^{-1} F.W. min^{-1}). In general, when the silicon dose was kept constant, the increased potassium level caused a decrease in APX activity (Figure 6 and Table 13).

Table 13. Effect of NaCl, K and Si applications on ascorbate peroxidase (APX) enzyme activity in the plant (mmol g^{-1} F.W. min^{-1})

Si Doses (mg/kg)	K Doses (mg/kg)	$NaCl_0$ Average	$NaCl_1$ Average
Si_0	K_0	B 1.282 b	A 2.738 a *
	K_1 (150)	A 2.200 a	A 2.695 a *
	K_2 (300)	A 1.980 a	B 2.200 b
Si_1 (75)	K_0	B 1.673 a	A 2.210 a
	K_1 (150)	B 1.615 ab	B 1.988 a *
	K_2 (300)	B 1.408 b	A 2.433 a *
Si_2 (150)	K_0	A 2.075 a	A 2.665 a *
	K_1 (150)	A 2.148 a	B 1.968 b
	K_2 (300)	B 1.273 b	C 1.425 c

a,b, c: The difference between potassium levels that take on different lowercase letters at the same silicon and NaCl level is important (p<0.05).
A, B,C: The difference between different capitalized silicon levels at the same potassium and NaCl levels is important (p<0.05).
*: The difference between NaCl1 administration and control (NaCl0) is significant (p<0.05).

4. DISCUSSION

In the pot experiment conducted with wheat plants, application of 100 mM NaCl significantly reduced plant fresh weight, plant dry weight and plant height (Tables 4, 5 and 6). In a similar experiment, it was determined that salt stress negatively affected plant development [45]. Increasing the amount of salt in the root zone creates osmotic stress in the plant and prevents the plant from using water [16]. Decreasing the amount of available water causes cell expansion to decrease and shoot development to slow down. In their study, Hu and Schmidhalter (2005) reported that increased osmotic stress, caused by higher concentrations of Na+ and Cl- ions, reduced the uptake of ions such as K+, Ca²+, and NO₃⁻, leading to nutrient deficiencies or imbalances in the plant [17]. In the experiment conducted, while increasing potassium doses under saline conditions did not cause a significant change in plant height at all silicon levels, plant fresh and dry weights generally decreased with the addition of potassium (Tables 4, 5 and 6). In a similar study, the negative effects of salinity were eliminated by potassium application [46]. Zheng et al. (2008) suggested in their study that potassium application reduced salt stress and increased plant growth [47]. In the experiment, potassium did not show the expected results in eliminating the harmful effects of salinity on plant growth parameters. This may be due to the high salt concentration used in the experiment.

While the effect of silicon applications on plant fresh weight and plant height was not found to be significant, plant dry weight increased significantly with silicon application. The effect of NaClxKxSi interaction on plant dry weight was found to be significant (Table 3). In saline conditions, increasing silicon doses at constant K_0 and K_1 levels significantly increased plant dry weight compared to the control (Table 5). In a similar study, a significant increase in plant growth was observed with the addition of silicon to wheat plants grown under salt stress [48]. Gurmani et al. (2013) suggested in their study with two types of wheat under saline conditions that silicon inhibited the transport of Na+ and increased plant growth [32]. In a study conducted with wheat plants under salt stress conditions, it was determined that silicon and potassium nitrate applications increased plant weight, grain weight, spike height and photosynthesis rate [49].

Table 6 shows that the interaction of NaCl, K, and Si applications had a statistically significant effect on K and Na levels in the plant . This effect caused the K content to decrease in saline conditions and increased the Na content (Tables 8 and 9). In many plants, salt generally causes the Na+ level to increase and the K+ level to decrease [15, 50-51]. Erdal et al. (2000) suggested that other cations should be taken in addition to Na in order to make the plant tolerant to salinity in the presence of Na [52]. In salt stress, application of silicon and potassium together or alone increased the potassium uptake of the plant [49]. Gurmani et al. (2013) suggested that silicon applied to wheat plants under salt stress inhibited Na+ transport and reduced the Na+/K+ ratio [32]. There are generally two basic concepts in studies on salt stress. These are salt stress and salt

shock. While salt shock is not very visible in the soil in agricultural areas, salt stress disappears after a certain time and its effect gradually increases. In salt stress studies, NaCl or sea water is applied to plants in a controlled manner under laboratory or greenhouse conditions. These applications are generally applied to the experiment at increasing concentrations of 25, 50 or 100 mM NaCl, and the plant is exposed to stress in this way [11, 53-55]. In this experiment, the decrease in potassium content in salty conditions compared to the control can be explained by the fact that the high salt level applied creates an antagonistic effect between Na and K in the root region of the plant, preventing the uptake of potassium.

In the experiment, the application of 100 mM NaCl inhibited the productivity of the plant and directly caused an increase in the activity of antioxidant enzymes. In particular, it caused a significant increase in the activity of the plant's superoxide dismutase and ascorbate peroxidase enzymes. This indicates that the plant is stressed. NaCl, K and Si applications significantly affected antioxidant enzyme activities in wheat plants (Table 11, 12, 13). In the study conducted by Karanlık (2001), it was explained that free oxygen radicals synthesized at increasing levels in the plant under stress damage the cells [56]. As in all living things under stress, antioxidant enzymes that convert free oxygen radicals into harmless compounds during stress in plants are resistant to damage. Enzymes such as SOD, CAT and APX are the most effective enzymes in destroying free oxygen radicals [41, 57-58]. Çakmak (1997) suggested that potassium deficiency may further increase the tissue damage that can be caused by free oxygen radicals synthesized due to salt stress [59]. Potassium applied in salt-stressed cereal crops improved antioxidant activity [60]. Al-Whaibi et al. (2012) reported that silicon applied in salt stress improved SOD, CAT and APX enzyme activities [61]. In another study, significant improvement in SOD and APX enzyme activities was seen with the application of silicon in salt stress [62-64]

5. CONCLUSION

The amount of saline soils in the world and in our country is increasing day by day. This increase reduces yields, and some areas are completely out of production due to excessive salinization. Only in our country, there is a salinity problem in approximately 2.5 million hectares of agricultural area and it is increasing. In this pot trial, the effect of single or combined applications of potassium and silicon under salt stress conditions on some antioxidative enzyme activity in the plant was investigated.

The first wall of strength of plants when exposed to stress is antioxidant enzymes. Antioxidants, which are a defense mechanism in the plant at the time of stress, help the plant to tolerate stress up to a certain limit. In the experiment, the addition of salt to the wheat plant generally reduced superoxide dysmutase activity, while ascorbate caused an increase in peroxidase activity. This increase is indicative of stress caused by salinity. When the dose of silicon was kept constant under saline conditions, administration of

K_1 (150 ppm K) significantly increased SOD activity (Table 11). This is an indication that potassium and silicon $NaCl_1K_1Si_0$ and $NaCl_1K_1Si_2$ applications increase SOD activity against salt stress. The administration of salt did not cause a significant change in CAT activity. In all applications with salinity, APX activity is increased. However, when Si_0 and Si_2 doses were kept constant, the increased potassium doses caused a significant reduction in increased APX activity due to salt stress.

As a result, salt applications caused the plant to stress. Although the KxSi interactions used to relieve this stress provided the plant with tolerance to salinity up to a certain point, they could not prevent the plant from stressing sufficiently. This may have been due to the high concentration of salt used in the experiment, or it may have been due to the fact that the wheat plant used was overly sensitive to salinity.

Author Contributions
All authors contributed to the conceptualization and design of the study. Material preparation, data collection and analysis were carried out by Orhan İNİK and Mehmet Ali BOZKURT. The first draft of the manuscript was written by Orhan İNİK, and the other author commented on previous versions of the manuscript. The other author finally read and approved the manuscript.

REFERENCES

[1] Shao, H. B., Chu, L. Y., Jaleel, C. A., & Zhao, C. X. (2008). Water-deficit stress-induced anatomical changes in higher plants. Comptes rendus biologies, 331(3), 215-225.

[2] Kalaji, M. H., & Pietkiewicz, S. (1993). Salinity effects on plant growth and other physiological processes.

[3] Akıncı, S. (1997). Physiological responses to water stress by Cucumis sativus L. and related species (Doctoral dissertation, University of Sheffield).

[4] Akinremi, O. O., Janzen, H. H., Lemke, R. L., & Larney, F. J. (2000). Response of canola, wheat and green beans to leonardite additions. Canadian Journal of Soil Science, 80(3), 437-443.

[5] Tunçtürk, M., Tunçtürk, R., Oral, E., & Baran, İ. (2020). Humik asitin baklada (Vicia faba L.) tuz (NaCl) stresinin azaltılması üzerine etkisi. Journal of the Institute of Science and Technology, 10(3), 2168-2179.

[6] Lichtenthaler, H. K. (1996). Vegetation stress: an introduction to the stress concept in plants. Journal of plant physiology, 148(1-2), 4-14.

[7] Larcher, W. (2003). Physiological plant ecology: ecophysiology and stress physiology of functional groups. Springer Science & Business Media.

[8] Blum, A., & Jordan, W. R. (1985). Breeding crop varieties for stress environments. Critical Reviews in Plant Sciences, 2(3), 199-238.

[9] Botella, M. A., Rosado, A., Bressan, R. A., & Hasegawa, P. M. (2005). Plant adaptive responses to salinity stress. Plant abiotic stress, 37-70.

[10] Munsuz, N., Çaycı, G., & Sözüdoğru Ok, S. (2001). Toprak Islahı ve Düzenleyiciler (Tuzlu ve Alkali Toprakların Islahı). Ankara Üniv. Ziraat Fak. Yayınları, (1518).

[11] Munns, R., & Tester, M. (2008). Mechanisms of salinity tolerance. Annu. Rev. Plant Biol., 59(1), 651-681.

[12] Çulha, Ş., & Çakırlar, H. (2011). Tuzluluğun bitkiler üzerine etkileri ve tuz tolerans mekanizmaları. Afyon Kocatepe Üniversitesi Fen ve Mühendislik Bilimleri Dergisi, 11(2), 11-34.

[13] Pessarakli, M., & Szabolcs, I. (2019). Soil salinity and sodicity as particular plant/crop stress factors. In Handbook of Plant and Crop Stress, Fourth Edition (pp. 3-21). CRC press.

[14] Doğru, A., & Canavar, S. (2020). Bitkilerde tuz toleransının fizyolojik ve biyokimyasal bileşenleri. Academic Platform-Journal of Engineering and Science, 8(1), 155-174.

[15] Parida, A. K., & Das, A. B. (2005). Salt tolerance and salinity effects on plants: a review. Ecotoxicology and environmental safety, 60(3), 324-349.

[16] Tuteja, N. (2007). Mechanisms of high salinity tolerance in plants. Methods in enzymology, 428, 419-438.

[17] Hu, Y., & Schmidhalter, U. (2005). Drought and salinity: a comparison of their effects on mineral nutrition of plants. Journal of plant nutrition and soil science, 168(4), 541-549.

[18] Türkhan, A., Kaya, E. D., Sarı, S., Tohumcu, F., & Özden, E. (2021). Farklı tuzluluk sınıfındaki topraklarda yetiştirilen domates tohumlarında bazı antioksidan enzim aktivitelerinin belirlenmesi. Journal of the Institute of Science and Technology, 11(özel sayı), 3406-3415.

[19] Hong, C. Y., Chao, Y. Y., Yang, M. Y., Cho, S. C., & Kao, C. H. (2009). Na+ but not Cl− or osmotic stress is involved in NaCl-induced expression of glutathione reductase in roots of rice seedlings. Journal of Plant Physiology, 166(15), 1598-1606.

[20] Cramer, G. R., & Nowak, R. S. (1992). Supplemental manganese improves the relative growth, net assimilation and photosynthetic rates of salt-stressed barley. Physiologia plantarum, 84(4), 600-605.

[21] Roberts, J. K., Linker, C. S., Benoit, A. G., Jardetzky, O., & Nieman, R. H. (1984). Salt stimulation of phosphate uptake in maize root tips

74

studied by 31P nuclear magnetic resonance. Plant Physiology, 75(4), 947-950.

[22] Litifi, A., Beek, J. G., & Van-de-Beek, J. G. (1992). Capsicum-Newsletter. Special Issue, 51-56, Eucarpia VIII th. In Meeting on Genetics and Breeding on Capsicum and Egg Plant, Rome, Italy (pp. 7-10).

[23] Ashraf, M., Zafar, Z. U., & Cheema, Z. A. (1994). Effect of low potassium regimes on some salt-and drought-tolerant lines of pearl millet. Phyton, 34(2), 219-227.

[24] Gong, H. J., Chen, K. M., Chen, G. C., Wang, S. M., & Zhang, C. L. (2003). Effects of silicon on growth of wheat under drought. Journal of plant nutrition, 26(5), 1055-1063.

[25] Romero-Aranda, M. R., Jurado, O., & Cuartero, J. (2006). Silicon alleviates the deleterious salt effect on tomato plant growth by improving plant water status. Journal of plant physiology, 163(8), 847-855.

[26] Anderson, D. L., Snyder, G. H., & Martin, F. G. (1991). Multi-year response of sugarcane to calcium silicate slag on Everglades Histosols. Agronomy Journal, 83(5), 870-874.

[27] Rafi, M. M., Epstein, E., & Falk, R. H. (1997). Silicon deprivation causes physical abnormalities in wheat (Triticum aestivum L). Journal of plant physiology, 151(4), 497-501.

[28] Liang, Y., Chen, Q. I. N., Liu, Q., Zhang, W., & Ding, R. (2003). Exogenous silicon (Si) increases antioxidant enzyme activity and reduces lipid peroxidation in roots of salt-stressed barley (Hordeum vulgareL.). Journal of plant physiology, 160(10), 1157-1164.

[29] Liang, Y., Zhu, J., Li, Z., Chu, G., Ding, Y., Zhang, J., & Sun, W. (2008). Role of silicon in enhancing resistance to freezing stress in two contrasting winter wheat cultivars. Environmental and Experimental Botany, 64(3), 286-294.

[30] Ashraf, M., Rahmatullah, Afzal, M., Ahmed, R., Mujeeb, F., Sarwar, A., & Ali, L. (2010). Alleviation of detrimental effects of NaCl by silicon nutrition in salt-sensitive and salt-tolerant genotypes of sugarcane (Saccharum officinarum L.). Plant and Soil, 326, 381-391.

[31] Ali, A., Tahir, M., Amin, M., Basra, S. M. A., Maqbool, M., & Lee, D. (2013). Si induced stress tolerance in wheat (Triticum aestivum L.) hydroponically grown under water deficit conditions. Bulgarian Journal of Agricultural Science, 19(5), 952-958.

[32] Gurmani, A. R., Bano, A., Najeeb, U., Zhang, J., Khan, S. U., & Flowers, T. J. (2013). Exogenously applied silicate and abscisic acid ameliorates the growth of salinity stressed wheat ('Triticum aestivum'L) seedlings through Na+ exclusion. Australian Journal of Crop Science, 7(8), 1123-1130.

[33] Kardoni, F. S. J. S. M., Mosavi, S. S., Parande, S., & Torbaghan, M. E. (2013). Effect of salinity stress and silicon application on yield and component yield of faba bean (Vicia faba).

[34] Rohanipoor, A., Norouzi, M., Moezzi, A., & Hassibi, P. (2013). Effect of silicon on some

physiological properties of maize (Zea mays) under salt stress. Journal of Biological and Environmental Sciences, 7(20).

[35] Jackson, M. (1958). Soil chemical analysis prentice Hall. Inc., Englewood Cliffs, NJ, 498(1958), 183-204.

[36] Hızalan, E., & Ünal, H. (1966). Topraklarda önemli kimyasal analizler. AÜ Ziraat Fakültesi Yayınları, 278, 5-7.

[37] Kacar, B. (1994). Bitki ve toprağın kimyasal analizleri. Ankara Üniversitesi Ziraat Fakültesi Eğitim, Araştırma ve Geliştirme Vakfı.

[38] Walkley, A. (1947). A critical examination of a rapid method for determining organic carbon in soils-effect of variations in digestion conditions and of inorganic soil constituents. Soil science, 63(4), 251-264.

[39] Olsen, S. R. (1954). Estimation of available phosphorus in soils by extraction with sodium bicarbonate (No. 939). US Department of Agriculture.

[40] Thomas, G., (1982). Exchangeable cations. In 'Methods of soil analysis. Part 2. Chemical and microbiological properties'.(Eds AL Page, RH Miller, DR Keeney) pp. 159–165. Soil Science Society of America, Inc.: Madison, WI, 1982.

[41] Cakmak, I., Strbac, D., & Marschner, H. (1993). Activities of hydrogen peroxide-scavenging enzymes in germinating wheat seeds. Journal of experimental botany, 44(1), 127-132.

[42] Giannopolitis, C. N., & Ries, S. K. (1977). Superoxide dismutases: I. Occurrence in higher plants. Plant physiology, 59(2), 309-314.

[43] Nakano, Y., & Asada, K. (1981). Hydrogen peroxide is scavenged by ascorbate-specific peroxidase in spinach chloroplasts. Plant and cell physiology, 22(5), 867-880.

[44] Düzgüneş, O., Kesici, T., Kavuncu, O., & Gürbüz, F. (1987). Araştırma ve deneme metotları. Ankara Üniversitesi Ziraat Fakültesi Yayınları, 1021, 1-381.

[45] Karakullukçu, E. (2008). Bazı nohut (Cicer arietinum L.) çeşitlerinin tuza toleranslarının belirlenmesi. Journal of Agricultural Sciences, 14(04).

[46] Yagmur, M., Kaydan, D., & Okut, N. (2006). Effects of potassium application on photosynthetic pigments, osmotic potential, kþ/naþ ratio and plant growth of barley under salinity. J. Agric. Sci, 12(2), 188-194.

[47] Zheng, Y., Jia, A., Ning, T., Xu, J., Li, Z., & Jiang, G. (2008). Potassium nitrate application alleviates sodium chloride stress in winter wheat cultivars differing in salt tolerance. Journal of plant physiology, 165(14), 1455-1465.

[48] Ali, A., Basra, S. M., Iqbal, J., Hussain, S., Subhani, M. N., Sarwar, M., & Haji, A. (2012). Silicon mediated biochemical changes in wheat under salinized and non-salinized solution cultures. African Journal of Biotechnology, 11(3), 606-615.

[49] Ahmad, B. (2014). Interactive effects of silicon and potassium nitrate in improving salt tolerance of wheat. Journal of Integrative Agriculture, 13(9), 1889-1899.

[50] Clarkson, D. T., & Hanson, J. B. (1980). The mineral nutrition of higher plants.

[51] Kuşvuran, Ş., Yaşar, F., Abak, K., & Ellialtıoğlu, Ş. (2008). Tuz stresi altında yetiştirilen tuza tolerant ve duyarlı Cucumis sp.'nin bazı genotiplerinde lipid peroksidasyonu, klorofil ve iyon miktarlarında meydana gelen değişimler. Yuzuncu Yıl University Journal of Agricultural Sciences, 18(1), 13-20.

[52] Erdal, İ., Türkmen, Ö., & Yıldız, M. (2000). Tuz stresi altında yetiştirilen hıyar (Cucumis sativus L.) fidelerinin gelişimi ve kimi besin maddeleri içeriğindeki değişimler üzerine potasyumlu gübrelemenin etkisi. Yuzuncu Yıl University Journal of Agricultural Sciences, 10(1), 25-29.

[53] Shavrukov, Y. (2013). Salt stress or salt shock: which genes are we studying?. Journal of Experimental Botany, 64(1), 119-127.

[54] Öner, F., Özkorkmaz, F., & Yilmaz, N. (2018). Tuz stresi altında gibberellik asit uygulamalarının yulafta bazı çimlenme parametreleri üzerine etkisi. International Journal of Agricultural and Natural Sciences, 1(1), 33-

[55] Tiryaki, İ. (2018). Bazı tarla bitkilerinin tuz stresine gösterdikleri adaptasyon mekanizmaları. Kahramanmaraş Sütçü İmam Üniversitesi Tarım ve Doğa Dergisi, 21(5), 800-808.

[56] Karanlik, S. (2001). Değişik buğday genotiplerinde tuz stresine dayanıklılık ve dayanıklılığın fizyolojik nedenlerinin araştırılması.

[57] Cakmak, I., & Marschner, H. (1992). Magnesium deficiency and high light intensity enhance activities of superoxide dismutase, ascorbate peroxidase, and glutathione reductase in bean leaves. Plant physiology, 98(4), 1222-1227.

[58] Gossett, D. R., Millhollon, E. P., & Lucas, M. C. (1994). Antioxidant response to NaCl stress in salt-tolerant and salt-sensitive cultivars of cotton. Crop science, 34(3), 706-714.

[59] Cakmak, I. (1997). Role of potassium in protecting higher plants against photo-oxidative damage. Food security in the WANA region, the essential need for balanced fertilization, International Potash Institute, Basel Switzerland, 345-352.

[60] Heidari, M., & Jamshidi, P. (2011). Effects of salinity and potassium application on antioxidant enzyme activities and physiological parameters in pearl millet. Agricultural Sciences in China, 10(2), 228-237.

[61] Al-Whaibi, M. H., Siddiqui, M. H., & Basalah, M. O. (2012). Salicylic acid and calcium-induced protection of wheat against salinity. Protoplasma, 249, 769-778.

[62] Zhu, Y. X., Gong, H. J., & Yin, J. L. (2019). Role of silicon in mediating salt tolerance in plants: a review. Plants, 8(6), 147.

[63] Zhu, Y., Guo, J., Feng, R., Jia, J., Han, W., & Gong, H. (2016). The regulatory role of silicon on carbohydrate metabolism in Cucumis sativus L. under salt stress. Plant and Soil, 406, 231-249.

[64] Zhu, Z., Wei, G., Li, J., Qian, Q., & Yu, J. (2004). Silicon alleviates salt stress and increases antioxidant enzymes activity in leaves of salt-stressed cucumber (Cucumis sativus L.). Plant Science, 167(3), 527-533.

Türk Doğa ve Fen Dergisi
Turkish Journal of Nature and Science
www.dergipark.gov.tr/tdfd

A Study on OSH Performance Measurement by PROMETHEE Method in Coal-Fired Thermal Power Plants

Nagihan ERSOY[1]*

[1]Manisa Celal Bayar University, Soma Meslek Yüksekokulu, Occupational Health and Safety Department, Manisa, Türkiye
Nagihan Ersoy ORCID No: 0000-0002-9807-9786

*Corresponding author: nagihanersoy89@gmail.com

Abstract: Occupational accidents in the world and in our country affect the energy sector as a serious problem. It has become important to take the necessary precautions for the uninterrupted continuation of energy. The effective prevention of occupational accidents and diseases by coal-fired power plants depends on their evaluation of OHS performance and continuing their improvement efforts. In the implementation phase of the OHS performance model in coal-fired thermal power plants, a total of 170 OHS performance measurement criteria, including 8 main criteria and 162 sub-criteria, were determined and 162 sub-criteria were evaluated with the PROMETHEE method. As a first step, the sub-criteria of the three riskiest sections in terms of OHS in coal-fired thermal power plants, which were previously selected with AHP, were evaluated by 10 occupational safety experts in the range of 0-100 for each coal-fired power plant alternative. Performance factor results were obtained by using the "Visual PROMETHEE" package program to obtain PROMETHEE results with criterion weights. The data obtained from alternative power plants were evaluated and prioritized with the PROMETHEE method based on the weights determined with the help of AHP according to the OHS performance measurement model we proposed, and coal-fired power plants were ranked. This study; An objective OHS performance measurement method based on measurable indicators, reflecting OHS performance in the most accurate way, practical to use, has been developed and applied in coal-fired thermal power plants.

Kömürlü Termik Santrallerde PROMETHEE Yöntemi ile İSG Performans Ölçümü Üzerine Bir Çalışma

Öz: Dünyada ve ülkemizde iş kazaları ciddi bir sorun olarak enerji sektörünü etkilemektedir. Enerjinin kesintisiz devam etmesi için gerekli önlemlerin alınması önem kazanmıştır. Kömürlü termik santrallerin iş kazası ve meslek hastalıklarını etkili bir şekilde önlemesi, İSG performanslarını değerlendirmeleri ve iyileştirme çalışmalarını sürdürmelerine bağlıdır. Kömürlü termik santrallerde İSG performans modelin uygulama aşamasında, temelde 8 ana kriter ve 162 alt kriter olmak üzere toplamda 170 İSG performans ölçüm kriteri belirlenmiş ve PROMETHEE yöntemi ile 162 alt kriter değerlendirilmiştir. İlk iş olarak, kömürlü termik santrallerde İSG açısından daha önceden AHP ile seçilmiş olan en riskli üç bölümün alt kriterleri her kömürlü termik santral alternatifi için 0-100 aralığında 10 iş güvenliği uzmanı tarafından değerlendirilmiştir. Kriter ağırlıkları ile PROMETHEE sonuçlarını elde etmek için "Visual PROMETHEE" paket programı kullanılarak performans faktör sonuçlarına ulaşılmıştır. Alternatif santrallerden alınan veriler önerdiğimiz İSG performans ölçüm modeline göre AHP yardımıyla belirlenmiş ağırlıklara dayanarak PROMETHEE yöntemiyle değerlendirilip ve önceliklendirilmiş ve kömürlü termik santraller sıralanmıştır. Bu çalışma; ölçülebilir göstergelere dayalı, objektif, İSG performansını en doğru şekilde yansıtan, kullanımı pratik bir İSG performans ölçümü yöntemi geliştirilmiş ve kömürlü termik santrallerde uygulaması yapılmıştır.

1. INTRODUCTION

It is seen that the primary growth sector to meet the future electricity demand will be coal-fired power plants. Even if the use of renewable energy sources in energy production is increased, it is imperative to have coal-fired power plants to ensure continuity and reliability. It is necessary to analyze the situation of existing coal-fired power plants, to reveal the deficiencies in the field of OHS and to develop solutions that can be applied.

Today's intense competition environment requires businesses to manage their business processes more effectively. The golden rule for managing processes is to determine performance criteria and manage performance effectively. At this point, first performance needs to be defined and the method of performance measurement needs to be determined. Since performance measurement is directly related to the company's outputs, it is important both in terms of comparing the company's performance with previous periods and making comparisons with its competitors [1].

For the development of the system, it is important to measure and analyze it. It is necessary to analyze the current situation of the businesses and observe where the changes made take the businesses. Measuring the impact of improvement studies in the field of OHS on OHS performance is an important problem. The OHS performances of coal-fired power plants were generally based on a limited number of information, such as the number of occupational accidents that occurred in previous years, and the observations made by an expert in a limited time at the plant. The information obtained using a limited number of indicators does not reflect actual performance. There is no sector-specific objective, commonly-accepted, simple measurement system that measures the OHS performance of multiple coal-fired power plants. Many criteria are evaluated when examining the occupational health and safety performance of coal-fired thermal power plants. These criteria are effective risk factors that can help to measure the occupational health and safety performance of thermal power plants in all parts of thermal power plants. All of the performance indicators that are used to measure the OHS performance of coal-fired thermal power plants are values that can be measured numerically and practically. In our study, the data to be obtained from thermal power plants are sufficient to measure the performance scores based on these developments. The occupational health and safety performances of the power plants were measured practically, quickly and objectively using the PROMETHEE method with the numerical data obtained from the occupational safety experts working in X, Y and Z thermal power plants [2].

In the Analytical Hierarchy Process (AHP) method was developed by Thomas L. Saaty and alternatives are listed and then compared pairwise according to their contribution to reaching each objective or criterion. This method (AHP) an important indicator which is the number of criteria and it affects result consistency because more than seven criteria lead to an increase in inconsistency.In application of this AHP method to calculate weight it is important to use experts to evaluate criteria because this affects the alternative's values in the future when MCDA methods are using criteria weight. When weights are calculated using the AHP method, these values can be used in every MCDA method. Also, after the AHP method, results can make conclusions about the indicated values and which indicator can solve the problem [3].

A distinctive feature of the Promethee method compared to other methods is that different function types can be selected while comparing alternatives for different evaluation criteria. Although this method is a simple sorting method that can be easily applied, it is the disadvantage of being subjective [4].

PROMETHEE is the most attractive outranking method because of its mathematical simplicity and transparency.PROMETHEE where a large number of alternatives arise reaches its computational limits quickly [5].

The PROMETHEE method has two main stages, which are PROMETHEE I and PROMETHEE II. The main difference that distinguishes the PROMETHEE method is that it takes into account the importance weights of each evaluation criterion and can apply different function types for each evaluation criterion [6].

The PROMETHEE and PROMETHEE II methods found applications in disciplines such as urban planning and architecture, land management, logistics, healthcare, banking, energy and quality analysis in general.

In their paper, Zorkirişçi and Rençber measured the financial performances of 20 public, private or foreign capital banks operating in Turkey using BWM-based TOPSIS, PROMETHEE and COPRAS methods and interpreted the findings comparatively. However, they concluded that the PROMETHEE method is more applicable in terms of ease of application and useful information it provides[7]. In their paper, Bağcı and Esmer the ranking of 8 public factoring companies was conducted by using Promethee Method which are registered in the Public Disclosure Platform [8].

In their paper, Atıcı and Ulucan in the first application, various hydroelectric plant projects are ranked using ELECTRE method. The second application ranks multiple wind plant projects using PROMETHEE technique [9].

In their paper, Vivas et al., who compared reports on sustainable development. Using the PROMETHEE method [10].

In the implementation phase of the proposed model, a total of 170 OHS performance measurement criteria,

78

including 8 main criteria and 162 sub-criteria, were determined and 162 sub-criteria were evaluated with the PROMETHEE method. As a first step, the sub-criteria of the three riskiest sections in terms of OHS in coal-fired thermal power plants, which were previously selected with AHP, were evaluated by 10 occupational safety experts in the range of 0-100 for each coal-fired power plant alternative. The points given for the determined criteria were entered into the program. In the next step, normalization was applied to the importance weights obtained by the AHP method. After normalizing the importance weights, the program was introduced. In the normalization process, first of all, the lowest criteria of each branch in each main criterion were determined and the totals of all these criteria were taken.

In the second step, each lowest criterion was divided into this sum and normalized weights were obtained. In the last step, each of the obtained criterion weights was multiplied by its main criterion weight and the weights entered into the program were obtained. Afterwards, the preference function was selected according to the criteria. The V type function was chosen as the preference function. The reason for this is; This type of function is suitable for quantitative data and the criteria are especially intended to be used with values above a certain average, while even small deviations below this value are taken into account.

A high positive advantage indicates that one alternative option is a better choice or performs better than others. If the negative superiority value is high; indicates that that option is a worse choice than the others, or that its performance is poorer.

The PROMETHEE method differs from other multi-criteria decision-making methods in that it gives a ranking among the alternatives and calculates according to the ideal solution [11,12,13].

The method evaluates coal-fired power plants, which are the basis of the decision-making problem, based on the determined criterion weights and prioritizes the alternatives partially and fully with pairwise comparisons. A screenshot of the program is shown in Figure 1.

PK9	PK10	PF1	PF2	PF3	PF4	PF5	PF6	PS1	PS2	PS3	PS4	PS5	PS6
☑	☑	☑	☑	☑	☑	☑	☑	☑	☑	☑	☑	☑	☑
unit	unit	unit	unit	unit	unit	unit	unit	unit	unit	unit	unit	unit	unit
◆	◆	◆	◆	◆	◆	◆	◆	◆	◆	◆	◆	◆	◆
max	max	max	max	max	max	max	max	max	max	max	max	max	max
0,10	0,09	0,16	0,13	0,17	0,11	0,19	0,24	0,21	0,13	0,25	0,13	0,13	0,06
V-shape	V-shape	V-shape	V-shape	V-shape	V-shape	V-shape	V-shape	V-shape	V-shape	V-shape	V-shape	V-shape	V-shape
absolute	absolute	absolute	absolute	absolute	absolute	absolute	absolute	absolute	absolute	absolute	absolute	absolute	absolute
n/a	n/a	n/a	n/a	n/a	n/a	n/a	n/a	n/a	n/a	n/a	n/a	n/a	n/a
2,00	2,00	2,00	2,00	2,00	2,00	2,00	2,00	2,00	2,00	2,00	2,00	2,00	2,00
n/a	n/a	n/a	n/a	n/a	n/a	n/a	n/a	n/a	n/a	n/a	n/a	n/a	n/a
70,00	100,00	60,00	40,00	50,00	10,00	0,00	50,00	20,00	20,00	100,00	20,00	80,00	20,00
100,00	100,00	90,00	100,00	90,00	100,00	70,00	100,00	90,00	100,00	100,00	100,00	100,00	100,00
83,33	100,00	80,00	76,67	76,67	50,00	30,00	73,33	50,00	63,33	100,00	50,00	93,33	66,67
12,47	0,00	14,14	26,25	18,86	37,42	29,44	20,55	29,44	33,00	0,00	35,59	9,43	33,99
100,00	100,00	90,00	100,00	90,00	100,00	0,00	100,00	90,00	100,00	100,00	100,00	100,00	100,00
80,00	100,00	60,00	40,00	50,00	10,00	20,00	50,00	20,00	70,00	100,00	20,00	80,00	80,00
70,00	100,00	90,00	90,00	90,00	40,00	70,00	70,00	40,00	20,00	100,00	30,00	100,00	20,00

Figure 1: The "Visual PROMETHEE" startup solution screen

Performance factor results were obtained by using the "Visual PROMETHEE" package program to obtain PROMETHEE results with criterion weights. With this software, PROMETHEE I and alternatives were compared on the basis of determined criteria, partial priorities were obtained, and then interpreted with graphics.

As a result of the comparison of PROMETHEE II and alternatives on the basis of the determined criteria, clear priorities are shown in the tables. Performance score results are explained below; The data obtained from alternative power plants were evaluated and prioritized with the PROMETHEE method based on the weights determined with the help of AHP according to the OHS performance measurement model we proposed, and coal-fired power plants were ranked.

Initial matrices are given and results are shown in the program used for PROMETHEE calculation separately for the coal parking area, ash slag disposal plant and boiler maintenance service. Values for the ideal solution are indicated. The same processes were evaluated with the PROMETHEE method for a total of 162 sub-criteria by entering the data obtained from all power plants at once.

2. MATERIAL AND METHOD

2.1. Determination of OHS Performance Rankings of Coal-Fired Thermal Power Plants by PROMETHEE Method

2.1.1. Evaluation of coal parking yard OHS performance results by PROMETHEE method

63 units of 1,000 performance criteria were evaluated for the coal parking site. The results obtained are described in Figure 2 and Figure 3.
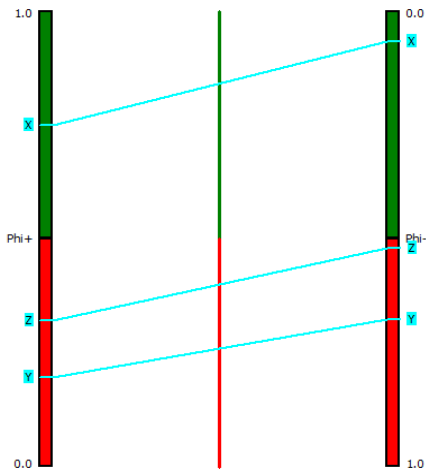
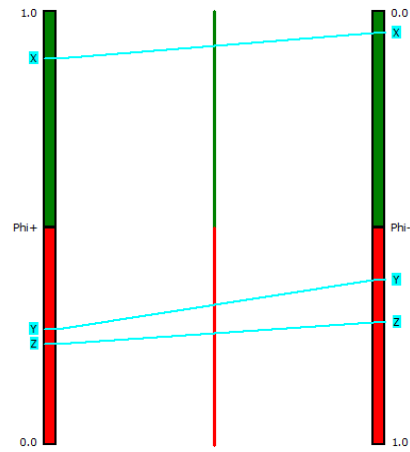**Figure 2:** PROMETHEE I partial ranking of coal parking sites

Figure 4: Partial sequencing of ash slag disposal plants with PROMETHEE I
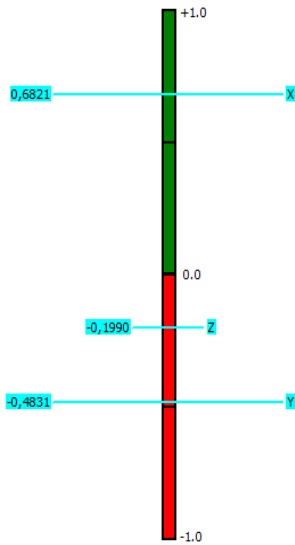

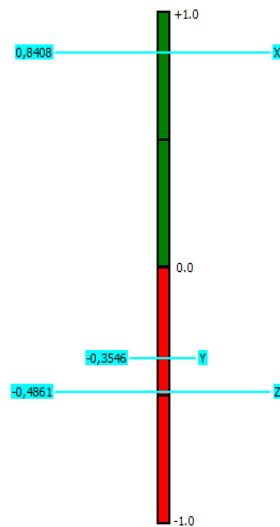**Figure 3:** Full sequencing of coal parking sites with PROMETHEE II

Figure 5: Full sequencing of ash slag disposal plants with PROMETHEE II

According to PROMETHEE I; As a result of the calculations, as can be seen in Figure 2, X coal-fired power plant was the best alternative in terms of partial ranking of the coal parking area section. It is followed by the Z and Y coal-fired power plants. For clear benchmarking, PROMETHEE 2 analysis is required. As a result of the calculations made according to Promethee II, the full ranking result is given in Figure 3.

2.1.2. Evaluation of OHS performance results of ash slag disposal plant by PROMETHEE method

39 OHS performance criteria of the ash slag disposal plant were evaluated. The results obtained are described in Figure 4 and Figure 5.

According to PROMETHEE I; As a result of the calculations, as can be seen in Figure 4, the X coal-fired thermal power plant was the best alternative in terms of partial ranking of the ash slag disposal plant section. It is followed by the Y and Z coal-fired thermal power plants. For net benchmarking, PROMETHEE II analysis is required. As a result of the calculations made according to Promethee II, the full ranking result is given in Figure 5.

2.1.3. Evaluation of OHS performance results of boiler maintenance service with PROMETHEE method

Boiler maintenance service 60 OHS performance criteria were evaluated. The results obtained are described in Figure 6 and Figure 7.
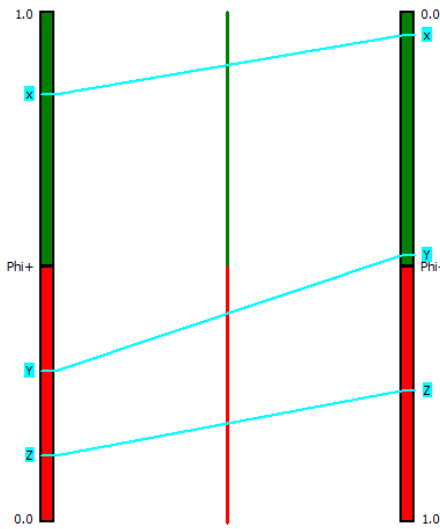
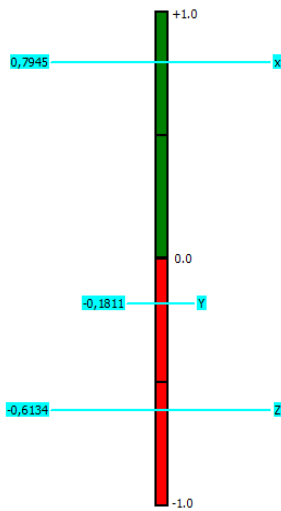**Figure 6.** Partial ranking of boiler maintenance services with Promethee

Figure 7. Full ranking of boiler maintenance services with Promethee II

2.1.4. Evaluation of OHS performance results of coal-fired power plants handled by PROMETHEE method

A total of 162 performance criteria were evaluated for all coal-fired power plants. The results obtained were evaluated according to PROMETHEE I and II with the Visual PROMETHEE program, and the results obtained are explained in Figure 8 and Figure 9.

As a result of the calculations made with the data obtained from coal-fired thermal power plants, X coal-fired thermal power plant was the best alternative in terms of partial ranking of OHS performance in Figure 8. Then it became the Y and Z coal-fired power plants. For net benchmarking, PROMETHEE II analysis is required. As

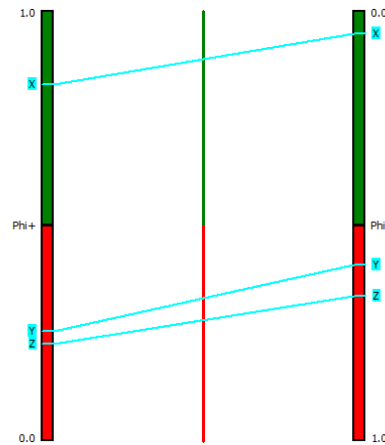a result of the calculations made according to Promethee II, the full ranking result is given in Figure 9.

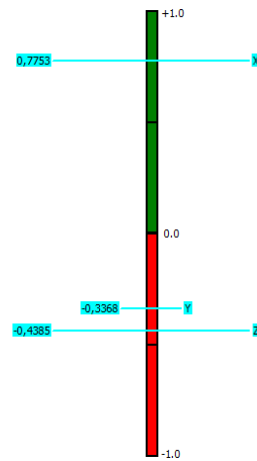**Figure 8.** Partial ranking of coal-fired power plants with Promethee I

Figure 9. Full ranking of coal-fired power plants with Promethee II

3. RESULTS

In this study, an OHS performance model based on measurable indicators with multi-criteria decision-making methods, objective, fast, practical reflecting the occupational health and safety performance in coal-fired power plants in the most accurate way was developed and the OHS performance of 3 coal-fired thermal power plants was measured. Since the current situation is analyzed practically and quickly before accidents occur with the multi-criteria decision-making methods we have made for coal-fired thermal power plants and the OHS performance measurement model, it makes it possible to prevent occupational accidents by proactively taking preventive and corrective measures.

With the latest ranking observed in Table 1, OHS performance results can be seen more clearly.

Table 1. Coal parking area PROMETHEE II ideal solution values

Sıra	Kömürlü termik santraller	Phi	Phi+	Phi-
1	X	0.6821	0.7491	0.0670
2	Z	-0.1990	0.3204	0.5194
3	Y	-0.4831	0.1946	0.6777

According to PROMETHEE I; As a result of the calculations, as can be seen in Figure 6, the X coal-fired power plant was the best alternative in terms of partial ranking of the boiler maintenance service section. It is followed by the Y and Z coal-fired thermal power plants. For net benchmarking, PROMETHEE II analysis is required. As a result of the calculations made according to Promethee II, the full ranking result is given in Figure 7.

According to the net ranking made in Table 1, it is the X coal-fired thermal power plant with the best OHS performance. Then, this ranking; Z coal-fired power plant was followed by Y coal-fired power plant.

With the latest ranking observed in Table 2, OHS performance results can be seen more clearly.

Table 2. PROMETHEE II ideal solution values of Ash slag disposal plant

Sıra	Kömürlü termik santraller	Phi	Phi+	Phi-
1	X	0.8281	0.8776	0.0495
2	Y	-0.3673	0.2539	0.6212
3	Z	-0.4608	0.2310	0.6918

According to the net ranking made in Table 2, it is the X coal-fired power plant with the best performance. According to our ranking study; Y coal-fired power plant was followed by Z coal-fired power plant.

With the latest ranking observed in Table 3, OHS performance results can be seen more clearly.

Table 3. Boiler maintenance service PROMETHEE II ideal solution values

Sıra	Kömürlü termik santraller	Phi	Phi+	Phi-
1	X	0.7945	0.8396	0.0451
2	Y	-0.1811	0.2964	0.4774
3	Z	-0.6134	0.1303	0.7437

According to the net ranking made in Table 3, it is the X coal-fired power plant with the best performance. Then, this ranking; Y coal-fired power plant was followed by Z coal-fired power plant.

By subtracting negative advantages from positive advantages, full sequencing was obtained with PROMETHEE II. With the latest ranking observed in Table 4, OHS performance results can be seen more clearly.

Table 4: PROMETHEE II ranking values of coal-fired thermal power plants

Sıra	Kömürlü termik santraller	Phi	Phi+	Phi-
1	X	0.7753	0.8286	0.0533
2	Y	-0.3368	0.2549	0.5917
3	Z	-0.4385	0.2253	0.6638

4. DISCUSSION AND CONCLUSION

According to the net ranking with Promethee II, it is the X coal-fired power plant with the best performance. Then, this ranking; Y coal-fired power plant was followed by Z coal-fired power plant.

This study provides superiority over other studies in terms of the fact that all of the performance indicators are quantitative, measurable, fast for performance measurement and require low expertise. This study is important in terms of giving an idea to researchers about measuring OHS performance, paving the way and applying it in the energy sector.

REFERENCES

[1] Bağcı, H., & Yüksel Yiğiter, Ş. (2019). BİST'te yer alan enerji şirketlerinin finansal performansının SD ve WASPAS yöntemleriyle ölçülmesi.

[2] Ersoy N. A study on occupational health and safety performance model in thermal power plants. Ph.D. Thesis, Üsküdar University, Istanbul, 2023.

[3] Zlaugotne, B., Zihare, L., Balode, L., Kalnbalkite, A., Khabdullin, A., & Blumberga, D. (2020). Multi-criteria decision analysis methods comparison. *Rigas Tehniskas Universitates Zinatniskie Raksti*, *24*(1), 454-471.

[4] Yılmaz, B., Dağdeviren, M. Comparative Analysis of PROMETHEE and Fuzzy PROMETHEE Methods in the Equipment Selection Problem, Gazi University Journal of Engineering and Architecture Faculty. 2010; 25(4), 811-826.

[5] Sotiropoulou, K. F., & Vavatsikos, A. P. (2021). Onshore wind farms GIS-Assisted suitability analysis using PROMETHEE II. *Energy Policy*, *158*, 112531.

[6] Şenkayas, H., Hekimoğlu, H. Application of PROMETHEE Method to the Multi-Criteria Supplier Selection Problem. Journal of Productivity. 2013; (2), 63-80.

[7] Zorkirişçi, E. D., & Rençber, Ö. F. BWM Tabanlı TOPSIS, PROMETHEE ve COPRAS Yöntemlerinin Karşılaştırılması: Bankaların Finansal Performansları Üzerine Bir Uygulama. *Süleyman Demirel Üniversitesi Vizyoner Dergisi*, *14*(39), 1030-1045.

[8] Bağcı, H., & Esmer, Y. (2016). PROMETHEE yöntemi ile faktoring şirketi seçimi. Beykent Üniversitesi Sosyal Bilimler Dergisi, 9(2).

[9] Atıcı, K. B., & Ulucan, A. (2009). Enerji Projelerinin Değerlendirilmesi Sürecinde Çok Kriterli Karar Verme Yaklaşımları ve Türkiye Uygulamaları. *Hacettepe Üniversitesi İktisadi ve İdari Bilimler Fakültesi Dergisi*, *27*(1), 161-186.

[10] Vivas, R.; Sant'anna, Â.; Esquerre, K.; Freires, F. Çok kriterli model ile sürdürülebilirlik performansının ölçülmesi: Bir vaka çalışması. *Sürdürülebilirlik* 2019, *11*, 1–13.

[11] Brans, J.P., Vincke, P. A Preference Ranking Organization Method: The PROMETHEE Method for MCDM. Management Science, 1985; 31(6), 647-656.

[12] Brans, J.P., Vıncke, P., Mareschal, B. How to Select and How to Rank Projects: The PROMETHEE Method. European Journal of Operational Research, 1986;24, 228-238.

[13] Dağdeviren, M., Eraslan, E. Supplier Selection with PROMETHEE Ranking Method. Gazi University Journal of Engineering and Architecture, 2008; 23(1), 69-75.

Diagnostic Process of Periprosthetic Joint Infection in Painful Arthroplasty Patients Referred to a Tertiary Care Center: Orthopedics and Pathology Perspective

Berna ERITEN [1] ID **, Serdar MENEKŞE** [2*] ID

[1] Şehit Prof. Dr. İlhan Varank Education and Research Hospital, Pathology Department, İstanbul, Türkiye
[2] Adana Seyhan State Hospital, Orthopedics and Traumatology Department, Adana, Türkiye
Berna ERITEN ORCID ID: 0000-0003-3710-1502
Serdar MENEKŞE ORCID ID: 0000-0002-4121-8917

Corresponding author: dr.serdarmenekse@gmail.com

Abstract: Joint arthroplasty failure due to periprosthetic infection remains one of the most challenging complications in orthopedic surgery, with complex diagnostic requirements and the need for expert evaluation. This study was aimed at determining the method of diagnosis of periprosthetic infection in the patients with painful joint arthroplasty referred to a tertiary center. Between January 2021 and January 2024, 85 patients referred for painful hip and knee arthroplasty were retrospectively evaluated. The median age of the patients was 67 years and 58.8% underwent total knee arthroplasty. Pathologically, 52.9% of the cases were reported as non-infectious, 29.4% as infectious and 17.7% as indeterminate. The presence of infectious pathology was strongly associated with the diagnosis of PEE (OR: 4.92, p=0.001), while the presence of non-infectious pathology was negatively associated (OR: 0.31, p=0.026). Neutrophil infiltration and bacterial colonization were independent markers for the diagnosis of infection. Fibrohistiocytic reaction was the dominant finding in cases of aseptic loosening. After controlling for demographic factors, the diagnostic contribution of pathologic evaluation was statistically significant. The results of this study demonstrate that detailed pathological examination is essential for accurate diagnosis, while emphasizing that successful management of painful arthroplasty cases requires coordination between orthopedics and pathology departments. Our findings underscore the need for pathological assessment and highlight the importance of a team approach with different specializations in managing arthroplasty who complain of pain.

83

Üçüncü Basamak Merkeze Sevk Edilen Ağrılı Artroplasti Hastalarında Periprostetik Eklem Enfeksiyonu Tanı Süreci: Ortopedi ve Patoloji Perspektifi

Öz: Periprostetik eklem enfeksiyonuna bağlı artroplasti başarısızlığı, karmaşık tanı gereklilikleri ve uzman değerlendirme ihtiyacı ile ortopedik cerrahinin en zorlu komplikasyonlarından biri olmaya devam etmektedir. Bu çalışmanın amacı, üçüncü basamak merkeze sevk edilen ağrılı artroplasti hastalarında periprostetik eklem enfeksiyonu (PEE) tanı sürecini incelemektir. Ocak 2021-Ocak 2024 tarihleri arasında ağrılı kalça ve diz artroplastisi nedeniyle sevk edilen 85 hasta retrospektif olarak değerlendirildi. Hastaların yaş ortancası 67 yıl olup %58.8'ine total diz artroplastisi uygulanmıştı. Patolojik değerlendirmede olguların %52.9'u non-enfeksiyöz, %29.4'ü enfeksiyöz ve %17.7'si belirsiz olarak raporlandı. Enfeksiyöz patoloji varlığı PEE tanısıyla güçlü ilişki gösterirken (OR:4.92, p=0.001), non-enfeksiyöz patoloji varlığı negatif ilişki gösterdi (OR:0.31, p=0.026). Nötrofil infiltrasyonu ve bakteriyel kolonizasyon, enfeksiyon tanısında bağımsız belirteçler olarak saptandı. Aseptik gevşeme olgularında fibrohistiyositik reaksiyon baskın bulgu olarak öne çıktı. Demografik faktörler kontrol edildikten sonra, patolojik değerlendirmenin tanısal katkısı istatistiksel olarak anlamlı bulundu. Bu çalışmanın sonuçları, doğru tanı için detaylı patolojik incelemenin gerekli olduğunu göstermekte ve ağrılı artroplasti olgularının başarılı yönetiminin ortopedi ve patoloji bölümleri arasındaki koordinasyona bağlı olduğunu vurgulamaktadır. Sonuçlarımız, ağrılı artroplasti hastalarında patolojik incelemenin tanısal değerini ve multidisipliner yaklaşımın önemini vurgulamaktadır.

1. INTRODUCTION

Diagnosis of periprosthetic joint infection (PEE) in painful arthroplasty patients is a complex process requiring a multidisciplinary approach. Especially in patients referred to tertiary care centers, the importance of standardized diagnostic protocols increases [1]. The systematic approach to PEE diagnosis has been well-established through clinical practice guidelines developed by the American Academy of Orthopaedic Surgeons (AAOS) [2].

Various factors play a role in the etiology of painful prosthetic joints. Aseptic loosening, implant wear, infection, mechanical problems, and soft tissue imbalance are prominent among these, as reported by several investigators [3, 4]. Pathologic examination plays a critical role in the differential diagnosis of these pathologies, especially in the differentiation of infectious and non-infectious causes, as demonstrated by Smith et al. [3] and Johnson et al. [5].

Various diagnostic tests such as serum inflammatory markers, joint aspiration, and synovial fluid analysis are used in the diagnostic process. The use of these tests in accordance with AAOS guidelines and the active participation of the pathology department in the process provide high diagnostic accuracy, especially in the differentiation of infectious and non-infectious pathologies [6, 7, 8].

In this study, two main points were investigated in patients with painful or failed hip and knee arthroplasty referred to a tertiary care center: referring physicians' adherence to AAOS guidelines and the diagnostic contribution of pathological examination. The hypothesis of the study is that referring physicians' adherence to guidelines is inadequate and that pathology-orthopedics collaboration may improve diagnostic accuracy. With this approach, the importance of multidisciplinary evaluation in the PEE diagnostic process is emphasized.

2. MATERIAL AND METHOD

This is a retrospective study conducted between January 1, 2021 and January 1, 2024. Patients over the age of 18 who were referred from our hospital to a tertiary care center due to painful or failed hip and knee arthroplasty were included in the study. In order to ensure standardization, patients referred from other centers and referred by non-orthopedists were excluded [9, 10].

2.1 Data Collection and Analysis

In a systematic approach, demographic data of the patients, specialty status of the referring physicians and diagnostic test protocols (ESR, CRP, joint aspiration, synovial fluid analysis) were examined in detail. Histopathological examination results and tertiary care center feedback were analyzed comparatively to assess the contribution of the pathology department. Compliance with AAOS guidelines was assessed through the use of recommended diagnostic tests and the order in which they were performed [11].

2.2 Patient Classification

The study population was divided into two main groups: with and without PEE based on tertiary center feedback. To evaluate the effect of the multidisciplinary approach, subgroup analyses were performed in terms of referring physicians' specialty levels and arthroplasty types (hip/knee) [12, 13, 14]. This classification system was based on similar studies in the literature [15].

2.3 Statistical Analysis:

Statistical analyses were performed using SPSS software (version 26.0, IBM Corp., Armonk, NY, USA). The data were analyzed in three stages. First, descriptive statistics were calculated, including median and distribution values for continuous variables and frequency and percentages for categorical variables. The Kolmogorov-Smirnov test was used to assess the normality of continuous variables. For variables with normal distribution, parametric tests were applied, while non-parametric tests were used for non-normally distributed variables. Statistical significance was set at $p < 0.05$.

Second, AAOS guideline compliance analysis was conducted with 95% confidence intervals. For subgroup comparisons, Chi-square test was used when expected frequencies were sufficient (>5 in all cells), and Fisher's exact test was applied when expected frequencies were low. The diagnostic value of pathologic examination was evaluated using McNemar's test.

Finally, risk factors for PEE were determined through logistic regression analysis. For numerical variables showing normal distribution, independent samples t-test was used, while Mann-Whitney U test was applied for non-normally distributed variables. Multiple logistic regression was performed to identify independent predictors, with variables showing $p < 0.20$ in univariate analyses included in the model.

2.3 Ethics:

This study was approved by the Scientific Research Ethics Committee of Adana City Training and Research Hospital (Meeting number: 7, Date: 07.11.2024, Decision number: 233).

3. RESULTS

The median age of the 85 patients included in the study was 67 (58-76) years and the median duration of arthroplasty was 48 (24-96) months. Total knee arthroplasty was performed in 58.8% (n=50) and total hip arthroplasty in 41.2% (n=35) of the patients. The side distribution was almost equal (49.4% left, 50.6% right). Pathologically, 52.9% of cases were reported as non-infectious, 29.4% as infectious and 17.7% as indeterminate. Periprosthetic joint infection (29.4%) and mechanical problems (23.5%) were the most common causes of failure in tertiary care center feedback (Table 1).

Table 1. Demographic and Clinical Characteristics of Study Sample

Variable	n (%)
Total N	85 (100.0%)
Demographic Information	
Median Duration of Arthroplasty (IQR)	48 months (24-96 months)
Median Age (IQR)	67 years (58-76 years)
Operation Types	
Total Hip Arthroplasty (THA)	35 (41.2%)
Total Knee Arthroplasty (TKA)	50 (58.8%)
Side	
Left	42 (49.4%)
Right	43 (50.6%)
Pathology Findings	
Non-infectious	45 (52.9%)
Infectious	25 (29.4%)
Indeterminate	15 (17.7%)
Failure Modes	
Hardware/Mechanical Failure	20 (23.5%)
Periprosthetic Joint Infection	25 (29.4%)
Instability	15 (17.6%)
Aseptic Loosening	18 (21.2%)
Other	7 (8.3%)

When the relationship between pathology types and failure modes was analyzed, the presence of infectious pathology showed a strong association with the diagnosis of periprosthetic joint infection (OR: 4.92, 95% CI: 1.86-13.02, p=0.001). The presence of non-infectious pathology was negatively associated with the diagnosis of infection (OR: 0.31, 95% CI: 0.11-0.87, p=0.026). Although a positive trend was observed for the presence of non-infectious pathology in aseptic loosening (OR: 1.86, 95% CI: 0.65-5.32, p=0.247), there was no statistically significant association between other failure modes and pathology types (Table 2).

Table 2. Odds Ratios for Failure Modes According to Pathology Types

Failure Mode	Pathology Type	Odds Ratio (95% CI)	p-value
Hardware/Mechanical Failure			
	Non-infectious pathology	1.32 (0.45-3.85)	0.614
	Infectious pathology	0.42 (0.12-1.46)	0.172
	Indeterminate pathology	0.85 (0.25-2.89)	0.795
Periprosthetic Joint Infection			
	Non-infectious pathology	0.31 (0.11-0.87)	0.026*
	Infectious pathology	4.92 (1.86-13.02)	0.001*
	Indeterminate pathology	0.62 (0.18-2.14)	0.448
Instability			
	Non-infectious pathology	1.24 (0.41-3.74)	0.702
	Infectious pathology	0.45 (0.11-1.84)	0.266
	Indeterminate pathology	1.15 (0.31-4.26)	0.836
Aseptic Loosening			
	Non-infectious pathology	1.86 (0.65-5.32)	0.247
	Infectious pathology	0.38 (0.10-1.44)	0.155
	Indeterminate pathology	0.92 (0.25-3.38)	0.898

Note: Statistical significance was set at $p \leq 0.05$. Significant associations are marked with an asterisk.

When specific pathologic findings were analyzed, neutrophil infiltration (B=0.885, p=0.004) and presence of granulation tissue (B=0.428, p=0.002) showed a strong association with periprosthetic joint infection. Fibrosis (B=0.352, p=0.038) and histiocytic infiltration (B=0.495, p=0.031) were the dominant findings in cases of mechanical failure. Foreign body reaction (B=0.245, p=0.026) was observed as a significant finding in cases of aseptic loosening. All these findings were evaluated as independent predictors in multiple regression analysis (Table 3).

Table 3. Multiple Regression Analysis for Independent Pathological Findings and Failure Modes

Failure Mode and Findings	Unstandardized Coefficient (B)	Standard Error (SE)	Standardized (β)	Coefficient	p-value	R²
Hardware/Mechanical Failure						0.324
Fibrosis	0.352	0.165	0.243		0.038	
Histiocytic infiltration	0.495	0.218	0.232		0.031	
Tissue necrosis	-0.228	0.092	-0.238		0.021	
Periprosthetic Joint Infection						0.412
Neutrophilic infiltration	0.885	0.298	0.345		0.004	
Granulation tissue	0.428	0.132	0.312		0.002	
Bacterial colonization	0.442	0.187	0.204		0.028	
Aseptic Loosening						0.286
Foreign body reaction	0.245	0.108	0.228		0.026	

Note: Multiple regression analysis was performed for each failure mode separately. R² values represent the total variance explained by the model for each failure mode. All reported associations are statistically significant ($p < 0.05$).

On detailed pathologic examination, specific histopathologic findings for different failure modes were evaluated by stepwise regression analysis. Neutrophil infiltration (B=0.892, p=0.006, VIF=1.32) and bacterial colonization (B=0.445, p=0.018, VIF=1.28) were independent predictors in infection cases. In cases of component loosening, fibrohistiocytic reaction (B=0.458, p=0.004, VIF=1.24) was the strongest predictor. Synovial hyperplasia (B=0.245, p=0.026, VIF=1.18) and inflammatory infiltrate (B=0.185, p=0.038, VIF=1.15) were significant predictors in instability cases (Table 4).

Table 4. Stepwise Multiple Regression Analysis for Histopathological Predictors of Specific Failure Modes

Failure Mode and Findings	Unstandardized Coefficient (B)	Standard Error (SE)	Standardized Coefficient (β)	p-value	VIF	Model R^2
Infection						0.452
Neutrophilic infiltration	0.892	0.308	0.365	0.006	1.32	
Bacterial colonization	0.445	0.182	0.208	0.018	1.28	
Granulation tissue	0.332	0.128	0.252	0.012	1.25	
Component Loosening						0.386
Fibrohistiocytic reaction	0.458	0.148	0.332	0.004	1.24	
Necrosis	0.525	0.248	0.228	0.038	1.20	
Foreign body reaction	0.228	0.098	0.232	0.028	1.18	
Instability						0.284
Synovial hyperplasia	0.245	0.108	0.228	0.026	1.18	
Inflammatory infiltrate	0.185	0.088	0.218	0.038	1.15	

Note: VIF = Variance Inflation Factor. VIF values <2 indicate absence of significant multicollinearity. Model R^2 represents the total variance explained by each failure mode model. All reported associations are statistically significant ($p < 0.05$).

The association of pathologic categories and comorbidities with failure modes was evaluated by hierarchical multiple regression analysis. After controlling for demographic factors (age, gender) in the first step, the contribution of comorbidities and pathology types was analyzed. Comorbidities were strongly associated with mechanical failure (R=0.682, adjusted R^2=0.315, F=15.24, p<0.001). The presence of infectious pathology was a significant predictor for the diagnosis of periprosthetic joint infection (R=0.492, adjusted R^2=0.242, F=12.86, p<0.001). Non-infectious pathology was moderately associated with aseptic loosening (R=0.386, adjusted R^2=0.149, F=8.45, p=0.008) (Table 5).

Table 5. Hierarchical Multiple Regression Analysis for Pathological Categories and Comorbidities

Failure Mode and Predictor Block	R	R^2	Adjusted R^2	F Change	p-value
Hardware/Mechanical Failure					
Demographics	0.245	0.082	0.060	3.24	0.075
Demographics + Comorbidities	0.682	0.465	0.315	12.45	0.001
Periprosthetic Joint Infection					
Demographics	0.186	0.058	0.035	2.86	0.095
Demographics + Infectious pathology	0.492	0.286	0.242	10.86	0.001
Demographics + Infectious pathology + Comorbidities	0.585	0.392	0.342	8.24	0.032
Aseptic Loosening					
Demographics	0.165	0.048	0.027	2.45	0.122
Demographics + Non-infectious pathology	0.386	0.182	0.149	8.45	0.008

Note: Demographics include age and gender. R^2 represents the total variance explained at each step, while Adjusted R^2 accounts for the number of predictors in the model. All final models are statistically significant ($p < 0.05$).

4. DISCUSSION AND CONCLUSION

In this study, we evaluated the compliance of referring physicians with AAOS guidelines and the diagnostic contribution of the pathology department in painful arthroplasty patients referred to tertiary care centers. In our study, which included a total of 85 patients, significant correlations were found between the results of pathologic evaluation and tertiary center feedback. It is noteworthy that the presence of infectious pathology was strongly associated with the diagnosis of periprosthetic joint infection (OR: 4.92, p=0.001) and this relationship persisted after controlling for demographic factors (R²=0.286, p<0.001). Specific histopathological findings such as neutrophil infiltration (B=0.892, VIF=1.32, p=0.006) and bacterial colonization (B=0.445, VIF=1.28, p=0.018) were found to have high diagnostic value as independent predictors. In non-infectious pathologies, fibrohistiocytic reaction (B=0.458, p=0.004) was the predominant finding in cases of aseptic loosening, and the presence of these pathologies showed diagnostic value

independent of demographic factors (R² increase from 0.048 to 0.182, p=0.008). These results evidence-based emphasize the critical role of a multidisciplinary approach and especially pathologic examination in the evaluation of painful arthroplasty patients.

Despite advanced imaging methods and diagnostic tests, periprosthetic joint infection remains one of the most challenging complications of total joint arthroplasty. The 29.4% PEE rate in our study and the strong correlation between pathologic evaluation and infection diagnosis (OR: 4.92, p=0.001) emphasize the importance of accurate and rapid diagnosis. Especially the culture time of low virulence pathogens can be prolonged up to 14 days [16], which complicates the diagnostic process. Although our pathological examination results reveal the diagnostic value of specific findings such as neutrophil infiltration and granulation tissue, the time required for histopathological evaluation in clinical practice and the inability to perform all diagnostic tests in some centers

may limit the effective use of the standard diagnostic algorithm.

Although we demonstrated the diagnostic value of pathologic examination in our study, it is clear that new technologies should be developed to obtain faster and more reliable results in the diagnosis of periprosthetic joint infection [17]. In particular, the cellular examination method we used to differentiate infectious and non-infectious cases in synovial fluid analysis yielded significant results in the presence of infectious pathology (p=0.001). Considering the limitations of conventional methods in the diagnostic process of PEE cases with a rate of 29.4% in our study, the importance of rapid and reliable diagnostic methods such as pathologic examination increases, especially in cases where all MSIS criteria cannot be evaluated.

The pathologic examination method applied in our study allowed detailed evaluation of the synovial tissue. The value of this approach is consistent with the findings of Van Landuyt et al. [18] in synovial tissue analysis. While previous studies have focused on specific cell populations to differentiate infectious and non-infectious cases [19, 20, 21], our study provides a more comprehensive analysis by evaluating multiple histopathological parameters such as neutrophil infiltration (B=0.885, p=0.004), granulation tissue (B=0.428, p=0.002) and bacterial colonization (B=0.445, p=0.018) in PEE cases. In particular, the strong association of the presence of infectious pathology with the diagnosis of PEE (OR: 4.92, p=0.001) supports the diagnostic value of this approach.

As with any other study, these limitations were some included the fact that some data was absent or limited owing to its retrospective design. Additionally, patients were recruited from a tertiary level center, hence the study population would not be generalized to a wider patient group. Moreover, it is also possible that some noninvasive, diagnostic tests may be performed differently from one patient to another in that not all centers may have histopathological examination and synovial fluid analysis as part of the criteria for diagnosis which would then greatly hinder the diagnostic accuracy. The other issue that bears relevance to the results is the differences in the diagnostic criteria and guidelines that were adopted in the study. Last, the evaluation of the primary outcome measure of PEE diagnosis could only be short term because of unavailability of follow-up long term results. These limitations highlight the potential advantages of multi-center studies which can provide more data and uniformity in the diagnostic measures in future relevant studies.

In conclusion, this research has proven that the pathology examination is an indispensable adjunct in the diagnosis of PJI. Specifically, the fact that infectious pathology was of great help in the diagnosis of PEE and the significance of a few histopathology features for diagnosis urge the need for a pathologist to be part of the team. On the other hand, the assessment of the referring doctors' adherence to the AAOS recommendations pointed out the inconsistency in the assessment of this outcome. The need

of a multidisciplinary approach to these processes is even more emphasized by the high diagnostic value of neutrophil infiltration, granulation tissue and bacterial colonization as pathological findings. Larger populations, prospectively designed studies, and standardized diagnostic protocols are needed to corroborate this finding in future research which will help in formulating a diagnostic algorithm for PEE. A take home message that arises from the current study is the relevance of a systematic approach and teamwork between pathology and orthopaedics in assessing painful arthroplasty patients.

REFERENCES

[1] Zagra L, Maccario C, Mondini A, et al. Treatment of failures related to articulation material in THA. A comprehensive algorithm of surgical options and open questions. Hip Int. 2014;24(Suppl 10)–S57.

[2] Bieger R, Kappe T, Fraitzl CR, et al. The aetiology of total knee arthroplasty failure influences the improvement in knee function. Arch Orthop Trauma Surg. 2013;133(2):237–241.

[3] Margulies BS, DeBoyace SD, Parsons AM, et al. Functionally deficient mesenchymal stem cells reside in the bone marrow niche with M2-macrophages and amyloid-beta protein adjacent to loose total joint implants. J Orthop Res. 2015;33(5):615–624.

[4] Miller DD, Yaar R, Posnik O, et al. Reactive granular histiocytosis secondary to arthroplasty prosthesis: a novel reaction pattern. J Cutan Pathol. 2012;39(5):558–561.

[5] Eftekhar NS, Doty SB, Johnston AD, et al. Prosthetic synovitis. Hip. 1985;1:169–183.

[6] Zysk SP, Gebhard H, Plitz W, et al. Influence of orthopedic particulate biomaterials on inflammation and synovial microcirculation in the murine knee joint. J Biomed Mater Res B Appl Biomater. 2004;71(1):108–115.

[7] Xu J, Yang J, Chen J, et al. Activation of synovial fibroblasts from patients at revision of their metal-on-metal total hip arthroplasty. Part Fibre Toxicol. 2020;17(1):42.

[8] Kwon YM, Thomas P, Summer B, et al. Lymphocyte proliferation responses in patients with pseudotumors following metal-on-metal hip resurfacing arthroplasty. J Orthop Res. 2010;28(4):444–450.

[9] Bémer P, Léger J, Milin S, et al. Histopathological diagnosis of prosthetic joint infection: does a threshold of 23 neutrophils do better than classification of the periprosthetic membrane in a prospective multicenter study? J Clin Microbiol. 2018;56(9).

[10] Bori G, Muñoz-Mahamud E, Garcia S, et al. Interface membrane is the best sample for histological study to diagnose prosthetic joint infection. Mod Pathol. 2011;24(4):579–584.

[11] Kumar VA, Abbas A, Aster J. Robbins and Cotran pathologic basis for disease (ed. V Kumar). Philadelphia, PA: Elsevier; 2015.

[12] Hasegawa M, Yoshida K, Wakabayashi H, et al. Pseudotumor with dominant B-lymphocyte infiltration after metal-on-metal total hip arthroplasty with a modular cup. J Arthroplasty. 2012;27(3):493.e5–e7.

[13] Watters TS, Cardona DM, Menon KS, et al. Aseptic lymphocyte-dominated vasculitis-associated lesion. Am J Clin Pathol. 2010;134(6):886–893.

[14] Kurmis AP, Herman A, McIntyre AR, et al. Pseudotumors and high-grade aseptic lymphocyte-dominated vasculitis-associated lesions around total knee replacements identified at aseptic revision surgery: findings of a large-scale histologic review. J Arthroplasty. 2019;34(10):2434–2438.

[15] Calliess T, Ettinger M, Hülsmann N, et al. Update on the etiology of revision TKA—evident trends in a retrospective survey of 1449 cases. Knee. 2015;22(3):174–179.

[16] Randelli F, Brioschi M, Randelli P, Ambrogi F, Sdao S, Aliprandi A (2018) Fluoroscopy- vs ultrasound-guided aspiration techniques in the management of periprosthetic joint infection: which is the best? Radiol Med 123(1):28–35. https://doi.org/10.1007/s11547-017-0811-1

[17] Fritz J, Lurie B, Miller TT (2013) Imaging of hip arthroplasty. Semin Musculoskelet Radiol 17(3):316–327. https://doi.org/10.1055/s-0033-1348098

[18] Hargunani R, Madani H, Khoo M, Fotiadou A, Pressney I, Calleja M, O'Donnell P (2016) Imaging of the painful hip arthroplasty. Can Assoc Radiol J 67(4):345–355. https://doi.org/10.1016/j.carj.2015.11.003

[19] Dinneen A, Guyot A, Clements J, Bradley N (2013) Synovial fluid white cell and differential count in the diagnosis or exclusion of prosthetic joint infection. Bone Jt J 95:554–557. https://doi.org/10.1302/0301-620X.95B4.30388

[20] Schinsky MF, Della Valle CJ, Sporer SM, Paprosky WG (2008) Perioperative testing for joint infection in patients undergoing revision total hip arthroplasty. J Bone Joint Surg Am 90(9):1869–1875. https://doi.org/10.2106/JBJS.G.01255

[21] Cipriano CA, Brown NM, Michael AM, Moric M, Sporer SM, Della Valle CJ (2012) Serum and synovial fluid analysis for diagnosing chronic periprosthetic infection in patients with inflammatory arthritis. J Bone Joint Surg Am 94(7):594–600. https://doi.org/10.2106/JBJS.J.01318

Türk Doğa ve Fen Dergisi
Turkish Journal of Nature and Science
www.dergipark.gov.tr/tdfd

Experimental Investigation of the Thermal Performance of Iron Oxide-Water Nanofluid Subjected To a Magnetic Field in a Horizontal Tube

Hamza ERTÜRK[1] , Tarkan KOCA[2*]

[1]İnonu University, Engineering Faculty, Mechanical Engineering Department, Malatya, Türkiye
[2]İnonu University, Engineering Faculty, Mechanical Engineering Department, Malatya, Türkiye
Hamza ERTÜRK ORCID No: 0009-0001-0517-9949
Tarkan KOCA ORCID No: 0000-0002-6881-4153

Corresponding author: tarkan.koca@inonu.edu.tr

Keywords
Nanofluid,
Magnetic field,
Heat transfer,
Iron oxide

Abstract: In this study, an experimental analysis was performed to evaluate the thermal behavior of iron oxide-water nanofluid as it traverses a straight copper tube, under the influence of a constant heat capacity and the application of a magnetic field. Four types of fluids were used in the experiment. These are pure water, 0.5% concentration of Fe_3O_4-water nanofluid, 1% concentration of Fe_3O_4-water nanofluid and 1.5% concentration of Fe_3O_4-water nanofluid. Experiments were conducted at two distinct flow rates as 10×10^{-5} m^3 s^{-1} and 13×10^{-5} m^3 s^{-1}. The inlet temperatures of the fluids and the surface temperature of the copper tube were maintained at the same level throughout all experiments. The Nusselt number was determined at Reynolds numbers of 4200 and 5400 in experiments conducted under turbulent flow conditions. The thermal performances of the fluids were compared by comparing the obtained Nusselt numbers. The experiments demonstrated that as the Reynolds number increased, the Nusselt number also increased, with the most notable enhancement of 20.7% observed in the iron oxide-water nanofluid at a 1.5% concentration and a Reynolds number of 5400 under a magnetic field. Additionally, both the heat transfer coefficient and the Nusselt number improved with the use of nanofluids.

89

Yatay Bir Boruda Manyetik Alan Uygulanan Demir Oksit-Su Nanoakışkanının Isıl Performansının Deneysel Olarak İncelenmesi

Anahtar Kelimeler
Nanoakışkan,
Manyetik alan,
Isı transferi,
Demir oksit

Öz: Bu çalışmada sabit ısı sığası ve manyetik alan etkisi altındaki düz bir bakır borudan akan demir oksit-su nanoakışkanının ısıl performansı deneysel olarak incelenmiştir. Deneyde dört tip akışkan kullanılmıştır. Bunlar; saf su, %0,5 konsantrasyonunda Fe_3O_4-Su nanoakışkanı, %1,0 konsantrasyonunda Fe_3O_4-Su nanoakışkanı ve %1,5 konsantrasyonunda Fe_3O_4-Su nanoakışkanıdır. Deneyler 10×10^{-5} m^3 s^{-1} ve 13×10^{-5} m^3 s^{-1} olmak üzere iki farklı debide gerçekleştirilmiştir. Akışkanların giriş sıcaklıkları ve bakır borunun yüzey sıcaklığı tüm deneylerde eşit tutulmuştur. Türbülanslı akış şartlarında gerçekleşen deneylerde iki farklı Reynolds (Re=4200 ve Re=5400) sayısındaki Nusselt sayısı hesaplanmıştır. Elde edilen Nusselt sayıları karşılaştırılarak akışkanların ısıl performansları karşılaştırılmıştır. Yapılan deneyler sonucunda Reynolds sayısının artması ile Nusselt sayısının da artış gösterdiği, nanoakışkanların kullanımı ile toplam ısı transfer katsayısının ve Nusselt sayısının artış gösterdiği gözlemlenmiştir. Nusselt sayısındaki en büyük artış, manyetik alan etkisi altında, Re=5400 değerinde %1,5 konsantrasyonunda demir oksit-su nanoakışkanda gerçekleşmiştir ve saf suya göre %20,7 oranında artış tespit edilmiştir.

1. INTRODUCTION

The movement of heat from an object at a higher temperature to one at a lower temperature occurs due to the existence of a temperature gradient. The process of heat energy transitioning between systems or objects is referred to as heat transfer. Naturally, heat transfer always occurs from high to low temperatures; however, modern

systems equipped with advanced equipment also enable heat transfer from low to high temperatures.

With energy resources quickly running out, humanity is striving to utilize what we have in the most effective manner possible. In many energy systems, heat transfer occurs. Therefore, scientists want to increase heat transfer efficiency. The application of nanofluids in thermal systems represents a significant advancement in heat transfer technology. Nanofluids are produced by incorporating solid particles with dimensions ranging from 1 to 100 nanometers into a base fluid. The primary objective of this procedure is to enhance heat transfer due to the interaction of the solid particles within the fluid. The term nanofluid was first used by Maxwell in 1881. Maxwell [1] conducted studies by adding solid particles to liquids. Various studies in this area have been reviewed.

Tekir et al. [2] investigated the thermal properties of a nanofluid made from different proportions of iron oxide, copper, and water ($Fe_3O_4 - Cu - H_2O$) under the influence of a magnetic field. In their study, they conducted experiments between the values of 994<Re<2337. The researchers noted that the Nusselt (Nu) number rose as the fluid velocity increased. At the same time, they observed that water Fe_3O_4 and Cu nanoparticles increased the heat transfer. The study found that applying a magnetic field to the nanofluids improved heat transfer by 14% compared to when no magnetic field was present. They determined that the hybrid nanofluids used; %1 Fe_3O_4 − %1 Cu − %98 water type showed the best performance under magnetic field. Demirpolat and Uyar [3], determined the thermal conductivities of the nanoparticles produced in order to evaluate the use of nanoparticle materials in thermal insulation materials, which a new perspective on energy is saving. The heat transfer coefficients of Al2O3 and CuO nanoparticles were found to be 34.2 and 65.4 W/mK, respectively. Uyar et al. [4] calculated that there was a 1.1% increase in thermal efficiency due to the MgO nanoparticle additive. Keklikcioğlu and Özceyhan [5] conducted a numerical analysis of the thermal performance of a hybrid nanofluid composed of graphene, iron oxide, and water, with varying concentrations between 0.5% and 1%. This analysis was performed within a flat heat exchanger tube featuring a circular cross-section, under conditions of constant surface heat flux, turbulent flow, and Reynolds numbers ranging from 10000 to 50000. The analysis revealed that the use of nanofluid significantly enhanced heat transfer while maintaining a relatively stable friction coefficient. The study found that using nanofluid instead of base fluid water increased the Nusselt number by up to 24%. The highest thermo hydraulic performance coefficient observed in this study was calculated as 1.2 for Re=10000 in the use of 1% graphene-iron oxide-water hybrid nanofluid. An experimental investigation was carried out by Çiftçi et al. [6] to assess the thermal performance of a closed heat pipe, particularly focusing on a thermo siphon that employed titanium dioxide-water ($TiO_2 - H_2O$) nanofluid. Three distinct cooling water flow rates ($5g\,s^{-1}$, $7.5g\,s^{-1}$, $10g\,s^{-1}$) and three varying heater power levels (200 Watt, 300 Watt, and 400 Watt) were utilized in the evaporation section of the study. The experiments employed both water and nanofluid as the working fluids. It was found that the titanium dioxide-water nanofluid enhanced thermal performance by 16.5% when subjected to a heating power of 200 Watt and a cooling water flow rate of 5 g/s. Kılınc et al. [7] conducted an experimental study to examine the cooling performance of vehicle radiators using nanofluids. This investigation incorporated pure water, along with graphene oxide-water and graphene nanoribbon-water nanofluids. The experimental setup included three different inlet temperatures and four varying flow rates as variable parameters. The experiments revealed an increase in the total heat transfer coefficient of 6.9% for a 0.001% GO-water solution, 32% for a 0.02% GO-water solution, and 18.9% for a 0.01% GNR-water solution. Kılınç [8] examined the thermal efficiency of a thermo syphon by employing nanofluid within a thermo syphon-type heat pipeIn the experiment, he used nanofluid containing 2% iron oxide particles and 0.2% surface activator in water. The cooling water flow rate of the condenser zone was used as $3g\,s^{-1}$, $6g\,s^{-1}$, $9g\,s^{-1}$, and two different parameters were used for the heat value given to heat the evaporator as 300 Watt and 400 Watt. As a result, it was observed that the magnetic nanofluid increased the thermal performance by 20%. Sadeghinezhad et al. [9] examined the thermal performance of fluid flow in the pipe in the range of 5000<Re<22000 using graphene-water nanofluid with various weight ratios ranging from 0.025% to 1%. In their research, they found that using nanofluid enhanced heat transfer and Nusselt number. The thermal performance of graphene and iron oxide nanoparticles separately and in hybrid nanofluids was examined by Askari et al. [10]. The nanofluids they prepared had three different weight ratios of 0.1%, 0.2% and 1.0%. As a result of the experiments, they found an improvement between 14% and 32% in the thermal conductivity coefficient compared to the base fluid. For the value of Re=4248, the heat transfer coefficient increased by 8.5% in the iron oxide-water nanofluid, while it increased by 14.5% in the iron oxide-graphene-water hybrid nanofluid. The thermal transfer properties of water-based nanofluids containing copper oxide and iron oxide were investigated by Peyghambarzadeh et al. [11], who suggested using them in place of conventional water in car radiators. Three distinct volumetric concentrations of 0.15%, 0.4%, 0.65% were used to prepare the nanofluids. The total heat transfer coefficient increased by 9% in this experimental investigation. A study on the heat transfer properties of nanofluids based on carbon nanotubes in a horizontal pipe was carried out by Ding et al. [12]. The pipe used for the study was 970 mm long with an inner diameter of 4.5 mm. Under laminar flow and fixed wall heat flux boundary conditions, they discovered that the convection heat transfer coefficient increased by more than 350% at Re=800 and 0.5% nanofluid. Abreu et al. [13] observed a 23% increase in Nusselt number for 0.25% concentration under the condition of Re=1650 for multilayer CNT with 80mm outer diameter and $20x10^{-3}$ nm length in a 6 mm inner diameter and 200 mm long pipe. Based on the research undertaken, it has been noted that the incorporation of nanofluids in heat transfer systems significantly improves efficiency. As global energy

resources continue to diminish at a rapid pace, the efficiency of current systems has gained paramount importance. Therefore, the high efficiency observed in nanofluids is anticipated to play a more significant role in our lives in the future.

This research examined the thermal performance of water-iron oxide $H_2O - Fe_3O_4$ nanofluid at volumetric ratios of 0.5%, 1%, and 1.5%, across various flow rates, while maintaining a constant heat capacity. The study also considered the effects of a magnetic field and the subsequent removal of the magnetic field. The findings were analyzed in the context of the thermal performance of water.

2. MATERIAL AND METHOD

In this experimental study, the thermal performance of water and iron oxide-water $(Fe_3O_4 - H_2O)$ nanofluids (volume ratios; 0.5%, 1%, and 1.5%) flowing through a straight copper pipe at two different flow rates $(10x10^{-5}$ m^{3}s^{-1}, $13x10^{-5}$ m^{3}s^{-1}), under constant heat capacity (25,000 Wm^{-2}), constant inlet temperature (15°C), without a magnetic field and then under the influence of a magnetic field were investigated. During the experiments, the inlet temperature of all fluids was maintained constant. After each experiment, the fluids were cooled in refrigeration units, and the tests were repeated once the fluids returned to the specified inlet temperature conditions. Experiments were conducted for four different fluid types at two flow rates without a magnetic field. Following this, the identical experiments were conducted in the presence of a magnetic field. In total, 14 distinct experiments were carried out.

2.1. Nanofluid Preparation

In the experimental study, pure water and iron oxide-water nanofluids with three different volumetric ratios (0.5%, 1%, 1.5%) were used as fluids. Nanofluids were synthesized using a two-step approach. Iron oxide particles supplied in the form of nanoparticles were mixed in pure water and kept in an ultrasonic mixer for approximately 5 hours. As a result of the process, homogeneous and stable iron oxide-water nanofluids were prepared.

The formulas used to determine the thermal properties of fluids are as follows;

Volumetric concentration: Pak and Cho [14] proposed Equation 1;

$$\phi_v = \frac{1}{(100\ \phi_m^{-1})(\rho_p\ \rho_f^{-1}) + 1}\ x100 \qquad (1)$$

Density: Equation 2 was utilized for density calculations;

$$\rho_n = (1 - \phi)\rho_f + \phi x \rho_p \qquad (2)$$

Specific heat: Bhimani et al. [15] employed Equation 3;

$$c_{p_n} = \frac{(1 - \phi)x\rho_f x c_{p_f} + \phi x \rho_p x c_{p_p}}{\rho_n} \qquad (3)$$

Dynamic viscosity: Wen and Ding [16] provided Equation 4;

$$\mu_n = \mu_f(1 + 2.5\phi) \qquad (4)$$

Thermal conductivity: Yu and Choi [17] used Equation 5;

$$k_n = \left| \frac{k_p + 2k_f + \{2(k_p - k_f)(1 + \beta)^3\phi\}}{k_p + 2k_f - \{(k_p - k_f)(1 + \beta)^3\phi\}} \right| x k_f \qquad (5)$$

Prandtl number showed in Equation 6;

$$Pr = \frac{\mu c_p}{k} \qquad (6)$$

The formula includes the parameters: ρ_n for nanofluid density, ρ_f for base fluid density, and ρ_n for nanoparticle density.

The parameter ϕ refers to the volumetric or mass fraction, while ϕ_v signifies the volumetric fraction of the nanofluid, and ϕ_m indicates the mass fraction of the nanofluid. The specific heat capacities are represented as c_{p_n} for the nanofluid, c_{p_f} for the base fluid, and c_{p_p} for the nanoparticles. Furthermore, μ_n represents the dynamic viscosity of the nanofluid, while μ_f denotes the dynamic viscosity of the base fluid, k_n stands for the thermal conductivity of the nanofluid, k_f symbolizes the thermal conductivity of the base fluid, and k_p refers to the thermal conductivity of the nanoparticles. The parameter β represents the ratio of the thickness of the nanoparticle layer to the original particle radius, with a determined value of 0.1 in this study.

The thermophysical characteristics of the fluids were determined utilizing the designated formulas. These properties are detailed in Table 1.

Table 1. Thermophysical properties of fluids

	H_2O Water	%0.5 $Fe_3O_4 - H_2O$ Iron Oxide-Water	%1 $Fe_3O_4 - H_2O$ Iron Oxide-Water	%1.5 $Fe_3O_4 - H_2O$ Iron Oxide-Water	Fe_3O_4 Iron Oxide
Intensity (ρ) kg m^{-3}	999.0	1019.9	1040.8	1061.7	5180
Specific Heat (c_p) J kgK^{-1}	4186	4082	3982	3887	104
Dynamic Viscosity (μ) kg ms^{-1}	1.120x10^{-3}	1.134x10^{-3}	1.148x10^{-3}	1.162x10^{-3}	
Heat Conduction Coefficient (k) W mK^{-1}	0.59	0.6007	0.6116	0.6226	17.65
Prandtl Number (Pr)	7.940	7.706	7.475	7.255	

2.2. Experimental Setup

To facilitate the flow, a two-stage circulation pump with a total power of 250 Watts was utilized. In the experimental setup, copper tubing was used to effectively

transfer heat energy to the fluid. The copper tube has an outer diameter of 28 mm, an inner diameter of 26 mm, and a length of 75 cm. Clamp heaters are placed on a 50 cm section of the copper tube. The remaining sections are equipped with magnets, thermocouple probes and

manometer inlets. Twelve clamp heaters are utilized, each having an outer diameter of 30 mm and a length of 40 mm, with a power rating of 200 Watts per heater. To achieve a consistent heat flux of 25,000 W/m², the system's electrical power is controlled using a 3000W-15A dimmer. For insulation, the heaters were first wrapped with rock wool and then covered with aluminum sheathing.

In the experimental setup, copper pipes were used to effectively give heat energy to the fluid. The copper pipe is length of $l = 75$ cm and diameters of $D_d = 28$ mm, $d_i = 26$ mm. At the starting position of the heaters, 10 neodymium magnets were placed to generate a magnetic field. Each magnet had dimensions of 50 x 10 x 5 mm measurements with a gauss meter revealed that the total magnetic field intensity produced by the magnets was 1600 Gauss. Thermocouples were placed at the inlet and outlet of the copper tube to measure the fluid temperatures at both ends. Two more thermocouples were positioned between the heaters to monitor the surface temperature of the copper tube. Additionally, the pressure drops within the flow were investigated using a U-type manometer integrated into the system. The diagrammatic illustration of the experimental arrangement created using the computer software is presented in Figure 1, while the actual visual depiction of the experimental setup can be found in Figure 2.
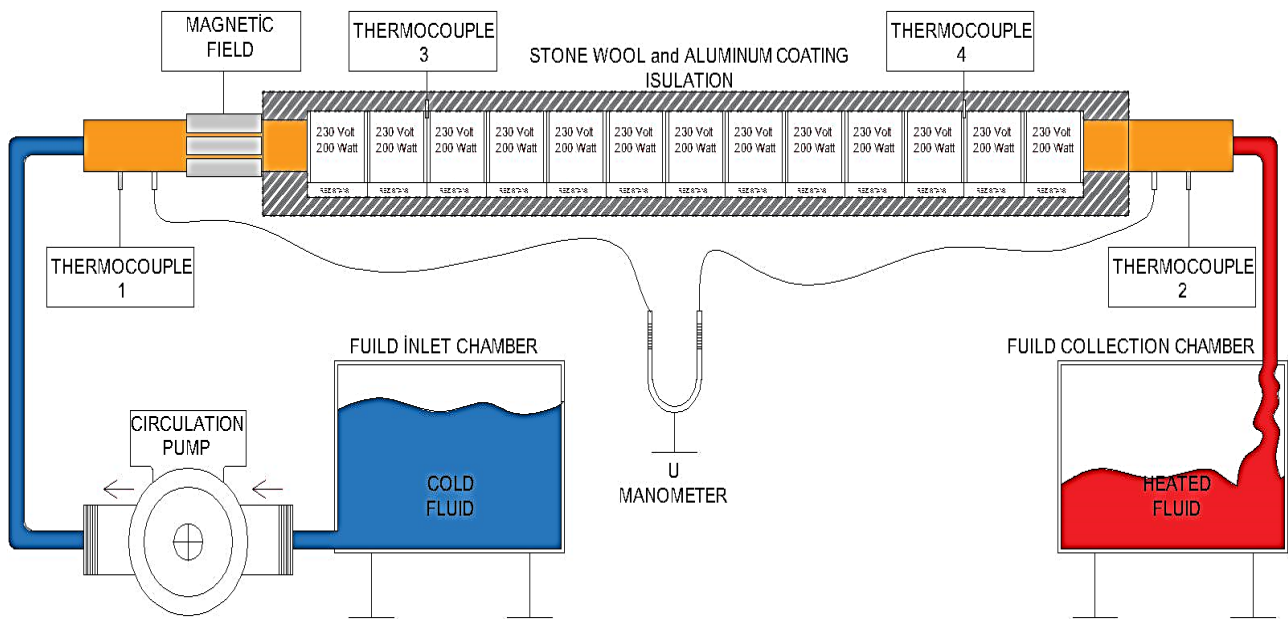
Figure 1. Schematic representation of the experimental set prepared in the computer program
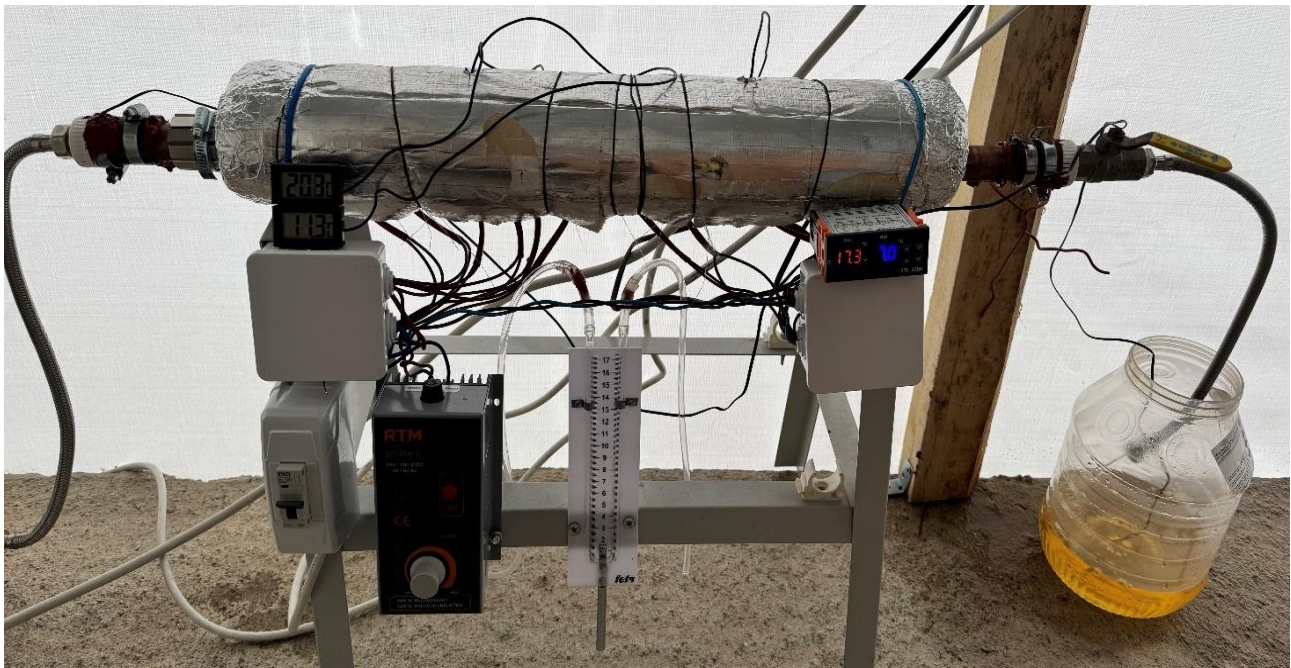
Figure 2. Visual of the experimental setup

3. CONCLUSION AND DISCUSSION

The thermal performance of an iron oxide-pure water nanofluid under the influence of a magnetic field was the main experimental focus of this study. Fourteen distinct experiments were conducted, and the outcomes were compared. Using the collected data, the necessary computations were carried out, and the thermal performance of nanofluids relative to pure water was evaluated. The formulas used in the calculations (Equation 7 to 15) are as follows;

Temperature difference;
$$\Delta T \ (K) = T_ç - T_g \tag{7}$$
Average temperature;
$$T_{ort}(K) = \frac{T_g + T_ç}{2} \tag{8}$$
Heat absorbed by the fluid;
$$\dot{Q}(W) = \dot{m}c_p(T_ç - T_g) \tag{9}$$
Heat transfer coefficient;
$$h \ (W \ mK^{-1}) = \frac{\dot{q}}{T_y - T_{ort}} \tag{10}$$
Thermal capacity;
$$\dot{q}(W \ m^{-1}) = \frac{\dot{Q}}{A} \tag{11}$$
Pressure drop;
$$\Delta P = (\rho_{Hg} - \rho)gx\Delta h \tag{12}$$
Reynolds number;
$$Re = \frac{\rho * V * D_h}{\mu} \tag{13}$$
Nusselt number;
$$Nu = \frac{h.Dh}{k} \tag{14}$$
Friction factor;
$$f = \frac{P_{in} - P_{out}}{\left(\frac{L}{D}\right).\left(\frac{\rho V^2}{2}\right)} \tag{15}$$

The formulas indicate the following parameters: ΔT represents the temperature difference between the inlet and outlet of the fluid; T_g denotes the inlet temperature of the fluid; $T_ç$ signifies the outlet temperature of the fluid; T_y refers to the surface temperature of the copper pipe; T_{ort} is the average of the inlet and outlet temperatures; and $\dot{m}$ indicates the mass flow rate, h heat convection coefficient, A Field, ρ_{Hg} density of mercury, ρ the density of the fluid, g Acceleration of gravity, Δh the difference in height on the pressure gauge, V velocity of the fluid, D_h hydrodynamic diameter, L characteristic length, P_{in} fluid inlet pressure, P_{out} the fluid outlet pressure.

3.1. Experiments without Magnetic Field

The experiments were conducted at two distinct flow rates while maintaining a constant temperature capacity in the absence of a magnetic field. The ambient temperature, the copper pipe's surface temperature, and the fluids' inlet temperatures were maintained constant during the experiment. The results indicated that as the Reynolds number increased, the Nusselt numbers also increased. When compared to pure water, nanofluids show higher Nusselt number values at equivalent Reynolds numbers. Figure 3 displays the Re-Nu graph, which was produced by computations using the experimental data.

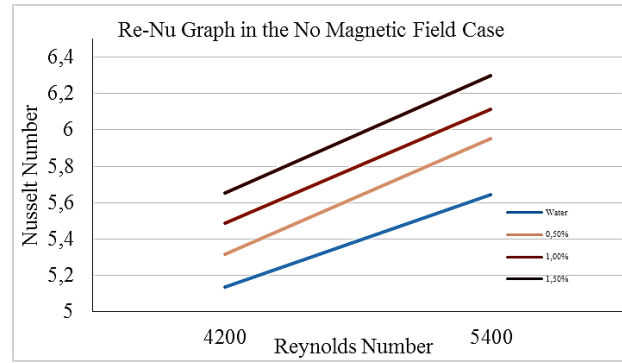Furthermore, the graph of the computed friction factor is shown in Figure 4.

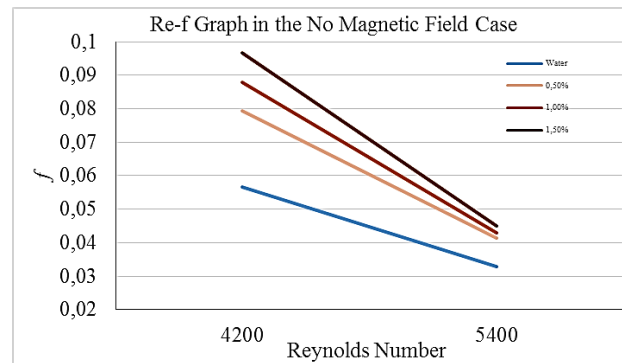**Figure 3.** Re-Nu plot of fluids in the absence of magnetic field effect

Figure 4. Re-f plot of fluids in the absence of magnetic field effect

3.2. Experiments under Magnetic Field

The studies were carried out with two different flow rates and a constant temperature capacity while being affected by a magnetic field. Throughout the experimentation, the inlet temperatures of the fluids, the surface temperature of the copper pipe, and the ambient temperature were maintained at constant levels. The results yielded graph curves that resembled those obtained in the absence of a magnetic field. The same data was utilized for pure water, as the magnetic field is not expected to affect it. In the experiments performed within the magnetic field, an increase in the Nusselt number of nanofluids was observed. No significant variations were observed in the fluid's inlet and outlet pressure values. Therefore, there is no obvious difference in the coefficient of friction. The Re-Nu graph formed as a result of the calculations made according to the experimental data is shown in Figure 5. The calculated friction factor is illustrated in Figure 6.
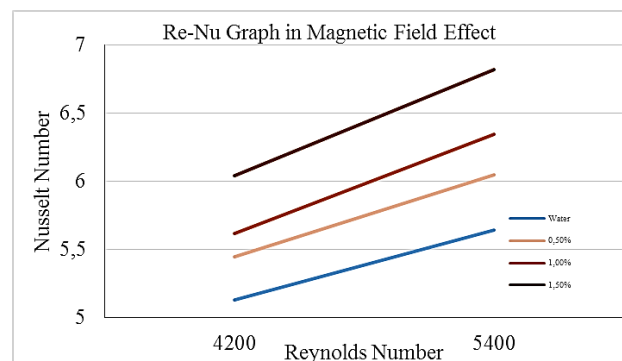

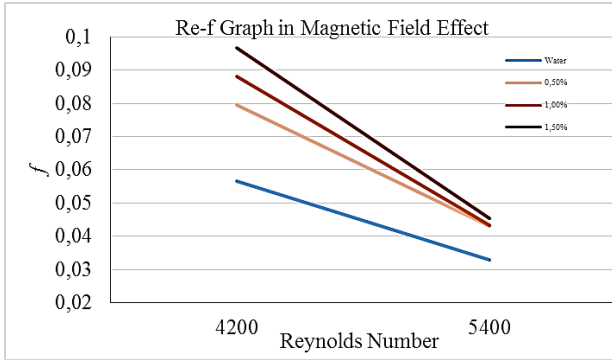**Figure 5.** Re-Nu plot of fluids under magnetic field effect

93

Figure 6. Re-f plot of fluids under magnetic field effect

3.3. Effect of Magnetic Field on Nanofluids

The experimental data collected without a magnetic field were compared to evaluate the effect of the magnetic field on nanofluids. Analysis of the results reveals that the magnetic field significantly influences the properties of the nanofluid. The Nusselt number increase value brought on by the magnetic field in the same nanofluid was compared with the graphs below in experiments conducted at two different Reynolds numbers. It is generally observed that the iron oxide-water nanofluid is affected by the magnetic field. Figure 7 and Figure 8 compare the Nusselt numbers of fluids with Re=4200 and Re=5400 values based on the magnetic field.
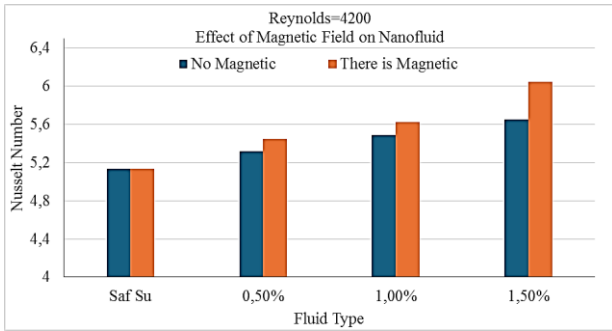
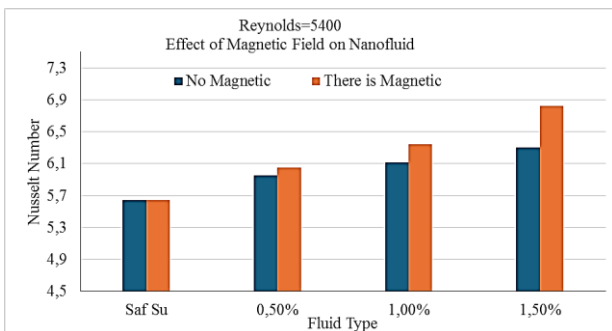**Figure 7.** The effect of magnetic field at Re=4200 on the Nusselt number of fluids

Figure 8. The effect of magnetic field at Re=5400 on the Nusselt number of fluids

3. RESULTS

The experiments demonstrated that the Nusselt number increased as the Reynolds number rose for all the fluids tested. It was also observed that the Nusselt number was further increased when pure water was replaced with an iron oxide-water nanofluid. In the experiments conducted without the influence of a magnetic field, it was noted that the Nusselt number rose as the volumetric ratio of the iron oxide-water nanofluid increased. In experiments conducted at Re=4200, the Nusselt number of pure water was 5.135, while the Nusselt number of 1.5% Iron oxide-water nanofluid increased by 10.1% and was found to be 5.653. In experiments conducted at Re=5400, the Nusselt number of pure water was 5.645, while the Nusselt number of 1.5% Iron oxide-water nanofluid increased by 11.6% and was found to be 6.299.

In experiments conducted under the influence of magnetic field, the Nusselt number of 1.5% Iron oxide-water nanofluid at Re=4200 was found to be 6.043. This value is 17.7% higher than the Nusselt number of pure water. At a Reynolds number of 5400, the Nusselt number of the 1.5% iron oxide-water nanofluid increased by 20.8% compared to water, reaching a value of 6.819. The observation indicated that the application of a magnetic field enhanced the thermal performance of nanofluids. The greatest effect of the magnetic field occurred in the 1.5% iron oxide-water nanofluid. While the Nusselt number of a 1.5% iron oxide-water nanofluid without a magnetic field is 6.299, the Nusselt number increases by approximately 8.25% to 6.819 when a magnetic field is applied to this fluid. It has been observed that it increases the Nusselt number by creating a linear effect in nanofluids at other concentrations. When the results are compared with previous studies, parallel results are seen. Like many nanofluids, the iron oxide-water nanofluid has increased heat transfer. The Nusselt number increases when a magnetic field is added to the nanofluid. Thus, we can conclude that magnetic nanofluids benefit from the magnetic field. There are multiple reasons for the iron oxide-water nanofluid's improved heat transfer. Initially, the total heat transfer coefficient of the nanofluid is higher than that of water alone, as iron oxide nanoparticles have a greater heat transfer coefficient than water. Additionally, the heat transfer coefficient increases due to the random motion of the nanoparticles within the fluid, along with their interactions and collisions. Moreover, the impact of the magnetic field on the movement of nanoparticles adds complexity to the fluid dynamics, thereby improving the heat transfer coefficient. The fact that nanofluids increase the heat transfer coefficient shows that their use in heat transfer systems is inevitable in the future. In today's technology, nanofluids are not widely used due to their high production costs and not at the desired level of homogeneity/stability. With the developing technology, nanoparticles in smaller sizes can be produced and nanofluids with high homogeneity and stability levels can be produced. With these nanofluids produced, it will be possible to obtain more heat transfer coefficient.

94

REFERENCES

[1] Maxwell, JC. A treatise on electricity and magnetism. Oxford University Press. 1th ed. Cambridge: 1904.

[2] Tekir M, Taskesen E, Gedik E, Arslan K, Aksu B. Effect of constant magnetic field on Fe_3O_4-Cu/Water hybrid nanofluid flow in a circular pipe. Heat and Mass Transfer. 2022; 58: 707-717.

[3] Demirpolat AB, Uyar MM. Investigation of the use of nanoparticles in thermal insulation materials. IJIEA. 2024; 8(2): 89-94.

[4] Uyar MM, Çıtlak A, Demirpolat AB. Investigation of performance and emission values of new type of fuels obtained by adding MgO nanoparticles to biodiesel fuels produced from waste sunflower and cotton oil. Industrial Crops and Products.2024; 222:1-12.

[5] Keklikcioğlu O, Özceyhan V. Grafen-demir oksit-su hibrit nanoakışkanlarının ısıl ve hidrolik performanslarının sayısal olarak incelenmesi. Erciyes Üniversitesi Fen Bilimleri Enstitüsü Dergisi. 2021; 37(2); 286-288.

[6] Çiftçi E, Sözen A, Karaman E. TiO_2 içeren nanoakışkan kullanımının ısı borusu performansına etkisinin deneysel olarak incelenmesi. Politeknik Dergisi. 2016; 19(3): 367-376.

[7] Kılınç F, Buyruk E, Karabulut K. Grafen tabanlı nanoakışkanların araç radyatörü soğutma performansı üzerindeki etkisinin deneysel analizi. Iğdır Üniversitesi Fen Bilimleri Enstitüsü Dergisi. 2019; 9(2): 1046-1056.

[8] Kılınç C. Manyetik Nanoakışkanın Termosifon Tipi Isı Borusunun Performansına Etkisi. Politeknik Dergisi. 2021; 24(3): 1309-1316.

[9] Sadeghinezhad E, Mehrali M, Tahan LS, Mehrali M, Kazi SN, Oon CS, et al. Experimental investigation of convective heat transfer using graphene nanoplatelet based nanofluids under turbulent flow conditions. Industrial & Engineering Chemistry Research. 2014; 53(31): 12455–12465.

[10] Askari S, Koolivand H, Pourkhalil M, Lotfi R, Rashidi A. Investigation of Fe_3O_4/Graphene nanohybrid heat transfer properties: experimental approach. International Communications in Heat and Mass Transfer. 2017; 87: 30-39.

[11] Peyghambarzadeh S, Hashemabadi S, Naraki M, Vermahmoudi Y. Experimental study of overall heat transfer coefficient in the application of dilute nanofluids in the car radiator, Applied Thermal Engineering. 2013; 52(1): 8–16.

[12] Ding Y, Alias H, Wen D, Williams R.A. Heat transfer of aqueous suspensions of carbon nanotubes (CNT nanofluids). Int. J. Heat Mass Transfer. 2006; 49(1): 240-250.

[13] Abreu B, Lamas B, Fonseca A, Martins N, Oliveira MSA. Experimental characterization of convective heat transfer with MWCNT based nanofluids under laminar flow conditions. Heat and Mass Transfer. 2014; 50(1): 65-74.

[14] Pak BC, Cho YI. Hydrodynamic and heat transfer study of dispersed fluids with submicron metallic oxide particles. Experimental Heat Transfer an International Journal. 1998; 11(2): 151– 170.

[15] Bhimani VL, Rathod PP, Sorathiya AS. Experimental study of heat transfer enhancement using water based nanofluids as a new coolant for car radiators. International Journal of Emerging Technology and Advanced Engineering. 2013; 3(6): 295-302.

[16] Wen D, Ding Y. Experimental investigation into convective heat transfer of nanofluids at the entrance region under laminar flow conditions. International Journal of Heat and Mass Transfer. 2004; 47: 5181-5188.

[17] Yu W, Choi SUS. The role of interfacial layers in the enhanced thermal conductivity of nanofluids: a renovated Maxwell model. Journal of Nanoparticle Research. 2003; 5: 167.

Design of A New Metamaterial and Investigation of Its Effect on The Gain of A Circular Patch Antenna

Bülent URUL[1*] ID

[1]Isparta University of Applied Sciences University, Vocational School of Technical Sciences, Electronics and Automation Department, Isparta, Türkiye
Bülent URUL ORCID No: 0000-0003-2656-2450

Corresponding author : bulenturul@isparta.edu.tr

Keywords
Metamaterials,
Antenna,
Gain

Abstract: Metamaterials have emerged as a revolutionary innovation in science and technology, offering properties not found in natural materials, such as negative refractive indices, which enable novel applications in photonics and optics. This study focuses on designing a novel metamaterial structure, with the specific goal of enhancing the performance of a circular patch antenna (CPA). The unique properties of metamaterials, particularly their ability to manipulate electromagnetic waves in unconventional ways, are leveraged to increase antenna gain and directivity. The proposed metamaterial, referred to as the four-armed symmetric metamaterial (FASM), was designed and simulated using CST software. The study explores the interaction between the FASM and the CPA by examining various configurations and distances between the two components. Simulation results reveal that applying the FASM in single and double layers significantly boosts the antenna's performance, achieving a maximum gain increase of 83.57% with a double-layer FASM at a specific distance. This finding demonstrates the potential of metamaterials to optimize antenna designs for improved efficiency and compactness, with applications spanning communication, radar, and satellite systems.

Yeni Bir Metamateryalin Tasarımı ve Dairesel Yama Antenin Kazancına Etkisinin İncelenmesi

Anahtar Kelimeler
Metamateryal,
Anten,
Kazanç

Öz: Metamalzemeler, fotonik ve optikte yeni uygulamalara olanak tanıyan negatif kırılma indisleri gibi doğal malzemelerde bulunmayan özellikler sunarak bilim ve teknolojide devrim niteliğinde bir yenilik olarak ortaya çıkmıştır. Bu çalışma, dairesel yama anteninin (DYA) performansını artırma özel hedefi ile yeni bir metamalzeme yapısı tasarlamaya odaklanmaktadır. Metamalzemelerin benzersiz özellikleri, özellikle elektromanyetik dalgaları alışılmadık şekillerde manipüle etme yetenekleri, anten kazancı ve yönlülüğünü artırmak için kullanılır. Dört kollu simetrik metamalzeme (DKSM) olarak adlandırılan önerilen metamalzeme, CST yazılımı kullanılarak tasarlanmış ve simüle edilmiştir. Çalışma, iki bileşen arasındaki çeşitli yapılandırmaları ve mesafeleri inceleyerek DKSM ile DYA arasındaki etkileşimi araştırmaktadır. Simülasyon sonuçları, DKSM'yi tek ve çift katmanlarda uygulamanın antenin performansını önemli ölçüde artırdığını ve belirli bir mesafede çift katmanlı bir DKSM ile %83,57'lik maksimum kazanç artışı elde ettiğini ortaya koymaktadır. Bu bulgu, metamalzemelerin haberleşme, radar ve uydu sistemlerini kapsayan uygulamalarda, anten tasarımlarının daha iyi verimlilik ve kompaktlık için optimize edilmesinde potansiyelini ortaya koymaktadır.

1. INTRODUCTION

Metamaterials are emerging as a revolutionary innovation in the world of science and technology, offering materials with properties not found in nature. These materials are structures where the coefficients of electrical permittivity (ε) and magnetic permeability (μ) can reach negative values, displaying extraordinary optical and electromagnetic characteristics. The discovery of these features has enabled scientists to go beyond the physical

96

limits of traditional materials, opening up new technological opportunities. Particularly, properties such as negative refractive index provide innovative solutions across a wide range of applications, especially in photonics and optics.

Firstly in 1968, Veselago introduces the theoretical framework for materials where both the electric permittivity (ε) and magnetic permeability (μ) are negative. It discusses the unique electromagnetic wave propagation characteristics in such materials, including reversed Doppler and Vavilov-Cerenkov effects, and the concept of "left-handed" substances with negative refractive indices. While no real substances with these properties were identified at the time, the paper suggests potential experimental approaches and their implications for physics [1]. In 2000, Smith and colleagues succeeded in producing the first metamaterial with negative permittivity properties in the laboratory [2]. This was confirmed by experiments conducted in the microwave region of the electromagnetic spectrum, and this discovery rapidly turned metamaterials into a growing field of research.

One of the fundamental properties of metamaterials is having a negative refractive index. The refractive index is a value that expresses how a material bends light or other electromagnetic waves. While most materials in nature have a positive refractive index, metamaterials possess a negative refractive index. This means that light or electromagnetic waves bend in the "negative direction," contrary to what is typically observed. This characteristic was detailed in Pendry's theoretical work and later confirmed by numerous experimental studies [2-5]. The negative refractive index forms the basis for extraordinary applications, such as directing, controlling, and bending light. One of the most striking applications of metamaterials is super lens technology. Proposed by Pendry, this technology suggests that materials with a negative refractive index could offer far superior resolution than conventional optical lenses. Super lenses allow light to focus even on extremely small, unconstrained scales, enabling the imaging of nanoscale details. This technology holds great potential for revolutionizing fields such as biomedical imaging and semiconductor manufacturing [6, 7].

Although metamaterials offer extraordinary properties, their applicability faces some limitations. For example, producing and scaling metamaterials can be quite challenging. These structures, successfully manufactured in laboratory environments, need further development to be integrated into large-scale commercial applications [8]. Additionally, applying negative permittivity properties over broader frequency bands remains a significant challenge. Overcoming these issues could enable the wider use of metamaterials, particularly in areas such as telecommunications, energy storage, and sensor technologies [9].

In recent years, a notable trend in the development of metamaterials is the emergence of a new class of materials known as "topological metamaterials." These structures have the potential to revolutionize the manipulation and control of both optical and acoustic waves. Topological metamaterials allow waves to be transmitted without loss, thanks to their perfect edge modes, which can significantly enhance energy efficiency [10, 11].

Studies have shown that metamaterials have the ability to enhance antenna performance when used together with antennas. The primary reason for this is that metamaterials allow electromagnetic waves to be focused and help reduce losses during wave propagation. A study conducted in 2020 examined the effects of the parameters of electrical substrates and metamaterial lens layers on antenna gain. The study found that these materials increased gain by 22% in single-layer applications and by 87% in double-layer applications [12]. The use of such materials, especially in microstrip antennas, enables small antennas to achieve high gain and directional performance. Another study from 2022 demonstrated that using flower-shaped metamaterial (FSMM) structures, optimized by the particle swarm optimization (PSO) algorithm, resulted in a 77% gain increase in satellite communication antennas. Additionally, another study revealed that by employing metamaterial structures etched onto the antenna substrate using the Defected Ground Structure (DGS) method, antenna gain was increased by 12% [13, 14].

The article by Li et al. (2024) presents the design of a broadband metamaterial absorber based on a metal-dielectric disc-ring structure. The proposed absorber achieves over 90% absorption in the 1500–4000 nm wavelength range, demonstrating polarization insensitivity and wide-angle absorption properties. The design leverages surface plasmon resonance and cavity resonance to enhance absorption, with potential applications in infrared detection and imaging [15]. Another study in 2024 examines recent advancements in tunable metamaterial absorbers (MAs). It focuses on various tuning methods, such as optical excitation, thermal radiation, and electrical modulation, to optimize the electromagnetic absorption properties of these structures using innovative materials and designs. Additionally, it discusses future challenges and potential application areas[16].

In conclusion, the use of metamaterials in antenna designs significantly enhances antenna performance, enabling widespread applications in fields such as communications, radar, and defense systems. With further development of these materials, more efficient and compact antennas are expected to emerge in the future. It is evident that, in addition to the metamaterials found in current literature, there is an ongoing and future need for various forms of metamaterials to be used across different frequency bands.

In this study, the primary goal is to design a novel metamaterial that does not exist in the current literature. Following this, to facilitate comparison, the newly designed metamaterial will be used in various combinations with a circular patch antenna, which is frequently used as a reference antenna in many studies.

97

The impact of the new metamaterial on the performance of the circular patch antenna will then be analyzed.

2. MATERIAL AND METHOD

2.1. Design of A New Metamaterial

Materials exhibit different behaviors in response to electromagnetic waves based on their electrical permittivity (ε) and magnetic permeability (μ) coefficients. In natural materials, these coefficients are typically positive values. In contrast, special materials known as metamaterials, which are produced in laboratory settings, can have both electrical (ε) and magnetic permeability (μ) coefficients that are negative. Depending on these coefficients, the materials designed and produced in the laboratory exhibit a negative refractive index. To classify a cell as a metamaterial, its refractive index must be negative, determined by the values of ε and μ. This can occur in three scenarios: Case 1, where only ε is negative within a specific frequency range; Case 2, where μ is negative; and Case 3, where both ε and μ are negative. A cell exhibiting any of these conditions within a given frequency range can be identified as a metamaterial for that range. Various approaches, such as the Nicholson-Ross-Weir method and other robust techniques, are commonly employed in the literature to compute these material parameters [17,18]. Thanks to these properties, metamaterials demonstrate electromagnetic characteristics that are not found in nature. To create such a metamaterial, a four-armed symmetric metamaterial (FASM) as shown in Figure 1 has been designed using the CST electromagnetic program. Both sides of the FASM have been designed in the same manner. The design parameters of the FASM are presented in Table 1.
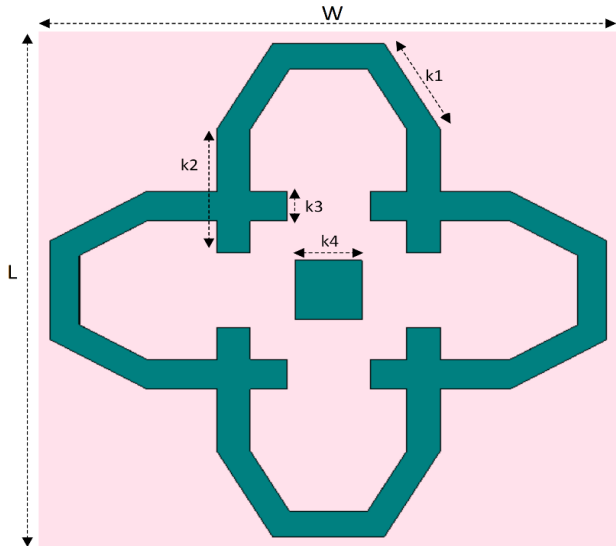

Figure 1. Four-armed symmetric metamaterial (FASM)

Table 1. FASM Design Parameters

Parameters	Value(mm)
Width(G)	5.5
Length(U)	5.5
Substrate Thickness	1.55
Metal Thickness	0.035
k1	1
k2	1.25
k3	0.3

k4	0.6

The FASM structure designed according to the parameters provided in Table 1 was simulated using the CST electromagnetic program, and the graphs of ε, μ and n refractive indices were obtained, as shown in Figure 2. The values given in the graph are the real parts of the expressions ,,. The simulation process was conducted in the frequency domain.
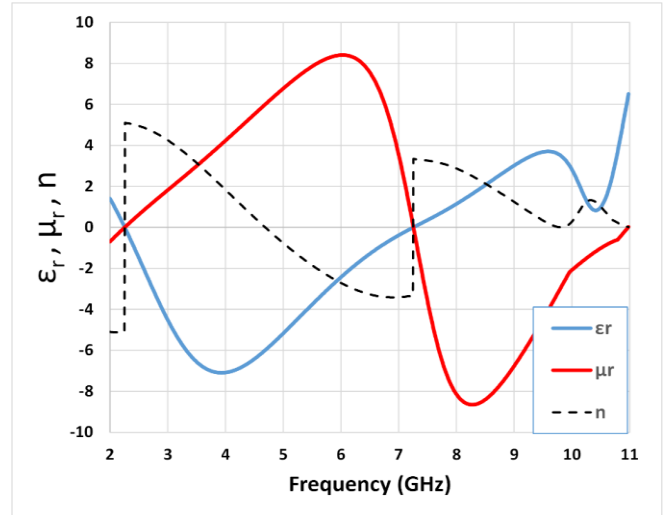

Figure 2. Graphs of ε_r, μ_r, n for the FASM

Upon examining Figure 2, it is clearly observed that the electrical permittivity of the FASM unit cell exhibits negative values between 2.38 GHz and 7.27 GHz. Similarly, it is noted that the cell demonstrates negative magnetic permeability between 7.27 GHz and 10.58 GHz. When these two observations are combined, it becomes evident that the refractive index (n) of the FASM cell is negative in the frequency range of 5.06 GHz to 7.27 GHz. Considering all these data collectively, it can be stated that the FASM unit cell exhibits metamaterial properties in a bandwidth of approximately 2.21 GHz. This characteristic indicates that the FASM cell has significant potential for advanced technology applications.

2. 2. Design of A Circular Patch Antenna (CPA)

In this study, a circular patch antenna was chosen as the reference antenna due to its ease of comparison, design, and production. The design process was carried out using the CST electromagnetic software, and a circular patch antenna (CPA) was designed on an FR4 substrate. The thickness of the substrate was selected as 1.55 mm, which is a standard used in the market. For the FR4 material, the loss tangent tan δ = 0.025 and Ɛr = 4.3 were chosen. All design parameters of the antenna were given in Table 2.

Table 2. CPA Reference Antenna Parameters

Parameters	Value(mm)
Width(W)	18
Length (L)	18
Substrate Thickness	1.55
Metal Thickness	0.035
R	7
m1	1.5
m2	3.6
m3	6.9

The antenna design, as shown in Figure 3, has been realized using an electromagnetic simulation program, with the parameters adjusted so that the resonance frequency of the antenna is 6.5 GHz.
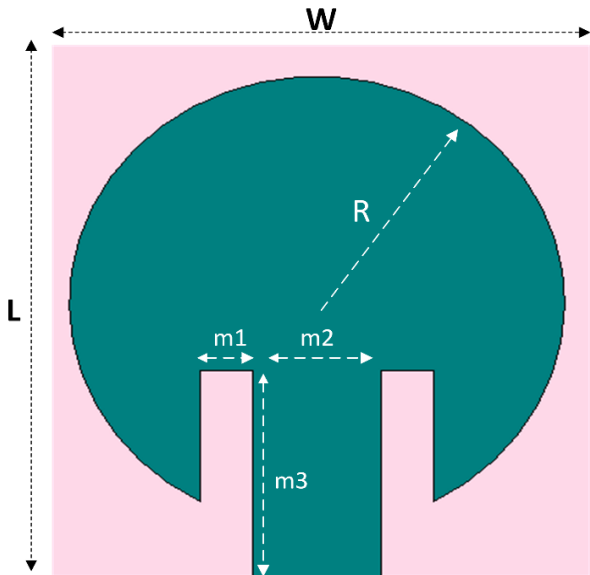

Figure 3. View of the reference antenna (CPA)

Subsequently, the antenna was simulated in the 5-8 GHz frequency range to obtain the gain and S11 values. Based on the simulation results, the antenna's return loss graph was generated, as illustrated in Figure 4.
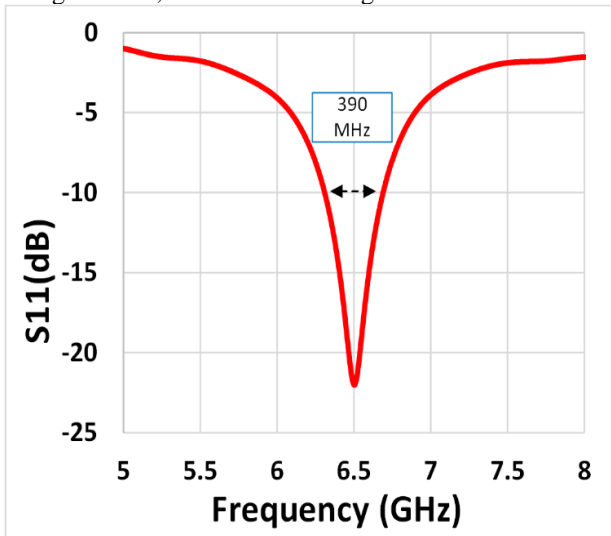

Figure 4. Return loss graph of the antenna (S11)

When the graph in Figure 4 is examined, it is noted that the antenna operates at a resonant frequency of 6.5 GHz within the 5-8 GHz range, and a return loss of 22.01 dB and bandwidth as 390 MHz are obtained at this value. Furthermore, the simulation conducted with the CST program produced the antenna's gain graph, which is displayed in Figure 5. According to this graph, the maximum gain was obtained as 2.8 dBi at an angle of -4 degrees.
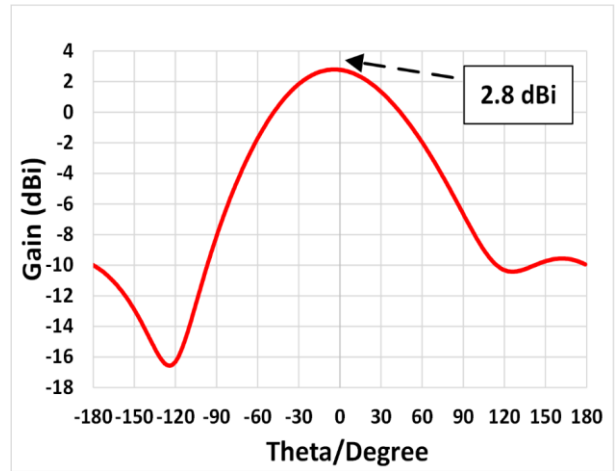

Figure 5. Gain graph of the CPA

3. RESULTS AND DISCUSSION

3.1. Application of The FASM Cell on The CPA

Metamaterial applications with electromagnetic antennas offer an innovative solution to improve antenna performance. The negative refractive index and unique electromagnetic properties of metamaterials can enhance antenna efficiency, reduce their size, and improve undesired radiation patterns. By placing metamaterials on or around circular patch antennas, they provide advantages such as lowering the operating frequency, increasing gain, and improving directivity. Especially in narrow-space applications, metamaterials can elevate the performance parameters of the antenna to levels that cannot be achieved through traditional methods. Such integration paves the way for more efficient and compact antenna designs in wireless communications, radar systems, and satellite communication [19, 20]. In this section, the impact of using FASM unit cells in conjunction with a circular patch antenna on the antenna's performance has been examined. To achieve this, a lens layer consisting of 9 unit cells (3x3), as shown in Figure 6, was created using FASM unit cells, with identical front and back layers.
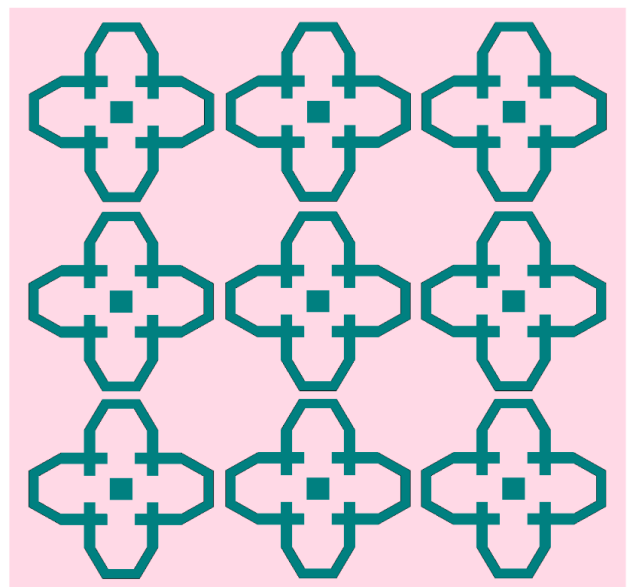

Figure 6. View of the FASM lens layer

In the next step, a lens layer composed of FASM unit cells was placed in front of the CPA as a single layer, as shown in Figure 7. The resulting structure was simulated at various distances between the antenna and the lens layer by utilizing the parameter sweep function of the CST program, and the results were given in Table 3. When Table 3 is examined, it is observed that the best gain value was obtained as 3.77 dBi for a distance of 15 cm, which is 34.64% higher than the gain of the reference antenna.
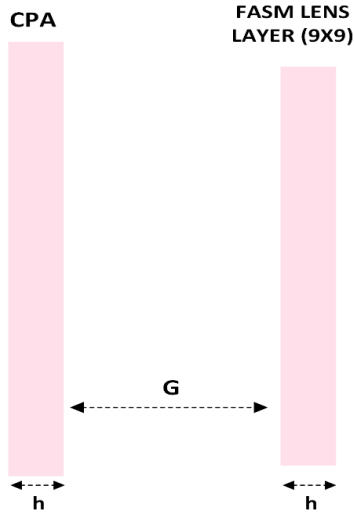

Figure 7. Usage of the CPA together with the FASM lens layer

Table 3. Antenna gain values according to the distance between single layer FASM lens-CPA

Gap (G)(mm)	Gain(dBi)	Gain Increase (%)
5	1.76	-37.14%
7.5	2.93	4.64%
10	3.51	25.36%
12.5	3.7	32.14%
15	3.77	34.64%
17.5	3.71	32.50%
20	3.73	33.21%

In the next step, as shown in Figure 8 and Figure 9, another lens layer made with FASM was added in front of the CPA, and the resulting structure was re-simulated by varying the distances between the antenna and the lens layers. The gap between the antenna and the first lens layer was fixed at 15 mm (G), while the simulation was conducted by varying the distance (T) between the two lens layers. The gain values obtained according to the changes in the intermediate distances are given in Table 4. Additionally, to allow for comparison on the graph, the gain graph (maximum value taken) for the reference antenna and the proposed antenna's single-layer and double-layer usage is provided in Figure 10. Additionally, the S11 graph of the reference antenna and the proposed structure is given in Figure 11.
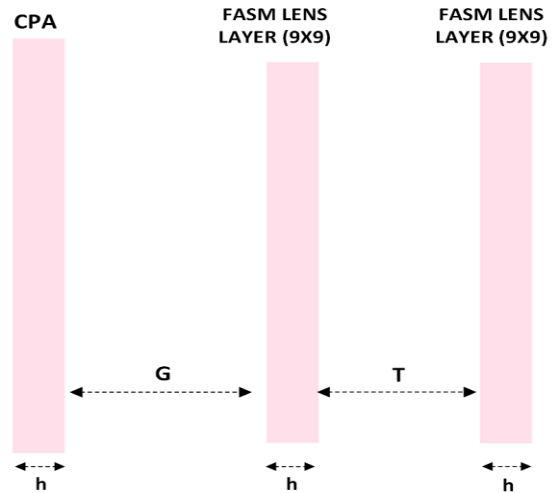

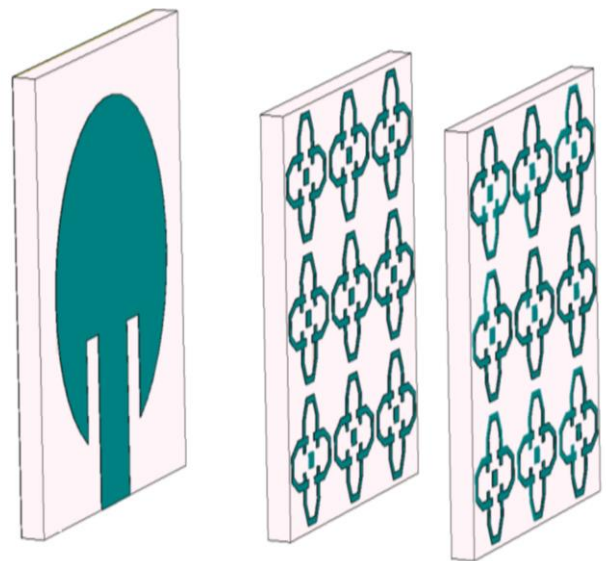**Figure 8.** Usage of the CPA together with the double layers FASM lens

Figure 9. 3D view of the CPA together with the double layers FASM lens

Table 4. Antenna gain values according to the distance between FASM lens layers

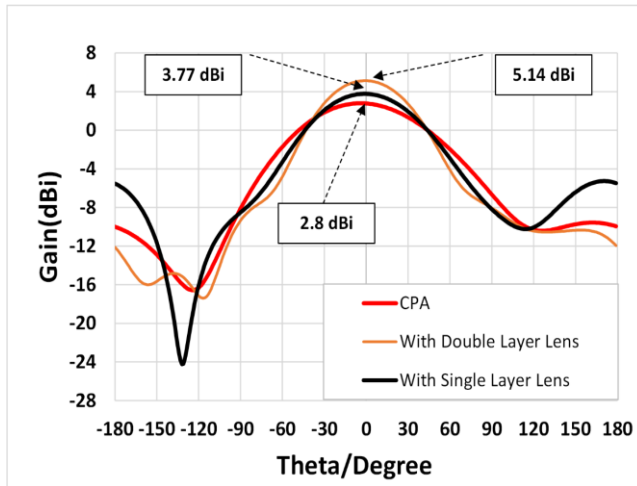| Gap (T)(mm)	Gain(dBi)	Gain Increase (%)
5	4.25	51.79%
7.5	4.57	63.21%
10	4.95	76.79%
12.5	5.14	83.57%
15	5.07	81.07%
17.5	4.98	77.86%
20	4.7	67.86%

Figure 10. Comparison of the gain graphs between reference antenna and proposed antenna.
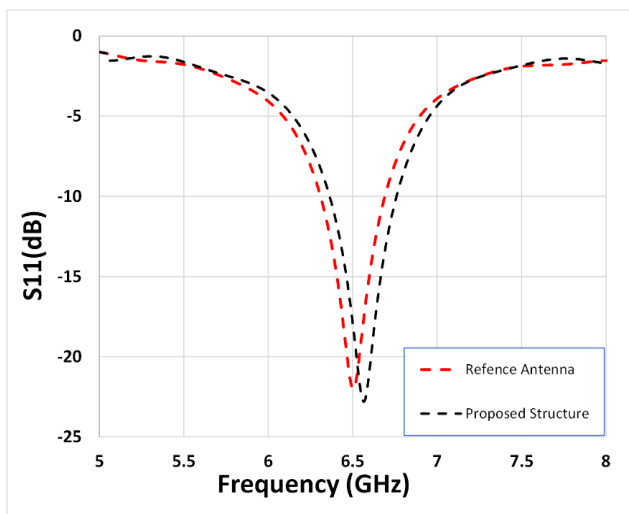

Figure 11. S11 graphs of reference antenna and proposed antenna.

When Table 4 and Figure 10 is examined, it is observed that the highest gain value, 5.14 dBi, is obtained when the distance (T) between the lens layers is 12.5 mm (with G=15 mm). This gain value is 83.57% higher than the gain of the reference antenna. In light of these results, it has been demonstrated that the use of lens layers made with FASM unit cells together with the CPA results in a significant increase in the antenna's gain. In addition, as seen in Figure 11, the resonant frequency of the proposed antenna shifted slightly to 6.7 GHz and its bandwidth was obtained as 527 MHz. This value is 137 MHz more than the bandwidth of the reference antenna.

4. CONCLUSION

In conclusion, this study successfully designed and demonstrated the effectiveness of a novel four-armed symmetric metamaterial (FASM) in improving the performance of a circular patch antenna (CPA). The FASM, when applied as a lens layer in both single and double configurations, yielded substantial gains in antenna performance. The maximum gain increase observed was 83.57%, which was achieved with a double-layer FASM configuration. These results confirm that metamaterials can provide significant enhancements in antenna gain and directivity, making them valuable for a

wide range of applications in wireless communications, radar, and satellite technologies. The integration of metamaterials into antenna designs presents a promising approach to achieving more compact, efficient, and high-performing antennas. Future research may focus on further optimizing these structures for different frequency bands and exploring their potential for other applications in advanced technologies.

REFERENCES

[1] Veselago VG. The electrodynamics of substances with simultaneously negative values of ε and μ. Soviet Physics Uspekhi. 1968, 10(4), 509-514. https://doi.org/10.1070/PU1968v010n04ABEH003699

[2] Smith DR, Padilla WJ, Vier DC, Nemat-Nasser SC, Schultz S. Composite medium with simultaneously negative permeability and permittivity. Physical Review Letters. 2000; 84(18):4184-4187. https://doi.org/10.1103/PhysRevLett.84.4184

[3] Pendry JB. Negative refraction makes a perfect lens. Physical Review Letters. 2000; 85(18):3966-3969. https://doi.org/10.1103/PhysRevLett.85.3966

[4] Shalaev VM. Optical negative-index metamaterials. Nature Photonics. 2007; 1(1): 41-48. https://doi.org/10.1038/nphoton.2006.50

[5] Valentine J, Zhang S, Zentgraf T, Ulin-Avila E, Genov DA, Bartal G, Zhang X. Three-dimensional optical metamaterial with a negative refractive index. Nature. 2008; 455(7211): 376-379. https://doi.org/10.1038/nature07238

[6] Fang N, Zhang X. Imaging properties of a metamaterial superlens. Applied Physics Letter.2003; 82(2): 161-163. https://doi.org/10.1063/1.1539261

[7] Liu Z, Lee H, Xiong Y, Sun C, Zhang X. Far-field optical hyperlens magnifying sub-diffraction-limited objects. Science. 2007; 315(5819):1686-1686. https://doi.org/10.1126/science.1139890

[8] Cui TJ, Smith DR, Liu R. Metamaterials: Theory, Design, and Applications. Springer; 2010. https://doi.org/10.1007/978-3-642-03453-2

[9] Zheludev NI, Kivshar YS. From metamaterials to metadevices. Nature Materials. 2012; 11(11), 917-924. https://doi.org/10.1038/nmat3341

[10] Khanikaev AB, Mousavi SH, Tse WK, Kargarian M, MacDonald AH, Shvets G. Photonic topological insulators. Nature Materials. 2013; 12: 233-239. https://doi.org/10.1038/nmat3520

[11] Lu L, Joannopoulos JD, Soljačić M. Topological photonics. Nature Photonics. 2014; 8 (11): 821-829. https://doi.org/10.1038/nphoton.2014.227

[12] Urul B. Dielektrik alt tabaka parametrelerinin metamateryal ile mikroşerit anten kazancının artırılmasına etkisi. Igdir University Journal of the Institute of Science and Technology. 2020; 10(2): 944-955. https://doi.org/10.21597/igusbd.751301

[13] Urul B. High-gain UWB antenna optimized with particle swarm optimization using metamaterial lens layer for satellite communication applications. International Journal of RF and Microwave

Computer-Aided Engineering. 2022; 32(9): e23280. https://doi.org/10.1002/mmce.23038

[14] Urul B. The effect of etched FSMM on the circular patch antenna using DGS method. International Congress on Human-Computer Interaction, Optimization and Robotic Applications (HORA). IEEE, 2020; p. 1-4. https://doi.org/10.1109/IMS.2020.9149721

[15] Li X, Wu SB, Wang Y, Hu Y. Design of broadband metamaterial absorbers in the near-infrared region. Advanced Theory and Simulations. 2024; 7(1), Article 2400839. https://doi.org/10.1002/adts.202400839

[16] Yixin L, Chenxia L, Bo F, Liang C, Jianfeng X, Fuhai L, Lizhen X, Xiao L, Ying T, Zhi H, Xufeng J. Research Progress in Tunable Metamaterial Absorbers. Advanced Photonics Research. 2024; Vol. 5, no. 2.

[17] Shi Y, Hao T, Li L, Liang CH. An improved NRW method to extract electromagnetic parameters of metamaterials. Microwave Optical Technology Letters, 2016; Vol. 58, Issue 3, Pages 647-652, 2016.

[18] Shi Y, Li ZY, Li L, Liang CH. An electromagnetic parameters extraction method for metamaterials based on phase unwrapping technique. Waves Random Complex Medium, 2016, Vol. 26, Issue 4, Pages 417-433.

[19] Chen X, Grzegorczyk TM, Wu BI, Kong JA. Robust method to retrieve the constitutive effective parameters of metamaterials. Physical Review E. 2004; 70(1): 016608. https://doi.org/10.1103/PhysRevE.70.016608

[20] Barroso JJ, Hasar UC. Resolving phase ambiguity in the inverse problem of transmission/reflection measurement methods. Journal of Infrared, Millimeter, and Terahertz Wave.2011; 32(7): 857-866. https://doi.org/10.1007/s10762-011-9800-1

Türk Doğa ve Fen Dergisi
Turkish Journal of Nature and Science

Cascade Control of Single Input Multi Output Buck Converter for Synchronous Charging Applications of Battery/Ultracapacitor Hybrid Energy Storage Systems

Muhammed Reşit ÇORAPSIZ[1*] iD

[1] Erzurum Technical University, Faculty of Engineering and Architecture, Department of Electrical & Electronics Engineering, Erzurum, Türkiye
Muhammed Reşit ÇORAPSIZ ORCID No: 0000-0001-5477-5299

*Corresponding author: r.corapsiz@erzurum.edu.tr

Abstract: In the near future, seeing more than one energy storage device in mobile device power systems will be possible. In today's technology, although Lithium-ion (Li-ion) battery cells stand out with their high energy density and superior cell voltage advantages, they suffer from limited cycle lives. A highly efficient hybrid power system can be created when high-power density ultracapacitors (UC) are combined with battery cells. However, since the cell voltages and power densities of these two energy storage devices are not equal, both the charge voltages and charge currents will be different from each other. This study proposes a single-input, multi-output cascade buck converter structure to synchronously charge battery and ultracapacitor cells. Converter parameters are calculated according to the charge powers of energy storage devices, and a cascade controller structure is designed to control charge current and cell voltage separately. The proposed synchronous charging system is tested using two different procedures: constant current (CC) mode, where reference currents are closely monitored, and constant voltage (CV) mode, where the charge voltage is limited. According to the results obtained, it was observed that the proposed system closely followed the reference currents in a short time of $6ms$ with a slight overshoot rate of approximately 8% in all tests.

103

Pil/Ultrakapasitör Hibrit Enerji Depolama Sistemlerinin Senkron Şarj Uygulamaları İçin Tek Girişli Çok Çıkışlı Düşürücü Dönüştürücünün Kademeli Kontrolü

Öz: Yakın gelecekte, mobil cihaz güç sistemlerinde birden fazla enerji depolama aygıtı görmek mümkün olacaktır. Günümüz teknolojisinde Lityum-iyon (Li-ion) pil hücreleri yüksek enerji yoğunluğu ve üstün hücre voltajı avantajlarıyla öne çıksa da sınırlı çevrim ömürlerinden muzdariptir. Yüksek güç yoğunluklu ultra kapasitörler (UC) pil hücreleriyle birleştirildiğinde, oldukça verimli bir hibrit güç sistemi oluşturulabilir. Ancak, bu iki enerji depolama aygıtının hücre voltajları ve güç yoğunlukları eşit olmadığından hem şarj voltajları hem de şarj akımları birbirinden farklı olacaktır. Bu çalışmada, pil ve ultra kapasitör hücrelerini senkron olarak şarj etmek için tek girişli, çok çıkışlı bir kademeli düşürücü dönüştürücü yapısı önerilmiştir. Dönüştürücü parametreleri, enerji depolama aygıtlarının şarj güçlerine göre hesaplanmış ve şarj akımlarının ve hücre voltajlarının ayrı ayrı kontrolü için bir kademeli denetleyici yapısı tasarlanmıştır. Önerilen senkron şarj sistemi, referans akımlarının yakından izlendiği sürekli akım (CC) modu ve şarj voltajının sınırlandırıldığı sürekli voltaj (CV) modu olmak üzere iki farklı prosedür kullanılarak test edilmiştir. Elde edilen sonuçlara göre önerilen sistemin tüm testlerde yaklaşık %8'lik hafif bir aşma oranıyla $6ms$ gibi kısa bir sürede referans akımlarını yakından takip ettiği gözlenmiştir.

1. INTRODUCTION

Governments and countries' global economic growth targets and the increased industrialization rate have caused a significant increase in energy consumption levels in recent years [1, 2]. The development of energy storage systems has an active role in spreading portable electronic devices and advancing minimum carbon footprint targets [3-5]. The energy and power capacities of energy storage devices are very important for the sustainability of these systems. In addition to these critical features, power converters provide bidirectional power flow from energy storage devices to the load side and from the load side to the energy storage devices [6]. Power electronic converters are frequently used in renewable energy systems due to the constant DC bus voltage required for high power quality [7-9]. As is known, the cell voltages of energy storage devices (e.g., battery or ultracapacitor cells) decrease over time in the discharge state [10]. This situation continues up to a specific cut-off voltage in battery cells. In contrast, the terminal voltage of an ultracapacitor can continue till close to zero depending on the discharge current amplitude in the ultracapacitor cell. Power electronic converters are designed not to reflect this change on the load side. In addition, since the terminal voltages and discharge capacities of the mentioned energy storage cells are limited, series and parallel connection of these devices may not meet this demand in loads that require high supply voltage or high supply current. In energy storage systems, if the terminal voltage on the source side is greater than the supply voltage on the load side, buck converters (conventional buck [11], quadratic buck [12], buck-boost [13], etc.) are used. If the supply voltage on the load side is greater than the terminal voltage on the source side, boost converters (conventional boost [14], Cuk [15], SEPIC [16], buck-boost, etc.) are used to equalize the source-load potential. Energy storage devices should be charged with a limited terminal current generated at a limited terminal voltage. These limited values are usually provided by the manufacturer. These values should not be exceeded during the charging and discharging processes for long-term use and safe operation of the devices [17]. Therefore, in an energy storage system designed using power converters, only averaged voltage mode control or averaged current mode control may not fully meet a high-performance and high-security charging process. As a result, separate control of the charging voltage and charging current is essential for performance and efficiency, especially safety in energy storage devices. In [12], a second-order buck converter was proposed as a competitive alternative to battery charging systems. In the study where the cascade control technique was used in charge control, a constant current constant voltage (CC-CV) charging protocol was adopted using three control loops. This protocol is the most common method for charging battery cells or packs. In [18] a bidirectional buck-boost converter was used to provide power from the sources to the vehicle drive system and store regenerative braking currents for electric vehicles consisting of battery and supercapacitor packs. A fully active topology structure was used in the study, and a two-stage control technique was applied over the

inductor current and DC bus voltage. However, the external charging states of the battery and supercapacitor packs were not examined. Most studies on energy storage systems consisting of battery and supercapacitor packs have focused on efficiently sharing energy and power between these two sources [19-21]. In systems with hybrid energy storage units, the charging conditions of the devices are as important as the effective power sharing between the devices. Especially in electric vehicles containing battery and supercapacitor packs, the state of charge (SoC) of the battery and supercapacitor packs may differ after a specific driving cycle [22]. This is usually due to the power-sharing technique adopted in energy management. In addition, the different energy and power densities of the devices are another factor affecting the SoC difference [23]. It has been reported that operating lithium-ion batteries, which are frequently used in electric vehicles, in the $10\% - 70\%$ SoC range positively affects battery health and life [24]. This range can be used for much more expansive limits for ultracapacitor packs. However, ultracapacitors used in hybrid energy storage systems are generally preferred to protect the battery packs from high currents during charging and discharging [25]. Therefore, the supercapacitor packs in these systems should be operated in a SoC range that can provide power to the load at any time on demand and store the recovered energy from the load at any time [26]. Considering these critical limits, at the end of a certain driving cycle for electric vehicles or the end of a certain load supply for energy storage systems, the battery and ultracapacitor must be charged to meet the next load requirements. The charging process can be carried out in three ways: i) While the battery group is charged, the ultracapacitor group can be charged using only the recovered energy, considering it operates within a specific SoC range, ii) After the battery group is charged, the charging requirement of the ultracapacitor group can be provided by the battery group with the help of a power converter. Both techniques mentioned above can extend the charging time of the ultracapacitor group, shorten the battery usage time, and negatively affect the system's efficiency. iii) The battery and ultracapacitor group can charge synchronously via a cascade-connected power converter. Thus, the battery and ultracapacitor groups are charged to the determined maximum SoC level at the end of the charging process. The third step emphasizes the main contribution of this study. A new technique based on synchronous charging of both battery and ultracapacitor packs via a single-input multi-output buck converter is proposed to make a critical contribution to this process. The proposed synchronous charging technique will prevent the negatives mentioned in i) and ii) since it will charge the battery and ultracapacitor packs simultaneously. Thus, the ultracapacitor can provide the necessary power at any time and store the necessary energy.

The present paper is organized as follows. Section 2 and Section 3 explain the energy storage principles and electrical equivalent circuits of Li-ion battery and ultracapacitor cells, respectively. Section 4 examines the structure, design and control of the cascade buck converter in detail. Results and discussion are presented

in Section 5, while Section 6 includes the main findings of this study.

2. LITHIUM-ION (LI-ION) BATTERIES

Critical features such as high energy density, long service life, wide operating temperature range, and low self-discharge are desired in batteries used in energy storage systems [27]. Among these critical features, energy density affects the energy supply time of the battery, while service life refers to the service period until the battery reaches the end of life (EoL). It is generally assumed that a battery cell has reached EOL when it has lost 20% of its initial capacity [28]. The battery cell must have high SoC retention capability and low self-discharge under negative temperature conditions, especially in electric vehicles with battery/ultracapacitor packs located in regions with intense winter conditions or in energy storage systems. Considering the features explained above, Lithium-ion batteries, which have these critical advantages, are frequently preferred in today's technology in electric vehicles and energy storage systems. Figure 1 represents the internal structure of a Li-ion battery cell [29].
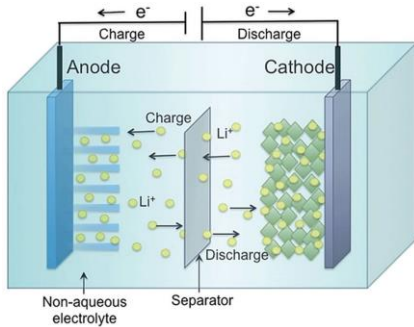

Figure 1. Behavior of a Lithium-ion battery (LiB) under charge and discharge conditions

Lithium-ion batteries, commercialized by SONY in the last quarter of the 20th century, consist of a lithium metal oxide cathode, an electrolyte made of lithium salt, and a graphite anode [30]. In addition, a separator in the electrolyte prevents the electron transfer from the anode to the cathode during charging and from the cathode to the anode during discharging. In a commercialized Li-ion battery cell, the cathode is usually coated on a copper layer and the anode on an aluminum layer. The positively charged Li+ ions are attracted to the negative terminal when the cell is charged. During this time, the electrons flow in the opposite direction of the current path and pass to the cathode region. The cell is said to be fully charged when this process is completed. During the discharge process, this reaction occurs oppositely. An electrical equivalent circuit can usually represent this complex electrochemical transformation. The Li-ion battery cell in MATLAB/Simulink Simscape/Electrical was used for the simulation tests in this study. This cell uses the Shepherd electrical equivalent circuit model shown in Figure 2.

The Shepherd battery model in Figure 2 is shown among the best-known electrical equivalent circuit models, and the relationships in the charge-discharge state are given as follows [31].

$$v_{bat} = E_{bat} - R_{bat}i_{bat} \tag{1}$$

$$E_{ch} = E_0 - K\left(\frac{Q}{it + 0.1Q}\right)i^* - K\left(\frac{Q}{Q - it}\right)it - R_{bat}i + Ae^{-B.it} \tag{2}$$

$$E_{disch} = E_0 - K\left(\frac{Q}{Q - it}\right)i^* - K\left(\frac{Q}{Q - it}\right)it - R_{bat}i + Ae^{-B.it} \tag{3}$$
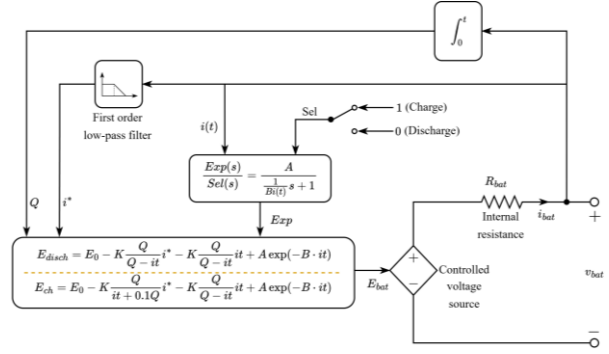

Figure 2. Shepherd battery model

In the notations in Equations 1-3, E_{disch} and E_{ch} represent the discharge and charge voltages (V), E_0 is the open circuit voltage (OCV) (V), V_{bat} is the battery terminal voltage (V), K is the polarization resistance coefficient (Ω), Q is the battery capacity (Ah), i_{bat} is the battery current (A), i^* is the filtered battery current (A), R_{bat} is the battery internal resistance (Ω), t is the time (h), A, B are empirical constants (V), (1/Ah), respectively. While the inside of the i^* term in Equation 3 represents the polarization resistance, the inside of the it term represents the polarization voltage. The parameters E_0, R_{bat}, K, A, B in Equations 2 and 3 are determined using the nominal voltage (V) and rated capacity (Ah) values. In this model, the ampere-hour counting technique given in Equation 4 is used to determine the battery state of charge (SoC).

$$SoC_{bat} = SoC_{init-bat} - \frac{1}{3600 * Q}\int i_{bat}dt \tag{4}$$

In this study, a single cell known as the cylindrical 18650 model, which many battery manufacturers commercialize, is used to perform the proposed synchronous charging process. Various electrical characteristics of this cell are given in Table 1.

Table 1. Electrical parameters of the battery cell

Parameter	Description	Value	Unit
R_{bat}	Internal resistance	14.4	mΩ
V_{bat}	Nominal voltage	3.6	V
Q_{rated}	Rated Capacity	2.5	Ah
$V_{cut-off}$	Cut-off voltage	2.7	V
V_{full}	Fully charged voltage	4.19	V
I_{d-nom}	Nominal discharge current	1.087	A
$SoC_{init-bat}$	Initial state of charge	50(%)	-

The electrical parameters given in Table 1 were determined by considering the values of a commercialized

battery cell. These battery parameters can be found in the following reference [32].

3. ULTRACAPACITORS

The limited power density, limited cycle life, and limited charge and discharge currents of battery technologies used in energy storage systems can cause range problems in electric vehicles and intermittent power flow in grid-connected systems. Since battery groups convert chemical energy into electrical energy, they have slow dynamics due to a series of chemical reactions. In addition, the lithium inventory loss (LLI) during each charge and the active material loss (LAM) that arises depending on the number of cycles limit the battery service life. Therefore, using ultracapacitors with high power density and cycle life [33], and can withstand sudden current changes in energy storage systems containing battery packs has contributed to solving the abovementioned problems. Another feature of ultracapacitors is that they can store energy produced from intermittent renewable energy sources (e.g., wind and solar) or high regenerative currents occurring in electric vehicles.
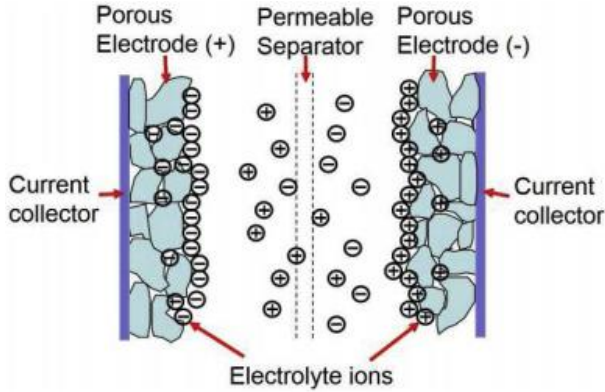

Figure 3. Structure of an ultracapacitor in the charged state

A schematic diagram of an ultracapacitor in the charged state is shown in Figure 3 [34]. An ultracapacitor or electric double layer capacitor (EDLC) consists of two porous electrodes, two electrolytes, a separator, and a current collector. Since the porous electrodes increase the surface area, these devices can be manufactured up to thousands of Farads. The capacitance of an ultracapacitor is similar to that of conventional capacitors and can be given as follows.

$$C_{UC} = \frac{\varepsilon_r \varepsilon_0 A}{d} \qquad (5)$$

In Equation 5, C represents the capacitance of the ultracapacitor, ε_r is the dielectric constant of the electrolyte, ε_0 is the dielectric constant of the vacuum, d is the effective thickness of the double layer, and A is the accessible surface area. In addition, the separator immersed in the electrolyte prevents electrical contact between the electrodes [35]. The energy stored in an ultracapacitor is given as follows:

$$W_{uc} = \frac{1}{2} C_{uc} V_{uc}^2 \qquad (6)$$

In Equation 6, W_{uc} represents the amount of stored energy, C_{uc} represents the capacitance, and V_{uc} represents the terminal voltage. As in battery applications, ultracapacitors can also be represented by electrical equivalent circuit models. The Zubieta model [36] is often preferred among these equivalent circuits, as it provides close values in both simulation and experimental applications.
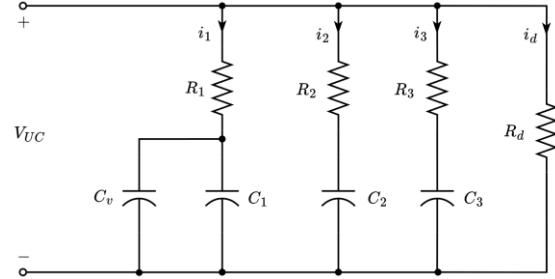

Figure 4. Zubieta ultracapacitor model

In the notations in Figure 4, C_1, C_2, and C_3 represent fixed capacitances, and C_v represents voltage-dependent capacitance (Differential capacitance). R_1, R_2, and R_3 represent fixed resistances, R_d represents self-discharge resistance, i_1, i_2, i_3, and i_d represent the branch current to which they are connected. To represent the voltage-dependent capacitance gain K_v, the i_1 current in the electrical equivalent circuit can be expressed as follows depending on the voltage (V_{C_1}) between the C_v and C_1 capacitors.

$$i_1 = \left(C_1 + K_v V_{C_1}\right)\frac{dV_{C_1}}{dt} \qquad if \ V_{C_1} > 0 \qquad (7)$$

$$i_1 = C_1 \frac{dV_{C_1}}{dt} \qquad if \ V_{C_1} < 0 \qquad (8)$$

The currents of the second and third branches can be determined by $i_n = C_n \frac{dV_{C_n}}{dt}, \{n \in 2,3\}$. The SoC of the ultracapacitor is directly proportional to the terminal voltage and can be determined as follows.

$$SoC_{uc} = \frac{Q_{init-uc}}{C_{uc}V_{uc}} \int i_{uc} dt \qquad (9)$$

The electrical properties of the cylindrical model ultracapacitor cell for the synchronous charging process proposed in this study are given in Table 2.

Table 2. Electrical parameters of the ultracapacitor cell

Parameter	Description	Value	Unit
R_{ESR}	Equivalent series resistance	8.9	mΩ
V_{rated}	Rated voltage	2.7	V
C_{rated}	Rated Capacity	30	F
V_{init}	Initial voltage	1.5	V
$SoC_{init-uc}$	Initial state of charge	49.5(%)	-

The electrical parameters given in Table 2 were determined by considering the values of a commercialized

ultracapacitor cell. These ultracapacitor parameters can be found in the following reference [37].

4. BUCK CONVERTER

DC-DC converters are power electronic devices used to meet load requirements with different voltage and current levels. Buck converters with low voltage gain can theoretically change the voltage applied from the input stage to the output stage between zero and the input voltage thanks to the appropriate switch duty ratio ($d = V_o/V_s$). For this reason, they are widely used in mobile devices, wearable technologies, battery applications, electric vehicles, and energy harvesting systems where low voltage is required [38].
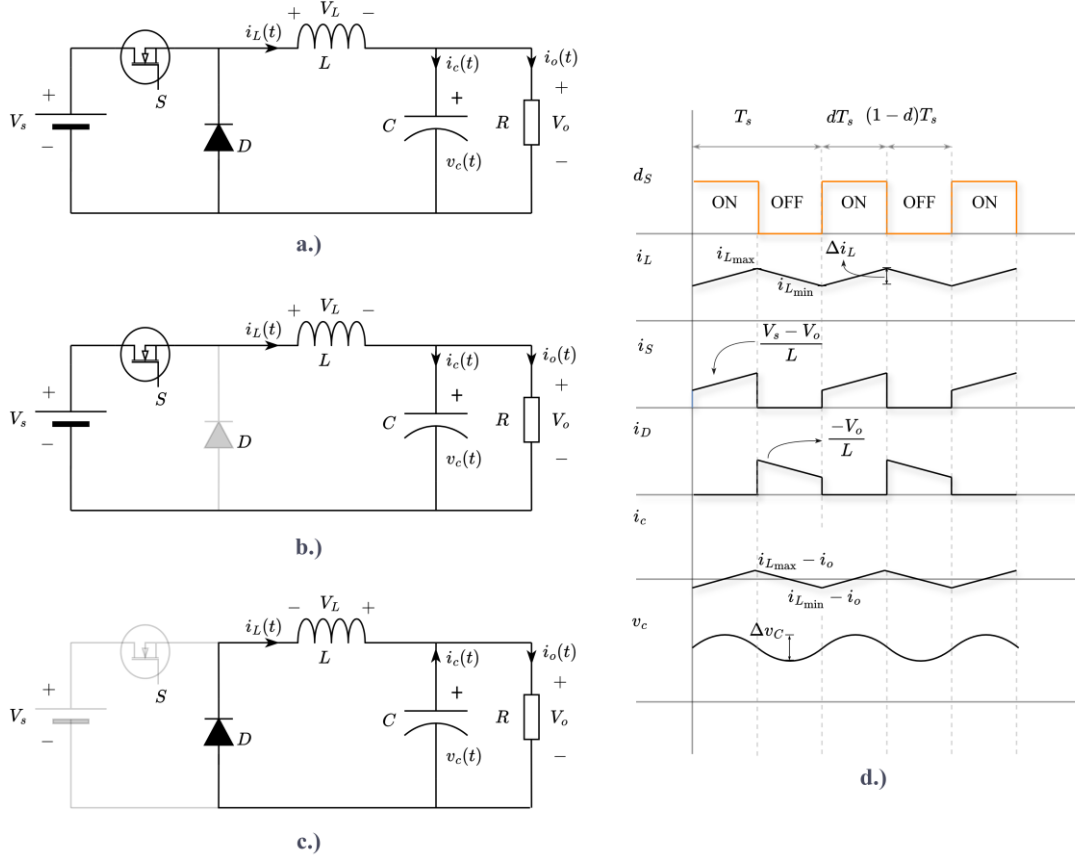

Figure 5. Buck converter operating modes and waveforms

Buck converters consist of an inductor (L) to ensure the continuity of the load current (i_o), a power MOSFET (S) positioned between the source (V_s) and the load (R) to adjust the load voltage (V_o), a diode (D) that will work complementarily with this MOSFET and a capacitor (C) to prevent load voltage ripples. The equivalent circuit of a conventional buck converter is shown in Figure 5a. As in conventional DC-DC power converters, the operation of the buck converter is examined in two modes. These modes are determined by the on and off states of the switch S.

$$L\frac{di_L(t)}{dt} = V_s - (1 - d(t))V_c(t) \qquad (10)$$

$$C\frac{dV_c(t)}{dt} = i_L(1 - d(t)) - \frac{V_c(t)}{R} \qquad (11)$$

Mode 1 starts with the S switch turning on, as shown in Figure 5b, and theoretically, the inductor current is assumed to increase linearly (dT_s). Mode 2, shown in Figure 5c, starts when switch S completes its duty cycle. In this case, D is turned on. The switching between S and D occurs immediately in simulation applications but requires a very short dead time interval (usually in the microsecond levels) in experimental applications. In this case, the inductor current is assumed to decrease linearly $(1 - dT_s)$. In the buck converter circuit in Figure 5a, $\dot{x}(t) = [i_L(t) \quad V_C(t)]^T$ are the state variables. When the switching function d is considered, the state equations of the circuit are as in Equations 10 and 11.

The linear model of the DC-DC buck converter can be modeled in the MATLAB/Simulink simulation environment using Equations 10 and 11. In addition, using these equations, the state space matrices and transfer functions of the buck converter can be written as follows.

$$A = \begin{bmatrix} 0 & -1/L \\ 1/C & -1/RC \end{bmatrix}, B = \begin{bmatrix} 1/L \\ 0 \end{bmatrix} V_s, C = [0 \quad 1] \quad (12)$$

$$G(s) = \frac{V_s/LC}{s^2 + (1/RC)s + 1/LC} \qquad (13)$$

107

3.1. Buck Converter Design

Power converters are generally examined in two operating modes, namely continuous conduction mode (CCM) and discontinuous conduction mode (DCM) [39]. In Mode 1 in CCM, the load power is supplied by the input source, while it is supplied by the inductor only in Mode 2. In DCM, Mode 1 occurs the same way as CCM, but the load power drops to zero in Mode 2. The charging current and voltage should be continuous in power converters operating in energy storage systems. Otherwise, thermal problems will likely occur in battery cells exposed to intermittent charging currents. Therefore, the minimum values of the passive elements operating the battery and ultracapacitor in CCM mode must be determined. While determining these values, some assumptions are made for the fluctuation levels of the inductor current, capacitor voltage, and switching frequency. The manufacturer provides the charging and discharging current limits of the battery cells. In these values, charging limits are usually $1C$, while discharging limits can go up to $10C$ [32]. The C value is used to express battery capacities and is defined as the discharge current that will discharge a fully charged battery in 1 hour. Considering the electrical properties of the battery cell used in our study, the maximum charge current should be limited to $1C$ ($2500mA$). If the charge voltage is $4.2V$, the converter output power (P_o) should be $10.5W$. When switching and conduction losses are considered, it can be said that a converter with a power of $15W$ will be sufficient. Assuming that the ripple in the inductor current (Δi_L) in Figure 5d is $0.2A$ (this value is usually between 20% and 40% of the output current), the ripple in the capacitor voltage (Δv_C) is $2mV$, and the switching frequency (f_s) is $100kHz$, the filter inductor and capacitor values can be calculated as follows.

$$L_j = \frac{V_o(V_s - V_o)}{f_s \Delta i_L V_s}, j \in \{bat, uc\} \tag{14}$$

$$C_j = \frac{\Delta i_L}{8 f_s \Delta V_C}, j \in \{bat, uc\} \tag{15}$$

According to Equations 14 and 15, converter inductances $L = 0.682mH$ and capacitances $C = 30\mu F$ were selected considering converter losses. The values of passive elements should be selected higher than the calculated minimum values, considering the operating conditions of the converter at a very low duty ratio.

Table 3. Electrical parameters of the buck converters

Parameter	Description	Value	Unit
V_s	Input voltage	12	V
L	Inductance	0.628	mH
C_{dc}	DC link Capacitance	30	μF
R_{dc}	DC link resistance	200	kΩ
f_s	Switching frequency	100	kHz

Especially in buck converters with intermittent input current, operating conditions at high switching frequencies and low duty ratios may disrupt the continuity of the output current. Therefore, it should not be forgotten that the calculated passive element values are the critical values required to provide the specified conditions. In this study, the electrical parameters of the single-input multi-output buck converter designed at the same power for battery and ultracapacitor synchronous charging are given in Table 3. The DC link resistance (R_{dc}), not included in the design phase in Table 3, prevents the output current from dropping to zero when the battery or ultracapacitor cell is disconnected from the charging terminal. If not, the output voltage increases excessively, creating a safety risk. The R_{dc}, limits the voltage by keeping the converter output current at a minimum level, eliminating this risk.

3.2. Cascade Control of Cascade Buck Converter for Proposed Synchronous Charge Architecture

In charging applications of energy storage devices, cell voltage and current must be controlled separately. This process is achieved by the CC-CV charging technique, which is frequently used to extend the battery's service life and increase charging efficiency [40]. Power electronic converters are usually controlled by average voltage or current control. However, terminal voltage may reach dangerous limits in energy storage systems if only current control is performed. Similarly, when only voltage control is performed, unlimited cell current may cause irreversible damage to the physical and chemical properties of the cell [41]. Compared to ultracapacitors, the critical control limits mentioned above are more effective in battery cells. Since ultracapacitors have high power density, they can withstand high charging currents without compromising their cycle life and physical properties. Since the battery and the ultracapacitor cell will be charged synchronously in this study, the buck converter designed in Section 4.1 was modified to be single-input and multi-output. Figure 6 shows the general structure of the system designed for synchronous charging. The power stage is formed by cascading two buck converters in such a way that the input voltages are the same and the output voltages are different. Detailed information on the implementation of the Cascade control structure for power converters can be found in the following reference [13]. The outputs of the converters are connected to the battery and ultracapacitor cells, respectively. The control algorithms implemented for cascade control of the relevant converter are shown in the upper part of the battery converter and the lower part of the ultracapacitor converter. In both control flows, the input reference voltages ($V_{j,ref}, j \in \{bat, uc\}$) are cell charge limit voltages [42]. The reference voltages are compared with the cell voltages, and a reference current value is generated to adjust the charge current. This value is limited by the maximum charge and discharge currents provided by the manufacturer with dynamic saturation. Ultracapacitors can withstand much higher charge currents than this limit current. However, the battery and ultracapacitor currents were selected with closer amplitudes for the synchronous charging application carried out in this study. The dynamic saturation generates the reference charge current ($I_{j,ref}, j \in \{bat, uc\}$), which is compared with the output current.
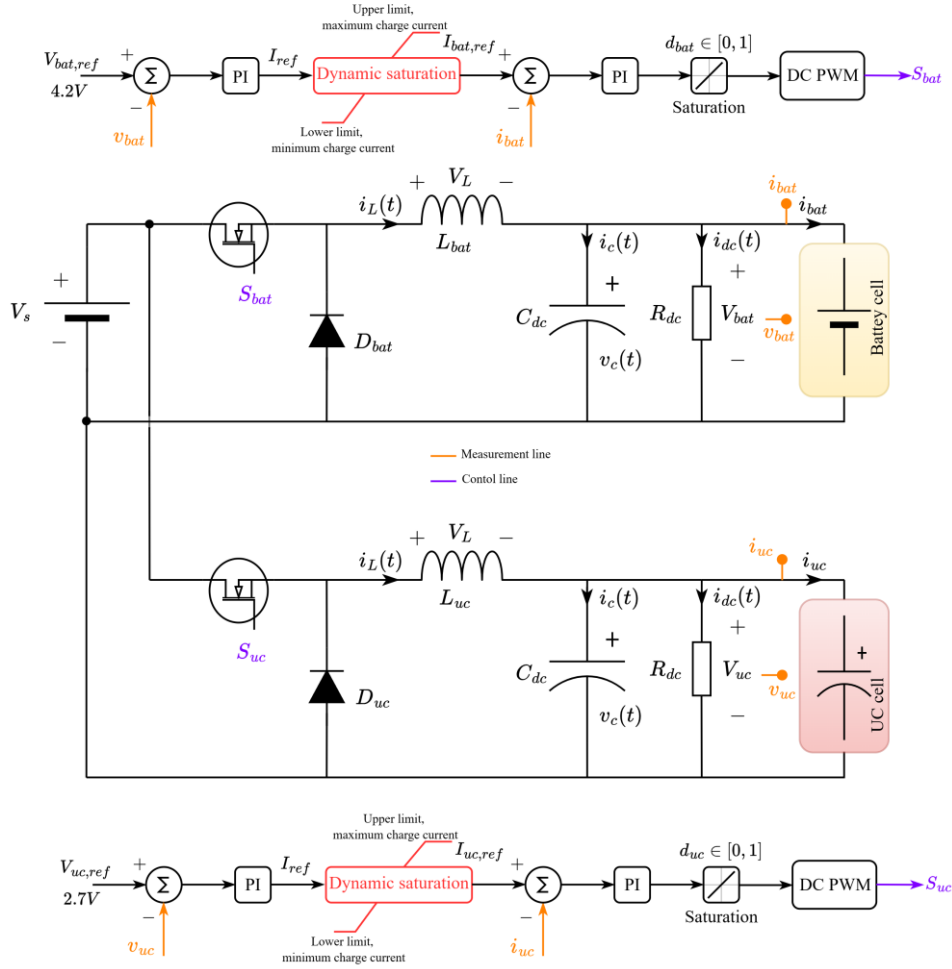
Figure 6. Overall architecture of synchronous charge of battery and ultracapacitor cells

The output of the second controller used to eliminate the current error produces the converter duty ratio required to provide the given reference values. In the control algorithm, the inner loop controls the charge currents while the outer loop controls the charge voltages. Therefore, cascade control is achieved by controlling more than one output variable. In the cascade buck converter in Figure 6, since the capacitor current (i_c) and the protection resistor current (i_{dc}) are negligibly small in CCM, the output current (i_{bat}) can be assumed to be equal to the inductor current (i_L). The transfer function between the input variable duty ratio (d) and the output variable inductor current (i_L) can be given as follows [43].

$$G_{id}(s) = \frac{i_L(s)}{d(s)} = \frac{V_s}{dR}\left(\frac{1 + sRC}{s^2LC + (L/R)s + 1}\right) \quad (16)$$

Similarly, the transfer function between the input variable duty ratio (d) and the output variable battery voltage (V_{bat}) can be given as follows [44].

$$G_{vd}(s) = \frac{v_c(s)}{d(s)} = \frac{V_s}{d}\left(\frac{1}{s^2LC + (L/R)s + 1}\right) \quad (17)$$

Controller design can be performed using the pidTuner toolbox in the MATLAB environment using Equations 16

and 17. For this study, the proportional integral (PI) controller structure, which is used in many applications due to its simple structure and robustness, was preferred. The PI controller transfer function is:

$$G_{PI}(s) = K_p\left(1 + \frac{1}{T_i s}\right) \quad (18)$$

In Equation 18, K_p represents the proportional gain, and T_i represents the integral time constant. When implementing the cascade control structure, it should be considered that the inner control loops (current control) will change much faster than the outer control loops (voltage control). For this reason, the integral time of the inner control loops is selected 5 to 10 times smaller than the outer control loops.

4. RESULT AND DISCUSSION

To prove the effectiveness of the proposed technique, the synchronous charging architecture consisting of a battery, ultracapacitor, and buck converter components, the details of which are shown in Figure 6, were modeled in the MATLAB/Simulink environment. The results were obtained separately since the energy storage devices are charged independently. Similar charging procedures were created for both the battery and the ultracapacitor cells. The charging procedure of the battery cell can be

summarized as follows: In the first step, a charging current of $0.2C$ is given to the battery cell as a reference. In the following steps, this rate is increased by $0.2C$ every $0.5s$ by giving sufficient rest periods to the battery cell until the battery cell reaches the maximum charging current. When the charging current reaches the maximum level ($1C = 2500mA$ for the battery cell used in this study), this current level is maintained until the battery is in continuous voltage mode. The simulation results of the battery cell are shown in Figure 7. Figure 7a shows the SoC change of the battery cell during the test procedure. The battery cell started the charging process from the

initial SoC level of 50% and was charged to approximately 50.25% at the end of the simulation. Increasing the charging current at the beginning of the charging process caused a slow change in the SoC. However, it is seen that the charging speed increases when the charging current reaches $1C$. The reason for the very low increase in the battery SoC is due to the short test period. The simulation period was kept short to show the cell changes during charging clearly. The change in the battery terminal voltage according to the reference charging currents is shown in Figure 7b.
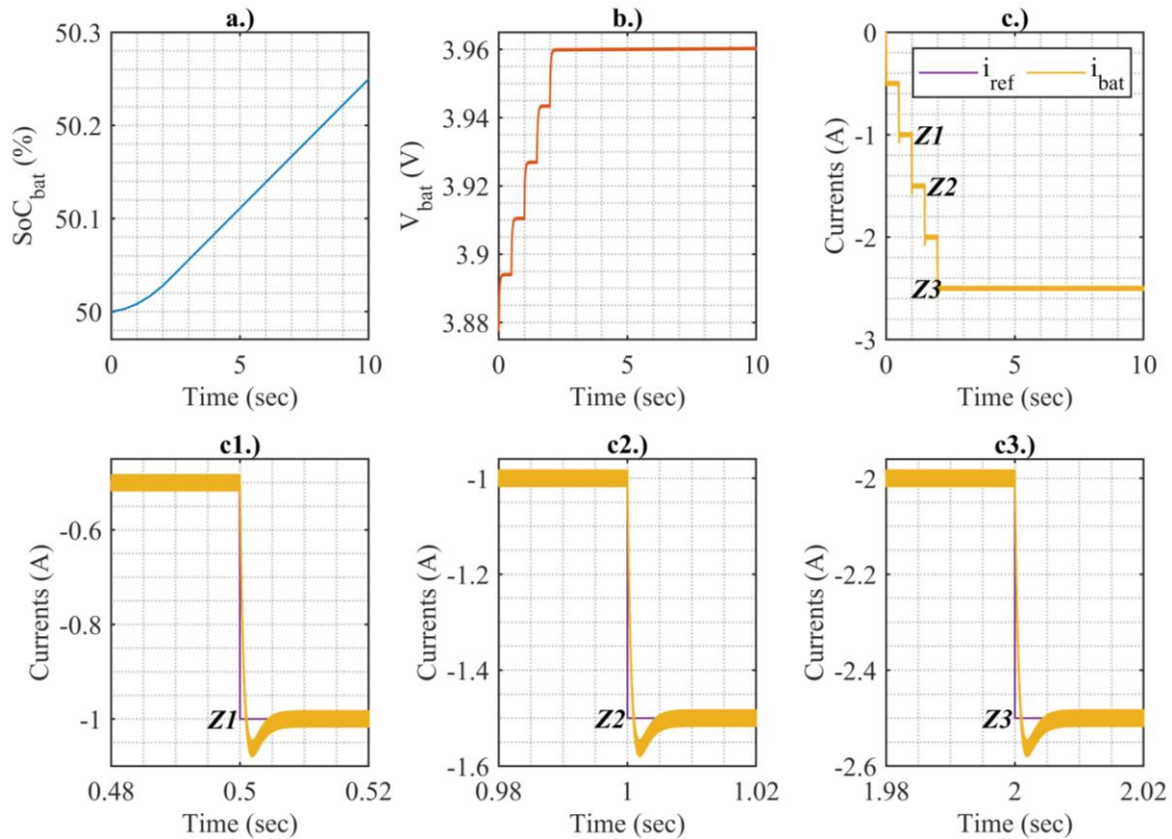

Figure 7. Simulation results of battery cell, a.) SoC, b.) Terminal voltage, c.) Battery current and reference current (c1.), c2.), and c3.) are zoom of c.) at Z1, Z2, and Z3 regions)

Two increasing effects are seen on the battery terminal voltage in parallel with the increase in the charging current. The first is the increase in the internal resistance voltage with the increase in the current passing through the battery's internal resistance. The second is due to the increased battery potential due to the charged Lithium ions passing to the cathode side under the effect of the charging current. The reason for the gradual increase in terminal voltage is directly related to the change in battery charging current. The changes in terminal voltage after each charging pulse were measured as $3.893V$, $3.910V$, $3.926V$, $3.943V$, and $3.960V$. In Figure 7c, the reference charging current and battery charging current are shown in the same graph. The charging current was applied at times $(t = k, \{k \epsilon 0, 0.5, 1, 1.5, 2\})$ and $(i_{ref} = n, \{n \epsilon 0.2C, 0.4C, 0.6C, 0.8C, 1C\})$, respectively. This procedure aims to test the robustness of the designed cascade control system. Since the simulation time is short

and the charging current is changed in a very narrow interval, Figure 7c was examined closely at three different points (Z1, Z2, Z3) in order to clearly show the battery current tracking states of the reference. The specified Z1, Z2, Z3 regions are shown closely in Figure 7c1, Figure 7c2 and Figure 7c3, respectively, as an extension of Figure 7c. In all three results, it is seen that the charging current reaches the reference value in a very short time and closely follows the reference with a very small overshoot. For the examined Z1, Z2 and Z3 regions, the overshoot values are measured as 7.939%, 7.944%, 7.953%, and the settling times are approximately $6ms$. These values prove the buck converter's accuracy and the adopted control method. In addition, to test the suitability of both the design values and the control algorithm for the buck converter, the time-dependent changes of the effective duty ratio (d_{bat}), diode current $(i_{D,bat})$, and MOSFET current $(i_{fet,bat})$ during the charging process

110

are shown in Figure 8. Zoomed images are given on the right side of the relevant graph in a short period of time interval when the reference charging current is $0.3C$ to closely monitor the changes on the converter side during the test. Figure 8a shows the change in the duty ratio. At the beginning of the charging process, the effective duty ratio is captured quickly and robustly. The increase in the duty ratio because of the change in the charging currents can be observed in the range of $0 < t < 2$ seconds and increases with time when the charging current is fixed at $1C$. This is because the battery cell terminal voltage (i.e.

converter output voltage) continues to increase during the charging period. Figure 8b and Figure 8c show the converter diode and MOSFET currents, respectively. When looking at the zoomed-in view of Figure 8b, it is seen that the diode current is zero during the duty cycle and carries the reference current in the regions outside the duty cycle $(1 - d)$. Since the diode and MOSFET in the converter structure work in complementary to each other, it is expected that the reference current will be seen on the MOSFET during the duty cycle. Figure 8c proves this expected situation.
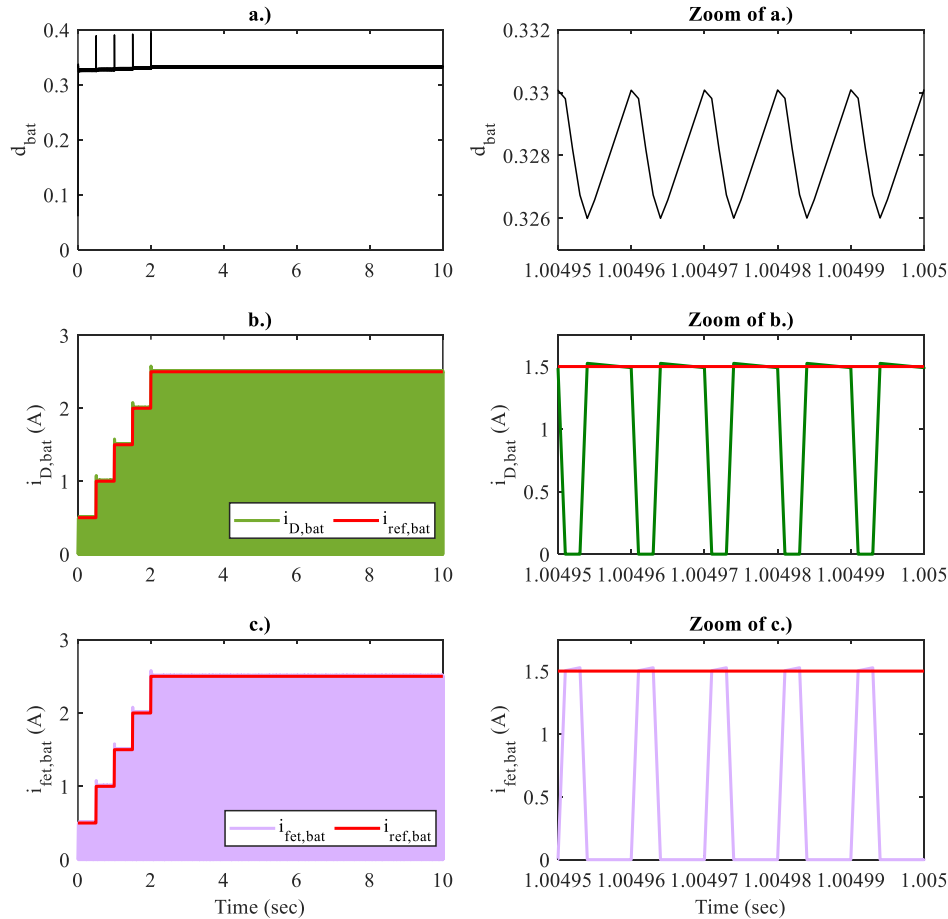

Figure 8. Results of battery buck converter, a.) Duty cycle, b.) Reference and diode current, c.) Refence current and MOSFET current

The results in Figure 7 and Figure 8 mainly focus on the current control, which is the inner loop of the designed cascade control system. The robustness of the voltage control, which constitutes the outer loop of the control system, can be tested when the cell terminal voltage reaches the charging voltage or when the battery cell is charged with a higher than the nominal charging voltage. During charging, the cell terminal voltage increases almost linearly to approximately 80% SoC. It is clear that the cell is charged in the continuous current (CC) mode in this region. The charging current starts to decrease when the cell terminal voltage reaches the charging voltage. After this decrease, the charging process continues in the continuous voltage (CV) mode. In order to test the effectiveness of the outer loop control mechanisms, a second simulation procedure was applied by starting the battery cell SoC from 80%. In this procedure, the minimum value of the charging current was selected as $0.4C$ and the maximum value as $3.2C$. The charging

current comprises pulses with a period of $0.3s$ and a duty cycle of 80%. Figure 9 shows the changes in the battery cell exposed to these pulses. The time-dependent change of the charge currents (i_{ch}) is shown in Figure 9a. Figure 9b shows the change of the battery cell current depending on the application of the charge currents. As can be seen, despite applying a charge current of $8A$ at $t = 0$, the external loop control mechanisms have successfully ensured that the terminal voltage does not exceed the specified limit value and have started to reduce the charging current. In this case, the battery cell continues to charge in CV mode. Afterward, the charge current is reduced to $1A$, and the CC mode is observed, where the charging process continues continuously at this value. Figure 9c and Figure 9d show the battery terminal voltage and the battery SoC, respectively. Limiting the battery terminal voltage against high charging currents again demonstrates the robustness of the control system.
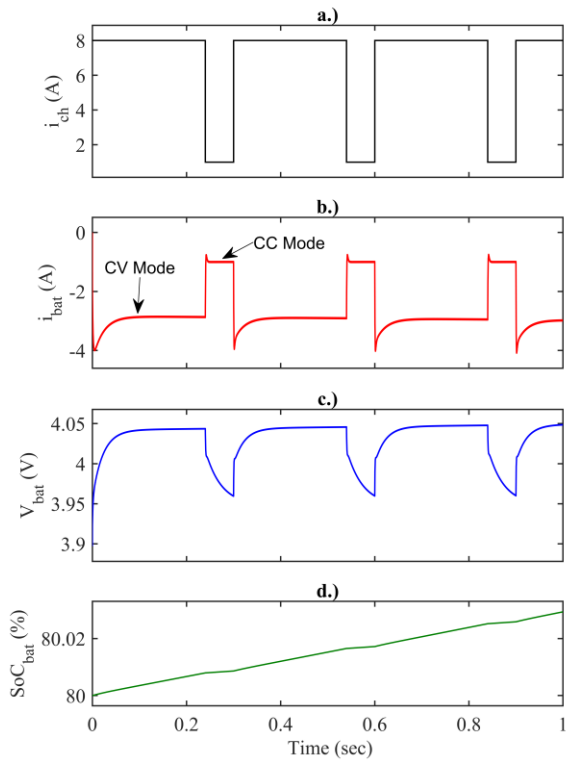
Figure 9. Test results of designed control algorithm in Continuous Current (CC) and Continuous Voltage (CV) modes for battery cell

The charging procedure of the ultracapacitor cell was applied similarly to the charging procedure of the battery cell. The only difference was that the charging currents were selected $0.2A$ lower than the battery cell, considering that the ultracapacitor cell would charge very quickly. Therefore, the ultracapacitor charging current

was applied at times $(t = k, \{k \in 0, 0.5, 1, 1.5, 2\})$ and $(i_{ref} = n, \{n \in 0.3A, 0.8A, 1.3A, 1.8A, 2A\})$, respectively. Figure 10 shows the simulation results of the ultracapacitor cell. The ultracapacitor SoC shown in Figure 10a started with a charge rate of approximately 50% and reached approximately 75% SoC at the end of the test. Since the SoC of the ultracapacitor cells is directly proportional to the terminal voltage, it is expected that the response in the SoC is similar to the cell voltage in Figure 10b. The reason why the ultracapacitor voltage increases linearly depending on the charging current is due to the use of electrostatic principles in the energy storage process. Unlike batteries, since no electrochemical transformation occurs, the dynamics in the cell voltage are more linear. The ultracapacitor voltage was measured as $1.512V$ at $t = 0$ and $2.229V$ at the end of the charging process. The time-dependent change of the selected reference current (i_{ref}) and ultracapacitor current (i_{uc}) in the ultracapacitor charging process is shown in Figure 10c. Since the simulation time is short and the charging current is changed in a very narrow range, Figure 10c was examined closely at three different points (Z4, Z5, Z6) in order to show the reference tracking states of the ultracapacitor current clearly. The specified regions Z4, Z5, and Z6 are shown closely in Figure 10c1, Figure 10c2, and Figure 10c3, respectively, as an extension of Figure 10c. In all three results, it is seen that the charging current reaches the reference value in a very short time and follows the reference closely with a very small overshoot. For the examined Z4, Z5, and Z6 regions, the overshoot values are measured as 7.281%, 7.288% , 7.312% , and the settling times are approximately $6ms$.
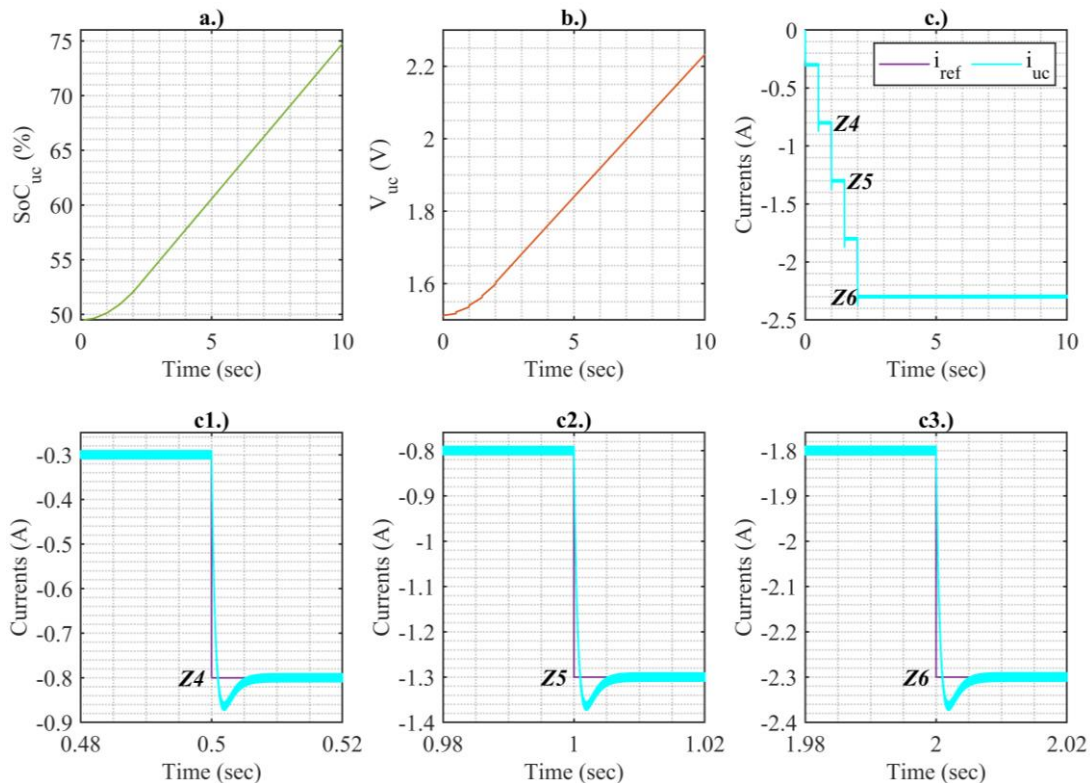
Figure 10. Simulation results of ultracapacitor, a.) SoC, b.) Terminal voltage, c.) Battery current and reference current (c1.), c2.), and c3.) are zoom of c.) at Z4, Z5, and Z6 regions)

Figures 11a, 11b and 11c show the time-dependent changes of the duty ratio (d_{uc}), diode current $(i_{D,uc})$, and MOSFET current $(i_{fet,uc})$ of the ultracapacitor converter, respectively. In order to closely monitor the changes on the converter side during the test, close-up images of a short region of the time interval when the reference charge current is $1.3A$ are given on the right side of the relevant graph.
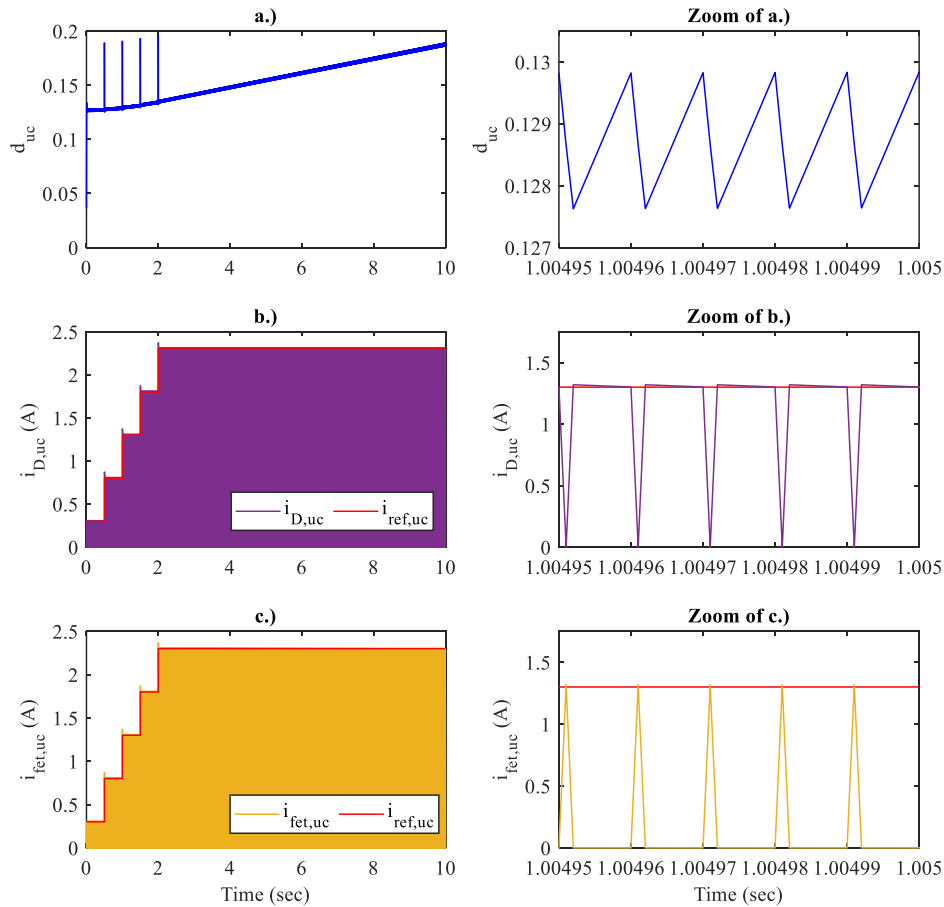

Figure 11. Results of ultracapacitor buck converter, a.) Duty cycle, b.) Reference and diode current, c.) Refence current and MOSFET current

It is seen that the duty ratio in Figure 11a increases linearly. This is due to the rapid increase in the ultracapacitor cell voltage. It is seen that the peaks in the duty cycle in current changes are very short time, and the control algorithm quickly tracks the duty ratio. It is expected that similar effects are seen in the diode current in Figure 11b and the MOSFET current in Figure 11c as in the battery cell. The difference is that the charge reference current is $0.2A$ lower for the ultracapacitor tests. Although the charge currents differ, the reference currents can be closely monitored thanks to the superior success of the designed control algorithm. Similar to the test procedure of the battery cell, the ultracapacitor converter controls the external loop mechanisms so that the cell limit voltage is not exceeded. Therefore, charging current increasing the cell voltage above the nominal voltage is not allowed. To check the external loop mechanisms of the ultracapacitor, a second test procedure was performed by starting the cell SoC from 80%. This procedure is the same as the second procedure for the battery cell. Figure 12 shows the test results of the inner (cell current control) and outer (cell voltage control) control mechanisms. Figure 12a shows the reference pulsed charging current effective at 80% at a maximum of $8A$ and a minimum of $1A$. The cell current (i_{uc}), cell voltage (V_{uc}) and state of charge (SoC_{uc}) in the ultracapacitor cell under the influence of these charging currents are shown in Figures 12b, 12c and 12d, respectively. It is observed that the charging current gradually decreases by increasing the cell voltage close to the nominal voltage, thanks to the effective operation of the external loop mechanisms (CV Mode). As the charging current is reduced to $1A$, the terminal voltage drops rapidly, and the charging current becomes continuous (CC Mode).

Today, most electric vehicles use only battery packs as energy storage devices. Hybrid electric vehicles use battery packs as auxiliary energy sources, while fully electric vehicles use them as the primary energy source. In renewable energy systems, battery packs are indispensable energy storage and supply devices. In hybrid power systems containing battery/ultracapacitors, ultracapacitors meet peak currents and prevent thermal and cycle life problems of battery packs. Ultracapacitors must be operated within a specific SoC range to meet the peak currents demanded by the load as both source and storage device. Ultracapacitors can fulfill this mission by storing either the energy of the battery packs or the recovered energy originating from the load. However,

113

while sharing the battery energy with the ultracapacitor can cause the battery SoC to decrease rapidly, the ultracapacitor cannot meet the peak currents if insufficient recovered energy exists. Therefore, charging the ultracapacitor to a specific SoC while the battery is charging will prepare the system for power supply and energy storage.
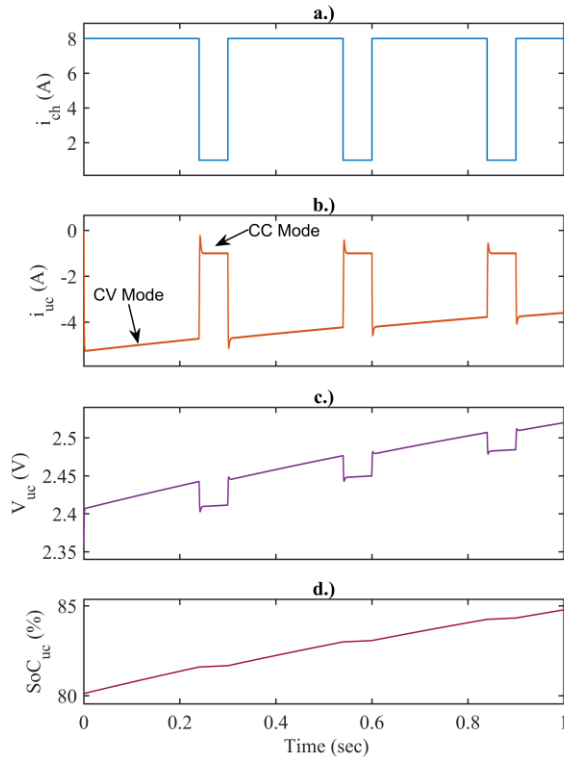

Figure 12. Test results of designed control algorithm in Continuous Current (CC) and Continuous Voltage (CV) modes for ultracapacitor cell

4. CONCLUSION

In the near future, when hybrid power systems using more than one energy storage device are widespread, the process of charging these devices separately will come to light. Especially in battery/ultracapacitor systems, which have been the subject of a serious research attack in recent years, the synchronous charging process may be of vital importance in terms of charging time. In this study, a battery and ultracapacitor synchronous charging system has been developed for small power applications. Although all simulation tests have been performed at cell size, the proposed system can easily be applied to larger-volume hybrid power systems. The superior success of the designed buck converter in capturing the reference charging currents proves that the critical calculations of the control algorithm are performed effectively. In addition, the designed control structure has shown superior success in obtaining both medium-level duty ratios (battery cell test) and low-level duty ratios (ultracapacitor cell test). In addition, the proposed synchronous charging system has provided serious performance by monitoring all reference charging currents with approximately 8% overshoot and $6ms$ settling time. The obtained results prove the applicability of the cascading control technique implemented in the

buck converter structure in both continuous current and continuous voltage modes. In future studies, it is planned to realize a cell-sized hardware prototype for HESS containing battery and ultracapacitor cells using the technique proposed in this study.

REFERENCES

[1] Emrani A and Berrada A, A comprehensive review on techno-economic assessment of hybrid energy storage systems integrated with renewable energy, Journal of Energy Storage. 2024; 84, 111010.

[2] Kaan M, Bozkurt A, Genç M S, and Genç G, Optimization study of an energy storage system supplied solar and wind energy sources for green campus, Process Safety and Environmental Protection. 2024; 190, 863-872.

[3] Zhu Z *et al.*, Versatile carbon-based materials from biomass for advanced electrochemical energy storage systems, eScience. 2024; 4, 5, 100249.

[4] Tian J, Fan Y, Pan T, Zhang X, Yin J, and Zhang Q, A critical review on inconsistency mechanism, evaluation methods and improvement measures for lithium-ion battery energy storage systems, Renewable and Sustainable Energy Reviews. 2024; 189, 113978.

[5] Nivolianiti E, Karnavas Y L, and Charpentier J-F, Energy management of shipboard microgrids integrating energy storage systems: A review, Renewable and Sustainable Energy Reviews. 2024; 189, 114012.

[6] Robles-Campos H R, Valderrabano-Gonzalez A, Rosas-Caro J C, Gabbar H A, and Babaiahgari B, Double Dual High Step-Up Power Converter with Reduced Stored Energy, Energies. 2023; 16, 7, 3194.

[7] Çorapsiz M R, PV-fed multi-output buck converter-based renewable energy storage system with extended current control for lifetime extension of Li-ion batteries, Computers and Electrical Engineering. 2024; 120, 109757.

[8] Çorapsız M R and Kahveci H, Double adaptive power allocation strategy in electric vehicles with battery/supercapacitor hybrid energy storage system, International Journal of Energy Research. 2022; 46, 13, 18819-18838.

[9] Uswarman R, Munawar K, Ramli M A M, and Mehedi I M, Bus Voltage Stabilization of a Sustainable Photovoltaic-Fed DC Microgrid with Hybrid Energy Storage Systems, Sustainability. 2024; 16, 6, 2307.

[10] Çorapsiz M R and Kahveci H, A study on Li-ion battery and supercapacitor design for hybrid energy storage systems, Energy Storage. 2023; 5, 1, e386.

[11] Chakraborty S, Hasan M M, Worighi I, Hegazy O, and Razzak M A, Performance Evaluation of a PID-Controlled Synchronous Buck Converter Based Battery Charging Controller for Solar-Powered Lighting System in a Fishing Trawler, Energies. 2018; 11, 10, 2722.

[12] López-Santos O *et al.*, Robust Control for a Battery Charger Using a Quadratic Buck Converter, IEEE Access. 2024; 12, 125480-125492.

114

[13] Florescu A, Bacha S, Munteanu I, Bratcu A I, and Rumeau A, Adaptive frequency-separation-based energy management system for electric vehicles, Journal of Power Sources. 2015; 280, 410-421.

[14] Yılmaz M, Kaleli A, and Çorapsız M F, Machine learning based dynamic super twisting sliding mode controller for increase speed and accuracy of MPPT using real-time data under PSCs, Renewable Energy. 2023; 219, 119470.

[15] Kushwaha R and Singh B, A Power Quality Improved EV Charger With Bridgeless Cuk Converter, IEEE Transactions on Industry Applications. 2019; 55, 5, 5190-5203.

[16] Singh K, Anand A, Mishra A K, Singh B, and Sahay K, SEPIC Converter for Solar PV Array Fed Battery Charging in DC Homes, Journal of The Institution of Engineers (India): Series B. 2021; 102, 3, 455-463.

[17] Acosta L N and Flexer V, Accelerated charging protocols for lithium-ion batteries: Are fast chargers really convenient?, Journal of Solid State Electrochemistry. 2024; 28, 3, 1107-1119.

[18] Wu Y *et al.*, Adaptive power allocation using artificial potential field with compensator for hybrid energy storage systems in electric vehicles, Applied Energy. 2020; 257, 113983.

[19] Raut K, Shendge A, Chaudhari J, Lamba R, and Alshammari N F, Modeling and simulation of photovoltaic powered battery-supercapacitor hybrid energy storage system for electric vehicles, Journal of Energy Storage. 2024; 82, 110324.

[20] Shen Y, Xie J, He T, Yao L, and Xiao Y, CEEMD-Fuzzy Control Energy Management of Hybrid Energy Storage Systems in Electric Vehicles, IEEE Transactions on Energy Conversion. 2024; 39, 1, 555-566.

[21] Reddy R M, Das M, and Chauhan N, Novel Battery-Supercapacitor Hybrid Energy Storage System for Wide Ambient Temperature Electric Vehicles Operation, IEEE Transactions on Circuits and Systems II: Express Briefs. 2023; 70, 7, 2580-2584.

[22] Snoussi J, Elghali S B, Benbouzid M, and Mimouni M F, Optimal Sizing of Energy Storage Systems Using Frequency-Separation-Based Energy Management for Fuel Cell Hybrid Electric Vehicles, IEEE Transactions on Vehicular Technology. 2018; 67, 10, 9337-9346.

[23] Zuo W, Li R, Zhou C, Li Y, Xia J, and Liu J, Battery-Supercapacitor Hybrid Devices: Recent Progress and Future Prospects, Advanced Science. 2017; 4, 7, 1600539.

[24] Watanabe S, Kinoshita M, Hosokawa T, Morigaki K, and Nakura K, Capacity fading of LiAlyNi1−x−yCoxO2 cathode for lithium-ion batteries during accelerated calendar and cycle life tests (effect of depth of discharge in charge–discharge cycling on the suppression of the micro-crack generation of LiAlyNi1−x−yCoxO2 particle), Journal of Power Sources. 2014; 260, 50-56.

[25] Trovão J P, Silva M A, and Dubois M R, Coupled energy management algorithm for MESS in urban EV, IET Electrical Systems in Transportation. 2017; 7, 2, 125-134.

[26] Castaings A, Lhomme W, Trigui R, and Bouscayrol A, Comparison of energy management strategies of a battery/supercapacitors system for electric vehicle under real-time constraints, Applied Energy. 2016; 163, 190-200.

[27] Usman Tahir M, Sangwongwanich A, Stroe D-I, and Blaabjerg F, Overview of multi-stage charging strategies for Li-ion batteries, Journal of Energy Chemistry. 2023; 84, 228-241.

[28] Saxena S, Le Floch C, MacDonald J, and Moura S, Quantifying EV battery end-of-life through analysis of travel needs with vehicle powertrain models, Journal of Power Sources. 2015; 282, 265-276.

[29] Roy P and Srivastava S K, Nanostructured anode materials for lithium ion batteries, Journal of Materials Chemistry A. 2015; 3, 6, 2454-2484.

[30] Lu Y, Zhang Q, Li F, and Chen J, Emerging Lithiated Organic Cathode Materials for Lithium-Ion Full Batteries, Angewandte Chemie. 2023; 135, 7, e202216047.

[31] Campagna N *et al.*, Battery Models for Battery Powered Applications: A Comparative Study, Energies. 2020; 13, 16, 4085.

[32] URL-1, ORION 18650P/25 2500mAh 10C. https://static.ticimax.cloud/37661/uploads/dosyalar/orion18650p250010.pdf (accessed 31.10.2024).

[33] Miller J R and Simon P, Electrochemical Capacitors for Energy Management, Science. 2008; 321, 5889, 651-652.

[34] Drummond R, Huang C, Grant P S, and Duncan S R, Overcoming diffusion limitations in supercapacitors using layered electrodes, Journal of Power Sources. 2019; 433, 126579.

[35] González A, Goikolea E, Barrena J A, and Mysyk R, Review on supercapacitors: Technologies and materials, Renewable and Sustainable Energy Reviews. 2016; 58, 1189-1206.

[36] Zubieta L and Bonert R, Characterization of double-layer capacitors for power electronics applications, IEEE Transactions on Industry Applications. 2000; 36, 1, 199-205.

[37] URL-2, Maxwell Ultracapacitor Cell. https://maxwell.com/products/ultracapacitors/cells/ (accessed 10.01.2025).

[38] Sani S G, Banaei M R, and Hosseini S H, Investigation and implementation of a common ground DC-DC buck converter with a novel control method for loss reduction in the converter, IET Power Electronics. 2024; 17, 14, 1840-1851.

[39] Kim H C, Biswas M, and Park J W, Discontinuous Conduction Mode Analysis of Two-Phase Interleaved Buck Converter With Inversely Coupled Inductor, IEEE Access. 2024; 12, 91944-91956.

[40] He L, Wang X, and Lee C-K, A Study and Implementation of Inductive Power Transfer System Using Hybrid Control Strategy for CC-CV Battery Charging, Sustainability. 2023; 15, 4, 3606.

[41] Zhang S S, Identifying rate limitation and a guide to design of fast-charging Li-ion battery, InfoMat. 2020; 2, 5, 942-949.

115

[42] Kollimalla S K, Ukil A, Gooi H B, Manandhar U, and Tummuru N R, Optimization of Charge/Discharge Rates of a Battery Using a Two-Stage Rate-Limit Control, IEEE Transactions on Sustainable Energy. 2017; 8, 2, 516-529.

[43] Argyrou M C, Marouchos C C, Kalogirou S A, and Christodoulides P, Modeling a residential grid-connected PV system with battery–supercapacitor storage: Control design and stability analysis, Energy Reports. 2021; 7, 4988-5002.

[44] Hong X, Wu J-F, and Wei C-L, 98.1%-Efficiency Hysteretic-Current-Mode Noninverting Buck–Boost DC-DC Converter With Smooth Mode Transition, IEEE Transactions on Power Electronics. 2017; 32, 2008-2017.

Investigation of the Effects of Environmental and Geothermal Resource Temperature on Carnot Efficiency

Mert GÜRTÜRK [1] , **Murat ERDEM** [2*]

[1] Fırat University, Technology Faculty, Department of Energy Systems Engineering, Elazığ, Türkiye
[2] Fırat University, Vocational School of Technical Sciences, Elazığ, Türkiye
Mert GÜRTÜRK ORCID No: 0000-0003-0380-5704
Murat ERDEM ORCID No: 0000-0003-0287-1881

Corresponding author: muratrdm01@gmail.com

Abstract: Geothermal energy is a domestic energy source that is renewable, clean, and environmentally friendly. Türkiye is in a rich position among the world countries regarding geothermal energy due to its geological and geographical location. The vast majority of these resources are located in the western Anatolia region of the country. Today, geothermal energy obtained in the country is used in areas such as electricity generation, heating, thermal and health tourism, industrial mineral extraction, drying, etc. In this study, the potential of a geothermal energy source in Denizli was evaluated using the volumetric method. The effects of time-dependent both ambient and resource temperatures were investigated on an hourly, monthly, and annual basis between 2001 and 2026. The analysis focused on the variation of resource temperature with ambient temperature and the efficiency of the Carnot cycle. The geothermal resource temperature was assumed to be 160°C, with a resource lifespan of 25 years. The lowest source temperature is 100.8°C, and the highest and lowest Carnot efficiencies are obtained as 40.4% and 16.5%. The geothermal resource potential has been calculated to be 74.97 MWe, and the thermal energy stored in the reservoir has been determined to be 5.94×10^{15} J.

117

Çevre ve Jeotermal Kaynak Sıcaklığının Carnot Verimliliğine Etkilerinin Araştırılması

Öz: Jeotermal enerji, yenilenebilir, temiz ve çevre dostu yerli bir enerji kaynağıdır. Türkiye, jeolojik ve coğrafi konumu nedeniyle jeotermal enerji açısından dünya ülkeleri arasında zengin bir konumdadır. Bu kaynakların büyük çoğunluğu ülkenin batı Anadolu bölgesinde bulunmaktadır. Günümüzde ülkede elde edilen jeotermal enerji; elektrik üretimi, ısınma, termal ve sağlık turizmi, endüstriyel mineral çıkarımı, kurutma vb. alanlarda kullanılmaktadır. Bu çalışmada, Denizli'deki bir jeotermal enerji kaynağının potansiyeli hacimsel yöntem kullanılarak değerlendirilmiştir. Zamana bağlı hem çevre sıcaklığının hem de kaynak sıcaklığının etkileri 2001-2026 yılları arasında saatlik, aylık ve yıllık bazda incelenmiştir. Analiz, kaynak sıcaklığının ortam sıcaklığına göre değişimine ve Carnot çevriminin verimliliğine odaklanmıştır. Jeotermal kaynak sıcaklığının 160°C olduğu ve kaynak ömrünün 25 yıl olduğu varsayılmıştır. En düşük kaynak sıcaklığı 100.8°C olup en yüksek ve en düşük Carnot verimleri sırasıyla %40.4 ve %16.5 olarak elde edilmiştir. Jeotermal kaynak potansiyeli 74.97 MWe olarak hesaplanmış olup rezervuarda depolanan termal enerji 5.94×10^{15} J olarak belirlenmiştir.

1. INTRODUCTION

Global energy consumption is expanding daily due to population growth, industrialization, and technological advancements. The limited lifespan of fossil fuels and the environmental consequences drive up demand for renewable energy sources [1–5]. Global warming is commonly associated with climate change, increased pollution, and urbanization, as well as the usage of fossil fuels, which primarily contribute to CO_2 emissions [3]. While renewable energy increased historically, fossil fuels still accounted for 82% of total primary energy consumption [6]. Türkiye adopted the United Nations Framework Convention on Climate Change (UNFCCC)

in 1992, the Kyoto Protocol in 1997, and the Paris Agreement in 2015, demonstrating its commitment to combating climate change on a global scale. The Paris Agreement marked a paradigm shift in addressing climate change, introducing numerical targets to limit the rise in global temperatures. It was emphasized that to achieve the goal of limiting the global temperature increase to 1.5°C, emissions must be reduced by 45% by 2030, to reach net-zero emissions by mid-century [7]. At the same time, as in many countries, Türkiye also offers various incentives to investors by updating the renewable incentive program called YEKDEM at certain intervals to achieve renewable energy targets [8]. According to the results of the Türkiye National Energy Plan study, electricity consumption is expected to reach 380.2 TWh in 2025, 455.3 TWh in 2030 and 510.5 TWh in 2035. In October 2024, the country's installed power reached 114,599 MW. As of the end of October 2024, the distribution of Türkiye 's installed power by resources is; 28.1% hydropower, 21.5% natural gas, 19.1% coal, 10.9% wind, 16.6% solar, 1.5% geothermal, and 2.4% other resources [9]. It is seen that the share of geothermal energy usage has decreased compared to 2023. This decrease is not related to the decrease in the use of geothermal resources but to the increase in the use of other energy sources. For example, while the share of solar energy was 6.7% in 2023, it reached 16.6% in 2024 [9]. Türkiye ranks 4th among the top 10 countries in the world and first in Europe in electricity production from geothermal resources [1]. However, it is still not able to benefit from this resource at the desired level. For this reason, feasibility studies need to be increased. Geothermal energy was first employed to create electricity in Italy's volcanic regions [10]. In Türkiye, in geothermal energy applications, the first electricity production was started in 1975 with the Kızıldere Power Plant, established by the General Directorate of MTA and having a power of 0.5 MWe [11]. 78% of the areas constituting the country's geothermal potential are located in Western Anatolia, 9% in Central Anatolia, 7% in the Marmara Region, 5% in Eastern Anatolia, and 1% in other regions [11]. Today, geothermal energy obtained in Türkiye is used in heating, thermal and health tourism, industrial mineral extraction, fishing, drying, etc. Geothermal energy production relies heavily on innovative system techniques. These are often referred to as improved geothermal systems. These system techniques include a fuel cell, combined cycle, absorption chiller, cascade system, multi-generation, Organic Rankine Cycle (ORC), Combined Cooling Heating and Power (CCHP), zeotropic, Tri-generation, and Poly-generation. The research provides vital data for investors. The studies show that the first stage is to determine the features of the geothermal resource. The primary reason is that geothermal energy is classed based on its source temperature. There are two distinct systems in the cycle. These systems, which rely on the Rankine cycle principle, are classified as binary and flash-based.

Flash systems use an evaporative heat rejection system at high geothermal source temperatures (above 170 ºC),

while binary systems use a heat exchanger at lower temperatures (above 140 ºC). It is commonly used for heating in areas with lower geothermal source temperatures [12]. Geothermal power plants are systems that operate based on ORC. By incorporating solar-hydrogen-carbon capture systems into existing systems, the goal is to increase the gain parameter. Examining the analysis, it is evident that several studies provide hot water, heating, and cooling all year long. Geothermal energy is characterized as a clean, sustainable, steady, and safe energy source [13].

Since geothermal power plants are operated at high capacity, cooling occurs at the source. This cooling spreads over years and negatively affects the efficiency and production of the geothermal power plant over time. The main reason here is that investors try to amortize the cost of the power plant investment as soon as possible and to meet the energy needs of countries first from renewable energy sources. Governments are required to reduce emission rates within a certain period of time in accordance with the Paris climate agreement. Electricity produced from renewable energy sources is prioritized according to the legislations put forward by governments. In other words, priority is given to renewable energy sources in electricity purchases. The biggest disadvantage of renewable energy sources such as wind and sun is that they are not permanent. However, there is no such disadvantage in geothermal energy production. Therefore, the energy produced from geothermal energy sources is continuously fed into the main grid. At the same time, priority is given to the electrical energy produced from these facilities. However, although the use of geothermal resources increases every year, the usage rate remains low compared to the country's geothermal resource potential. The main reason for this is that the resource potential cannot be fully determined due to the inadequacy of technical and economic feasibility studies and the inadequacy of the incentives provided to investors stand out. For this purpose, this study determined a geothermal resource potential for Denizli, the province with the second-highest geothermal energy resources in Türkiye, and examined the impact of ambient and geothermal resource temperatures on the efficiency on an annual, daily, and hourly basis.

2. MATERIAL AND METHOD

As understood from the literature, Türkiye is in a very good position due to its geological structure in terms of geothermal energy. Although Türkiye is benefiting more from this clean, renewable domestic energy source every year with various supports, it is seen that it uses this energy source less than other energy sources. The top five countries in electricity production from geothermal energy are the USA, Indonesia, Philippines, Türkiye, and New Zealand [9]. The distribution of the country's geothermal energy sources is given in the map in Figure 1.

118
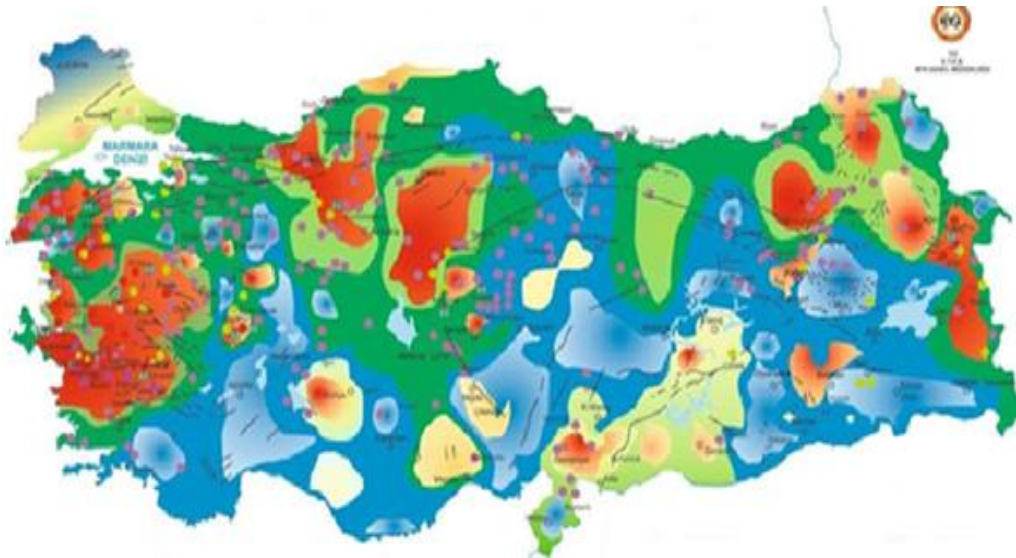
Figure 1. Türkiye's geothermal energy resources and application map [9]

The areas marked in red on the map represent sources with temperatures ranging between 70–100°C, indicating the highest temperature zones. Green areas correspond to sources with temperatures between 50–69°C, while purple areas indicate temperatures of 20–49°C. The blue areas represent regions with the lowest temperatures. The map demonstrates that the most effective geothermal sources are concentrated in the western part of the country, particularly in the Aegean region [9]. Figure 2(a) illustrates the annual progression of Türkiye's installed geothermal energy capacity (in MW), while Figure 2(b) depicts its proportion within the total installed power capacity (in MW).

a)

b)
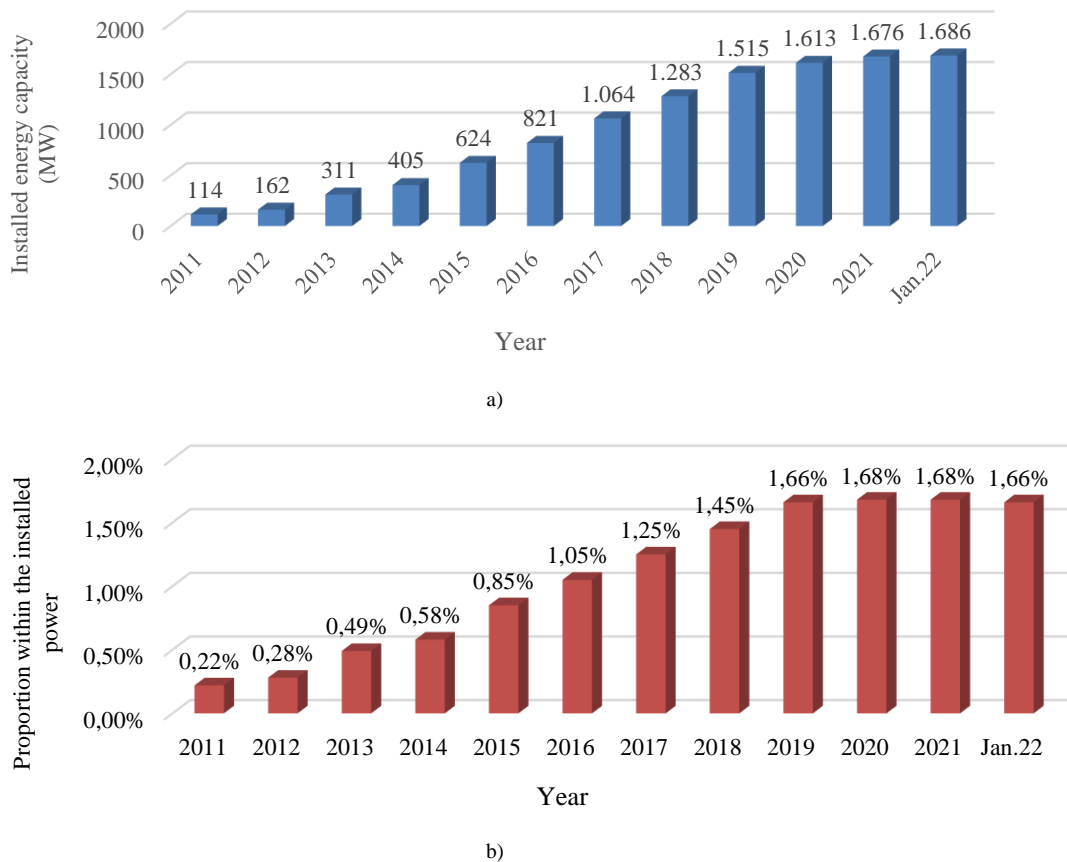
Figure 2. Installed power distributions from geothermal energy (MW), Geothermal energy ratio in installed power (%) [9]

From 2011 to June 2022, geothermal energy use has increased steadily every year in both quantity and rate. By the end of June 2022, the installed geothermal energy capacity widely utilized for electricity generation and regional heating reached 1,686 MW, representing 1.66% of the total installed power capacity. However, considering Türkiye's geothermal potential, it is evident that this data is still insufficient.

2.1. Theoretical Calculation

In the study, Türkiye is considered the location. Geothermal energy source temperature values in Türkiye vary between 130 ºC and 232 ºC depending on the area [14]. The location considered in the survey is Denizli (Lat. 37.77 - Lon. 29.1). The volume of the geothermal source whose theoretical analysis was made is up and down 16 km^3 [15]. In the present study, the geothermal source temperature is considered as 160 ºC. Several methods have been employed in the literature to estimate geothermal resource potential, including surface heat flux, planar fracture analysis, magmatic heat budget, total well flow, volumetric estimation, mass-in-place evaluation, and power density assessment [16]. In this study, the geothermal resource potential was determined using the volumetric method. The calculations were conducted by Equation 1 [16].

$$MWe = \frac{Q_{geo} \times R_f \times \eta_{conv}}{L \times F} \quad (1)$$

F in Equation 1 indicates the power plant capacity factor (%90). R$_f$ represents the recovery factor (%15). L represents the power plant life. In this study, L is considered as 25 years. The Q$_{geo}$ (J) value in Equation 1 represents the thermal energy stored in the reservoir. It was calculated using Equation 2 [16].

$$Q_{geo} = \rho_r c_r V (T_i - T_\infty) \quad (2)$$

Here, volumetric heat capacity of the reservoir rock $\rho_r = 2550$ kg/m^3 - $c_r = 1000$ J/kgK is expressed [17]. V is the volume of productive reservoir (m^3). Volume of productive reservoir is an important parameter. A small volume reservoir directly affects the working life of the geothermal power plant [17]. In the current study, the V value is considered as 16 km^3 [17]. T$_i$ and T$_\infty$ values are the initial temperature of lithology and environmental temperature (ºC), respectively. The environmental temperature value is taken from NASA POWER WEB (2024) [18]. The received data covers the years from 2001 to 2026 depending on the location. The received data is hourly environmental temperature value (NASA POWER WEB, 2024). The source from which the data is taken shares only 20 years of hourly data. Therefore, the values considered in the analyzes are the same between the values between 2016-2021 and 2022-2026. The data source used for location-dependent ambient temperature was chosen because it has been used reliably in many articles [4,8]. In this application that NASA has made available to users, many meteorological data can be obtained hourly, daily and annually depending on the specified location. To calculate the geothermal resource temperature at the end of 25 years, the energy loss in the resource was calculated with Equation 3.

$$Q_{geoloss} = Q_{geo} \cdot (1 - e^{-\lambda t}) \quad (3)$$

In Equation 3, λ and t values in the third equation indicate the loss coefficient and hourly time, respectively. The λ value takes values between 0.02 and 0.5 [19] annually in the analyses in the literature. However, these figures may change based on the geothermal resource's properties. In this study, the hourly λ value has been taken as 2.282x10^{-6}. After the losses in the geothermal resource depending on the environmental temperature on an hourly basis, the final temperature value of the geothermal resource was calculated with Equation (4), (5).

$$Q_{geofinal} = Q_{geo} - Q_{geoloss} \quad (4)$$

$$T_{geofinal} = \frac{Q_{geofinal}}{\rho_r \cdot c_r \cdot V} + T_\infty \quad (5)$$

The T$_{geo}$ value in Equation 5 represents the hourly final temperature value of the geothermal source. η$_{conv}$ is conversion efficiency. This value is determined in the literature using two alternative approaches, based on the geothermal source temperature or reservoir enthalpy value [20]. In this study, a method based on enthalpy (710 kJ/kg) is adopted. conversion efficiency is calculated via using Equation 6 [20].

$$\eta_{conv} = 6.6869 \ln(h) - 37.930 \quad (6)$$

It should be noted that Equation 3 is appropriate for binary plants. Researchers choose these strategies based on their input parameters. The Carnot efficiency of the plant is calculated with Equation 7.

$$\eta_{carnot} = 1 - \frac{T_c}{T_h} \quad (7)$$

Here, η$_{carnot}$ is Carnot efficiency (%), T$_h$ is the temperature of the heat source (K), and T$_c$ is the temperature of the ambient (K).

3. RESULTS

Denizli province is one of Türkiye's leading regions in renewable energy production due to its abundant geothermal resources and significant investments. According to data from NASA POWER WEB, the average temperature in the region between 1997 and 2022 is 14.55 ºC, while the average wind speed is 2.8 m/s [16,18]. As geothermal energy serves as the primary energy source in the area, accurately identifying and assessing the potential of this resource is of great importance. In the study, the first step involves determining the geothermal resource potential. In this context, the geothermal resource potential has been calculated as 74.97 MWe using Equation 1. It has been observed that numerous analyses on this topic have been conducted in the literature. The geothermal resource potential is reported to vary between 4 and 100 MWe, depending on the parameters considered [16]. The thermal energy stored in the reservoir was calculated using Equation 2 and determined to be 5.94 x 10^{15} J. In the literature, for source temperatures between 150–250°C and a depth of 3 km, the heat content value is reported to range between 5.1×10^9 J [21] and 5×10^{22} J [22].

The geothermal resource temperature was calculated hourly over a period of 25 years, providing insight into the long-term thermal behavior of the reservoir. These findings contribute to a better understanding and evaluation of geothermal energy potential and allow for comparisons with other studies in the literature. If additional details or analysis are required, further support can be provided.

The hourly change in a geothermal source in a day is presented in Figure 3. It is seen from the figure (Figure 3) that the change in the ambient temperature does not change significantly. The axis on the right of the graphs shows the Carnot efficiency (η). Since the ambient temperature is generally high between 8:00 a.m. and 6:00 p.m., it has been observed that the Carnot efficiency increases inversely during this time period. While the efficiency reached a maximum of 35.6 % in 2002, it was observed to decrease to 25.8 % by January 2026.
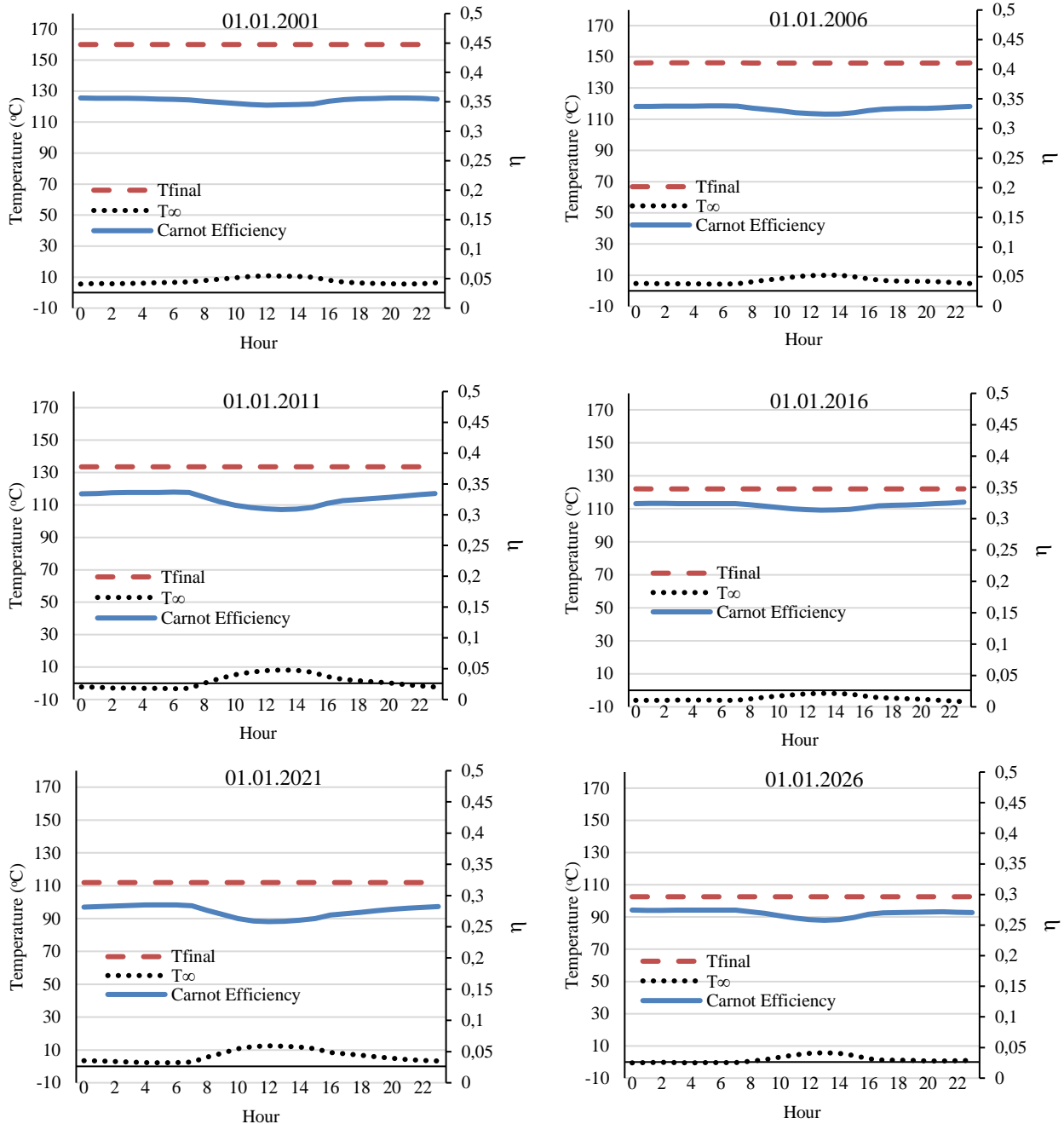
Figure 3. Hourly change in a geothermal resource in a day

121

The direct effect of the hourly decrease in ambient temperature on the geothermal resource potential for the years 2001-2026 is clearly seen. The initial source temperature of 160°C decreased over time, reaching 146.0 °C in 2006, 133.5 °C in 2011, 122.1°C in 2016, and 111.8 °C in 2021, 102.6 °C in 2026 depending on the ambient

temperature (As of January 1st). The Carnot efficiency in these years is 35.6 % - 34.4 % in 2001, 33.8 %- 32.4 % in 2006, 33.3 %-30.8 % in 2011, 32.6 % - 31.3% in 2016, 28.4 % -25.8 % in 2021 and 27.3 % - 25.8 % in 2026. The ambient temperature is 5.5-10.8 °C in 2001, 4.3-10.2 °C in 2006, -3.3 °C - 8.1 °C in 2011, -6.9 °C to -1.8 °C in

2016, 2.1 °C -12.2 °C in 2021 and -0.5 °C -5.7 °C in 2026 (January, 01).

There is a clear inverse relationship between Carnot efficiency and ambient temperature, as lower ambient temperatures generally correspond to higher efficiency values. This correlation aligns with the theoretical principles of Carnot efficiency, which improves as the temperature difference between the heat source and the ambient increases. Over the years, fluctuations in ambient temperature appear to have influenced efficiency levels, with the trend toward decreasing efficiency in recent years partially attributable to rising minimum ambient temperatures and reduced temperature differentials.

The hourly change in geothermal resources for a month is given in Figure 4.
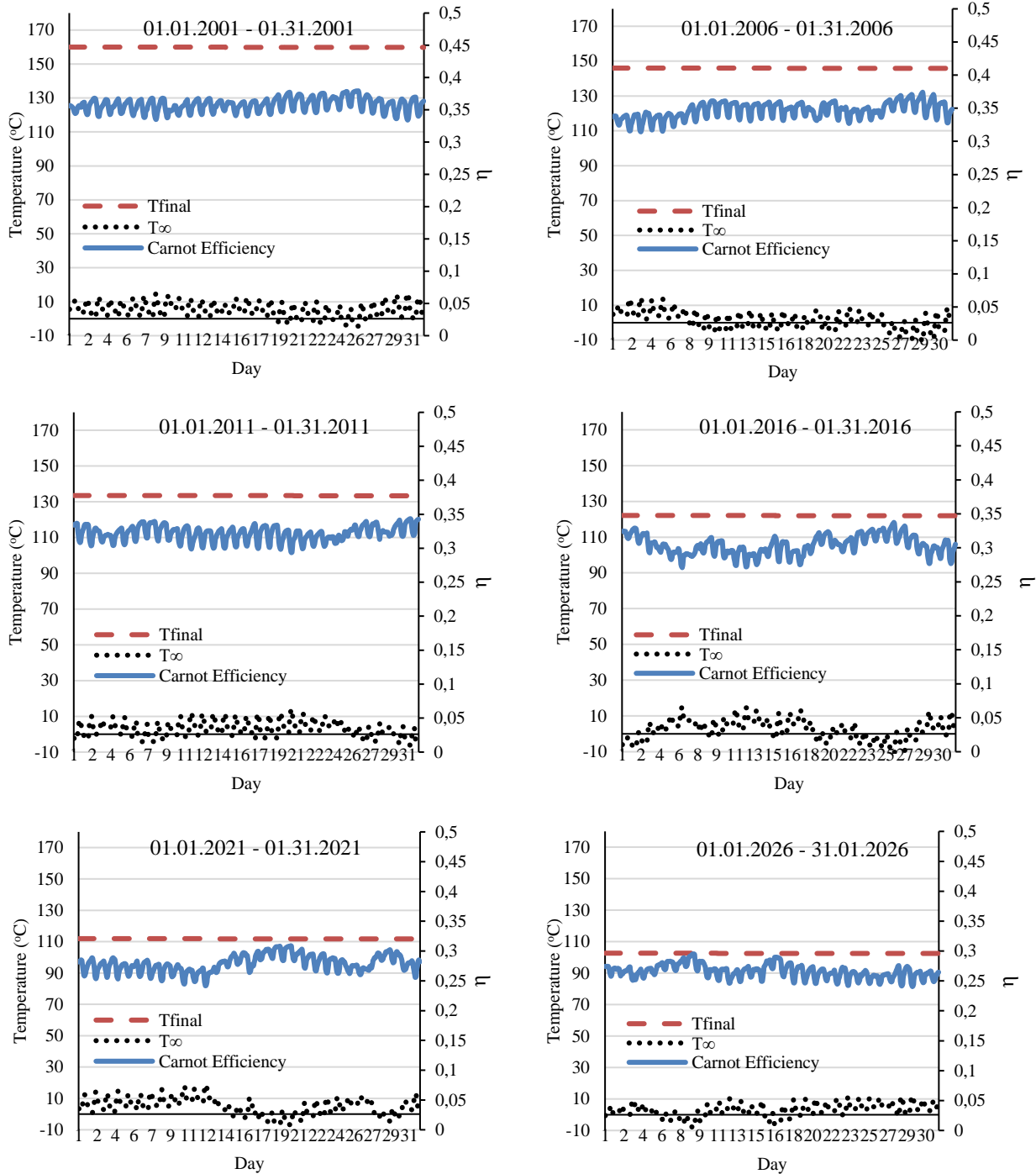
Figure 4. Hourly change in a month's geothermal resource

The change in geothermal resource potential over one month (January 1–31) is presented in Figure 4, covering the years 2001–2026. While no significant variability is observed in geothermal resource temperature, notable fluctuations are evident in geothermal resource potential values. These fluctuations appear to have a cumulative effect over time, as illustrated in Figure 4. Additionally, the ambient temperature during this period ranges from -4.4 °C to 15.1 °C. The variability in ambient temperature has a pronounced impact on the geothermal resource

122

potential. During the specified period, the geothermal resource potential fluctuates between 160 ºC and 102.4ºC. The geothermal resource temperatures reached at the end of each month at 5-year intervals from 2001 to 2026 are 159.7 ºC, 145.8 ºC, 133.3 ºC, 121.9 ºC, 111.7 ºC and 102.4 ºC, respectively. Depending on the geothermal resource and ambient temperature, minimum and maximum Carnot efficiency varied between 33.4-37.6% in 2001, 31.4-

37.2% in 2006, 29.3-34.2% in 2011, 27.1-33.6% in 2016, 24.1-30.8% in 2021 and 24.0-29.4% in 2026. As expected, there were decreases in Carnot efficiency depending on the increasing ambient temperature at the end of each year.

In Figure 5, it shows the hourly change in the geothermal resource according to years.
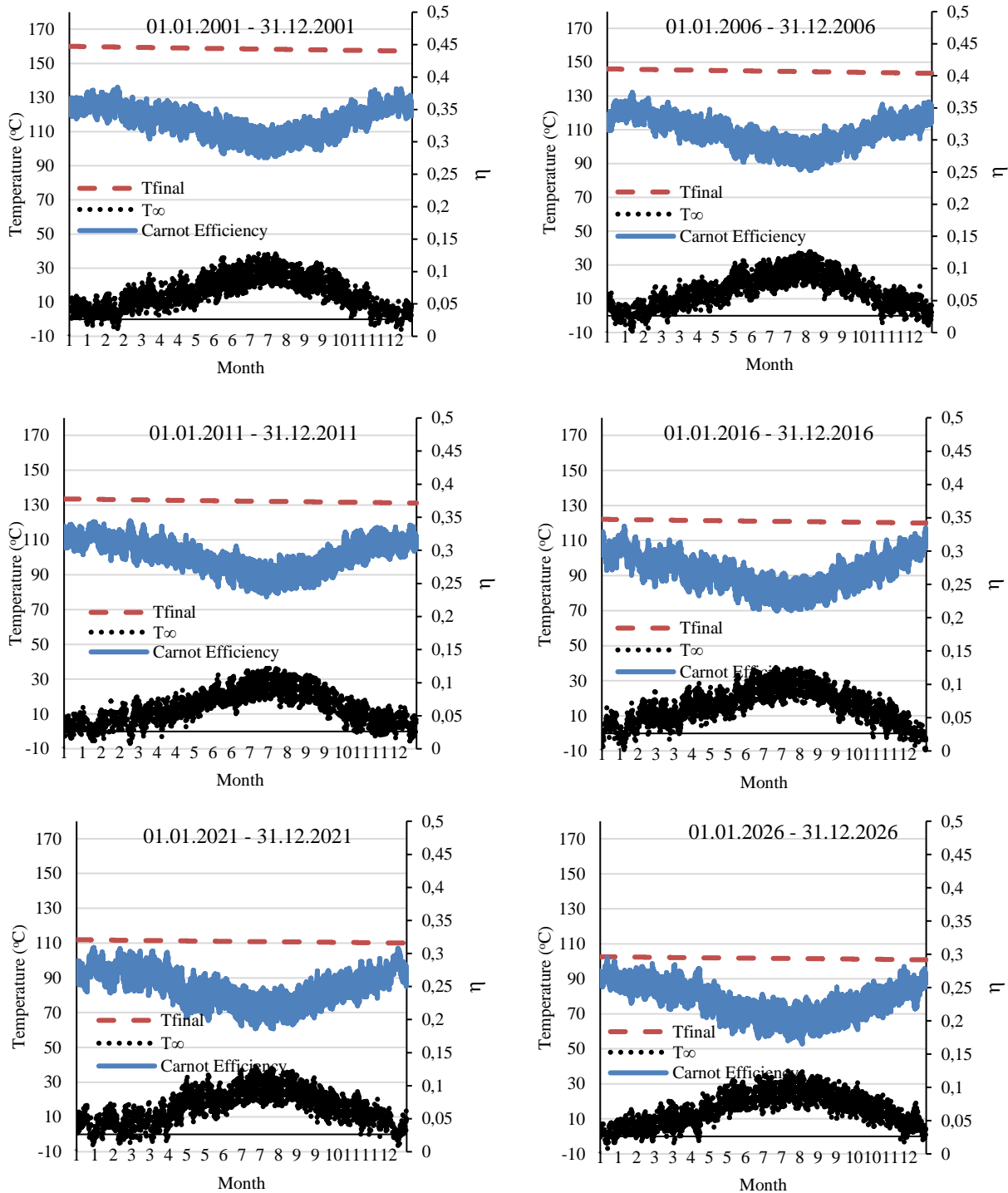
Figure 5. Hourly change in the geothermal resource according to years

As can be seen from the graphs here (Fig.5), the examination was carried out for each year (January 1 - December 31) at five-year intervals (2001-2026). The results were generated using daily data. During this period, the geothermal resource temperature values

decreased to 157.1 ºC at the end of 2001, 143.5 ºC at the end of 2006, 131.1 ºC at the end of 2011, 120.0 ºC at the end of 2016, 109.9 ºC at the end of 2021 and 100.8 ºC at the end of 2026. The decrease difference for each five years was calculated as 13.6 ºC, 12.4 ºC, 11.1 ºC, 10.1 ºC

and 9.1ºC, respectively. As can be seen from these data, the difference has tended to decrease over the years. Figure 5 more clearly illustrates the inverse relationship between Carnot efficiency and ambient conditions. The Carnot efficiencies calculated for every five years under examination are as follows: 27.5%-38.1%, 25.7%-37.0%, 23.6%-34.1%, 21.6%-33.2%, 18.5%-30.3%, and 16.5%-29.3%, respectively. This trend highlights the progressive

decline in Carnot efficiency over the years, further emphasizing the impact of environmental factors on thermodynamic performance.

Figure 6 shows the change in Carnot efficiency and temperature of the geothermal resource depending on the ambient temperature between 2001-2026.
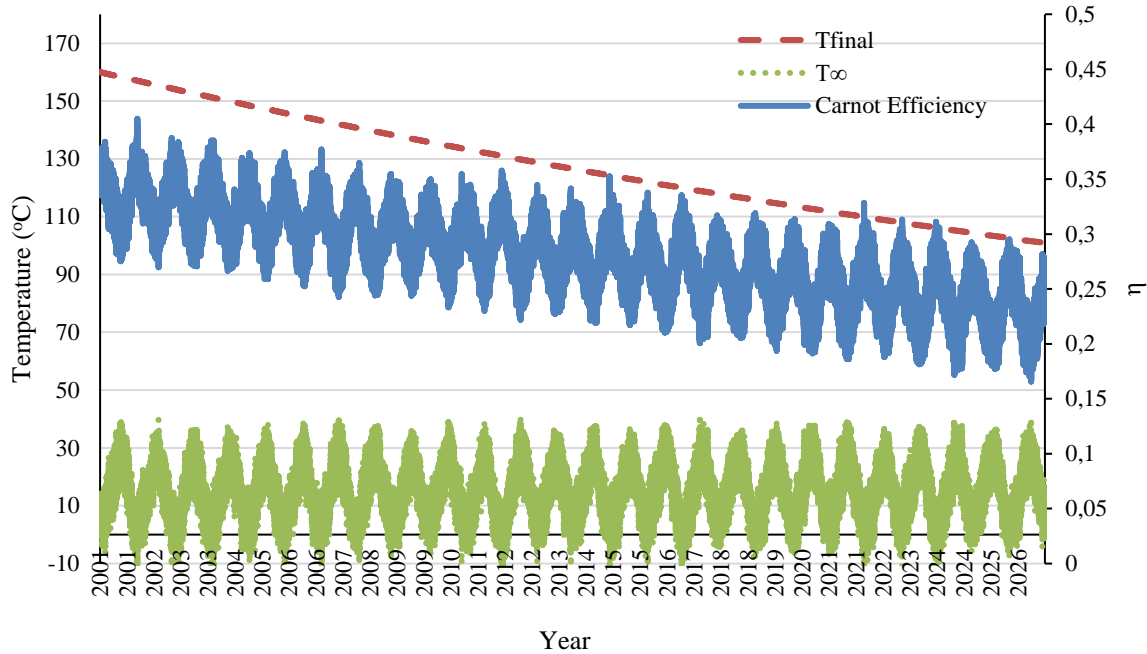
Figure 6. Comparisons of Carnot efficiency, temperature of geothermal resource and ambient temperature between 2001-2026

In Figure (Fig.6), geothermal resource temperature, ambient temperature, and Carnot efficiency changes are presented yearly from 2001 to 2026. The source temperature and Carnot efficiency exhibit a similar linear decrease over the years, whereas the ambient temperature shows relatively smaller annual variations. This phenomenon is due to the slower rate of increase in ambient temperature compared to the rate of decrease in source temperature. In the initial years, the difference between the Carnot efficiency and source temperature is more pronounced; however, this difference diminishes later. This trend is closely associated with the continued decrease in source temperature and the gradual increase in ambient temperature up to 2026, influencing the observed Carnot efficiency. Calculations were made starting from the first hour.

Accordingly, the maximum and minimum values of the source temperature and Carnot efficiencies obtained for each year are given in Table 1.

Table 1. Maximum and minimum values of the source temperature and Carnot efficiency for 2001-2026

Year	T_{source} (ºC)		Carnot efficiency (%)	
	Max.	Min.	Max.	Min.
2001	160.0	157.1	38.3	27.5
2002	157.1	154.2	40.4	26.9
2003	154.2	151.4	38.3	27.0
2004	151.4	148.7	38.5	26.6
2005	148.7	146.0	37.3	25.8
2006	146.0	143.4	37.4	25.2
2007	143.4	140.9	37.6	24.2
2008	140.9	138.3	36.4	24.3
2009	138.3	135.9	35.4	24.3
2010	135.9	133.5	35.4	23.3
2011	133.5	131.1	34.4	22.9
2012	131.1	128.8	35.7	22.1
2013	128.8	126.5	34.4	22.7
2014	126.5	124.3	32.9	21.9
2015	124.3	122.1	35.2	21.7
2016	122.1	119.9	33.7	21.0
2017	119.9	117.8	33.4	20.0
2018	117.8	115.8	31.7	20.5
2019	115.8	113.8	31.9	19.3
2020	113.8	111.8	31.3	19.1
2021	111.8	109.9	30.8	18.5
2022	109.9	108.0	32.8	18.8
2023	108.0	106.2	31.3	18.1
.2024	106.2	104.3	31.0	17.1
2025	104.3	102.6	29.3	17.7
2026	102.6	100.8	29.5	16.5

The highest and lowest geothermal source temperatures calculated for the first year (2001) are 160°C and 157.1°C, respectively. Throughout the life of a geothermal power plant it is seen that the source temperature drops from 160 °C to 100.8 °C. This data is important for the proper management of investments. At the beginning, the temperature drop difference was approximately 2.9 °C, but by the end, it had decreased to 1.8 °C. This change can be attributed to a heat transfer phenomenon driven by the reduction in the temperature gradient. As the source temperature gradually declined over the years, the temperature difference also diminished. However, the highest temperature value recorded for 2026 during this decline was calculated as 102.6°C.

Although the Carnot efficiency generally declines over the plant's lifespan, this decrease is not linear. As shown in the table, the Carnot efficiency values fluctuate. For instance, while an increase in the maximum value is observed from 2001 to 2002, an increase in the minimum value occurs between 2002 and 2003. However, during the same period (2002 to 2003), there is a significant decrease in the maximum value. The maximum and minimum Carnot efficiencies achieved over the plant life are 40.4% and 16.5%, respectively. Maximum Carnot efficiency (40.4%) was achieved in 2002, and minimum efficiency in 2026. These values are directly related to the ambient temperature. Over time, efficiency has decreased due to the decrease in source temperature and the effect of global warming.

4. DISCUSSION AND CONCLUSION

Geothermal energy constitutes a strategic advantage for sustainable energy production in Türkiye. To maximize the efficiency and sustainability of this resource, parameters such as reservoir temperature, depth, pressure, and long-term sustainability must be accurately determined. Additionally, the effects of climatic conditions on energy production should be considered. The average temperature in the region supports the stable and efficient operation of geothermal plants. In this context, accurately defining Denizli's geothermal potential is critical for achieving sustainable energy production and economic development goals. Advanced geothermal modeling, real-time monitoring systems, and environmental impact assessments will play a significant role in increasing the efficiency of energy investments in the region. In this study, the potential of a geothermal energy source located in Denizli district of Türkiye was determined and the environmental effects on the source were examined over time. The results obtained in this context are presented below.

- During the first year of the investment, source temperature was 157.1°C, respectively, with corresponding Carnot efficiencies of 38.3% and 27.5%. By the end of 2026, these values decreased to 102.6°C and 100.8°C for the source temperatures, and 29.5% and 16.5% for the Carnot efficiencies.
- The geothermal resource potential is calculated as 74.97 MWe, and the thermal energy stored in

the reservoir is determined as 5.94×10^{15} J. At the same ambient temperatures, these numbers become larger in sources with higher temperatures.

- The source temperature initially decreased by approximately 2.9°C – 1.7°C, but this difference diminished toward the end. The Carnot efficiency exhibited a fluctuating trend, namely, sometimes decreasing after a year and at other times increasing.
- The maximum and minimum rates of Carnot efficiency vary between 40.4% and 16.5%, respectively. The maximum and minimum rates were achieved in 2002 and 2026, respectively.
- The ambient and source temperatures corresponding to the maximum and minimum rates are 156.3°C (2002) and 101.5°C (2026), respectively. These values take different values at the same source temperature but in different locations due to the environmental temperature.

Acknowledgement

REFERENCES

[1] Yalcin M, Kalaycioglu S, Basaran C, Sari F, Gul FK. Exploration of potential geothermal fields using GIS-based entropy method: A case study of the Sandikli. Renew Energy 2024;237:121719. https://doi.org/10.1016/j.renene.2024.121719.

[2] Jess A. What might be the energy demand and energy mix to reconcile the world's pursuit of welfare and happiness with the necessity to preserve the integrity of the biosphere? Energy Policy 2010;38:4663–78. https://doi.org/10.1016/j.enpol.2010.04.026.

[3] Laming C. Renewable energy - The way forward. Eng Technol 2001;4:18-22.

[4] Gürtürk M, Ucar F, Erdem M. A novel approach to investigate the effects of global warming and exchange rate on the solar power plants. Energy 2022;239:122344. https://doi.org/10.1016/j.energy.2021.122344.

[5] Gürtürk M, Erdem M, Uçar F. Solar energy technical feasibility comparison: an alternative proposal for the Industry. Energy Effic 2024;17. https://doi.org/10.1007/s12053-024-10226-9.

[6] British Petroleum. bp Energy Outlook 2023 edition 2023 explores the key trends and uncertainties. Stat Rev World Energy 2023:1–53.

[7] Republic of Turkey Ministry of Environment U and CC. No Title 2024. https://netsifirturkiye.org/en/the-2053-net-zero-target-and-turkiyes-long-term-climate-change-strategy/.

[8] Erdem M, Gürtürk M. Economic analysis of the impact of Turkey's renewable support mechanism on solar energy investment. Util Policy 2025;92:101862.

125

https://doi.org/10.1016/j.jup.2024.101862.

[9] Republic of Turkey Ministry of Energy and Natural Resources. No Title 2024. https://enerji.gov.tr/bilgi-merkezi-enerji-elektrik#:~:text=2024 yılı Ekim ayı sonu itibarıyla kurulu gücümüzün kaynaklara göre,ü ise diğer kaynaklar şeklindedir.

[10] Bodvarsson G. Evaluation of geothermal prospects and the objectives of geothermal exploration. Geoexploration 1970;8:7–17. https://doi.org/https://doi.org/10.1016/0016-7142(70)90015-3.

[11] GENERAL DIRECTORATE OF MINERAL RESEARCH AND EXPLORATION (MTA). No Title 2024. https://www.mta.gov.tr/.

[12] Ahmadi A, El Haj Assad M, Jamali DH, Kumar R, Li ZX, Salameh T, et al. Applications of geothermal organic Rankine Cycle for electricity production. J Clean Prod 2020;274. https://doi.org/10.1016/j.jclepro.2020.122950.

[13] Song Y, Xu C. Design and performance analysis of a solar-geothermal-hydrogen production hybrid generation based on S–CO2 driven and waste-heat cascade utilization. Int J Hydrogen Energy 2022;47:28353–71. https://doi.org/10.1016/j.ijhydene.2022.06.177.

[14] Erdogdu E. A snapshot of geothermal energy potential and utilization in Turkey. Renew Sustain Energy Rev 2009;13:2535–43. https://doi.org/https://doi.org/10.1016/j.rser.2009.06.020.

[15] Yildirim D, Ozgener L. Thermodynamics and exergoeconomic analysis of geothermal power plants. Renew Sustain Energy Rev 2012;16:6438–54. https://doi.org/https://doi.org/10.1016/j.rser.2012.07.024.

[16] Ciriaco AE, Zarrouk SJ, Zakeri G. Geothermal resource and reserve assessment methodology: Overview, analysis and future directions. Renew Sustain Energy Rev 2020;119:109515. https://doi.org/https://doi.org/10.1016/j.rser.2019.109515.

[17] Mohan AR, Turaga U, Subbaraman V, Shembekar V, Elsworth D, Pisupati S V. Modeling the CO2-based enhanced geothermal system (EGS) paired with integrated gasification combined cycle (IGCC) for symbiotic integration of carbon dioxide sequestration with geothermal heat utilization. Int J Greenh Gas Control 2015;32:197–212. https://doi.org/https://doi.org/10.1016/j.ijggc.2014.10.016.

[18] NASA POWER Data Access Viewer n.d. https://power.larc.nasa.gov/data-access-viewer/.

[19] Gregory L. Mines. GETEM User Manuel, 2016.

[20] Zarrouk SJ, Moon H. Efficiency of geothermal power plants: A worldwide review. Geothermics 2014;51:142–53. https://doi.org/https://doi.org/10.1016/j.geothermics.2013.11.001.

[21] EPRI. Geothermal Energy Prospects for the Next 50 Years. Electr Power Res Inst. 1978.

[22] Korkmaz ED, Serpen U, Satman A. Geothermal boom in Turkey: Growth in identified capacities and

potentials. Renew Energy 2014;68:314–25. https://doi.org/https://doi.org/10.1016/j.renene.2014.01.044.

Effects of *Berberis vulgaris* L. Extract on the Physicochemical, Sensory, and Textural Properties of Raw and Cooked Patties

Kübra CINAR TOPCU[1*] iD **, Gamze UGUR[2]** iD

[1]Bayburt University, Aydıntepe Vocational School, Department of Food Science, Bayburt, Türkiye
[2]Bayburt University, Aydıntepe Vocational School, Food Technology, Bayburt, Türkiye
Kübra CINAR TOPCU ORCID No: 0000-0002-3715-8739
Gamze UGUR ORCID No: 0009-0009-9238-9589

Corresponding author: kcinar@bayburt.edu.tr

Keywords	**Abstract:** The effects of adding different concentrations (0.1%, 0.2%, and 0.4%) of *Berberis vulgaris* fruit extract to raw beef patties on their physicochemical properties were investigated. Physicochemical, sensory, and textural analyses were also performed on cooked beef patties. The addition of the extract did not cause a significant change in the approximate composition of the patties. (P<0.01). Initially, it significantly affected the TBARS value in all groups (P<0.05). However, there was no significant difference in TBARS values after cooking (p>0.05). While no significant difference was observed in the color values before cooking, cooking reduced L*, a*, and b* values. The cooking yield significantly affected all groups (P<0.01) and was reduced by adding Berberis extract. The incorporation of the extract did not induce any statistically important alterations in the sensory attributes of the patties. Furthermore, texture analysis revealed highly significant effects on the hardness, gumminess, and chewiness values across all groups (P<0.01). The results demonstrate that the extract did not notably change the patties' physicochemical properties. However, it effectively reduced lipid oxidation and enhanced their textural qualities. This study supports the potential use of *B. vulgaris* extract as a natural additive to improve the quality of beef patties.
Berberis vulgaris L., Pattie, TBARS, Texture	

127

Berberis vulgaris L. Ekstraktının Çiğ ve Pişmiş Köftelerin Fizikokimyasal, Duyusal ve Tekstürel Özelliklerine Etkisi

Anahtar Kelimeler	**Öz:** Farklı konsantrasyonlarda (%0,1, %0,2 ve %0,4) *Berberis vulgaris* meyve ekstraktı eklenmesinin çiğ sığır köftelerinin fizikokimyasal özellikleri üzerindeki etkileri araştırılmıştır. Ayrıca, pişmiş sığır köfteleri üzerinde fizikokimyasal, duyusal ve tekstürel analizler yapılmıştır. Ekstraktın ilavesi, köftelerin yaklaşık bileşiminde önemli bir değişikliğe neden olmamıştır. pH değerlerindeki değişim, tüm gruplarda anlamlı şekilde etkilenmiştir (P<0.01). İlk başta, TBARS değerini tüm gruplarda önemli ölçüde etkilemiştir (P<0.05). Ancak, pişirme sonrasında TBARS değerlerinde önemli bir fark gözlenmemiştir (p>0.05). Pişirmeden önce renk değerlerinde anlamlı bir fark gözlenmezken, pişirme L*, a* ve b* değerlerini azaltmıştır. Pişirme verimi, tüm grupları önemli ölçüde etkilemiştir (P<0.01). Köftelere Berberis ekstraktı eklenmesi pişirme verimini azaltmıştır. Ekstraktın ilavesi, köftelerin duyusal özelliklerinde istatistiksel olarak anlamlı bir değişiklik oluşturmamıştır. Ayrıca, tekstür analizi, tüm gruplarda sertlik, yapışkanlık ve çiğnenebilirlik değerleri üzerinde yüksek derecede anlamlı etkiler ortaya koymuştur (P<0.01). Sonuçlar, ekstraktın köftelerin fizikokimyasal özelliklerini kayda değer şekilde değiştirmediğini göstermektedir. Ancak, lipid oksidasyonunu etkili bir şekilde azaltır ve onların tekstürel niteliklerini artırır. Bu çalışma, sığır köftelerinin kalitesini artırmak için *B. vulgaris* ekstraktının doğal bir katkı maddesi olarak potansiyel kullanımını desteklemektedir.
Berberis vulgaris L., Köfte, TBARS, Tekstür	

1. INTRODUCTION

Adequate and balanced nutrition is essential for individuals to live healthily, develop economically and socially, and improve their overall well-being [1]. Among the vital nutrients, protein plays a crucial role, with meat and meat products being excellent sources of animal protein [2].. They are rich in essential amino acids and low in carbohydrates [3]. Additionally, meat is an excellent source of iron, zinc, selenium, niacin, vitamins A, B6, and B12, as well as essential fatty acids [4].

Beef patties are a traditional and popular food product with rich nutritional value and distinct flavor. However, due to factors such as processing, storage, and preservation methods, the quality of beef patties can be easily compromised, limiting their competitive position in the market [5]. Besides, suitable conditions for microorganisms, appropriate pH, high water activity, and the presence of unsaturated fatty acids, also contribute to the limited shelf life of beef patties, whether they are sold raw or partially cooked [6]. Therefore, attention must be given to every step of the production process to maintain product quality [5].

Lipid oxidation is one of the significant changes affecting the sensory properties of meat products, particularly in terms of flavor and texture, leading to a reduced shelf life. To extend shelf life and improve the overall quality of beef patties, various natural additives, spices, and plants are commonly used in the meat industry [7, 8]. In particular, the addition of natural antioxidants to meat products has become a key focus in recent research to enhancee oxidative stability and prevent microbial degradation [9, 10].

One such natural additive is *B. vulgaris*, a plant belonging to the Berberis genus of the Berberidaceae family. *B. vulgaris* is known for its red color and sour taste, and its fruit contains significant levels of antioxidant compounds that are beneficial for human health [11, 12]. This plant is commonly used in the food industry to produce jam, sweets, wine, and tea [13], and it has traditionally been used for medicinal purposes, particularly in treating kidney, urinary, and digestive disorders, as well as for improving circulation [14, 15].

In this study, *B. vulgaris* fruit extract was incorporated into beef patties as a natural antioxidant to assess its impact on the patties' physicochemical, sensory, and textural properties. The purpose of using *B. vulgaris* extract is to enhance the product's oxidative stability while preserving its nutritional and sensory characteristics. The study also aims to evaluate the extract's potential to improve the overall quality of beef patties.

2. MATERIAL AND METHOD

In the research, minced beef and beef fat obtained from a local butcher were used. *B. vulgaris* L. (barberry) fruit was collected from local gardens in Bayburt province. The minced beef and beef fat used in the study were brought to Bayburt University Aydıntepe Vocational School Department of Food Processing Laboratory under suitable conditions and stored at 4 °C until use as research material.

1.1. Preparation of Fruit Extract

100 grams of the fruit were weighed and dried in an oven at 50°C for two days. The dried fruit was then ground in porcelain mortars until it reached the desired grain size. Afterward, 100 mL ethanol (80%) was added to 10 g of sample and the mixture was left to extract for 48 hours in a water bath with temperature maintained below 40 °C. The extract was subsequently filtered and underwent evaporation in an evaporator. The obtained extract was dried in a lyophilizer and the fruit extract was prepared [16, 17].

1.2. Patties preparation and sampling

Minced beef and beef fat obtained from a local butcher were used in patty production at +4 °C. The fat proportion was set to 20% of minced beef, and a homogeneous mixture was obtained. The lyophilized extract was added to the mixture at rates of 0.1%, 0.2%, and 0.4%. The control group had no extract added. All groups had 1.5% salt added. The prepared mixtures were kneaded until homogeneous. The patties were shaped with a diameter of 9.0 ± 0.2 cm and a thickness of 1.0 ± 0.3 cm using Petri dishes. After shaping, the patties were left to rest at 4°C for 1 day. The weight of each patty was standardized to approximately 50 g. The patties, which had rested in the refrigerator, were cooked on a preheated heating plate set to 180°C for 12 minutes. During the cooking process, the patties were turned every two minutes.

1.3. Antioxidant Evaluations and Overall Phenolic Substance Content

The study employed three fundamental analysis methods to evaluate the antioxidant properties and total phenolic content of plant extracts. First, the DPPH analysis determined the extract's capacity to scavenge DPPH radicals, expressing antioxidant activity as Trolox equivalent (mg g^{-1}) based on the optical density measured at 517 nm [18]. Similarly, the ABTS analysis evaluated the extract's ability to reduce ABTS substrate, correlating the absorbance change at 734 nm with Trolox equivalent (mg g^{-1}) [19]. Additionally, the Folin–Ciocalteu phenol analysis determined the total phenolic components of the extract, presenting the results in terms of Gallic acid equivalent (mg g^{-1}) [20]. These analysis methods comprehensively assessed different aspects, including antioxidant capacity, radical scavenging ability, and total phenolic content, providing a detailed evaluation of the biological activity of plant extracts.

1.4. Physicochemical Analyses

Raw samples of patties from each group were analyzed for moisture [21], pH [22], ash [21], color, and thiobarbituric acid reactive substances (TBARS) [23]. Cooked patties from each group were analyzed for pH, TBARS, color, sensory analysis, and textural properties

128

after microbiological analyses were carried out. Additionally, the cooking yield of the patties was identified. Color values (L*, a*, b*) of the samples were determined using a Chroma Meter (CR-200, Minolta Co, Osaka, Japan) colorimeter. Color measurements were assessed according to the criteria determined by the Commission Internationale de l'E Clairage based on three-dimensional color measurements. Accordingly, color intensities are represented by L*; L*=0, black; L*=100 white (darkness/brightness); a*; +a*=red, -a*=green and b*; +b*=yellow, b*=blue. Before use, the device was calibrated with a standard calibration scale. The following equation was used to identify cooking yield [24].

$$Cooking\ yield = \left(\frac{patties\ weight\ after\ cooking\ (g)}{patties\ weight\ before\ cooking\ (g)}\right) * 100 \quad (1)$$

1.5. Total Aerobic Mesophilic Bacterial Count (TAMB)

Seeding was performed with the plate count agar (PCA, Merck) spreading method, and samples were incubated under aerobic conditions for 2 days at 30 °C in Petri dishes. Count results were determined as log cfu g^{-1} at the end of incubation [25].

1.6. Enterobacteriaceae Count

For the detection of Enterobacteriaceae counts, seeding was performed using the spreading method on violet red bile dextrose (VRBD, Merck) agar. Plates were incubated under anaerobic conditions for 2 days at 30 °C. Red colonies larger than 1 mm were counted after incubation and were given as log cfu g^{-1} [26].

1.7. Sensory Analysis

For sensory analysis, patties were cooked for 12 minutes on a heating plate at 170-180 °C, turning them until the internal temperature reached 72 °C. A panel of 10 panelists conducted sensory assessments of the ready-to-eat cooked patty samples using the following hedonic scale (1-9) [27].

1.8. Texture Profile Analysis

Texture analysis was carried out using a device (CT3, Brookfield Engineering Laboratories, USA). Cylindrical samples taken from the patties (20 mm diameter, 10 mm height) underwent TPA analysis (conditions: pretest velocity 1 mm g^{-1}, test velocity and post-test velocity 2 mm g^{-1}, 5 s between first and second compression and compression rate 50%) at room temperature with two compression cycles using a 50 mm cylindrical probe. Textural parameters were calculated from the obtained force-time curves (hardness, adhesiveness, cohesiveness, springiness, chewiness, gumminess, and resilience) [28].

1.9. Statistical Analyses

In the study, four different extract proportions (control, 0.1%, 0.2%, and 0.4% fruit extract) were used as factors. The research was arranged and carried out with two repetitions using a randomized complete block design. Only beef samples were used in the study, and the statistical analysis was performed accordingly. The results underwent variance analysis, and the means of significant main effects and interactions were compared using Duncan's multiple comparison test (SPSS 20.0).

3. RESULTS AND DISCUSSION

In this study, the antioxidant potential of *B. vulgaris* fruit extract was measured as 25.45±0.35 mg TE g^{-1} using the DPPH method and 42.42±2.59 mg TE g^{-1} using the ABTS method (Figure 1). Significant variations in antioxidant values reported in the literature were observed. Och et al. [29] reported higher DPPH and ABTS values compared to our study, whereas Gündoğdu et al. [30], Özgen et al. [31], and Yıldız et al. [32] reported lower ABTS values compared to our findings. These variations suggest that antioxidant activity is influenced by various factors such as geographical origin, environmental conditions, growing season, soil type, and post-harvest processing methods. Specifically, the climate and soil conditions in different cultivation regions can significantly affect the phenolic compounds and antioxidant capacities of plants. Additionally, variations in post-harvest processing techniques and extraction methods can determine the effectiveness and quantity of these compounds.

The high antioxidant values obtained in our study indicate that the extraction conditions used were more effective in isolating antioxidant compounds. These results highlight the potential of *B. vulgaris* as a rich source of antioxidants and emphasize the contribution of phenolic compounds to its antioxidant capacity.
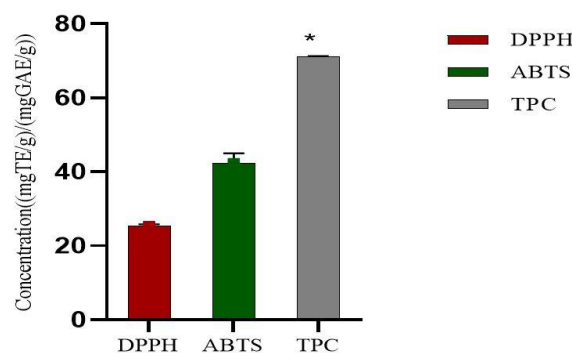
Figure 1. Antioxidant activity and total phenolic content of fruits

The total polyphenol content of *B. vulgaris* fruit in this study was determined to be 71.09±0.28 mg GAE g^{-1} as shown in Figure 1. Eroğlu et al. [33] reported lower and higher total phenolic contents in water and ethanol extracts, respectively. Similarly, Özgen et al. [31], Yıldız et al. [32], and Ersoy et al. [34] reported lower total phenolic contents compared to our study, while Motalleb et al. [35] reported higher phenolic content. These variations can be attributed to factors such as the geographical origin of the samples, environmental conditions, growing season, soil type, and post-harvest processing methods. For example, high UV radiation and low water stress in some regions may lead to an increase

in phenolic compounds, while more humid and temperate climates in other regions may result in lower levels of these compounds [36, 37].

Our study found that *B. vulgaris* fruit extract has high antioxidant potential and total phenolic content of. These findings suggest that *B. vulgaris* is an important source of antioxidants and that phenolic compounds contribute significantly to its antioxidant capacity.

Moreover, variations in antioxidant and total phenolic contents highlight the need for standardized methodologies to accurately compare these compounds across different studies and better understand the factors influencing their accumulation in *B. vulgaris*.

The physicochemical analysis results for the beef patties are presented in Table 1.

Table 1. Moisture, pH, ash, color, TBARS value, and cooking yield in raw and cooked beef patties (Mean ± SD)

		Ratio (%)				
		0	0.1	0.2	0.4	Sig
R	Moisture (%)	71.19±9.20a	63.13±0.47a	63.73±0.48a	64.94±0.35a	ns
C	Moisture (%)	55.21±0.51a	50.91±0.65a	54.90±4.99a	53.41±0.79a	ns
R/C Moisture (%) Interaction						**
R	pH	5.68±0.01c	5.62±0.01c	5.48±0.05b	5.32±0.06a	**
C	pH	5.91±0.01d	5.83±0.02c	5.71±0.01b	5.54±0.02a	**
R/C pH Interaction						**
R	Ash (%)	2.22±0.34a	1.29±0.55a	2.61±0.47a	1.94±0.59a	ns
C	Ash (%)	2.83±0.18a	2.76±0.11a	2.98±0.07a	2.75±0.06a	ns
R/C Ash (%) Interaction						*
R	L^*	65.46±4.31b	59.96±5.59ab	54.68±5.86a	60.37±3.16ab	ns
C	L^*	55.95± 1.77a	50.44± 7.56a	49.06±1.88a	51.88± 3.95a	ns
R/C L^* Interaction						ns
R	a^*	25.61±1.92a	26.32±6.26a	25.87±4.95a	29.18±0.65a	ns
C	a^*	23.09± 2.16b	17.46± 2.02a	17.49±0.96a	15.64± 3.77a	ns
R/C a^* Interaction						**
R	b^*	13.68±0.68a	13.34±2.24a	12.39±1.72a	12.61±2.79a	ns
C	b^*	9.40±1.38a	9.02± 1.58a	8.89±1.79a	8.89±2.74a	ns
R/C b^* Interaction						*
R	TBARS (mgMDA/kg)	1.95±0.04b	1.72±0.16b	1.53±0.08a	1.63±0.01a	**
C	TBARS (mgMDA/kg)	2.29±0.33a	1.72±0.36a	2.01±0.21a	1.86±0.14a	ns
R/C TBARS (mgMDA/kg) Interaction						ns
Cooking Yield (%)		75.72±1.22c	70.17±0.33b	68.87±0.72ab	67.41±0.57a	**

Sig (Significance), R (Raw), C (Cooked), SD (Standard Deviation), ** p<0.01, * p<0.05 (Significance Levels), ns (Non-significant for p>0.05), and different letters in the same column (a-c) indicating significant differences (p<0.05) are utilized.

As stated in the literature, the addition of the extract did not significantly alter the approximate composition of the patties, particularly with respect to moisture and ash content [6, 38]. These findings indicate that the extract's impact on the initial composition of the patties is limited. The observed loss of moisture during the cooking of patties aligns with a common outcome observed in meat and meat product cooking processes [39, 40].

However, the interaction between raw and cooked patties (R/C) showed significant changes in moisture retention, suggesting that the extract may influence the moisture retention capacity during cooking. Specifically, while the extract did not significantly alter the initial moisture content of the patties, it seems to modulate moisture loss during cooking, with a more pronounced effect seen in cooked patties. This finding supports the hypothesis that the addition of the extract may have an augmenting effect on moisture loss, particularly during cooking, and underscores the dynamic changes in composition that occur during the cooking process.

Thus, the addition of the extract maintains the stability of the patties' composition while inducing changes in moisture content, particularly during cooking. The interaction between raw and cooked patties indicates that the extract may influence the extent of moisture loss in the final cooked product.

The pH values of raw patties exhibit a significant effect across all experimental groups (P<0.01), indicating that the addition of the extract significantly lowered the pH levels. This decrease can be attributed to the naturally low pH value (2.85) of *B. vulgaris*. The pronounced effect of the extract on the acidic properties of the raw patties demonstrates a significant alteration in the pH profile induced by the botanical extract. During the cooking process, the interaction on pH becomes more complex, and a pronounced change is observed in all groups (P<0.01). This indicates how the extract interacts with the initial pH of the raw materials and the changes occurring during cooking. The extract appears to play a role in shaping the acidity profile in raw patties during cooking, with this effect becoming more pronounced in the cooked

patties. Furthermore, instead of the expected pH increase during cooking [41, 42], a lower pH value was observed in the raw patties, suggesting that the acidic components of the extract become more pronounced during cooking. Although an increase in pH during cooking is generally expected in meat [41, 42], the low pH of *B. vulgaris* has been shown to alter this expectation. The low pH of the extract influences the acidity profile in both raw and cooked patties, creating a more acidic environment during the cooking process. These findings emphasize the role of the botanical extract in this interaction and contribute to our understanding of its effects on acidity control throughout the cooking process. In conclusion, the pH interaction between raw and cooked patties shows that the addition of the extract not only influences the initial pH levels but also shapes the changes in acidic properties during cooking. This suggests a more dynamic interaction with pH during cooking and highlights the extract's significant influence on this process.

The TBARS values of raw patties exhibited a significant impact in all groups (P<0.05). The presence of antioxidants and phenolic components in the extract reduced lipid oxidation and free radical formation, thereby enhancing the product's antioxidant capacity. An increase in the extract proportion resulted in lower TBARS values compared to the control group. These findings align with studies conducted by Ahn and Grün [43], Mahapatra et al., [44], and Erdoğan and Özdestan-Ocak [38]. During the cooking process, no significant difference was observed between TBARS values (p>0.05). This suggests that the cooking procedure did not influence TBARS values. However, it is important to note that the interaction between the raw and cooked patties revealed dynamic changes in TBARS values. While no significant differences were observed during cooking, the antioxidant properties of the extract in the raw patties still effectively mitigated lipid oxidation and free radical formation. This suggests that the extract's role in controlling lipid oxidation is most prominent in the raw patties, with its impact on TBARS values remaining stable throughout the cooking process. These results affirm that the low TBARS values in raw patties can be attributed to the antioxidant properties of the extract, effectively mitigating lipid oxidation and free radical formation. The interaction highlights that while the extract reduces lipid oxidation in raw patties, its effect does not change significantly during cooking, suggesting that the antioxidant capacity is retained during thermal processing. These findings underscore the significant potential of plant extracts in enhancing the quality of raw patties while maintaining their antioxidant efficacy during cooking.

Although no statistically significant differences were observed in color values, cooking resulted in a notable decrease in L*, a*, and b* values. These color changes can be attributed to biochemical processes, such as an increase in metmyoglobin concentration or myoglobin denaturation. The findings align with similar results in the literature, supporting the impact of decreases in color values during cooking on meat pigments [8]. During cooking, a significant interaction between raw and cooked patties was observed, leading to changes in color parameters. While no significant differences were found between groups, the cooking process affected the color properties of the patties, with a decrease in L*, a*, and b* values. This suggests that the extract may modulate color changes during cooking, possibly influencing myoglobin stability or the rate of metmyoglobin formation. The interaction between raw and cooked patties highlights the dynamic nature of color changes during cooking, which could have implications for the visual properties of the product. Considering that color changes directly affect the visual and sensory characteristics of a product, these findings emphasize the importance of understanding the physical and chemical transformations occurring during the cooking process. Ultimately, the study contributes valuable insights into the potential effects of color changes during cooking on product quality. The interaction findings suggest that cooking not only affects color values but also influences the extract's role in color stability during the process.

The cooking of meat is a crucial step for flavor enhancement. Microbiological analyses play a pivotal role in evaluating the microbiological quality of the product, aligning with product specifications or legally applicable standards [45]. In this study, microbiological analyses indicated that the total aerobic mesophilic bacteria and Enterobacteriaceae counts were below the detectable limit (<2 log cfu g^{-1}) after the cooking process. The microbiological results underscore the notion that the cooking process enhances microbiological quality, contributing significantly to the overall quality of the product. The use of extract is believed to potentially contribute to maintaining microbial stability. This aspect holds particular importance for the product's consequently and consumer health. However, a more detailed analysis is warranted to elucidate the specific effects of the extract on microbiological stability. Further investigation into how the extract may exert antimicrobial effects and impact microbial growth would provide valuable insights. Such in-depth analyses can inform specific strategies to maintain and improve the microbiological quality of the product.

Cooking yield is a critical parameter for evaluating quality changes in meat products during the cooking process [46]. In this study, a significant reduction in cooking yield (P<0.01) was observed in patties formulated with Berberis extract. This result may be attributed to the extract's potential to enhance fat and moisture loss during cooking. The literature frequently highlights the influence of additive composition and thermal properties on cooking yield [47].

The reduction in cooking yield caused by Berberis extract suggests that it may limit water and fat binding capacity, affecting the stability of the protein matrix. This finding contrasts with the results of Naveena et al. [48], who reported that additives improved cooking yield in chicken burgers. Differences between studies could arise from variations in the chemical composition of the extract, the type of meat, and the applied processes.

131

The results underscore the need for further investigation into the effects of Berberis extract on fat and moisture loss. Future research could guide the development of novel formulations to optimize these effects.

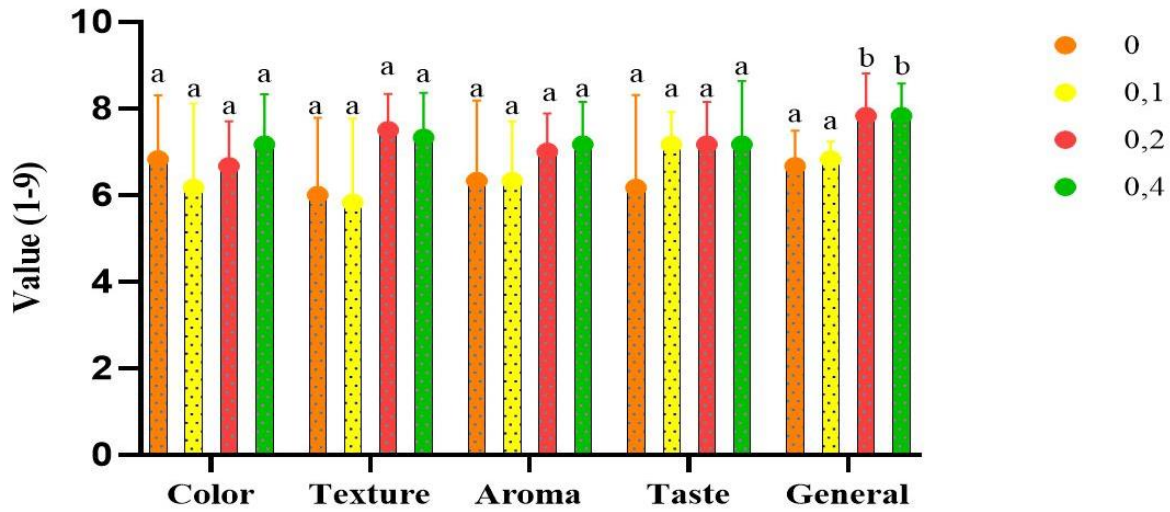The sensory analysis results for the beef patties were given in Figure 2.

Figure 2. The sensory analysis results for the beef patties.

The columns in the table represent the mean of three replicates, and the vertical bars indicate the standard error of the mean. Distinct letters denote statistically significant variances based on Duncan's multiple range test (p < 0.05).

The addition of the extract did not result in significant changes in the sensory characteristics of the patties. However, according to the panelists' evaluations, an improvement in sensory properties was observed as the extract proportion increased. Although no statistically significant differences were found, these observations suggest that the extract may have a subtle but positive effect on sensory profiles such as flavor, aroma, and texture. Similarly, in a study by Naveena et al. [49], plant extracts showed a tendency for improved flavor and texture profiles as extract concentrations increased,

although no statistically significant differences were found. These findings are consistent with the data from our study, where a trend of improvement in sensory characteristics was observed with an increase in extract proportion, despite the lack of statistical significance. Additionally, Bouarab-Chibane et al. [50] reported that plant extracts had varying effects on sensory characteristics such as color, texture, and taste. While some extracts led to distinct sensory changes, others did not result in meaningful differences in sensory perception. This is in line with our findings, suggesting that plant extracts have the potential to improve sensory attributes, with the degree of impact varying depending on the extract type and concentration.

Texture analysis results for the beef patties are presented in Table 2.

132

Table 2. Texture analysis results (Mean ± SD)

	Raito (%)				
	0	0.1	0.2	0.4	Sig
Hardness (N)	62.49±6.89a	72.29±8.87ab	88.78±7.016c	82.40±5.013bc	**
Adhesiveness (mJ)	0.40±0.29a	0.30±0.13a	0.13±0.14a	0.13±0.15a	ns
Resilince	0.24±0.015a	0.28±0.01a	0.26±0.022b	0.25±0.01ab	ns
Cohesiveness	0.52±0.01a	0.55±0.05a	0.60±0.03b	0.56±0.03ab	ns
Springeness (mm)	9.24±0.48a	9.10±0.59a	9.06±0.44a	9.44±0.68a	ns
Gumminess (N)	32.56±3.07a	40.54±9.01ab	53.65±5.64c	46.03±3.16bc	**
Chewiness (mJ)	299.82± 14.19a	358.90±53.01a	485.85±57.78b	433.50±30.30b	**

Sig (Significance), SD (Standard Deviation), ** p<0.01, * p<0.05 (Significance Levels), ns (Non-significant for p>0.05), and different letters in the same column (a-c) indicating significant differences (p<0.05) are utilized.

The effects of different concentrations of *B. vulgaris* extract on the texture properties of meatballs were investigated. Significant statistical differences in hardness, gumminess, and chewiness values were observed across all groups (P<0.01). An increase in extract concentration resulted in a notable rise in the hardness, gumminess, and chewiness values of the meatball samples. These findings suggest that Berberis

vulgaris extract has a reinforcing effect on the protein matrix. Plant polyphenols can interact with proteins, forming cross-links that may enhance the structural integrity of the meatballs [51]. However, variability in the mechanisms of action of different plant extracts has been observed in the literature. For example, in the study by Mahapatra et al. [52], it was reported that certain fruit extracts reduced the hardness of meat products. On the

other hand, Salejda et al. [53] reported that the addition of cherry cornis juice had an increasing effect on the hardness of model beef meatballs. These differences may be attributed to the chemical composition of the extracts, application ratios, and the physicochemical properties of the meat product [54].

The increase in gumminess and chewiness values may be linked to the extract's capacity to enhance the mechanical stability of the meatballs. The extract's effect of increasing water and fat loss during cooking may have contributed to the formation of a denser protein matrix, thereby improving gumminess and chewiness. Additionally, the phenolic compounds in plant extracts may strengthen protein-protein interactions, creating a tighter structure that further enhances these properties. Literature on the effects of plant extracts on gumminess and chewiness shows varied results. For instance, Choi et al. [55] found that increasing lotus leaf powder levels from 1% to 3% led to a significant decrease in the hardness, stickiness, and chewiness values of chicken meatballs.

These findings suggest that *B. vulgaris* extract has the potential to improve the texture properties of meatballs. The results of this study highlight the practical potential of using Berberis vulgaris extract as a natural food additive. Future research could further explore the effects of varying extract concentrations and evaluate their impact on sensory properties.

4. CONCLUSION

This study investigated the effects of *B. vulgaris* extract on the physicochemical, sensory, and textural properties of beef patties. The results demonstrated that while the extract did not significantly alter the moisture, ash content, or color, it reduced lipid oxidation (TBARS values) and enhanced textural parameters such as hardness, gumminess, and chewiness. However, the extract caused a significant reduction in cooking yield, potentially due to its effect on fat and moisture retention.

These findings suggest that *B. vulgaris* extract can be utilized as a natural antioxidant in meat products, contributing to oxidative stability and textural improvements. Further studies are necessary to optimize extract concentrations and minimize adverse effects on cooking yield. Additionally, exploring its interaction with other additives and its impact under different cooking conditions could broaden its industrial application. This research highlights the potential of *B. vulgaris* extract as a sustainable alternative to synthetic additives, paving the way for healthier and more natural meat products.

REFERENCES

[1] Wells JC, Marphatia AA, Amable G, Siervo M, Friis H, Miranda JJ, et al. The future of human malnutrition: rebalancing agency for better nutritional health. Globalization and health. 2021;17(1):1-25.

[2] Lee HJ, Yong HI, Kim M, Choi YS, Jo C. Status of meat alternatives and their potential role in the future meat market—A review. AJAS. 2020;33(10):1533.

[3] Ogundipe OO, Fasogbon BM, Ayeke AO, Nwosu PN, Adebayo-Oyetoro AO, Faloye OR. Quality evaluation of beef patties formulated with wheat and sweet potato flour blends. Food Sci Appl Biotechnol. 2023;6(2):187-199.

[4] Majeed T, Maqbool N, Sajad A, Aijaz T, Khan ZS. Meat as a functional food for health. ın functional foods. 1st Ed. CRC Press; 2024.

[5] Meng X, Wu D, Zhang Z, Wang H, Wu P, Xu Z, et al. An overview of factors affecting the quality of beef meatballs: Processing and preservation. Food Scı Nutr. 2022;10(6):1961-1974.

[6] Ergezer H, Serdaroğlu M. Antioxidant potential of artichoke (Cynara scolymus L.) byproducts extracts in raw beef patties during refrigerated storage. J Food Meas Charact. 2018;12:982-991.

[7] Manessis G, Kalogianni AI, Lazou T, Moschovas M, Bossis I, Gelasakis AI. Plant-derived natural antioxidants in meat and meat products. Antioxidants. 2020; 9(12):1215.

[8] Kirkyol M, Akköse A. Effects of animal fat replacement with almond flour on quality parameters of beef patties. Food Scı Nutr. 2023;11(11):7091-7099.

[9] Karre L, Lopez K, Getty KJK. Natural antioxidants in meat and poultry products. Meat Sci. 2013;94:220–227.

[10] Falowo AB, Fayemi PO, Muchenje V. Natural antioxidants against lipid-protein oxidative deterioration in meat and meat products: a review. Food Res Int. 2014;64:171–181.

[11] Yang L, Zhang Z, Hu X, You L, Khan RAA, Yu Y. Phenolic contents, organic acids, and the antioxidant and bio activity of wild medicinal Berberis plants-as sustainable sources of functional food. Molecules. 2022;27(8):2497.

[12] Gacche RN, Dhole NA. Antioxidant and possible anti-inflammatory potential of selected medicinal plants prescribed in the Indian traditional system of medicine. Pharm Biol. 2006;44:389–395.

[13] Gruenwald J, Brendler T, Jaenicke C. PDR for herbal medicines fourth edition. Thomson; 2007.

[14] Sobhani Z, Akaberi M, Amiri MS, Ramezani M, Emami SA, Sahebkar A. Medicinal species of the genus Berberis: a review of their traditional and ethnomedicinal uses, phytochemistry and pharmacology. Pharmacological Properties of Plant-Derived Natural Products and Implications for Human Health, 2021;547-577.

[15] Blumenthal M, Busse WR, Goldbert A, Gruenwald J, Hall T, Klein SR. The complete German E monographs-therapeutic guide to herbal medicines. American Botanical Council, Austin, TX;1998.

[16] Deliorman Orhan D, Hartevioglu A, Kupeli E, Yesilada E. In vivo anti-inflammatory and antinociceptive activity of the crude extract and fractions from Rosa canina L. fruits. J Ethnopharmacol. 2007;112:394–400.

[17] Kasımoğlu C, Uysal H. Farklı test sistemleri ile somatik hücrelerde profenofos genotoksisitesine karşı kuşburnu (Rosa canina L.) ekstrelerinin doğal bir antigenotoksik ajan olarak kullanılması. Cumhuriyet Üniversitesi Fen Fakültesi Fen Bilimleri Dergisi (CFD), 2016;37:1.

[18] Kumaran A, Karunakaran RJ. In vitro antioxidant activities of methanol extracts of five Phyllanthus species from India. LWT. 2007;40(2):344-352.

[19] Re R, Pellegrini N, Proteggente A, Pannala A, Yang M, Rice-Evans C. Antioxidant activity applying an improved ABTS radical cation decolorization assay. Free Radıcal Bıo Med.1999;26(9-10):1231-1237.

[20] McDonald S, Prenzler PD, Antolovich M, Robards K. Phenolic content and antioxidant activity of olive extracts. Food Chem. 2001;73(1):73-84.

[21] AOAC. Meat and meat products. Chapter 39. In W. Horwitz (Ed.), Official methods of analysis (18th ed., pp. 8). AOAC International; 2005.

[22] Gökalp HY, Kaya M, Tülek Y, Zorba O. Et ürünlerinde kalite kontrolü ve laboratuar uygulama klavuzu (4. Baskı). Atatürk Üniversitesi Yayınları, Yayın No: 751. Ziraat Fakültesi Yayın No: 318, Atatürk Üniviversitesi Ofset Tesisi, Erzurum. 2010.

[23] Lemon DW. An improved TBA test for rancidity new series circular. No:51.Halifax-Laboratory, Halifax, Nova Scotia;1975.

[24] Murphy EW, Criner PE, Gray BC. Comparisons of methods for calculating retentions of nutrients in cooked foods. J Agric Food Chem.1975;23(6):1153-1157.

[25] Ismail SAS, Deak T, Abd El-Rahman HA, Yassien MAM, Beuchat LR. Presence and changes in populations of yeasts on raw and processed poultry products stored at refrigeration temperature. Int J Food Microbiol. 2000;62(1-2):113-121.

[26] Santos MHS. Amino acid decarboxylase capability of microorganisms isolated in Spanish fermented meat products. Int J Food Microbiol. 1998;39(3):227-230.

[27] Reihani SFS, Tan T-C, Huda N, Easa AM. Frozen storage stability of beef patties incorporated with extracts from ulam raja leaves (Cosmos caudatus). Food Chem. 2014;155:17-23.

[28] Bourne MC. Texture profile analysis. Food Technol. 1978;32:62-66.

[29] Och, A, Olech M, Bąk K, Kanak S, Cwener A, Cieśla M, et al. Evaluation of the antioxidant and anti-lipoxygenase activity of Berberis vulgaris L. leaves, fruits, and stem and their LC MS/MS polyphenolic profile. Antioxidants. 2023;12(7):1467.

[30] Gündoğdu M. Determination of Antioxidant Capacities and Biochemical Compounds of Berberis vulgaris L. Fruits. AEB. 2013;7(2):344-348.

[31] Ozgen M, Saraçoglu O, Geçer EN. Antioxidant capacity and chemical properties of selected barberry (Berberis vulgaris L.) fruits. HEB. 2012;53(6):447–451.

[32] Yildiz H, Ercisli S, Sengul M. Topdas EF, Beyhan O, Cakir O, et al. Some physicochemical characteristics, bioactive content and antioxidant characteristics of non-sprayed barberry (Berberis vulgaris L.) fruits from Turkey. Erwerbs-Obstbau, 2014;56(4):123–129.

[33] Eroğlu AY, Çakır Ö, Sağdıç M, Dertli E. Bioactive characteristics of wild Berberis vulgaris and Berberis crataegina fruits. J Chem. 2020;1-9.

[34] Ersoy N, Kupe M, Sagbas HI, Ercisli S. Physicochemical diversity among barberry (Berberis vulgaris L.) fruits from eastern Anatolia. Not Bot Horti Agrobo. 2018;46(2):336–342.

[35] Motalleb G, Hanachi PS, Kua H, Othman F, Asmah R. Evaluation of phenolic content and total antioxidant activity in Berberis vulgaris fruit extract. J Biol Sci. 2005;5(5):648–653.

[36] Çağlar M, Demirci M. Üzümsü meyvelerde bulunan fenolik bileşikler ve beslenmedeki önemi. EJOSA. 2017;7(11):18-26.

[37] Gökçen İS, Keskin N. Asmanın UV (ultraviyole) stresine yanıtları. In: Türkoğlu N, Cantürk S editörs. Ziraat ve doğa bilimleri. 1st ed. Cetinje-Karadağ: Ivpe; 2020. P. 1-18.

[38] Erdoğan B, Özdestan-Ocak Ö. Inhibitory effects of carob and propolis extracts on the formation of heterocyclic aromatic amines in beef patties cooked with different methods. J Food Process Pres. 2022;46(7):16623.

[39] Sheridan PS, Shilton NC. Analysis of yield while cooking beef-burger patties using far infrared radiation. J Food Eng. 2002;51:3–11.

[40] Del Pulgar JS, Gázquez A, Ruiz-Carrascal J. Physico-chemical, textural and structural characteristics of sous-vide cooked pork cheeks as affected by vacuum, cooking temperature, and cooking time. Meat Sci. 2012;90(3):828-835.

[41] Puolanne EJ, Ruusunen MH, Vainionpää JI. Combined effects of NaCl and raw meat pH on water-holding in cooked sausage with and without added phosphate. Meat Sci. 2001;58(1):1-7.

[42] Choi YS, Sung JM, Park JD, Hwang KE, Lee CW, Kim TK, et al. Quality and sensory characteristics of reduced fat chicken patties with pork back fat replaced by dietary fiber from wheat sprout. Korean J Food Scı An. 2016;36(6):799–806.

[43] Ahn J, Grün IU. Heterocyclic amines: 2. Inhibitory effects of natural extracts on the formation of polar and nonpolar heterocyclic amines in cooked beef. J Food Scı. 2005;70(4):C263-C268.

[44] Mahapatra G, Biswas S, Banerjee R. Improving the quality and shelf-life of chevon meatballs by incorporating fruit and fruit by-products. Indian J Anim Sci. 2021;90:1655-1662.

[45] Blackburn CW. 'Microbiological testing in food safety and quality'. Mead, G. (Ed.) Microbiological analysis of red meat, poultry and eggs. management' Woodhead Publishing; 2006.

[46] Pietrasik Z, Li-Chan ECY. Binding and textural properties of beef gels as affected by protein, κ-

carrageenan and microbial transglutaminase addition. Food Res Int. 2002;35(1):91-98.

[47] Turp GY, Icier F, Kor G. Influence of infrared final cooking on color, texture and cooking characteristics of ohmically pre-cooked meatball. Meat Sci. 2016;114: 46-53.

[48] Naveena BM, Muthukumar M, Sen AR, Babji Y, Murthy TRK. Quality characteristics and storage stability of chicken patties formulated with finger millet flour (Eleusine coracana). J Muscle Foods. 2006;17(1):92-104.

[49] Naveena BM, Sen AR, Vaithiyanathan S, Babji Y, Kondaiah N. Comparative efficacy of pomegranate juice, pomegranate rind powder extract and BHT as antioxidants in cooked chicken patties. Meat Sci, 2008;80(4):1304-1308.

[50] Bouarab-Chibane L, Ouled-Bouhedda B, Leonard L, Gemelas L, Bouajila J, Ferhout H, et al. Preservation of fresh ground beef patties using plant extracts combined with a modified atmosphere packaging. Eur Food Res Technol. 2017;243:1997-2009.

[51] Atacan K. Polifenollerle fonksiyonelleştirilmiş Fe3O4 nanopartiküllerine tripsin ımmobilizasyonu ve sindirim uygulaması. Doktora Tezi. Sakarya Universitesi Türkiye. 2016.

[52] Mahapatra G, Biswas S, Patra G, Vidyarthi AK. Enhancement of storage stability, textural profile, physico-chemical parameters and sensory attributes of chevon meatballs by guava powder incorporation. IJBSM, 2019;10(4):346-351.

[53] Salejda AM, Kucharska AZ, Krasnowska G. Effect of Cornelian cherry (Cornus mas L.) juice on selected quality properties of beef burgers. J Food Qual. 2018;(1):1563651.

[54] Olkiewicz M, Tyszkiewicz S, Wawrzyniewicz M. Effect of basic chemical composition and functional additives on rheological characteristics of selected meat products, Acta Agrophysica. 2007;9:147–169.

[55] Choi YS, Choi JH, Kim HY, Kim HW, Lee MA, Chung HJ, et al. Effect of lotus (Nelumbo nucifera) leaf powder on the quality characteristics of chicken patties in refrigerated storage. Food Sci Anim Resour. 2011;31(1):9-18.

135

Türk Doğa ve Fen Dergisi
Turkish Journal of Nature and Science
www.dergipark.gov.tr/tdfd

BINGÖL UNIVERSITY

Renewable Energy and Hydrogen Storage System Analysis for Carbon Neutral Campuses with HOMER

Faruk BARLAZ[1*] iD, Yahya AKIL[2] iD, Cem HAYDAROĞLU[3] iD, Heybet KILIÇ[2] iD

[1] Dicle University, Institute of Science, Diyarbakır, Türkiye
[2] Dicle University, Department of Electrical Energy and Energy, Diyarbakır, Türkiye
[3] Dicle University, Department of Electrical and Electronics Engineering, Diyarbakır, Türkiye

Faruk BARLAZ ORCID No: 0009-0003-2703-0234
Yahya AKIL ORCID No: 0000-0002-7497-6458
Cem HAYDAROĞLU ORCID No: 0000-0003-0830-5530
Heybet KILIÇ ORCID No: 0000-0002-6119-0886

*Corresponding author: cem.haydaroglu@dicle.edu.tr

Abstract: This study presents a detailed techno-economic analysis of a Hybrid Renewable Energy System (HRES) designed to achieve carbon neutrality for Dicle University in Diyarbakır, Turkey. Leveraging the region's high solar potential and moderate wind availability, the system integrates photovoltaic panels (PV), wind turbines (WT), battery storage systems (BSS), electrolyzers, and hydrogen storage tanks (HST). Despite the wind potential being less pronounced than solar energy in Diyarbakır, wind turbines are included to ensure energy diversity and reliability, particularly during non-sunny periods. The analysis, conducted using HOMER Pro software and local meteorological data, evaluates the system's capacity to meet a daily energy demand of 34.3 kWh. The optimized system comprises an 123 kW PV array, a 10 kW WT, an 1 kWh BSS, a 113 kW electrolyzer, and a 1000 kg hydrogen storage capacity. The economic analysis reveals a total capital cost of $483,650, a Net Present Cost (NPC) of $537.006,57, and a Levelized Cost of Energy (LCOE) of $10.66/kWh. Results demonstrate the feasibility and efficiency of integrating renewable energy sources with hydrogen storage to achieve energy sustainability, reliability, and significant carbon emission reductions. This work provides a scalable model for deploying HRES in similar climates and institutions.

136

Karbon Nötr Kampüsler için Homer ile Yenilenebilir Enerji ve Hidrojen Depolama Sistemleri Analizi

Anahtar Kelimeler
Yenilenebilir Enerji,
Hidrojen depolama,
Hibrit yenilenebilir
enerji sistemi
(HYES),
Karbon nötrlüğü,
Teknik ve ekonomik
analiz,
HOMER

Öz: Bu çalışma, Diyarbakır'daki Dicle Üniversitesi için karbon nötrlüğe ulaşmayı hedefleyen Hibrit Yenilenebilir Enerji Sistemi'nin (HYES) ayrıntılı bir teknik ve ekonomik analizini sunmaktadır. Bölgenin yüksek güneş enerjisi potansiyeli ve orta düzeydeki rüzgar potansiyeli değerlendirerek sistem, fotovoltaik paneller (PV), rüzgar türbinleri (WT), batarya depolama sistemleri (BSS), elektrolizörler ve hidrojen depolama tanklarını (HDT) entegre etmektedir. Diyarbakır'da rüzgar potansiyeli güneş enerjisine kıyasla daha düşük olmasına rağmen, rüzgar türbinleri, özellikle güneşsiz dönemlerde enerji çeşitliliği ve güvenilirliği sağlamak amacıyla sisteme dahil edilmiştir. HOMER Pro yazılımı ve yerel meteorolojik veriler kullanılarak gerçekleştirilen analiz, günlük 34,3 kWh enerji talebini karşılayacak sistemin kapasitesini değerlendirmektedir. Optimize edilen sistem, 123 kW PV dizisi, 10 kW WT, 1 kWh BSS, 113 kW elektrolizör ve 1000 kg hidrojen depolama kapasitesinden oluşmaktadır. Ekonomik analiz, toplam sermaye maliyetini 483.650 $, Net Mevcut Maliyeti (NPC) 537.006,57 $ ve Düzlenmiş Enerji Maliyetini (LCOE) 10,66 $/kWh olarak ortaya koymaktadır. Sonuçlar, yenilenebilir enerji kaynaklarının hidrojen depolama ile entegre edilmesinin enerji sürdürülebilirliği, güvenilirliği ve karbon emisyonlarının önemli ölçüde azaltılmasında etkin ve uygulanabilir bir çözüm sunduğunu göstermektedir. Bu çalışma, benzer iklim ve kurumlarda HRES uygulaması için ölçeklenebilir bir model sağlamaktadır

1. INTRODUCTION

The demand for electricity is rising in line with the growth of the global population.[1] The principal factors contributing to this growth can be attributed to the accelerated pace of technological and industrial advancement, as well as the proliferation of electrical devices utilized by consumers across various facets of life [2]. This necessity is typically fulfilled by fossil fuels, which are detrimental to the environment and finite in supply [3]. The global energy crisis has emerged concurrently with the global health crisis triggered by the advent of the COVID-19, the Red Sea crisis, and Russia's invasion of Ukraine [4]. The aforementioned crises have resulted in a scarcity of environmentally detrimental fossil fuels and a surge in their market value. In consequence of this unfavorable situation, investments in renewable energy sources (RES), which consist of environmentally friendly and limited energy sources such as solar, wind, and biomass, have accelerated [5]. For example, the installed capacity of wind power plants worldwide reached 1 TW by the end of 2023 [6]. Furthermore, Turkey, with its growing population and developing industry, derives 44.8% of its energy needs from fossil fuels and 55.2% from renewable sources of energy (RES) as a result of its investments in RES [7].

In 2035, a peak in energy consumption will be reached, indicating a subsequent increase in greenhouse gas emissions [8]. To address these concerns, countries are formulating policies aimed at eliminating these emissions. These policies are designed to promote carbon neutral transitions across various sectors, including transportation and grid stabilization [9]. A significant approach to achieving this objective involves the utilization of green hydrogen, which involves the storage and transportation of excess energy produced by renewable energy sources [10]. Nuclear energy is poised to emerge as a reliable alternative for reducing greenhouse gas emissions [11].

The immediate fluctuations in RES production levels, which are contingent upon atmospheric and environmental circumstances, diminish the dependability of energy provision. This has a detrimental impact on energy efficiency and sustainability [12]. To address this challenge, hybrid renewable energy systems (HRES), which integrate multiple energy sources, have been developed [13]. The implementation of HRES has resulted in enhanced sustainability, security, and efficiency in energy utilization [14]. Moreover, depending on the design region-specific criteria, a HRES can incorporate some or all of these sources, including wind, biomass, geothermal, hydro, diesel generator (DG), batteries, pumped storage, and flywheel [15], [16] . In light of the region-specific criteria, it is imperative to devise an optimal HRES design for stochastic load cases that is both reliable and cost-effective. To this end, comprehensive technical, economic, and environmental analyses must be conducted, and the most suitable components must be selected and positioned based on the findings of these analyses [17].

A number of commercial software programs are available for designing HRES including Hybrid Optimization of Multiple Energy Resources (HOMER Pro), RETScreen, PVWatts, EnergyPLAN, KomMod, PVSyst software, Hybrid2, Helioscope, iHOGA software, and TRNSYS [18]. These software programs facilitate the design, sizing, technical, and economic evaluation of HRES [19]. HOMER Pro offers notable advantages, including a straightforward user interface, effective graphical representation of results, and an hourly data processing capacity [20]. Moreover, in comparison to other software programs, HOMER Pro boasts a more extensive repository of renewable resources, the capacity to model grid-connected or standalone systems, and the capability to conduct economic assessments. However, the most significant advantage of HOMER Pro over other programs is its ability to simulate and optimize according to techno-economic evaluations in varying scenarios [21].

In [22], conducted a technical and economic analysis of an electric vehicle charging station in Karampura, Delhi, for three different cases of photovoltaic (PV)-Hydrogen, Wind (WTG)-Hydrogen and PV-WTG-Hydrogen, employing the use of HOMER Pro software. In [23], a techno-economic analysis was conducted utilising the HOMER Pro software for a wind-powered hydrogen refuelling station in seven South African cities, designed to serve 25 hydrogen vehicles with a tank capacity of 5 kg per day. In [24], A technical and economic analysis was conducted of three different systems, namely a PV-Hydrogen system, a Wind-Hydrogen system and a PV-WTG-Hydrogen system, using the HOMER Pro software. In [25], provides financial resources for investment in clean energy infrastructure in Australia. For this purpose, the technical and economic viability of the WTG-Hydrogen system and the PV-WTG-Hydrogen system has been evaluated using HOMER Pro software, with the expectation that they will facilitate the production of hydrogen in Australia. In [26], conducted a technical and economic analysis of a HRES consisting of PV, WTG, electrolyser, hydrogen tank, battery, fuel cell (FC), hydrogen boiler and thermal load in Northern Alberta, Canada. This was achieved through the utilisation of the HOMER Pro software, with five different scenarios being considered. In [27], a HRES model comprising PV system, WTG, biogas generator (BGG) and battery storage system (BSS) was subjected to technical and economic analysis using the HOMER Pro software. The model was designed for a village situated in the rural Bingöl province. In [28], a technical and economic analysis of four different scenarios was conducted using HOMER Pro software: grid-connected grid-DG, grid-DG-PV, grid-DG-PV-BSS and grid-DG-BSS. In [29], conducted a technical and economic analysis for an off-grid HRES in Afyon province of Turkey using the HOMER Pro software, comprising PV system, electrolyser, hydrogen tank and FC. In [30], conducted a technical and economic analysis utilising HOMER Pro software for an off-grid HRES comprising PV, WTG, DG and BSS for the Navajo region in New Mexico.

In this study, a HRES system was developed in the software platform HOMER Pro for the purpose of reducing the carbon emissions of the Dicle University

campus in Diyarbakır province. The system comprises PV, WTG, BSS, hydrogen, a hydrogen tank and an electrolyser. Diyarbakır province is distinguished by its considerable solar potential. The objective is to utilise the surplus or irregular output generated by PV and WTG at the appropriate juncture by storing hydrogen. Consequently, techno-economic analyses have been conducted and evaluated for the system to be devised.

2. MATERIAL AND METHOD

The planned HRES system of Dicle University is situated at the following geographical coordinates: 40°16′ N longitude and 37°54′ N latitude. According to data from the General Directorate of Renewable Energy, Turkey and, in particular, the Southeastern Anatolia Region is a region with a high level of total global solar radiation, with a solar radiation of 1460 kWh/m²-year and an average sunshine duration of 2993 hours/year [31]. Figure 1 illustrates the fluctuations in global radiation and sunshine duration across months in Diyarbakır province. It can be observed that Diyarbakır receives approximately eight hours of sunshine annually on average. The province's higher sunshine levels than the national average in Turkey highlight the potential for effective utilisation of this energy source [32].
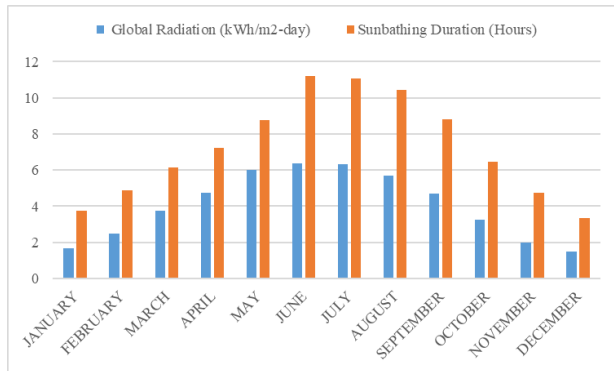

Figure 1. Average Global Radiation Values and Sunrise Durations

2.1. HOMER Pro

HOMER Pro is a user-friendly software, the use of which is free of charge, that has been developed for the purpose of facilitating the design of electric renewable energy systems. The software was designed in 1993 by the US National Renewable Energy Laboratory (NREL) for use with both on-grid and off-grid systems, and has since become widely used worldwide. The software simulates system configurations and provides optimised results in terms of net present cost, which can be analysed in tabular and graphical form. HOMER Pro is developed in C++ on the Windows platform and employs the HDKR anisotropic model for solar energy systems. The software allows users to input component costs, energy sources and other technical data in order to analyse different system configurations. The software is capable of simulating 8,760 hours per year and provides comprehensive outputs for economic and technical assessments. However, it should be noted that HOMER Pro has certain limitations. These include the fact that it only works with a single

objective function, does not consider battery depth of discharge (DOD), and ignores intra-hour variations and bus voltage variations. It may therefore be beneficial to enhance the flexibility and support for different optimisation techniques, which could further expand the use of HOMER [18], [33].

2.2. PV system

In this study, 8 Kw flat plate PV panel is used. HOMER Pro software calculates the power output of the PV array according to Equation 1 [7].

$$P_{PV} = A_{PV} k_{pv} \left(\frac{H_L}{H_{L,STC}} \right) \left[1 + \beta_P \left(L_c - L_{c,STC} \right) \right] \qquad (1)$$

In this context, A_{PV} represents the power output under test conditions (kW), k_{PV} denotes the PV depreciation factor [%], and H_L signifies the solar radiation incident on the PV array at the current time step [kW/m²]. $H_{L,STC}$ represents the incident radiation under standard test conditions, which is defined as 1 kW/m². β_P denotes the power temperature coefficient. L_c signifies the temperature of the PV cell at the current time step, whereas $L_{c,STC}$ denotes the temperature of the PV cell under standard test conditions, which is set at 25°C.

2.3. WTG System

The WTG utilised in the HOMER Pro simulation model from this study has a rotor diameter of 15.81 m, a nominal capacity of 10 kW, an on-start wind speed of 2.75 m/s and an off-start speed of 20 m/s. The HOMER Pro software employs the logarithmic law, as outlined in Equation 2, to calculate the wind speed at the hub height of the WTG.

$$H_b = H_m x \left(\frac{w_b}{w_m} \right) \gamma \qquad (2)$$

In this context, H_b represents the wind speed at the hub height of the wind turbine (m/s). H_m denotes the wind speed at the anemometer height (m/s). w_b signifies the hub height of the wind turbine (m). w_m is the anemometer height (m), and γ is the power law exponent [7].

2.4. Converter System

Converter technology facilitates bidirectional energy transfer, enabling the fulfilment of energy loads. This is achieved by converting energy generated from wind turbines from alternating current (AC) to direct current (DC) and power from photovoltaic (PV) panels from DC to AC. The HOMER software employs a comprehensive evaluation process to assess the performance of converters, taking into account key parameters such as efficiency, lifetime and cost [23].

138

2.5. Battery Storage System (BSS)

As the system is off-grid, 1 kWh of lead-acid batteries are employed for energy storage. The HOMER Pro software calculates the charge and discharge states of the BSS in accordance with Equations 3 and 4 [7].

$$O_n(t) = \frac{gR_1(t)e^{-g} + R(t)gc(1-e^{-g\Delta t})}{1-e^{-g\Delta t} + c(g\Delta t - 1 + 1 - e^{-g\Delta t})} \quad (3)$$

$$O_n(t) = \frac{-gR_{max}(t) + gR_1(t)e^{-g\Delta t} + R(t)gc(1-e^{-g\Delta t})}{1-e^{-g\Delta t} + c(g\Delta t - 1 + 1 - e^{-g\Delta t})} \quad (4)$$

In this context, R_{max} represents the total storage capacity, R_1 denotes the amount of energy stored in the batteries (kWh), R signifies the total amount of energy (kWh), c is the storage capacity ratio, g is the storage rate constant, and Δt is the time interval.

2.6. Electrolyser (ELC)

Electrolysers are instrumental in the field of energy storage, facilitating the splitting of water into hydrogen and oxygen. During daylight hours, the system produces hydrogen using solar energy and demineralised water. The hydrogen is then compressed and stored in the tank, ready for use in energy production when required. PEM (Proton Exchange Membrane) electrolysers offer several advantages over conventional alkaline electrolysers, including higher efficiency, faster response times and the production of hydrogen with a purity level of 99.999%. PEM technology addresses the limitations of alkaline electrolysers, such as low pressure operation and low current, thereby enabling a wide operating range. Furthermore, the utilisation of materials such as platinum as electrodes confers a distinct advantage in terms of performance. In the study, the PEM electrolyser was identified as the optimal choice due to its high efficiency and superior features. The capital cost of the system was calculated to be $80,000, the replacement cost was calculated to be $44,926.71, and the operation and maintenance cost was determined to be $30 with 85% efficiency [34]–[36].

2.6. Hydrogen Tank (HST)

Once the hydrogen has been produced by the electrolyser, it is stored in hydrogen tanks for subsequent use. The most common storage method is that of high-pressure gas cylinders. In recent years, technological advances have made it possible to use lightweight composite cylinders that can withstand 800 bar pressure and allow hydrogen to reach a density of 36 kg/m³ [37].

2.7. Economic Modeling

The economic viability of hydrogen refuelling stations was evaluated using the HOMER Pro software. The analysis was based on key economic indicators, including the net present cost (NPC), the levelised cost of energy (LCOE), and the hydrogen production cost (LCOH) [38], [39].

Net present cost:

The net present cost (NPC) can be calculated in accordance with equation 5 by subtracting the present value of the costs incurred over the life cycle of a project from the present value of the revenues to be generated over the same period. The calculation is made using the total annual cost (D_T) and the capital recovery factor ($DFG(j,K)$). $DFG(j,K)$ is a factor used to determine the present value of annual revenues and can be calculated in accordance with equation 6:

$$D_{NPC} = \frac{D_T}{DFG(j,K)} \quad (5)$$

$$DFG(j,K) = \frac{j(1+j)^K}{(1+j)^K - 1} \quad (6)$$

In this equation, the variable "j" represents the real interest rate, expressed as a percentage, while the variable "K" denotes the lifespan of the component, expressed in years.

Levelised cost of energy

The term 'Levelised Cost of Energy' (LCOE) is used to describe the average cost per kWh of useful energy produced by a power generation system. The LCOE is calculated in accordance with equation 7, where B_r represents the total electrical energy (kWh/year) required to maintain the operation of the hydrogen refuelling station [38], [39]

$$LCOE = \frac{D_T}{B_r} \quad (7)$$

Levelised cost of hydrogen production

The levelised cost of hydrogen production (LCOH) is a metric used to assess the economic efficiency of hydrogen production processes. In the HOMER Pro software, LCOH is calculated as the difference between the total annual cost and the annual cost of electricity, divided by the annual hydrogen production [40]. This metric is used to optimise the production costs of a hydrogen production system per kWh or kilogram, and is calculated according to equation 8:

$$LCOH = \frac{D_T - D_{elec}}{M_H} \quad (8)$$

This calculation method assesses the cost-effectiveness of the system, taking into account both capital investment and operating costs. Furthermore, it provides a basic tool for analysing the impact of hydrogen production costs on energy demand and production capacity. Consequently, it offers a comprehensive view of the long-term economic feasibility of the system [40]. In this context, D_T represents the total annual capital cost of the refuelling station, expressed in dollars per year. D_{elec}, on the other hand, denotes the annual revenue generated from electricity sales, also expressed in dollars per year. Finally, M_H represents the annual mass of hydrogen produced, expressed in kilograms per year.

139

3. RESULTS

The design of a microgrid for hydrogen production has been realized with Homer Pro to be used for various purposes on the Dicle University campus. In the designed system, temperature, solar, and wind data were obtained from NASA data in Homer Pro software. The hybrid energy system designed with Homer Pro software was analyzed. In this study, two different scenarios were considered. The unit costs of renewable energy equipment used for these scenarios are given in Table 1.

Table 1. Unit cost values

Component	Capital ($)	Replacement ($)	O&M ($)	Salvage ($)	Total ($)
Generic 10 Kw	50,000.00	15,590.00	6,391.68	8,737.45	63,244.47
Generic 1kWh Lead Acid	3,300.00	6,297.73	1,406.17	380.93	10,622.97
Generic Electrolyzer	5,250.00	2.190.64	536.90	407.75	7,569.79
Generic Flat Plate PV	369,000.00	0.00	15,723.53	0.00	384,723.53
Hydrogen Tank	31,500.00	0.00	6,391.68	0.00	37,891.68
System Converter	24,600.00	10,264.72	0.00	1,910.59	32,954.13
System	483,650.00	34,343.09	30,449,96	11,436.72	537,006,57

The present study is grounded in the same coordinates of the Dicle University campus depicted in Figure 2 for both scenarios, thereby ensuring the consistency of the simulation results.

In the present study, the utilization of a singular load model is advocated for two discrete scenarios. The annual modification of this load model is delineated in Figure 3.

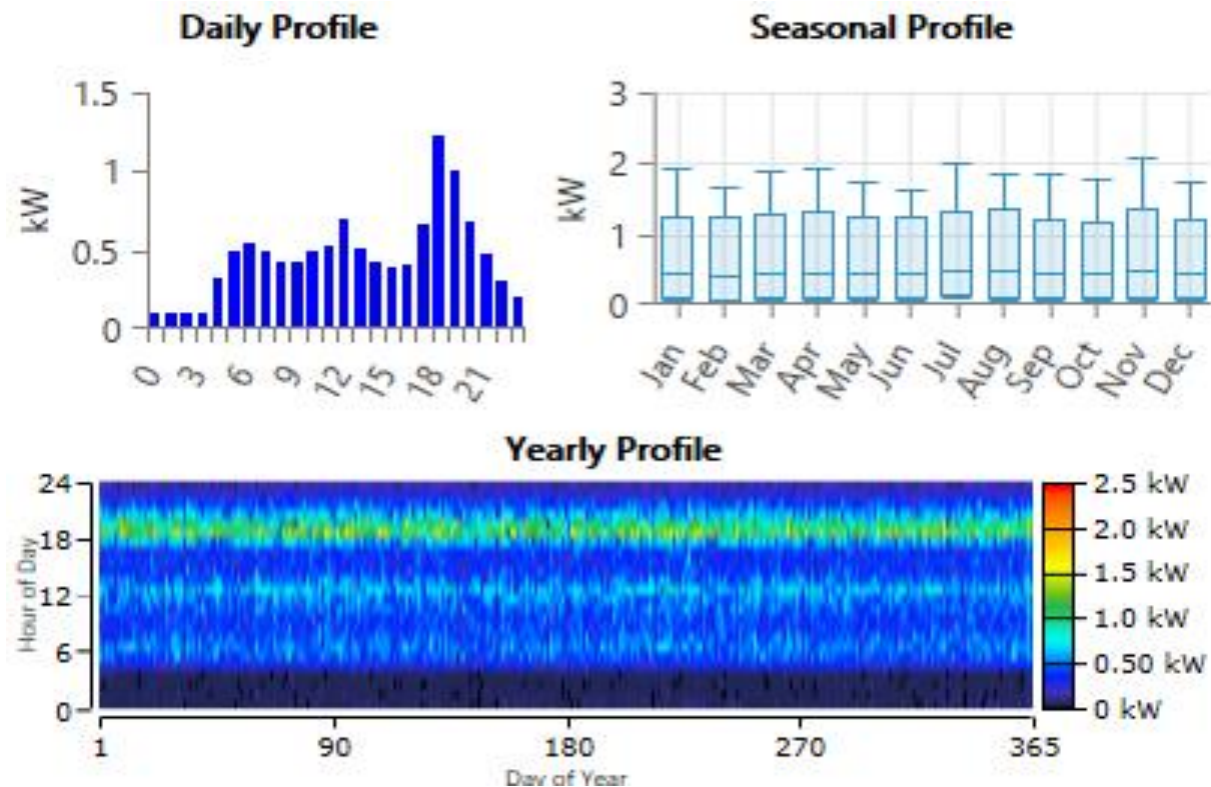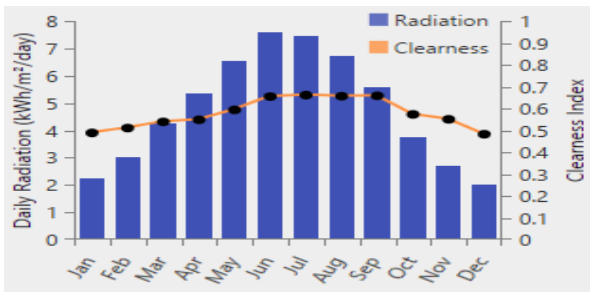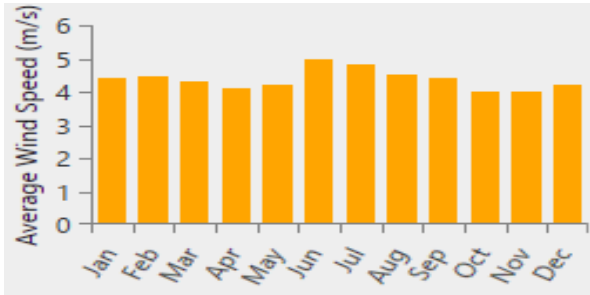**Figure 2.** Homer Pro Model Dicle University coordinates

Figure 3. Daily/monthly/annual change of load

The coordinates for the Dicle University campus were entered into the Homer Pro simulation program, which provides daily changes in radiation and average wind speed, as illustrated in Figure 4.

(a)

(b)

Figure 4. a) Daily Radiation Change b) Average Wind Speed Change

Given the application of identical coordinates in both scenarios examined in this study, it is reasonable to conclude that the weather change coordinates are equivalent in both scenarios.

3.1. Scenario 1

In this particular scenario, the HRES campus model, which consists of off-grid photovoltaics (PV), wind turbines (WTG), and electrolyzers (ELC), was developed in Homer Pro. This model encompasses 123 kW PV panels, 10 kW WTG, 1 kWh battery storage system, 113 kW electrolyzer, and a 1000 kg hydrogen storage tank (HST) for hydrogen production from solar energy. Homer Pro proposes an 82 kW converter to store electrical energy and meet energy demand. The Homer Pro campus model is depicted in Figure 5.
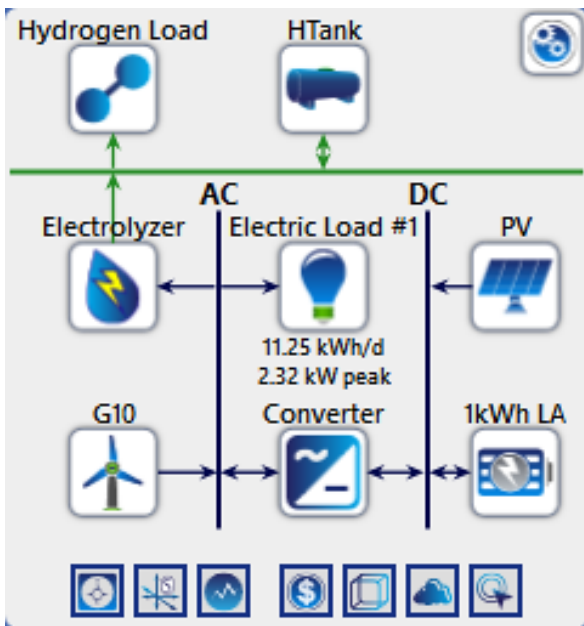

Figure 5. Off-grid HOMER Pro HRES model at Scenario 1

The proposed HRES system is designed to meet daily energy production of 34.3 kWh and peak energy demand of 4,102 kW. The capital cost of the system is calculated to be \$483,650.00, while the operation and maintenance costs are calculated to be \$30,449.96. The net present cost (NPC) of the system is \$537,006.57, while the levelized cost of energy (COE) is \$10.66/kWh. The off-grid PV-WTG system designed at Homer Pro is estimated to generate 202,302.31 kW of energy for one year. The PV component of the system is responsible for meeting 95% of the total energy demand, while the WTG component accounts for the remaining 5%. The energy production from each energy source over a one-year period is illustrated in Figure 6.
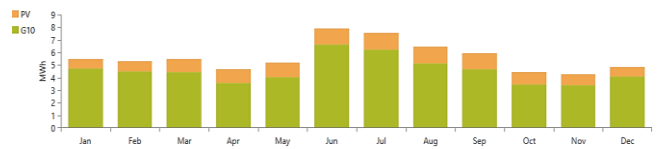
Figure 6. Production Quantities according to HOMER Pro

As illustrated in Figure 7, the power output of the PV exhibits a notable increase, particularly during the summer months. However, the presence of black gaps in the graph indicates a reduction in output on cloudy days. The PV contributes a significant amount to the annual electricity production, with a total of 192,583.60 kW.
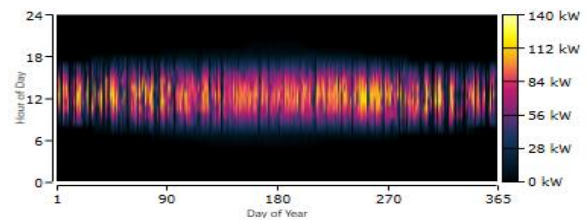
Figure 7. PV Generated Power Amount

141

The power output of the WTG is illustrated in Figure 8. Despite intermittent periods, the turbine generated electricity almost continuously throughout the year, contributing a total of 9,718.71 kW.
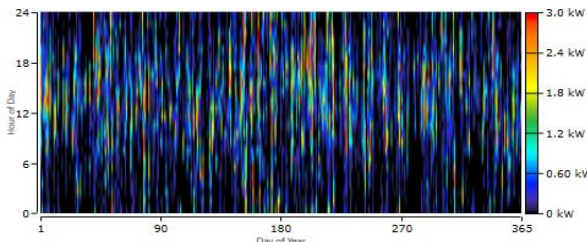
Figure 8. WTG Power Production Quantity

The purpose of the designed off-grid system is to utilize excess energy generated from PV, WTG and BSS. The system also employs an electrolyzer to store excess energy and produce hydrogen. Figure 9 illustrates the monthly energy consumption of the electrolyzer. Over the course of a year, the energy consumption amounted to 190,936.60 kW.
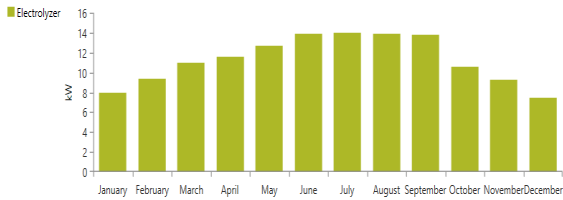
Figure 9. Electrolizer energy consumption change

It has been demonstrated that the electrolyzer functions at maximum capacity and produces hydrogen, particularly during daylight hours. In the off-grid PV-WTG system designed in the Homer Pro simulation program, the surplus energy is stored as hydrogen through the electrolyzer. Subsequently, the hydrogen is utilized to satisfy the energy requirements of the system via the fuel cell. The power input graph of the electrolyzer is depicted in Figure 10.
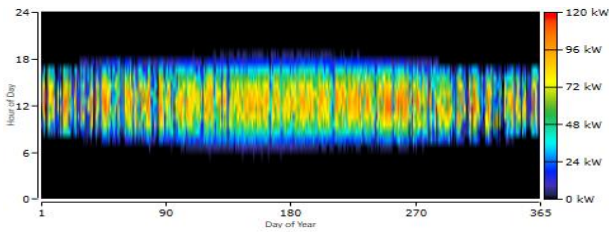
Figure 10. Electrolyzer Power Change Quantity

In scenarios where energy is inadequate for the load, the stored hydrogen is utilized to generate electricity through fuel cells. This system necessitates daily replenishment of the hydrogen tank, as illustrated in Figure 11. The total amount of hydrogen stored throughout the year is 1756,470.00 kilograms.
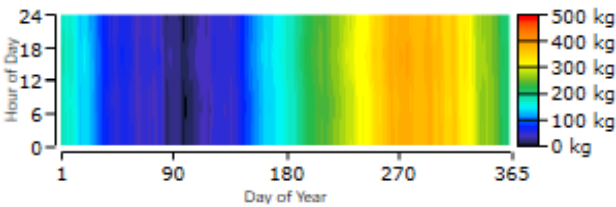
Figure 11. Hydrogen tank filling change

The charge change of the battery used in the off-grid PV-WTG system throughout the year is illustrated in Figure 12.
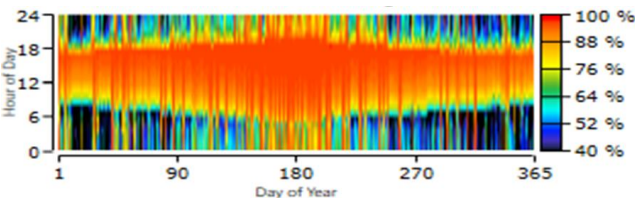
Figure 12. Battery Charge Replacement (SoC)

3.2. Scenario 2

In this scenario, the HRES campus model, consisting of off-grid PV and ELC systems, is constructed in Homer Pro. The model encompasses 123 kW PV panels, a 1 kWh battery storage system, an 113 kW electrolyzer, and a 1000 kg hydrogen storage tank (HST) for hydrogen

production from solar energy. Homer Pro proposes an 82 kW converter to store electrical energy and meet energy demand. The Homer Pro campus model is depicted in Figure 13.
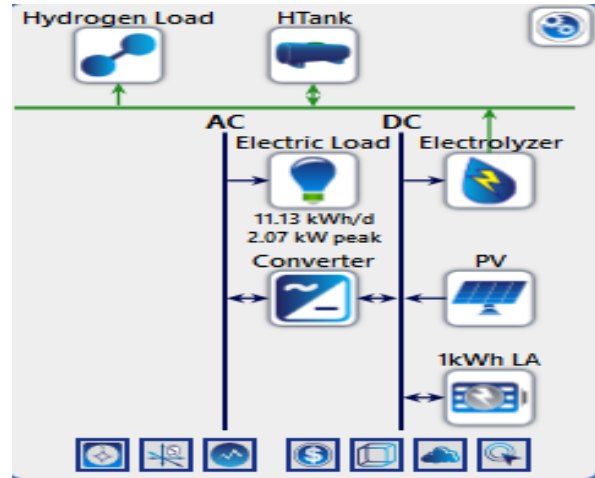
Figure 13. Off-grid HOMER Pro HRES model at Scenario 2

The capital cost of the proposed HRES system was calculated to be $433,650.00, while the operation and maintenance costs were calculated to be $24,058.28. The net present cost (NPC) of the system is thus $473,762.1, and the levelized cost of energy (COE) is $8.96/kWh.
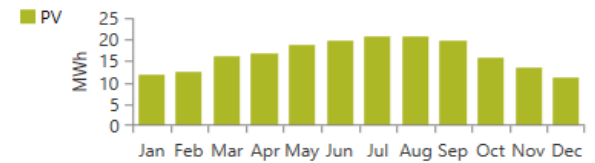
Figure 14. Of-grid PV system monthly generation change

The PV energy production for the Off-grid PV system designed in this scenario is shown in Figure 14. It produced a total of 197,280.75 kW of energy for one year.

Figure 15. Electrolizer energy consumption change

In the designed off-grid system, the excess energy produced by the PV system is utilized to store hydrogen through an electrolyzer. Figure 15 illustrates the monthly energy consumption of the electrolyzer. Over the course of a year, the energy consumption was 191,852.28 kW.
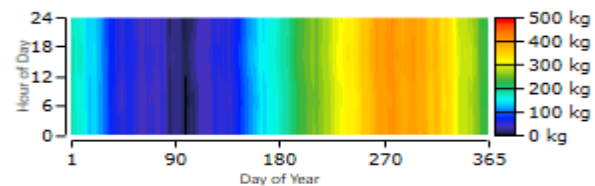
Figure 16. Hydrogen tank filling change

In scenarios where energy is limited or insufficient to meet the load, stored hydrogen is utilized to generate

142

electricity through the means of fuel cells or batteries, thereby supplying the system with energy. The necessity of daily replenishment of the hydrogen tank is illustrated in Figure 16. The total amount of hydrogen stored throughout the year is 1838,205.00 kilograms. Consequently, the average annual storage is 209.86 kilograms of hydrogen.

4. DISCUSSION AND CONCLUSION

Hydrogen has emerged as a pivotal energy carrier in the global transition towards sustainable and low-carbon energy systems. This study demonstrates the techno-economic feasibility of a hybrid renewable energy system (HRES) for Dicle University, integrating photovoltaic (PV) panels, wind turbines (WT), battery storage systems (BSS), and hydrogen storage technologies. By leveraging Diyarbakır's abundant solar potential and incorporating wind energy for diversity, the proposed system achieves a reliable and sustainable energy solution with minimized carbon emissions. The integration of hydrogen storage, particularly during surplus energy generation, addresses variability in renewable resources and ensures a stable energy supply.

This study investigates two distinct scenarios.In the first scenario, a fully independent hybrid energy system is modeled by integrating photovoltaic (PV), wind turbine (WTG), biomass-to-energy (BESS), electrolyzers, and hydrogen storage tanks. The excess electrical energy generated in this system is converted into hydrogen gas through electrolysis and stored. When energy demand arises, the system is sustained by converting the hydrogen back into electricity. The capital cost of this model was calculated as $483,650.00, while the levelized cost of energy (LCOE) was determined as $10.66/kWh.In the second scenario, an energy model was created using only PV panels. Wind turbines were removed from the system, and the role of the hydrogen storage system was increased. In this scenario, excess electricity is stored as hydrogen to ensure uninterrupted energy supply. The capital cost of this system was calculated as $433,650.00, and the LCOE value was determined as $8.96/kWh.In terms of hydrogen storage capacity, Scenario 2 increased the security of energy supply by producing and storing more hydrogen per year.

Hydrogen production through Proton Exchange Membrane (PEM) electrolyzers significantly enhances system performance with high efficiency and purity levels. The stored hydrogen provides flexibility for various applications, contributing to energy resilience during periods of low renewable energy availability. Future advancements in electrolyzer technology and reductions in storage costs are critical for further optimizing the system's economic and environmental benefits. Supportive policies and financial incentives can accelerate the adoption of similar HRES solutions in academic institutions and rural areas.

REFERENCES

[1] Doğan, S., Haydaroğlu, C., Gümüş, B., & Mohammadzadeh, A. (2024, November). Innovative fuzzy logic type 3 controller for transient and maximum power point tracking in hydrogen fuel cells. *International Journal of Hydrogen Energy*, (August).

[2] Aydın, F., & Öztürk, D. (2024, August). Design and techno-economic analysis of hybrid power systems for rural areas: A case study of Bingöl. *Electricity, 5*(3), 562–584.

[3] Iqbal, R., Liu, Y., Zeng, Y., Zhang, Q., & Zeeshan, M. (2024). Comparative study based on techno-economics analysis of different shipboard microgrid systems comprising PV/wind/fuel cell/battery/diesel generator with two battery technologies: A step toward green maritime transportation. *Renewable Energy, 221*(July), 119670.

[4] Haydaroğlu, C., Kılıç, H., & Gümüş, B. (2024, September). Performance analysis and comparison of performance ratio of solar power plant. *Turkish Journal of Electrical Power and Energy Systems*.

[5] Purlu, M., & Ozkan, U. (2023, February). Economic and environmental analysis of grid-connected rooftop photovoltaic system using HOMER. *Turkish Journal of Electrical Power and Energy Systems, 3*(1), 39–46.

[6] Haydaroğlu, C., Yıldırım, B., Kılıç, H., & Özdemir, M. T. (2024, November). The effect of local and interarea oscillations of wind turbine generators based on permanent magnet synchronous generators connected to a power system. *Turkish Journal of Electrical Power and Energy Systems*.

[7] Köprü, M. A., Öztürk, D., & Yıldırım, B. (2024, August). Farklı rüzgâr hızı ve güneş radyasyon oranına sahip bölgeler için mikro şebeke tasarımı ve karşılaştırmalı analizi. *DÜMF Mühendislik Dergisi, 3*, 607–613.

[8] Kilic, H. (2024). Improving the performance of microgrid-based Power-to-X systems through optimization of renewable hydrogen generation. *International Journal of Hydrogen Energy*, (November 2023).

[9] Shahzad, S., Alsenani, T. R., Kilic, H., & Wheeler, P. (2024, December). Techno-economic analysis of green hydrogen integration in smart grids: Pathways to sustainable energy systems. *International Journal of Hydrogen Energy*, (July).

[10] Haydaroğlu, C. (2025, January). Chaos-based optimization for load frequency control in islanded airport microgrids with hydrogen energy and electric aircraft. *International Journal of Hydrogen Energy*, (October 2024).

[11] Khaleel, M., et al. (2025, January). Harnessing nuclear power for sustainable electricity generation and achieving zero emissions. *Energy Exploration & Exploitation*, 1–23.

[12] Polat, S., & Bıyık, E. (2024, November). Evaluation of centralized and distributed energy storage systems in residential microgrid topologies. *Turkish Journal of Electrical Power and Energy Systems*, 1–14.

143

[13] Pinto, J. O. C. P., & Moreto, M. (2021, January). Protection strategy for fault detection in inverter-dominated low voltage AC microgrid. *Electric Power Systems Research, 190*(April 2020), 106572.

[14] Sabzehgar, R. A. A., Kazemi, M. A., Rasouli, M., & Fajri, P. (2020, January). Cost optimization and reliability assessment of a microgrid with large-scale plug-in electric vehicles participating in demand response programs. *International Journal of Green Energy, 17*(2), 127–136.

[15] Yimen, N., et al. (2022, October). Optimal design and sensitivity analysis of distributed biomass-based hybrid renewable energy systems for rural electrification: Case study of different photovoltaic/wind/battery-integrated options in Babadam, northern Cameroon. *IET Renewable Power Generation, 16*(14), 2939–2956.

[16] Zhang, G., Xiao, C., & Razmjooy, N. (2022, December). Optimal operational strategy of hybrid PV/wind renewable energy system using homer: A case study. *International Journal of Ambient Energy, 43*(1), 3953–3966.

[17] Talari, S., Shafie-khah, M., Osório, G. J., Aghaei, J., & Catalão, J. P. S. (2018, January). Stochastic modelling of renewable energy sources from operators' point-of-view: A survey. *Renewable and Sustainable Energy Reviews, 81*(June 2017), 1953–1965.

[18] Sinha, S., & Chandel, S. S. (2014, April). Review of software tools for hybrid renewable energy systems. *Renewable and Sustainable Energy Reviews, 32*, 192–205.

[19] Tozzi, P., & Jo, J. H. (2017). A comparative analysis of renewable energy simulation tools: Performance simulation model vs. system optimization. *Renewable and Sustainable Energy Reviews, 80*(August 2016), 390–398.

[20] Ammari, C., Belatrache, D., Touhami, B., & Makhloufi, S. (2022, October). Sizing, optimization, control and energy management of hybrid renewable energy system—A review. *Energy and Built Environment, 3*(4), 399–411.

[21] Caliskan, A., & Percin, H. B. (2024, July). Techno-economic analysis of a campus-based hydrogen-producing hybrid system. *International Journal of Hydrogen Energy, 75*(October 2023), 428–437.

[22] Syed Mohammed, A., Anuj, Lodhi, A. S., & Murtaza, Q. (2022, August). Techno-economic feasibility of hydrogen based electric vehicle charging station: A case study. *International Journal of Energy Research, 46*(10), 14145–14160.

[23] Ayodele, T. R., Mosetlhe, T. C., Yusuff, A. A., & Ntombela, M. (2021). Optimal design of wind-powered hydrogen refuelling station for some selected cities of South Africa. *International Journal of Hydrogen Energy, 46*(49), 24919–24930.

[24] Basu, S., John, A., Akshay, & Kumar, A. (2021). Design and feasibility analysis of hydrogen based hybrid energy system: A case study. *International Journal of Hydrogen Energy, 46*(70), 34574–34586.

[25] Okonkwo, P. C. (2024). A case study on hydrogen refueling station techno-economic viability. *International Journal of Hydrogen Energy, 49*(PD), 736–746.

[26] Priyanka, T. J., Atre, S., Billal, M. M., & Arani, M. (2023). Techno-economic analysis of a renewable-based hybrid energy system for utility and transportation facilities in a remote community of Northern Alberta. *Cleaner Energy Systems, 6*(September 2022).

[27] Köprü, M. A., Öztürk, D., & Yıldırım, B. (2024). A dispatch strategy for the analysis of the technical, economic, and environmental performance of a hybrid renewable energy system. *Sustainability, 16*(17), 7490.

[28] Yusupov, Z., & Almagrahı, N. (2023). Techno-economic and environmental analysis of microgrid: A case study of Karabuk University. *Sigma Journal of Engineering and Natural Sciences – Sigma Mühendislik ve Fen Bilimleri Dergisi, 41*(4), 758–769.

[29] Acar, C., Erturk, E., & Firtina-Ertis. (2023). Performance analysis of a stand-alone integrated solar hydrogen energy system for zero energy buildings. *International Journal of Hydrogen Energy, 48*(5), 1664–1684.

[30] Jenkins, P., & Sonar, A. C. (2020). Feasibility analysis of an islanded microgrid in Tohatchi, New Mexico using HOMER Pro. *Energy and Power Engineering, 12*(6), 357–374.

[31] Haydaroğlu, C., & Gümüş, B. (2016). Dicle Üniversitesi güneş enerjisi santralinin PVsyst ile simülasyonu ve performans parametrelerinin değerlendirilmesi. *Dicle Üniversitesi Mühendislik Fakültesi Mühendislik Dergisi, 00*(412), 491–500.

[32] Haydaroğlu, C., & Gümüş, B. (2017). Investigation of the effect of short term environmental contamination on energy production in photovoltaic panels: Dicle University solar power plant example. *Applied Solar Energy, 53*(1), 31–34.

[33] Deshmukh, M. K., & Singh, A. B. (2019). Modeling of energy performance of stand-alone SPV system using HOMER pro. *Energy Procedia, 156*(September 2018), 90–94.

[34] Mohammed, O. H., Amirat, Y., Benbouzid, M., Elbast, A., Mohammed, O. H., & Amirat, Y. (2014). Optimal design of a PV / fuel cell hybrid power system for the city of Brest in France. *[Conference paper or journal info missing]*, 119–123.

[35] Alazemi, J., & Andrews, J. (2015, August). Automotive hydrogen fuelling stations: An international review. *Renewable and Sustainable Energy Reviews, 48*, 483–499.

[36] Gorgun, H. (2006, January). Dynamic modelling of a proton exchange membrane (PEM) electrolyzer. *International Journal of Hydrogen Energy, 31*(1), 29–38.

[37] Luta, D. N., & Raji, A. K. (2018, May). Decision-making between a grid extension and a rural renewable off-grid system with hydrogen generation. *International Journal of Hydrogen Energy, 43*(20), 9535–9548.

[38] Abdelhady, S. (2021). Performance and cost evaluation of solar dish power plant: Sensitivity analysis of levelized cost of electricity (LCOE) and

144

net present value (NPV). *Renewable Energy, 168*, 332–342.

[39] Shen, W., et al. (2020). A comprehensive review of variable renewable energy levelized cost of electricity. *Renewable and Sustainable Energy Reviews, 133*(August), 110301.

[40] Siyal, S. H., Mentis, D., & Howells, M. (2015, August). Economic analysis of standalone wind-powered hydrogen refueling stations for road transport at selected sites in Sweden. *International Journal of Hydrogen Energy, 40*(32), 9855–9865.

Türk Doğa ve Fen Dergisi
Turkish Journal of Nature and Science

Antioxidant Activity, Amino Acid Composition and Trace Element Levels of *Verbascum lasianthum* Boiss. ex Bentham from Erzincan, Türkiye

Tugrul Cagri AKMAN[1]* (iD)

[1]Erzincan Binali Yıldırım University, Faculty of Pharmacy, Department of Analytical Chemistry, Erzincan, Türkiye
Tugrul Cagri AKMAN ORCID No: 0000-0002-5439-950X

Corresponding author: eczcagri87@gmail.com

Abstract: This study aims to investigate trace elements and amino acids in the root and stem of *Verbascum lasianthum* Boiss. ex Bentham (VL) from Erzincan and to understand the role of these compounds in adaptation to environmental stress conditions. In the study, ICP-MS and LC-MS/MS methods are used for analyses. In addition, the antioxidant activities of methanol: water extracts (70:30, v:v) of these parts were investigated. The results showed that VL in Erzincan accumulates elements such as sodium and silicium to adapt to arid and stressful environmental conditions and supports these processes by synthesizing amino acids such as L-proline, L-asparagine, and L-glutamine. The high amount of iron indicates that VL can be a potential iron source in the treatment of anemia. However, aluminum accumulation in plants is extremely risky due to its possible neurotoxic effect on humans and plant toxicity. Although these amino acids and trace elements contribute to the antioxidant potential of the plant, VL showed a low antioxidant activity when compared to VL species in other regions. In conclusion, this study emphasizes the importance of comprehensively analyzing phytochemical profiles such as trace elements, amino acids, and phenolic compounds to evaluate the efficacy and safety of medicinal plants.

146

Türkiye, Erzincan'dan *Verbascum lasianthum* Boiss. ex Bentham'ın Antioksidan Aktivitesi, Amino Asit Bileşimi ve Eser Element Seviyeleri

Öz: Bu çalışmada Erzincan'da yetişen *Verbascum lasianthum* Boiss. ex Bentham (VL) bitkisinin kök ve gövdesinde bulunan eser elementler ve aminoasitlerin araştırılması ve bu bileşiklerin çevresel stres koşullarına uyumda oynadığı rolün anlaşılması amaçlanmıştır. Çalışmada, analizler için ICP-MS ve LC-MS/MS yöntemleri kullanılmıştır. Ayrıca, bu kısımların metanol:su (70:30, v:v) ekstraklarının antioksidan aktiviteleri araştırılmıştır. Sonuçlar, Erzincan'daki VL'nin kurak ve stresli çevre koşullarına uyum sağlamak için sodyum ve silisyum gibi elementleri biriktirdiğini ve L-prolin, L-asparagin ve L-glutamin gibi amino asitleri sentezleyerek bu süreçleri desteklediğini göstermiştir. Yüksek demir miktarı, VL'nin anemi tedavisinde potansiyel bir demir kaynağı olabileceğini göstermektedir. Ancak alüminyumun bitkilerde birikmesi, insanlarda nörotoksik etki yaratması ve bitki toksisitesi nedeniyle son derece risklidir. Bu amino asitler ve eser elementler bu bitkinin antioksidan potansiyeline katkıda bulunsa da, diğer bölgelerdeki VL türleriyle karşılaştırıldığında düşük bir antioksidan aktivite gösterdi. Sonuç olarak, bu çalışma tıbbi bitkilerin tıbbi etkinliğini ve güvenliğini değerlendirmek için eser elementler ve amino asitler gibi fitokimyasal profillerin kapsamlı bir şekilde analiz edilmesinin önemini vurgulamaktadır.

1. INTRODUCTION

Medicinal plants have a long history as an important aspect of traditional medicine in many cultures throughout the world, and the World Health Organization (WHO) considers herbal medicines, in particular, to be a crucial component of healthcare for millions of people

[1]. The demand for these herbal treatment methods is constantly increasing in both developing countries and industrialized regions. Along with this interest, a global awareness is emerging on issues such as effectiveness, safety, quality, and regulation. WHO recommends the establishment of quality standards in herbal treatment. Botanical descriptions of plants, active compounds

analyses and detection of contaminants stand out as important elements [2].

Medicinal plants are frequently used both in the treatment of diseases and are also preferred as nutritional supplements due to the beneficial substances in their structure. These substances also include trace elements (TE) and amino acids (AA). These contents in plants can vary depending on the structure of the soil in which they grow, accumulation from the air, and the ability of the plant to collect elements [3,4]. Along with TE and AA, medicinal plants can also accumulate harmful heavy metals due to growth and environmental factors. Some elements that are necessary for living things can have toxic effects when found in excess. Therefore, the detection of elements in plants and the examination of their effects on human health and plant development have become more important with the increase in environmental pollution [5,6].

The biosynthesis of the AA in plants plays a vital role in plant development and resistance to environmental stresses. Some the AA form chelate complexes with micro and macro elements, facilitating the absorption of these elements by plant roots. Chelate complexes increase the solubility of metal ions, allowing them to be transported more effectively into plant tissues. In addition, the AA activate metabolic pathways and enzymatic processes that support the absorption of elements [7,8].

Turkey hosts a wide variety of plants thanks to the rich ecosystems provided by its various geographical regions. Within this variety, the Verbascum genus is included in the *Scrophulariaceae* family with 245 species and stands out with a high endemism rate of 80%. Plants in the Verbascum genus are used in folk medicine in the treatment of many diseases such as asthma, skin disorders, hemorrhoids, fungal infections, and diarrhea. Studies have reported that these species have anticarcinogenic, wound healing, anti-inflammatory, antifungal, and antioxidant properties [9,10].

Verbascum lasianthum Boiss. ex Bentham (VL), known as " Yünlü sığırkuyruğu", is a biennial plant that grows widely throughout Turkey and is preferred in the treatment of hemorrhoids, especially in Southwestern Anatolia. (Figure 1) Previous studies have reported that VL has wound healing, antioxidant, cytotoxic, antibacterial, antinociceptive, and anti-inflammatory properties [11–13]. Although the phenolic compounds and biological activities of the plant have been investigated in these studies, the AA content has not yet been reported. In a single study on the TE profile, it was reported that Ca and Mg were found in high concentrations, but Se and Co could not be detected [13].

In this study, TE analysis of root and stem parts of VL collected from Erzincan and its surroundings was carried out by Inductively Coupled Plasma Mass Spectrometry (ICP-MS) method. In addition, the AA profile of methanol-water extracts of root and stem parts was evaluated by liquid chromatography-tandem mass

spectrometry (LC-MS/MS) technique. In addition, the antioxidant activities of these extracts were also studied.
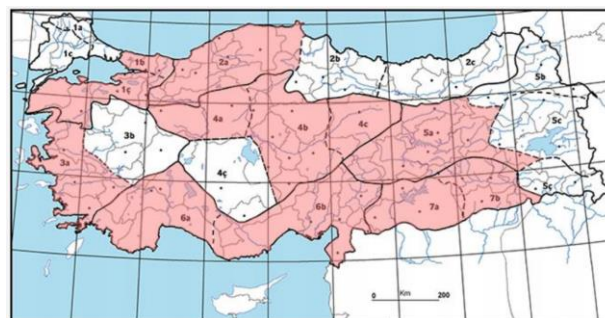
Figure 1. Distribution areas of VL species in Turkey

2. MATERIAL AND METHOD

2.1. Plant Collection and Extraction Protocol for Analytical Procedures

Plant samples were collected from the Kemah and İliç countryside of Erzincan in June 2023. One of these samples was identified by senior taxonomist Prof. Dr. Ali Kandemir and preserved in the herbarium of the Faculty of Arts and Sciences, Erzincan Binali Yıldırım University (EBYU), Turkey (Herbarium ID number: EBYU-000009).

The samples were separated into roots and stems to make them suitable for analysis, and both parts were dried under natural conditions at the room temperature. These dried parts were pulverized with a blender for ICP-MS analysis. On the other hand, hydromethanolic extracts were prepared for antioxidant capacity and AA analyses. In the extraction process, the root and stem parts of the plants were dried at the room temperature and then pulverized into fine powder. 10 grams of plant samples were macerated overnight in 500 mL of methanol and water mixture (7:3, v:v). This process was repeated three times in total. After removing the plant residues, the solvents were combined, and methanol was evaporated. Finally, the water phase was lyophilized to obtain an amorphous solid (1.2 g for root and 1.7 g for stem). The prepared extracts were stored in dark bottles at +4 °C until use.

2.2. Reagents

All aqueous solutions used in ICP-MS analysis were prepared with pure water obtained with Milli-Q Advanced A 10 purification system (Millipore, USA). A mixed solution containing 1% HNO_3 (Merck, USA) and 1% acetonitrile (Sigma Aldrich, Germany) was used for preparation of plant samples, internal standards, and standard solutions. All equipment used in the study, such as tubes, glass vials, and micropipette tips, were cleaned with 10% HNO_3 solution and rinsed with deionized water to prevent contamination during sample preparation and analysis. Agilent® Trace Elements solution contained the following TEs at a concentration of 100 mg L^{-1}: Boron (B), sodium (Na), aluminum (Al), silicium (Si), manganese (Mn), iron (Fe), cobalt (Co), nickel (Ni), copper (Cu), zinc (Zn), selenium (Se), molibdant (Mo), and cadmium (Cd). This solution was diluted to 1000 μg

147

dL^{-1} to establish a calibration curve for the TE. The HNO$_3$ solution used had 99.99% trace metal purity.

2.3. Sample Preperation for ICP-MS Analysis

Milestone Connect ETHOS UP microwave system and Direct-Q 8 UV Ultrapure Water system were used to prevent contamination of atmospheric pollutants during sample preparation for ICP-MS analyses. The microwave degredation method was applied to remove organic compounds in plant samples and to bring inorganic components into a soluble form. Root and stem samples were weighed 200 mg each and 1.8 mL of ultrapure water was added. A vortex device was used to ensure homogeneous dissolution of the mixture. 0.5 mL samples from the prepared mixtures were taken into Teflon containers, then 8 mL of HNO$_3$ and 2 mL of H$_2$O$_2$ solution were added and subjected to a microwave-assisted digestion process. Ramp parameters used in the microwave program are presented in detail in Table 1.

Table 1. The ramping conditions of the microwave program.

Step	Time	T1	T2	Pressure	Power
1	00:10:00	200 °C	100 °C	45 bar	Max power*
2	00:15:00	200 °C	100 °C	45 bar	Max power*

*Max power: 1500W for Ethos and 1200W for Start units.

After the degredation process was completed, ultrapure water was added to complete the sample volume to 15 mL. The mixtures were purified by passing through 0.45 μm syringe filters. Final samples were analyzed three times on the ICP-MS instrument to ensure the reliability of the analytical process and the average values were reported. Dilution factors were calculated using the formula "(final volume or weight / initial sample amount) * dilution coefficient" to verify the accuracy of the results.

2.4. ICP-MS Conditions

For the TE analysis, Agilent 7800 Quadrupole ICP-MS (Agilent Technologies, Japan) was used by operating it with a rotary pump. During the sample injection process, the Integrated Sample Input System (ISIS 3) and Agilent ASX-500 Series ICP-MS Autosampler (Agilent Technologies, Japan) were preferred. Instrument control and data analysis were performed by Mass Hunter 4.2 Workstation Software 7800 ICP-MS Top C.01.02. Measurements were made using a nickel sampler, MicroMist glass concentric nebulizer, and quartz Scott-type spray chamber in quantitative ICP-MS analysis mode. After activating the instrument, basic calibration procedures such as torch alignment, resolution calibration, standard lens settings, plasma optimization, spectrum analysis, and performance reports were applied. Instrument calibration was performed with an Agilent calibration solution containing cerium, cobalt, lithium, magnesium, thallium, and yttrium at a concentration of 1 μg mL^{-1}. Helium collision mode was used for sensitive determination of the TE, and argon was preferred as carrier gas. Before the measurement, the purification process was performed with helium gas for 45 minutes to ensure the accuracy of the ICP-MS system. Device settings and process parameters are presented in detail in Table 2. In the sample preparation phase, the tube and

probe of the autosampler were cleaned with 2% HNO$_3$ and 1% HCl solutions, then rinsed with ultrapure water and made ready for use.

Table 2. Agilent 7800 Quadrupole ICP-MS device parameters

Parameters	Value
Plasma conditions	Forward power 1200W
Plasma gas flow	15.0 L min^{-1}
Carrier gas flow	1 L min^{-1}
Carrier gas pressure	1.45 kPa
Dilution gas flow	1 L min^{-1}
He gas flow	4.5 mL min^{-1}
QP bias	-15 V
Oct bias	-18 V
Cell entrance	-40 V
Cell exit	60 V
Deflect	-0.8 V
Plate bias	-60 V
Nebulizer pump speed	0.30 rps
Sample uptake rate	1.5 mL min^{-1}

Before starting the analysis of plant samples, the instrument was calibrated and validated to ensure the reliability of the method. These operations were performed using Agilent certified reference materials accompanied by daily quality control tests in accordance with the instructions provided by the manufacturer. The calculation of measurements and data analysis process were completed by means of the software 'Mass Hunter 4.2 Workstation Software 7800 ICP-MS Top C.01.02'.

2.5. Chromatographic and Mass Spectroscopic Conditions for AA Analysis

The LC-MS/MS method described in previous studies was used for the separation of the AA [14]. Experiments were carried out using an Agilent 6470 triple quadrupole LC-MS/MS system (Agilent Technologies, Santa Clara, CA, USA). This system includes a 1290 fast pump (G7120A), a 1290 automatic sampler (G7129A), and a 1260 multi-column thermostat (G7116A). Electrospray ionization (ESI) source was preferred for the ionization process. Jasem Quantitative Amino Acids LC-MS/MS Analysis Kit (Altium International Lab. Cih. A.Ş., Istanbul, Turkey) was used to determine the AA concentrations in root and stem extracts. The kit has a CE-IVD certificate, and its validation has been completed. This analysis kit; Calibration curves consisting of 7 different standards include a mixture of 27 isotope-labeled amino acids used as internal standards (IS), two-level quality control samples (QC) and a dilution solution (reagent-1).

Standards, quality control, and extract samples were prepared in accordance with the sample preparation protocol of the kit. For calibration standards, 50 μL of standard solution was taken into a vial. 50 μL of IS and 700 μL of reagent-1 were added. The vial was vortexed for 5 seconds before being placed in the autosampler before being prepared for LC-MS/MS analysis. For extract samples, 10 mg of extract was dissolved in the Jasem's mobile phase (A: 3% formic acid–5% methanol–30 mM ammonium formate, B: Acetonitrile; 1:1, v:v). After filtration, 50 μL of extract sample was mixed with 50 μL of IS and 700 μL of reagent-1. The mixture was

vortexed for 5 seconds and centrifuged at 3600 *g* for 5 minutes at room temperature to precipitate insoluble particles. The supernatant was transferred to a vial for LC-MS/MS analysis.

Chromatographic separation of the AA was performed using the analytical column, gradient elution program, and mobile phases specified in the kit protocol. The analytical column was kept at 30 °C and 3 µL of standard, control, and sample solutions were injected into the HPLC system. Jasem's A and B mobile phases were applied at a flow rate of 0.7 mL min^{-1} with the gradient elution program specified in Table 3. The entire analysis took 7.5 minutes.

Table 3. The mobile phase composition during gradient elution

Time	Change Solvent Composition	
	A	B
1.00 min	22.00 %	78.00 %
4.00 min	70.00 %	30.00 %
5.00 min	70.00 %	30.00 %
5.10 min	22.00 %	78.00 %
9.00 min	22.00 %	78.00 %

*A: %3 formic acid–%5 methanol–30 mM ammonium formate, B: Acetonitrile

The mass spectrometer was operated in positive ion multiple reaction monitoring (MRM) mode to perform mass determination of the AA. The analysis method included the following mass parameters: capillary voltage of 2000 V, drying gas temperature of 150 °C, drying gas flow rate of 10 L min^{-1}, 40 psi nebulizer pressure, 400 °C sheath gas temperature, and 10 L min^{-1} sheath gas flow rate. MS/MS determinations were performed using the collision-induced dissociation (CID) process, with the dissociation of precursor ions into product ions. For each ion transition, the MRM of the the AA to monitor the transitions and determine the IS, appropriate breakdown voltage (FV), and collision energy (CE) values were set. Table 4 summarizes the mass spectrometry parameters and precursor/product ion mass transitions of each analyte.

Calibration curves were used to quantify analytes, considering matrix effects and procedural losses. During LC-MS/MS analysis, data collection, characterization, and quantification were performed with the help of Agilent MassHunter software (versions 10.1 and 10.0).

2.6. Antioxidant activity assays

2.6.1. Determination of total phenolic content (TPC)

The TPC of the extracts was measured by a spectrophotometric method using the Folin-Ciocalteu reagent [15]. In this analysis, first, each extract and standard solutions (1 mg mL^{-1}) were diluted with 4.5 mL of distilled water. Then, 100 µL of Folin-Ciocalteu reagent was added to the mixture, and the mixture was incubated at room temperature for 120 minutes. After the incubation period, 300 µL of 2% Na$_2$CO$_3$ solution was added to each sample. The samples were vortexed to make them homogeneous and the absorbance values were measured at a wavelength of 760 nm. All analyses were performed in triplicate, and the calibration curve was

obtained with the linear equation y = 0.117x - 0.011 using various gallic acid concentrations (1–1000 µg mL^{-1}). The results obtained were expressed in mg gallic acid equivalent phenolic compound per extract (mg GAE g extract^{-1}).

2.6.2. Determination of total flavonoid content (TFC)

The TFC of the extracts was analyzed according to the method described by Varol et al [16]. In this process, firstly, 100 µL of extract and standard solutions (1 mg mL^{-1}) were mixed with 4.7 mL of methanol. Then, 100 µL of ammonium acetate (NH$_4$CH$_3$COO, 1 M) and 100 µL of 10% aluminum chloride (AlCl$_3$) solution were added to the mixture. The resulting mixture was vortexed and incubated at room temperature for 45 minutes. At the end of the incubation period, absorbance measurements were made at 415 nm wavelength. All tests were performed in triplicate and the results were reported as mg quercetin equivalent/g extract based on the calibration curve (y = 0.117x - 0.011) obtained using various quercetin concentrations (1–1000 µg mL^{-1}).

2.6.3. DPPH• Radical scavenging activity

DPPH• radical scavenging capacities of the extracts were evaluated using the methods specified in the literature [17]. Samples prepared at different concentrations (5–100 µg mL^{-1}) were mixed with 1 mL of DPPH• (0.26 mM) solution and vortexed for homogenization. The mixtures were incubated at room temperature in the dark for 30 minutes. After incubation, absorbance measurements were performed at 517 nm wavelength. DPPH• activity was calculated with Equation 1.

$$\text{Activity (\%)} = [(A_0 - A_1)/A_0] \times 100 \qquad (1)$$

In this equation, A_0 is the absorbance of the control sample and A_1 is the absorbance of the test sample. Analyses were performed with triplicates and the results were given as IC$_{50}$ (µg mL^{-1}) value, mean ± standard deviation. The DPPH• scavenging activities of the extracts were compared with standard antioxidants such as Trolox, butylated hydroxytoluene (BHT), butylated hydroxy anisole (BHA), and ascorbic acid.

2.6.4. Ferric reducing antioxidant power (FRAP)

The ferric-reducing antioxidant power (FRAP) analysis of the extracts was performed according to the method described by Akman et al [18]. In this method, 250 µL of extracts or standard solutions (1 mg mL^{-1}) were mixed with 1 mL of phosphate buffer (0.2 M, pH 6.6) and 1.25 mL of 1% [K$_3$Fe(CN)$_6$] solution. The mixtures were incubated in a water bath at 50°C for 20 min. After incubation, 0.25 mL of 0.1% FeCl$_3$ and 1.25 mL of 10% trichloroacetic acid were added and the absorbance of the mixture was measured at 700 nm. All tests were performed in triplicate and the results were expressed as mg Trolox equivalent (TE) activity g extract^{-1} according to the calibration curve obtained with various concentrations of Trolox (10–100 µg mL^{-1}). FRAP values

of the extracts were compared with standard antioxidants BHT, BHA, and ascorbic acid.

Table 4. MRM conditions of the AA.

Amino Acid	Precursor Ion (m/z)	Product Ion (m/z)	FV* (V)	CE** (V)	Polarity	Retention time (min)
1-Methyl-l-Histidine	170.1	124.1	100	10	Positive	4.354
3-Methyl-l-Histidine	170.1	126.2	120	10	Positive	4.334
Argininosuccinic acid	291.0	70.2	140	30	Positive	3.982
Beta-Alanine	90.1	72.1	80	2	Positive	2.537
DL- 5-Hydroxylysine	163.1	128.1	90	6	Positive	4.083
DL-homocystine	269.0	136.0	90	8	Positive	3.789
Ethanolamine	62.1	44.2	80	4	Positive	2.518
Gamma-aminobutyric acid	104.0	87.1	100	6	Positive	2.188
Glycine	76.2	30.1	80	1	Positive	3.129
L-2-Aminoadipic acid	162.0	98.0	90	10	Positive	2.619
L-2-Aminobutyric acid	104.2	58.3	80	4	Positive	2.759
L-alanine	90.2	44.2	80	4	Positive	2.954
L-anserine	241.1	170.0	80	10	Positive	4.507
L-arginine	175.2	70.2	110	20	Positive	3.995
L-asparagine	133.1	74.2	70	10	Positive	3.184
L-aspartic acid	134.1	74.1	80	8	Positive	2.767
L-carnosine	227.1	110.1	110	22	Positive	4.255
L-citrulline	176.2	159.3	80	3	Positive	3.520
L-cystathionine	223.0	134.0	100	8	Positive	4.032
L-cystine	241.1	74.2	100	24	Positive	3.974
L-glutamic acid	148.1	84.2	80	12	Positive	2.494
L-glutamine	147.1	84.2	80	12	Positive	3.289
L-histidine	156.1	110.1	100	8	Positive	4.006
L-homocitrulline	190.1	173	80	12	Positive	3.461
L-isoleucine	132.2	69.2	100	14	Positive	2.147
L-leucine	132.2	43.3	100	24	Positive	2.060
L-lysine	147.1	84.2	80	12	Positive	4.113
L-methionine	150.1	104.1	80	4	Positive	2.174
L-norvaline	186.0	140.0	100	8	Positive	2.478
L-ornithine	133.2	70.3	80	14	Positive	4.075
L-phenylalanine	166.1	120.1	80	6	Positive	1.921
L-proline	116.2	70.2	90	12	Positive	3.273
L-serine	106.2	60.2	80	4	Positive	2.924
L-threonine	120.2	74.2	80	4	Positive	2.807
L-tryptophan	205.1	188.1	80	1	Positive	1.764
L-tyrosine	182.1	165	80	1	Positive	1.968
L-valine	118.2	72.2	80	4	Positive	2.478
o-phospo-L-serine	186.0	88.1	90	8	Positive	3.655
o-phosphoryl Ethanolamine	142.0	44.2	80	4	Positive	3.735
Sarcosine	90.1	44.2	90	8	Positive	3.468
Taurine	126.1	44.3	110	14	Positive	1.730
Trans-4-hydroxy-l-proline	132.2	68.2	90	20	Positive	3.165

*FV: Fragmentor voltage, **CE: Collision energy.

3. RESULTS

3.1. ICP-MS Analysis

In this study, the TE amounts in the root and stem of VL were determined using a validated ICP-MS method [19]. According to the analysis results, it was determined that the TE levels in the root and stem parts showed similar distributions. (Table 5) Na stood out as the most abundant TE in both parts. Especially high amount of Na accumulation was observed in the root and found remarkable (6226.7 µg g dry weight (dw)$^{-1}$). After Na, Si was detected in high amounts at 387.0 µg g dw^{-1}for root and 593.5 µg g dw^{-1} for stem and Fe was detected in high amounts at 208.8 µg g dw^{-1} for root and 216.3 µg g dw^{-1} for stem. B, Al, Mn, Co, Ni, Cu, Zn, and Se were determined in both parts but in very low concentrations. Mo was only detected in root with low concentration, while Cd was not detected in both parts.

Table 5 The TE concentrations in root and stem parts of VL. (µg g dw^{-1})

Parts	B	Na	Al	Si	Mn	Fe	Co	Ni	Cu	Zn	Se	Mo	Cd
Root	18.2	6226.7	126.6	387.0	8.8	208.8	0.1	8.5	9.8	63.2	0.1	0.1	<0.000
Stem	23.7	644.4	195.9	593.5	10.2	216.3	0.1	9.7	8.0	6.9	0.1	<0.000	<0.000

3.2. LC-MS/MS Analysis for AA

An LC-MS/MS analysis method with high sensitivity, accuracy, and precision was used to evaluate the AA profiles in the root and stem parts of VL. A total of 43 AA were quantitatively analyzed in these parts by LC-MS/MS. Figure 2 shows the MRM chromatograms obtained from the LC-MS/MS analysis of the root and stem extracts.
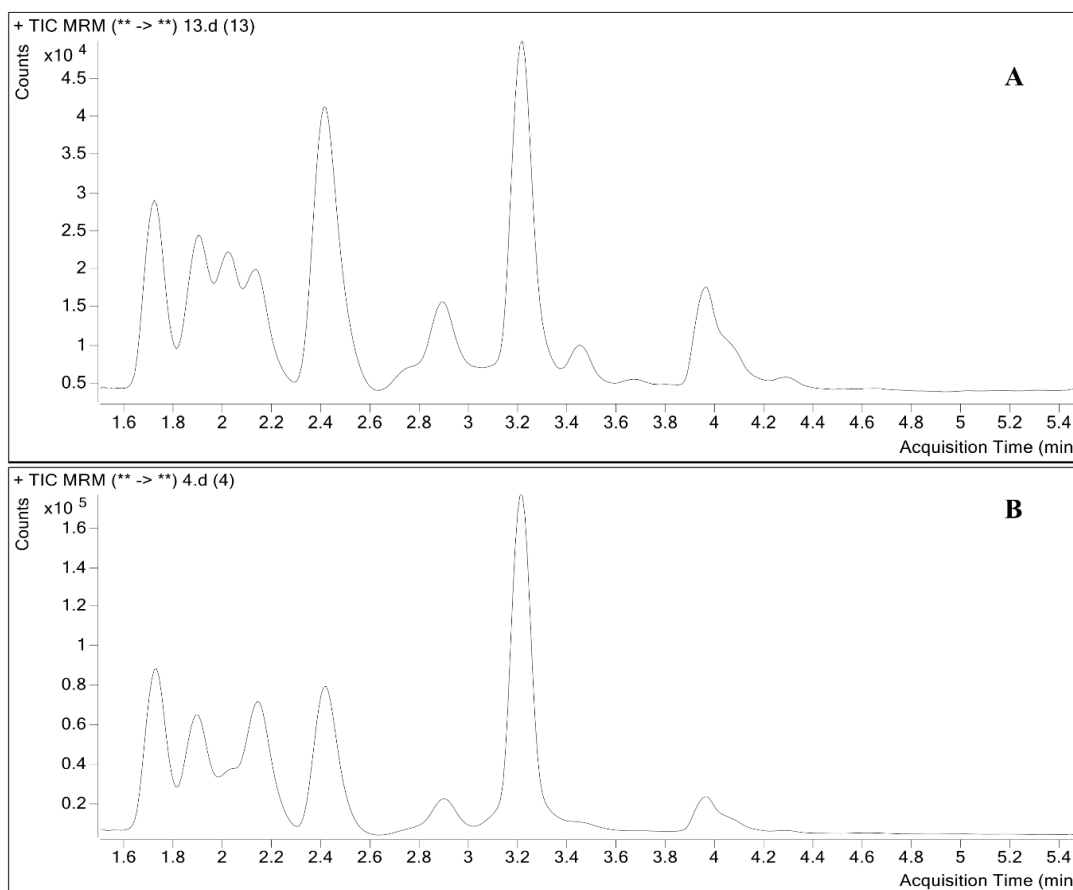
Figure 2. The MRM chromatograms of the A) root and B) stem extracts

The AA levels in these extracts were determined in nmol mL^{-1}. The linear regression equations, correlation coefficients (R^2), and quantification limit values (LOQ) of the AA are presented in Table 6.

Table 6. Calibration curve equations, correlation coefficients, and LOQ values of the AA in the LC-MS/MS method

Amino Acids	Calibration curve equations	R^2	LOQ (nmol L^{-1})
1-methylhistidine	y= 0.134550x + 0.030534	0.9963	1.0
3-methylhistidine	y= 0.007255x + 0.009899	0.9970	1.0
2-aminoadipic acid	y= 0.012476x - 0.005961	0.9924	0.5
2-aminobutyric acid	y= 0.164021x - 0.304197	0.9969	2.5
3-aminoisobutyric acid	y= 0.005320x + 0.006929	0.9979	1.0
5-hydroxylysine	y= 0.003114x + 0.003675	0.9971	1.0
Argininosuccinic acid	y= 0.013154x - 7.593827E-004	0.9992	1.0
Beta-alanine	y= 0.006016x + 0.002325	0.9970	0.2
Ethanolamine	y= 0.386430x + 1.384151	0.9961	2.0
Gamma-aminobutyric acid	y = 0.039074x + 0.058776	0.9962	1.0
Glycine	y= 0.001120x - 0.008773	0.9955	5.0
Homocitrulline	y= 0.004492x - 0.007928	0.9986	2.0
Homocystine	y= 0.039396x + 0.012211	0.9998	0.25
L-alanine	y= 0.002234x - 0.003392	0.9991	1.0
L-anserine	y= 0.020276x + 0.003041	0.9994	0.4
L-arginine	y= 0.012304x + 7.375877E-004	0.9994	2.0
L-asparagine	y= 0.012480x - 0.008593	0.9962	2.0
L-aspartic acid	y = 0.020336x – 0.028037	0.9995	1.0
L-carnosine	y= 0.025459x - 0.002913	0.9989	1.0
L-citrulline	y= 0.018775x + 0.039661	0.9986	0.5
L-cystathionine	y= 0.101093x + 0.001578	0.9998	0.1
L-cystine	y= 0.010862x - 0.007446	0.9987	2.0
L-glutamic acid	y= 0.017219x - 0.038986	0.9994	5.0
L-glutamine	y= -1.686812E-006x^2 + 0.006569x + 0.054237	0.9994	5.0
L-histidine	y= 0.010063x + 0.072616	0.9984	5.0
L-isoleucine	y= 0.002582x - 0.007951	0.9976	1.0
L-leucine	y= 0.001315x - 7.336834E-004	0.9980	5.0
L-lysine	y= 0.025117x + 0.130604	0.9984	1.0
L-methionine	y= 0.021032x + 0.025020	0.9966	1.0
L-norvaline	y= 0.002458x^2 + 00.042305x + 0.014883	0.9975	0.1
L-ornithine	y= 0.013625x + 0.526848	0.9993	2.0
L-phenylalanine	y= 0.020012x + 0.067728	0.9996	1.0

L-proline	y= 0.005376x + 0.024883	0.9979	5.0
L-serine	y= 0.013133x + 0.214409	0.9962	5.0
L-threonine	y= 0.010757x + 0.078723	0.9953	2.5
L-tryptophan	y= 0.028557x - 0.053366	0.9990	1.0
L-tyrosine	y= 0.013461x - 0.019332	0.9995	1.0
L-valine	y= 0.002968x + 0.014195	0.9989	5.0
o-phosporhyl ethanolamine	y= 9.059945E-004x - 1.944540E-004	0.9997	0.25
o-phosphoserine	y= 5.074562E-004x - 7.213929E-006	0.9999	0.25
Sarcosine	y= 0.050509x + 0.228475	0.9991	5.0
Taurine	y= 0.001442x – 0.001064	0.9979	5.0
Trans-4-hydroxy L-proline	y= 0.005091x - 0.003910	0.9993	1.0

*R^2: Correlation coefficient

In this study, it was determined that the root and stem parts of the plant have different AA profiles. It was observed that the concentrations of the AA generally found in the stem were higher than in the root. (Table 7)

Table 7. AA levels in the root and stem extracts of VL (nmol mL^{-1})

Amino Acids	Root	Stem	Amino Acids	Root	Stem
1-methylhistidine	0.0000	0.0000	L-glutamic acid	8.9035	28.4213
3-methylhistidine	0.0000	0.0000	L-glutamine	14.9213	379.9220
2-aminoadipic acid	2.4261	5.6595	L-histidine	0.0000	4.6044
2-aminobutyric acid	2.2302	3.2828	L-isoleucine	5.6796	34.5097
3-aminoisobutyric acid	21.0044	66.0686	L-leucine	6.2863	32.7559
5-hydroxylysine	0.0000	0.0000	L-lysine	1.2469	11.0819
Argininosuccinic acid	0.3042	1.4487	L-methionine	0.0000	0.0000
Beta-alanine	0.8958	0.7660	L-norvaline	0.2209	3.6957
Ethanolamine	2.3116	103.5776	L-ornithine	24.7736	0.0000
Gamma-aminobutyric acid	14.5879	53.9212	L-phenylalanine	0.0000	20.4949
Glycine	10.6834	38.2563	L-proline	0.0000	470.0972
Homocitrulline	1.7979	1.8431	L-serine	0.0000	83.7654
Homocystine	0.0000	0.0000	L-threonine	0.0000	31.4394
L-alanine	30.4803	93.4081	L-tryptophan	2.4485	23.8490
L-anserine	0.0000	0.0000	L-tyrosine	3.1378	11.5716
L-arginine	2.0282	53.5069	L-valine	3.0923	68.5982
L-asparagine	2.0480	403.7208	*o*-phosporhyl ethanolamine	0.8348	0.2532
L-aspartic acid	7.9867	36.4775	*o*-phosphoserine	0.1288	0.0609
L-carnosine	0.2780	0.3002	Sarcosine	0.0000	0.2969
L-citrulline	0.0000	5.3701	Taurine	1.1490	0.9507
L-cystathionine	0.3446	0.1189	Trans-4-hydroxy L-proline	1.5211	1.7520
L-cystine	1.7094	1.4065			

152

As a result of the analyses, a total of 30 AA were determined in the root part, and the ones with the highest concentration were L-alanine (30.4803 nmol mL^{-1}), L-ornithine (24.7736 nmol mL^{-1}) and 3-aminoisobutyric acid (21.0044 nmol mL^{-1}), respectively. L-citrulline, L-histidine, L-phenylalanine, L-proline, L-serine, L-threonine, and sarcosine were detected in the stem, but not in the root. Among the 36 AA detected in the stem, the ones with the highest concentrations were determined as L-proline (470.0972 nmol mL^{-1}), L-asparagine (403.7208 nmol mL^{-1}), and L-glutamine (24.7736 nmol mL^{-1}), respectively. (Figure 3) The concentrations of 3-aminoisobutyric acid, ethanolamine, gamma-aminobutyric acid, L-alanine, L-arginine, L-aspartic acid, L-isoleucine, L-leucine, L-serine and L-valine, which were found in very low amounts in the root, were detected at quite high levels in the stem (32.7559-103.5776 nmol mL^{-1}). However, L-ornithine, one of the most abundant AA in the root, was not detected in the stem. The AA such as 2-aminoadipic acid, 2-aminobutyric acid, argininosuccinic acid, beta-alanine, homocitrulline, L-carnosine, L-cystationine, L-cystine, L-glutamic acid, L-lysine, L-norvaline, L-tryptophan, L-tyrosine, *o*-phosphorylethanolamine, *o*-phosphoserine, taurine and trans-4-hydroxy L-proline were found in very low concentrations (0.1288-23.8490 nmol mL^{-1}) both in root and stem. Additionally, 1-methylhistidine, 3-methylhistidine, 5-hydroxylysine, homocystine, L-anserine, and L-methionine were not observed in any part of the plant.
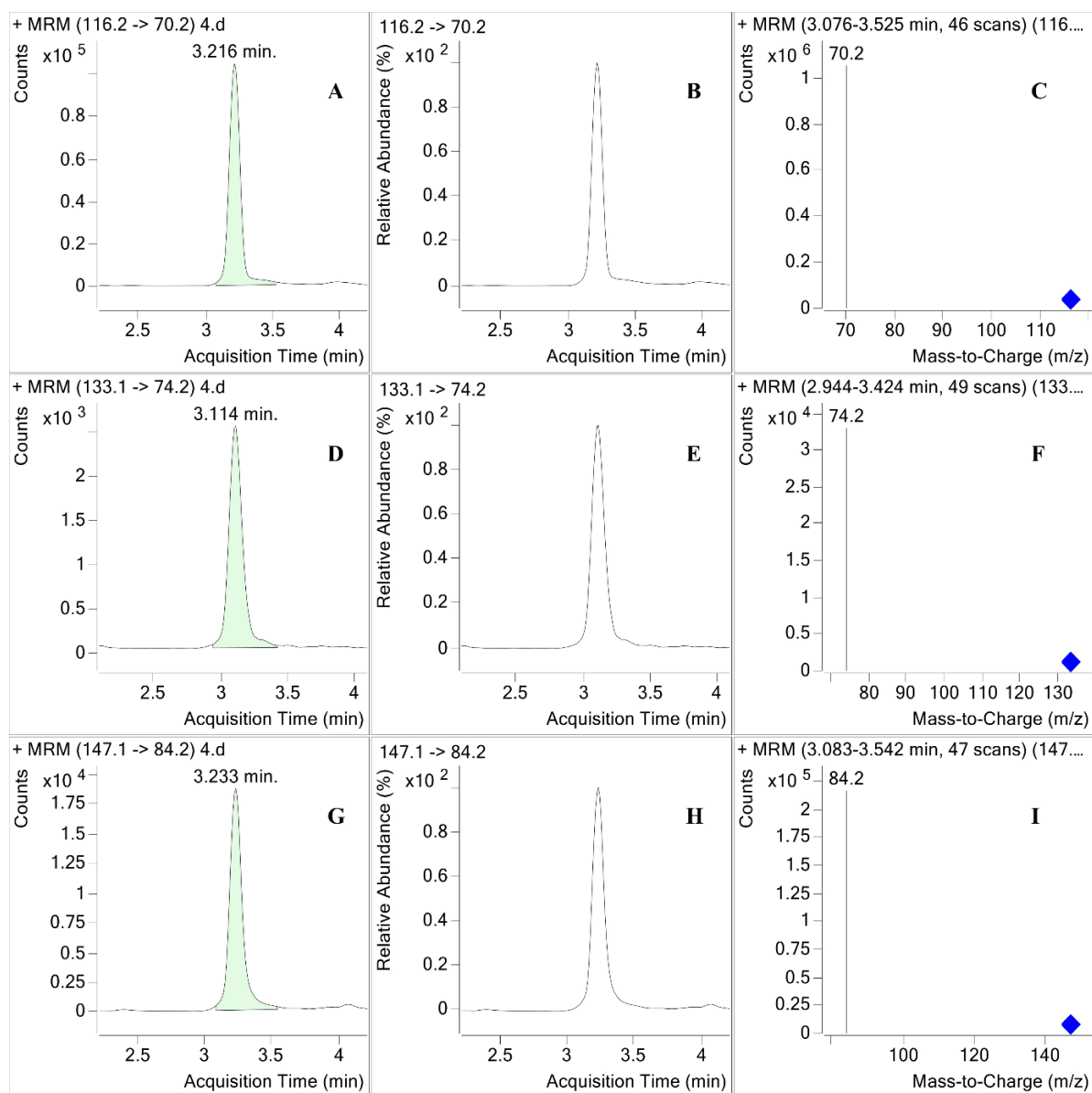
Figure 3. The typical chromatograms showed the peak area and relative abundance respectively of A, B) L-proline, D, E) L-asparagine, and G, H) L-glutamine. The mass spectrums of C) L-proline, F) L-asparagine, and I) L-glutamine.

3.3. Antioxidant Activity Assay

The antioxidant activity and total phenolic and flavonoid contents of root and stem extracts are detailed in Table 8. When DPPH• radical scavenging ability was evaluated in terms of IC_{50} (µg mL^{-1}), it was seen that the IC_{50} values of the root and stem extracts were 141.35±2.03 and 54.97±1.78 µg mL^{-1}, respectively. However, these values indicate lower activity when compared to standard antioxidants such as Trolox, BHA, and BHT. In addition, the TPC value of the stem extract was measured as 62.28±0.28 mg GAE g extract^{-1} and the TFC value was measured as 15.71±0.75 mg QE g extract^{-1}, which were significantly higher than the TPC (35.80±1.31 mg GAE g extract^{-1}) and TFC (10.52±0.56 mg QE g extract^{-1}) values of the root extract. The ferric ion-reducing capacity of root and stem extracts of VL was also investigated in the study. The results showed that the ferric reducing capacity of the stem extract was higher as 122.53±0.58 mg TE g extract^{-1} compared to the root extract (75.83±2.97 mg TE g extract^{-1}); however, this capacity was lower than the activity of ascorbic acid at 394.17±0.98 mg TE g extract^{-1}.

Table 8. Antioxidant activity, TPC and TFC of VL

Plant Species	DPPH IC_{50} (µg mL^{-1})	Total phenolics (mg GAE g Extract $^{-1}$)	Total flavonoids (mg QE g Extract^{-1})	Reducing power (mg TE g Extract^{-1})
Verbascum lasianthum (root)	141.35±2.03	35.80±1.31	10.52±0.56	75.83±2.97
Verbascum lasianthum (stem)	54.97±1.78	62.28±0.28	15.71±0.75	122.53±0.58
Trolox	11.95±0.15	-	-	-
BHA	8.04±0.69	-	-	338.57± 0.31
BHT	10.70±0.73	-	-	257.80± 1.24
Ascorbic acid	9.91±0.87	-	-	394.17±0.98

4. DISCUSSION AND CONCLUSION

Medicinal plants have various pharmacological and biological effects thanks to the primary and secondary metabolites, phytochemical compounds, and the TE in their structure. Therefore, their use in traditional medicine has become widespread in recent years as an alternative to both nutritional and pharmaceutical treatments. However, human-induced activities such as industrialization, mining, use of chemical fertilizers and pesticides, fossil fuel consumption, and accumulation of domestic waste have led to heavy metal accumulation and related toxicity in medicinal plants. This situation limits the safe use of medicinal plants. Medicinal plants can cause serious side effects when used above the recommended safe consumption limits [20]. Therefore, for the evaluation of the efficacy, safety, and toxicity of medicinal plants, their chemical compositions, especially the TE, AA, and heavy metals, should be examined by analytical methods.

In this study, the TE, heavy metal, and AA levels in the root and stem of VL collected from Erzincan were analyzed. In addition, the antioxidant activities of hydromethanolic extracts obtained from these parts were evaluated. In a previous study, the TPC, antioxidant activity, and TE compositions of methanol and acetone extracts of VL grown in Western Anatolia were reported. In this study, methanol (IC_{50}: 6.44 mg mL^{-1}) and acetone (IC_{50}: 17.07 mg mL^{-1}) extracts were shown to have higher antioxidant activity compared to BHT (23.58 mg mL^{-1}). The TPC values were reported as 30.82±2.10 and 64.47±4.84 mg GAE g $extract^{-1}$, respectively [13]. When these two studies were compared, it was determined that the TPC values of both regions were similar, but the plant in Western Anatolia showed higher antioxidant activity.

In the study of Hazman et al., the most abundant TE in VL were reported as Fe (446.98 ± 94.63 ppm), Zn (20.67 ± 1.08 ppm), Mn (38.12 ± 2.39 ppm), and Na (78.38 ± 10.08 ppm). In addition, Cu and Pb elements were found at low levels, while Se and Co were not detected [13]. Compared to VL in Erzincan, the arid climate of Eastern Anatolia caused stress in the plant, resulting in higher levels of Na (6226.7 and 644.4 µg g dry $weight^{-1}$) and Si (387.0 and 593.5 µg g dry $weight^{-1}$) accumulation in the root and stem. Plants require trace amounts of elements such as Fe, Cu, Zn, and Mn in their growth and development processes [21]. However, it is known that high concentrations of these elements in medicinal plants may have carcinogenic effects [22]. In both studies, it was observed that Cu, Mn, Ni, and B elements have similar profiles at low concentrations. However, the high Fe levels of VL in Erzincan stand out as important data. On the other hand, although the carcinogenic effects of Al have not yet been definitively confirmed, it is known that it can cause plant toxicity by dissolving in acidic soils, in addition to its neurotoxic effects in humans [20,23]. In our investigation, the absence of Cd among heavy metals was regarded as a favorable safety finding. Al accumulation in roots (126.6 µg g dry $weight^{-1}$) and stems (195.9 µg g dry $weight^{-1}$) may cause a potential risk to plant development and traditional medicinal practices. This is a concern that

should be carefully evaluated when using the plant for medicinal purposes.

AA biosynthesis is essential for the tolerance of plants to environmental stressors [7,8]. This study presents the first report of VL's AA profile. LC-MS/MS tests revealed that the stem part had high levels of L-proline, L-asparagine, and L-glutamine. Proline and glutamine serve as crucial defensive mechanisms against harmful environmental factors such as salt stress, dryness, and temperature variations. These AAs regulate the transport of Na ions in plants and prevent their harmful effects. Proline, in particular, promotes cell membrane integrity and restricts the entry of Al into the cell [24,25]. Glutamine and glycine help to retain and transport Fe on the root surface, making it easier to incorporate into metabolic processes [8,26]. Si generally accumulates in plants as a defense mechanism in response to stress conditions. L-asparagine helps stressed plants accumulate Na and Si while also playing an important role in nitrogen metabolism. It also protects the plant from environmental challenges by enhancing antioxidant production, such as glutathione, as well as antioxidant enzyme activity [27]. The adaptation mechanisms developed by VL in Erzincan arid climate against stress are consistent with the analysis results of the AA and the TE. The plant accumulated Na and Si to protect itself from water and salt stress. In addition, it produced large amounts of L-proline and L-asparagine to reduce Al toxicity and increase Na absorption. It also enhanced L-glutamine synthesis to support Fe absorption, which is required for metabolic functions. Although the found AA and the TE contributed to the plant's antioxidant capacity, it was determined that there was no appreciable antioxidant activity.

In conclusion, this study on *Verbascum lasianthum* from Erzincan emphasizes the importance of the AA and the TE in plant response to environmental stress situations. The accumulation of Na and Si, as well as the synthesis of L-proline, L-asparagine, and L-glutamine in the plant, were thought as a defense mechanism created against the effects of arid and stressful situations. However, it was emphasized that high levels of Al accumulation in the root and stem could offer potential risks in the medicinal use of the plant. The low antioxidant activity suggests that the pharmacological effects of this plant should be studied further for traditional medicine. These findings highlight the need to conduct a thorough investigation of chemical profiles for the safety and efficacy of medicinal plants.

REFERENCES

[1] Thomson GE. Further consideration of Asian medicinal plants in treating common chronic diseases in the West. Journal of Medicinal Plants Research. 2010;4:125–30.

154

[2] Sixty-second World Health Assembly: Resolutions and decisions, annexes. 2009.

[3] Sattar SA, Reddy BS, Rao VK, Pradeep A, Raju GN, Ramanarayana K, et al. Estimation of trace elements in some anti-epileptic medicinal plants by PIXE. Journal of Radioanalytical and Nuclear Chemistry. 2012;294:337–41.

[4] Silva PSC, Francisconi LS, Gonçalves RD. Evaluation of major and trace elements in medicinal plants. Journal of the Brazilian Chemical Society. 2016;27:2273–89.

[5] Ranđelović SS, Kostić DA, Zarubica AR, Mitić SS, Mitić MN. The correlation of metal content in medicinal plants and their water extracts. Hemijska Industrija (Chemical Industry). 2013;67:585–91.

[6] Ebrahim AM, Eltayeb MH, Khalid H, Mohamed H, Abdalla W, Grill P, et al. Study on selected trace elements and heavy metals in some popular medicinal plants from Sudan. Journal of Natural Medicines. 2012;66:671–9.

[7] Rengel Z, Cakmak I, White P. Marschner's mineral nutrition of plants. Acad Press. 2022.

[8] Baqir H, Zeboon N, Al-Behadili A. The role and importance of amino acids within plants: A review. Plant Archives. 2019;19:1402–10.

[9] Karamian R, Ghasemlou F. Total phenolic content, antioxidant and antibacterial activities of three Verbascum species from Iran. Journal of Medicinal plants and By-Products. 2013;2:43–51.

[10] Şimşek S, Akşit H, Aydın A, Köksal E. Ferruginoside D: A novel phenylethanoid from *Verbascum leiocarpum*. Chemistry & Biodiversity. 2023;20:e202301200.

[11] Süntar I, Tatli II, Küpeli Akkol E, Keleş H, Kahraman Ç, Akdemir Z. An ethnopharmacological study on Verbascum species: From conventional wound healing use to scientific verification. Journal of Ethnopharmacology. 2010;132:408–13.

[12] Kupeli E, Tatli II, Akdemir ZS, Yesilada E. Bioassay-guided isolation of anti-inflammatory and antinociceptive glycoterpenoids from the flowers of *Verbascum lasianthum* Boiss. ex Bentham. Journal of Ethnopharmacology. 2007;110:444–50.

[13] Hazman O, Aksoy L, Buyukben A, Kara R, Kargioglu M, Kumral ZB, et al. Evaluation of antioxidant, cytotoxic, antibacterial effects and mineral levels of *Verbascum lasianthum* Boiss. ex Bentham. Anais da Academia Brasileira de Ciências. 2021;93:e20210865.

[14] Atila A, Alay H, Yaman ME, Akman TC, Cadirci E, Bayrak B, et al. The serum amino acid profile in COVID-19. Amino Acids. 2021;53:1569–88.

[15] Gözcü S, Akşit Z, Aydın A, Yılmaz MA, Şimşek S. Comprehensive phenolic profiling and biological evaluation of *Centaurea glastifolia* L. (Asteraceae). Natural Product Research. 2024;1–12.

[16] Varol T, Osma E, Şimşek S, Elveren M. Antioxidant activities of plant species growing in different habitats (serpentine, gypsum and limestone). Frontiers in Life Sciences and Related Technologies. 2023;4:150–6.

[17] Gözcü S, Akşit Z, Şimşek S, Kandemir A, Aydin A, Yilmaz MA, et al. LC-MS /MS characterization and biological activities of *Morina persica* L. (Caprifoliaceae). Journal of Research in Pharmacy. 2024; 28:961–73.

[18] Akman TÇ, Şimşek S, Akşit Z, Aydın A, Yılmaz MA. Exploring the potential of *Psephellus huber-Morathi* (Wagenitz) Wagenitz: A comprehensive UHPLC-MS/MS analysis of phytochemical composition and evaluation of antioxidant, antimicrobial, and antiproliferative activities. Kahramanmaraş Sütçü İmam Üniversitesi Tarım ve Doğa Dergisi. 2024;27:782–92.

[19] Akman TC, Yazici M, Atila A, Mertoglu C. Analysis of Isotretinoin-Induced alterations in the levels of plasma trace elements: Investigation of the relationship between magnesium, phosphorus, potassium, zinc, and Treatment-Related side effects. Biological Trace Element Research. 2024;202:4858–4868.

[20] Palani K, Balasubramanian K, Kalaivani R. Study on aluminium contamination in mettur soil and its subsequent uptake by medicinal plants. Oriental Journal of Chemistry. 2018;34:3129.

[21] Kaur H, Kaur H, Kaur H, Srivastava S. The beneficial roles of trace and ultratrace elements in plants. Plant Growth Regulation. 2022;100:219–36.

[22] Jaishankar M, Tseten T, Anbalagan N, Mathew BB, Beeregowda KN. Toxicity, mechanism and health effects of some heavy metals. Interdisciplinary Toxicology. 2014;7:60–72.

[23] Swain S, Rautray TR. Estimation of trace elements, antioxidants, and antibacterial agents of regularly consumed indian medicinal plants. Biological Trace Element Research. 2021;199:1185–93.

[24] Alotaibi MO, Saleh AM, Sobrinho RL, Sheteiwy MS, El-sawah AM, Mohammed AE, et al. *Arbuscular mycorrhizae* mitigate aluminum toxicity and regulate proline metabolism in plants grown in acidic soil. Journal of Fungi. 2021;7:531.

[25] Alvarez M, Savouré A, Szabados L. Proline metabolism as regulatory hub. Trends in Plant Science. 2022;27:39–55.

[26] Buchanan B, Gruissem W, Jones R. Biochemistry and molecular biology of plants. John Wiley & Sons, Ltd; 2015.

[27] Lardos M, Marmagne A, Bonadé Bottino N, Caris Q, Béal B, Chardon F, et al. Discovery of the biostimulant effect of asparagine and glutamine on plant growth in *Arabidopsis thaliana*. Frontiers in Plant Science. 2023;14:1281495.

155

Türk Doğa ve Fen Dergisi
Turkish Journal of Nature and Science

www.dergipark.gov.tr/tdfd

BINGÖL UNIVERSITY

Development of an Effective Deep Learning Model for COVID-19 Detection from CT Images

Tanju CEYLAN[*] ID **, Özkan İNİK**[2] ID

[1] Tokat Gaziosmanpaşa University, Department of Computer Engineering, Tokat, Türkiye
[2] Tokat Gaziosmanpaşa University, Department of Computer Engineering, Tokat, Türkiye
Tanju CEYLAN ORCID No: 0009-0001-3843-5785
Özkan İNİK ORCID No: 0000-0003-4728-8438

*Corresponding author: tanju.ceylan@gop.edu.tr

Keywords
Deep learning,
Image classification,
COVID-19,
Computed tomography

Abstract: Coronavirus Disease (COVID-19) is an RNA-type virus that is spreading worldwide. COVID-19, which was first seen in Wuhan, China, in December 2019, quickly began to be seen in all countries of the world.Symptoms such as respiratory tract infections, fever, cough and shortness of breath are common in the diagnosis of the disease. The diagnosis of the disease is made in the first stage by applying the Polymerase Chain Reaction (PCR) test. The long duration of laboratory research has led researchers to different methods. In this study, a model was designed that can help radiologists detect the disease through Computed Tomography (CT) images. This system, based on deep learning, aims to detect the disease by classification method through COVID-19 positive and negative chest tomography images. The data set used in the study consists of a total of 5000 images. Experimental studies have been conducted on Convolutional Neural Network (CNN) models such as AlexNet, Densenet201, GoogleNet, ResNet-50, Vgg-16, EfficientNet and the proposed CNN model. COVID-19 prediction was made with the designed CNN model with a success rate of 99.20%. An effective and successful model is proposed for COVID-19 detection from CT images.

156

BT Görüntülerinden COVID-19 Tespiti İçin Etkili Bir Derin Öğrenme Modeli Geliştirilmesi

Anahtar Kelimeler
Derin öğrenme,
Görüntü sınıflandırma,
COVID-19,
Bilgisayarlı tomografi

Öz: Coronavirüs Hastalığı (COVID-19), dünya çapında yayılan RNA tipi bir virüstür. İlk olarak Aralık 2019'da Çin'in Wuhan kentinde görülen COVID-19, hızla dünyanın tüm ülkelerinde görülmeye başlandı. Hastalığın tanısında solunum yolu enfeksiyonları, ateş, öksürük ve nefes darlığı gibi belirtiler sık görülüyor. Hastalığın tanısı ilk aşamada Polimeraz Zincir Reaksiyonu (PCR) testi uygulanarak konmaktadır. Laboratuvar araştırmalarının uzun sürmesi araştırmacıları farklı yöntemlere yöneltmiştir. Bu çalışmada Bilgisayarlı Tomografi (BT) görüntüleri aracılığıyla radyologların hastalığı tespit etmesine yardımcı olabilecek bir model tasarlandı. Derin öğrenmeye dayanan bu sistem, COVID-19 pozitif ve negatif göğüs tomografisi görüntüleri üzerinden hastalığın sınıflandırma yöntemiyle tespit edilmesini hedefliyor. Çalışmada kullanılan veri seti toplam 5.000 adet görselden oluşmaktadır. AlexNet, Densenet201, GoogleNet, ResNet-50, Vgg-16, EfficientNet gibi Evrişimsel Sinir Ağı (CNN) modelleri ve önerilen CNN modeli üzerinde deneysel çalışmalar yapılmıştır. Tasarlanan CNN modeliyle %99.20 başarı oranıyla COVID-19 tahmini yapıldı. BT görüntülerinden COVID-19 tespiti için etkili ve başarılı bir model önerilmiştir.

1. INTRODUCTION

Coronavirus group diseases were first seen in world history in 1960 [1]. Considering the last 25 years, there have been virus epidemics with high lethal effects.

"Severe Acute Respiratory Syndrome (SARS-CoV) respiratory disease was seen in Asia, Europe and North America in 2003 [2]. The Middle East Respiratory Syndrome-coronavirus (MERS-CoVS) virus, which occurs with serious respiratory failure problems, affected

humanity in the Arabian Peninsula in 2012 [3]. Finally, in December 2019, pneumonia cases began to be seen in Wuhan, China's Hubei Province, with symptoms such as high fever, cough, weakness and shortness of breath. The symptoms were first seen in animal markets and areas where seafood is sold. The World Health Organization (WHO) has defined this new virus as "COVID-19". This name consists of the initials of "co" corona, "vi" virus and "d" English word "dease". WHO has named this virus that causes COVID-19 disease as Severe Acute Respiratory Syndrome-Coronavirus-2 (SARS-COV-2). WHO announced COVID-19 to the world as a pandemic, that is, a global epidemic, on March 11, 2020. The first case in our country was officially recorded on this date.

The most used method for detecting COVID-19 is the PCR method [4]. It is known that PCR test results take an average of 6 hours. While the main goal in combating the disease is to use time in the most effective way, using kits sometimes delays the result and may cause high economic costs. Even if the PCR test result is negative in the early stages of the disease, the advantage of radiology imaging methods such as X-ray or CT is that the disease can be detected from images at every stage. In the later stages of the disease, comments can be made about the patient's condition and necessary precautions can be taken thanks to these detailed imaging techniques. CT images provide the opportunity to obtain detailed information about many vital structures such as the status of organs, lesions, developing pneumonia, soft tissues, and the status of vessels. Although the CT imaging method has such advantages, the patient's condition must be reported by a physician. After reporting, appropriate treatment must be administered to the patient as quickly as possible. It is vital that the sooner the reporting process ends, the isolation of the patient and the initiation of treatment will reduce the risk of transmission. Reporting the diagnoses made significantly increases the workload of radiologists. The exponential increase in the number of patients during the pandemic has led the scientific world to seek various solutions to reduce this burden on physicians. One of these solutions is work done with artificial intelligence. Artificial intelligence-based systems are used to detect many diseases [5-8]. Various deep learning models are used to mark disease-related parts on X-Ray imaging and CT images and to process the generated data. When looking at these studies, it can be seen that deep learning models are generally used. Because deep learning models have been shown to provide results with high accuracy in many areas [9-15]. In addition, many artificial intelligence models and experimental studies developed for COVID-19 detection are also included in the literature. Some of the studies in the literature are mentioned below.

Hemdan et al. (2020) designed a CNN model called COVIDDX-Net. They carried out their studies with the aim of early diagnosis of COVID-19 disease with this design. COVIDX-Net includes 7 CNN methods such as VGG19 and GooglleNet. They used 50 chest X-ray images as the data set. They reached a success rate of 89% with VGG-19 and 91% with DenseNet [16]. Bozkurt (2021) conducted a study using deep learning techniques

to prevent the spread of COVID-19 disease and make a rapid diagnosis. With the applied methods, He aimed to examine lung X-Ray images in 3 classes: COVID-19, normal and viral pneumonia patients. In the study conducted with 11 different methods, he achieved the highest success rate of 97.17% using the DenseNet121 method [17]. Seyyed Mohammad et al. (2021) aimed to detect COVID-19 with the help of artificial intelligence through CT images and used data from 2 separate public hospitals for this study. The data set consists of 3 categories. The number of images used in the categories consists of 5.705 pneumonia cases, 4.001 COVID-19 patients and 9.979 normal people. In the study, they compared different DNN models. They achieved the best result with their proposed model called Wavelet CNN-4 with a success rate of 99.03% [18]. Oğuz (2021) worked on a COVID-19 diagnostic model to support radiologists. 1.345 CT images taken from Siirt Training and Research Hospital were used as a data set. He used 80% of the data for training and 20% for testing. Feature extraction was performed using ResNet-50, ResNet-101, AlexNet, Vgg-16, Vgg-19, GoogLeNet, SqueezeNet, Xception models. The most successful results were achieved with a success rate of 96.29% through the ResNet-50 model [19]. Panahi et al. (2021) believed that the interpretation of PCR test kits and CT methods by physicians in detecting COVID-19 disease delayed the process and aimed to make a faster diagnosis with the help of artificial intelligence. For this purpose, they used X-Ray images of 940 people as the data set for their study. They developed a classification method called Fast COVID-19 Detector (FCOD) and achieved a 96% accuracy rate with the developed method [20]. Urut and Özdağ (2022) aimed to detect COVID-19 with the recurrent neural network method Recurrent Neural Network (RNN) using a deep learning algorithm on chest x-ray images. They aimed to reduce the burden of diagnosis on physicians. The data set used in the study consists of 576 positive cases and 1.583 normal person images. They worked on models such as Resnet, VGG and DenseNet for the system that will perform the classification process. They achieved the highest success rate with the Resnet method with a prediction accuracy of 97% [21]. Ceylan and İnik (2022) developed an original deep learning model aiming to detect COVID-19. The data set used in the study was obtained from the open access Kaggle platform. In the data set they created from a total of 6.000 images, they used 3.600 images for training, 1.800 images for testing, and 600 images for verification. During the experimental studies, they reached the highest success rate of 99.7%. They reported that conditions such as the clarity, size, and learning frequency of the visuals affected the success rate [22]. Çelik and İnik (2023) used artificial intelligence-based computer vision systems to diagnose monkeypox disease in their study. Monkeypox disease is similar to other chickenpox diseases. They aimed to reduce the workload of experts with the study. The dataset was trained on VGG-19, VGG-16, MobileNet V2, GoogLeNet, and EfficientNet-B0 models. It has been observed that the success rate increases as the number of images in the data set increases. They achieved the highest success rate of 99.25% with the increased data set [23]. Pacal (2023) used the data set named COVID-QU-Ex in his study. In his

157

study, he trained with the ViT-L16 model. 11.956 COVID-19 images, 11.263 non-COVID pneumonia cases and 10.701 Normal case images were used in the dataset. As a result of the study, they reached a 96% accuracy rate with the ViT-L16 model [24]. Doğan (2023) used the widely used COVID-19 data set in his study and performed a cross-data set evaluation. ResNet50 model was used in the research and the highest success rate (71.47%) was achieved with this model [25]. In their study, Tüfekçi and Gezici (2023) aimed to distinguish between COVID_19 and Pneumonia diseases. Cross-validation was performed 10 times on the data set used and the highest success rate (99.90%) was obtained with the Alexnet model. [26].

The contributions made to the literature in this study are given below:

• The data set used in the study consists of CT images of people treated at Tokat Gaziosmanpaşa University Hospital. This data set was created originally.

• An novel CNN model was designed and a high success rate was achieved with the original data set.

• The success of the proposed original CNN model was compared with state-of-the-art models.

In the second part of the article, information will be given about the methods and materials used, in the third part, information will be given about the experimental studies, and in the fourth part, information will be given about the obtained results and inferences.

2. MATERIAL AND METHOD

2.1. Deeep Learning

In this section, information about artificial intelligence and deep learning concepts will be given. Under the title of deep learning, information about Convolutional Neural Networks (CNN) architecture will be given. Information is given about layers such as Input Layer, Convolution Layer, Pooling Layer, Fully Connected Layer, Dropout and Classification Layer in the CNN architecture. With its ability to think and interpret, the human brain can decide in a very short time what its next move will be or easily solve a numerical operation. A person can interpret what may happen to him and what consequences his actions will have based on his previous experiences. Although computers can solve very complex operations instantly, they do not have direct abilities such as interpretation and decision-making[27]. The development process of artificial intelligence started with studies using these skills that the human brain can do as a model. Artificial intelligence can be defined as a machine performing tasks such as solving a problem, extracting meaning, and producing a solution by imitating human characteristics. Although the history of deep learning does not date back to ancient times, it is a very popular subject in terms of application areas and experimental studies. The concept of deep learning attracted attention for the first time thanks to the large-scale visual recognition competition

(ImageNet. Large-Scale Visual Recognition Challenge / ILSVRC) held in the object recognition category in 2012 [28]. While there are scientists who see deep learning as a sub-branch of machine learning, there are also scientists who argue the opposite and argue that it is a completely different field of study. With deep learning, tasks that may take a long time for humans to do, as well as tasks in daily life, can be done easily, and humanoid disadvantages such as mental state or fatigue are not encountered [29]. Deep learning consists of multi-layer artificial neural networks and can process large amounts of data simultaneously. The increase in Big Data day by day and the continuous development of graphics card (GPU) features have improved the capabilities of deep learning and it has become increasingly popular after 2000.

Deep learning is used in many areas such as image processing, facial recognition systems, natural language processing, voice recognition, fingerprint readers, robotics, gene analysis, and driverless cars. The most commonly used features of deep learning are classification, recognition and detection [30].

2.2. Convolutional Neural Network (CNN)

Convolutional Neural Network (CNN) architecture is frequently used in computer vision applications. CNN architecture consists of various layers such as input layer, convolution layer, pooling layer, fully connected layer, relu layer, scaling layer, classification layer. A classical CNN architecture is given in Figure 1.
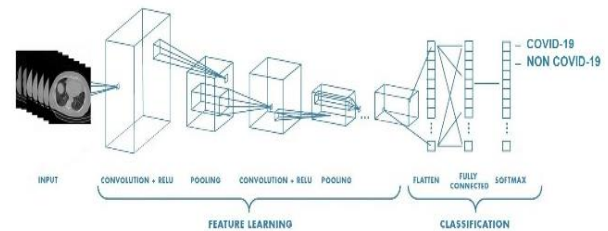
Figure 1. Classic CNN architecture

Input Layer: The input layer is the first layer of the CNN architecture. The data enters the system as it is from this layer. The size of the data transferred to the system is important. If the size is chosen small, the memory requirement will decrease, the training time will decrease, but the success rate may decrease. If it is chosen larger, the training time increases, the memory requirement increases and the success rate may increase. Finding the perfect input size for our system is important for training time and performance.

Convolution Layer: This layer, which is the most basic component in the CNN architecture, is also known as the convolution layer or transformation layer. The most basic operation of this transformation occurs by creating new matrices by moving a certain filter of 3x3, 5x5, 7x7, 9x9 size over the entire image.

Pooling Layer: Pooling layer usually comes after the relu layer. The input data studied may be large in size, which causes complexity and prolongation of training time. The

pooling layer aims to gradually reduce this large size of data, preventing memorization while preserving important parts of the feature map. This reduction affects length and width but not depth. These reductions in the number of parameters also prevent system confusion.

Fully Connected Layer: In the CNN architecture, the fully connected layer comes after the convolution layer, relu layer and pooling layer. The neurons in this layer connect to all the neurons of the previous layer and work by transferring their outputs to the next layer [31]. It is used in studies such as fully connected layer classification processes, natural language processing and image processing. The feature in the layer is obtained by connecting the matrices on this layer.

Dropout Layer: It is a method developed to prevent multilayer neural networks from memorizing. After a determined threshold value, information that may be considered unimportant is forgotten. The system prevents excessive loss of time and prevents memorization. Dropout process is accomplished by deleting some random links.

Classification Layer: In this layer, results are produced as many as the number of items to be classified. For example, if 4 different types of objects are to be classified, the classification layer output value should be 4. Different classification types are used for the classifier layer applied as the last layer. Softmax can be said to be the most well-known classifier [30].

2.3. Data Set

The data set used in the study consists of CT images of people receiving treatment at Tokat Gaziosmanpaşa University Hospital, as a result of the permissions obtained in accordance with the ethics committee decision no. 26. 23-KAEK-033 and 83116987-092. The data set was created from CT images of patients and healthy people diagnosed as COVID-19 positive, who were examined at the relevant polyclinic between 2019 and 2023. The data set consists of 5.000 images in total, including 2.500 images of 250 Covid-19 patients and 2.500 images of 250 healthy individuals. Images representing CT image classes of COVID-19 Positive and COVID-19 Negative people in the data set are given in Figure 2.
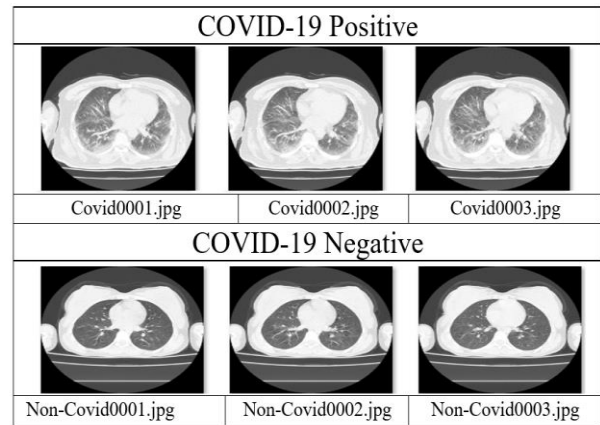

Figure 2. CT images of COVID-19 Positive and COVID-19 Negative people

As a result of dozens of experimental studies conducted on the data set, the highest accuracy rate was achieved with the figures in Table 1.

Looking at Table 1, we see that 70% are used for training, 15% for validation, and 15 for testing. In total, 3,500 training, 750 validation and 750 test images were used.

Table 1. Number of images of the data set used in experimental studies

Data Set Class	Training	Validation	Test
	% 70	% 15	% 15
COVID-19 Positive	1.750	375	375
COVID-19 Negative	1.750	375	375
Total	**3.500**	**750**	**750**

2.4. Proposed Method

The processing steps applied for this study are given in Figure 3. In the first stage, the data set was created, and in the second stage, the dcm format of the data was converted to .jpg image format. Pre-processing steps such as classifying the data and changing the names to make them meaningful were carried out. In the third stage, the distribution of data to be used for training, validation and testing was determined. In the fourth stage, it was determined which deep learning network models would be used for training. In the final stage, performance metrics and accuracy rates were obtained, allowing the results to be compared.
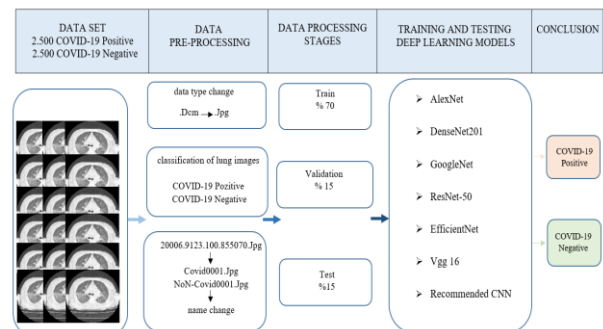

Figure 3. Methodology of the proposed method

The network design of the proposed model is given in Figure 4. The model has a two-class output and consists of a total of 50 layers.

159

Figure 4. Network design of the proposed model

3. EXPERIMENTAL STUDIES

Information about the sources of hardware and software used in experimental studies is given in Table 2.

Table 2. Information about the hardware and software used

Hardware	Specification
Processor:	12th Gen Intel(R) Core(TM) i7-1255U 1.70 GHz
Ram:	16 GB
Graphics Card:	Intel(R) UHD Graphics
Display Memory:	8.129 MB

Within the scope of the study, an original data set was created to be used for the first time. The data set consists of lung CT images of people whose reporting results are COVID-19 Positive and COVID-19 negative. For the classification of these images, a study was conducted on the proposed CNN model and 6 models frequently used in the literature. Models were trained on a data set of 5.000

images. MATLAB R2023a software was used to train the models.

3.1. Performance Metrics

Convergence graphs, performance values obtained as a result of experimental studies and results obtained from the studied models were compared. The confusion matrix reflects the performance values of the trained network. The table of confusion matrix is given in Table 3.

Table 3. Confusion Matrix

Confusion Matrix		Predicted Values	
		Positive	Negative
Actuald Values	Positive	True Positive (TP)	False Positive (FP)
	Negative	False Negative (FN)	True Negative (TN)

TP: It is the process of correct classification of a positive sample.
TN: It is the process of correctly classifying the negative sample.
FP: It is the process of misclassifying the negative sample.
FN: It is the process of misclassifying a positive sample.
The ROC curve is created by plotting the true positive rate (Sensitivity) against the false positive rate at varying thresholds. The part below the ROC curve threshold constitutes the AUC value. AUC represents the degree of discriminability. It shows the model's ability to distinguish between classes. The higher the AUC rating, the better the model's ability to predict true negatives as negative and true positives as positive. The performance metrics used in the study are stated below.

$$\text{Accuracy} = \frac{TP + TN}{TP+TN+FP+FN} \text{ x } 100 \qquad (1)$$

$$\text{Precision} = \frac{TP}{TP+FP} \text{ x } 100 \qquad (2)$$

$$\text{Recall} = \frac{TP}{TP + FN} \text{ x } 100 \qquad (3)$$

$$\text{F1-Score} = \frac{2 \text{ x Percision x Recall}}{\text{Precision + Recall}} \qquad (4)$$

Results Obtained with Deep Learning Models

The data set was trained on six different commonly used CNN models and the proposed network model, and different success rates were obtained. Experimental results obtained during the training phase are given under model headings.

Performance Evaluation of Alexnet Model

Looking at the confusion matrix in Figure 5, it can be seen that 330 of 369 COVID-19 positive patients were classified correctly and 39 were classified incorrectly. While 336 of 381 healthy samples were classified correctly, 45 were classified incorrectly.

The experimental results obtained during the training of the data set with the Alexnet model are 89.51% precision rate, 87.88% recall rate, 88.69% F1 score, as seen in Table 4. It can be seen that the model reached an accuracy rate of 88.79%.
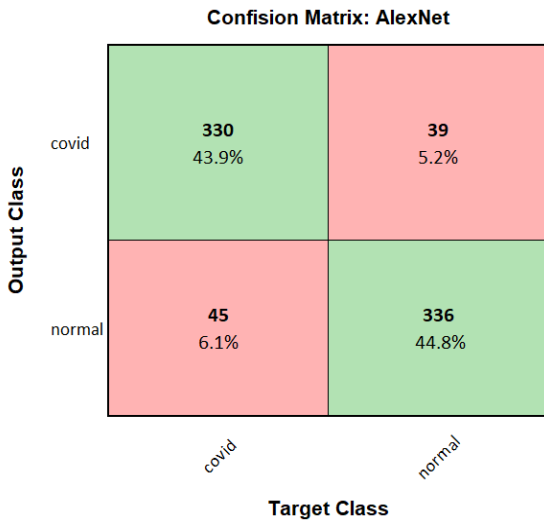
Figure 5. Confusion matrix obtained by the Alexnet model on test data

Table 4. Experimental results of the AlexNet model

Accuracy (%)	Precision (%)	Recall (%)	F1-Score (%)
88.79	89.51	87.88	88.69

Performance Evaluation of DenseNet201 Model

Looking at the confusion matrix in Figure 6, it can be seen that 326 of 384 COVID-19 positive patients were classified correctly and 58 were classified incorrectly. While 320 of 366 healthy samples were classified correctly, 46 were classified incorrectly. The experimental results obtained during the training of the data set with the DenseNet201 model are 84.89% precision rate, 87.61% recall rate, 86.23% F1 score, as seen in Table 5. It can be seen that the model reached an accuracy rate of 86.14%.
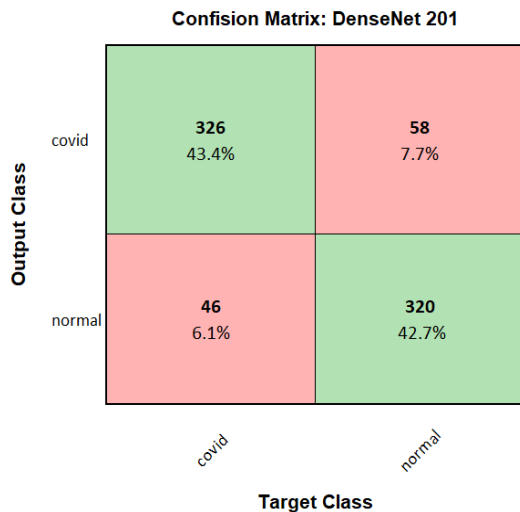

Figure 6. Confusion matrix obtained by DenseNet201 model on test data

Table 5. Experimental results of the DenseNet201 model

Accuracy (%)	Precision (%)	Recall (%)	F1-Score (%)
86.14	84.89	87.61	86.23

Performance Evaluation of the EfficientNet Model

Looking at the confusion matrix in Figure 7, it can be seen that 357 of 362 COVID-19 positive patients were classified correctly and 5 were classified incorrectly. While 375 of 388 healthy samples were classified correctly, 13 were classified incorrectly. The experimental results obtained during the training of the data set with the EfficientNet model are 98.64% precision rate, 86.46% recall rate, 97.54% F1 score, as seen in Table 6. It can be seen that the model reached an accuracy rate of 97.60%.

Figure 7. Confusion matrix obtained by the EfficientNet model on the test data

Table 6. Experimental results of the EfficientNet model

Accuracy (%)	Precision (%)	Recall (%)	F1-Score (%)
97.60	98.64	96.46	97.54

Performance Evaluation of GoogleNet Model

Looking at the confusion matrix in Figure 8, it can be seen that 360 of 384 COVID-19 positive patients were classified correctly and 24 were classified incorrectly. While 353 of 365 healthy samples were classified correctly, 12 were classified incorrectly. The experimental results obtained during the training of the data set with the GoogleNet model are 93.71% precision rate, 96.75% recall rate, 95.21% F1 score, as seen in Table 7. It can be seen that the model reached an accuracy rate of 95.16%.

Figure 8. Confusion matrix obtained by the GoogleNet model on test data

Table 7. Experimental results of the GoogleNet model

Accuracy (%)	Precision (%)	Recall (%)	F1-Score (%)
95.16	93.71	96.75	95.21

Performance Evaluation of ResNet-50 Model

Looking at the confusion matrix in Figure 9, it can be seen that 370 of 414 COVID-19 positive patients were classified correctly and 44 were classified incorrectly. While 331 of 336 healthy samples were classified correctly, 5 were classified incorrectly. The experimental results obtained during the training of the data set with the ResNet-50 model are 89.47% precision rate, 98.71% recall rate, 93.87% F1 score, as seen in Table 8. It can be seen that the model reached an accuracy rate of 93.55%.
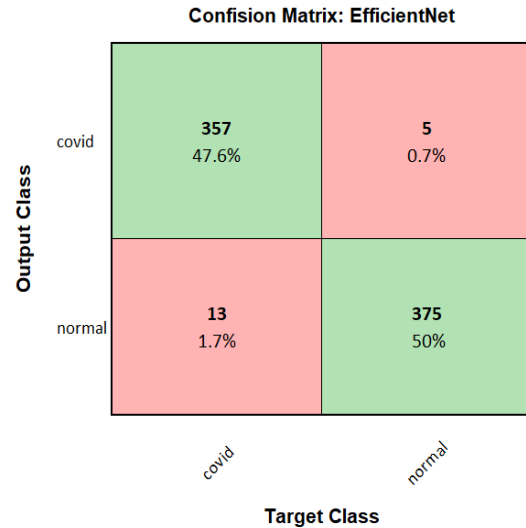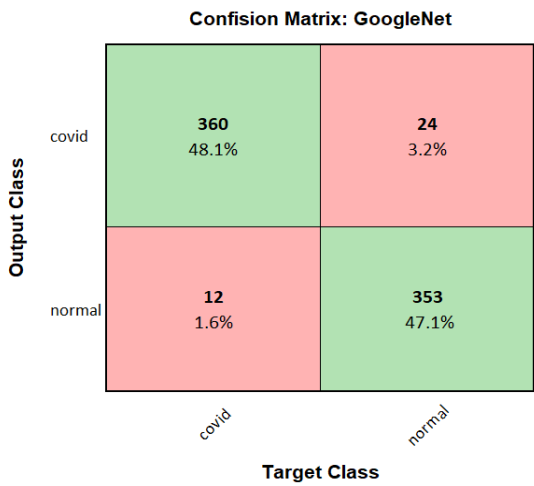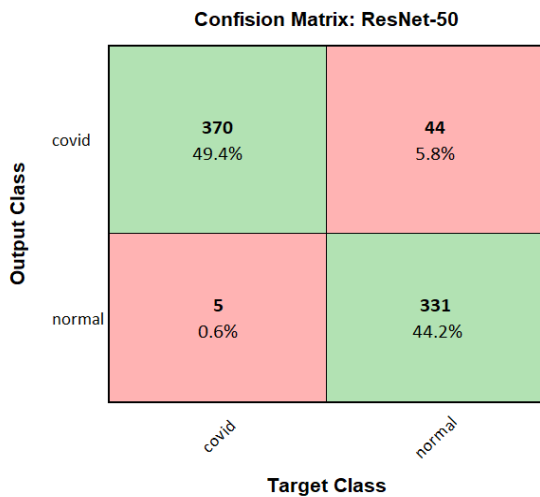

Figure 9. Confusion matrix obtained by ResNet-50 model on test data

Table 8. Experimental results of the ResNet-50 model

Accuracy (%)	Precision (%)	Recall (%)	F1-Score (%)
93.55	89.47	98.71	93.87

Performance Evaluation of VGG-16 Model

Looking at the confusion matrix in Figure 10, it can be seen that 334 of 350 COVID-19 positive patients were classified correctly and 16 were classified incorrectly. While 354 of 400 healthy samples were classified correctly, 46 were classified incorrectly. The experimental results obtained during the training of the data set with the VGG-16 model are 95.39% precision rate, 87.88% recall rate, 91.48% F1 score, as seen in Table 9. It can be seen that the model reached an accuracy rate of 91.72%.
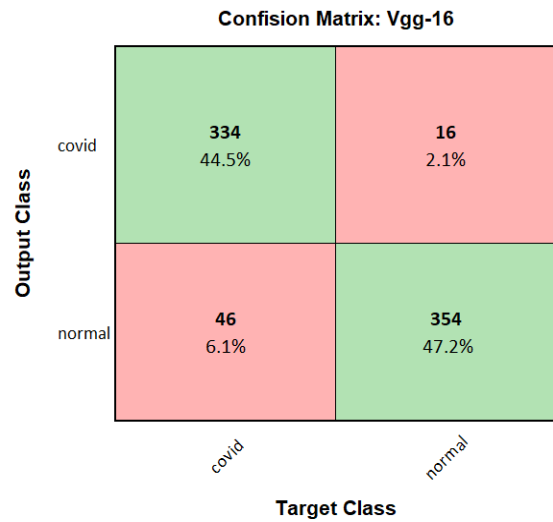
Figure 10. Confusion matrix obtained by the VGG-16 model on test data

Table 9. Experimental results of the VGG-16 model

Accuracy (%)	Precision (%)	Recall (%)	F1-Score (%)
91.72	95.39	87.88	91.48

Performance Evaluation Of The Proposed Model

The convergence chart of the data set with the proposed model during the training phase is given in Figure 11. When the proposed model convergence graph is examined, a graph gradually increasing to 95% levels is seen until the 17th cycle. There is an increase, albeit low, from the 18th cycle to the 32nd cycle. Although the error rate increases between the 32nd and 35th cycles, it is seen that the accuracy rate after the 36th level converges to 99.20%.
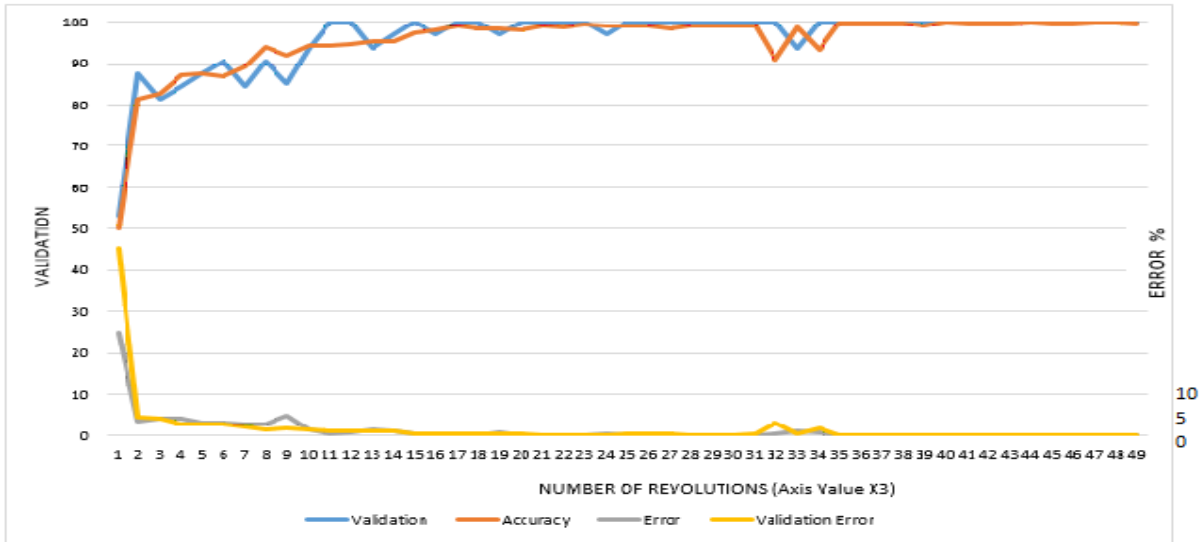
Figure 11. Convergence graph of the proposed model

The confusion matrix obtained on the test data with the proposed model is given in Figure 12. Looking at the confusion matrix, 372 of 375 COVID-19 positive patients were classified correctly and 3 were classified incorrectly. Of 375 healthy samples, 372 were correctly classified and 3 were misclassified as COVID-19 positive. When we look at the general accuracy of the model, it was seen that it achieved an accuracy rate of 99.20%.
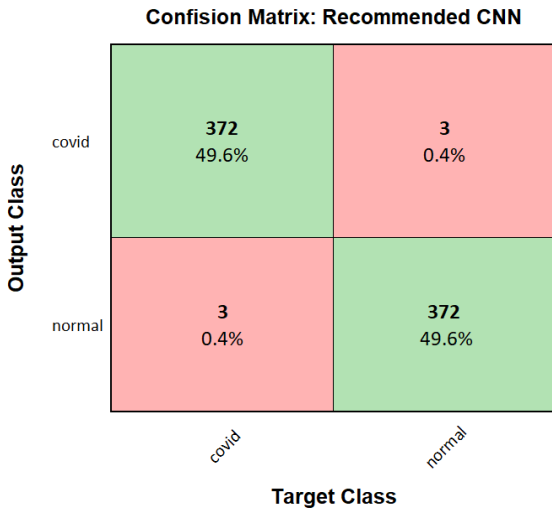
Figure 12. Confusion matrix obtained by the proposed model on the test data

The ROC Curve obtained during the training phase with the proposed model is given in Figure 13.
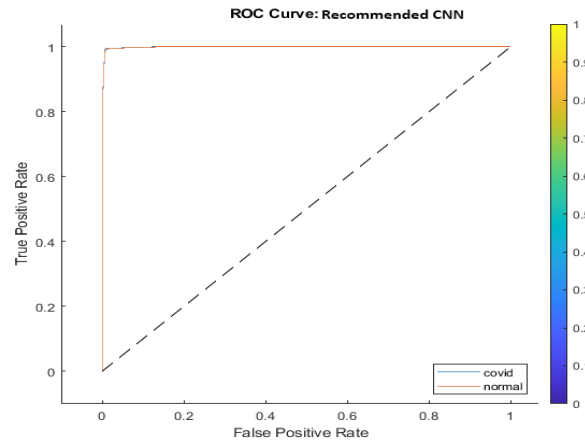
Figure 13. ROC Curve of the proposed model

The AUC diagram obtained during the training phase with the proposed model is given in Figure 14.

Figure 14. AUC Chart of the proposed model

The performance metrics obtained during the training phase with the proposed model are given in Table 10.

Table 10. Experimental results of the proposed model
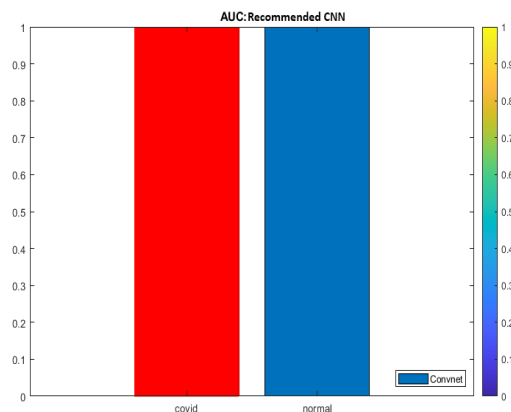
Accuracy (%)	Precision (%)	Recall (%)	F1-Score (%)
99.20	99.20	99.20	99.20

163

4. DISCUSSION AND CONCLUSION

COVID-19 disease has become a global problem and has caused serious problems.

Diagnosis of the disease, isolation of patients, application of the correct treatment and, as a result, minimizing the impact of the epidemic have been the common goal of all healthcare professionals and everyone who feels responsible. In this direction, image classification studies on COVID-19 have been carried out in the field of science and technology and experimental studies have been carried out that can predict the disease. This study was conducted to detect the disease and assist physicians. Experimental studies were conducted with 7 different CNN models on lung CT images of healthy people and people diagnosed with COVID-19. The data set used in experimental studies consists of 5.000 images. Comparison of performance metrics of the examined models is given in Figure 15. When parameters such as 99.20% accuracy, 99.20% precision, 99.20% sensitivity, 99.20% F1 score are examined, it is seen that the proposed model has the highest success rate. Considering these obtained values, we think that the proposed network model will be useful in detecting COVID-19.

	Accuracy (%)	Precision (%)	Recall (%)	F1-Score (%)
Recommended Model	99,20	99,20	99,20	99,20
EfficientNet	97,60	98,64	96,46	97,54
GoogleNet	95,16	93,71	96,75	95,21
ResNet-50	93,55	89,47	98,71	93,87
VGG-16	91,72	95,39	87,88	91,48
AlexNet	88,79	89,51	87,88	88,69
DenseNet201	86,14	84,89	87,61	86,23
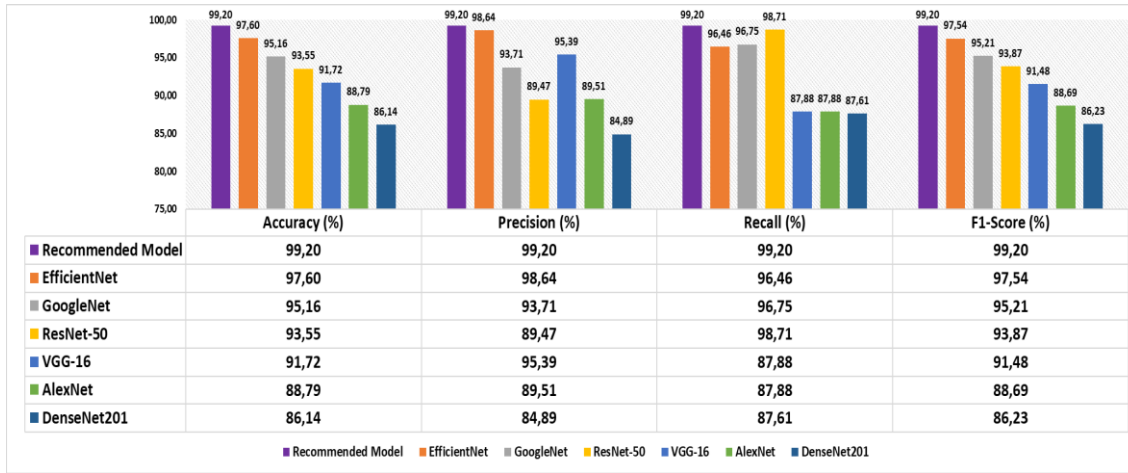
Figure 15. Comparison of experimental results of models

Looking at the performance metrics and accuracy rates given in Figure 15, the EfficientNet model is 97.60%, the GoogleNet model is 95.16%, the ResNet-50 model is 93.55%, the Vgg-16 model is 91.72%, the AlexNet model is 88.79%, DenseNet201 model is calculated as 86.14%.

The accuracy rate of the proposed model was calculated as 99.20%, and the highest rate was obtained with this model among the models studied experimentally.

Roc curves are created by plotting the number of true positives as a function of false positives, looking at varying classification thresholds. ROC curves also provide information about the success rates of the results obtained. The Roc curve process, which is frequently used in clinical diagnosis, was created for each of the experimental studies conducted for the detection of COVID-19.

It is known that positives are completely separated from negatives when the ROC score reaches 1. The curve that the Roc curve will create in the coordinate system is the true positive value (sensitivity) and false positive value of the diagnostic test on the Y axis. (1-specificity) on the X-axis. At each loop point, the Roc curve is created by connecting the points where true positives and false positives intersect [32].

An image showing the distinction between a perfect classifier, a typical classifier, and a classifier that makes random predictions based on the performance of the Roc curves is shown in Figure 16.

Perfect classifier   A typical classifier   Random classifier
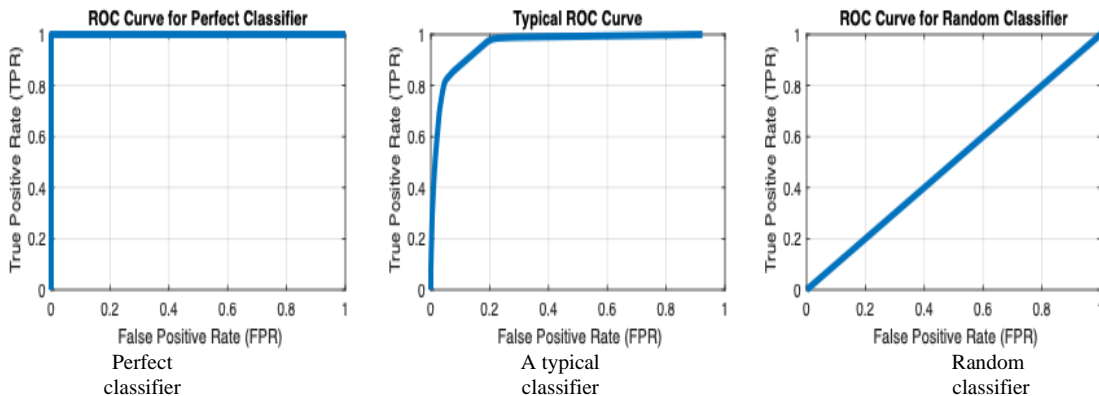
Figure 16. Graphs based on classification levels [33]

Figure 17 shows the Roc curves of the models in which experimental studies were carried out. Looking at the performance values, it can be seen that the model that makes the best discrimination is the recommended model. In the study, model performances are listed from high to low as Recommended Model, EfficientNet, GoogleNet, ResNet-50, Vgg-16, AlexNet, DenseNet20.
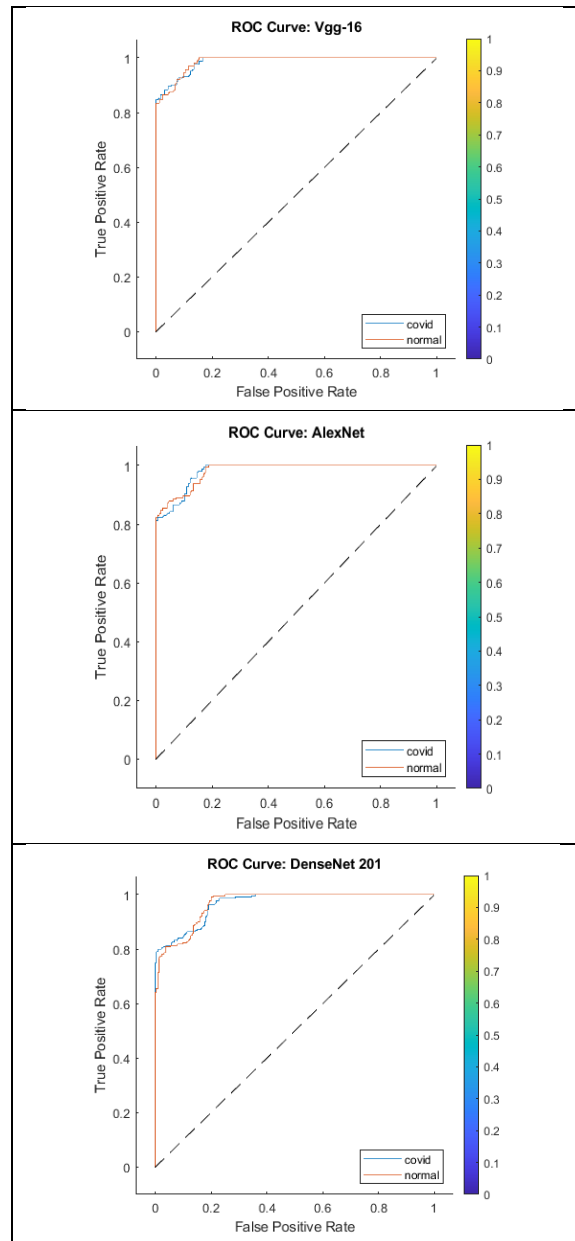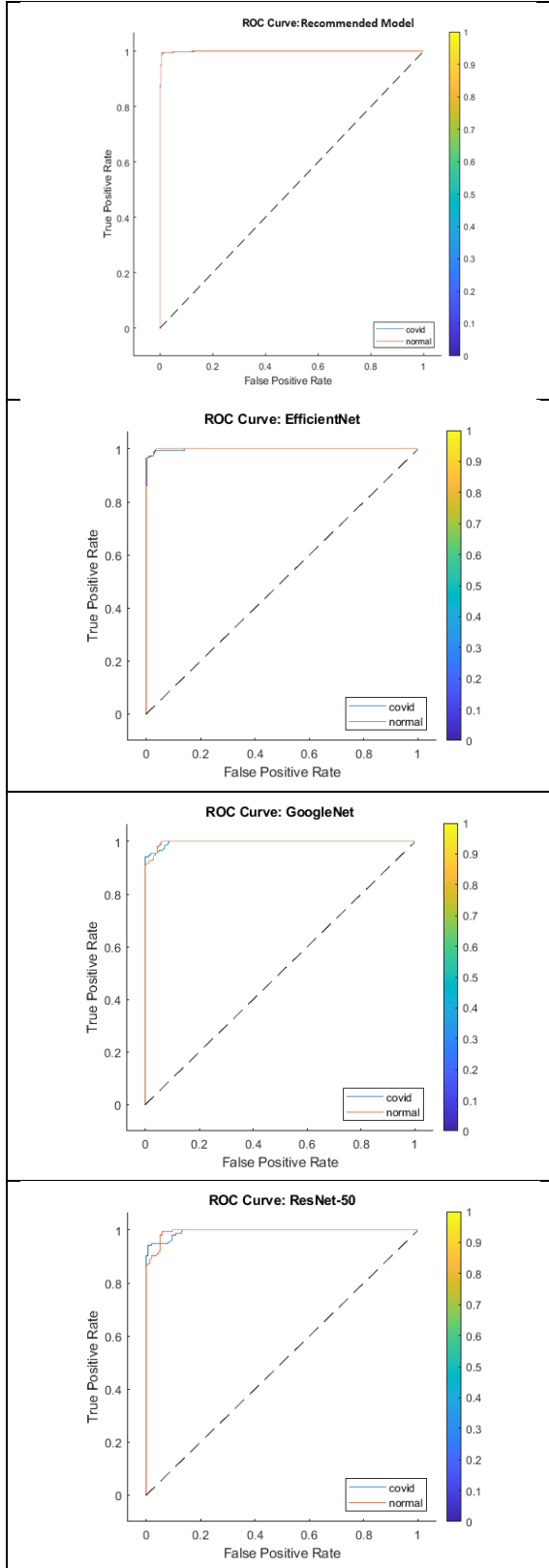
Figure 17. ROC curves of the models

As a result, when the studies were evaluated, it was understood that CNN models could be designed for image classification purposes. The trained data set has been used in a study for the first time, and it is aimed to further develop it by adding a pneumonia class and to conduct studies on pneumonia, COVID-19 positive and COVID-19 negative classes accordingly.

REFERENCES

[1] Selçuk EB. Pandemic Spread Process in the World and Turkey. Inonu University Faculty of Medicine Department of Family Medicine. 2020;12(3):87-91.

[2] Akyol, AD. Sars Severe Acute Respıratory Syndrome. Ege University Faculty of Nursing Journal.2005; 21(2):107-123.

[3] Nemli, SA. Middle East Respiratory Syndrome-Coronavirus (MERS-CoV). Kocatepe Medical Journal. 2016; 17:77-83.

165

[4] Ökçün S, Kurnaz M, Koçkaya G, Acar A. Overvıew Of Covıd-19 Dıagnosıs Methods: Rapid Review. Eurasian Journal Of Health Technology Assessment. 2020; 4(2):10-35.

[5] İnik Ö, Ceyhan A, Balcıoğlu E, Ülker E. A new method for automatic counting of ovarian follicles on whole slide histological images based on convolutional neural network. Computers in biology and medicine. 2019; 112:103350.

[6] Celik M, İnik Ö. Development of hybrid models based on deep learning and optimized machine learning algorithms for brain tumor Multi-Classification. Expert Systems with Applications. 2024;238: 122159.

[7] İnik Ö, Ülker E. Optimization of deep learning based segmentation method. Soft Computing. 2022; 26(7): 3329-3344.

[8] Çelik M, İnik Ö. Multiple Classification Of Brain Tumors For Early Detection Using A Novel Convolutional Neural Network Model. Eskişehir Osmangazi University Faculty of Engineering and Architecture Journal. 2023; 31(1) 491-500.

[9] İnik Ö, Balcıoğlu E, Ceyhan A, Ülker E. Using Convolution Neural Network for Classification of Different Tissue Images in Histological Sections. Annals of the Faculty of Engineering Hunedoara. 2019; 17.1: 101-104..

[10] İnik O, İnik Ö, Öztaş T, Demir Y, Yüksel A. Prediction of Soil Organic Matter with Deep Learning. Arabian Journal for Science and Engineering. 2023; 1-21.

[11] İnik Ö, Uyar K, Ülker E. Gender classification with a novel convolutional neural network (CNN) model and comparison with other machine learning and deep learning CNN models. Journal Of Industrial Engineering Research. 2018; 57-63.

[12] Nasip ÖF, Zengin K. Deep learning based bacteria classification. In. Tokat, Türkiye: 2nd International Symposium on Multidisciplinary Studies and Innovative Technologies (ISMSIT). 2018; 1-5.

[13] Singhal T. A Review of Coronavirus Disease-2019 (COVID-19). The Indian Journal of Pediatrics. 2020; 281–286.

[14] Kaya B, Önal M. Segmentation of Lung CT Images for COVID-19 Detection. European Journal of Science and Technology. 2021; 28:1296-1303.

[15] Çalışkan A. Detection Of Coronavirus Disease Using Wavelet Convolutional Neural Network Method. Kahramanmaraş Sütçü İmam University Journal of Engineering Sciences. 2023; 26(1):203-212.

[16] Hemdan EE, Shouman MA, Karar ME. COVIDX-Net: A Framework of Deep Learning Classifiers to Diagnose COVID-19 in X-Ray Images. 2020;2003.11055.

[17] Bozkurt F. COVID-19 Detection from Chest X-Ray Images Using Deep Learning Techniques. European Journal of Science and Technology. 2021;(24):149-156.

[18] JavadiMoghaddam S, Gholamalinejad H. A Novel Deep Learning Based Method For COVID-19 Detectıon From CT İmage. Biomedical Signal Processing and Control V70, (2021).

[19] Oğuz Ç. Determination Of COVİD 19 Possible Cases By Using Deep Learning Techniques. Master's Thesis, Ataturk University Institute of Science, Erzurum.2021.

[20] Panahi AH, Rafiei A, Rezaee A. FCOD: Fast COVID-19 Detector based on deep learning techniques. Informatics in Medicine Unlocked. 2020; (22):100506.

[21] Urut S, Özdağ R. COVID-19 Forecasting And Feature Detection Using Recurrent Neural Networks. Uluslararası Bilişim Kongresi. 2022; 523-530.

[22] Ceylan T, İnik Ö. COVID-19 Detection on Radiological Images with Deep Learning. 3rd International Conference on Applied Engineering and Natural Sciences. 2022;1807-1811.

[23] Çelik M, İnik Ö. Detection of Monkeypox Among Different Pox Diseases with Different Pre-Trained Deep Learning Models. Journal of the Institute of Science and Technology. 2023;13(1): 10-21.

[24] Pacal I. A Vision Transformer-based Approach for Automatic COVID-19 Diagnosis on Chest X-ray Images. Journal of the Institute of Science and Technology. 2023; 13(2):778-791.

[25] Doğan Y. COVID-19 Detection with Deep Learning Methods Under Cross-Dataset Evaluation. Gazi Universty Journal of Science Part C: Desıgn And Technology. 2023; 11(3) 813-823.

[26] Tüfekçi P, Gezici B. Detection of COVID-19 and Viral Pneumonia from Chest X-Ray Images with DeepLearning. Afyon Kocatepe University Journal of Science and Engineering. 2023; 23(1), 89-100.

[27] Yilmaz A. Artificial Intelligence, ISBN 978-605-9118-80-4, Irem Soylu, Istanbul. Kodlab; 2022.

[28] İnik Ö, Ülker E. Deep Learning and Deep Learning Models Used in Image Analysis. Gaziosmanpasa Journal of Scientific Research. 2017; 6(3): 85-104.

[29] Talan T, Aktürk C. Theoretical and Applied Research in Computer Science. Istanbul: Efe Academy Publications; 2021.

[30] Doğan F, Türkoğlu İ. The Comparison Of Leaf Classification Performance Of Deep Learning Algorithms. Sakarya University Journal Of Computer And Information Sciences. 2018; (1):10–21.

[31] Büyükarıkan B, Ülker E. Fruit Classification With Convolution Neural Network Models Using Illumination Attribute. Uludag University Faculty of Engineering Journal. 2020; (25), 81-100.

[32] Obuchowski NA. Receiver Operating Characteristic Curves And Their Use İn Radiology. Radiology. 2003; 229(1):3-8.

[33] mathworks.com [internet]. 2023 [cited 2023 november22].Available from:https://www.mathworks.com/products/new_products/release2023a.html/

166

Türk Doğa ve Fen Dergisi
Turkish Journal of Nature and Science
www.dergipark.gov.tr/tdfd

Determination of Wave Parameters of Bandirma Bay Using Wave Prediction Methods

Selahattin Alp ERKURTULMUS[1*] , **Emre PESMAN[2]**

[1] Yalova University, Altinova Vocational School, Ship Construction Program, Yalova, Türkiye
[2] Karadeniz Technical University, Surmene Faculty of Marine Sciences, Naval Arch. and Marine Eng. Department, Trabzon, Türkiye
Selahattin Alp ERKURTULMUS ORCID No: 0000-0001-5129-7228
Emre PESMAN ORCID No: 0000-0003-3529-3619

Corresponding author: alp.erkurtulmus@yalova.edu.tr

Abstract: Coasts are with complex dynamics where the interaction of the air, water, and land is effectively perceived. Wave height is the most important parameter that affects the coastal zone and the most significant parameter of coastal engineering problems. For this reason, wave statistics and wave height estimations are important. In Türkiye, as in the rest of the world, wave predictions are based on wind measurements or wind models. However, since there is no measurement of wave data that can be used in wave climate studies on the Turkish coasts and since such research has just started, wave models are obtained by various methods in the design process. In this study, wave predictions for Bandirma Bay were carried out with methods proposed in the literature (CEM, JONSWAP, SMB, Wilson) using the 12-month hourly average wind speed data of the State Meteorological Service for 1991, and the results were discussed and compared to those reported in other studies in the literature.

167

Dalga Tahmin Yöntemleri Kullanılarak Bandırma Körfezi için Dalga Parametrelerinin Belirlenmesi

Öz: Kıyılar; hava, deniz ve kara etkileşimlerinin etkin bir şekilde gözlemlendiği karmaşık dinamiklere sahip bölgelerdir. Belirgin dalga yüksekliği, bir kıyı bölgesini etkileyen en önemli parametredir. bu parametre kıyı ve liman mühendislikleri problemleri için de büyük önem arz etmektedir. Bu nedenle dalga istatistikleri ve dalga yüksekliği tahmini önemlidir. Ülkemizde de dünyada olduğu gibi dalga tahminleri rüzgâr ölçümlerine veya rüzgâr modellerine dayanmaktadır. Ancak, ülkemiz kıyılarında dalga iklimi çalışmalarında kullanılabilecek ölçülmüş dalga verisi olmadığından ve bu tarz çalışmalar yeni başladığından, kıyı yapıları tasarım sürecinde çeşitli yöntemlerle dalga modelleri elde edilmektedir. Gerçekleştirilen bu çalışmada, Bandırma için ölçülen Devlet Meteoroloji İşleri Genel Müdürlüğü'nün 1991 yılına ait 12 aylık saatlik ortalama rüzgâr şiddeti verileri kullanılarak literatürdeki CEM, JONSWAP, SMB, Wilson gibi dalga tahmini yöntemleri kullanılarak Bandırma körfezi için dalga tahmini gerçekleştirilmiş ve literatür çalışmaları ile sonuçlar karşılaştırılmıştır.

1. INTRODUCTION

Coasts are areas with complex dynamics where the interaction of the air, water, and land is effectively observed. The most important parameter affecting the coastal zone and the most significant parameter of coastal engineering problems is wave height [1]. Wave height is the vertical distance between the wave crest and the wave trough. The estimation of wave height through wave statistics is important. In Türkiye, as in the rest of the world, wave predictions are based on wind measurements or models. Additionally, as a parameter with important roles in coastal engineering activities such as coastal planning, coastal structure design, sediment transport, and coastal erosion analyses, wave height can also be estimated by methods such as artificial intelligence techniques, numerical models, and parametric methods [2].

Since direct wave measurements are costly and difficult, wind data are used for wave prediction. The main wave prediction methods in the literature are the Sverdrup, Munk, and Bretschneider (SMB) method [3], Wilson method [4], JONSWAP method [5], Donelan method [6], Shore Production Manual (SPM) method [7], and Coastal Engineering Manual (CEM) method [8].

In this study, wave predictions for Bandirma Bay were carried out using four widely applied methods reported in the relevant literature: CEM, JONSWAP, SMB, Wilson. These methods were selected due to their proven reliability in various coastal engineering applications and their compatibility with available 12-month hourly average wind speed data.

1.1. Physical Conditions

Bandirma is a gulf region protected by the Kapidag Peninsula in the south of the Marmara Sea. Since the Marmara Sea is an inland sea, it has a soft wave climate, and the heights of the waves coming into this gulf are quite small. The gulf is closed to west and northwest waves due to the Kapidag Peninsula and is only open to northeast and east waves with $20°$-$70°$ angles as shown in Figure 1 [9].
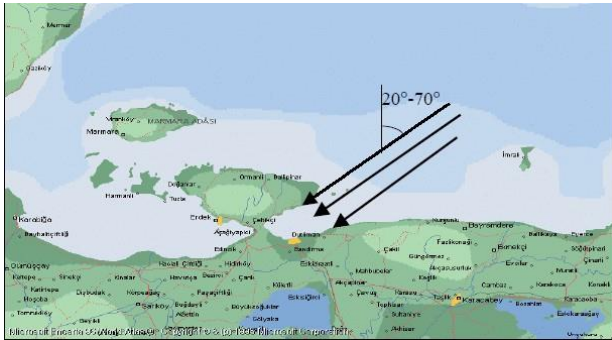

Figure 1. Bandirma bay and wave directions [9].

2. MATERIAL AND METHOD

One of the factors affecting wave formation is wind speed. Wind speed is the speed of the wind in the atmosphere. This speed should be known before wave predictions. However, due to factors such as the fact that the measurement sites are encompassed by settlement borders over time, incorrect measurements and potentially incorrect calculations may be a problem [10].

Considering this situation, it was seen that the measurement site was idle, the State Meteorological Service (DMI) data of 1991 were used in the study, and this information is provided in Appendix A [11].

The surface area on the sea where the wind creates the waves is called fetch (F) [12]. Wind speed, U, fetch distance, F, and wind blowing time, t, determine the height and period of wind-driven waves [13]. The situation in which the fetch and wind blowing time are sufficient is a fully developed sea state. The opposite is called a developing sea state. If the wind blowing time is shorter than the required wind blowing time, this

constitutes a fully developed sea state, and there is a time-limited situation, while if the fetch distance is smaller than the required fetch distance, there is a fetch-limited situation. The effective fetch distance (F_e) is calculated by measuring the fetch lengths at $7.5°$ intervals in a band of $45°$ from the wave direction ± and using Equation 1 [14]. Figure 2 shows effective fetch lengths for Bandirma Bay.
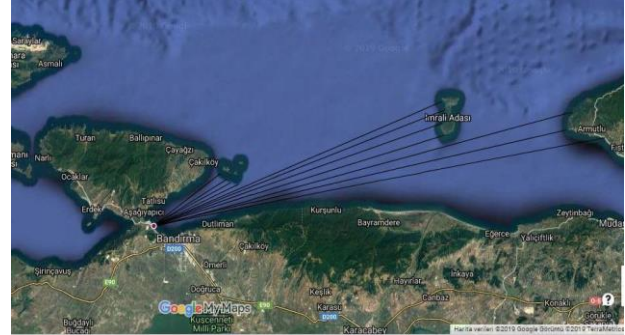
Figure 2. Effective fetch lengths

$$F_{eff} = \frac{\sum F_i \cos \alpha^2}{\sum \cos \alpha} \qquad (1)$$

Significant wave heights are calculated depending on the effective fetch lengths, wind blowing time, and wind speed at a height of 10 m from the sea. Fetch is the distance of the swell area of the wave. Significant wave height was estimated using the CEM, JONSWAP, SMB, and Wilson methods considering fetch-limited, time-limited, or fully developed sea states.

2.1. CEM Method

The calculation in the CEM method is made as in Equations 2 and 3 depending on the significant wave height H_s, wave period T_z, minimum wind blowing time t_{min}, effective fetch length F_e, wind speed at 10 m U_{10}, and gravitational acceleration g:

$$\frac{g H_s}{U_*^2} = 4.13 \times 10^{-2} \left(\frac{g F_e}{U_*}\right)^{0.5} \qquad (2)$$

$$\frac{g T_z}{U_*} = 0.651 \left(\frac{g F_e}{U_*^2}\right)^{1/3} \qquad (3)$$

Here, U_* is the frictional speed, and it is calculated as in Equation 4:

$$U_* = U_{10} (C_D)^{0.5} \qquad (4)$$

Here, C_D is the coefficient of friction, and it is calculated as in Equation 5:

$$C_D = 0.001 (1.1 + 0.035 \, U_{10}) \qquad (5)$$

In time-limited cases, the effective fetch distance (F_e) is calculated using Equation 6 depending on the minimum wind blowing time (t_{min}).

$$\frac{g F_e}{U_*^2} = 5.23 \times 10^{-3} \left(\frac{g t_{min}}{U_*}\right)^{1.5} \qquad (6)$$

2.2. JONSWAP Spectrum Method

The JONSWAP method is frequently used in developing sea states. The significant wave height H_S defined for a fetch-limited case is calculated as in Equation 7, and wave period T_Z is calculated as in Equation 8:

$$H_s = 0.0163 \, F^{0.5} \, U \qquad (7)$$

$$T_z = 0.439 \, F^{3/10} \, U^{2/5} \qquad (8)$$

For time-limited cases the formulae given in Equations 9 and 10 are used [5]:

$$H_s = 0.0146 \, t^{5/7} \, U^{9/7} \qquad (9)$$

$$T_z = 0.419 \, t^{3/7} \, U^{4/7} \qquad (10)$$

Here, H_S is the significant wave height (m), T_Z is the mean wave period (s), F is the fetch length (km), U is the wind speed (m s^{-1}), and t is the wind blowing duration time (s). The formulae written for the fetch-limited case are valid if the condition in Equation 11 is met:

$$t > 1.167 \, F^{0.7}/U^{0.4} \qquad (11)$$

Otherwise, time-limited formulae should be used.

2.3. SMB Method

The first method of determining design values using wind data was presented by Sverdrup and Munk [15]. The wave prediction curves given by Sverdrup and Munk were revised by Bretschneider using empirical data [16]. Therefore, this method is often referred to as the Sverdrup-Munk-Bretschneider (SMB) method.

Using the nomogram given for the SMB method shown in Appendix B, T_S and H_S can be found with the help of the fetch distance, wind speed, and wind blowing time [16]. During the use of this nomogram, T_S and H_S values are found by the interpolation intersecting the wind speed with the given fetch distance and blowing time [13].

However, if the intersection first encounters the blowing lines (time-limited waves), it is understood that the event and fetch can be taken as infinite. If the fetch levels are encountered first (fetch-limited waves), it is understood that the fetch distance controls the event, and the wind blowing time is insignificant [17]. The significant wave height H_S for time-limited waves and fetch-limited waves and period T_S are calculated as in Equations 12, 13, and 14, respectively:

$$\frac{g \, H_s}{U^2} = 0.283 \, tanh \left[0.0125 \left(\frac{g \, F}{U^2} \right)^{0.42} \right] \qquad (12)$$

$$\frac{g \, H_s}{U^2} = 0.283 \, tanh \left[0.0125 \left(\frac{g \, F}{U^2} \right)^{0.42} \right] \qquad (13)$$

$$\frac{g \, t}{U} = K \, e^{\left\{ \left[A \left(ln\left(\frac{g \, F}{U^2}\right) \right)^2 - B \, ln\left(\frac{g \, F}{U^2}\right) + C \right]^{1/2} + D \, ln\left(\frac{g \, F}{U^2}\right) \right\}} \qquad (14)$$

Here, K=6.5882, A=0.0161, B=0.3692, C=2.2024, and D=0.08798. These expressions contain the fetch geometry ϕ as in Equation 15 [13]:

$$\phi = \frac{g \, F}{U^2} \qquad (15)$$

The fetch parameter is given in graphical form in Figure 3. These equations are valid only for the deep-sea state. This method can also be applied using the nomogram given in Appendix B.
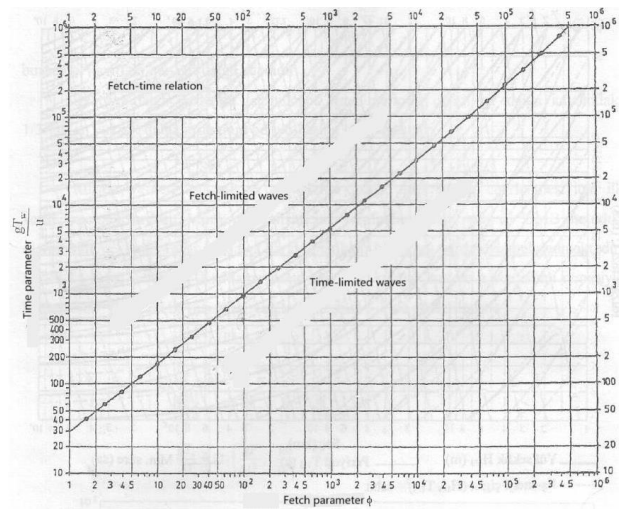
Figure 3. ϕ Fetch parameters [13].

Using these equations,

a) T, U, and F are determined based on the available wind data,

b) In Equation 14, the fetch parameter ϕ is determined,

c) The parameter g T/U is calculated,

d) If the value found by using steps (b) and (c) remains above the curve when marked in Figure 3, the significant wave height is determined by the fetch, and the fetch parameter found in step (b) is used. If this value is below the curve, the significant wave height is calculated based on the wind blowing time, and for this, the smaller value of ϕ, which is determined by intersecting the curve using the time parameter (g t/ U), is used,

e) Based on these calculated values of ϕ, H_S and T_S are calculated using Equations 12 and 13 [18].

169

2.4. Wilson Method

In this method, the minimum wind blowing time for the fetch-limited condition to end is calculated using Equation16:

$$t_{min} = 1.0 \, F^{0.73} \, U^{-0.46} \qquad (16)$$

Here, t_{min} is the fetch distance in an hour, and U is the wind speed (m s^{-1}) at 10 m above sea level. The significant wave height and period in the fetch-limited condition are expressed by Equations 17 and 18:

$$H_S = 0.30 \, \frac{U^2}{g} \left[1 - \left[1 + 0.004 \left(\frac{g \, F}{U^2} \right)^{0.5} \right]^{-2} \right] \qquad (17)$$

$$T_S = 8.61 \, \frac{U}{g} \left[1 - \left[1 + 0.008 \left(\frac{g \, F}{U^2} \right)^{1/3} \right]^{-5} \right] \qquad (18)$$

If the wind blows at a speed lower than t_{min}, fetch-limited case assumptions cannot be met. In the Wilson method, if the formation of waves is time-limited, an equivalent fetch distance F_{eq} is found using Equation 19. by replacing t_{min} with the wind blowing time in Equation 16. Wave parameters are recalculated using this equivalent fetch value in Equations 17 and 18.

$$F_{eq} = 1.0 \, t^{1.37} \, U^{0.63} \qquad (19)$$

Here, F_{eq} (km) is the equivalent fetch distance, t (s) is the wind blowing duration, and U is the wind speed (m s^{-1}) at 10 m above sea level [19].

3. RESULTS

The significant wave heights H_S and periods T_Z obtained by wave estimation methods which are CEM, JOBSWAP, Wilson, and SMB, using wind data from the meteorological station located around Bandirma Bay are shown in Table 1. The results were compared to TPAO measurements in the literature using bias and RE (relative error) statistics. Bias and RE is calculated using Equations 20 and 21.

Table 1. Simplified wave model results for Bandirma Bay

Method	H_S (m)	T_S (s)
CEM	0.42	3.30
JONSWAP	0.83	3.09
Wilson	0.81	3.47
SMB	1.71	5.92

The observed wave is the TPAO wave height value used for comparison, which is 0.55 m at a 10% risk time [20].

$$bias = \frac{1}{N} \sum_{i=1}^{N} P_i - Q_i \qquad (20)$$

$$RE = \frac{1}{N} \sum_{i=1}^{N} \frac{|P_i - Q_i|}{Q_i} \times 100 \qquad (21)$$

In these equations, P_i represents the estimated values, and Q_i represents the observed values. In Table 2, the error statistics of the estimation-based methods are given by comparing them to the results of other studies conducted in the Marmara Sea [21], the Black Sea [19], and Lake Ontario [22].

Table 2. Comparative error statistics of simplified estimation methods

Forecast Method	Error Statistics	Bandirma Bay	Sacu et al. (2018)	Akpinar et al. (2011)	Etemad et al. (2007)
CEM	bias	0.1	-0.25	-0.53	-0.36
	RE	18	74	-	68
JONSWAP	bias	0.53	-0.23	-0.5	-
	RE	96	67	-	-
Wilson	bias	0.59	-0.19	-0.49	-0.21
	RE	107	58	-	51
SMB	bias	1.9	-	-	-
	RE	345	-	-	-

In this study, bias values were found to be positive, unlike those in the literature. This was because no calibration was made in the formulae in this study, as opposed to other studies in the literature. Nevertheless, it can be observed in the comparisons that simplified methods are inadequate.

4. DISCUSSION AND CONCLUSION

In this study, while the results of simplified methods for wave models were found as shown in Table 2, calculations were made according to the average values of 1/3 of the data for high speeds. However, as seen in the comparative error analyses in Table 2, since the TPAO data were gathered according to a 10% risk, calculations were made according to the average values of 1/10 of the high speeds.

According to the results of this study, the CEM method gives the closest result to the observed TPAO values with an error rate of 18%. This is consistent with previous studies that highlight the accuracy of the CEM method in regions with moderate wind climates. On the other hand, the values found using simplified wave estimation methods gave results above the observed values of up to 300%, contrary to the results in other studies in the literature. This difference was due to the fact that this study was conducted without performing any calibration process.

It is recommended that these values be taken into consideration in any coastal and marine engineering studies and that more care be taken when using simplified wave models. It is also suggested that, if possible, some numerical methods should be used, calibration processes should be carried out, and sensitivity analyses should be performed in engineering studies to be conducted for the same site.

For more detailed wave analyses for Bandirma Bay, improving the temporal and spatial quality of existing measurements will increase the reliability of studies to be carried out in the future.

REFERENCES

[1] Erkurtulmus, SA, Yahsi, M., Pesman. E. Wave estimation methos for Bandirma bay. International Symposium of Bandırma and Its Surroundings-UBS'19. Bandırma, 2019.

[2] Berbić, J, Ocvirk, E, Carević, D, Lončar, G. Application of neural networks and support vector machine for significant wave height prediction. Oceanologia. 2017;59(3):331-349.

[3] Bretschneider, CL, Tamaye, EE. Hurricane wind and wave forecasting techniques. Coastal Engineering. 1976:202-237.

[4] Wilson, B. Seiches. Advences in Hydroscience. 1972;8:1-94.

[5] Hasselmann K, Barnett, T, Bouws, E, Carlson, H, Cartwright, D, Enke, K, et al. Measurements of wind-wave growth and swell decay during the Joint North Sea Wave Project (JONSWAP). Deutschen Hydrographischen Zeitschrift; 1973.

[6] Donelan, MA, Waters, CCINWR. Similarity Theory Applied to the Forecasting of Wave Heights, Periods and Directions. National Water Research Institute; 1980.

[7] USACE. Shore protection manual us army corps. Coastal Engineering. 1984;4(2):652.

[8] USACE. Coastal engineering manual. 2006.

[9] Demir, EN, Savran, H, Otay, S. Bandırma Alternative Coastal Fill Project Feasibility Study. 3rd National Coastal Engineering Symposium. Bandırma: 2000: p.1-15.

[10] Kenisarin, M, Karslı, VM, Caglar, M. Wind power engineering in the world and perspectives of its development in Turkey. Renewable Sustainable Energy Revolotion. 2006;10(4):341-369.

[11] Akdag, S, Dinler, S, Menteş, A. Analysis of wind energy characteristic for Bandırma. 4th Renewable Energy Sources Symposium. 2007.

[12] Yuksel, O, Cevik, Y. Coastal Engineering. Beta Publications; 2009.

[13] Capanoglu, BD. Wind and wave climate research for the coastal region- Ayvalık, Bozcaada and Bandırma. [Master dissertation]. Balikesir: Balikesir University; 2015.

[14] Tur, R, Soylu Pekpostalci, D, Kucukosmanoglu, A. Wave prediction methods Based on wind data in Gulf of Antalya. 9. Coastal Engineeering Symposium. 2018: p. 653-665.

[15] Sverdrup, HU, Munk, WH. Wind, sea and swell: Theory of relations for forecasting. Hydrographic Office; 1947.

[16] Bretschneider, CL. Forecasting relations for wave generation. Look Lab. 1970; 1(3):31-34.

[17] Yuksel, Y, Cevik, E, Celikoglu, Y. Coastal and port engineering. TMMOB Publications; 1998.

[18] Sahin, C. Parametric wind wave modelling: Western Black Sea case study. [Master dissertation]. Istanbul: Yildiz Technical University ; 2007.

[19] Akpinar, M, Ozger, A, Komurcu, M. Comperative wave forecasting in the Black Sea: Hopa case study. 7th Coastal Engineeering Symposium. 2011: p. 281-292.

[20] Erdik, T, Beji, S. Statistical analysis of wave height and wind velocity distributions for the Sea of Marmara. International Journal of Environment and Geoinformatics. 2018;5(1):6-83.

[21] Sacu, S, Erdik, T, Sen, O. Comparison of simplified wave prediction methods for Sea of Marmara. 9th Coastal Engineering Symposium. 2018.

[22] Kazeminezhad, MH , Etemad-Shahidi, A, Mousavi, S.J. Evaluation of neuro fuzzy and numerical wave prediction models in Lake Ontario. Journal of Coastal Research. 2007:317-321.

171

Appendices

Appendix A. Wind direction, speed and frequency [11].

Speed (kt)	N	NNE	NE	ENE	E	ESE	SE	SSE	S	SSW	SW	WSW	W	WNW	NW	NNW	TOTAL
0-1	59	127	80	116	97	141	79	86	36	45	24	24	31	15	39	76	1075
1-2	114	305	85	146	117	189	130	165	31	47	19	18	26	32	23	169	1616
2-3	99	393	10	10	21	127	72	118	34	30	9	29	15	35	12	89	1103
3-4	78	542	9	3	5	50	27	68	21	10	6	8	16	26	3	25	897
4-5	70	648	7	0	0	7	8	23	18	12	2	7	5	8	4	6	825
5-6	85	623	4	0	0	1	3	30	27	10	6	6	1	4	0	9	809
6-7	128	600	0	0	0	0	4	8	26	6	4	3	0	2	0	3	784
7-8	148	451	0	0	0	0	2	5	11	2	2	2	0	0	0	0	623
8-9	101	338	1	0	0	0	0	0	2	2	0	1	0	0	0	0	445
9-10	34	172	0	0	0	0	0	0	2	1	0	1	0	0	0	0	210
10-11	25	140	1	0	0	0	0	0	1	1	0	0	0	0	0	0	168
11-12	14	67	0	0	0	0	0	0	1	0	0	0	0	0	0	0	82
12-13	3	0	0	0	0	0	0	0	0	0	0	0	0	0	0	0	3
13-14	2	32	0	0	0	0	0	0	0	0	0	0	0	0	0	0	34
14-15	1	0	0	0	0	0	0	0	0	0	0	0	0	0	0	0	1
15-16	4	12	0	0	0	0	0	0	0	0	0	0	0	0	0	0	16
16-17	6	0	0	0	0	0	0	0	0	0	0	0	0	0	0	0	6
17-18	6	14	0	0	0	0	0	0	0	0	0	0	0	0	0	0	20
18-19	6	0	0	0	0	0	0	0	0	0	0	0	0	0	0	0	6
Total	983	4464	197	275	240	515	325	503	210	166	72	99	94	122	81	377	8273
Pct. (%)	11.27	51.18	2.26	3.15	2.75	5.90	3.73	5.77	2.41	1.90	0.83	1.13	1.08	1.40	0.93	4.32	100

Appendix B. SMB method [16].

Türk Doğa ve Fen Dergisi
Turkish Journal of Nature and Science
www.dergipark.gov.tr/tdfd

Determination of Serum Vaspin Levels in Diabetic Rats and Investigation of Possible Relationships Between Vaspin and Some Other Adipocytokines

Gülsüm ASİLKAN KALDIK[1]* , Abdurrahman ŞERMET[2]

[1] Bingöl University, Vocational School of Health Services, Elderly Care Department, Bingöl, Türkiye
[2] Dicle University, Medicine Faculty, Physiology Department, Diyarbakır, Türkiye
Gülsüm ASİLKAN KALDIK ORCID No: 0000-0002-1179-7719
Abdurrahman ŞERMET ORCID No: 0000-0001-5579-8310

*Corresponding author: gasilkan@bingol.edu.tr

Abstract: Adipose tissue plays an important role in many critical processes, especially diabetes, due to the adipokines it secretes. It is known that there is a relationship between diabetes and obesity. This work was conducted to analyze the relationship between insulin resistance occurring in diabetics and adipokines secreted from adipose tissue in obese rats. In addition, the relationship between diabetes and adipokines is not clear enough and there are limited studies on this subject. Therefore, the current work was also focused on examining the relationship between serum vaspin, adiponectin and leptin levels and diabetes parameters in STZ-induced diabetic rat model (Wistar Albino rats). Groups were control (C), diabetic (D), diabetic + metformin (D+Met) groups. Met (500 mg/kg/day) was applied for 8 weeks. The experiments elucidated that daily food intake and water consumption, fasting blood sugar, HbA1c levels and insulin resistance were higher in diabetic groups when compared to control and treatment groups. Serum vaspin, adiponectin and leptin levels and glucose-6-phosphate dehydrokinase (G6PD), pyruvate kinase (PK) and hexokinase (HK) activities were significantly lower in diabetic rats. Metformin treatment improved insulin resistance and glucose levels, and increased G6PD, PK and HK activities and plasma vaspin, adiponectin and leptin levels. All these results revealed that adipokines can play important roles in glucose metabolism, insulin resistance and pathogenesis.

174

Diyabetik Sıçanlarda Serum Vaspin Düzeylerinin Belirlenmesi ve Diğer Bazı Adipositokininlerle Vaspin Arasındaki Olası İlişkilerin Araştırılması

Öz: Adipoz doku salgıladığı adipokinler nedeniyle başta diyabet olmak üzere birçok kritik süreçte önemli rol oynamaktadır. Diyabet ile obezite arasında ilişki olduğu bilinmektedir. Bu yüzden, mevcut çalışma diyabetiklerde ortaya çıkan insülin direnci ile obez kişilerdeki yağ dokusundan salgılanan adipokinler arasındaki ilişkiyi araştırmak amacıyla gerçekleştirilmiştir. Ayrıca diyabet ile adipokinler arasındaki ilişki yeterince açık değildir ve bu konuda sınırlı çalışmalar vardır. Bu yüzden mevcut çalışma ayrıca STZ ile indüklenen diyabetik ratlarda (Wistar Albino sıçan) serum vaspin, adiponektin ve leptin düzeyleri ile diyabet parametreleri arasındaki ilişkiyi incelemeye odaklanmıştır. Gruplar kontrol (C), diyabetik (D), diyabetik+metformin (D+Met) gruplarıydı. Met (500 mg/kg/gün) 8 hafta süreyle uygulandı. Deneyler diyabetik ratların günlük besin alımı ve su tüketimi, açlık kan şekeri, HbA1c düzeyleri ve insülin direnci kontrol ve tedavi gruplarına göre daha yüksek olduğunu ortaya çıkardı. Diyabetik ratlarda serum vaspin, adiponektin ve leptin seviyeleri ile glukoz-6-fosfat dehidrokinaz (G6PD), pürüvat kinaz (PK) ve hekzokinaz (HK) aktiviteleri önemli ölçüde düştü. Metformin tedavisiyle insülin direnci ve glukoz seviyelerinde iyileşme, G6PD, PK ve HK aktivitelerinde ve plazma vaspin, adiponektin ve leptin düzeylerinde artış belirlendi. Tüm bu sonuçlar adipokinlerin glukoz metabolizması, insülin direnci ve patogenezinde önemli bir rol oynayabileceğini göstermektedir.

1. INTRODUCTION

Diabetes mellitus, which is increasingly seen all over the world, is a metabolic and chronic disorder characterized by irregularities in lipid, carbohydrate and protein metabolism and accompanied by one or both of the insulin resistance in the tissues and impaired insulin secretion that occur due to the destruction of β-cells in the pancreas [1].

The disease risks of diabetes, which lead to serious damage to vital organs including the heart, kidney and eye as well as the vascular system, are associated with exposure to genetic and environmental factors. All of these factors affect diabetes with almost the same intensity. Insulin resistance is associated with factors such as obesity, genetic factors, aging and sedentary lifestyle. Obesity occurs due to excessive consumption of foods with high energy content and decreased physical movements, which leads to diabetes [2]. The risk factors for the development of diabetes are basically divided into two as unchangeable and changeable factors. Ethnicity, age and positive family history are unchangeable risk factors, while physical inactivity, obesity and alcohol are changeable risk factors. The factors in these two groups are closely interconnected [3].

Many biological amines and hormones play a role in maintaining energy balance in the body. However, adipose tissue plays a major role in ensuring that the excess energy taken into our body is used by other tissues in the event of prolonged starvation and in storing this energy [4]. It has been proven that adipose tissue not only stores and releases energy but also contributes to energy balance through endocrine, paracrine and autocrine signals. However, although the important functions of adipose tissue in energy metabolism and disorders are known, the mechanisms that shape its formation and functions are still not fully known [1]. It has been previously shown that in some critical disorders affecting vital organs in our body, the metabolic, physiological and morphological functions of adipose tissue change, as well as the lipid and glucose storage capacity, cell number and size change [5]. Adipose tissue secretes bioactive peptides called adipokines and thus has both systemic (endocrine) and local (autocrine/paracrine) effects. Together with these effects, it contributes to the immune and inflammatory response, appetite, glucose and lipid metabolism [6]. The secretion levels of most adipokines are highly variable in the presence of obesity. For example, the secretion of adipokines such as vaspin, adiponectin and leptin is directly related to adipose tissue mass, and adipose tissue mass plays a vital role in emergence of insulin resistance. Insulin resistance forms a critical pathological link between cardiovascular diseases and some metabolic functions associated with diabetes [1].

Vaspin secretion occurs in the stomach, liver, subcutaneous and visceral fat tissue, peripheral blood cells, macrophage foam cells and pancreas in humans, while vaspin secretion has also been detected in the hypothalamus of db/db and C57BL/6 mice [7]. Among the cells that express vaspin in humans, the liver has the highest vaspin expression [8]. This hormone acts as a serine protease inhibitor, but when we look at the literature studies on vaspin, it has been seen that this effect is low. However, it is stated that vaspin affects metabolism by reducing food intake and blood glucose levels [1].

Leptin is an adipocyte-derived hormone which functions as a basic regulator of energy balance and food intake, and it reduces blood sugar and prevents lipid formation [9]. Leptin resistance or deficiency can cause obesity and diabetes. It has been found that there is a positive correlation between serum leptin concentrations and body mass index and body fat percentage, and that leptin levels decrease in obese individuals due to weight loss [10].

Adiponectin is a hormone generated mostly by adipocytes, and to a lesser extent by skeletal and cardiac myocytes, and is secreted into the bloodstream as a hexamer, trimer, and high molecular weight multimer. Adiponectin plays a role in preventing the formation of plaque deposits in arteries and in the development of atherosclerosis with its anti-inflammatory effects. Serum adiponectin levels decrease in individuals possessing coronary artery disease, obesity, and type 2 diabetes [10].

The aim of the current work was to investigate the relationship between insulin resistance in diabetic rats and adipokines secreted from fat tissue in obese rats, i.e. whether adipokines cause insulin resistance. In addition, the relationship between diabetes and adipokines is not clear enough and there are limited studies on this subject. Therefore, the work also focused on investigating the relationship between serum vaspin, adiponectin and leptin levels and liver enzymes related to diabetes parameters and glucose metabolism in STZ-induced diabetic rats

2. MATERIAL AND METHOD

2.1. Animals

The work was approved by Dicle University with the decision numbered 2017/05. The experiments were performed in accordance with the international declaration and guide.

This study was conducted on 21 male Wistar albino rats (latin name), aged 8–12 weeks, with a body weight of 260–300 g. Animals were housed in groups of 7 in 40×60 cm stainless steel cages under standard lighting conditions (12 hours of daylight and 12 hours of darkness) at constant temperature (22 ± 2°C) and 50%±10% humidity with standard 8 mm pellet feed and fresh tap water daily. Animals were divided into 3 groups: a healthy control group (C), a diabetic control group (D), and a metformin treatment group (D+met).

2.2. Creation of Experimental Diabetes

A solution of 60 mg/kg streptozotocin (STZ, Sigma Chemical Company) prepared in citrate buffer (pH 4.5) was injected intraperitoneally (i.p.) as a single dose to all rats except the healthy control group for the induction of diabetes in rats. The healthy control group received the same amount of citrate buffer as placebo. Rats with plasma glucose levels of $\geq$ 250 mg/dl in glucose measurements performed 48 hours after the injection were classified as diabetic rats to be included in the diabetes group. Following the administration of streptozotocin, feed and water intake were allowed.

2.3. Study Design and Formation of Experiment Groups

Diabetic rats were divided into 2 groups: diabetic control (D) and metformin treatment group (D+met). The healthy control group and diabetic control group were provided with water and feed only. The metformin group received metformin at a dose of 500 mg/kg/day orogastrically over the course of 8 weeks.

2.4. Finalization of The Experiment

Following an 8-week period, rats were fasted for 12 hours before being sacrificed by cardiac puncture while under ketamine anesthesia in order to obtain blood samples for subsequent analysis. Blood samples were placed in gel tubes and centrifuged at 3700 rpm for 15 minutes to obtain the serum extract, and the supernatants were transferred to Eppendorf tubes. Liver samples were rinsed with physiological saline after collection and kept at -80 °C until further analysis.

2.5. Biochemical Analysis

Serum glucose, TC, TG, and HDL-C were measured spectrophotometrically on an Abbott Architect C16000 autoanalyzer (Abbott Laboratories, Abbott Park, IL, USA) using Abbott Diagnostics original kits. Serum LDL-C was calculated using the formula LDL-C (mg/gl)=Total cholesterol (HDL+Triglyceride/5) and VLDL was calculated using the formula VLDL=TG/5 [11]. Serum insulin levels were measured with Roche Diagnostics original kits and the Cobas e601 module (Roche Diagnostics, Mannheim, Germany) by the electrochemiluminescence measurement method. Insulin resistance was calculated as follows:

HOMA-IR= fasting insulin (μu/ml) x fasting glucose (mg/dl)/405] [12].

Serum levels of vaspin, adiponectin, and leptin were measured spectrophotometrically with SunRed brand ELISA (Enzyme-Linked Immunosorbent Assay) kits according to the protocol.

For the determination of liver enzyme levels, 1 g of liver tissue was weighed on a precision scale and taken into a homogenization tube. 9 ml of PBS (phosphate buffer solution) (1:10) was added and homogenized in an ultraturrax T25-type mechanical homogenizer at 13500 rpm for 60 seconds. Within a centrifuge tube, the homogenate was centrifuged at 3700 rpm for 15 min at 4°C. The supernatant portion of the centrifuged samples was transferred to Eppendorf tubes, and HK, PK, and G6PD determinations were measured spectrophotometrically with SunRed brand ELISA (Enzyme-Linked Immunosorbent Assay) kits according to the protocol on the same day.

3. RESULTS

3.1. Fasting Blood Glucose Values and Weights

When initial and final weights were compared, weight loss was recorded in the D and D+met groups, while weight gain was recorded in the healthy control group. When initial and final glucose levels were compared, the D and D+met groups had higher final glucose levels, whereas there was no significant change in the healthy control group.

Table 1. Comparison of initial and final weights values

Parameters	Groups-Median (min-max)		
	C	D	D+Met
Initial weight (gr)	160.2 (125-185)	417.2 (385-484)	399.4 (298-531)
Final weight (gr)	265.1 (242-324)	214.7 (195-229)	194.1 (173-224)

Data represent median (min-max). C=Healthy control, D=Diabetic, D+Met= Group given metformin at a dose of 500 mg/kg/day for eight weeks.

Table 2. Comparison of initial and final plasma glucose values.

Parameters	Groups - Median (min-max)		
	C	D	D+Met
Initial glucose value (mg dl^{-1})	98.4 (89-105)	97.1 (86-107)	96 (87-103)
Final glucose value (mg dl^{-1})	100.2 (88-112)	363.5 (295-410)	569.5 (547-595)

Data represent median (min-max). C=Healthy control, D=Diabetic, D+Met= Group given metformin at a dose of 500 mg/kg/day for eight weeks.

3.2. Glycemic Parameters

When insulin resistances of the healthy control group and diabetic group were compared, the differences were found to be statistically significant (Table 3).

Table 3. Fasting blood glucose, insulin level and insulin resistance

Parameters	Groups - Median (min-max)	
	C	D
Fasting insulin Level (IU)	1.43 (1.30-1.60)	0.74 (0.60-0.90)
Insulin Resistance (HOMA-IR)	10.51 (10.0-11.2)	14.50 (13.0-17.0)

Data represent median (min-max). C=Healthy control, D=Diabetic Group

3.3. Enzymes Related to Glucose Metabolism

The activities of hexokinase (HK), glucose-6-phosphate dehydrogenase (G6PD), pyruvate kinase (PK), which are

enzymes related to glucose metabolism, were evaluated and the results are presented in the Table 4.

Table 4. Comparison of enzymes related to glucose metabolism

Parameters	Groups - Median (min-max)		
	C	D	D+Met
G6PD (mU mL^{-1})	501.22± 2.23	250.42± 1.64	395.57± 29.56
PK (mU mL^{-1})	205.67± 1.12	92.52± 1.25	160.83± 5.24
HK (mU mL^{-1})	252.21± 2.24	125.08± 1.88	267.67± 1.23

Data represent median (min-max). C=Healthy control, D=Diabetic, D+Met= Group given metformin at a dose of 500 mg/kg/day for eight weeks.

G6PD levels were higher in D+Met group in comparison to D group, and the difference was statistically significant (p<0.05). G6PD levels in group C were found to be the highest in comparison to the D and D+Met groups. These results were statistically significant in both the D and D+Met groups (p<0.05).

The PK levels of group C were recorded to be higher than those of the D and D+Met groups, indicating a statistically significant difference (p<0.05) in favor of group C. PK values were higher in group D+Met in comparison to group D and were found to be significant in favor of the D+Met group (p<0.05).

The HK values of rats in groups C and D+Met were found to be higher than those of rats in group D, which was significantly in favor of rats in groups C and D+Met (p<0.05). However, the HK levels of rats in groups C and D+Met were similar to each other, and no noticable statistical difference was found between them (p > 0.05).

3.4. Serum vaspin-adiponectin-leptin values

In comparison with the control group, adiponectin levels were determined to be significant in both diabetic and D+Met groups (p≤0.05). Leptin and vaspin levels were also significant in groups D and D+Met (p≤0.05).

Table 5. Serum vaspin-adiponectin-leptin values

Parameters	Groups - Median (min-max)		
	C	D	D+Met
Adiponectin (mg L^{-1})	5.55 (5.11-5.87)	4.61 (4.24-5.08)	5.62 (5.17-5.97)
Vaspin (ng L^{-1})	686.31 (660.77-695.22)	578.36 (538.55-645.22)	591.94 (516.44-711.88)
Leptin (pg mL^{-1})	369.77 (340.86-407.13)	303.16 (265.86-368.04)	370.69 (345.87-395.85)

When the three groups were compared, group medians were found to be different for adiponectin (P = 0.002). For vaspin, group medians showed no difference (P = 0.90). However, for leptin, group medians showed a difference (P = 0.006).

3.5. Serum Lipid Profile

TG and VLDL levels were higher in group D compared to groups C and D+Met. Cholesterol and HDL levels were lower in the groups D and D+Met compared to group C. LDL values showed no significant difference between the diabetic group and the healthy control group.

Table 6. Parameters Related to Fat Metabolism

Parameters	Groups - Median (min-max)		
	C	D	D+Met
TG (mg dl^{-1})	149.8 (72-395)	188.7 (75-230)	170.1 (105-489)
Cholesterol (mg dl^{-1})	84.8 (65-111)	62.2 (41-74)	66.7 (52-121)
HDL (mg dl^{-1})	54.8 (37.6-75.5)	29.0 (22.7-38.9)	41.2 (32.4-52.9)
LDL (mg dl^{-1})	2.5 (0.1-3.5)	2.5 (1.6-3.3)	2.1 (1.5-2.9)
VLDL (mg dl^{-1})	28.8 (14.4-79.0)	39.8 (15-48)	35.2 (21.2- 97.8)

Data represent median (min-max). C=Healthy control, D=Diabetic, D+Met= Group given metformin at a dose of 500 mg/kg/day for eight weeks.

4. DISCUSSION AND CONCLUSION

Adipose cells, also regarded as specific endocrine cells, are both energy storage and a tissue in which cytokines and hormones called adipokines are produced [13]. Furthermore, adipokines and cytokines produced by adipose tissue contribute to the inflammatory process and have inflammatory (TNF-α, IL-6, etc.) or anti-inflammatory (adiponectin, etc.) properties [14,15]. Cytokines secreted from adipose tissue initiate proinflammatory events and subsequently contribute to the development of insulin resistance [16].

Insulin, secreted from the islets of Langerhans of pancreatic beta cells, is a hormone that reduces plasma glucose levels. When insulin binds to the receptor on the plasma membrane, it causes a sequence of protein-protein interactions within the cell, which is how insulin achieves its effect. Insulin resistance is defined as a less than normal response to insulin at a certain concentration or impairment of its effect on glucose balance and deficiency in the response to insulin [17].

Certain mechanisms are involved in the underlying potential factors of insulin resistance. Increased visceral adiposity, fetal malnutrition, and genetic problems in one or more proteins have been reported as causes of insulin resistance. HOMA-IR > 2.5 is accepted as an indicator of insulin resistance [14].

The current experiments revealed that diabetic rats had a higher fasting blood glucose level and lower fasting insulin level in comparison to the control group. Insulin resistance (HOMA-IR) was ascertained to be higher in diabetic rats in comparison with the control. A study performed by Ghadge et al. [15] on gender-related effects of fasting blood glucose levels and disease duration on biochemical markers in type 2 diabetics revealed that fasting blood glucose levels were higher in

177

diabetics. The high blood glucose level obtained in the diabetic group was similar to the level found in the present study. Zaidi et al. [18] investigating the relationship between obesity and insulin resistance elucidated that the diabetic group had higher levels of both insulin resistance and fasting blood glucose than the control group. Park et al. [19] conducted a study on hyperglycemia and dyslipidemia in Type 2 DM mice in which plasma insulin levels were determined to be lower in diabetics compared to the control group. In the present study, hexokinase (HK), pyruvate kinase (PK), and glucose-6-phosphate dehydrogenase (G6PD) activities, which are enzymes related to glucose metabolism, were investigated to determine the level of G6PD in diabetic rats compared to healthy rats, and an increase was observed with metformin treatment. Furthermore, HK and PK levels of enzymes related to glucose metabolism were determined to be lower in diabetic rats as compared to the control group but slightly increased with metformin treatment. In the study, leptin levels were ascertained to be higher in the healthy control group in comparison to the diabetic group. The decreased leptin level in the diabetic group started to increase again in the metformin group. The leptin levels found at lower levels in the diabetic group in comparison to the healthy control group in the current work were similar to the leptin levels obtained in the study conducted by Bluher et al. regarding leptin in adipose tissue, suggesting that the decreased leptin level in the diabetes process can be associated with insulin resistance [20]. Several research groups (Ghadge et al., Gu X et al.) [15, 21] reported lower leptin levels in the diabetic group compared to healthy individuals. In the study conducted by Divan AG et al. [22] on the relationship between serum adiponectin and leptin levels in obesity as well as Type 2 DM, in contrast to the present study, leptin levels were determined to be higher in diabetic rats.

Evaluation of adiponectin levels in this study revealed that adiponectin levels were lower in the diabetic group in comparison with the healthy control group and increased again in the metformin-treated group, reaching their previous levels. The adiponectin levels found by Kershaw et al. [23] in their study were similar to the adiponectin levels found in the present study. Similar to Kershaw et al., Ghadge et al. [15] reported lower adiponectin levels in diabetics compared to healthy individuals, suggesting that the value found in adiponectin levels in this study is consistent with that of Ghadge et al. Likewise, Zapata et al. found adiponectin to be lower in diabetics, which was similar to the adiponectin levels obtained in the current study [24] .

Lower levels of adiponectin in the diabetic group in comparison to the control group suggested that adiponectin levels may cause diabetes or may be associated with increased resistance to insulin, impaired glucose tolerance, and diabetes.

Vaspin is a significant, newly discovered adipocytokine and has a regulatory role in glucose and lipid metabolism [25]. Upon analyzing the vaspin levels in this study, it was discovered that the healthy control group had higher serum vaspin levels than the diabetic group. These levels decreased over the course of the diabetes, but then slightly increased again when metformin was administered. According to the results of the study on vaspin conducted by Hida et al. [26], levels of vaspin were found to be similar to those obtained in the present study, suggesting that low levels of vaspin obtained during diabetes mellitus can be linked with glucose tolerance and insulin resistance.

The results from the present study elucidated that VLDL and TG levels were higher in the diabetic group in comparison to the metformin and healthy control groups. These results were similar to the results obtained by Ghadge et al. [15] in their study on the gender-related impacts of fasting blood glucose levels and disease duration on biochemical markers in type 2 diabetics, which showed that very low-density lipoprotein (VLDL) and triglyceride levels were higher in the diabetic group, as was found in the present study. Zapata et al. [24] carried out a study on various circulating concentrations of adipokines, glucagon, and adropin in a clinical population of lean, overweight, and diabetic cats, in which the diabetic group had higher triglyceride concentrations, as in our study. HDL and cholesterol levels were lower in the metformin and diabetic groups when compared to the healthy rats. In terms of LDL levels, the difference between the groups was found to be insignificant.

This work revealed that serum adiponectin, leptin and vaspin levels were low in diabetic rats, suggesting that these hormones may increase diabetes and insulin resistance and worsen glucose tolerance. These findings led us to think that adiponectin, leptin and vaspin may improve insulin sensitivity and increase glucose tolerance. VLDL and TG levels were determined to be higher in the diabetic group. This finding suggested that there may be a link between diabetes and obesity and that obesity may contribute to diabetes. The presence of insulin resistance in diabetics and the factors underlying the effect of adipokines in this process will provide a better understanding of the cause-effect relationship between diabetes and obesity for the development of better treatment methods. Although research on the effects of adipokines, which are thought to be anti-inflammatory, such as adiponectin, leptin and vaspin, on the insulin mechanism continues, it is thought that they may be effective in the treatment of conditions such as type 2 diabetes and insulin resistance.

Acknowledgement

REFERENCES

[1] Tripathi BK, Srivastava AK (2006) Diabetes mellitus: complications and therapeutics. Med Sci Monit, 12(7), 130-47.

[2] Dendup T, Feng X, Clingan S, et al. Environmental Risk Factors for Developing Type 2 Diabetes Mellitus: A Systematic Review. International Journal of Environmental Research and Public Health, 2018; 15(1).

[3] Aravinda J. Risk factors in patients with type 2 diabetes in Bengaluru: A retrospective study. World Journal of Diabetes, 2019; 10(4), 241–248.

[4] Reilly SM, Saltiel AR. Adapting to obesity with adipose tissue inflammation. Nature Reviews Endocrinology. 2017;13, 633–643.

[5] Alipoor E, Mohammad Hosseinzadeh F, Hosseinzadeh-Attar MJ. Adipokines in critical illness: A review of the evidence and knowledge gaps. Biomedicine ve Pharmacotherapy, 2018; 108, 1739–1750.

[6] [Unamuno X, Gomez-Ambrosi J, Rodriguez A, et al. Adipokine dysregulation and adipose tissue inflammation in human obesity. 2018

[7] Sato K, Shirai R, Yamaguchi M, et al. Anti-atherogenic effects of vaspin on human aortic smooth muscle cell/macrophage responses and hyperlipidemic mouse plaque phenotype. International Journal of Molecular Sciences, 2018; 19(6).

[8] Escote X, Gomez-Zorita S, Lopez-Yoldi M, et al. Role of omentin, vaspin, cardiotrophin-1, TWEAK and NOV/CCN3 in obesity and diabetes development. International Journal of Molecular Sciences, 2017;18.

[9] Pereira S, Cline DL, Glavas MM, et al. Tissue-specific effects of leptin on Rglucose and lipid metabolism. Endocrine Reviews, 2021; 42(1), 1-28.

[10] İncilay-Torunoğlu E, Yarım GF. Inflammation Markers Associated with Metabolic Syndrome. East Black Sea Journal of Health Sciences. 2022; 1,

[11] Friedewald WT, Levy RI, Fredrickson DS. Estimation of the concentration of low-density lipoprotein cholesterol in plasma, without use of the preparative ultracentrifuge. Clin Chem. 1972;18(6):499-502.

[12] Matthews DR, Hosker JP, Rudenski AS, Naylor BA, Treacher DF, Turner RC. Homeostasis model assessment: insulin resistance and beta-cell function from fasting plasma glucose and insulin concentrations in man. Diabetologia. 1985;28(7):412-9.

[13] Scherer PE. Adipose tissue: From lipid storage compartment to endocrine organ. Diabetes. 2006;55(6):1537-45.

[14] Matthews DR, Hosker JP, Rudenski AS, Treacher DF, Turner RC. Homeostasis model assessment: insulin resistance and fl-cell function from fasting plasma glucose and insulin concentrations in man. Diabetelogia. 1985; 28:412-419

[15] Ghadge, A. A., Diwan, A. G., Harsulkar, A. M., & Kuvalekar, A. A. (2017). Gender dependent effects of fasting blood glucose levels and disease duration on biochemical markers in type 2 diabetics: A pilot study. Diabetes & Metabolic Syndrome: Clinical Research & Reviews, 11, S481-S489.

[16] Timar R, Timar B, Degeratu D, Serafinceanu C, Oancea C. Metabolic syndrome, adiponectin and proinflammatory status in patients with type 1 diabetes mellitus. J Int Med Res. 2014;42(5):1131-8.

[17] Reaven GM. Banting Lecture. Role of insülin resistance in humandisease. Diabetes 1988;37:1595-607

[18] Zaidi SI, Shirwany TA. The Relationship Between Isulin Resistance and Obesity and Serum Resistance. J Ayub Med Coll Abbottabad. 2015; 27 (3): 552-5

[19] Park MH, Han JS. Padina arborescens Improves Hyperglycemia and Dyslipidemia in C57BL / KsJ-db / db Mice with Type 2 Diabetes Mellitus. J Med Food. 2015; 18 (10): 1088-94.

[20] Blüher M. Adipokines–removing road blocks to obesity and diabetes therapy. Mol Metab. 2014;3(3):230-40.

[21] Gu X, Chen Z. Serum leptin levels in obese women with and without type 2 diabetes mellitus. Minerva Endocrinol. 2014; 39 (3): 223-9.

[22] Divan AG, Kuvalekar AA, Dharamsi S, Vora PM, Nikam VA, Ghadge AA. The relationship between serum adiponectin and leptin levels in obesity and type 2 diabetes mellitus. Indian J Endocrinol Metab. 2018; 22 (1): 93-99.

[23] Kershaw EE, Flier JS. Adipose Tissue as an endocrin organ. J Clin Endocrinol Metab 2004;89:2548-56.

[24] Zapata RC, Meachem MD, Cardoso NC, Mehain SO, McMillan CJ, Snead ER, et al. Different circulating concentrations of adipokines, glucagon and adropine in the clinical population of fat-free, overweight and diabetic cats. BMC Veterinary Res. 2017;13 (1): 85

[25] Li Q, Chen R, Moriya J, Yamakawa J, Sumino H, Kanda T. A novel adipocytokines visceral adipose tissue-derived serine protease inhibitör (vaspin), and obesity. J Int Med Res 2008; 36: 625-9.

[26] Hida K, Wada J, Eguchi J, Zhang H, Baba M, et al. Visceral Adipose Tissue –Derived Serine Protease İnhibitör: a unique insülin-sensitizing adypocytokine in obesity. Proc Natl Acad Sci USA 2005;102:10610-5

Türk Doğa ve Fen Dergisi
Turkish Journal of Nature and Science

www.dergipark.gov.tr/tdfd

BINGÖL UNIVERSITY

Artificial Intelligence-Assisted Multi-Criteria Decision-Making Methodology: From Research Trends to the Future Roadmap

Mahmut BAYDAŞ[1*] ID **, Nazlı ERSOY[2]** ID

[1] Necmettin Erbakan University, Faculty of Applied Sciences, Department of Accounting and Finance Management, Konya, Türkiye
[2] Osmaniye Korkut Ata University, Faculty of Economics and Administrative Sciences, Department of Business Administration, Osmaniye, Türkiye
Mahmut BAYDAŞ ORCID No: 0000-0001-6195-667X
Nazlı ERSOY ORCID No: 0000-0003-0011-2216

Corresponding author: mbaydas@erbakan.edu.tr

Abstract: Bibliometric analysis is a popular methodology in recent years that provides valuable insights for literature and researchers by visualizing interesting trends, relationship patterns, and information flow in research areas. This study aims to evaluate the publication trends, author contributions, institutional collaborations, and citation dynamics of this field by examining the integration of Multi-Criteria Decision Making (MCDM) and Artificial Intelligence (AI) with bibliometric analysis methods. This integration optimizes complex decision-making processes and provides faster, consistent, and effective solutions. The analysis was performed using performance analysis and science mapping techniques. Data were collected from the WoS database and 993 articles covering the period from 1992 to 2024 were analyzed. Co-citation, keyword co-occurrence, and co-authorship analyses were visualized with VOSviewer software. Accordingly, India, China and Iran stand out as the countries with the most publications, while the Indian Institute of Technology has the highest contribution. 'Annals of Operations Research' and 'Expert Systems with Applications' were among the most frequently cited journals. University of Technology Sydney and King Abdulaziz University stood out in institutional collaboration. This study is a pioneering study that conducts bibliometric analysis for AI-MCDM methods, especially in terms of the subject, scope and some of the findings obtained, and has produced valuable insights through data analytics.

Yapay Zekâ Destekli Çok Kriterli Karar Verme Metodolojisi: Araştırma Eğilimlerinden Gelecek Yol Haritasına

Öz: Bibliyometrik analiz, son yıllarda araştırma alanlarında ilginç eğilimleri, ilişki desenlerini ve bilgi akışını görselleştirerek literatür ve araştırmacılar için değerli bilgiler sağlayan popüler bir yöntemdir. Bu çalışma, Çok Kriterli Karar Verme (ÇKKV) ve Yapay Zekâ (AI) entegrasyonunun bibliyometrik analiz yöntemleriyle incelenerek, bu alanın yayın eğilimlerini, yazar katkılarını, kurumsal iş birliklerini ve atıf dinamiklerini değerlendirmeyi amaçlamaktadır. Bu entegrasyon, karmaşık karar verme süreçlerini optimize ederek ve daha hızlı, tutarlı ve etkili çözümler sunmaktadır. Analiz, performans analizi ve bilim haritalama teknikleri kullanılarak yapılmıştır. Veriler, WoS veritabanından toplanmış ve 1992-2024 yıllarını kapsayan 993 makale analiz edilmiştir. Ortak atıf, eş birliktelik ve ortak yazar analizleri VOSviewer yazılımı ile görselleştirilmiştir. Buna göre, Hindistan, Çin ve İran en fazla yayına sahip ülkeler olarak öne çıkarken, Indian Institute of Technology en yüksek katkıyı sağlamaktadır. 'Annals of Operations Research' ve 'Expert Systems with Applications' en sık atıf yapılan dergiler arasında yer almıştır. University of Technology Sydney ve King Abdulaziz University, kurumsal iş birliği alanında öne çıkmıştır. Bu çalışma, özellikle konu, kapsam ve elde edilen bazı bulgular açısından, AI-ÇKKV yöntemleri için bibliyometrik analiz yapan öncü bir çalışmadır ve veri analitiği ile çok değerli içgörüler üretmiştir.

1. INTRODUCTION

Artificial Intelligence (AI) has become a very important decision support system today thanks to its ability to detect meaningful patterns in large and complex data sets, to solve problems quickly and accurately, and the advanced predictive accuracy of machine learning. AI-based systems, which can carry out tasks at high levels of difficulty even autonomously, have made radical transformations in every conceivable field, accelerating efficiency, accuracy, prediction, and innovation. It is thought that artificial intelligence, which is considered a branch of engineering, will one day reach a very advanced level of intelligence beyond predictions with speed, capacity, and software developments, and will be a decision support mechanism needed in almost every field [1].

Decision making is a rational implementation process where decision makers (DMs) are faced with operational decisions and choose among various options to achieve certain goals or address the interests of stakeholders [2]. A decision-making methodology that emerged in the fields of operations research and applied mathematics and has found widespread use in the field of computer and artificial intelligence in recent years is Multi-Criteria Decision Making (MCDM). MCDM is a systematic approach that has hundreds of types in different approaches where multiple criteria and alternatives are taken into account, processes crisp, fuzzy or probability data, and can simultaneously solve complex problems such as data transformation, weighting, and basic calculation equations [3-4]. An important advantage of MCDM methods is that they can simultaneously address benefit-oriented and cost-oriented criteria with different weight coefficients. Thus, the decision maker will have the ability to easily choose the most appropriate one among the alternatives. In this context, MCDM is not only an academic tool but also an indispensable method of decision-making practices.

It is clear that MCDM methods, which can normally be applied with difficulty for each problem separately in human execution, can be used to solve hundreds of problems simultaneously thanks to the autonomous and powerful processing power ability of artificial intelligence. In this sense, MCDM-AI integration can be a vital solution support or assistant. The integration of AI and MCDM methods is a hybrid approach that will be increasingly used to overcome complex problems in modern decision-making processes. The combination of powerful data processing capabilities of AI and systematic analysis and evaluation skills of MCDM provides fast, consistent and optimized solutions to multi-dimensional and dynamic problems. This integration, which was founded in the 1990s, has gained momentum with the developments in computer-based algorithms, programming, software and especially artificial intelligence and machine learning in recent years.

However, the lack of comprehensive bibliometric analyses in the literature regarding the emphasis on the AI-MCDM title is very striking. Bibliometric studies

provide guidance for researchers by using quantitative methods to understand the development of scientific literature and research trends. These analyses help discover new research areas by encouraging interdisciplinary collaborations. They also support policy makers and research institutions in making strategic decisions in resource allocation. Analysis of trends in research outputs stimulates scientific innovation by providing information on innovative technologies and fields. Finally, it increases the impact of research and strengthens academic networks by mapping international collaborations [5-9].

This study aims to analyze the scientific production at the intersection of AI and MCDM, and to reveal the historical development, basic trends, and future research opportunities of this integration. Within the scope of the study, articles published from 1992 to 2024 were collected from the Web of Science (WoS) database and examined with bibliometric analysis methods. Using performance analysis and science mapping techniques, this study identifies important authors, journals, institutions, and countries in the literature; while also revealing the basic dynamics of the field with co-citation, keyword co-occurrence, and co-authorship analyses.

In this context, the study aims to both fill the knowledge gap in the literature and provide an awareness for understanding the current and potential effects of AI-MCDM integration on decision-making processes and valuable insights in the background.

2. METHODOLOGY

2.1. Aim

This study aims to offer a comprehensive analysis of the integrated application of MCDM and AI by exploring publication trends, author patterns, institutional contributions, and citation dynamics through bibliometric techniques. While numerous studies have examined MCDM and AI individually in recent years, research that combines these two fields remains relatively scarce in the existing literature. The fusion of MCDM and AI methods provides significant advantages in contemporary decision-making processes, particularly for addressing complex problems involving the interplay of multiple factors. This synergy not only enhances the efficiency of decision-making but also yields more accurate, optimized, and reliable outcomes. In this regard, the study seeks to illuminate the overarching trends in the joint application of these fields, as revealed through bibliometric analysis.

2.2. Method

In this study, bibliometric analysis was employed to provide an overview of the MCDM-AI field. Bibliometric analyses conducted to identify key topics and trends in a research field provide valuable insights for shaping future research directions and addressing existing gaps [10]. Bibliometric analysis combines two key approaches: science mapping analysis and performance analysis [11]. Performance analysis assesses the contributions of

research entities, science mapping aims to explore the relationships among these entities [12]. Science mapping, also known as bibliometric mapping, provides a visual representation of the connections between fields, specialties, disciplines, and individual works or authors [13]. In this regard, this study utilizes bibliometric analysis to present key authors, leading journals, organizations, and countries related to this field. Additionally, through science mapping, co-citation, co-occurrence of keywords analysis, and co-authorship analysis are provided.

2.3. Analysis Technique

Various software programs, such as VOSviewer [14], BibExcel [15], CitNetExplorer [16], SciMAT [17], RStudio Bibliometrix (Bibliometrix), and CiteSpace [18] are used to perform bibliometric analysis. In this study, the relationships between terms and the visualization of bibliometric networks were analyzed using the VOSviewer 1.6.16 software [14]. VOSviewer, with its detailed visual representations of the literature, facilitates a deeper exploration of research trends related to material selection [19].

2.4. Data Collection

In this study, the WOS database was used to gather the necessary data. WOS is among the most commonly utilized databases in the field of scientometrics [20]. Several procedures were followed to collect the data from WOS. Initially, keywords related to MCDM and AI topics were created, and a search was conducted in the topic section, yielding 1248 studies. To enhance the quality of the study and considering the role of high-quality journals in academic development [21], only journals indexed in SSCI (211), SCIE (863), and ESCI (147) were included. Given that English is the dominant language of publication (99%), only English-language articles were considered in this study (N=1245). No time constraints were imposed on data collection. Only articles were included in the analysis (N=993). The data was collected on 14/12/2024. After applying the filtering process, 993 articles were included in the analysis. The list of terms used for the query and the methodology are presented in Figure 1.

182
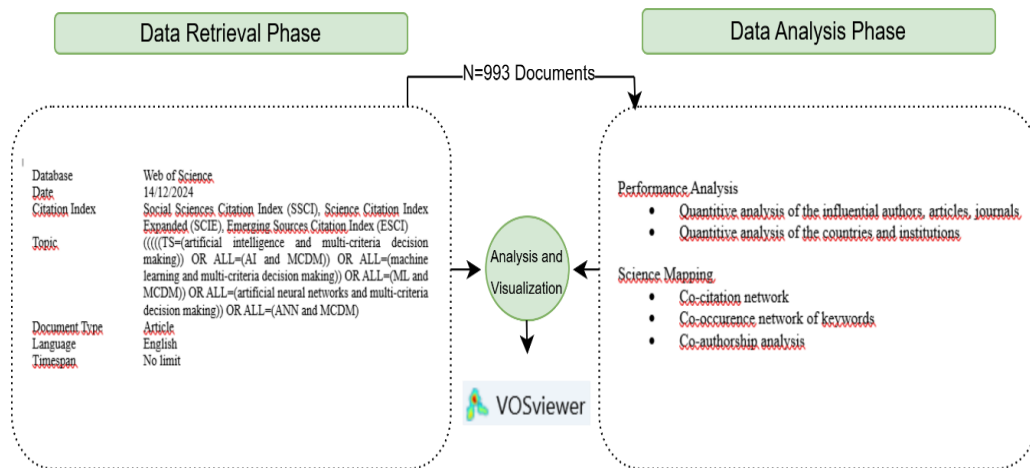
Figure 1. Research methodology

3. APPLICATION
3.1. Performance Analysis

In this section, a performance analysis has been conducted to present an overview of the studies in the MCDM-AI field, key authors, leading journals, organizations, and countries.

3.1.1. Publication trend

The trend of total publications and citations over time in the MCDM-AI field is shown in Figure 2.
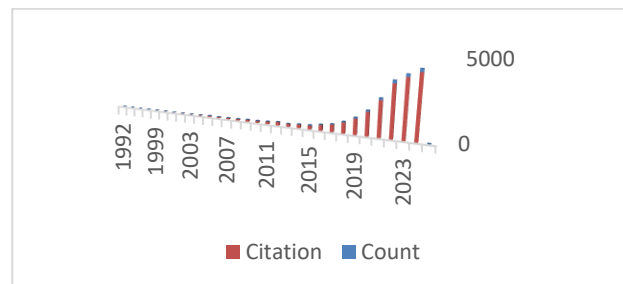
Figure 2. Number of publications and citations over time

According to Figure 2, the first publication in this field appeared in 1992. The study titled "Integrating Case-Based Reasoning In Multicriteria Decision Support Systems" was published by [22]. Another key study, titled "Feedforward Artificial Neural Networks For Solving Discrete Multiple Criteria Decision-Making Problems," was published by [23]. It can be observed that the number of MCDM-AI studies has gradually increased over the years. A noticeable upward trend emerged particularly

from 2018 onwards, with a peak in the number of publications observed in 2024. On the other hand, the total number of citations (excluding self-citations) for the 993 studies reviewed is 19.286, with an h-index of 66. Until 2012, the citation count was relatively low (N=227), but a sharp increase in citations started in 2018 (N=717), reaching its highest point in 2024 (N=4178).

3.1.2. Leading countries and institutions

An analysis was conducted to evaluate the contributions of prominent countries and institutions to the MCDM-AI field. In the initial phase, the contributions of various countries were examined, identifying a total of 93 countries involved in this domain. The publication counts of the top 10 contributing countries are presented in Table 1.

Table 1. The top 10 productive countries

Countries	N	%
India	222	21.83
Peoples R China	183	17.99
Iran	133	13.08
USA	116	11.41
Saudi Arabia	72	7.08
Taiwan	69	6.78
Australia	60	5.90
England	58	5.70
Turkiye	53	5.21
Malaysia	51	5.01

The analysis reveals that India ranks first with 222 publications, followed by People's Republic of China in second place with 183 publications, and Iran in third with 133 publications. Other notable countries in terms of

publication count include the USA (n = 116), Saudi Arabia (n = 72), Taiwan (n = 69), Australia (n = 60), England (n = 58), Turkey (n = 53), and Malaysia (n = 51). Figure 3 presents the top 10 most productive institutions among the 200 organizations in the relevant field. The Indian Institute of Technology System (IIT) ranks first with 36 publications and 411 citations. In second place is the National Institute of Technology (NIT) System, with 34 publications and 672 citations, followed by the University of Tehran, also with 34 publications, but 604 citations, securing the third position. Additionally, 178 universities have published fewer than 10 articles.
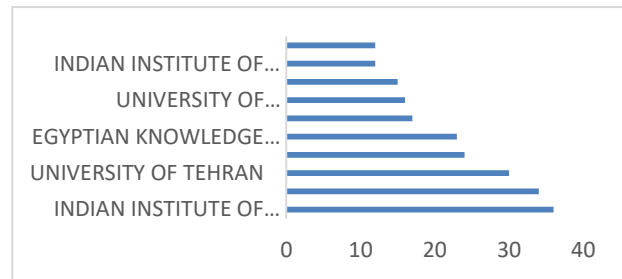

Figure 3. The most productive institutions

3.1.3. Leading authors, articles, and journals

This section provides an overview of studies on the topic of MCDM-AI, the authors responsible for these works, and the journals in which they were published. Between 1992 and 2024, a total of 200 authors contributed to 664 publications. Notably, only 7 authors (3.5%) produced 10 or more publications. Table 2 lists the top 10 researchers in this field.

183

Table 2. The top authors and their publication details

Rank	Author	Country/Institution	PYS	TP	TC	h-index	C/P
1	Pradhan, Biswajeet	Australia / University of Technology Sydney	2000	678	41817	112	61.68
2	Pamucar, Dragan	Serbia/ University of Belgrade	1991	486	12261	58	25.23
3	Wang, Chia-Nan	Taiwan/National Kaohsiung University of Science and Technology	2002	258	2464	28	9.55
4	Zaidan, A. A.	Australia / P Jain School of Global Management	2009	226	5888	57	26.05
5	Albahri, A.S.	Iraq/ Imam Ja'afar Al-Sadiq University	2018	142	3288	44	23.15
6	Albahrey, Osamah Shihab	Malaysia/ Universiti Pendidikan Sultan Idris	2018	122	3332	47	27.31
7	alamoodi, abdullah	Malaysia/ Universiti Tenaga Nasional	2019	96	2306	30	24.02
8	Dang, Thanh-Tuan	Taiwan/National Kaohsiung University of Science and Technology	2019	51	792	18	15.53
9	Nguyen, Ngoc-Ai-Thy	Taiwan/National Kaohsiung University of Science and Technology	2020	23	572	14	24.87
10	Maghsoodi, Abtin Ijadi	New Zealand /The University of Auckland	2018	21	457	14	21.76

Note: PYS (Publication Year Start), TP (Number of Publication), TC (Tocal Citations without self citation), C/P = citations per paper (TC/TP).

The rankings in Table 2 are based on the number of publications. According to this, Pradhan, Biswajeet is the most prolific author with 678 publications, followed by Pamucar, Dragan with 486 publications, and Wang, Chia-Nan with 258 publications, securing the third position. In terms of citation count, the top three authors are Pradhan, Biswajeet (n=41.817), Pamucar, Dragan (n=12.261), and Zaidan, A. A. (n=5.888). When evaluating the h-index, Pradhan, Biswajeet (n=112) ranks first, followed by Pamucar, Dragan (n=58) in second place, and Zaidan, A. A. (n=57) in third.

The top 10 most highly cited and influential papers in the field of MCDM-AI are presented in Table 3. The ranking is based on the number of citations. The most cited paper is "Pymoo: Multi-Objective Optimization in Python," published by [24]. The second most cited paper, with 424 citations, is "A comparative assessment of flood susceptibility modeling using Multi-Criteria Decision-Making Analysis and Machine Learning Methods," authored by [25]. These papers were published in the IEEE Access and the Journal of Hydrology, respectively.

Table 3. The top 10 most cited publications

Rank	Title	First Author	Year	Source	TC
1	"Pymoo: Multi-Objective Optimization in Python"	Blank [24]	2020	IEEE Access	872
2	"A comparative assessment of flood susceptibility modeling using Multi-Criteria Decision-Making Analysis and Machine Learning Methods"	Khosravi [25]	2019	Journal of Hydrology	424
3	"A GIS-based flood susceptibility assessment and its mapping in Iran: a comparison between frequency ratio and weights-of-evidence bivariate statistical models with multi-criteria decision-making technique"	Khosravi [26]	2016	Natural Hazards	325
4	"Flash-Flood Susceptibility Assessment Using Multi-Criteria Decision Making and Machine Learning Supported by Remote Sensing and GIS Techniques"	Costache [27]	2020	Remote Sensing	163
5	"GIS-based landslide susceptibility modeling: A comparison between fuzzy multi-criteria and machine learning algorithms"	Ali [28]	2021	Geoscience Frontiers	130
6	"Benchmarking Methodology for Selection of Optimal COVID-19 Diagnostic Model Based on Entropy and TOPSIS Methods""	Mohammed [29]	2020	IEEE Access	113
7	"Building supply-chain resilience: an artificial intelligence-based technique and decision-making framework"	Belhadi [30]	2021	International Journal of Production Research	108
8	"Accurate multi-criteria decision making methodology for recommending machine learning algorithm"	Ali [31]	2017	Expert Systems with Application	103
9	"Landslide susceptibility assessment at the Wuning area, China: a comparison between multi-criteria decision making, bivariate statistical and machine learning methods"	Hong [32]	2019	Natural Hazards	89
10	"A comparison among fuzzy multi-criteria decision making, bivariate, multivariate and machine learning models in landslide susceptibility mapping"	Pham [33]	2012	Geomatıcs Natural Hazards & Risk	85

The leading 10 journals in the field of MCDM-AI are ranked by publication count in Figure 4. According to this ranking, *Annals of Operations Research* (n=101) holds the first position, followed by *International Journal of Machine Learning and Cybernetics* (n=32), *IEEE Access* (n=29), and *Expert Systems with Applications* (n=24).

Furthermore, 94.5% of the journals have published 10 or fewer articles. The analysis reveals that these top 10 journals account for 36.67% of the total publications during the study period. The contribution of *Annals of Operations Research* to the field is particularly notable.

184

Figure 4. Top 10 most leading journals

3.2. Science Mapping

Bibliometric methods can be utilized at the levels of titles, keyword lists, publication abstracts, and even entire citation records to analyze trends related to specific topics and topic categories [14]. This section will present the science mapping analysis, including the results of co-occurrence of keywords analysis, co-citation analysis, and co-authorship analysis.

3.2.1. Top keywords for MCDM-AI field

This analysis was performed to identify the most frequently used keywords in studies within the MCDM-AI field. A total of 3.416 indexed keywords were found across 993 documents, as provided by VOSviewer. A threshold of 5 occurrences was applied, with 111 keywords meeting this criterion (Figure 5). The analysis resulted in 11 distinct clusters, which are depicted in similar colors. The node size represents the frequency of the keywords, while the proximity of the nodes within each cluster indicates the frequency of their co-occurrence.

Figure 5. Keyword cloud

VOSviewer has organized the 111 keywords into 11 distinct clusters. Cluster 1, indicated in red (18 items), includes keywords such as AI, artificial intelligence, decision making, fuzzy AHP, fuzzy TOPSIS, and simulation. Cluster 2, indicated in green (13 items), contains terms like analytic hierarchy process, ANP, DEMATEL, fuzzy, neural network, and sensitivity analysis. Cluster 3, indicated in blue (11 items), features keywords such as ANN, data envelopment analysis, MCDM, hazard, PROMETHEE, and prediction. Cluster 4, also indicated in green (11 items), highlights terms like

"CoCoSo", "CRITIC", "entropy", "machine learning" (ML), "multi-criteria decision making", "multi-criteria decision-making", "supply chain management", and "TOPSIS". Similarly, Cluster 5 (11 items), Cluster 6 (10 items), Cluster 7 (9 items), Cluster 8 (9 items), Cluster 9 (8 items), Cluster 10 (7 items), and Cluster 11 (4 items) form a total of 11 clusters. The top 10 most frequently used keywords have been ranked according to their total connection strength (Table 4).

Table 4. Top 10 keywords

Keywords	Occurences	Total Link Strengths	Cluster membership
Machine learning	124	184	7
topsis	89	184	4
mcdm	104	182	3
Multi-criteria decision making	95	122	4
Artificial intelligence	73	111	1
Multi-criteria decision-making	65	111	4
Decision making	36	75	1
Ahp	31	67	5
Artificial neural network	42	65	6
sustainability	30	52	5
Fuzzy logic	21	49	6

Machine learning and topsis have the highest value, with a total connection strength of 184 and 124 and 89 co-occurrences, respectively. Other nodes with high total link strengths include mcdm (n=182), Multi-criteria decision making (n=122), Artificial intelligence (n=111), Multi-criteria decision-making (n=111).

3.2.2. Co-citation analysis

Co-citation analysis is used to examine the relationships between authors, topics, journals, and keywords [34].

This section provides the co-citation analysis in two stages: author and journal co-citation analysis.

3.2.2.1. Co-citation of authors and journals

Author co-citation analysis involves mapping the prominent and influential authors in the field within a network. In this study, a citation threshold of 20 was set as the minimum, and only authors with a minimum of 20 citations were included in the analysis. Out of a total of 34.376 citations, 166 authors surpassed this threshold, and the density visualization of these 166 authors is shown in Figure 6.
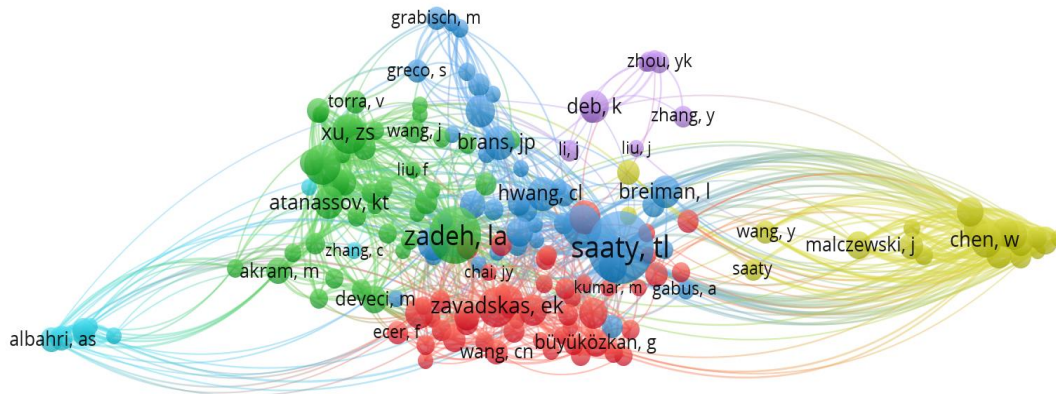
Figure 6. Author co-citation network

Based on this analysis, the author co-citation network is divided into six clusters: Cluster 1 (49 items), Cluster 2 (41 items), Cluster 3 (38 items), Cluster 4 (21 items), Cluster 5 (9 items), and Cluster 6 (8 items). Authors who are frequently co-cited are grouped together in the same cluster. The largest clusters are labeled in red (Cluster 1), while the most-cited authors are identified in black. Table 5 lists the top authors with the highest citation counts

associated with the themes of the research clusters. Saaty, T.L., a member of Cluster #3, has the highest citation count (n=366). Zadeh, L.A. (n=232), and Opricovic, S. (n=128), from Clusters #2 and #3, are ranked second and third, respectively. Xu, Z.S. (n=116) and Yager, R.R. (n=116), members of Cluster #2, are tied for fourth place in citation count.

Table 5. Most cited authors

Author	Number of citations	Total link strength	Cluster membership
Saaty, tl	366	3110	3
Zadeh, la	232	2387	2
Opricovic, s	128	1381	3
Xu, zs	116	1795	2
Yager, rr	116	1668	2

A journal co-citation occurs when two articles from different journals are cited together in a third publication [34]. The threshold was established at 20, and among

16,418 journals, 402 surpassed this limit. Figure 7 illustrates the co-citation of journals in the field of MCDM-AI.
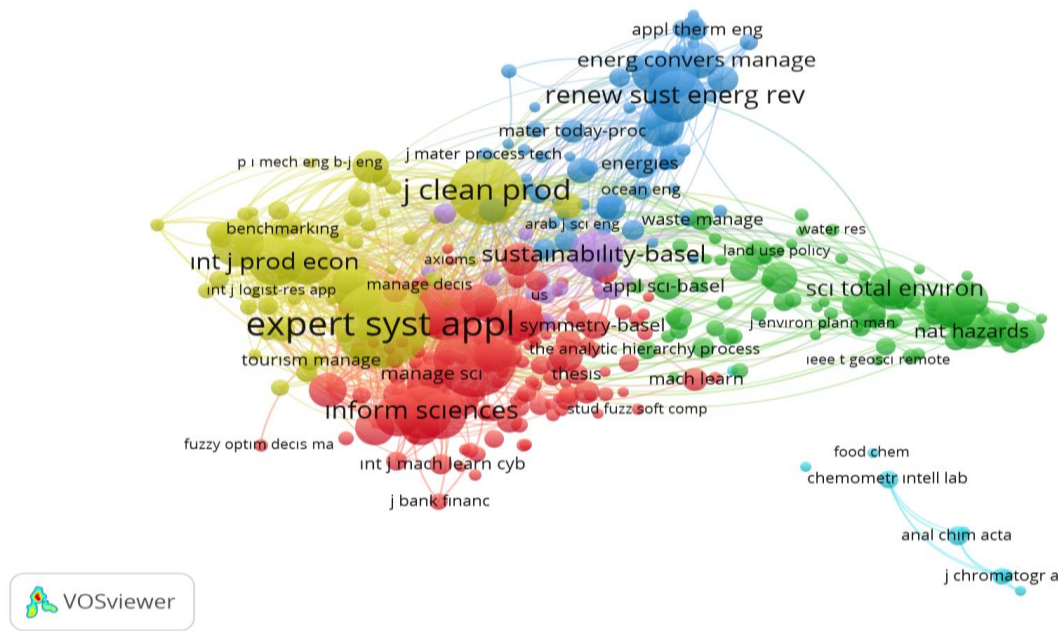
186

Figure 7. Journal co-citation network

This map clearly demonstrates the division into six clusters, each represented by a different color. The three largest circles on this color-coded map correspond to "*Expert Systems with Applications*", "*European Journal of Operational Research* (EUR J Open Res)", and "*Journal of Cleaner Production*" (J Clean Prod), indicating that these journals have the highest citation counts and the largest networks.

In Cluster 4, "*Expert Systems with Applications*" is connected to 395 other journals, including "*Applied Mathematical Modelling*", "*International Journal of Information Management*", and "*Annals of Operations Research*". In Cluster 1, "*EUR J Open Res*" ranks second with a total of 398 connections, with journals such as "*Soft Computing*", "*Information Control*", "*IEEE Access*", and "*Information Sciences*" among its connections. Lastly, "*J Clean Prod*", located in Cluster 4, has a connection strength of 393 and is linked to journals like "*Sustainable*"

Production" *and* "*Consumption*, *Journal of Manufacturing Systems*", "*Transportation Research E-Logistics*", and "*Production and Operations Research*".

3.2.3. Co-authorship analysis

Co-authorship analysis explores the relationships and collaborations between researchers [12]. The analysis was conducted to identify which researchers, countries, and institutions are collaborating with each other.

3.2.3.1. Co-authorship networks for authors, countries and instutions

During the analysis period, among the 3.379 authors working on MCDM-AI topics, the minimum publication threshold was set to 2, and the minimum citation count required for an author was set at 30. A total of 182 authors exceeded these thresholds (Figure 8).
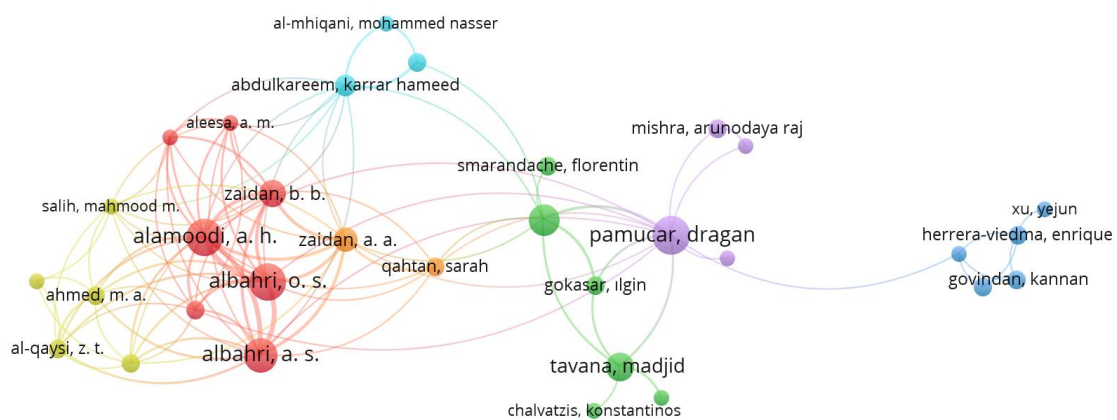
Figure 8. Author co-authorship network

The authors addressing the topic of MCDM-AI are grouped into seven clusters based on the author co-authorship network map. Figure 8 illustrates these clusters, where nodes are connected when collaborative

work occurs. Each cluster consists of at least two authors. In the above network map, Alamoodi, AH (citations: 167, documents: 11, total link strength: 47), Albahri, OS (citations: 167, documents: 11, total link strength: 47),

and Albahri, AS (citations: 134, documents: 10, total link strength: 42) exhibit stronger connection strengths compared to other authors. The higher connection strength is further confirmed by their placement within the red circles. The density map indicates that the blue, green, yellow, and red colors represent no density, low density, moderate density, and high density, respectively.

Among the 97 countries contributing to the field of MCDM-AI, 78 nations have published a minimum of two papers, while 62 countries have published at least five papers. The analysis was conducted based on countries with a minimum of five publications. Figure 9 presents the country co-authorship network within the field of MCDM-AI.
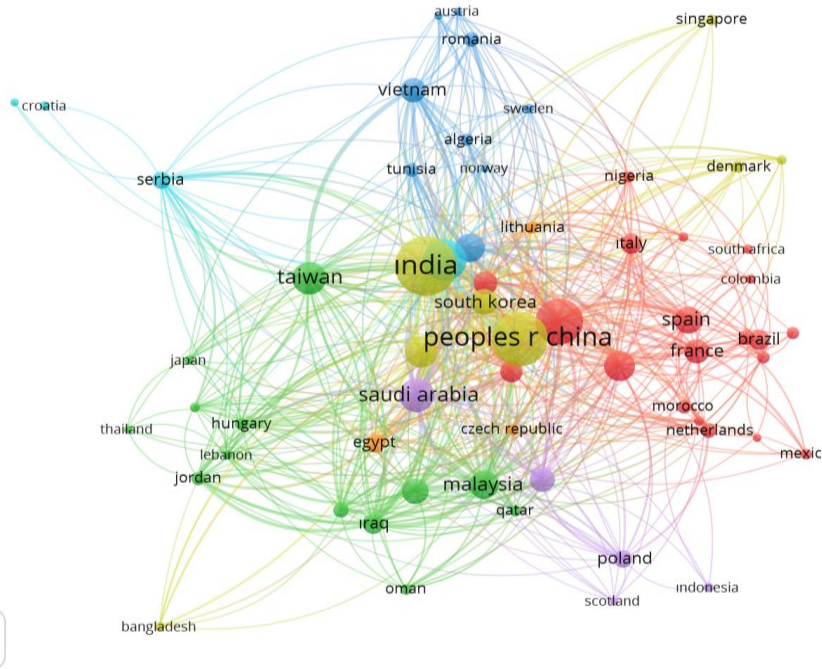
Figure 9. Country co-authorship network

The network is composed of seven clusters. India, with 222 documents, 52 connections, and a total connection strength of 221, along with the People's Republic of China, which has 183 documents, 40 connections, and a total connection strength of 206, and Iran, with 133 documents, 44 connections, and a total connection strength of 198, are the top three countries demonstrating the highest level of collaboration.

An analysis was conducted to explore the collaborative efforts of institutions within the MCDM-AI field. Among 1.582 research institutions, 87 have published at least five papers. The analysis identified 12 clusters (Figure 10). The University of Technology Sydney, with 16 documents, 807 citations, 15 links, and a total connection strength of 38, ranks first. King Abdulaziz University follows in second place with 17 documents, 246 citations, 27 links, and a total connection strength of 36.
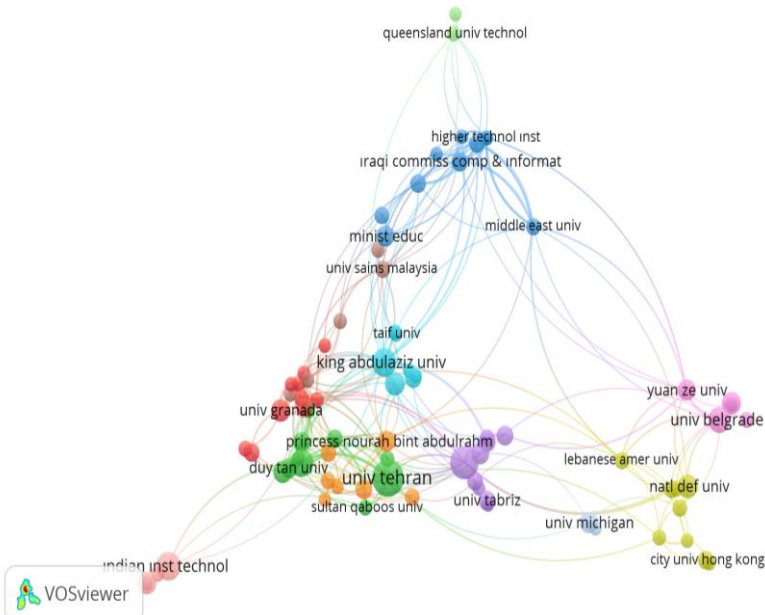

Figure 10. Institutes' co-authorship network

4. RESULT AND DISCUSSION

AI refers to the application of computers to model cognitive behavior with minimal human intervention, and it is generally considered to have originated with the invention of robots [1]. AI is a rapidly advancing technological field that is demonstrating its impact across various aspects of life. Since 2010, a number of AI technologies have emerged, driven by innovative advancements in computer hardware and internet Technologies [35]. These AI technologies have been incorporated into diverse fields such as communication [36], health [37], sustainability [38], etc. In recent years, another important area where artificial intelligence has been integrated is MCDM. MCDM evaluates various qualitative and quantitative criteria that need to be considered in order to find the most optimal solution [39]. The increasing complexity of problems has enhanced the importance of these methods. On the other hand, the integration of MCDM and AI is considered significant for managing complex decision-making processes more effectively and efficiently. In recent years, it has become possible to access numerous studies where these two fields are used in an integrated manner [2, 40-44]. The integration of MCDM and artificial intelligence enables the rapid and accurate analysis of complex data, thereby providing a more solid foundation for the decision-making process. Furthermore, this integration allows for the optimization of the balance among complex criteria, enhancing the consistency of the decision-making process.

This study presents a bibliometric analysis of the MCDM-AI integration, aiming to provide insights into key trends, developments, and opportunities in the research activities at the intersection of these two fields. The methodology of the research consists of two main stages: performance analysis and science mapping. In the performance analysis section, key authors, leading journals, organizations, and countries related to this field are presented. Through science mapping, co-citation analysis, co-occurrence of keywords analysis, and co-authorship analysis are provided. According to the performance analysis results, the quantity of publications and citations in the MCDM-AI field has seen a significant increase, particularly since 2018, reaching its peak in 2024. India has been identified as the leading country in this field, with the "Indian Institute of Technology System" (IIT System) ranking first for the highest number of publications. Furthermore, it was found that most of the universities in the top 10 are based in Saudi Arabia and India. The most influential author in this field has been identified as Pradhan, Biswajeet. The articles titled "Pymoo: Multi-Objective Optimization in Python" and "A Comparative Assessment of Flood Susceptibility Modeling Using Multi-Criteria Decision-Making Analysis and Machine Learning Methods" were found to have a high impact. Additionally, the most influential journal in this field is *Annals of Operations Research*, which accounts for 36% of the total publications in the top 10 journals. According to the science mapping analysis results, frequently used terms in both integrated areas include "Machine Learning," "TOPSIS," and "MCDM."

Co-citation analysis results show that Saaty, TL holds the highest connection strength among authors. *Expert Systems with Applications* is the journal with the highest connection strength. According to the co-authorship analysis, Alamoodi, AH, Albahri, OS, and Albahri, AS exhibit stronger connection strengths compared to other authors. Similar to the performance analysis results, the leading three countries in the MCDM-AI field are India, the People's Republic of China, and Iran. In terms of institutional collaborative efforts, the University of Technology Sydney and King Abdulaziz University rank at the top with the highest connection strength.

In the literature, although there have been a significant number of recent studies on the applications of artificial intelligence (AI) in the MCDM field, only one study has been identified that presents the general trends of integration between the two areas. In the study conducted by Düzen et al. [45], a bibliometric analysis of the combined use of machine learning and MCDM was performed. It has been determined that some key findings obtained through performance analysis and science mapping analysis are consistent with the results of the aforementioned study. Our study covers the literature from a wider period without any time limitation (1992-2024). It is the pioneer study to perform bibliometric analysis for AI-MCDM methods in terms of title emphasis. Moreover, our study shows that it contributes to the field from different perspectives in terms of the most influential author, institutional contribution, leading country, distribution in literature, and general, theoretical, and methodological terms. These findings show that the study is a road map in the literature.

5. CONCLUSION

This study evaluated the integration of MCDM and AI with bibliometric analysis, revealing important trends, developments and opportunities in the combined use of these two fields. The study showed that this integration has increased rapidly, especially since 2018, and reached its peak in 2024. India, China and Iran stand out as the leading countries in this field, while the Indian Institute of Technology (IIT) provided the highest publication contribution.

It was determined that keywords such as "Machine Learning," "TOPSIS," and "MCDM" with performance analysis and science mapping methods are strong connection points in the integrated use of this field. Pradhan, Biswajeet in particular were identified as the leading authors in this field, and Annals of Operations Research and Expert Systems with Applications were the most widely cited journals. In addition, University of Technology Sydney and King Abdulaziz University were at the forefront of institutional collaboration.

These findings prove that the combined applications of MCDM and AI provide more solid foundations for decision-making processes by analyzing complex data sets quickly and accurately. This integration not only increases the effectiveness of decision-making processes, but also provides an important roadmap for shaping the

future directions of the literature in this field. The research covers a wider period (1992-2024) in the literature and is a pioneering study in this field, especially at some points. Moreover, it constitutes a roadmap for the future applications of these methods.

In this context, the study has made significant contributions to both theoretical and applied literature in the integration of MCDM and AI and has established a basis for future research.

5.1. Limitations of Study and Future Research

The limitations of this study can be expressed as follows. The use of data obtained from only one database (WOS) may have limited the scope of the research. Additionally, the study focused solely on journal articles, excluding conference proceedings, book chapters, or other types of academic publications. Furthermore, it should be noted that the dataset and sample would vary depending on the selected keywords. Moreover, since the analysis only includes studies published up to a certain date, significant research conducted after the publication of this study could not be included in the analysis. Future research could allow for a more comprehensive analysis by expanding beyond the Web of Science database. Additionally, multidisciplinary approaches integrating methods from different disciplines, alongside MCDM and AI, could be explored.

REFERENCES

[1] Hamet P, Tremblay J. Artificial intelligence in medicine. Metabolism. 2017; 69, 36-S40.

[2] Zakeri S, Konstantas D, Sorooshian S, Chatterjee P. A novel ML-MCDM-based decision support system for evaluating autonomous vehicle integration scenarios in Geneva's public transportation. Artificial intelligence review. 2024; 57(11), 1-64.

[3] Stević Ž, Ersoy N, Başar EE, Baydaş M. Addressing the global logistics performance index rankings with methodological insights and an innovative decision support framework. Applied sciences. 2024; 14(22), 1-21.

[4] Baydaş M, Elma OE, Stević Ž. Proposal of an innovative MCDA evaluation methodology: knowledge discovery through rank reversal, standard deviation, and relationship with stock return. Financial Innovation. 2024; 10(1), 1-35.

[5] Odoi-Yorke F, Kabiru SA, Sanful RE, Otoo GS, Lamptey FP, Abbey AA, et al. A review of recent trends, advancements, and future directions in near-infrared spectroscopy applications in biofuel production and analysis. Infrared physics & technology. 2024; 1-41.

[6] Lăpădat C, Bădîrcea RM, Manta AG, Georgescu AI. Bibliometric analysis of the common agricultural policy: intersections of agriculture, economy and environment. Finante-provocarile viitorului (Finance-Challenges of the Future). 2024; 1(26), 46-65.

[7] Matta-Pacheco J, Tsukamoto-Jaramillo A, Tinedo-Lôpez PL, Espinoza-Carhuancho F, Pacheco-Mendoza J, Mayta-Tovalino F. Bibliometric study of periodontitis and alzheimer\'s disease: trends, collaboration, and emerging patterns. The journal of contemporary dental practice. 2024; 25(9), 863-868.

[8] Toker Z, Aksoy E. A bibliometric review of studies on mathematics teacher professional development with an emphasis on mathematics coaching research. Journal of mathematics teacher education. 2024; 1-75.

[9] Roucham B, Lefilef A, Zaghdoud O, Mohammed KS. The evolution of green hydrogen in renewable energy research: Insights from a bibliometric perspective. Energy reports. 2025; 13, 576-593.

[10] Şengöz A, Orhun BN, Konyalilar N. A holistic approach to artificial intelligence-related research in the transportation system: bibliometric analysis. Worldwide hospitality and tourism themes. 2024; 16(2), 138-149.

[11] Farooq R. A review of knowledge management research in the past three decades: a bibliometric analysis. VINE journal of ınformation and knowledge management systems. 2024; 54(2), 339-378.

[12] Donthu N, Kumar S, Mukherjee D, Pandey N, Lim WM. How to conduct a bibliometric analysis: An overview and guidelines. Journal of business research. 2021; 133, 285-296.

[13] Small, H. Visualizing science by citation mapping. Journal of the american society for information science. 1999; 50(9), 799–813.

[14] Van Eck NJ, Waltman L. Software survey: VOSviewer, a computer program for bibliometric mapping. Scientometrics. 2010; 84 (2), 523–538.

[15] Persson O, Danell R, Schneider JW. How to use Bibexcel for various types of bibliometric analysis. Celebrating scholarly communication studies: a festschrift for olle persson at his 60th birthday. 2009; 5, 9–24.

[16] Van Eck NJ, Waltman L, CitNetExplorer: a new software tool for analyzing and visualizing citation networks. Journal of informetrics. 2014; 8(4), 802–823.

[17] Cobo MJ, López-Herrera AG, Herrera-Viedma E, Herrera F. SciMAT: A new science mapping analysis software tool. Journal of the american society for information science and technology. 2012; 63(8), 1609-1630.

[18] Chen C. CiteSpace II: detecting and visualizing emerging trends and transient patterns in scientific literature. Journal of the american society for information science and technology. 2006; 57 (3), 359–377.

[19] Sahoo SK, Choudhury BB, Dhal PR. A bibliometric analysis of material selection using MCDM methods: trends and insights. Spectrum of mechanical engineering and operational research. 2024; 1(1), 189-205.

[20] Medina-Mijangos R, Seguí-Amórtegui L. Research trends in the economic analysis of municipal solid waste management systems: A bibliometric analysis from 1980 to 2019. Sustainability. 2020;12(20), 1-20.

[21] Judge AT, Cable DM, Colbert AE, Rynes SL. What causes a management article to be cited—Article, author, or journal?. Academy of Management Journal. 2007; 50(3): 491-506.

[22] Angehrn AA, Dutta S. Integrating case-based reasoning in multi-criteria decision support systems. Proceedings of the IFIP Tc8/wg8.3 Working Conference on Decision Support Systems: Experiences and Expectations, Fontainebleau. North-Holland; 1992. p. 133-150.

[23] Malakooti B, Zhou YQ. Feedforward artificial neural networks for solving discrete multiple criteria decision making problems. Management Science. 1994; 40(11), 1542-1561.

[24] Blank J, Deb K. Pymoo: Multi-objective optimization in python. Ieee Access. 2020; 8, 89497-89509.

[25] Khosravi K, Shahabi H, Pham BT, Adamowski J, Shirzadi A, Pradhan B, et al. A comparative assessment of flood susceptibility modeling using multi-criteria decision-making analysis and machine learning methods. Journal of hydrology, 2019; 573, 311-323.

[26] Khosravi K. et al. A GIS-based flood susceptibility assessment and its mapping in Iran: a comparison between frequency ratio and weights-of-evidence bivariate statistical models with multi-criteria decision-making technique. Natural hazards, 2016; 83: 947-987.

[27] Costache R. et al. Flash-flood susceptibility assessment using multi-criteria decision making and machine learning supported by remote sensing and GIS techniques. Remote Sensing, 2019; 12(1), 106.

[28] Ali SA., et al. GIS-based landslide susceptibility modeling: A comparison between fuzzy multi-criteria and machine learning algorithms. Geoscience frontiers, 2021; 12(2): 857-876.

[29] Mohammed MA., et al. Benchmarking methodology for selection of optimal COVID-19 diagnostic model based on entropy and TOPSIS methods. Ieee access, 2020; 8: 99115-99131.

[30] Belhadi A, et al. Building supply-chain resilience: an artificial intelligence-based technique and decision-making framework. International journal of production research, 2022; 60(14): 4487-4507.

[31] Ali R, Lee S, Chung TC. Accurate multi-criteria decision making methodology for recommending machine learning algorithm. Expert systems with applications, 2017; 71: 257-278.

[32] Hong H, et al. Landslide susceptibility assessment at the Wuning area, China: A comparison between multi-criteria decision making, bivariate statistical and machine learning methods. Natural hazards, 2019; 96: 173-212.

[33] Pham QB, et al. A comparison among fuzzy multi-criteria decision making, bivariate, multivariate and machine learning models in landslide susceptibility mapping. Geomatics, Natural hazards and risk, 2021; 12.1: 1741-1777.

[34] Small H. Co-citation in the scientific literature: A new measure of the relationship between two documents. J. Am. Soc. Inf. Sci. 1973; 24, 265–269.

[35] Chen P, Chu Z, Zhao M. The Road to corporate sustainability: The importance of artificial intelligence. Technology in Society. 2024; 76(2024), 1-9.

[36] Wang J, Du H, Niyato D, Kang J, Cui S, Shen XS, et al. Generative AI for integrated sensing and communication: Insights from the physical layer perspective. IEEE Wireless Communications. 2024; 246-255.

[37] König H, Frank D, Baumann M, Heil R. AI models and the future of genomic research and medicine: True sons of knowledge? Artificial intelligence needs to be integrated with causal conceptions in biomedicine to harness its societal benefits for the field. BioEssays. 2021; 43(10), 1-12.

[38] Bibri SE, Alexandre A, Sharifi A, Krogstie J. Environmentally sustainable smart cities and their converging AI, IoT, and big data technologies and solutions: an integrated approach to an extensive literature review. Energy Informatics. 2023; 6(1), 1-39.

[39] Taherdoost H, Madanchian M. Multi-criteria decision making (MCDM) methods and concepts. Encyclopedia. 2023; 3(1), 77-87.

[40] Alshahrani R, Yenugula M, Algethami H, Alharbi F, Goswami SS, Naveed QN, Lasisi A, et al. Establishing the fuzzy integrated hybrid MCDM framework to identify the key barriers to implementing artificial intelligence-enabled sustainable cloud system in an IT industry. Expert systems with applications. 2024; 238(2024): 1-28.

[41] Nguyen TMH, Nguyen VP, Nguyen DT. A new hybrid pythagorean fuzzy AHP and CoCoSo MCDM based approach by adopting artificial intelligence technologies. Journal of experimental & theoretical artificial intelligence. 2024; 36(7), 1279-1305.

[42] Ghoushchi SJ, Haghshenas SS, Vahabzadeh S, Guido G, Geem ZW. An integrated MCDM approach for enhancing efficiency in connected autonomous vehicles through augmented intelligence and IoT integration. Results in Engineering. 2024; 23, 1-21.

[43] Hsueh SL, Feng Y, Sun Y, Jia R, Yan MR. Using AI-MCDM model to boost sustainable energy system development: A case study on solar energy and rainwater collection in guangdong province. Sustainability. 2021; 13(22), 1-25.

[44] Arabameri A, Lee S, Tiefenbacher JP, Ngo PTT. Novel ensemble of MCDM-artificial intelligence techniques for groundwater-potential mapping in arid and semi-arid regions (Iran). Remote Sensin. 2020; 12(3), 1-27.

[45] Düzen MA, Bölükbaşı İB, Çalık E. How to combine ML and MCDM techniques: an extended bibliometric analysis. Journal of innovative engineering and natural science. 2024; 4(2), 642-657.

191

BİNGÖL UNIVERSITY

Does High Blood Pressure Have an Effect on Intervertebral Fibrocartilage Histology?

Erhan ŞAHİN[1]* , Damla Gül FINDIK[2] , Özlem TÜRELİK[3]

[1:] Bilecik Seyh Edebali University, Faculty of Medicine, Histology and Embryology Department, Bilecik, Türkiye
[2:] Bilecik Seyh Edebali University, Faculty of Medicine, Histology and Embryology Department, Bilecik, Türkiye
[3:] Bilecik Seyh Edebali University, Faculty of Medicine, Pathology Department, Bilecik, Türkiye

Erhan SAHIN ORCID No: 0000-0003-2152-0542
Damla Gul FINDIK ORCID No: 0000-0001-8028-627X
Ozlem TURELIK ORCID No: 0000-0001-6057-9171

Corresponding author: erhansahinn@gmail.com

Abstract: Since the cartilage tissue is fed by the vessels in the surrounding connective tissue, it is a very difficult tissue to repair. Therefore, cardiovascular diseases primarily affect the cartilage tissue. In this study, the possible effects of high blood pressure on discus intervertebralis were examined histopathologically and histomorphometrically. Discus intervertebralis of 13 normotensive and 13 hypertensive patients were compared histopathologically and histomorphometrically. Demographic information of the patients was obtained from the patient registration system of the hospital. Hematoxylin-eosin stained slices were used for histopathological evaluation. In histological sections, chondrocytes and lacunae diameters were measured at 400x magnification in 10 different areas with a computer morphometric measurement program. Discus intervertebralis of normotensive and hypertensive patients did not differ in terms of chondrocyte count and lacunae diameter. The mean age of hypertensive patients (61.69±13.55) was higher than the mean age of normotensive patients (42±8.84) (p<0.05). The gender ratio of the groups did not show a statistical difference (p>0.05). In this study, it was shown that the discus intervertebralis of normotensive and hypertensive patients who underwent lumbar discectomy were not different in terms of histopathologically and histomorphometrically (in terms of chondrocyte number and lacunae diameter).

192

Yüksek Tansiyonun Omurlar Arası Fibröz Kıkırdak Histolojisi Üzerinde Etkisi Var Mıdır?

Öz: Kıkırdak doku, çevresindeki bağ dokusunda bulunan damarlarla beslendiğinden onarımı çok zor bir dokudur. Bu nedenle kardiyovasküler hastalıklar öncelikle kıkırdak dokusunu etkiler. Bu çalışmada, yüksek tansiyonun discus intervertebralis üzerindeki olası etkileri histopatolojik ve histomorfometrik olarak incelenmiştir. 13 normotansif ve 13 hipertansif hastanın discus intervertebralis'i histopatolojik ve histomorfometrik olarak karşılaştırılmıştır. Hastaların demografik bilgileri hastanenin hasta kayıt sisteminden elde edilmiştir. Histopatolojik değerlendirme için hematoksilen-eozin boyalı kesitler kullanılmıştır. Histolojik kesitlerde, kondrosit ve lakün çapları, morfometrik ölçüm programı ile 10 farklı alanda 400x büyütmede ölçülmüştür. Normotansif ve hipertansif hastaların discus intervertebralis'i kondrosit sayısı ve lakün çapı açısından farklılık göstermemiştir. Hipertansif hastaların yaş ortalaması (61.69±13.55), normotansif hastaların yaş ortalamasından (42±8.84) yüksekti (p<0.05). Grupların cinsiyet oranı istatistiksel olarak fark göstermedi (p>0.05). Bu çalışmada lomber disektomi uygulanan normotansif ve hipertansif hastaların discus intervertebralislerinin histopatolojik ve histomorfometrik (kondrosit sayısı ve lakün çapı) olarak farklı olmadığı gösterildi.

1. INTRODUCTION

Intervertebral discs (ID) are located between our vertebrae. In intervertebral discs, the outer structure, which we call annulus fibrosus, surrounds the nucleus pulposus structure in the center. While the annulus fibrosus is in the structure of fibrous cartilage, the nucleus pulposus consists of a gel-like substance. Fibrous cartilage is a tissue with few chondrocytes and abundant matrix. The extracellular matrix contains abundant type I collagen, chondroitin sulfate and dermatan sulfate. Nucleus pulposus is a gel-like matrix containing abundant hyaluronic acid. Since there is no perichondrium in the cartilage tissue of the ID, their nutrition is provided by the capillaries in the subchondral plate of vertebrae and the surrounding connective tissue [1, 2]. Vascular support of the ID is very important in this respect.

Lumbar disc herniation is an ID pathology that significantly reduces the quality of life of patients. The herniated nucleus pulposus compresses the nerve root and causes inflammation in that area. Its treatment has an important place in the country's health expenditures. Depending on the condition of the pathology, treatment methods such as physiotherapy, rest, lifestyle changes, analgesic and antispasmodic agents are applied first. The latest surgical methods are used [3]. As in many diseases, cardiovascular causes come to the fore in cartilage injuries. Ischemia-induced osteoarthritis is a good example [4]. There are studies in the literature showing that arterial hypertension is directly related to joint osteoarthritis [5, 6].

Hypertension is defined as a condition in which arterial blood pressure is above normal values. In other words, it is the condition that the blood pressure is higher than 140 mm/Hg in systole and 90 mm/Hg in diastole. Hypertension is a chronic disease whose prevalence is increasing day by day both in our country and in the world. Hypertension is the etiology of many diseases, especially cardiovascular diseases. Considering the diseases that affect human and public health, it is a disease that is relatively easy to treat compared to others [7].

In this study, the IDs of patients with high arterial blood pressure and those with normal arterial blood pressure who have undergone lumbar disc herniation surgery will be compared histopathologically and histomorphometrically.

2. MATERIAL AND METHOD

2.1. Experimental Design

This study is a retrospective study. Tissues of patients who had undergone lumbar disc herniation surgery without any metabolic disease were used as the control group. Tissues of patients who were hypertensive and had lumbar disc herniation surgery (blood pressure higher than 140 mm/Hg in systole, 90 mm/Hg in diastole) were used for the experimental group.

2.2. Ethical Statements

The study was carried out in compliance with the Declaration of Helsinki with the approval of Bilecik Seyh Edebali University, Faculty of Medicine, Non-Invasive Clinical Research Ethics Committee, dated 27.12.2022 and numbered 8-2.

2.3. Study Population, Inclusion and Exclusion Criteria for Samples

26 patients who underwent lumbar discectomy at Bilecik Training and Research Hospital between January 2022 and June 2023 were included in the study. Age and gender parameters were also reported for demographic analysis. Patients with possible independent external factors such as cervical discectomy, hypo/hyperthyroidism and diabetes mellitus were excluded.

2.4. Histopathological and Histomorphometric Evaluation

After the tissues were surgically removed, they were immediately placed in 10% neutral buffered formaldehyde for fixation. Tissues were embedded in paraffin after dehydration, clearing and paraffin impregnation. Sections of 5 μm thickness were taken from paraffin blocks to slides. Slides were kept in the oven for deparaffinization. Then, the slides were passed through xylol and decreasing ethyl alcohol series (100%, 90%, 80%, and 70%) respectively. After the slides were stained with hematoxylin & eosin stain, they were passed through increasing series of ethyl alcohol (70%, 80%, 90% and 100%). Slides were kept in xylol for 30 minutes and then mounted with entellan. Tissues were examined and photographed under a microscope (Olympus CX23) with an Olympus camera (Olympus EP50). The groups were first evaluated histopathologically by a pathologist. Chondrocytes were counted in 10 different fields of slides at 400× magnification [8] . In addition, lacunae diameters were measured in counted chondrocytes.

2.5. Statistical Analysis

Statistical package program was used for statistical analysis. Continuous variables were checked for normality using the Kolmogorov-Smirnov test. Student's t-test was used to compare parametric data. Chi-square test was used for the analysis of categorical data. A p-value below 0.05 was considered statistically significant.

3. RESULTS

3.1. Histopathologic Results

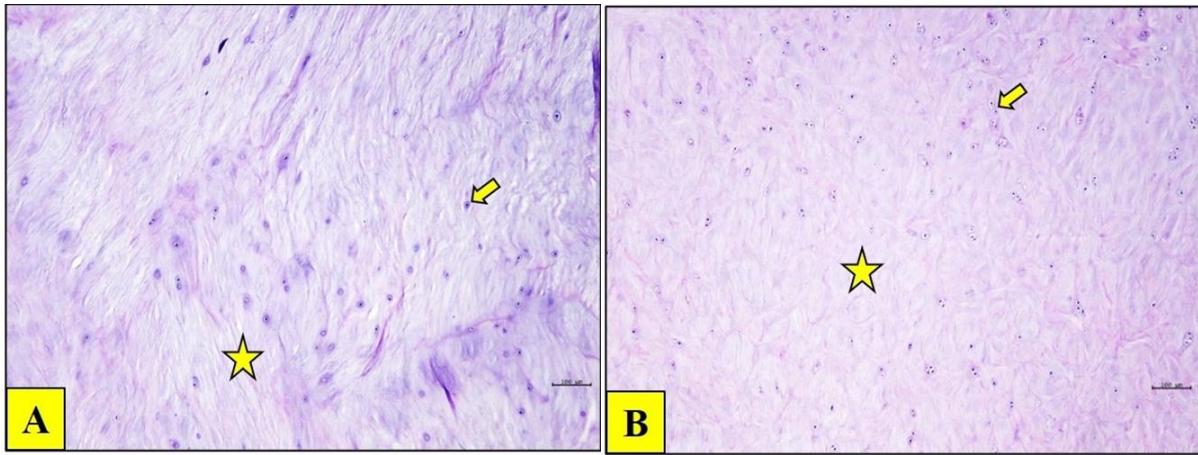Normotensive and hypertensive sections had histopathologically similar appearance (Figure 1).

Figure 1. Hematoxylin-eosin staining of discus intervertebralis from normotensive (A) and hypertensive (B) patients. Normotensive and hypertensive sections had similar chondrocyte (yellow arrow) and extracellular matrix (yellow star) histology. In image A and B, the bars are 100µm.

3.2. Comparison of Chondrocyte Morphology in Normotensive and Hypertensive Patients

The mean chondrocyte count per field at x400 magnification of the groups was 3.22±0.77 in normotensive patients and 3.15±0.75 in hypertensive patients. The mean lacunae diameters were measured as 13.05±0.47 in normotensives and 13.53±1.41 in hypertensives. There was no significant difference between the groups in terms of chondrocyte count and lacunae diameter (p>0.05) (Figure 2).
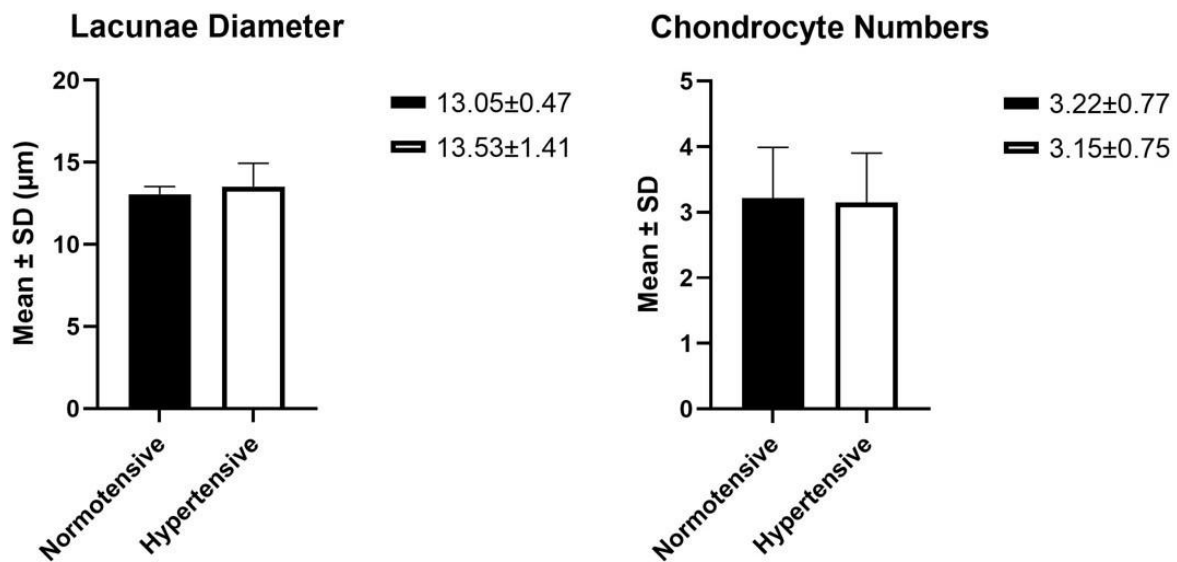
Figure 2. The mean chondrocyte numbers and lacunae diameter in normotensive and hypertensive patients. Student's t-test, p>0,05.

3.3. Demographic Characteristics of Normotensive and Hypertensive Patients

In the study population, the mean age of hypertensive patients (61.69±13.55) was higher than the mean age of normotensive patients (42±8.84) (p<0.05). While the female/male ratio was 46.2/58.8% in the hypertensive group, it was 79.9/23.1% in the normotensives. The gender ratio of the groups did not show a statistical difference (p>0.05) (Table 1).

Table 1. Demographic characteristics of normotensive and hypertensive patients. Chi-square and Student's t-test, SD: Standart deviation, Statistical significance: *p<0.05

	Normotensive	Hypertensive	p value
Gender			0.227
Male *(n)*	10 (79.9 %)	6 (46.2%)	
Female *(n)*	3 (23.1%)	7 (53.8%)	
Age			*0,000197
Mean±SD	42±8.84	61.69±13.55	

194

4. DISCUSSION AND CONCLUSION

In this study, it was shown that the discus intervertebralis of normotensive and hypertensive patients who underwent lumbar discectomy were not different in terms of histopathologically and histomorphometrically (in terms of chondrocyte number and lacunae diameter). This is the first study to compare the discus intervertebralis of normotensive and hypertensive patients histopathologically and histomorphometrically.

Although the effects of cardiovascular system diseases such as arterial hypertension and hyperlipidemia on cartilage tissue are known, more studies are needed to detail this relationship. Kabalyk et al. investigated the effects of arterial hypertension on articular cartilage in their experimental study. Researchers have shown in their studies that arterial hypertension damage the articular cartilage histopathologically and histomorphometrically [5]. Our study showed different results from this study. We found that there was no difference between normotensive and hypertensive patients in terms of histopathology, chondrocyte count and lacunae diameter. When we look the reasons for this difference; the first thing that stood out was that while we worked on intervertebral discs, they worked on articular cartilage. There are three different types of cartilage in humans: fibrous, hyaline and elastic cartilage. Articular surfaces are covered with hyaline cartilage. Intervertebral discs are fibrous cartilage. These two cartilages differ histologically. These two cartilage vascularization and nutrition pathways also differ. We think that the difference in results is due to this. The relationship between osteoarthritis and high blood pressure has been the subject of curiosity by many researchers. Ashmeik et al. magnetic resonance imaging in 1126 volunteers showed that increased diastolic blood pressure caused increased articular cartilage matrix damage [9]. Wang et al. and Ashmeik et al. obtained similar results [10]. Ashmeik et al. and and Wang et al. obtained very important findings, but these studies are related to articular cartilages like the previous study. The difference between these two studies and our study actually reveals the hypothesis of our future study. In our study, the effects of arterial hypertension on cartilage tissue were similar in men and women. However, Yeater et al. it appears to have obtained different results compared to our study. Yeater et al. showed that hypertension increases osteoarthritis in the articular cartilage in a gender related manner [11]. The presence of serious nervous system problems in discus intervertebralis diseases makes it easier to choose the surgical option in the treatment. Articular cartilage diseases are examined over a longer period of time and after alternative treatments are tried, surgical procedures are applied. The pathophysiological and anatomical differences of these two cartilages lead treatment providers to different diseases and different priorities. These differences perhaps lead the researchers' hypotheses on hypertension and cartilage damage to articular cartilage.

In parallel with our study, Maurer et al. in their magnetic resonance imaging (MRI) study on 400 patients, they revealed that factors such as obesity, hypertension, diabetes, elevated LDL-c, low HDL-c, elevated triglycerides, smoking status, and alcohol consumption are not related to disc degeneration. Our data support this study histopathologically and histomorphometrically [12]. Although we and Maurer et al. showed that hypertension did not make any difference in intervertebral discs, Samartzis et al. in an MRI scan of 1800 volunteers, they showed that high blood pressure was associated with different stages of lumbar disc degeneration [13]. If different results are obtained with the same methods in science, the existing hypothesis must be repeated. These repetitions will provide us with powerful data in proving or ignoring the hypothesis. Our focus is on a detailed examination of the subject of hypertension and disc degeneration.

The data obtained from this study reveal important results regarding fibrous cartilage histopathology and hypertension. It shows that the fibrous cartilage in the discus intervertebralis of normotensive and hypertensive patients is not different histopathologically and histomorphometrically. Future studies should include larger populations in terms of the number of volunteer patients and advanced imaging techniques such as MRI with molecular examination methods together.

Conflicts of interest
The authors declare that there is no conflict of interest.

REFERENCES

[1] Grunhagen T, Wilde G, Soukane DM, Shirazi-Adl SA, Urban JP. Nutrient supply and intervertebral disc metabolism. J Bone Joint Surg Am. 2006;88(2):30-5.

[2] Roberts S, Evans H, Trivedi J, Menage J. Histology and pathology of the human intervertebral disc. J Bone Joint Surg Am. 2006;88(2):10-4.

[3] Eygi E, Balkaya AN, Gurbet A, Şahin Ş. Non-Opere Tek Mesafe Lomber Disk Herniasyonlarinda Transforaminal Epidural Steroid Enjeksiyonu Etkinliğinin Değerlendirilmesi. Kocatepe Tıp Dergisi. 2023;24(2):148-53.

[4] Khamidov O, Khodzhanov IY, Mamasoliev B, Mansurov DS, Davronov A, Rakhimov A. The role of vascular pathology in the development and progression of deforming osteoarthritis of the joints of the lower extremities (Literature review). Annals of RSCB. 2021;25(1):214-25.

[5] Kabalyk M, Kovalenko T, Nevzorova V, Sukhanova G. Effect of Arterial Hypertension and Hyperlipidemia on the Remodeling of Articular Cartilage and the Development of Osteoarthritis (Experimental Study). Adv Gerontol 2020;10(1):79-85.

[6] Mazurov V, Stolov S, Vorobyeva O, Dolgikh S, Martynov IV, Pobyegai O. Cardiovascular problems

in rheumatology. Medical academic journal. 2009;9(1):59-65.

[7] Mills KT, Stefanescu A, He J. The global epidemiology of hypertension. Nat Rev Nephrol. 2020;16(4):223-37.

[8] Bilge O, Doral MN, Atesok K, Atay OA, Donmez G, Turhan E, et al. The effects of the synovium on chondrocyte growth: an experimental study. Knee Surg Sports Traumatol Arthrosc. 2011;19(7):1214-23.

[9] Ashmeik W, Joseph GB, Nevitt MC, Lane NE, McCulloch CE, Link TM. Association of blood pressure with knee cartilage composition and structural knee abnormalities: data from the osteoarthritis initiative. Skeletal Radiol. 2020;49(9):1359-68.

[10] Wang Y, Meng T, Ruan G, Zheng S, Zhu J, Cen H, et al. Associations of blood pressure and arterial stiffness with knee cartilage volume in patients with knee osteoarthritis. Rheumatology (Oxford). 2021;60(10):4748-54.

[11] Yeater TD, Griffith JL, Cruz CJ, Patterson FM, Aldrich JL, Allen KD. Hypertension contributes to exacerbated osteoarthritis pathophysiology in rats in a sex-dependent manner. Arthritis Research & Therapy. 2023;25(1):1-13.

[12] Maurer E, Klinger C, Lorbeer R, Hefferman G, Schlett CL, Peters A, et al. Association between cardiovascular risk factors and degenerative disc disease of the thoracolumbar spine in the general population: results from the KORA MRI Study. Acta Radiol. 2022;63(6):750-9.

[13] Samartzis D, Bow C, Karppinen J, Luk KDK, Cheung BMY, Cheung KMC. Hypertension is Independently Associated with Lumbar Disc Degeneration: A Large-Scale Population-Based Study. Global Spine Journal. 2014;4(1).

196

Türk Doğa ve Fen Dergisi
Turkish Journal of Nature and Science
www.dergipark.gov.tr/tdfd

Deterministic Lateral Displacement System with Inclined Elliptical Obstacles for Efficient Size-Based Separation of Microparticles

Döne SAYARCAN[1*] [iD] **, Ahmet CİCEK[2]** [iD] **, Nurettin KOROZLU[2]** [iD]

[1] Opticianry Programme, Gölhisar Vocational School of Health Services, Burdur Mehmet Akif Ersoy University, Burdur, Türkiye
[2] Department of Nanoscience and Nanotechnology, Art and Science Faculty, Burdur Mehmet Akif Ersoy University, Burdur, Türkiye
Döne SAYARCAN ORCID No: 0000-0001-7000-0354
Ahmet CİCEK No: 0000-0002-7686-0045
Nurettin KOROZLU No: 0000-0002-0899-0227

Corresponding author: donesayarcan@mehmetakif.edu.tr

Abstract: A deterministic lateral displacement system with inclined elliptical posts is demonstrated to sort spherical micrometer-sized solid particles. Numerical simulations via the finite-element method are performed to investigate the microfluidic system performance. Soft microparticles undergo deformations in designs with cylindrical posts or posts with sharp corners. Such deformations occur due to particle clogging between obstacles, which can disrupt the flow lanes. The proposed approach aims to eliminate these challenges. The calculations reveal a much-reduced rate of change in flow velocity between vertically inclined elliptical posts, compared to circular posts. The calculated critical particle sizes are more likely to follow the equation associated with the first flow lane width derived from a parabolic velocity profile at high fluid inlet rates, rather than the two semi-analytical models proposed for circular posts. The experimental and theoretical critical diameter data exhibited greater agreement with the critical diameter equation obtained using the curve-fitting method at lower fluid inlet rates. Overall, the minimum particle size decreased as the rate of flow increased. When assessing the connection between the two, a smaller critical diameter is achieved by decreasing the inclination angle. The adjustability of the system by rotating the posts is a major advantage of the proposed approach.

197

Miroparçacıkların Boyutlarına Göre Verimli Ayrıştırılması İçin Eğimli Eliptik Engeller İçeren Bir Deterministik Yanal Yerdeğiştirme Sistemi

Öz: Eğik eliptik sütunlar içeren bir Deterministik Yanal Yerdeğiştirme sistemi, mikrometre boyutundaki küresel katı parçacıkları ayırmak için gösterilmiştir. Mikroakışkan sistem performansını araştırmak için Sonlu Elemanlar Yöntemi ile sayısal simülasyonlar yapılmıştır. Yumuşak mikroparçacıklar, silindirik sütunlar veya keskin köşelere sahip sütunlarla tasarımlarda deformasyonlara uğrar. Bu tür deformasyonlar, parçacıkların engeller arasında tıkanmasından kaynaklanır ve bu da akış yollarını bozabilir. Önerilen yaklaşım, bu zorlukları ortadan kaldırmayı hedeflemektedir. Hesaplamalar, dairesel sütunlara kıyasla dikey eğimli eliptik sütunlar arasında akış hızındaki değişim oranının çok daha düşük olduğunu ortaya koymaktadır. Hesaplanan kritik parçacık boyutlarının, yüksek sıvı giriş hızlarında parabolik bir hız profilinden türetilen ilk akış yolu genişliğiyle ilişkili denklemi, dairesel sütunlar için önerilen iki yarı-analitik modelden daha fazla takip etme olasılığı vardır. Deneysel ve teorik kritik çap verileri, daha düşük sıvı giriş hızlarında eğri uydurma yöntemi kullanılarak elde edilen kritik çap denklemi ile daha büyük bir uyum sergilemiştir. Genel olarak, minimum parçacık boyutu akış hızı arttıkça azalmıştır. İkisi arasındaki bağlantı değerlendirildiğinde, eğim açısının azaltılmasıyla daha küçük bir kritik çap elde edilir. Sütunları döndürerek sistemi ayarlayabilme imkanı, önerilen yaklaşımın büyük bir avantajıdır.

1. INTRODUCTION

Microfluidic devices for particle sorting in suspensions have attracted attention in the fields of biomedical research, biochemistry, pharmacology, and clinical diagnostics [1, 2]. Typically, such sorting procedures can be carried out via centrifugation, flow cytometry, gel electrophoresis, and chromatography. Although these techniques are effective for samples with a high volume, they are not suitable for small-scale operations. Microfluidic systems provide the reduction in size and combination of different functionalities to carry out laboratory tasks on a small scale. These systems can handle, combine, and examine small amounts of samples, while significantly reducing the amount of time needed to conduct such operations.

Microfluidic systems have extensive applications in the manipulation, sorting, and classification of micro- and nanoparticles [3]. Particle manipulation is frequently employed in the detection of biomolecules [4], as well as in the sorting and separation of cells [5, 6]. Particle sorting strategies in microfluidics can be categorized into active and passive schemes. Active sorting devices including magnetophoresis [7], dielectrophoresis [8], acoustophoresis [9], and thermophoresis [10] control the movement of particles by applying external forces. These approaches depend on the interaction between the particles and either the flow, magnetic, electric, acoustic, or optical field available in the microchannel. Passive microfluidics employs fluid forces and channel geometry to accomplish particle sorting. This involves techniques such as hydrodynamic filtration [11], pinched flow fractionation [12], inertial microfluidics [13], viscoelastic separation [14], and deterministic lateral displacement (DLD) [15]. DLD has gained significant popularity as a technique for particle separation and detection in the last two decades. DLD employs hydrodynamic forces, channel shape, and flow to achieve separation without the need for external forces.

The concept of DLD was first presented by Huang et al. in 2004 [16]. Researchers discovered that in a microchannel, when obstacles are organized in a particular periodic order, laminar flows with Reynolds numbers less than one (Re<1) result in the formation of a specific number of flow lanes (N) between the posts. Microparticles that are smaller than a critical diameter (D_c) have a distinct flow lane, while particles that are larger than Dc follow consecutive flow lanes. These patterns of movement, referred to as zigzag and displacement modes, were described by Huang et al. (2004) [16]. The observed differentiation in the particle trajectories enables the particles to be selectively steered towards specific exit pathways according to their size.

The paths followed by particles passing through a DLD system depend on the geometric parameters of the system. The first of these parameters are: the gap size (G) between two obstacles, the center-to-center distance (λ) between two obstacles, the shift amount ($\Delta\lambda$) of the next obstacle row, and the row shift fraction (ε), which is defined as $\varepsilon = \Delta\lambda/\lambda$. There are various approaches for determining the critical particle size.

Inglis et al. [17] proposed an analytical approach to determine the critical particle diameter (D_c) in a DLD device with equal downstream and lateral gap sizes. The number of flow lanes between obstacles is equal to the period of the obstacle arrays, and the number of flow lanes N is related to the row shift fraction as $N = 1/\varepsilon$ [17]. Each of these flow lanes contains an equal amount of fluid, and the width of each lane can be calculated considering a symmetric parabolic flow profile. According to the theory, if the particle radius is smaller than the width of the first flow lane, the particle follows the lane path, which is termed as the 'zigzag mode' [17]. On the other hand, if the particle radius is larger than the flow lane width, the particle follows successive lanes, termed as the 'displacement mode'. The width β of the "first" flow lane passing through each row gap (adjacent to the row) is given as a first-order approximation by

$$D_c = 2\beta \tag{1}$$

Considering a parabolic velocity profile between adjacent obstacles and the equal flux carried by the flow lanes, β can be analytically calculated [17]. Beech [19] simplified the critical particle diameter equation to

$$\frac{D_c}{G} = 1.155\varepsilon^{0.5} \tag{2}$$

Davis [18] derived an empirical formula for the critical particle size in a DLD device:

$$D_c = 1.4G\varepsilon^{0.48} \tag{3}$$

Equation (3) according to Davis' [18] theory is obtained by investigating approximately 20 different devices in experiments, in which polystyrene beads were used to collect data [15]. Non-spherical and deformable particles were not considered in Davis' [18] study.

Conducting a theoretical analysis of DLD devices improves the accuracy of predicting the paths of particles. Many DLD systems with varying obstacle configurations have been investigated to the date. Analyses have been conducted on systems that feature posts with different shapes, including airfoil-shaped [20], teardrop-shaped [21], triangular [22], I-shaped [23], and optimized-shaped [24]. Asymmetric systems, characterized by unequal lateral and downstream gaps, have also been studied to determine the critical particle diameter. Inglis et al. [17] introduced a theoretical method to calculate the critical particle size in asymmetric DLD designs. Zhang et al. [13] conducted a numerical analysis to investigate the impact of several column forms (cylindrical, diamond, and triangular) on the dynamic behavior of red blood cells in DLD devices. Sharp and pointed obstacles drastically increase the probability of red blood cells to deform and result in considerable damage.

As previously stated, numerous DLD systems have been developed by leveraging the characteristics of the particles that need to be sorted. The efficiency of the proposed DLD systems is significantly influenced by

various characteristics, including the geometric parameters of the DLD system, the shapes of obstacles, the properties of the fluid, and the properties of the particles. Due to the numerous parameters that affect the system, additional research and the development of more DLD systems are required.

This research focuses on a DLD system including inclined elliptical posts, a design that has not been previously investigated. First, the performance of the proposed device is assessed. After that, an analysis is conducted on the efficacy of particle sorting, the impact of fluid velocity on particle paths, and the influence of obstacle inclination angles. The separation capability of the designed system is assessed by comparing the calculated critical diameters with those predicted through the formulas presented by Inglis [17] and Davis [18] for DLD systems that have circular obstacle posts. The velocity profile between the elliptical obstacle posts is compared to the profile in a conventional design, taking into account the impact of the velocity profile on the sorting of particles. The effect of the inclination angle of the elliptical obstacle posts on the critical diameter has been examined. The system under consideration has been modeled through two-dimensional (2D) finite element method (FEM) simulations. A module for particle tracking, which includes an interface for fluid-particle interaction, was used to simulate the interactions between the particles and the obstacle posts. This method enabled more accurate prediction of the particle movements. The study employed time-dependent bidirectional particle tracking to determine the threshold particle diameter and track the paths of the particles.

2. MATERIAL AND METHOD

2.1. Simulation Domain Design and Boundary Conditions

To model particle movements in the DLD array, COMSOL Multiphysics software is employed. The model is created using the Particle Tracing for Fluid Flow interface added to the fluid flow module with 2D FEM. The fluid-particle interaction interface is used to account for the effect of particle movement on the fluid flow profile. The microchannel structure was designed using the microfluidic module (Figure 1(a)) and the design parameters of the DLD system (Figure 1(b,c)) are shown in Figure 1.
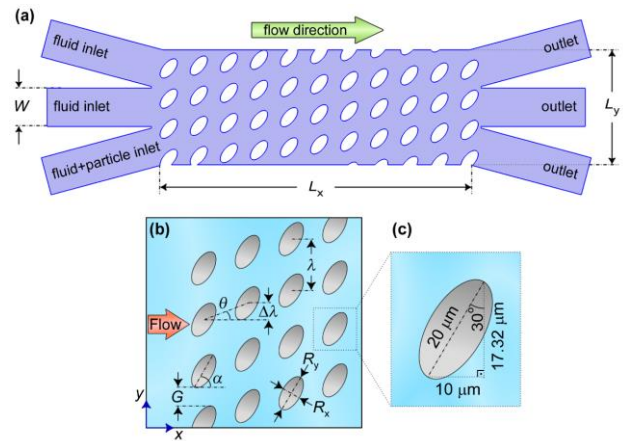

Figure 1: (a) Full-scale depiction of the planned microchannel structure, (b) design of the elliptical DLD posts and the relevant geometrical parameters, (c) geometric position and dimensions of an obstacle post within the DLD system.

The left section of the microfluidic channel is partitioned into three distinct channels for fluid inflow (Figure 1(a)). The right section is further partitioned into three distinct channels for the discharge of fluids and particles (Figure 1(a)). The lowest inlet channel is configured to release particles simultaneously with the stream. The fluid phase utilized water at ambient temperature. The input flow is characterized by a parabolic velocity profile and a fully developed creeping flow. The outflow boundary condition is specified as having zero viscous stress and Dirichlet conditions on pressure. The fluid in the simulation is subjected to a 'no-slip' condition by the domain walls and fixed obstacle walls. Particles with a density of 1200 kg m³ are specified (Table 1). The drag force, which is influenced by the characteristics of the fluid, operates upon the solid particles. The boundary condition for the particles is specified as 'bounce' when they bumped into the walls. The DLD system is encountered by water and particles immediately after they pass through the entrance channel. The channel width of the DLD system is L_y=99 µm, and its length is L_x=285 µm (Figure 1(a)). The microchannel contains eleven rows of elliptical obstacles, which results in the minimum DLD system length for efficient particle separation. The elliptical obstacle posts are designed with a width of 10 µm and a length of 20 µm to create a fully formed elliptical structure (Figure 1(b)). The minor-to-major axis ratio of the posts is set at ½. The elliptical obstacle posts are placed at a 60° angle relative to the direction of flow (the x axis) (Figure 1(c)). G is the gap size between the obstacle posts, λ is the row shift step (same for both x and y directions), and $\Delta\lambda$ is the shift amount between neighboring rows. The row shift fraction is $\varepsilon = \Delta\lambda/\lambda$, and the row shift angle of the obstacle posts is $\theta = \tan^{-1}(\varepsilon)$. Table 1 contains the parameters of the DLD system.

199

Table 1: Geometrical and physical parameters assumed in the design of the DLD system.

	Parameter	(Unit)	Value	Description
Geometrical	L_x	(µm)	285	Channel length in the propagation (x) direction
	L_y	(µm)	99	Channel height in the lateral (y) direction
	W	(µm)	33	Fluid inlet channel width
	R_x	(µm)	10	Elliptical posts' minor axis length
	R_y	(µm)	20	Elliptical posts' major axis length
	α	(°)	60	Elliptical posts' inclination angle
	G	(µm)	6	The gap between two posts
	$\Delta\lambda$	(µm)	2.25	The row shift
	λ	(µm)	26	Center-to-center distance between posts
	$\varepsilon = \Delta\lambda/\lambda$		0.0865	Row shift fraction
	$\theta = \tan^{-1}(\varepsilon)$	(°)	11.53	Row shift angle
Physical	ρ_f	(kg m^3)	1000	Fluid density
	ρ_p	(kg m^3)	1200	Particle density
	U_f	(µl min-1)	125	Inlet flow rate

To solve the governing equations, it is necessary to create a mesh for the simulation domain. COMSOL utilizes the governing equations to solve for the most precise outcome at every mesh location. A free triangular mesh with a maximum and minimum element size of 4.22×10⁻⁶ and 6.03×10⁻⁸, respectively, is utilized for the calculations. The mesh is specifically designed to comply with the boundary conditions and geometry of the calculation domain. The mesh quality for the present simulation is determined to be 0.8306, implying a high level of mesh quality [25].

Particle motion in a dilute flow is influenced by the fluid. This phenomenon is commonly known as two-way coupling. The Particle Tracing for Fluid Flow interface utilizes the fluid-particle interaction physics to compute the two-way coupling between particles and the fluid. A drag force proportional to the fluid velocity is applied to the particles under laminar flow. The fluid-particle interaction physics solves the Navier-Stokes equations [26, 27] and the continuity equation in a time-dependent manner. The Bidirectionally Coupled Particle Tracing interface, which addresses all particle degrees of freedom in a time-dependent solution, is employed. The remaining degrees of freedom are computed using a stationary solver. A for-end for loop is used to iterate the two solvers and get a self-consistent solution, taking into account the bidirectional interactions between moving particles and the stationary flow field. The time-dependent solver is configured with time steps of 0.001 milliseconds. The 'generalized alpha' method, which is an implicit solver, is used for the time steps. The MUMPS algorithm is the direct solver of choice.

3. RESULTS

This section evaluates the validity of the designed device through numerical calculations and determines the optimal physical conditions for this system.

3.1. Velocity Field

The velocity field between the obstacle gaps significantly affects particle orientation and the deformation of deformable particles. The creeping flow module is used to model the flow behavior within the DLD system. The velocity profiles between traditional circular posts (Figure 2(a)) and the elliptical obstacle posts in this design (Figure 2(b)) are shown in Figure 3. The circular post diameter is chosen to be equal to the sine of the elliptical obstacle diameter given in Figure 2(b) (17.32 µm), and all other DLD parameters are set the same as in this study, with a fluid flow rate of 125 µl min⁻¹.
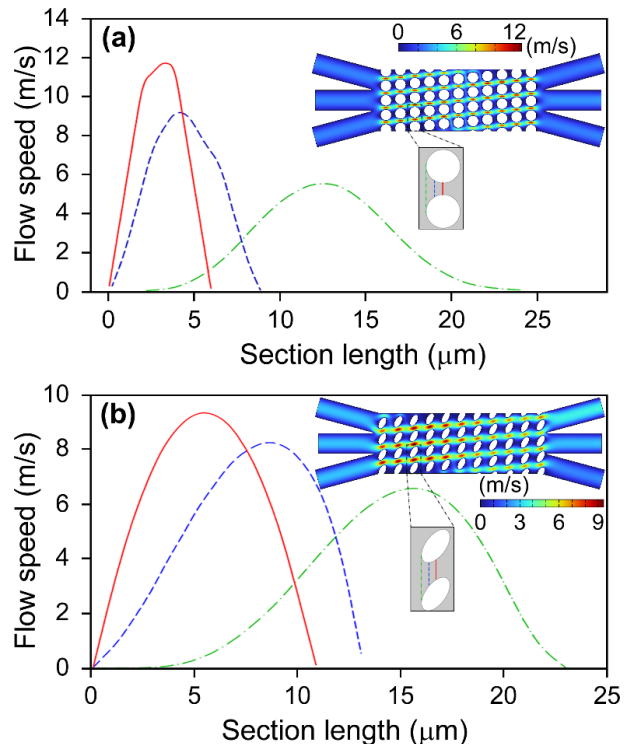
Figure 2: The fluid velocity gradient and flow field between obstacle posts in a DLD system comprised of (a) conventional circular posts and (b) the designed elliptical obstacle posts.

The velocity gradient in the gap between traditional circular post arrays (Figure 2(a)) is relatively higher than the velocity gradient in the gap between elliptical obstacles in the proposed design (Figure 2(b)). The

acceleration in the flow field from the inlet to the closest distance between obstacles (green-blue-red sections, respectively) is almost twice the value calculated for elliptical rods. Besides, the flow speed reaches its maximum values at the closest distance between obstacles (red curve) in both designs. In the traditional design, the flow compresses in the red section, causing the fluid velocity to nearly double compared to the green section (Figure 2(a)). In the proposed design, however, the velocity trend undergoes less variation from the inlet (green section) to the closest distance between obstacles (red section) (Figure 2(b)).The high velocity gradient in the traditional circular post array design has a significant impact on the motion of soft particles, as such particles tend to be rotated, deformed, and subsequently aligned with the average flow direction, leading to no further displacement. In contrast, in our proposed design, the orientation of the elliptical obstacles distributes the velocity gradient over a wider area, creating a more uniform velocity field. Therefore, it can be stated that the elliptical obstacles act as a guide for pressure on transported particles. Additionally, the deformation process of soft particles will be less affected, and the particles will be influenced less by this velocity field.

3.2. Critical Particle Size

For analyzing the impact of changes in $\Delta\lambda$ on critical diameter, simulations of particle trajectories across a range of sizes are conducted. The $\Delta\lambda$ values are systematically increased from 1 μm to 2.75 μm in increments of 0.25 μm. The results are compared with the critical particle sizes obtained from Beech's [28] (Equation 2) and Davis' [18] (Equation 3) formulas (Figure 4). The critical particle size range is determined by finding the smallest diameter of particles in displacement mode and the largest diameter in zigzag mode.

Figure 3 shows the particle movement modes at different ε values and different speeds. Figure 3(a), (b) and (c) shows the particle trajectories at a fluid inlet rate of 100 μl min⁻¹, 125 μl min⁻¹, and 150 μl min⁻¹, respectively, at all inlet channels in Figure 1(a), according to the displacement fraction.
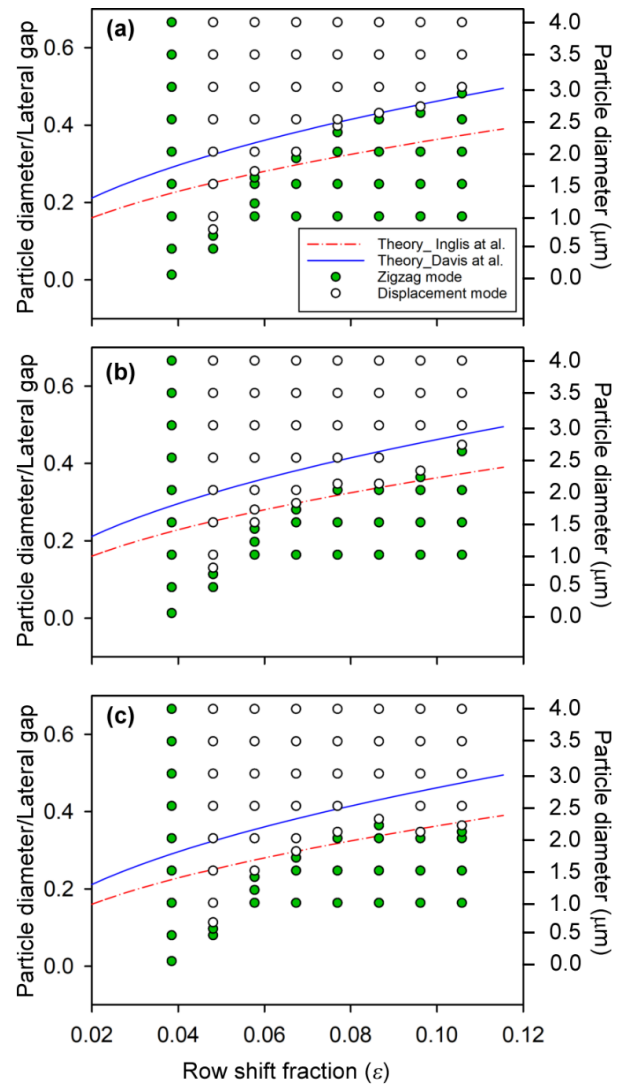
Figure 3: Particle trajectories normalized by obstacle gap size and fluid velocities of **(a)** 100 µl min⁻¹, **(b)** 125 µl min⁻¹, and **(c)** 150 µl min⁻¹ based on row shift fraction. The filled and hollow circles represent the zigzag mode and the displacement mode, respectively. Burada The red dashed curve represents the critical diameter curve derived from Inglis et al.'s [17] critical diameter theory, while the blue curve illustrates the critical diameter curve introduced by Davis et al. [18].

The particle size normalized by the lateral obstacle gap size is presented in Figure 3. As the row shift fraction decreases, the hydrodynamic resistance against the switching flow increases, resulting in a very thin first flow lane width (β) for small ε values compared to the direct flow. Since the critical diameter is directly related to the switching flow, the critical diameter decreases as ε decreases. As shown, for $\Delta\lambda$ values of 1 μm and below, particles of all sizes are found to move in zigzag mode, indicating that the obstacle row shift amount should be above 1 μm for the system to operate efficiently. As the row shift fraction increases, the sizes of particles moving in zigzag mode also increase. The critical diameter values for fluid velocities of 125 µl min⁻¹ (Figure 3(b)) and 150 µl min⁻¹ (Figure 3(c)) are more consistent with the critical diameter model proposed by Inglis et al. [17]. For a fluid velocity of 100 µl min⁻¹ (Figure 3(a)), the critical diameter values are more consistent with Davis' [18] proposal.

Besides the row shift fraction, inlet flow rate also affects the critical diameter. The impact of this rate on particle trajectories is shown in Figure 4. A particle with a diameter of 2.5 μm is observed to move in zigzag mode after the eighth obstacle for a rate of 100 μl min⁻¹, while it moves in displacement mode for 125 μl min⁻¹. As the rate increases, the Reynolds number also increases, causing flow lane compression, influencing particle trajectories, and altering separation dynamics [21]. An increase in the Reynolds number generally leads to a decrease in critical diameter, and higher fluid velocities result in denser flow lanes, reducing critical diameter. This result is consistent with the study by Dincau et al [21], which showed that fluid velocity and Reynolds number affect particle trajectories in a DLD system with circular posts.

(a)

Inlet flow rate: 100 μl/min
Particle diameter: 2.5 μm → **zigzag mode**

(b)

Inlet flow rate: 125a μl/min
Particle diameter: 2.5 μm → **displacement mode**
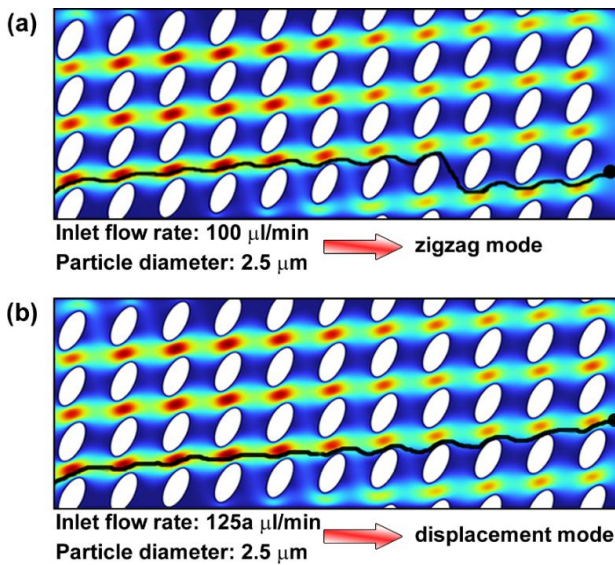
Figure 4: Trajectories of a solid spherical particle with a diameter of 2.5 μm in the DLD system for inlet flow rates of **(a)** 100 μl min⁻¹ and **(b)** 125 μl min⁻¹.

The proposed design allows the evaluation of the effect of the inclination angle of elliptical obstacle posts on particle trajectories for an inlet rate of 125 μl min⁻¹ and $\Delta\lambda$=2.25 μm. Here, particle trajectories are tracked at various inclination angles. Figure 5 shows particle trajectories based on the inclination angle of the obstacle posts. The selected inclination angle (60°) did not affect the critical diameter within ±5°. When the inclination angle is 70°, the critical particle size decreases, whereas it increases for 50°. Additionally, the critical diameter increases significantly with a decrease in the inclination angle.
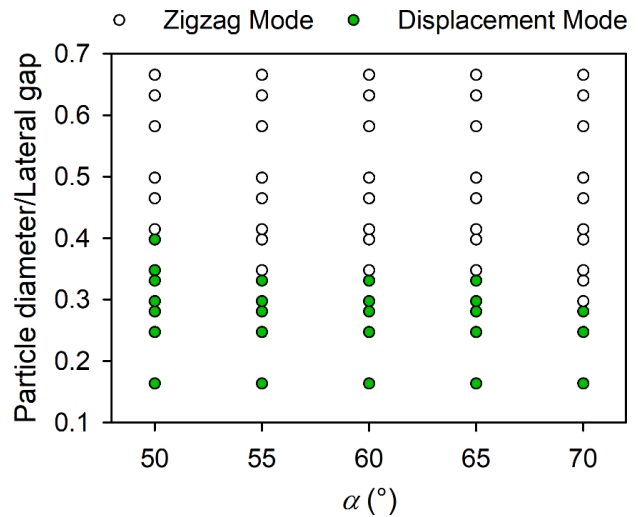

Figure 5: Trajectories of particles of various sizes based on the inclination angle of elliptical obstacle posts.

4. DISCUSSION AND CONCLUSION

In conclusion, an alternative microfluidic device that utilizes the deterministic lateral displacement principle to effectively sort particles within the diameter range of 1 to 4 μm is proposed. The elliptical post design is intended to alleviate the challenges associated with employing conventional circular or sharp-cornered (e.g. triangular, rectangular, etc.) post arrays and presents an original obstacle post design. Hence, adverse effects, such as particle clogging and unintended deformation of soft particles are eliminated through the introduced design.

It is shown that a DLD system including inclined elliptical obstacle posts results in a smoother velocity profile, as the velocity gradient between the circular posts is significantly higher, resulting in a strong tendency for particle rotation, deformation, and alignment with the average flow direction. The use of inclined elliptical posts mitigates these problems by increasing the spacing between the posts, which led to an approximately 50% rise in flow velocity from the input to the midgap between vertically neighboring obstacles. The DLD system displayed behavior that closely aligned with the proposed equation for the initial flow lane width, which was derived from a parabolic velocity profile at high fluid velocities, when compared to the two suggested techniques for circular posts.

The critical diameter equation developed by curve fitting actual and theoretical data showed greater consistency at low inlet flow rates (100 μl min⁻¹). The critical particle diameter reduced as the inlet rate increases. Furthermore, the degree of inclination of the elliptical obstacle posts has an impact on the trajectories of particles since the critical particle diameter is almost constant at inclinations of 55°, 60°, and 65°, but decreases at an inclination of 70° and increases at an inclination of 50°. Thus, the proposed approach is practically adjustable through the rotation of the posts.

Acknowledgement

REFERENCES

[1] Whitesides GM. The origins and the future of microfluidics. Nature. 2006;442(7101):368-73.

[2] Yager P, Edwards T, Fu E, Helton K, Nelson K, Tam MR, Weigl BH. Microfluidic diagnostic technologies for global public health. Nature. 2006;442(7101):412-8.

[3] Salafi T, Zeming KK, Zhang Y. Advancements in microfluidics for nanoparticle separation. Lab on a Chip. 2017;17(1):11-33.

[4] Xu X, Sarder P, Kotagiri N, Achilefu S, Nehorai A. Performance analysis and design of position-encoded microsphere arrays using the Ziv-Zakai bound. IEEE Transactions on Nanobioscience. 2012;12(1):29-40.

[5] Choi J-W, Oh KW, Thomas JH, Heineman WR, Halsall HB, Nevin JH, et al. An integrated microfluidic biochemical detection system for protein analysis with magnetic bead-based sampling capabilities. Lab on a Chip. 2002;2(1):27-30.

[6] Dittrich PS, Schwille P. An integrated microfluidic system for reaction, high-sensitivity detection, and sorting of fluorescent cells and particles. Analytical chemistry. 2003;75(21):5767-74.

[7] Munaz A, Shiddiky MJ, Nguyen N-T. Recent advances and current challenges in magnetophoresis based micro magnetofluidics. Biomicrofluidics. 2018;12(3).

[8] Jubery TZ, Srivastava SK, Dutta P. Dielectrophoretic separation of bioparticles in microdevices: A review. Electrophoresis. 2014;35(5):691-713.

[9] Connacher W, Zhang N, Huang A, Mei J, Zhang S, Gopesh T, Friend J. Micro/nano acoustofluidics: materials, phenomena, design, devices, and applications. Lab on a Chip. 2018;18(14):1952-96.

[10] Vigolo D, Rusconi R, Stone HA, Piazza R. Thermophoresis: microfluidics characterization and separation. Soft Matter. 2010;6(15):3489-93.

[11] Debnath N, Sadrzadeh M. Microfluidic mimic for colloid membrane filtration: a review. Journal of the Indian Institute of Science. 2018;98(2):137-57.

[12] Lenshof A, Laurell T. Continuous separation of cells and particles in microfluidic systems. Chemical Society Reviews. 2010;39(3):1203-17.

[13] Zhang J, Yan S, Yuan D, Alici G, Nguyen N-T, Warkiani ME, Li W. Fundamentals and applications of inertial microfluidics: A review. Lab on a Chip. 2016;16(1):10-34.

[14] Lu X, Liu C, Hu G, Xuan X. Particle manipulations in non-Newtonian microfluidics: A review. Journal of colloid and interface science. 2017;500:182-201.

[15] McGrath J, Jimenez M, Bridle H. Deterministic lateral displacement for particle separation: a review. Lab on a Chip. 2014;14(21):4139-58.

[16] Huang LR, Cox EC, Austin RH, Sturm JC. Continuous particle separation through deterministic lateral displacement. Science. 2004;304(5673):987-90.

[17] Inglis DW, Davis JA, Austin RH, Sturm JC. Critical particle size for fractionation by deterministic lateral displacement. Lab on a Chip. 2006;6(5):655-8.

[18] Davis JA. Microfluidic separation of blood components through deterministic lateral displacement: Princeton University; 2008.

[19] Beech JP. SEPARATION AND ANALYSIS OF BIOLOGICAL PARTICLES.

[20] Al-Fandi M, Al-Rousan M, Jaradat MA, Al-Ebbini L. New design for the separation of microorganisms using microfluidic deterministic lateral displacement. Robotics and computer-integrated manufacturing. 2011;27(2):237-44.

[21] Dincau BM, Aghilinejad A, Chen X, Moon SY, Kim J-H. Vortex-free high-Reynolds deterministic lateral displacement (DLD) via airfoil pillars. Microfluidics and Nanofluidics. 2018;22:1-9.

[22] Liu L, Loutherback K, Liao D, Yeater D, Lambert G, Estévez-Torres A, et al. A microfluidic device for continuous cancer cell culture and passage with hydrodynamic forces. Lab on a Chip. 2010;10(14):1807-13.

[23] Zeming KK, Ranjan S, Zhang Y. Rotational separation of non-spherical bioparticles using I-pillar arrays in a microfluidic device. Nature communications. 2013;4(1):1625.

[24] Hyun J-c, Hyun J, Wang S, Yang S. Improved pillar shape for deterministic lateral displacement separation method to maintain separation efficiency over a long period of time. Separation and Purification Technology. 2017;172:258-67

[25] Burlington MA. Multiphysics, C. O. M. S. O. L. Introduction to comsol multiphysics®. COMSOL Multiphysics, 1998. accessed Feb, 9(2018), 32.

[26] Bruus H. *Theoretical microfluidis* (Vol. 18): Oxford University Press; 2007

[27] Batchelor GK. *An introduction to fluid dynamics*: Cambridge University Press; 2000

[28] Beech J. Microfluidics separation and analysis of biological particles: Lund University; 2011.

Türk Doğa ve Fen Dergisi
Turkish Journal of Nature and Science

www.dergipark.gov.tr/tdfd

Rare Cardiac Tumor: Diagnosis And Management Of Atrial Myxoma With Computerized Tomography

Ahmet BAYTOK[1*] iD

[1] Karapınar State Hospital, Radiology Department, Konya, Türkiye
Ahmet BAYTOK ORCID No: 0000-0003-1615-5771

Corresponding author: drahmetbaytok@gmail.com

Abstract: Atrial myxomas are the most common benign primary cardiac tumors, predominantly located in the left atrium and frequently diagnosed between the ages of 30 and 60, with a higher prevalence in women. Although often asymptomatic, these tumors can present with various symptoms, including dyspnea, palpitations, and systemic embolic events, depending on their size, location, and mobility. We report the case of a 62-year-old female patient with a left atrial myxoma, presenting with mild dyspnea and palpitations. The patient's past medical history included hypertension and type 2 diabetes, with no prior history of cardiovascular disease. Initial transthoracic echocardiography (TTE) revealed a pedunculated mass in the left atrium, partially obstructing the mitral valve opening. Contrast-enhanced computed tomography (CT) further confirmed the diagnosis of atrial myxoma. Surgical resection was performed successfully, with histopathological confirmation of the myxoma. Postoperative imaging showed no residual mass, and the patient's symptoms resolved entirely. This case underscores the importance of prompt diagnosis and surgical intervention in atrial myxoma cases to prevent potential embolic complications and hemodynamic deterioration. Early surgical removal offers an excellent prognosis, minimizing the risk of recurrence. Regular follow-ups remain essential to monitor for potential recurrence, although rare. This case emphasizes the role of echocardiography and CT in the diagnostic process and highlights the favorable outcome achievable with early intervention in atrial myxoma cases.

Nadir Kardiyak Tümör: Atriyal Miksomanın Bilgisayarlı Tomografi ile Tanı ve Yönetimi

Öz: Atriyal miksomalar, en yaygın görülen benign primer kardiyak tümörlerdir ve genellikle sol atriyumda yerleşir. En sık 30 ile 60 yaşları arasında teşhis edilir ve kadınlarda daha yüksek prevalansa sahiptir. Çoğu zaman asemptomatik olmalarına rağmen, boyut, konum ve hareketliliklerine bağlı olarak dispne, çarpıntı ve sistemik embolik olaylar gibi çeşitli semptomlarla ortaya çıkabilirler. Bu makalede, hafif dispne ve çarpıntı şikayetleriyle başvuran 62 yaşında bir kadın hastanın sol atriyal miksoma vakası sunulmaktadır. Hastanın tıbbi geçmişinde hipertansiyon ve tip 2 diyabet bulunmakta olup, kardiyovasküler hastalık öyküsü yoktu. İlk transtorasik ekokardiyografi (TTE) incelemesinde mitral kapak açıklığını kısmen tıkayan pedinküllü bir kitle tespit edildi. Kontrastlı bilgisayarlı tomografi (BT) tetkiki, atriyal miksoma tanısını doğruladı. Cerrahi olarak tümör başarılı bir şekilde çıkarıldı ve histopatolojik inceleme miksoma tanısını kesinleştirdi. Ameliyat sonrası görüntülemelerde rezidü kitle saptanmadı ve hastanın semptomları tamamen düzeldi. Bu vaka, atriyal miksomalarda erken tanı ve cerrahi müdahalenin önemini vurgulamaktadır. Erken cerrahi eksizyon, embolik komplikasyonları ve hemodinamik bozulmayı önleyerek mükemmel bir prognoz sunar ve nüks riskini en aza indirir. Nadir de olsa olası nüksleri izlemek için düzenli takipler gereklidir. Bu olgu, atriyal miksoma tanısında ekokardiyografi ve BT'nin kritik rolünü ortaya koymakta ve erken müdahalenin sağladığı olumlu sonuçları vurgulamaktadır.

1. INTRODUCTION

Atrial myxomas are the most common primary tumors of the heart.They are usually benign, and are located in the left atrium in 75% of cases [1]. It is seen in approximately 0.5 out of 100,000 people and constitutes approximately 50% of all primary cardiac tumors [2]. These tumors, more commonly seen in women, are usually diagnosed between the ages of 30 and 60 [3]. Clinical presentations are quite variable; patients may be asymptomatic or present with various findings such as decreased cardiac output, embolic events and systemic symptoms depending on the size, location and movement of the myxoma [4]. Among these symptoms, cardiovascular symptoms such as shortness of breath, palpitations, dizziness, and syncope are prominent. If the tumor is located in the left atrium near the mitral valve, it can narrow the mitral valve opening, leading to findings similar to mitral stenosis [5].

Transthoracic echocardiography (TTE) is usually the first choice for the diagnosis of atrial myxomas. TTE is a reliable method for assessing the size, mobility and hemodynamic effects of the myxoma. However, advanced imaging methods such as computed tomography (CT) and magnetic resonance imaging (MRI) are also used to examine the characteristics of the tumor in more detail and to evaluate its relationship with surrounding tissues [6]. These methods also play an important role in the surgical treatment planning of atrial myxoma.

Surgical removal of atrial myxomas is the mainstay of treatment recommended to prevent embolic complications and cardiac symptoms. The prognosis after surgical intervention is generally good, but recurrence of myxomas has been reported in rare cases [7]. In this case report, an atrial myxoma detected by CT and TTE in a 62-year-old female patient will be discussed in light of the literature.

2. CASE REPORT

A 62-year-old female patient presented to the cardiology outpatient clinic with complaints of palpitations and occasional shortness of breath. Her medical history included primary hypertension and type 2 diabetes, and she had been receiving antihypertensive and antidiabetic treatment for approximately five years. The patient had no history of smoking or alcohol use, and there was no known family history of heart disease. She had no history of surgery or cardiovascular disease. Her blood pressure values were generally around 140/90 mmHg, and her blood sugar levels were kept under control with oral antidiabetic treatment.

On physical examination, the patient was alert, cooperative, and hemodynamically stable. No significant murmur was detected during cardiac auscultation. Although the patient had mild bilateral edema in the legs, no pathological findings were observed on lung auscultation. Electrocardiography (ECG) revealed a sinus rhythm, and the cardiac axis was evaluated as normal. TTE was planned before recommending an exercise test or further non-invasive evaluations.

In the TTE examination, a pedunculated, mobile mass approximately 1.9 x 2 cm in size was detected in the posterior wall of the left atrium, located between the mitral annulus and the papillary muscle. It was considered that the mass had the potential to partially obstruct the mitral valve opening and could affect mitral valve functions. The left ventricular ejection fraction (EF) was measured at 55%

To clarify the diagnosis, a contrast-enhanced thoracic CT scan was performed. The CT scan revealed a well-defined mass in the left atrium with intense contrast enhancement. The CT findings were consistent with an atrial myxoma. The pedunculated nature of the mass, its mobility, and potential for growth posed a risk of obstructing the mitral valve opening. This condition was thought to potentially lead to hemodynamic deterioration in the patient over time. Additionally, due to the mass's size and location within the left atrium, the increased risk of embolism was considered, and urgent surgical treatment was planned.

The patient was referred to the cardiovascular surgery team and underwent surgery. During the operation, a pedunculated and mobile myxoma located in the left atrium was excised. The mitral valve structure was carefully examined, and it was determined that the damage caused by the mass to the valve was minimal. No complications occurred during surgery or in the postoperative period. The excised tumor was sent for histopathological examination, which confirmed the diagnosis of atrial myxoma.

In the postoperative TTE, no residual tumor or recurrence was observed in the left atrium. The left ventricular EF was measured within normal limits at 60%. Although mild fibrotic changes and minimal valve regurgitation were detected in the mitral valve, overall valve function was satisfactory. No pathological findings were observed in the aortic and tricuspid valves, and there was no evidence of pulmonary hypertension or other complications. The patient's cardiac functions returned entirely to normal in the postoperative period, and her symptoms subsided. The patient is stable and continues to be monitored with regular cardiology follow-ups.
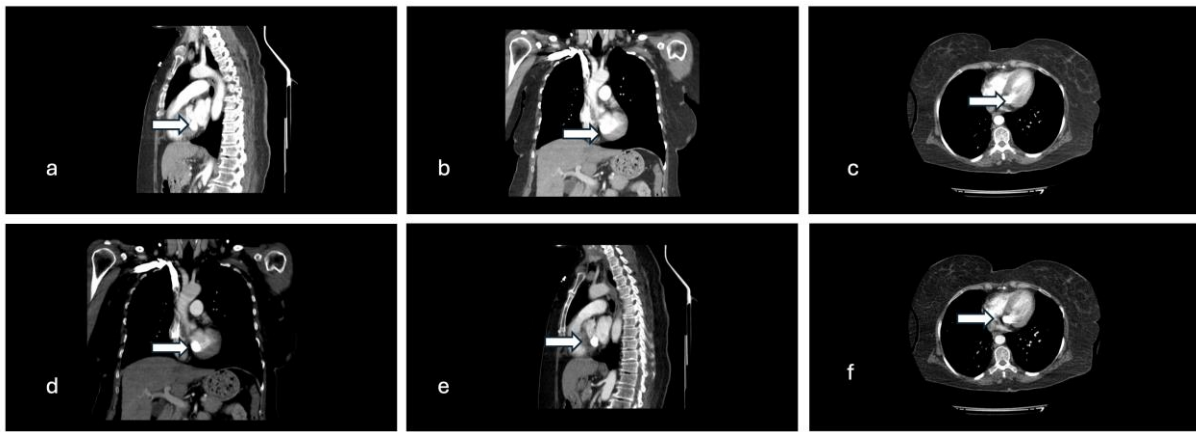
Figure 1. Different views of the atrial myxoma located in the left atrium as seen on CT images: a, e) Sagittal view of the atrial myxoma, b, d) Coronal view of the atrial myxoma, c, f) Axial view of the atrial myxoma indicated by white arrows.

4. DISCUSSION AND CONCLUSION

Atrial myxomas, though among the most common primary benign tumors of the heart, can exhibit a highly variable course in terms of clinical symptoms and prognosis. In this case, a pedunculated and mobile myxoma located in the left atrium was identified in a 62-year-old female patient who presented with complaints of palpitations and shortness of breath. While these tumors may remain asymptomatic, they can also lead to severe cardiac dysfunction through embolic complications or obstructive symptoms. In this case, the decision for surgical intervention was made due to the myxoma's partial obstruction of the mitral valve opening and its associated embolic risk.

This case stands out in the clinical literature as an example of atrial myxoma being detected with mild symptoms in a patient presenting with cardiac symptoms and successfully treated with early diagnosis. The majority of atrial myxomas are located in the left atrium and, as stated in the literature, are more common in women [8]. In our case, the patient's female gender and the location of the myxoma in the left atrium are consistent with this information in the literature.

In the literature, surgical removal of atrial myxomas is considered the standard treatment method due to the high risk of these tumors causing embolic complications [9]. Myxomas may increase the risk of cerebral, pulmonary or peripheral embolism due to their mobile and pedunculated structure [10]. In this case, it was determined in CT and TTE that the myxoma was mobile and affected the mitral valve functions. This situation shows that early surgical intervention is mandatory. In the literature, the prognosis after early surgical intervention is generally good and the complication rates are low [11]. In our case, no complications developed after surgery and cardiac functions completely returned to normal.

Atrial myxomas are rare tumors that can recur. A study by Jiang et al. emphasized the importance of careful postoperative follow-up despite the low recurrence rate after myxoma removal [7]. In our patient, postoperative TTE examinations confirmed the complete removal of the tumor with no residual presence. However, in light of the literature, long-term follow-up remains necessary.

This case highlights the importance of detecting atrial myxoma in a patient presenting with asymptomatic or mild symptoms. Cardiac symptoms can often be nonspecific, and the diagnosis of a rare tumor such as myxoma can be missed, especially if not provided by TTE. Furthermore, it is essential to distinguish atrial myxomas from other cardiac masses, as highlighted in recent reports of atypical presentations and confounding imaging findings in cases of giant cardiac masses [12]. Rare malignant cardiac tumors such as malignant fibrous histiocytomas can mimic benign masses like myxomas, emphasizing the importance of accurate imaging and histopathological confirmation [13]. Furthermore, considering the hemodynamic effects of myxoma and the risk of embolic complications, this case demonstrates that favorable outcomes can be achieved with prompt surgical treatment.

This case reflects the typical clinical features of atrial myxoma as frequently described in the literature and its favorable prognosis after successful surgical treatment, once again demonstrating the importance of careful clinical and imaging evaluations in the diagnosis and treatment of myxomas.

Acknowledgement

REFERENCES

[1] St John Sutton M, Mercier L-A, Giuliani ER, Lie J, editors. Atrial myxomas: a review of clinical experience in 40 patients. Mayo Clinic Proceedings; 1980.

[2] Pinede L, Duhaut P, Loire RJM. Clinical presentation of left atrial cardiac myxoma: a series of 112 consecutive cases. 2001;80(3):159-72.

[3] Griborio-Guzman AG, Aseyev OI, Shah H, Sadreddini MJH. Cardiac myxomas: clinical presentation, diagnosis and management. 2022;108(11):827-33.

[4] Latifi AN, Ibe U, Gnanaraj JJEHJ-CR. A case report of atrial myxoma presenting with systemic embolization and myocardial infarction. 2019;3(3):ytz104.

[5] Raicea VC, Suciu H, Raicea AD, Macarie GC, Mezei T, Maier MSJRJoM, et al. Giant left atrial myxoma–literature review and case presentation. 2021;62(2):361.

[6] Hrabak-Paar M, Muršić M, Balaško-Josipović T, Dilber D, Bulj NJRiCM. Multimodality Imaging of Cardiac Myxomas. 2024;25(6):204.

[7] Jiang C-X, Jian-Gang W, Rui-Dong Q, Wei W, Li-Jian G, Jing-Hua Z, et al. Long-term outcome of patients with atrial myxoma after surgical intervention: analysis of 403 cases. 2019;16(4):338-43.

[8] Hartig I, Kraatz E-G, Beurich H-W, Moosig FJZfR. Atrial myxoma with clinical signs of systemic inflammatory disease. 2014;73:281-4.

[9] Tetsuka S, Ikeguchi KJCRiM. Prevention of cerebral embolism progression by emergency surgery of the left atrial myxoma. 2015;2015(1):151802.

[10] De Carli S, Alberto Sechi L, Ciani R, Barillari G, Dolcetti G, Bartoli EJC. Right atrial myxoma with pulmonary embolism. 1994;84(4-5):368-72.

[11] Mikić A, Đukić P, Obrenović-Kirćanski B, Gluvić Z, Putnik S, Vraneš M, et al. Cardiac myxoma: The influence of surgical technique on long-term prognosis. 2012;64(1):1-6.

[12] Tatar S, Sahin AT, Işık M, Görmüş NJTEHJ. Confounding giant right atrial mass. 2024;76(1):108.

[13] Sarı H, Tatar S, Alsancak YJJoS, Medicine. A rare case of cardiac tumor: Malignant fibrous histiocytoma. 2020;4(8):713-5.

207

Türk Doğa ve Fen Dergisi
Turkish Journal of Nature and Science

Monkeypox Virus: Current Status And Global Health Ipmlications

Semih Eriten[1] iD

[1] Sultanbeyli State Hospital, Emergency Department. İstanbul, Türkiye
Semih Eriten: 0000-0001-8516-372X

Corresponding author: semiheriten@hotmail.com

Abstract: Monkeypox virus (MPOV), formerly known as MPOX, is a zoonotic disease agent belonging to the Orthopoxvirus family.. First discovered in monkeys in 1970, the virus was later detected in humans and became endemic in Central and West African countries. In 2022, MPOV turned into a global pandemic and was declared a Public Health Emergency of International Concern by the World Health Organisation. This review article comprehensively examines the current status of MPOV, its transmission routes, prevention strategies and implications for global health. The study highlights areas for future research and emphasizes the importance of global collaboration against this emerging health threat. With the aim of raising awareness about MPOV, supporting informed decision-making and developing intervention strategies to reduce transmission, this review aims to contribute to efforts to protect public health.

208

Maymun Çiçeği Virüsü: Güncel Durum ve Küresel Sağlık Etkileri

Özet: Önceden MPOX olarak bilinen Maymun çiçeği virüsü (MPOV), Ortopoksvirüs ailesine ait zoonotik bir hastalık etkenidir. İlk olarak 1970 yılında maymunlarda keşfedilen virüs daha sonra insanlarda tespit edildi ve Orta ve Batı Afrika ülkelerinde endemik hale geldi. 2022 yılında MPOV küresel bir pandemiye dönüştü ve Dünya Sağlık Örgütü tarafından Uluslararası Endişe Verici Halk Sağlığı Acil Durumu ilan edildi. Bu derleme makalesi, MPOV'un mevcut durumunu, bulaşma yollarını, önleme stratejilerini ve küresel sağlık üzerindeki etkilerini kapsamlı bir şekilde incelemektedir. Çalışma, gelecekteki araştırma alanlarını vurgulamakta ve bu ortaya çıkan sağlık tehdidine karşı küresel iş birliğinin önemini vurgulamaktadır. MPOV hakkında farkındalığı artırma, bilinçli karar vermeyi destekleme ve bulaşmayı azaltmak için müdahale stratejileri geliştirme amacıyla bu derleme, halk sağlığını koruma çabalarına katkıda bulunmayı amaçlamaktadır.

1. INTRODUCTION

Monkeypox virüs (MPOV) is a zoonotic disease caused by a virus in the Orthopoxvirus family. The disease was first discovered in monkeys in 1970 in countries where cases of monkeypox were monitored, hence the name [1]. The virus was later found in humans and has since become endemic in Central and West African countries. Monkeypox virus can cause significant morbidity and mortality in humans and there is currently no specific treatment [2]. In 2022, monkeypox became a global epidemic when a large number of cases were reported in several countries where the disease had previously been rare or absent. The World Health Organisation declared

monkeypox a Public Health Emergency of International Concern as it continued to spread rapidly around the world and public health measures failed to prevent it [3].

It is important to provide a comprehensive overview of MPOV to raise awareness and inform informed decision-making and intervention strategies to reduce transmission and protect public health. In this study, we examined the current status of monkeypox virus, transmission routes, prevention strategies, and global health impacts. Potential areas for future research and the importance of global collaboration to counter this emerging health threat are highlighted.

1.1. History and First Cases of Monkeypox Virus

Monkeypox virus was first discovered in laboratory monkeys at a research center in Copenhagen in 1958, but the first case in humans was detected in 1970 in a 9-year-old boy in the Democratic Republic of Congo (then Zaire) [4]. After this discovery, sporadic cases were reported in Central and West Africa throughout the 1970s. In the 1980s, the incidence of the disease increased and in 2003, the United States experienced an outbreak outside the African continent for the first time [1] and may have arisen as a result of transmission from infected prairie dogs to humans [5].

The geographical distribution and sociocultural implications of monkeypox virus form an important complement to understanding the global health impact of the disease. The virus has historically been endemic in the rainforest regions of Central and West Africa, but has become particularly widespread in the Democratic Republic of Congo, Nigeria and Cameroon [6]. Due to globalization and increased international travel, in recent years, cases have also been seen in Europe, North America and Asia [7]. Thus, geographical spread has also affected the approach of different cultures to the disease. For example, in some African societies, traditional medical practices and the consumption of wild animal meat (bushmeat) play a role in the spread of the disease, while in Western societies the disease is generally perceived as an exotic threat [8]. Misperceptions due to the name of the disease and the conditions under which it was first discovered (in laboratory monkeys) have led to some discriminatory attitudes such as stigmatization in some societies [9].

Over time, with the increase in travel and trade, monkeypox cases have started to be seen in different parts of the world. The patterns of spread of MPOV in different geographical regions reflect the complex interactions between the ecology of the virus, human behaviour and global health systems. These patterns can be summarised as follows:

1.2. Endemic Regions in Africa

MPOV was first detected in the Democratic Republic of Congo (DRC) in 1970 and remained endemic in Central and West Africa for many years [10]. Regular outbreaks have been observed in DRC, Congo Basin and Nigeria. In these regions, the virus is usually spread through zoonotic transmission and is more prevalent in rural areas [11].

1.3. West African Strain and Congo Basin Strain

MPOV has two main genetic clades: West African (WA) and Congo Basin (CB) strains. The CB strain is considered more virulent and infectious [12]. While the WA strain is usually seen in West African countries, the CB strain is more common in Central Africa.

1.4. First Outbreaks Outside Africa

The 2003 outbreak in the USA showed that the virus could spread outside Africa. This outbreak was associated with infected rodents imported from Ghana [5].

1.5. 2022 Global Pandemic

The 2022 pandemic, which started in 2022 and spread rapidly, represents a significant change in the spread patterns of the virus. In this outbreak, the virus emerged simultaneously in many countries, especially in previously non-endemic regions [7].

a) Europe: Cases were seen in many European countries, especially in the UK, Spain, Portugal and Germany [13].
b) North America: A significant number of cases have been reported in the USA and Canada [14].
c) Latin America: Cases have also been detected in countries such as Mexico and Argentina, [15].
d) Asia and Oceania: The number of cases has been relatively low in these regions, but cases have also been reported in countries such as Japan, Australia and New Zealand [16].

1.6. New Propagation Dynamics

In the 2022 outbreak, the spread of the virus occurred mostly through human-to-human transmission. High transmission rates were observed especially in the men who have sex with men (MSM) community [15].

1.7. Global Mobility and Spread

International travel and migration have been effective in the rapid spread of the virus to new regions [6].

1.8. Spread in Urban Areas

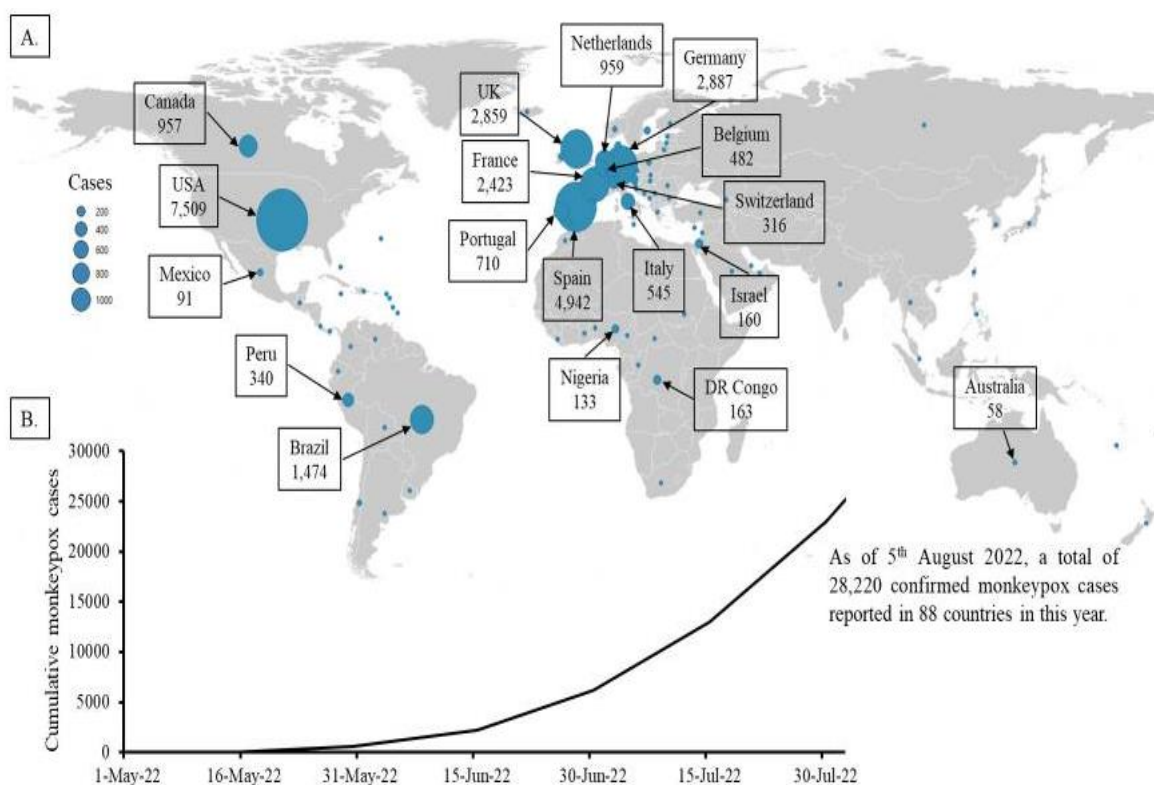Unlike previous outbreaks, the virus was more prevalent in urban areas in the 2022 outbreak [17].

Figure 1. Current global monkeypox (MPOV) infection patterns as of August 5, 2022 [16].

2. BİOLOGİCAL STRUCTURE AND TRANSMİSSİON ROUTES OF MONKEYPOX VİRUS

MPOV is an enveloped DNA virus belonging to the genus Orthopoxvirus of the family Poxviridae. Its genetic structure includes a double-stranded DNA genome of approximately 197 kb in length, characterised by inverted repeat sequences at the ends [18]. The MPOV genome contains approximately 190 protein-coding genes and these genes encode structural proteins, enzymes and immune modulators of the virus [19].

The protein components of the virus are structurally and functionally diverse. Chore proteins package the DNA genome and form the nucleoprotein complex. Membrane proteins are located in the envelope of the virus and play a role in binding to cell receptors. In addition, enzymes encoded by the virus (e.g. DNA polymerase, RNA polymerase) are critical in the replication process [20]. The central core consists of core fibril and viral double-stranded DNA (dsDNA) and is surrounded by the palisade layer, a tightly arranged rod-shaped structure [21](Figure 2).
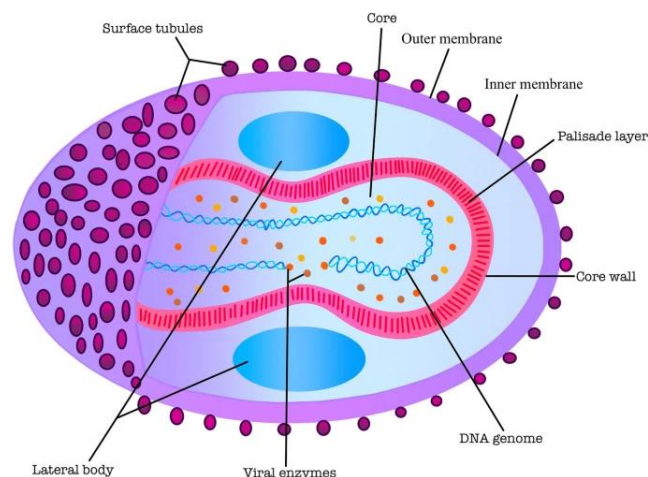
Figure 2. Structure of MPOV [21]

The replication mechanism of MPOV, similar to other poxviruses, occurs entirely in the cytoplasm. This process includes the following steps [22]:
1. Entry of the virus into the cell: This occurs via membrane fusion or endocytosis.
2. Early gene expression: Partial unfolding of viral DNA and transcription of early genes.
3. DNA replication: Replication of viral DNA is carried out by virus-encoded DNA polymerase.
4. Middle and late gene expression: Synthesis of structural proteins and enzymes.
5. Virion assembly and maturation: Formation of new virus particles and their release from the cell.
It covers virus identification, isolation and laboratory diagnostic methods. Identification and isolation of MPOV is usually done with samples taken from lesions. These samples are collected in viral transport medium and processed in biosafety level 3 (BSL-3) laboratories [23].

Virus isolation is performed in cell culture using Vero E6 or BSC-40 cell lines [24]. Laboratory diagnostic methods include polymerase chain reaction (PCR), real-time PCR (RT-PCR), electron microscopy and immunohistochemistry [25]. PCR, especially RT-PCR, is the preferred method due to its high sensitivity and specificity and targets specific gene regions of the virus [26]. Serological tests, especially ELISA and Western blot, are used to detect previous infections, but should be interpreted with caution due to cross-reactivity [27]. Next-generation sequencing technologies are increasingly used for genomic characterisation of the virus and outbreak monitoring [28]. These methods enable rapid and accurate diagnosis of monkeypox infections, which is critical for disease control and management.

When the epidemiological characteristics, transmission routes, host range and spread dynamics of the virus are considered, a complex picture emerges. The routes of transmission of MPOV are diverse: Direct contact with infected animals, close physical contact with infected persons, and contact with contaminated objects are among the main routes [29]. The virus can be transmitted through respiratory droplets, body fluids and material from lesions. Sexual contact has also been identified as an important route of transmission, especially in the global outbreak in 2022 [15]. In terms of host range, MPOV can infect a wide range of mammalian species. The natural reservoir host is thought to be rodents, but primates, squirrels and other small mammals can also be infected [30]. Humans are considered intermediate hosts and are usually infected through contact with infected animals. However, human-to-human transmission is also possible and this type of transmission has come to the fore in recent outbreaks [6]. In terms of spread dynamics, the R_0 value (basic reproduction number) of MPOV is generally estimated to be below 1, indicating that continuous human-human transmission is limited [31]. However, in certain populations and conditions, this value may be higher. For example, in the 2022 outbreak, higher transmission rates were observed within some communities [32]. In terms of geographical distribution, MPOV has historically been endemic in Central and West Africa, but in recent years, cases have been observed in other continents [33]. Factors such as globalization, travel and climate change cause the virus to spread to new regions [34]. In addition, factors such as human behaviour, social networks and the response capacity of health systems also affect the dynamics of spread. Epidemiological surveillance, contact tracing and early warning systems are critical to control the spread of MPOV [35]. In conclusion, the epidemiology of MPOV reflects complex interactions between the ecology of the virus, human behaviour and global health systems, and a holistic understanding of these factors is required to develop effective control strategies.

3. CLİNİCAL SYMPTOMS İN MONKEYPOX CASES

Monkeypox infection usually presents a clinical picture with two distinct stages: the prodromal period and the rash period. The prodromal period follows an incubation period lasting an average of 6-13 days (sometimes 5-21 days) after contact with the virus [24]. During this initial phase, patients typically experience high fever, severe headache, lymphadenopathy (swelling of the lymph nodes), back pain, myalgia (muscle aches) and intense weakness [15]. Lymphadenopathy is an important feature that distinguishes monkeypox from smallpox [36].

The lesions seen in monkeypox infection are remarkable for their characteristic features. They are typically hard or rubbery, well circumscribed and deep-seated. They often develop a punctate structure at the apex of the lesions, which is called an umbilication. The evolution of the lesions occurs in four stages: macular, papular, vesicular and pustular, followed by crusting and shedding. The current global outbreak has revealed some variation in the clinical presentation of monkeypox infection. Lesions are frequently seen on the genital and anorectal areas or in the mouth. Contrary to the classical description, the rash does not always spread to many parts of the body, sometimes limited to only a few lesions or a single lesion. In addition, the appearance of a rash on the palms of the hands and soles of the feet is not observed in all cases in this outbreak [37] (Figure 3).

Figure 3. Mpox Rash [37]

Despite this variable presentation, the development of the lesions usually follows a similar pattern. The lesions start as a maculopapular rash and rapidly progress to vesicular and pustular stages, finally culminating in crusting and shedding [29]. A patient may have lesions in different stages at the same time. The number of lesions may vary from a few to thousands [38]. The clinical course usually lasts 3-4 weeks and most cases heal spontaneously. However, a more severe course may be seen in immunocompromised individuals, young children and pregnant women [6]. In severe cases, skin lesions may coalesce and cover large areas, leading to peeling of the skin [24]. Rare but serious complications include secondary bacterial infections, sepsis, pneumonia, encephalitis and vision loss, especially due to corneal

infection [39]. In recent outbreaks, atypical presentations have also been reported, especially in patients infected with the strain of West African origin. These include localised lesions without prodromal symptoms, a single lesion in the anogenital region and oral/perineal lesions suggestive of secondary sexual transmission [40].

The lesions are usually described as painful until the healing phase, when they become itchy [41]. Although fever and other prodromal symptoms (e.g. chills, lymphadenopathy, malaise, myalgia or headache) classically precede the rash, in this outbreak they may also occur after the rash or not at all [42,43].

4. EPİDEMİOLOGİCAL SURVEİLLANCE AND CONTROL STRATEGİES

Epidemiological surveillance and control strategies for MPOV encompass various methods used to monitor, prevent and control the spread of the disease. These strategies can be analysed under the following main headings:

4.1. Epidemiological Surveillance: a) Case Definition and Notification: Using standardized case definitions, suspected, probable and definite cases are rapidly identified and notified [44]. b) Active Surveillance: Active case searches are carried out through health institutions and community-based surveillance systems [45]. c) Laboratory Surveillance: Verification of cases and monitoring of virus strains are ensured by using methods such as PCR tests and genomic sequencing [46]. d) Animal Reservoir Surveillance: Monitoring of potential animal reservoirs and assessment of zoonotic transmission risks [30].

4.2. Control Strategies: a) Case Isolation: Rapid isolation of detected cases and provision of appropriate medical care [47]. b) Contact Tracing: Identifying and monitoring the contacts of the cases and quarantining them when necessary [48]. c) Vaccination: Vaccination of high-risk groups and post-contact cases (e.g. smallpox vaccine or newly developed MPOV vaccines) [49]. d) Risk Communication and Community Engagement: Raising public awareness, informing the public about risk factors and encouraging preventive behaviors [50]. e) Border Controls: Screening and informing international travellers [51].

4.3. Epidemic Management: a) Early Warning Systems: Analysing and interpreting surveillance data for early detection of potential outbreaks [51]. b) Outbreak Response Teams: Formation and deployment of trained teams for rapid response [52]. c) Mobilization of Resources: Rapid mobilization of necessary medical equipment, personnel and financial resources in case of an outbreak [53].

4.4. International Cooperation: a) Data Sharing: Sharing surveillance data between countries and international organizations [7]. b) Capacity Building: Strengthening surveillance and control capacity in low- and middle-income countries [2]. c) Research

Collaborations: Coordination of vaccine and antiviral drug development studies [54].

4.5. Technological Innovations: a) Digital Surveillance Tools: Use of mobile applications and artificial intelligence-supported systems [55]. b) Genomic Surveillance: Monitoring virus evolution through the use of next-generation sequencing technologies [56].

Effective implementation of these strategies is critical for early detection, rapid response and effective control of MPOV outbreaks.

5. EVOLUTİONARY BİOLOGY OF MPOV

The origin of the virus, its evolutionary relationship with other poxviruses and its genetic changes over time reflect a complex evolutionary process. Although the exact origin of MPOV is unknown, molecular clock analyses suggest that the virus emerged approximately 70,000 years ago [57]. MPOV is genetically closely related to smallpox virus (Variola virus) and phylogenetic analyses suggest that these two viruses evolved from a common ancestor approximately 3000-4000 years ago [58]. The relationship of MPOV to other poxviruses shows similarities in terms of genomic structure and gene content. For example, the MPOV genome, like other orthopoxviruses, consists of linear double-stranded DNA containing inverted repeat sequences at the ends and is approximately 200 kb in length [18]. In terms of genetic changes over time, two major genetic clades of MPOV have been identified: West African (WA) and Congo Basin (CB) clades. There are significant genetic differences between these two clades and the CB clade is thought to be more virulent [12]. Recent genomic analyses have shown that the rate of evolution of MPOV may be higher than previously thought. In particular, the strains seen in the 2022 pandemic were found to accumulate much more mutations than expected [56]. This rapid evolution may increase the adaptation of the virus to new hosts and potentially increase its infectiousness. Furthermore, its increased circulation in human populations may affect the evolutionary trajectory of the virus and lead to the emergence of new variants [59]. Understanding the evolutionary biology of MPOV is critical for predicting the future behaviour of the virus, developing vaccine and antiviral strategies, and assessing potential zoonotic threats.

6. EFFECTS OF MONKEYPOX VİRUS ON PUBLİC HEALTH AND PUBLİC HEALTH MEASURES

The monkeypox virus outbreak has led to significant social impacts and behavioural changes. Firstly, as with HIV/AIDS virus [60], the faster spread of MPOV among certain groups will increase stigma and discrimination against these groups. Studies of the monkeypox outbreak in 16 countries showed that 98 per cent of cases were gay or bisexual men, 75 per cent of whom were white and 41 per cent were HIV positive [15]. Sexual transmission has emerged as an important route of transmission because lesions are usually seen in the genital and perianal areas and most patients are men who have sex with men [39,61].

However, these data may lead to the association of the disease with certain groups and potentially lead to stigmatization. Jaiswal et al. (2020) highlighted the harmful consequences of labelling the disease as a 'gay virus' [62]. This stigmatization can affect not only at-risk groups but also the general population, as people may avoid getting tested or seeking treatment for fear of being stigmatised. Therefore, when presenting and discussing this data, health authorities and the media should use careful language to avoid social stigmatization and make clear that the disease is not limited to any sexual orientation or identity.

The effects of outbreaks can have more devastating effects on vulnerable segments of the population [63]. Without urgent action, they pose a significant risk to immunocompromised groups and families. The health system faces challenges related to diagnosis, treatment and disease prevention during an outbreak. The lives of healthcare workers are at significant risk, especially when the supply chain of healthcare equipment is disrupted [64]. If health workers or their family members become ill, their ability to provide care is also reduced as they will have to look after each other. An outbreak of MPOV could further increase the burden on the health system, which is already facing numerous other problems [65].

Outbreaks of MPOV can lead to lower tax revenues and increased expenditure, causing fiscal stress, especially in low-middle-income countries (LMICs) where fiscal constraints are high and tax systems need to be improved. Therefore, the MPOV outbreak could have short-term fiscal and long-term economic impacts on nations. All efforts to contain the virus will cost a significant amount of resources and will significantly affect the national economy. The productivity of the population is significantly affected, affecting national economies and overall development [65]. In the labour market, there may be productivity losses due to sick or quarantined employees, and increased pressure on health systems may increase the cost of testing and treatment, while the tourism and leisure sectors may also be adversely affected by travel restrictions.

7. CONCLUSİON

MPOV has become a global health threat in recent years and has attracted the attention of the international community. This review comprehensively examined the current status of MPOV, its transmission routes, and its impact on global health. The rapid spread of the virus and the inadequacy of existing public health measures highlight the need for an urgent and coordinated global response.

The following important steps need to be taken to be successful in combating MPOV in the future:

- Research and Development: More resources should be devoted to research to develop effective treatments and vaccines against MPOV. In particular, the focus should be on the development of broad-spectrum antiviral drugs and next-generation vaccines.

- Strengthening Surveillance Systems: Surveillance systems should be improved for early detection and monitoring of MPOV cases globally, especially in high-risk areas.
- International Co-operation: International co-operation should be increased to share information between countries, develop joint research projects and coordinated response strategies.
- Community Education and Awareness: Comprehensive education programmes should be implemented to inform the public about the transmission routes, symptoms and prevention methods of MPOV.
- Strengthening Health Systems: Health systems should be strengthened to diagnose, treat and isolate MPOV cases, especially in resource-limited areas.
- Prevention of Zoonotic Transmission: The risk of zoonotic transmission should be minimised through measures such as reducing human-animal contact and regulating wildlife trade.
- Developing Global Health Security Policies: Global health security policies should be reviewed and strengthened to ensure rapid and effective response to emerging infectious diseases such as MPOV.

To be prepared for similar outbreaks in the future, lessons learnt from the fight against MPOV should be carefully considered and applied.

REFERENCES

[1] CDC. About Mpox [Internet]. 2024 [cited 2024 Sep 3]. Available from: https://www.cdc.gov/poxvirus/mpox/about/index.html

[2] Durski KN. Emergence of monkeypox—west and central Africa, 1970–2017. MMWR Morb Mortal Wkly Rep [Internet]. 2018 [cited 2024 Sep 5];67. Available from: https://www.cdc.gov/mmwr/volumes/67/wr/mm6710a5.htm

[3] Lamptey E, Yaidoo S, Asiedua E, Boakye EO, Banoya M tia, Senkyire EK. Monkey pox: Rethinking COVID-19 to project future strategies against emerging and evolving pathogens. Health Care Sci. 2022;1(2):129–33.

[4] WHO. Mpox [Internet]. 2024 [cited 2024 Sep 3]. Available from: https://www.who.int/news-room/fact-sheets/detail/mpox

[5] Reed KD, Melski JW, Graham MB, Regnery RL, Sotir MJ, Wegner MV, et al. The Detection of Monkeypox in Humans in the Western Hemisphere. N Engl J Med. 2004 Jan 22;350(4):342–50.

[6] Bunge EM, Hoet B, Chen L, Lienert F, Weidenthaler H, Baer LR, et al. The changing epidemiology of human monkeypox—A potential threat? A systematic review. PLoS Negl Trop Dis. 2022;16(2):e0010141.

[7] Kraemer MU, Tegally H, Pigott DM, Dasgupta A, Sheldon J, Wilkinson E, et al. Tracking the 2022 monkeypox outbreak with epidemiological data in real-time. Lancet Infect Dis. 2022;22(7):941–2.

[8] Bonwitt J, Dawson M, Kandeh M, Ansumana R, Sahr F, Brown H, et al. Unintended consequences of the 'bushmeat ban' in West Africa during the 2013-2016 Ebola virus disease epidemic. Soc Sci Med 1982 [Internet]. 2018 Mar [cited 2024 Sep 4];200. Available from: https://pubmed.ncbi.nlm.nih.gov/29421463/

[9] WHO. Monkeypox: public health advice for gay, bisexual and other men who have sex with men [Internet]. 2022 [cited 2024 Sep 4]. Available from: https://www.who.int/news/item/25-05-2022-monkeypox--public-health-advice-for-gay--bisexual-and-other-men-who-have-sex-with-men

[10] Breman JG, Steniowski MV, Zanotto E, Gromyko AI, Arita I. Human monkeypox, 1970-79. Bull World Health Organ. 1980;58(2):165.

[11] Rimoin AW, Mulembakani PM, Johnston SC, Lloyd Smith JO, Kisalu NK, Kinkela TL, et al. Major increase in human monkeypox incidence 30 years after smallpox vaccination campaigns cease in the Democratic Republic of Congo. Proc Natl Acad Sci. 2010 Sep 14;107(37):16262–7.

[12] Likos AM, Sammons SA, Olson VA, Frace AM, Li Y, Olsen-Rasmussen M, et al. A tale of two clades: monkeypox viruses. J Gen Virol. 2005 Oct 1;86(10):2661–72.

[13] Vivancos R, Anderson C, Blomquist P, Balasegaram S, Bell A, Bishop L, et al. Community transmission of monkeypox in the United Kingdom, April to May 2022. Eurosurveillance [Internet]. 2022 Jun 2 [cited 2024 Sep 4];27(22). Available from: https://www.eurosurveillance.org/content/10.2807/1560-7917.ES.2022.27.22.2200422

[14] CDC. Centers for Disease Control and Prevention. 2023 [cited 2024 Sep 4]. Monkeypox Technical Reports. Available from: https://www.cdc.gov/poxvirus/mpox/cases-data/technical-report/report-3.html

[15] Thornhill JP, Barkati S, Walmsley S, Rockstroh J, Antinori A, Harrison LB, et al. Monkeypox Virus Infection in Humans across 16 Countries — April–June 2022. N Engl J Med. 2022 Aug 25;387(8):679–91.

[16] Khan S, Akbar SMF, Yahiro T, Mahtab MA, Kimitsuki K, Nishizono A. Unprecedented rise of monkeypox in Europe and America: Are Asian countries ready for a new outbreak during the ongoing COVID-19 pandemic? J Glob Health [Internet]. 2022 [cited 2024 Sep 4];12. Available from: https://www.ncbi.nlm.nih.gov/pmc/articles/PMC9425425/

[17] Vaughan A, Aarons E, Astbury J, Brooks T, Chand M, Flegg P, et al. Human-to-human transmission of monkeypox virus, United Kingdom, October 2018. Emerg Infect Dis. 2020;26(4):782.

[18] Alakunle E, Moens U, Nchinda G, Okeke MI. Monkeypox virus in Nigeria: infection biology, epidemiology, and evolution. Viruses. 2020;12(11):1257.

[19] Esposito JJ, Sammons SA, Frace AM, Osborne JD, Olsen-Rasmussen M, Zhang M, et al. Genome Sequence Diversity and Clues to the Evolution of Variola (Smallpox) Virus. Science. 2006 Aug 11;313(5788):807–12.

[20] Moss B. Poxviridae: the viruses and their replication. 2001 [cited 2024 Sep 5]; Available from: https://www.cabidigitallibrary.org/doi/full/10.5555/20023085623

[21] Begum JPS, Ngangom L, Semwal P, Painuli S, Sharma R, Gupta A. Emergence of monkeypox: a worldwide public health crisis. Hum Cell. 2023 May 1;36(3):877–93.

[22] McFadden G. Poxvirus tropism. Nat Rev Microbiol. 2005;3(3):201–13.

[23] CDC. Biosafety Laboratory Guidance for Handling and Processing Mpox Specimens [Internet]. 2024 [cited 2024 Sep 5]. Available from: https://www.cdc.gov/poxvirus/mpox/lab-personnel/lab-procedures.html

[24] Adler H, Gould S, Hine P, Snell LB, Wong W, Houlihan CF, et al. Clinical features and management of human monkeypox: a retrospective observational study in the UK. Lancet Infect Dis. 2022;22(8):1153–62.

[25] Gul I, Liu C, Yuan X, Du Z, Zhai S, Lei Z, et al. Current and Perspective Sensing Methods for Monkeypox Virus. Bioengineering. 2022 Oct;9(10):571.

[26] Neubauer H, Reischl U, Ropp S, Esposito JJ, Wolf H, Meyer H. Specific detection of monkeypox virus by polymerase chain reaction. J Virol Methods. 1998;74(2):201–7.

[27] Karem KL, Reynolds M, Braden Z, Lou G, Bernard N, Patton J, et al. Characterization of Acute-Phase Humoral Immunity to Monkeypox: Use of Immunoglobulin M Enzyme-Linked Immunosorbent Assay for Detection of Monkeypox Infection during the 2003 North American Outbreak. Clin Vaccine Immunol. 2005 Jul;12(7):867–72.

[28] Otieno JR, Ruis C, Onoja BA, Kuppalli K, Hoxha A, Nitsche A, et al. Global genomic surveillance of monkeypox virus. medRxiv. 2024;2024–08.

[29] ECDC. Factsheet for health professionals on mpox [Internet]. 2024 [cited 2024 Sep 5]. Available from: https://www.ecdc.europa.eu/en/all-topics-z/monkeypox/factsheet-health-professionals

[30] Doty JB, Malekani JM, Kalemba LN, Stanley WT, Monroe BP, Nakazawa YU, et al. Assessing monkeypox virus prevalence in small mammals at the human–animal interface in the Democratic Republic of the Congo. Viruses. 2017;9(10):283.

[31] Grant R, Nguyen LBL, Breban R. Modelling human-to-human transmission of monkeypox. Bull World Health Organ. 2020;98(9):638.

[32] Endo A, Murayama H, Abbott S, Ratnayake R, Pearson CAB, Edmunds WJ, et al. Heavy-tailed sexual contact networks and monkeypox epidemiology in the global outbreak, 2022. Science. 2022 Oct 7;378(6615):90–4.

[33] Petersen E, Kantele A, Koopmans M, Asogun D, Yinka-Ogunleye A, Ihekweazu C, et al. Human monkeypox: epidemiologic and clinical characteristics, diagnosis, and prevention. Infect Dis Clin. 2019;33(4):1027–43.

214

[34] Ullah M, Li Y, Munib K, Zhang Z. Epidemiology, host range, and associated risk factors of monkeypox: an emerging global public health threat. Front Microbiol. 2023;14:1160984.

[35] Meena RK. Monkeypox: A New Global Threat [Internet]. Springer India 7th Floor, Vijaya Building, 17, Barakhamba Road, New Delhi …; 2022 [cited 2024 Sep 5]. Available from: https://www.indianpediatrics.net/july2022/585.pdf

[36] Harapan H, Ophinni Y, Megawati D, Frediansyah A, Mamada SS, Salampe M, et al. Monkeypox: A Comprehensive Review. Viruses. 2022 Sep 29;14(10):2155.

[37] CDC. Clinical Recognition [İnternet]. 2023 [cited 2024 Sep 6]. Availablefrom: https://www.cdc.gov/poxvirus/mpox/clinicians/clinical-recognition.html

[38] Carvajal A, Gracia PVD. Monkeypox and pregnancy. Am J Obstet Gynecol Mfm. 2022 Nov;4(6):100746.

[39] Antinori A, Mazzotta V, Vita S, Carletti F, Tacconi D, Lapini LE, et al. Epidemiological, clinical and virological characteristics of four cases of monkeypox support transmission through sexual contact, Italy, May 2022. Eurosurveillance [Internet]. 2022 Jun 2 [cited 2024 Sep 6];27(22). Available, from: https://www.eurosurveillance.org/content/10.2807/1560-7917.ES.2022.27.22.2200421

[40] Patel A, Bilinska J, Tam JC, Fontoura DDS, Mason CY, Daunt A, et al. Clinical features and novel presentations of human monkeypox in a central London centre during the 2022 outbreak: descriptive case series. bmj [Internet]. 2022 [cited 2024 Sep 6];378. Available from: https://www.bmj.com/content/378/bmj-2022-072410.abstract

[41] Obermeier PE, Buder SC, Hillen U. Poxvirus infections in dermatology – the neglected, the notable, and the notorious. JDDG J Dtsch Dermatol Ges. 2024 Jan;22(1):56–93.

[42] Azzi A. Unusual Monkeypox virus outbreak in 2022: Phenotypic and molecular characteristics. Asp Mol Med. 2023;1:100001.

[43] Sardana K, Sachdeva S, Narula S, Gogate S. Triaging cases of fever with vesicular rash relevant to the monkeypox epidemic. Trop Doct. 2023 Oct;53(4):481–8.

[44] WHO. Surveillance, case investigation and contact tracing for Monkeypox: Interim guidance [Internet]. 2022 [cited 2024 Sep 5].

[45] Yinka-Ogunleye A, Aruna O, Dalhat M, Ogoina D, McCollum A, Disu Y, et al. Outbreak of human monkeypox in Nigeria in 2017–18: a clinical and epidemiological report. Lancet Infect Dis. 2019;19(8):872–9.

[46] Altindis M, Puca E, Shapo L. Diagnosis of monkeypox virus–An overview. Travel Med Infect Dis. 2022;50:102459.

[47] McCollum AM, Damon IK. Human monkeypox. Clin Infect Dis. 2014;58(2):260–7.

[48] Kaler J, Hussain A, Flores G, Kheiri S, Desrosiers D. Monkeypox: a comprehensive review of transmission, pathogenesis, and manifestation. Cureus [Internet]. 2022 [cited 2024 Sep 5];14(7). Available from: https://www.ncbi.nlm.nih.gov/pmc/articles/PMC9345383/

[49] Petersen BW. Use of vaccinia virus smallpox vaccine in laboratory and health care personnel at risk for occupational exposure to orthopoxviruses—recommendations of the Advisory Committee on Immunization Practices (ACIP), 2015. MMWR Morb Mortal Wkly Rep [Internet]. 2016 [cited 2024 Sep 5];65. Available from: https://www.cdc.gov/mmwr/volumes/65/wr/mm6510a2.htm

[50] WHO. Risk communication and community engagement (RCCE) for monkeypox outbreaks: interim guidance, 24 June 2022 [Internet]. World Health Organization; 2022 [cited 2024 Sep 5]. Available from: https://apps.who.int/iris/bitstream/handle/10665/357184/WHO-MPX-RCCE-2022.1-eng.pdf?sequence=1

[51] Rao AK. Monkeypox in a traveler returning from Nigeria—Dallas, Texas, July 2021. MMWR Morb Mortal Wkly Rep [Internet]. 2022 [cited 2024 Sep 5];71. Available from: https://www.cdc.gov/mmwr/volumes/71/wr/mm7114a1.htm

[52] Kmiec D, Kirchhoff F. Monkeypox: A New Threat? Int J Mol Sci. 2022 Jul 17;23(14):7866.

[53] WHO. Monkeypox Strategic Preparedness, Readiness, and Response Plan (SPRP) [Internet]. 2022 [cited 2024 Sep 5]. Available from: https://www.who.int/publications/m/item/monkeypox-strategic-preparedness--readiness--and-response-plan-(sprp)

[54] Titanji BK, Tegomoh B, Nematollahi S, Konomos M, Kulkarni PA. Monkeypox: a contemporary review for healthcare professionals. In: Open forum infectious diseases [Internet]. Oxford University Press; 2022 [cited 2024 Sep 5]. p. ofac310. Available from: https://academic.oup.com/ofid/article-abstract/9/7/ofac310/6615388

[55] Jenkins ZN. Understanding Monkeypox. 2022 [cited 2024 Sep 5]; Available,from: https://digitalcommons.cedarville.edu/pharmacy_media_contributions/314

[56] Isidro J, Borges V, Pinto M, Sobral D, Santos JD, Nunes A, et al. Phylogenomic characterization and signs of microevolution in the 2022 multi-country outbreak of monkeypox virus. Nat Med. 2022;28(8):1569–72.

[57] Babkin IV, Babkina IN. The origin of the variola virus. Viruses. 2015;7(3):1100–12.

[58] Hendrickson RC, Wang C, Hatcher EL, Lefkowitz EJ. Orthopovirus genome evolution: the role of gene loss. Viruses. 2010;2(9):1933.

[59] Happi C, Adetifa I, Mbala P, Njouom R, Nakoune E, Happi A, et al. Urgent need for a non-discriminatory and non-stigmatizing nomenclature for monkeypox virus. PLoS Biol. 2022;20(8):e3001769.

215

[60] Deacon H. Towards a sustainable theory of health-related stigma: lessons from the HIV/AIDS literature. J Community Appl Soc Psychol. 2006 Nov;16(6):418–25.

[61] Raccagni AR, Candela C, Mileto D, Canetti D, Bruzzesi E, Rizzo A, et al. Monkeypox infection among men who have sex with men: PCR testing on seminal fluids. J Infect. 2022;85(5):573.

[62] Jaiswal J, LoSchiavo C, Perlman DC. Disinformation, Misinformation and Inequality-Driven Mistrust in the Time of COVID-19: Lessons Unlearned from AIDS Denialism. AIDS Behav. 2020 Oct;24(10):2776–80.

[63] Manirambona E, Wilkins L, Lucero-Prisno III DE. COVID-19 and its threat to refugees in Africa. Health Promot Perspect. 2021;11(3):263.

[64] Shang Y, Li H, Zhang R. Effects of pandemic outbreak on economies: evidence from business history context. Front Public Health. 2021;9:632043.

[65] Manirambona E, Musa SS, Shomuyiwa DO, Salam FA, John OO, Dinyo DGA, et al. The monkeypox virus: A public health challenge threatening Africa. Public Health Chall. 2022;1(4):e33.